

THIS WEEK

EDITORIALS

ENVIRONMENT Europe must protect species before calamity strikes **p.496**

WORLD VIEW Countries must gather hard data to assess their disaster risks **p.497**

HEAVY LIFTING Nanotube yarns as artificial muscles **p.498**

Nature's sexism

The editors of this publication need to improve how we reflect women's contributions to science. For this, we must inject an extra loop into our thinking.

Earlier this year, we published a Correspondence that rightly took *Nature* to task for publishing too few female authors in our News and Views section (D. Conley and J. Stadmark *Nature* **488**, 590; 2012). Specifically, in the period 2010–11, the proportions of women News and Views authors in life, physical and Earth sciences were 17%, 8% and 4%, respectively. The authors of the Correspondence had taken us to task in 2005 with a similar analysis for the authorship of our Insight overview articles, and gave us slight credit for having improved that position.

Our minds were further focused on the problem by a much-discussed paper published in September (C. A. Moss-Racusin *et al. Proc. Natl Acad. Sci. USA* <http://doi.org/jkm>; 2012). The disturbing message of this blinded, randomized study was that US academics discriminated in hiring decisions and in salary against women who applied for a lab-manager position. Notably, female faculty members were as significantly discriminatory as males.

So here is a fuller litany of facts about *Nature's* performance in this arena, based on internal surveys.

Of the 70 editors and reporters around the globe who commission, select, write or oversee *Nature's* daily and weekly content, 38 (54%) are women. This proportion is reflected among team leaders. We feel confident that there is no discrimination in the recruitment and hiring practices of *Nature* and its publishers; the same applies to the writers whom we employ as freelancers.

Our performance as editors is much less balanced.

Of the 5,514 referees who assessed *Nature's* submitted papers in 2011, 14% were women.

Of the 34 researchers profiled by journalists in 2011 and so far in 2012, 6 (18%) were women.

Of externally written Comment and World View articles published in 2011 and so far in 2012, 19% included a female author.

There are well-known external factors that will lead to some imbalance. The proportion of female researchers active in certain disciplines is low. The proportion of women active in the upper reaches of all disciplines is low. As a result, women in science will be asked to help to ensure a gender balance on committees and will therefore collectively experience greater pressure of that sort than men, leaving less time for writing and reviewing. One can speculate that there also may be a tendency for women to be less willing than men to push themselves forward, which may lead to editors being less aware of them. But it is certainly the case that women typically spend more time than men as homemakers and looking after children, further reducing the time available for journal contributions.

However, we do not believe that these considerations can fully account for, or excuse, the imbalance in *Nature's* pages. Nor do we believe that our own editors consciously discriminate against women.

That leaves the unconscious factors, and here we believe that there is work to do. We believe that in commissioning articles or in thinking

about who is doing interesting or relevant work, for all of the social factors already mentioned, and possibly for psychological reasons too, men most readily come to editorial minds. The September paper speculated about an unconscious assumption that women are less competent than men. A moment's reflection about past and present

female colleagues should lead most researchers to correct any such assumption.

We therefore believe that there is a need for every editor to work through a conscious loop before proceeding with commissioning: to ask themselves, "Who are the five women I could ask?"

"There is a need for every editor to ask themselves, 'Who are the five women I could ask?'"

Under no circumstances will this 'gender loop' involve a requirement to fulfil a quota or to select anyone whom we do not know to be fully appropriate for the job, although we will set ourselves internal targets to help us to focus on the task. It is not yet clear just what difference this workflow loop will make. But it seems to us to be a step towards appropriately reflecting in our pages the contributions of women to science. ■

Too much to ask

A market-based malaria-control programme may not be perfect, but it deserves to continue.

The ravages of malaria are most damaging where they are hardest to combat: in rural areas in Africa that have little or no public health infrastructure. In response to that quandary, scientists and economists in 2004 dreamed up a scheme called the Affordable Medicines Facility — Malaria (AMFm). It aims to get artemisinin-based combination therapies (ACTs) — the most effective malaria treatments known — into the private pharmacies and village shops that are the only source of medicine in many rural African areas. Now, this grand experiment seems likely to end, its successes under-rated and potential improvements not yet explored.

The high costs of ACTs have often meant that few rural outlets stocked them. Instead, shops sold cheaper but often ineffective drugs such as chloroquine — or, worse, artemisinin monotherapies, which are a recipe for the emergence of drug resistance. To overcome these problems, the AMFm first secures much cheaper prices from makers of ACTs by generating and negotiating massive bulk orders. Next, it offers importers subsidies to bring prices down further, to levels that are affordable in rural Africa. The scheme has been tested since 2010 at the country level in Ghana, Kenya, Madagascar, Niger, Nigeria,

Tanzania and Uganda, and last month an independent evaluation found that it had performed remarkably well on the main benchmarks of success, increasing the number of outlets stocking ACTs and lowering prices (S. Tougher *et al. Lancet* <http://doi.org/js2; 2012>).

Last week, however, the Global Fund to Fight AIDS, Tuberculosis and Malaria decided to end the AMFm as a stand-alone programme, by integrating it into the fund's core system for awarding malaria-control grants to countries. This integration probably spells the end for AMFm, because there will be no new money for the programme after the end of next year.

The fund's decision may be related to long-standing US opposition to the AMFm. Congress has passed legislation discouraging support for the programme until the concept has been proven, and the US President's Malaria Initiative maintains that private-sector treatment efforts should be carried out in partnership with governments. Other critics say that trained community health workers, not shop-keepers, should be at the front line of malaria treatment. In an ideal world, that may all be true. But whatever its detractors might say, the programme has succeeded in getting effective antimalarials to the only places in rural areas where most parents can get treatment for a child whose life is threatened by malaria.

More sensibly, the AMFm's critics also note that because not all cases of fever are malaria, selling ACTs over the counter inevitably leads to

overtreatment, resulting in waste. But overtreatment has long plagued all malaria-control programmes, and would happen with or without the AMFm. It is only within the past few years that progress in rapid diagnostic tests for malaria — which use just a finger-prick of blood to check for proteins specific to the malaria-causing *Plasmodium* parasite — has made routine testing feasible. Only in 2010 did the World

Health Organization begin recommending the use of diagnostics before treatment of malaria.

There is plenty of scope for improving the AMFm's approach, which is still young. Combining diagnostics and treatment is clearly the next step, for example, and there is a major need — social scientists listen up — to devise clever ways to market tests and drugs together.

But it would be senseless to give up on the AMFm's strategy of using the vast existing private-sector infrastructure in Africa to get good medicines where there were none before. Anyone who doubts the power of the continent's private-sector distribution networks should consider how the free market has made Coca-Cola and other soft drinks available in even the remotest locations. That force should be harnessed equally for lifesaving malaria therapies. ■

"Whatever its detractors might say, the programme has succeeded in getting antimalarials to rural areas."

Water wars

Environmental protections must not wait until a population is about to disappear.

Where there are serious threats to the environment, governments should not postpone cost-effective preventative measures because the scientific evidence is inconclusive. So says the precautionary principle, an idea enshrined in several international treaties, including the declaration signed in 1992 at the Earth Summit in Rio de Janeiro, Brazil.

Many scientists think that this principle should have long ago triggered action to curb the damage to aquatic wildlife caused by the synthetic hormone ethynyl oestradiol (EE2), an ingredient of birth-control pills that passes through wastewater treatment plants and into streams and lakes (see page 503). In 2004, for example, the UK Environment Agency declared that the hormone feminizes male fish and is likely to damage entire fish populations. It later concluded that this damage is unacceptable in the long term.

Eight years on, the evidence against EE2 continues to mount, but the European Commission is only now proposing the first serious effort to tackle the problem, suggesting tight limits on the hormone's concentration in the environment. The legislation would set a global precedent. But its prospects look bleak, mainly because of concerns about how best to limit the escape of EE2 into the aquatic environment, what that would cost and who should pay.

Governments and members of the European parliament are right to consider the costs of implementing the legislation. But some governments and industry groups are stifling these crucial discussions when they have barely begun.

The UK government, for example, has suggested that the necessary changes to wastewater treatment plants would cost England and Wales between £26 billion (US\$41 billion) and £30 billion over ten years, a figure so breathtaking that it is likely to ensure that the legislation is kicked into the long grass. Other governments and industry groups have also branded the proposed rules unaffordable. Privately, scientists have told *Nature* that they suspect the calculations aim for the highest possible cost in order to portray the rules as financially unrealistic.

Nature's investigation shows that the UK estimate ignores significant cost-cutting opportunities. And is the cost really so high when the UK water industry has already committed to spend £22 billion from 2010–15 to improve infrastructure and water quality in England and Wales? What is more, the same measures that would limit EE2 in waste water would also reduce other potentially harmful pharmaceutical residues, including antibiotics and diclofenac — a second substance for which the European Commission has proposed stringent limits.

In addition, the discussion has focused on wastewater treatment, with little consideration of what the pharmaceutical and farming industries could do to keep their drugs out of the aquatic environment. Doctors and patients have a responsibility here, too, to make sure that the drugs are prescribed appropriately and that leftover pills are disposed of properly. To be clear, no one is seriously suggesting inhibiting patients' access to the drugs they need, even though some parties in the dispute have charged that the restrictions would do just that.

It is time to set aside scare tactics and to have an open and honest discussion about how to solve a potentially devastating environmental problem. The European Commission's proposed limits on the levels of EE2 in streams and lakes are a crucial first step.

That the regulation of EE2 faces such hurdles despite the mounting evidence of harm highlights a wider problem with environmental risk assessment. Governments may acknowledge the precautionary principle, but before taking action they often insist on strong evidence that populations, and not just individuals, are at risk. In the case of EE2, industry groups acknowledge that individual fish may have been harmed but note that there is no sign of a crash in Europe's freshwater fish numbers. Yet an unequivocal link between a specific chemical in the environment and harm to wildlife populations has been demonstrated in a mere handful of cases.

Often, the clinching evidence comes only after massive harm has been done, as was the case for North America's bald eagle (*Haliaeetus leucocephalus*) in the 1960s, when the population plummeted because residues of organochlorines such as DDT (dichlorodiphenyltrichloroethane) had caused the species' eggshells to thin. Governments and members of parliament have an opportunity to prevent a similar wildlife catastrophe, but they must act on the evidence before it is too late. ■

➔ **NATURE.COM**
To comment online,
click on Editorials at:
go.nature.com/xhbnq



How resilient is your country?

Extreme events are on the rise. Governments must implement national and integrated risk-management strategies, says Erwann Michel-Kerjan.

As the United States continues to mop up after Superstorm Sandy, we see again our vulnerability to extreme events. The destruction was massive: US\$50 billion in economic losses; large-scale evacuations; thousands of businesses closed in anticipation; and millions of Americans without power for days. But the catastrophe had a silver lining: the way that science was used to improve decision-making.

Still, much more is required to make nations truly resilient to extreme events — we need to develop national risk-management strategies.

The United States' response to Sandy contrasted vividly with that to Hurricane Katrina. In 2005, the inability to foresee and effectively communicate the possible failure of the levee system in New Orleans, and the incapacity of the government to address the basic needs of those affected, surprised the world.

Katrina caused 1,300 deaths in the United States, many of them avoidable. Many fewer died from Sandy. Comparisons are never perfect, but it is clear that the systematic use of scientific evidence by the government and the media led to more effective crisis management. Information on the most likely path Sandy would take and on conditions at landfall (based on national and international forecasts of wind speed and storm surge) all helped.

A few days after Sandy, I flew from New York to Mexico City to participate in the final round of G20 meetings, which drew the finance ministers and central bankers of 20 major economies. This year, the group formally recognized disaster-risk financing and management as a priority.

This sends an important signal to the international community because Sandy was not an outlier. It could even be the new norm, as continuing development in high-risk areas combines with intense disasters to produce ever-increasing damage.

Worldwide, economic losses from natural catastrophes rose from \$528 billion in 1981–90 to \$1,213 billion during 2001–10. In 2011 alone, they amounted to \$380 billion, in large part because of the earthquake, tsunami and nuclear accident in Japan. The previous year, earthquakes caused massive losses in Haiti, Chile and New Zealand. Large-scale floods have struck Australia, China, Pakistan and Thailand, and in the past decade, a series of hurricanes has generated economic losses of hundreds of billions of dollars in the Americas.

Given this situation, governments should be able to answer, comprehensively and quantitatively, five questions that I see as pillars of national risk management. What risks do we face and where? What assets and populations are exposed and to what degree? How vulnerable are they? What financial burden do these risks place on individuals, businesses and the government budget? How best can we invest to reduce risks and strengthen economic and social resilience?

Many governments do not know the answers.

In a 2011 survey by the Organisation for Economic Co-operation and Development, more than half of the governments that responded could not assess aggregate amounts of insured losses from disasters (this would require merely collecting data from the insurers). Most do not have systematic and publicly available data on total losses, which is necessary to assess disaster vulnerability.

Preparation for disasters — from early warning systems, urban planning and zoning, to mitigation and financial protection — requires detailed estimates for all segments of society, including the economic exposure of the government itself. Yet even the United States has no public national database of residences and buildings in flood-prone areas.

This is particularly frustrating given the tremendous improvement in our capacity to do large-scale probabilistic catastrophe risk assessments; to measure hazards; to assess the vulnerability of buildings, infrastructure and livelihoods; and to calculate the resultant expected losses.

The estimates are still not perfect, but they continue to improve. The insurance industry already uses them to manage trillions of euros of coverage around the world. Done on a national scale, they could form the basis of a coherent and science-based national risk-management strategy. It will not be cheap, but it would be a wise investment.

To do that for all the extreme events that a country can face, and to mitigate and finance them and overcome behavioural barriers, demands multi-disciplinary work and strong coordination, both among scientists and across government ministries. I recommend that governments appoint cabinet-level national-risk officers, similar to

what is done for enterprise-wide risk management in the private sector.

In 2008, the World Bank, with the Swiss Agency for Development and Cooperation, assembled a small group of dedicated experts to undertake such an effort in Morocco. I have been involved since the beginning, and having finished the initial assessment phase, we are now supporting Morocco in developing an integrated national strategy to mitigate the impact of floods, earthquakes, tsunamis, drought, commodity volatility and agriculture risks. I hope that Morocco will provide a concrete case of what can be done. And for us, as scientists, engineers and financiers, it is highly rewarding to know that our work will contribute directly to saving lives and helping millions of families recover from a disaster.

A growing number of heads of states want to make resilience a priority, but are unsure of the first step. Good practice demands a combination of quantitative knowledge and leadership at the top. Shall we start? ■

Erwann Michel-Kerjan is with the Wharton School of the University of Pennsylvania and managing director of its Wharton Risk Center. He is chairman of the OECD Board on Financial Management of Catastrophes, headquartered in France.
e-mail: erwannmk@wharton.upenn.edu

**SANDY
WAS NOT AN
OUTLIER.
IT COULD EVEN
BE THE
NEW NORM.**

➔ **NATURE.COM**
Discuss this article
online at:
go.nature.com/wazstu

RESEARCH HIGHLIGHTS

Selections from the
scientific literature

BIODIVERSITY

More creatures under the sea

Between one- and two-thirds of marine species remain to be discovered, researchers estimate.

Ward Appeltans of UNESCO's Intergovernmental Oceanographic Commission in Oostende, Belgium, headed up a group of 270 taxonomists from around the world to build the World Register of Marine Species. The researchers report between 222,000 and 230,000 known marine eukaryotes — species with complex cells containing membrane-bound organelles. On the basis of past rates of species discovery, statistical modelling suggests that the total number of eukaryotic species in the world's oceans comes to between 320,000 and 760,000.

The team also asked 120 of the taxonomists to estimate how many species were likely to be discovered in their areas of expertise. This yielded totals of 704,000 to 972,000.

Curr. Biol. <http://dx.doi.org/10.1016/j.cub.2012.09.036> (2012)

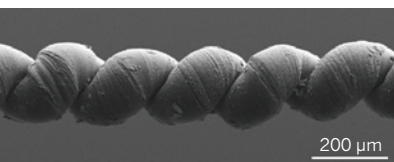
For a longer story on this research, see go.nature.com/qew2qq

MATERIALS

Catapult from nanotube yarns

Artificial muscle consisting of yarns spun from carbon nanotubes and soaked in paraffin wax can lift 200 times the weight that natural muscles the same size can carry.

The 'muscle' (pictured),



designed by Ray Baughman of the University of Texas at Dallas and his colleagues, produces torque by twisting and untwisting. Heating the yarn's wax component with a flash of light or by passing an electric current through the yarn causes it to expand, twist and shorten. The muscle rapidly contracted and relaxed over more than one million cycles.

The authors used a 100-micrometre-wide yarn to power a miniature catapult and launch a piece of foil, demonstrating a torque slightly

higher than that of large electric motors. The muscles could be used as sensors and actuators in a variety of systems, the authors say.

Science 338, 928–932 (2012)

For a longer story on this research, see go.nature.com/ygkxbr

ASTRONOMY

Encounter with a rogue planet

Astronomers have discovered the closest and most convincing known example of a planet wandering through

space without a parent star.

Candidate orphan planets have been found since the 1990s, but because no one knew their ages, researchers could not determine whether the objects were truly planets or were heavier, star-like bodies called brown dwarfs. But Philippe Delorme of the Institute of Planetology and Astrophysics in Grenoble, France, and his colleagues say that the newfound body, dubbed CFBDSIR2149, is the first orphan that seems to be associated with a stream of young stars, the AB Doradus



EARTH SCIENCE

Volcanoes swell before blasting

Pronounced uplift of volcano centres seems to be a reliable sign of imminent eruption along Indonesia's west Sunda arc, one of the most active volcanic regions on Earth.

Estelle Chaussard and Falk Amelung of the University of Miami in Florida conducted a radar remote-sensing survey of volcanic inflation in 76 historically active volcanoes on the islands of Sumatra, Java and Bali between 2006 and 2009. Of six volcanoes that showed a clear uplift signal

during this period, three — Sinabung (pictured), Kerinci and Slamet — erupted soon after.

The authors conclude that measurable inflation is a frequent precursor to volcanic eruptions in regions where magma reservoirs are typically located at relatively shallow depths, as in Indonesia. The findings could improve forecasts of volcanic activity.

Geophys. Res. Lett. <http://dx.doi.org/10.1029/2012GL053817> (2012)

BAY/SMOYO/AFP/GETTY

moving group, of known age — between 50 million and 120 million years.

The authors identified the object using data from the Canada–France Brown Dwarf Survey InfraRed, and suggest that it has a planet-like mass four to seven times that of Jupiter.

Astron. Astrophys. 548, A26 (2012)

BIOENGINEERING

Injectable gels spring into shape

Sponge-like polymer gels ‘remember’ and regain their shape after being injected into mice, demonstrating their potential to deliver drugs and cells for tissue repair and regeneration.

A team led by David Mooney at Harvard University in Cambridge, Massachusetts, made the hydrogels — porous structures that absorb water — out of alginate, a complex sugar extracted from seaweed. The researchers placed star- and heart-shaped gels in a syringe and injected them beneath the skin of mice; two days later, the materials had regained their original shapes. Gels that were preloaded with either growth-promoting proteins or cells and similarly injected into mice slowly released their contents before dissolving. Gel-delivered cells showed higher levels of survival and engraftment for up to 15 days than cells injected alone.

Proc. Natl Acad. Sci. USA
<http://dx.doi.org/10.1073/pnas.1211516109> (2012)

MICROBIOLOGY

Ancient origin for gut microbiome

Chimpanzees and humans share not only 96% of their DNA sequence, but also the basic make-up of their gut microbes.

The microbial communities that thrive in the human gut can typically be grouped into three ‘enterotypes’, each of which is dominated by

a specific set of bacteria. Howard Ochman at Yale University in New Haven, Connecticut, and his colleagues categorized the enterotypes of 35 chimpanzees from Gombe Stream National Park in Tanzania. Between them, the chimpanzees also harboured three enterotypes, and these were similar in composition to those found in humans.

The results suggest that this variation in gut microbial groups is an ancient trait that preceded the split between humans and chimpanzees.

Nature Commun. 3, 1179 (2012)

NEURODEGENERATION

Parkinson’s protein spreads

Injecting the abnormal protein associated with Parkinson’s disease into the brains of mice causes key symptoms of the disorder, seemingly by spreading from one neuron to another. The findings point to a causal link between the misfolded protein, α -synuclein, and the neurodegeneration seen in Parkinson’s.

Virginia Lee and her colleagues at the University of Pennsylvania in Philadelphia injected a synthetic abnormal form of α -synuclein into the mouse striatum, a brain region to which the neurons that die in Parkinson’s project. The injected protein clumped together to form Lewy bodies, a signature of Parkinson’s disease. Neurons then began to die, and neurons that link up with those near the injection site also developed Lewy bodies, indicating cell-to-cell transmission of α -synuclein. Six months after the injection, the animals’ motor coordination, strength and balance had deteriorated — all Parkinsonian symptoms.

Antibodies against α -synuclein could stop or slow down the spread of the disease, the authors suggest.

Science 338, 949–953 (2012)

For a longer story on this research, see go.nature.com/tcoflz

COMMUNITY CHOICE

The most viewed papers in science

NEUROSCIENCE

Faces warp as brain area is zapped

HIGHLY READ
on jneurosci.org
in October

Electrical stimulation of two specific brain regions distorts the perception of faces.

Facial recognition has been linked to the fusiform gyrus, but establishing a causal link and identifying the specific areas of this region involved have proved challenging. Josef Parvizi and his colleagues at Stanford University in California used three modes of brain-activity measurement to pinpoint a specific neural circuit involved in the visual perception of real faces. The authors stimulated electrodes implanted into the mid and posterior fusiform areas of a 45-year-old man. He reported that the faces he saw in the room appeared so distorted that they almost looked like different people. He was still able to name famous faces and recognize other objects. Stimulating electrodes implanted into nearby brain areas had no effect.

Electrophysiology and functional magnetic resonance imaging data confirmed that these two fusiform areas were active when the volunteer was viewing faces.

J. Neurosci. 32, 14915–14920 (2012)



MAYAKO KUTSUJAKE

ZOOLOGY

Aphids borrow plant plumbing

Some aphid species build nests that are attached to plants and remain sealed for months — so how do the insects avoid drowning in their own waste? It seems that they flush waste products using the fluid-transport systems of their host plants.

Takema Fukatsu of the National Institute of Advanced Industrial Science and Technology in Tsukuba, Japan, and his colleagues compared the nodule-like nests, or galls (pictured), of six species of aphid from the Hormaphidinae

subfamily. By injecting various fluids, including some containing dye, into the closed galls, the team found that several species build sealed nests with spongy, absorbent walls that drain into the host plant’s vascular system. By contrast, other species make open galls that have waxy, non-absorbent walls.

The authors suggest that aphid species evolved different strategies to balance colony hygiene with defence against predators and parasites.

Nature Commun. 3, 1187 (2012)

NATURE.COM

For the latest research published by Nature visit:

www.nature.com/latestresearch

SEVEN DAYS

The news in brief

POLICY

Climate warning

The world is on course for warming of 4 °C by the end of the century, with alarming consequences for natural ecosystems, agriculture and human well-being, according to an analysis commissioned by the World Bank. Released on 18 November, a week before the next round of United Nations climate talks kicks off in Doha, the report stresses that 4 °C of warming could overwhelm human efforts to adapt to climate change. Limiting warming to 2 °C — a formal goal of the United Nations — is possible, but would require urgent action, the report says.

Strict open access

The US National Institutes of Health (NIH) is stepping up enforcement of its public-access policy, which has a compliance rate of just 75%. The policy requires investigators to submit papers arising from NIH-funded research to the PubMed Central repository when they are accepted for publication; the papers must be freely accessible to the public within 12 months of publication. On 16 November, the NIH said that beginning as soon as spring 2013, it would withhold the next instalment of grant funds from recipients who have not complied.

Catch contained

The body that decides how many tuna can be caught in the Atlantic and Mediterranean has followed the advice of scientists and set a catch limit of some 13,500 tonnes of bluefin tuna per year from 2013 — up roughly 600 tonnes from this year. The move delighted conservationists, who had feared that the International Commission for

the Conservation of Atlantic Tunas would set a higher quota that could threaten signs of recovery in the troubled species. See go.nature.com/w4igy8 for more.

US flight exemption

Legislation that would keep US airlines out of the emissions-trading scheme set up by the European Union (EU) was passed by the US House of Representatives on 13 November. The EU folded aviation into its scheme this year, but on 12 November announced a one-year postponement for flights entering and leaving the EU. Environmental groups are pressing President Barack Obama to veto the US bill, which needs his signature to become law. See go.nature.com/zfcmmou for more.

Fishing action

The European Commission has warned eight nations that they risk being listed as 'uncooperative' in its fight against illegal fishing. If Belize, Cambodia, Fiji, Guinea, Panama, Sri Lanka, Togo and Vanuatu do not take action to combat such activity, which is generally regarded as one of the main barriers to sustainable fisheries, they could face trade sanctions. Maria Damanaki, the commissioner for fisheries, described the warning — the first of its kind — as "not a black list, but a yellow card".

Merger off

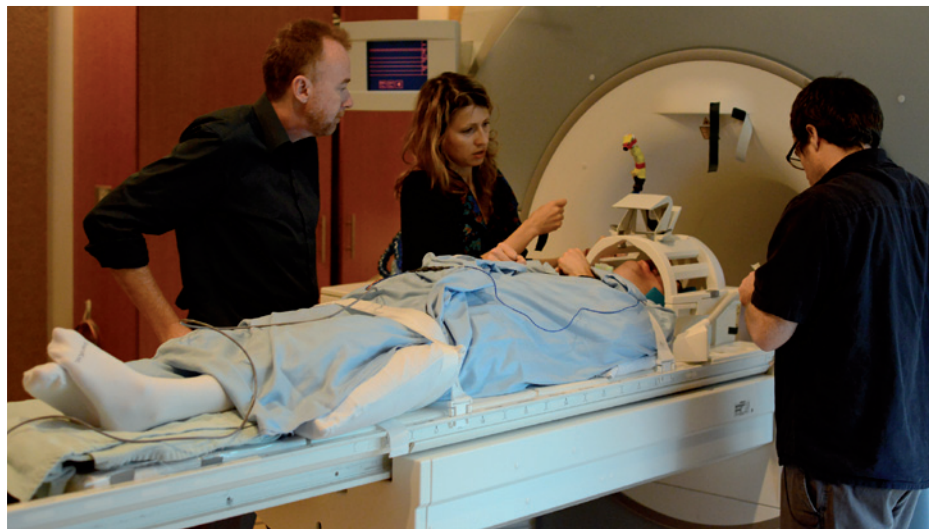
The US National Institutes of Health (NIH) last week abandoned a plan to create a single institute devoted to the study of substance abuse and

a neuroscientist at Canada's Western University in London, Ontario (see *Nature* **486**, 178–180; 2012). This is the first time that the method has been used to ask a patient substantive questions about their condition. See go.nature.com/atvwlw for more.

addiction. The plan would have required dissolving two existing NIH institutes, the National Institute on Drug Abuse, which has an annual budget of US\$1 billion, and the \$460-million National Institute on Alcohol Abuse and Alcoholism (see *Nature* **467**, 643; 2010). The expenditure of resources needed to set up a new institute was not justified in a time of fiscal strain for the agency, said NIH director Francis Collins. See go.nature.com/uibf6x for more.

Malaria funding

The future of a multimillion-dollar effort to subsidize malaria medicines looks shaky. Last week, the Global Fund to Fight AIDS, Tuberculosis and Malaria decided to fold the stand-alone programme (called the Affordable Medicines



FERGUS WALSH/BBC

No pain, 'says' patient in vegetative state

A man thought to have been in a vegetative state has told doctors 'no' when asked if he was in pain on a BBC documentary programme broadcast on 13 November. He communicated with the aid of a functional magnetic resonance imaging technique developed by Adrian Owen,

GALAPAGOS NATIONAL PARK/AP Facility — Malaria) into its existing grants system, and not set aside any money for it after 2013. The Global Fund, based in Geneva, Switzerland, has also appointed a new executive director, Mark Dybul, a physician and immunologist at Georgetown University, Washington DC. See pages 495 and 508 for more.

PEOPLE

Physicist paroled

Russian physicist Valentin Danilov has been granted parole after 11 years in jail and could be released this week. Danilov was head of the Institute of Thermodynamics at Krasnoyarsk State Technical University before he was arrested in 2001 on charges of selling classified satellite technology to a Chinese company. He was cleared of all charges in 2003 but a new jury overturned the decision a year later, sentencing him to a total of 14 years in prison. See go.nature.com/thq7pk for more.

RESEARCH

Higgs data unveiled

Physicists at the Hadron Collider Physics Symposium 2012 in Kyoto, Japan, last week presented the first new data on the Higgs boson since its discovery in July (see *Nature* <http://doi.org/jr2>; 2012). The

data so far indicate that the properties of the Higgs closely fit predictions made by the standard model of particle physics, disappointing those who were hoping to see signs of 'new physics'. See page 505 for more.

Space scope fails

A European satellite that in 2009 discovered the first known rocky planet outside the Solar System has suffered a computer failure that means it can no longer retrieve data from its telescope. The first computer aboard the Convection, Rotation and Planetary Transits (COROT) satellite failed in 2009, leaving the mission reliant on a second unit, which has now also failed. The mission team will try to reboot the first computer in December, after it failed to restart the second. See go.nature.com/qki5ox for more.

EVENTS

Galapagos poison

Last week, conservationists began dropping poisoned bait onto two islands in the famous Galapagos archipelago, Ecuador, to rid them of invasive rats that eat local flora and the eggs of native species such as iguanas, other lizards and tortoises. The US\$1.8-million dumping operation on Pinzón and Plaza Sur, carried



out by helicopter (pictured), is funded by the Ecuadorean government and a coalition of conservation groups. It marks the second phase of an effort to clear out all non-native rodents by 2020.

BUSINESS

Sea mining stopped

Nautilus Minerals, a deep-sea mining company based in Toronto, Canada, is to end its controversial plans to extract copper, gold and silver off the coast of Papua New Guinea, it announced on 13 November. The company had said in June that it was in dispute with the country's government over the payment of the costs of the project. Critics have argued that deep-sea mining needs to be better regulated to protect fragile ecosystems. See go.nature.com/xpqc3 for more.

Meningitis vaccine

Europe's drug regulators could soon approve the first broad-spectrum vaccine against meningitis B, after the

COMING UP

26 NOVEMBER

Climate negotiators start a fortnight of debate at the United Nations Framework Convention on Climate Change in Doha, geared towards a proposed 2015 global climate treaty. go.nature.com/wnhovv

29–30 NOVEMBER

In Brussels, the 2nd European Gender Summit discusses how to support women's scientific careers, and how to tackle gender issues in research. www.gender-summit.eu

European Medicines Agency's Committee for Medicinal Products for Human Use recommended its approval on 16 November. Called Bexsero, the vaccine contains four antigens that target the more than 3,000 strains of subtype B *Neisseria meningitidis*, the most common subtype in European meningitis cases. Analysts think that the therapy could generate about US\$1 billion a year for its maker, Novartis in Basel, Switzerland.

Spill settlement

Oil-and-gas giant BP will pay US\$4 billion in fines after pleading guilty to 14 criminal charges relating to the April 2010 Deepwater Horizon oil accident in the Gulf of Mexico (see nature.com/oilspill). The fine, the biggest such settlement in US history, includes \$2.4 billion for the National Fish and Wildlife Foundation and \$350 million for the National Academy of Sciences to support a 30-year programme that will study human health and the environment in the Gulf coast region. See go.nature.com/uwsfzd for more.

NATURE.COM

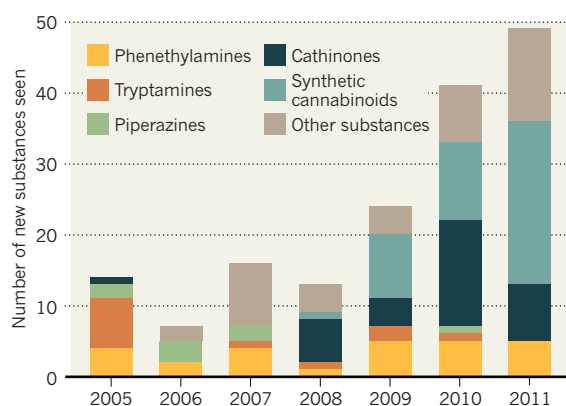
For daily news updates see: www.nature.com/news

TREND WATCH

The number of new psychoactive substances that are synthesized or extracted from plants to get around drug-control laws continues to rise, says a report by the European Monitoring Centre for Drugs and Drug Addiction in Lisbon. The agency says that it spotted 49 new drugs — known as 'legal highs' — last year (by analysis of drugs either seized or bought for testing). About two-thirds were synthetic cathinones (related to amphetamines) or cannabinoids, and most are said to be made in China and India.

DESIGNER DRUGS ON THE RISE

Europe's drugs monitor detected a record 49 new psychoactive substances last year.



NEWS IN FOCUS

PHYSICS Hopes ebb for particles beyond the Higgs **p.505**

EXOBIOLOGY Ice drillers fish for life in Antarctica's hidden lakes **p.506**

SPACE Lab astrophysics brings the heavens to Earth **p.509**

BIOCHEMISTRY Adding new letters to the genetic code **p.516**



ALESSANDRO ABBONIZIO/AFP/GETTY



European proposals to regulate pharmaceuticals in aquatic organisms could already be dead in the water.

ENVIRONMENT

Drug-pollution law all washed up

EU initiative to clean up waterways faces tough opposition.

BY NATASHA GILBERT

Europe is set to quash a precedent-setting initiative designed to tackle a disturbing side effect of common drugs — their impact on aquatic life. *Nature* has learned that landmark regulations intended to clean Europe's waterways of pharmaceuticals are likely to be dead on arrival when they reach a key vote in the European Parliament next week.

The proposal by the European Commission, which would limit the concentrations in water of a widely used contraceptive and an anti-inflammatory drug, have sparked intense lobbying

by the water and pharmaceutical industries, which say that the science is uncertain and the costs too high. European Union (EU) member states, alarmed by cost estimates of tens of billions of euros, seem to agree. Researchers and environmentalists question those estimates, and argue that the proposal should be judged principally on what they say is strong scientific evidence, rather than on financial concerns.

Many of Europe's rivers are home to male fish that are 'intersex' and so display female sexual characteristics,

including female reproductive anatomy. Some males also produce vitellogenin, a protein normally found in eggs that can be induced in males by hormone exposure^{1,2}. In one of the largest studies of the problem, the UK government's Environment Agency found in 2004 that 86% of male fish sampled at 51 sites around the country were intersex.

Toxicologists blame this feminization on endocrine-disrupting chemicals — particularly the active ingredient in the contraceptive pill, ethinyl oestradiol (EE2) — that dribble through municipal sewage effluents into the environment. The feminization affects fish health and lowers the sperm count in males, raising the risk of a population crash. "This is the most evidence we have on the impact of any chemical in the aquatic environment," says Susan Jobling, an environmental toxicologist at Brunel University in London.

With concerns growing over EE2 pollution, the European Commission proposed in January that the EU's member states limit the drug's annual average concentrations in surface waters to no more than 0.035 nanograms per litre (ng l⁻¹). One study² recorded adverse effects in species living in water containing 1 ng l⁻¹ of EE2, for example, and predicted a 'no effect' level of 0.2 ng l⁻¹. Environmental toxicologists typically extrapolate such evidence to estimate lower 'safe' limits that would cover a range of other species (see 'Raging hormones').

The commission has also proposed that lawmakers take action on diclofenac, an anti-inflammatory drug that disrupts cell function in the liver, kidneys and gills of fish³. Diclofenac is already notorious for having devastated vulture populations in Asia⁴.

The EE2 standard would represent a severe cut in pollution levels. For example, a study led by environmental chemist Mike Gardner at Atkins, an environmental consultancy headquartered in Epsom, UK, tested effluents from 160 wastewater treatment plants. He found that almost all effluents exceeded the commission's proposed standard for EE2, and that about half exceeded it by more than 13 times.

On 28 November, members of the European Parliament's environment committee will discuss and vote on the proposal. A rejection from the committee would almost certainly doom the proposal in the full parliamentary vote, scheduled for next year. On the basis of previous committee discussions of the topic, as well as policy documents seen by *Nature*, that ►

► **NATURE.COM**

Water under pressure.
go.nature.com/vrtrdc

► outcome now looks highly likely. “There was no proper discussion about the environmental impacts of these chemicals in the committee; it just boils down to politics,” says Axel Singhofen, a German Member of the European Parliament (MEP) for The Greens who sits on the environment committee.

Upgrading the technology for wastewater treatment could eliminate most of the pollution. Researchers and policy experts suggest sharing the costs among all responsible parties, including the water and drug industries, and that some expense would be passed on to the public. Toxicologists and the water industry also advocate stricter controls on the authorization, use and disposal of endocrine-disrupting chemicals — for example, by educating people not to flush unwanted drugs down the drain, or by prescribing fewer of them. The drugs are widely used in livestock, so preventing animals from urinating close to rivers could further reduce the amount of drugs leaking into surface waters.

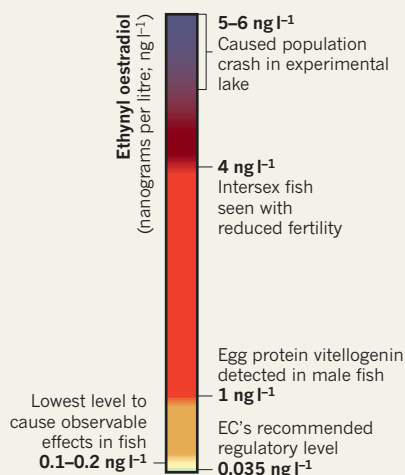
The water and pharmaceutical industries both acknowledge that EE2 is present in rivers, and that it is responsible for intersex fish. But they also say that there is little evidence of harm, noting that Europe’s freshwater fish populations are not plummeting. *Nature* has seen a pharmaceutical industry position statement, distributed to member states, that calls existing scientific data on EE2’s environmental impacts “limited” and “inconclusive”. The European Federation of National Associations of Water and Waste Water Services (EUREAU), based in Brussels, concurs, saying it has “significant concerns” about what it calls a lack of data on the environmental impact of the substances, as well as the potentially huge costs of eliminating them from waste water.

Unpublished position statements from the United Kingdom and the Netherlands echo the industries’ arguments. “Due to uncertainties in the assessment of benefit and costs, and until further monitoring data have been gathered to inform the policy making, it would not be appropriate to propose measures at EU level,” the Netherlands’ statement says.

A report prepared by environment committee member Richard Seeber, a Christian Democrat MEP from Austria, could also sway the vote. Seeber’s report suggests delaying any standards for pharmaceuticals in water until 2027. He agrees with the water industry that

RAGING HORMONES

The European Commission (EC) has proposed limiting the levels of the contraceptive hormone ethinyl oestradiol in surface water.



the issue should be tackled by restricting the authorization and use of the chemicals, rather than by treating waste water.

Seeber is also the founder and president of the European Parliament’s Intergroup on Water, which brings together MEPs, industry and non-governmental organizations to discuss water issues. That group receives “personnel support” and “material contributions” from EUREAU, according to financial statements that *Nature* obtained through a freedom of information request. Seeber says that EUREAU’s involvement was limited to providing organizational and administrative support: “At no point did a member of EUREAU work in our office or at the Parliament, nor did they advise us on content-related matters.”

The UK government, meanwhile, estimates that treated water from around 1,360 of the country’s wastewater treatment plants would fail the proposed environmental standards for EE2. Upgrading these plants to meet the standard would cost between £26 billion (US\$41 billion) and £30 billion, it says.

Yet the United Kingdom is applying an overly stringent standard of 0.016 ng l⁻¹ to estimate the cost of the EU rules, the European Commission told *Nature*. The UK government’s Department for Environment, Food and Rural Affairs has not responded

to repeated requests from *Nature* to explain its calculations. Applying the proposed 0.035 ng l⁻¹ standard would almost halve those costs, the commission says. Such sums are not without precedent: according to the UK water regulator, Ofwat, water companies in England and Wales have already committed to spend £22 billion between 2010 and 2015 on improving water infrastructure — including £4.1 billion for improving water quality in the environment.

Britain’s estimate also assumes that all plants would need to be fitted with the most advanced — and most expensive — treatment technology, which uses granular activated carbon to absorb pharmaceuticals from the water. But such measures will not be necessary at every plant, says Andrew Johnson, an environmental chemist at the Centre for Ecology and Hydrology in Oxfordshire, UK. He suggests that low-cost improvements to existing wastewater treatments, such as sand filters, may be sufficient in some cases.

The investment would bring additional benefits, because improved water treatment could remove many other pollutants of concern, says Michael Depledge of the Peninsula College of Medicine and Dentistry in Plymouth, UK, a former chief scientist for the UK Environment Agency who studies the environment and human health. Levels of many pharmaceuticals are rising in rivers across Europe, he says, posing a “significant risk” to the environment and health — through the emergence of antibiotic-resistant bacteria, for example.

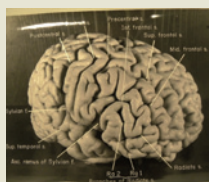
Environmental scientists say that the case for action will only get stronger. Fish populations may be stable now, but a study of fathead minnows (*Pimephales promelas*) in an experimental lake in Canada has shown that exposure to high levels of EE2 triggered a population crash⁵. And researchers think that the EU is missing a chance to set a global precedent. “It’s a test case for regulating pharmaceuticals in the water,” says Jobling. “If they don’t regulate on EE2, they won’t regulate anything.” ■ SEE EDITORIAL P.496

1. Jobling, S. et al. *Environ. Health Perspect.* **114**, 32–39 (2006).
2. Gross-Sorokin, M. Y., Roast, S. D. & Brighty, G. C. *Environ. Health Perspect.* **114**, 147–151 (2006).
3. Cuklev, F. et al. *Environ. Toxicol. Chem.* **30**, 2126–2134 (2011).
4. Oaks, J. L. et al. *Nature* **427**, 630–633 (2004).
5. Kidd, K. A. et al. *Proc. Natl Acad. Sci. USA* **104**, 8897–8901 (2007).



MORE
ONLINE

TOP STORY



Snapshots explore Einstein’s unusual brain
go.nature.com/ozmue1

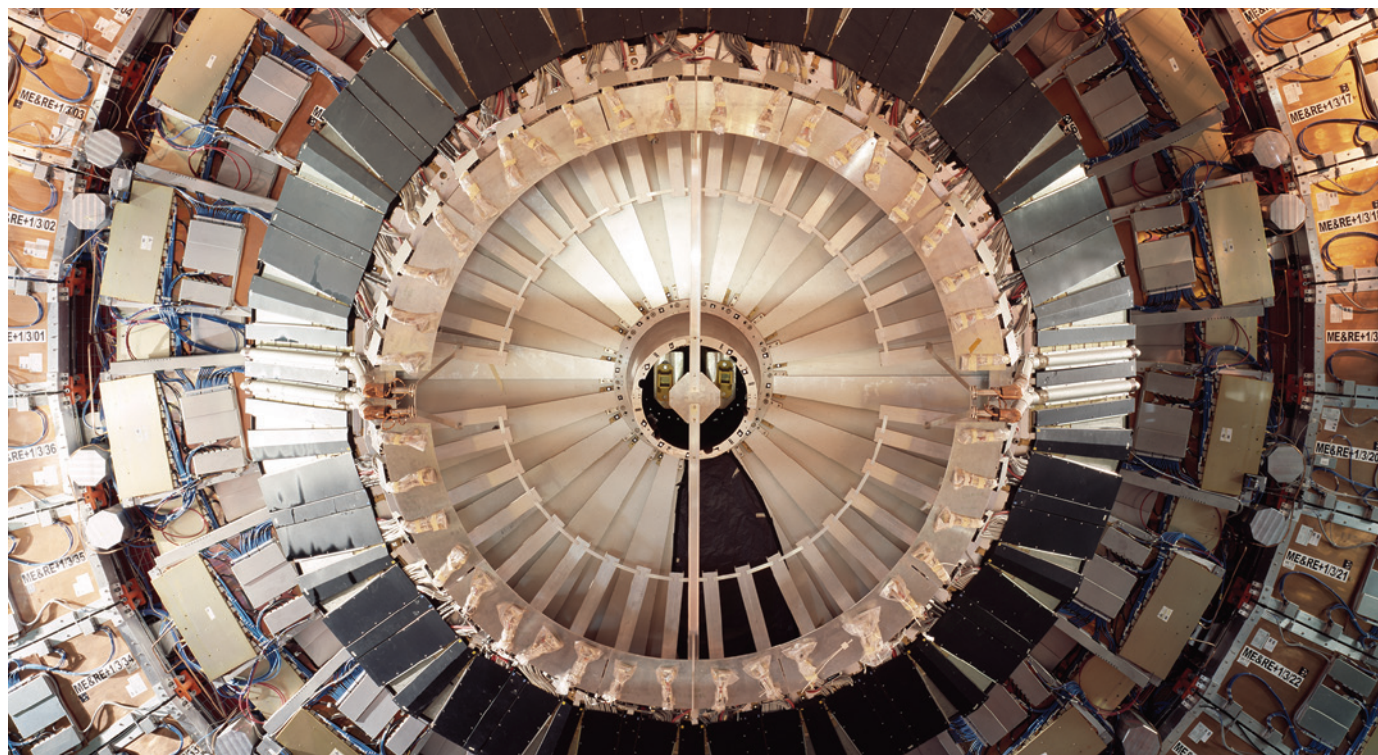
MORE NEWS

- Leonardo fossil sketch may depict early nests go.nature.com/eargns
- Human drugs make fish flounder go.nature.com/clh8ys
- Roaming robot may explore mysterious Moon caverns go.nature.com/2mii0z

WATCH



Brain scans of rappers shed light on creativity
go.nature.com/xy6onz



Data collected by experiments at the Large Hadron Collider (including its CMS detector, pictured) have provided little support for supersymmetry theory.

PARTICLE PHYSICS

Truant particles turn the screw on supersymmetry

Physicists hoping for signs of radically new particles get no joy from Large Hadron Collider.

BY MATTHEW CHALMERS

Absence of evidence is not necessarily evidence of absence. That's what theoretical physicist John Ellis of King's College London says of the latest result in the search for supersymmetry, an idea that has captivated particle physicists for 30 years.

Although researchers are still digesting the discovery of the Higgs boson, announced in July at CERN, Europe's particle-physics laboratory near Geneva in Switzerland, more exotic creations are needed to fill out their picture of the subatomic world. The Higgs provides the last missing particle of the standard model of particle physics, but this theory still has some major deficiencies — it is silent on gravity and on what makes up dark matter, among other things. Supersymmetry (SUSY), which predicts that every standard-model particle has a heavier partner, is a step towards a more unified theory of the particles and forces.

Last week at a conference in Kyoto, Japan, physicists working on the LHCb experiment

— one of four large detectors located around CERN's Large Hadron Collider (LHC) — announced the hotly anticipated results of an indirect search for new superparticles, known by the cognoscenti as 'sparticles'. The team clocked an extremely rare process in which a B_s meson — composed of a strange quark and a bottom antiquark — decays into a muon-antimuon pair. Only one in roughly every 300 million B_s mesons is predicted to do this, because the decay relies on a highly unlikely chain of events involving the fleeting appearance of virtual particles. But with the help of sparticles, the rate could increase by perhaps a factor of 100.

However, the LHCb team found that the B_s behaves just as the standard model says it should, although further data are needed to confirm the measurement. Some members of the 800-strong collaboration proclaimed the result as "very damaging" for SUSY. But SUSY

is a slippery animal — it introduces more than 100 new parameters into the standard model, all adjustable — and SUSY proponents don't seem particularly worried. "To paraphrase Mark Twain, news of SUSY's death has been greatly exaggerated," says theoretical physicist and SUSY pioneer Savvas Dimopoulos of Stanford University in California.

Nevertheless, the LHC has undoubtedly lengthened the odds of SUSY being correct, at least in its simplest, 'natural' incarnations. "Models of natural supersymmetry are looking increasingly hard to believe," says Brian Feldstein of the Kavli Institute for the Physics and Mathematics of the Universe at the University of Tokyo.

The LHCb result comes on top of tough direct constraints from the LHC's larger ATLAS and CMS detectors. These have seen no sign of sparticles such as squarks and gluinos — nor of any particles outside the standard model. Updates from ATLAS and CMS, presented in Kyoto, continue to show that the lightest superparticles, if they exist, must ▶

NATURE.COM
Read more at
Nature's LHC
special.
www.nature.com/lhc

► have truly elephantine masses of more than 1 teraelectronvolt (TeV).

Studies of the Higgs boson itself are yielding mixed signals for SUSY-seekers. So far, rough measurements of CERN's new boson — updated last week — suggest that it behaves just as the standard model predicts, with no hint that additional particles are influencing its behaviour. Yet the mass of the Higgs, 126 gigaelectronvolts (GeV), is pretty much what SUSY predicted, says Sven Heinemeyer at the Institute of Physics of Cantabria in Spain. "If it had been 140 GeV or more, the minimal supersymmetric standard model would have been dead without any possibility of resurrection," he says. SUSY also predicts the existence of four further Higgs particles, at different masses, which have yet to be discovered.

The next chance for some cheering news about SUSY will come in March, when physicists will present results encompassing much more of the data gathered by the LHC, which will continue to smash protons until 17 December. SUSY will probably then remain in limbo until early 2015, when the LHC will re-open for experiments after a long shutdown for maintenance, and will begin colliding protons at energies of 13 TeV. So far, the collider has operated at energies of up to only 8 TeV. The increase in energy will put discoveries of more massive particles within the LHC's reach.

Yet sparticles with masses of several TeV or higher might be too heavy to be produced in the LHC or any other conceivable experiment — a troubling possibility.

One of the main attractions of SUSY is that it solves a problem in the standard model, which predicts that the Higgs field — the constant sea of energy from which the Higgs boson arises — should be ramped up to ridiculously high values by the ever-present fluctuations of standard-model particles. SUSY's sparticles are supposed to prevent that by cancelling out the fluctuations, thereby stabilizing the Higgs. But there is disagreement about whether superheavy sparticles can offer enough stabilization.

In another blow to SUSY's explanatory power, such sparticles could also become too heavy to be convincing candidates for dark matter, the unseen stuff that astronomers believe has a key role in shaping cosmic structure.

Fans of SUSY are likely to lose faith only if the LHC finds nothing after a year or two of high-energy running. That would force them to look for an even more audacious idea to break free from the standard model. Even so, SUSY will probably live on in mathematical physics, says theorist Ben Allanach of the University of Cambridge, UK. "It is such a powerful new mathematical symmetry that it would be a shame if nature didn't make use of it," he says. ■



A British field camp in Antarctica will soon host efforts to drill through the ice to reach Lake Ellsworth.

EARTH SCIENCE

Hunt for life under Antarctic ice heats up

UK and US teams to drill into ancient subglacial lakes.

BY QUIRIN SCHIERMEIER

Nestled in a steep fjord beneath three kilometres of Antarctic ice, the lost world of Lake Ellsworth has haunted Martin Siegert's dreams ever since he got involved in subglacial research a dozen years ago. Finally, the time has come for him to explore its mysterious waters.

Next week, Siegert, a glaciologist at the University of Bristol, UK, packs his bags for the long journey to the opposite end of the world. Once he has reached the Rothera Research Station of the British Antarctic Survey (BAS) on an island off the Antarctic Peninsula, he and his science crew will fly about 1,000 kilometres into western Antarctica. On 5 December, the real work begins: drilling straight down through the ice to the pristine lake beneath. In its shadowy waters they hope to find forms of life that have not seen the light of day in millions of years (see 'Trapped under ice'). And in the lake bed sediments, the team will search for records of the poorly understood history of the West Antarctic Ice Sheet, potentially revealing

how the mighty glacier has waxed and waned over time.

Is Siegert excited? "This is the very pinnacle of the science I've been doing since the turn of the millennium," he says. "Now guess if I'm excited."

Almost 380 subglacial lakes have been discovered and mapped in Antarctica, and have been explored remotely with ice-penetrating radar, gravity measurements and seismic investigations (A. Wright and M. Siegert *Antarctic Science* <http://doi.org/jsn;2012>). These ancient lakes, large and small, owe their existence to geothermal heat that melts the Antarctic ice from below. Gravity and ice pressure force the melt water to flow, and it collects in the hollows and valleys of the continent under the ice.

If all goes to plan, Lake Ellsworth will be the second such lake to be breached. In February, a Russian team penetrated Lake Vostok — the largest and deepest Antarctic lake — completing a project that was launched more than 20 years ago (see *Nature* 482, 287; 2012). And

➔ **NATURE.COM**
Read more about the exploration of Lake Vostok:
go.nature.com/h55xgu

► have truly elephantine masses of more than 1 teraelectronvolt (TeV).

Studies of the Higgs boson itself are yielding mixed signals for SUSY-seekers. So far, rough measurements of CERN's new boson — updated last week — suggest that it behaves just as the standard model predicts, with no hint that additional particles are influencing its behaviour. Yet the mass of the Higgs, 126 gigaelectronvolts (GeV), is pretty much what SUSY predicted, says Sven Heinemeyer at the Institute of Physics of Cantabria in Spain. "If it had been 140 GeV or more, the minimal supersymmetric standard model would have been dead without any possibility of resurrection," he says. SUSY also predicts the existence of four further Higgs particles, at different masses, which have yet to be discovered.

The next chance for some cheering news about SUSY will come in March, when physicists will present results encompassing much more of the data gathered by the LHC, which will continue to smash protons until 17 December. SUSY will probably then remain in limbo until early 2015, when the LHC will re-open for experiments after a long shutdown for maintenance, and will begin colliding protons at energies of 13 TeV. So far, the collider has operated at energies of up to only 8 TeV. The increase in energy will put discoveries of more massive particles within the LHC's reach.

Yet sparticles with masses of several TeV or higher might be too heavy to be produced in the LHC or any other conceivable experiment — a troubling possibility.

One of the main attractions of SUSY is that it solves a problem in the standard model, which predicts that the Higgs field — the constant sea of energy from which the Higgs boson arises — should be ramped up to ridiculously high values by the ever-present fluctuations of standard-model particles. SUSY's sparticles are supposed to prevent that by cancelling out the fluctuations, thereby stabilizing the Higgs. But there is disagreement about whether superheavy sparticles can offer enough stabilization.

In another blow to SUSY's explanatory power, such sparticles could also become too heavy to be convincing candidates for dark matter, the unseen stuff that astronomers believe has a key role in shaping cosmic structure.

Fans of SUSY are likely to lose faith only if the LHC finds nothing after a year or two of high-energy running. That would force them to look for an even more audacious idea to break free from the standard model. Even so, SUSY will probably live on in mathematical physics, says theorist Ben Allanach of the University of Cambridge, UK. "It is such a powerful new mathematical symmetry that it would be a shame if nature didn't make use of it," he says. ■



A British field camp in Antarctica will soon host efforts to drill through the ice to reach Lake Ellsworth.

EARTH SCIENCE

Hunt for life under Antarctic ice heats up

UK and US teams to drill into ancient subglacial lakes.

BY QUIRIN SCHIERMEIER

Nestled in a steep fjord beneath three kilometres of Antarctic ice, the lost world of Lake Ellsworth has haunted Martin Siegert's dreams ever since he got involved in subglacial research a dozen years ago. Finally, the time has come for him to explore its mysterious waters.

Next week, Siegert, a glaciologist at the University of Bristol, UK, packs his bags for the long journey to the opposite end of the world. Once he has reached the Rothera Research Station of the British Antarctic Survey (BAS) on an island off the Antarctic Peninsula, he and his science crew will fly about 1,000 kilometres into western Antarctica. On 5 December, the real work begins: drilling straight down through the ice to the pristine lake beneath. In its shadowy waters they hope to find forms of life that have not seen the light of day in millions of years (see 'Trapped under ice'). And in the lake bed sediments, the team will search for records of the poorly understood history of the West Antarctic Ice Sheet, potentially revealing

how the mighty glacier has waxed and waned over time.

Is Siegert excited? "This is the very pinnacle of the science I've been doing since the turn of the millennium," he says. "Now guess if I'm excited."

Almost 380 subglacial lakes have been discovered and mapped in Antarctica, and have been explored remotely with ice-penetrating radar, gravity measurements and seismic investigations (A. Wright and M. Siegert *Antarctic Science* <http://doi.org/jsn;2012>). These ancient lakes, large and small, owe their existence to geothermal heat that melts the Antarctic ice from below. Gravity and ice pressure force the melt water to flow, and it collects in the hollows and valleys of the continent under the ice.

If all goes to plan, Lake Ellsworth will be the second such lake to be breached. In February, a Russian team penetrated Lake Vostok — the largest and deepest Antarctic lake — completing a project that was launched more than 20 years ago (see *Nature* 482, 287; 2012). And

➔ **NATURE.COM**
Read more about the exploration of Lake Vostok:
go.nature.com/h55xgu



places. At roughly 12 kilometres long by 3 kilometres wide, with a depth of around 150 metres, it is but a puddle compared with the vast Lake Vostok. Measuring about 250 kilometres long by 50 kilometres wide, Vostok ranks among the world's largest freshwater bodies. Ellsworth is neatly settled in a subglacial valley near the continental divide, where the overlying ice moves at its slowest. At around -30°C , ice at the site is also twice as 'warm' as the ice on the Vostok plateau in East Antarctica, and is thinner by almost a kilometre. All this will make Lake Ellsworth much easier to access and extensively sample than its prominent cousin, says Siegert.

Even if Ellsworth and Whillans turn out to be sterile, the exploration might provide clues about what constrains life on Earth and elsewhere in the Solar System. Siegert says that it would be a "phenomenal result" if the lakes were found to be devoid of life, because they offer everything that bacteria need — including liquid water and nutrients — and their water temperatures are just a few degrees below zero.

The UK team hopes to reach Ellsworth in a single three-day session, using a drill that will melt the ice with a high-pressure jet of water, heated to 90°C . Once the borehole is finished, the team will have around 24 hours to deploy a water-sampling probe and a sediment corer before the hole refreezes.

The equipment, fastidiously prepared to make sure that it does not contaminate the lake with microbes from the surface, was approved last year by the parties to the Antarctic Treaty. Siegert reckons that drilling will consume some 60,000 litres of water, produced by melting snow at the site. The water will pass through a five-stage filtration system and then be treated with ultraviolet light to sterilize it. "The water we will use to melt into the lake is cleaner than the ice that naturally melts into the lake," says Siegert. The 5-metre-long cylindrical titanium probe that will travel down the

hole on the end of a tether, taking samples at different depths in the lake, was assembled in a clean room in Southampton, UK, and will be unwrapped from its sterilized bag only once it sits in the clean borehole.

The main challenge, says Siegert, will be to complete all sampling operations within the very short window of time. If things go badly, however, the team has enough fuel to reopen the hole by pumping in more hot water. If the probe gets lost or stuck, the researchers may drill a second hole and deploy a second set of sampling instruments. Indeed, they might do this anyway to get an extra round of sampling, potentially adding confidence to the scientific results, says Siegert.

If Lake Ellsworth does host life, it could be identified by the end of the year. But the exploration of Antarctica's hidden lakes has just begun, says John Prisco, a glaciologist at Montana State University in Bozeman, who is overseeing the Lake Whillans foray. Data from more than just three sites are needed, he says, before scientists can hope to understand how the hidden lakes and rivers interact with the overlying ice sheet by lubricating its movement, for example. Studying more lakes could also reveal whether their discharges of minerals affect the chemistry and biological productivity of the Southern Ocean.

"We have come a long way since the time, not long ago, when people thought that Antarctica was but a benign block of ice," says Prisco. "It makes me happy to see the excitement surrounding our science. But I'm afraid we know still less about Antarctica's subglacial environments than we know about some places on Mars." ■

BAS a third effort is about to begin: next week, a US drilling team will set out for McMurdo Station in Antarctica. In January, the researchers will move to their target — subglacial Lake Whillans, a small, shallow body of water close to the edge of the Ross Ice Shelf.

The quest to find exotic microbial life that may have evolved in or beneath these lakes is for many the most thrilling aspect of the research. Scientists have discovered a catalogue of bacteria elsewhere that mine their energy from rocks and minerals, and many assume that specialized microbes living in Antarctica's hidden lakes might do the same.

"Life exists in extreme ecosystems, from the deep lithosphere to the high atmosphere," says David Pearce, an environmental microbiologist with the BAS who will join the UK expedition. "I would be incredibly surprised if we get there and find no organisms at all."

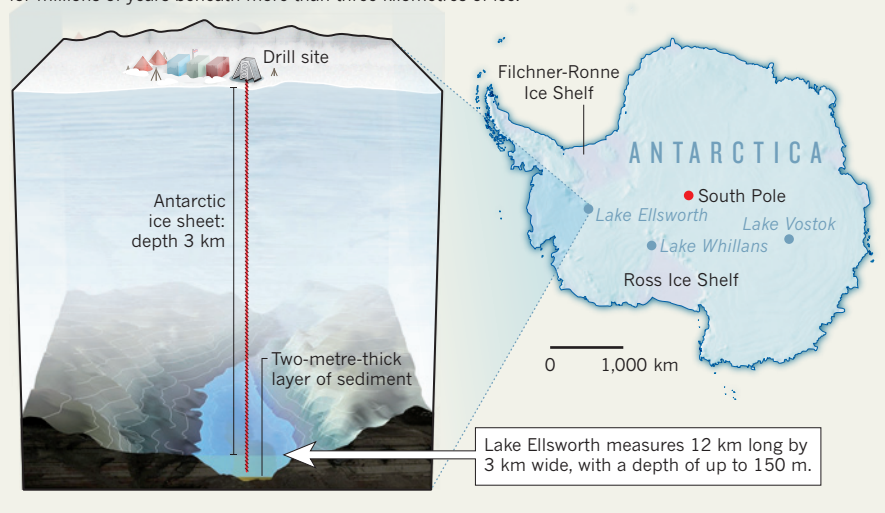
The Lake Vostok team found evidence that heat-loving bacteria may live in the bedrock surrounding that lake. The clues came from DNA in sediment that had become trapped in accretion ice — the lake water that freezes to the bottom of the massive glacier (S. A. Bulat *et al. Adv. Space Res.* **48**, 697–701; 2011).

But the upper layers of the lake itself seem to be lifeless, reported Sergey Bulat, a microbiologist at the Petersburg Nuclear Physics Institute in Russia, at the 12th European Workshop on Astrobiology in Stockholm last month. No native microbes turned up in a preliminary analysis of lake water that had frozen onto the Russians' drill bit, although the team will return to the site this season to collect more samples.

Lake Ellsworth might be a better bet for microbe-hunters, because it offers fewer hiding

TRAPPED UNDER ICE

A team of researchers is about to drill into Antarctica's subglacial Lake Ellsworth, which has been isolated for millions of years beneath more than three kilometres of ice.



Fresh start for global disease fund

But shake-up raises doubts over the future of a major malaria-control programme.

BY DECLAN BUTLER

It has been a rough couple of years for the Global Fund to Fight AIDS, Tuberculosis and Malaria, the world's largest funder of international health programmes. Since its creation in 2002, the organization, based in Geneva, Switzerland, has channelled US\$24.7 billion to delivering disease-control measures such as drugs, diagnostics and bed nets, saving millions of lives. But the global financial crisis has hit the fund hard, and its troubles mounted in 2011 when allegations of corruption among its grant recipients tarnished its reputation and alarmed donors.

Last week, the Global Fund tried to move on, announcing a new leader and unveiling major changes to its funding programme. The changes come, however, at a time of flat-lining donations to the fund, probably heralding an era of curtailed ambitions and risking the fund's unique role in scaling up control measures against the three killer diseases in response to specific countries' needs.

At its most recent fund-raising meeting, in October 2010, the fund had hoped to expand its efforts by raising \$20 billion for 2011–13, but donors pledged just \$11.7 billion, barely enough to maintain its existing programmes. Then followed the fraud allegations, which largely rehashed audits already made public by the fund itself. A retrospective audit published in July this year suggests that the allegations may have been overblown. It found that, in a sample of grants worth \$3.8 billion that were awarded from 2005 to 2012 in 27 countries, just 0.5% of grant funding was lost to outright fraud. Experts say that figure is not exceptional for funding programmes in poor nations that often struggle with corruption.

By November 2011, the organization's funding difficulties led it to cancel all new awards until 2014. On top of that, a management crisis ensued, with executive director Michel Kazatchkine resigning in January this year. Kazatchkine's departure followed the board's appointment in November 2011 of a temporary general manager alongside him to reform the agency.

Last week's appointment of Mark Dybul as executive director could signal a fresh start, and has been broadly welcomed. A physician and immunologist who co-directs the Global Health Law Program at the O'Neill Institute for National and Global Health Law

"A lot of the fund's problems look like they are behind it."



The Global Fund's AMFm project put cheap and effective malaria drugs on the shelves of rural shops.

at Georgetown University, Washington DC, Dybul helped to create the US President's Emergency Program for AIDS Relief, and led the much-lauded body from 2006 to 2009. "He did a really thoughtful, responsible and accountable job," says Barry Bloom of the Harvard School of Public Health in Boston, Massachusetts.

In response to a September 2011 report from a high-level review panel, the fund's board also adopted a new grant-funding model that departs from its revolutionary demand-driven model. Unlike typical aid organizations, which craft and spend a given budget, the fund has until now operated by soliciting and peer-reviewing requests for aid from countries, and then seeking donor financing for all the top-rated proposals.

Under the new model, funding will still be demand-driven to some extent, although constrained by the probable continued flatlining of the budget. Countries applying for funds will now be subjected to a means test that imposes funding caps depending on their wealth and their burdens of AIDS, malaria and tuberculosis. Some funds will still be made available outside this scheme for proposals that are judged to be of exceptional interest.

Another concern of global-health experts is that the new funding model risks neglecting poor populations living in middle-income countries.

The board also threw into question the future of the Affordable Medicines Facility — Malaria (AMFm),

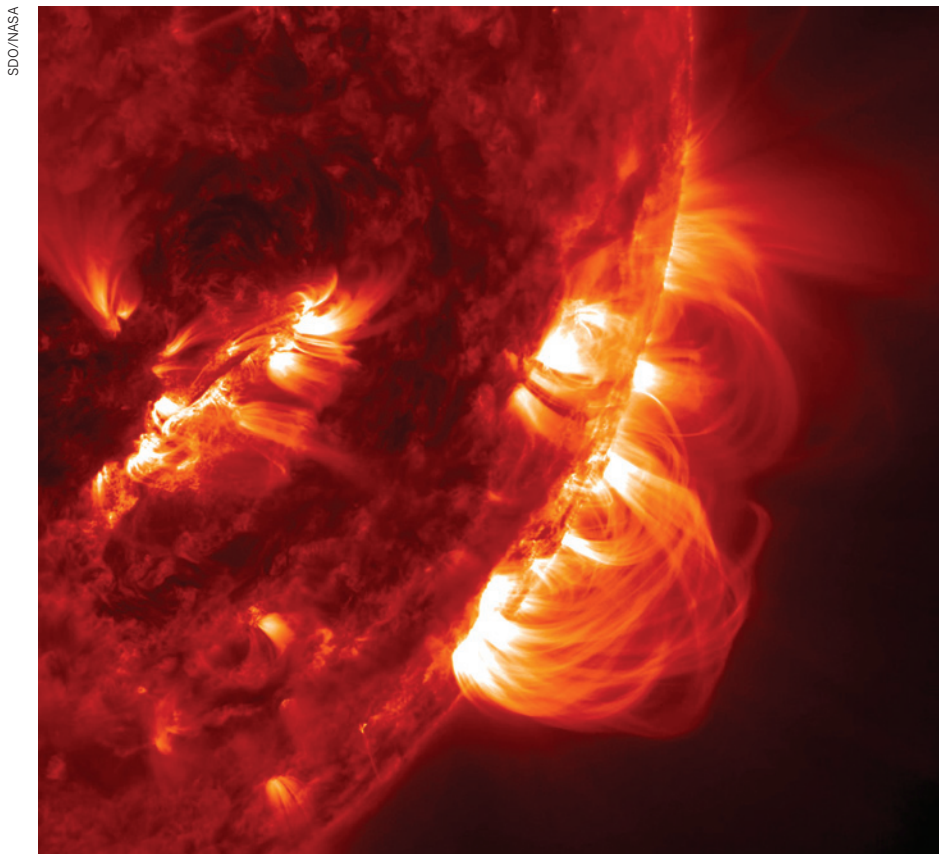
a multimillion-dollar programme aimed at providing subsidized artemisinin-based combination therapies for malaria to private-sector local stores and pharmacies. These are often the only point of supply for medicines for many in the rural developing world, particularly in Africa (see *Nature* **490**, 13–14; 2012).

The board decided that the stand-alone AMFm programme will now be integrated into the Global Fund's existing grants system, but did not ring-fence any new money for it. Because existing funds for the AMFm run out at the end of 2013, many experts assert that this move effectively kills the programme.

Kate Macintyre, executive director of Aidspan, a non-governmental organization based in Nairobi that acts as a watchdog of the Global Fund, says she is "optimistic" that the turmoil has come to an end, and that the fund is back on track. "A lot of the fund's problems look like they are behind it," she says. She adds that a key test for the fund's future will be the eagerness of donors to contribute at replenishment meetings in May and September 2013, which will cover its work from 2014 to 2016.

The fund is also working harder to win support from the corporate and philanthropic sectors. Jennifer Cohn, a medical coordinator at Médecins Sans Frontières, which provides medical humanitarian aid, hopes that a tax on financial transactions planned by ten European countries might also be tapped to provide the Global Fund with another source of support. The most urgent need for the fund, she says, is to start "getting money out the door" again. ■ SEE EDITORIAL P.495

➔ **NATURE.COM**
Read more in
Nature's Malaria
Outlook:
go.nature.com/spwwtf



A type of turbulence simulated in a lab experiment could help to explain why the Sun's corona is so hot.

PHYSICS

Lab astrophysics aims for the stars

Earth experiments deployed to understand data from space.

BY EUGENIE SAMUEL REICH

The giant orange magnets were built decades ago to confine hydrogen nuclei in the quest for fusion energy. But since 1998, Jan Egedal, a plasma physicist at the Massachusetts Institute of Technology in Cambridge, has used the magnets, from a massive, doughnut-shaped tokamak, to simulate magnetic fields in the thin wind of charged particles streaming from the Sun. Egedal hopes to learn how the solar wind transfers energy.

In the past, 'laboratory astrophysics' experiments such as Egedal's — efforts to mimic the behaviour of space plasmas and other astrophysical phenomena — have had to piggyback on the apparatus of energy research or fundamental physics. Now, practitioners are trying to enshrine the field as a discipline in its own right, with dedicated funding and equipment.

In June, the American Astronomical Society (AAS) in Washington DC created its first new division in 30 years, dedicated to lab astrophysics. The American Physical Society's plasma-physics meeting last month in Providence, Rhode Island, saw an unprecedented number of lab-astrophysics sessions. And some NASA scientists are saying that the agency should devote a small amount of funding from every space mission to lab astrophysics. "There's an increasing number of papers on lab astrophysics," says Fred Skiff, a plasma physicist at the University of Iowa in Iowa City, who chaired the physical-society meeting. "It's come of age."

One goal is to make the most of the data streaming in from spacecraft. Egedal, for example, is exploring questions posed by two solar-wind missions: the European Space Agency's Cluster and NASA's Wind. "We're in the heyday of Solar System spacecraft, and that's fuelled the

growth of lab-astrophysics experiments," he explains. Farid Salama, a lab astrophysicist at NASA's Ames Research Center in Moffett Field, California, says that the work is also attractive in times of tight budgets, because the cost of experiments tends to be hundreds of thousands of dollars, compared with hundreds of millions for space missions.

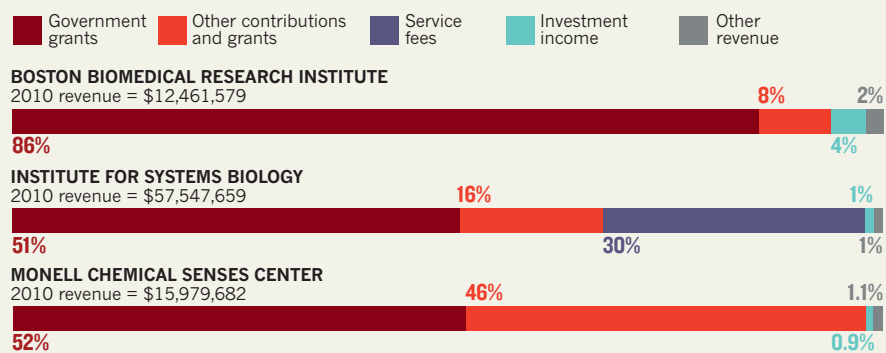
Significant results are emerging. Last month, Skiff and his colleagues described the first lab measurement of astrophysical turbulence in which two magnetic waves collide to generate a third one — a phenomenon that has been invoked to explain why the Sun's atmosphere, or corona, is thousands of times hotter than its surface and how massive amounts of energy move between galaxies. Using the Large Plasma Device, a 21-metre-long plasma generator at the University of California, Los Angeles, Skiff made two of these 'Alfvén' waves, collided them and mapped the daughter wave, confirming the mechanism (G. G. Howes *et al. Phys. Rev. Lett.* Preprint at <http://arxiv.org/abs/1210.4568>; 2012). "This is the first clear lab demo of something that is a cornerstone of theory," says Amitava Bhattacharjee, a theoretical astrophysicist at Princeton University in New Jersey. The experiment cost less than US\$100,000.

NASA has always funded some lab astrophysics, but Salama says that the agency should consider doing so as a matter of course for all space missions. A good first candidate for this funding model, he says, would be work connected with the Herschel Space Observatory, a European mission with NASA involvement that is collecting infrared spectra from thousands of different molecules in Galactic clouds of dust and gas. Many of the molecules have yet to be identified, but researchers could pin them down by synthesizing candidates and checking their spectra in the lab. Daniel Savin, an astrochemist at Columbia University in New York who was involved in the creation of the AAS lab-astrophysics division, says that theoretical work in lab astrophysics is also needed to set priorities for which experiments to do. For example, synthesizing every possible molecule that might be observed in space is not financially feasible. Models of cloud chemistry could guide the work by indicating which are the most important.

Dedicated funding for lab astrophysics would be good news for Egedal, who is beginning to outgrow his current apparatus. His group has predicted the existence of a plasma regime in which electrons can be unexpectedly and powerfully energized, a previously unexplained effect seen by spacecraft observing the solar wind. But to explore the mechanism, he needs to do experiments using a larger volume of plasma and higher magnetic fields (J. Egedal *et al. Nature Phys.* 8, 321–324; 2012). If lab astrophysics establishes itself as a worthy discipline, he might be able to graduate from his hand-me-down tokamak, he says. "I want to build a new one." ■

THE CASE FOR A BALANCED PORTFOLIO

The 2010 budget for the Boston Biomedical Research Institute, which is closing, demonstrates the risk of an over-reliance on NIH funding. In comparison, two other institutes of similar size have more diverse models.



FUNDING

Private labs caught in budget crunch

Biomedical-lab closure highlights plight of independent research institutes that rely heavily on federal grants.

BY HEIDI LEDFORD

On the eve of a ballot that would dissolve his institution, Charles Emerson fell silent when asked how he would cast his vote. A combination of declining federal support and the economic downturn had left the Boston Biomedical Research Institute (BBRI) in debt. Frantic attempts to raise money — soliciting philanthropists, seeking partnerships with academic institutions, even renting out space in the BBRI building in Watertown, Massachusetts — barely made a dent. “I’m going to vote for dissolution,” the BBRI’s director finally said. “There is just no other way.”

On 15 November, members of the BBRI corporation agreed, voting 61–15 to end the institute’s 44-year history of biomedical research, which has included the study of vaccines for Alzheimer’s disease and the launch of a centre funded by the National Institutes of Health (NIH) to focus on a form of adult muscular dystrophy. Across the country, other independent labs fear a similar fate. “The BBRI could be a bellwether,” says Jonathan Chernoff, chief scientific officer of the Fox Chase Cancer Center in Philadelphia, Pennsylvania. “The same thing may befall other institutes, even the larger ones.”

Independent institutes tend to offer freedom from the teaching

responsibilities and bureaucratic hassles that can burden researchers at a university or hospital. But they also lack revenue from tuition, or the administrative infrastructure and dedicated alumni that typically drive university fund-raising. “We have a nimbleness which you don’t get at a university,” says Chernoff. “But we little ships are in danger of sinking.”

Fox Chase ultimately sacrificed its independence to avoid a shipwreck. After struggling to recover from the 2008 economic crash, the institute was acquired in July by the Temple University Health System, also in Philadelphia, for US\$83.8 million. “We’re still trying to deal with the outcome of this,” says Chernoff. “We don’t know how it will change our culture.”

Many biomedical-research institutes rely heavily on revenue from NIH grants to individual investigators. But NIH budgets have been declining since 2010, a trend that is unlikely to change any time soon. This proved fatal for the BBRI: as many researchers began to struggle to get their grants renewed, key grant winners retired or moved to other institutions. In 2010, the institute received \$10 million in grants from the NIH — more than 80% of its budget that year (see ‘The case for a balanced portfolio’). By 2012, NIH grants had plummeted to \$6.5 million. In July, Emerson saw projections that put the BBRI’s 2013 NIH revenue at around \$3 million. It was then, he says, that he realized the institute was out of options.

Like the BBRI, the La Jolla Institute for

Allergy & Immunology in California gets about 80% of its budget from NIH grants. Chief technology officer Stephen Wilson says that the institute recognized the impending NIH funding crisis five years ago. Since then, it has cut non-essential staff. It now trains lab managers to use budgeting software, and even encourages employees to bring in coffee mugs rather than use paper cups. Like many institutes, it is also aggressively pursuing philanthropic donations.

But philanthropy has its drawbacks. Many donors bristle at being asked to cover the ‘indirect’ costs of research: unglamorous background expenses such as utilities and administrative staff. Accepting a large donation that does not fully cover overheads can end up costing institutions money. “When a philanthropist gives us a million dollars but says ‘I’ll pay no indirect costs’, we have to have another sizeable pool of money to cover those expenditures,” says Sanders Williams, president of the Gladstone Institutes in San Francisco, California.

Collaborations with pharmaceutical and biotechnology firms are another funding route. The Monell Chemical Senses Center in Philadelphia has buttressed itself by building relationships with some 50 companies worldwide. The Institute for Systems Biology in Seattle, Washington, holds equity in start-up companies that it helps to launch. And the Buck Institute for Research on Aging in Novato, California, has spun out two companies from its research.

But industry money is no easy fix either, says Monell director Gary Beauchamp. “Industry groups are suffering cutbacks,” he says. “It’s a continual struggle to maintain those alliances.” Williams agrees. “We are facing the perfect storm. All of our revenue streams are challenged,” he says.

For Emerson and the BBRI, it is too late. Earlier this year, Emerson presented a final list of alternative funding schemes to the BBRI’s board. In the end, it concluded, there simply was not enough money in the institute’s \$8.5-million endowment to tide it over and not enough time left for it to regroup. Emerson’s focus now is on helping faculty members to find placements at other institutions, and preparing for his own move to the University of Massachusetts Medical School in Worcester. “I didn’t want this to happen,” he says. “Now I just want to see that our scientists can carry on their work.” ■

CORRECTION

The story ‘Snow survey hopes for avalanche of data’ (*Nature* **491**, 312–313; 2012) gave the wrong affiliation for Rodica Nitu; she is a meteorological-instrument expert at Environment Canada in Toronto. And the data source for the map should have read: the Centre for Atmospheric Research Experiments.

➔ NATURE.COM

Follow the impact of the recession on science:

go.nature.com/h7ghyz

LIFE IN THE CONCRETE JUNGLE

Ecologists are exploring how people, buildings, wildlife and pollution interact in the world's cities.

BY COURTNEY HUMPHRIES

Nathan Phillips steps out onto the roof of Boston's Prudential Tower and looks down at the city 50 stories below. Up here, the rush of the wind has replaced the cacophony of car horns, screeching brakes and conversations filling the streets. And the rarefied air carries none of the odours that wrinkle an urban nose. The roof is "essentially a different atmospheric environment from the rest of the city", says Phillips, an ecologist at Boston University in Massachusetts.

That rarefied air is what brings Phillips to the top of the tower. He has set up four book-sized collectors, one at each corner of the roof, to capture air blowing across the city. Black tubing carries the air samples to a tank inside the building, where a computer analyses their levels of carbon dioxide, carbon monoxide, methane and water vapour.

Like most cities, Boston brews up a blend of gases that covers the urban area like a dome. The top of the Prudential Tower is inside or outside this metropolitan atmosphere, depending on the weather. From his rooftop eyrie, Phillips looks towards three other sampling sites around the city and another some 70 miles west, in the green hills outside the pollution zone.

Phillips and his colleagues are using data from these sites to model how carbon dioxide and other gases move through the city, and how the mix differs from the air in rural areas. The work is part of an interdisciplinary project to study Boston's 'metabolism' — how elements are exchanged between natural and human systems. Phillips and his



HIDDEN GAS LEAKS

Areas of Boston in which methane levels spike to more than 2.5 parts per million (p.p.m.) suggest points where natural gas might be escaping from underground pipes. Researchers used a mobile analyser to measure methane in the city.

SOURCES: REF. 5, GOOGLE, TERRAMETRICS, USGS, SIO, NOAA, US NAVY, NGA, GEBCO

team are now focusing on atmospheric carbon — particularly carbon dioxide and methane. Next, they plan to look at carbon in the city's soils and water, and to track the flow of water, nitrogen and pollutants. "The goal is to understand the function of a major city," Phillips says.

CITIES UNDER THE MICROSCOPE

The work is part of the growing field of urban ecology, in which scientists study cities as if they were ecosystems. In the past, artificial and natural elements have been studied separately, but urban ecologists seek to understand the interplay between them — such as how heat and high carbon dioxide levels boost plant growth, how trees cool cities and how green spaces improve animal habitat.

Using ecological methods to tease apart those relationships can improve urban areas for people as well as natural systems, says Phillips. "The scientific study of cities should yield practical benefits in terms of making our cities more sustainable," he says.

There is a growing need for this kind of research. With cities

launching efforts to slash carbon emissions, reduce water use and improve habitats, scientists are beginning to evaluate how such policies affect the overall health of the urban environment. “You need science to help you understand how you are going to best progress towards those goals,” says Steward Pickett, an urban ecologist at the Cary Institute of Ecosystem Studies in Millbrook, New York.

Viewed from the top of the Prudential Tower, Boston is all buildings, cars, pavement and people. But the metropolis also contains nearly 2 million trees, countless tonnes of soil and microbes and a web of wildlife that includes rats, coyotes, deer, more than 100 bird species and the occasional bear or moose in the suburbs. This mix makes for complex relationships — urban trees, for instance, are affected not only by soil pollutants and heat radiating from asphalt, but also by water-metering policies and landscaping. They can provide cooling shade, but they can also block winds that would blow away pollutants. To study these various factors requires a blend of biological, physical and social sciences.

SEEDS OF CHANGE

In 2009, the US National Science Foundation (NSF) and the US Forest Service gave urban ecology a boost by providing US\$6 million to fund 21 projects, including Phillips's, that directly address the environmental concerns of cities. Many scientists see these grants, dubbed ‘Urban Long-Term Research Areas: Exploratory’ (ULTRA-Ex) awards, as the first step towards fostering a much-needed research network for long-term projects in urban ecology.

The NSF has funded this type of work since the late 1990s, when it set up Long-Term Ecological Research (LTER) sites in Phoenix, Arizona, and Baltimore, Maryland. But such examples are rare. This year, an analysis of more than 8,000 ecological studies found that only 4% assessed densely populated areas¹, despite calls from some ecologists and the NSF for more investigation of how people shape environments.

“What has been very surprising,” says Morgan Grove, a research forester at the Forest Service who is involved in the Baltimore LTER study, “is how much of a demand there is for urban-ecology science and data.”

The results are not always what civic leaders want to hear. An ULTRA-Ex team at the University of California, Los Angeles (UCLA), for example, raised questions about the impacts of a plan to plant one million trees in that city. The study found that some property owners are reluctant to plant trees along streets, because of maintenance costs and concerns that trees reduce visibility and lead to more crime, says Stephanie Pincetl, a land-use researcher at UCLA, who led the study. And because trees vary in water requirements and how much shade they provide, some species could increase the need for irrigation in the arid region².

Another ULTRA-Ex project in Cleveland, Ohio, is studying the effects of converting vacant lots into urban farms. This process could benefit cities with shrinking populations, like Cleveland's, and save millions of dollars in annual maintenance costs, says Michael Walton, an ecologist at Cleveland State University, who is leading the project. Researchers at Ohio State University in Wooster have analysed pollutants, nutrients and food webs in soil from vacant lots, and found that they are generally suitable for planting crops³. Other studies show that gardens established in these plots can, over time, develop healthy populations of pest-killing microbes and ants⁴, suggesting that urban farming will not necessarily boost pesticide use in cities. Such studies are becoming more common worldwide, as organizations such as the Stockholm Resilience Centre commit to studying social and ecological interactions in cities.

With two ULTRA-Ex projects that are now joining forces, Boston is emerging as a major centre of urban-ecology research. While Phillips studies the city's gaseous metabolism, Paige Warren, an ecologist at the University of Massachusetts in Amherst, is leading a group to assess how efforts to plant vegetation throughout Boston have affected air quality, people and wildlife. “There should be predictable consequences, but we haven't studied them that much,” says Warren.

Phillips and his team are collaborating with Steven Wofsy, an

atmospheric scientist at Harvard University in Cambridge, Massachusetts, to model how carbon dioxide moves throughout the city. In addition to the rooftop measurements, the researchers are driving around Boston in a car outfitted with a sampling device to gather high-resolution data on street-level carbon dioxide. They are also studying how carbon dioxide levels and shade from buildings affect plants — and how trees, in turn, absorb carbon dioxide and cool buildings.

URBAN EXHALATIONS

Such studies will be crucial as nations move to reduce greenhouse-gas pollution, because cities are responsible for more than two-thirds of global carbon dioxide emissions from energy use. Most of what is known about cities' overall carbon output comes from combining emissions estimates for traffic, buildings and industries, but there is considerable uncertainty in such inventories. Road transportation is thought to account for about one-third of US greenhouse-gas emis-

“THE SCIENTIFIC STUDY OF CITIES SHOULD YIELD PRACTICAL BENEFITS IN TERMS OF MAKING OUR CITIES MORE SUSTAINABLE.”

sions, but credible inventories for that source in Massachusetts can differ by nearly 40%, says Lucy Hutyra, an environmental scientist and co-leader of the ULTRA-Ex project at Boston University. As cities begin to take carbon regulation more seriously, “we need to have a transparent, robust, verifiable reporting of carbon dioxide emissions”, she says. Otherwise, cities cannot track their successes and failures.

As the researchers complete the first analyses from their atmospheric model of Boston's carbon dioxide concentrations, they are finding some surprises. Their data indicate that traffic emissions in the core of the city are higher than some estimates have suggested.

Phillips and Hutyra are also working to identify natural-gas leaks from underground pipes⁵, and they have found more than 3,000 so far (see ‘Hidden gas leaks’). Their aim is to quantify how such leaks contribute to greenhouse-gas emissions and affect nearby plants and soil. Phillips says that methane from natural gas depletes oxygen in soils, causing plant roots to rot.

It is not yet clear whether any ULTRA-Ex sites will receive funding to establish expanded research programmes — which Tom Baerwald, a programme manager at the NSF, estimates would cost around \$1 million a year.

For Phillips, future funding concerns take a back seat as he wraps up his work on the Prudential Tower. His data show that carbon dioxide levels in Boston average 388 parts per million (p.p.m.) in summer — when photosynthesis is in high gear — and 413 p.p.m. in winter. But the breeze on this August day has brought fresh air to the rooftop, and the carbon dioxide concentration is a modest 379 p.p.m. That value, says Phillips, “is probably what you'd read over Hawaii right now”. With that, he packs up and boards an elevator for a ride down to the urban air of Boston proper. ■

Courtney Humphries is a freelance writer in Boston, Massachusetts.

1. Martin, L. J., Blossey, B. & Ellis, E. *Front. Ecol. Environ.* **10**, 195–201 (2012).
2. Pincetl, S., Gillespie, T., Pataki, D. E., Saatchi, S. & Saphores, J.-D. *GeoJournal* <http://dx.doi.org/10.1007/s10708-012-9446-x> (2012).
3. Grewal, S. S. *et al. Urban Ecosyst.* **14**, 181–194 (2011).
4. Yadav, P., Duckworth, K. & Grewal, P. S. *Landscape Urban Plan.* **104**, 238–244 (2012).
5. Phillips, N. G. *et al. Environ. Pollut.* (in the press).

DNA'S NEW ALPHABET

When Steven Benner set out to re-engineer genetic molecules, he didn't think much of DNA. "The first thing you realize is that it is a stupid design," says Benner, a biological chemist at the Foundation for Applied Molecular Evolution in Gainesville, Florida.

Take DNA's backbone, which contains repeating, negatively charged phosphate groups. Because negative charges repel each other, this feature should make it harder for two DNA strands to stick together in a double helix. Then there are the two types of base-pairing: adenine (A) to thymine (T) and cytosine (C) to guanine (G). Both pairs are held together by hydrogen bonds, but those bonds are weak and easily broken up by water, something that the cell is full of. "You're trusting your valuable genetic inheritance that you're sending on to your children to hydrogen bonds in water?" says Benner. "If you were a chemist setting out to design this thing, you wouldn't do it this way at all."

Life may have had good reasons for settling on this structure, but that hasn't stopped Benner and others from trying to change it. Over the past few decades, they have tinkered with DNA's basic building blocks and developed a menagerie of exotic letters beyond A, T, C and G that can partner up and be copied in similar ways. But the work has presented "one goddamn problem after another," says Benner. So far, only a few of these unnatural base pairs can be inserted into DNA consecutively, and cells are still not able to fully adopt the foreign biochemistry.

The re-engineering of DNA, and its cousin RNA, has practical goals. Artificial base pairs are already used to detect viruses and may find other uses in medicine. But scientists are also driven by the sheer novelty of it all. Eventually, they hope to develop organisms with an expanded genetic alphabet that can store more information, or perhaps ones driven by a genome with no natural letters at all. In creating these life forms, researchers could learn more about the fundamental constraints on the structure of genetic molecules and determine whether the natural bases are necessary for life or simply one solution of many. "Earth has done it a certain way in its biology," says Gerald Joyce, a nucleic-acid biochemist at the Scripps Research Institute in La Jolla, California. "But in principle there are other ways to achieve those ends."

Benner first became interested in those other ways as a graduate student in the 1970s. Chemists had synthesized everything from peptides to poisons, and some were trying to build molecules that could accomplish the same functions as natural enzymes or antibodies with different chemical structures. But DNA was largely ignored, he recalls.

"Chemists were looking at every other class of molecule from a design perspective except the one at the centre of biology," says Benner.

In 1986, Benner started a lab at the Swiss Federal Institute of Technology in Zurich and began to rebuild DNA's backbone. He quickly realized that what seemed like a flaw might be a feature. When he and his team replaced the backbone's negatively charged phosphates with neutral chemical groups¹, they found that any strand longer than about a dozen units folded up on itself — probably because repelling charges were needed to keep the molecule stretched out.

The bases proved more amenable to tinkering. Benner set out to create base pairs that are similar to nature's, but with rearranged hydrogen bonding units.

His team tested two new pairs: *iso*-C and *iso*-G (ref. 2) and κ and xanthosine³. It showed that polymerase enzymes — which copy DNA or transcribe it into RNA — could read DNA containing the unnatural bases and insert the complementary partners into a growing DNA or RNA strand. Ribosomes, the cellular machines that 'translate' RNA into protein, could also read an RNA snippet containing *iso*-C and use it to add an unnatural amino acid to a growing protein⁴. "The base pairing, which is at the centre of genetics, turned out to be for us the most malleable part of the molecule," says Benner. The researchers did encounter a problem, however. Because its hydrogen atoms tend to move around, *iso*-G often morphed into a different form and paired with T instead of *iso*-C.

UNNATURAL BONDS

Eric Kool, a chemist now at Stanford University in California, wondered whether his team could develop unnatural bases with fixed hydrogen-bonding arrangements. He and his colleagues made a base similar to the natural base T, but with fluorine in place of the oxygen atoms (see 'Designer DNA'), among other differences⁵. The structure of the new base, called difluorotoluene (designated F), mimicked T's shape almost exactly but discouraged hydrogen from jumping.

The team soon discovered that F was actually terrible at hydrogen bonding⁵, but polymerases still treated it like a T: during DNA copying, they faithfully inserted A opposite F (ref. 6) and vice versa⁷. The work suggested that as long as the base had the right shape, a polymerase could slot it in correctly. "If the key fits, it works," says Kool.

Other scientists were dubious. "I got outraged e-mails from people saying, 'How can you possibly tell us that hydrogen bonds are not needed for DNA replication?'," says Kool. "That was the centre of the

DNA HAS BEEN AROUND FOR BILLIONS OF YEARS — BUT THAT DOESN'T MEAN SCIENTISTS CAN'T MAKE IT BETTER.

CGACTG **F** **P** **Z**...

BY ROBERTA KWOK

helix. And people were so fixated on hydrogen bonds that it was hard to even conceive of alternatives.” Instead of forming hydrogen bonds — a property normally associated with hydrophilic, or water-loving, molecules — F and other shape-mimicking bases developed by Kool’s team were hydrophobic. Water repels them, which helps them to stabilize in the double helix. DNA is analogous to a stack of coins, says Kool, and staying in the stack shields an unnatural base from water.

Floyd Romesberg, a chemical biologist at the Scripps Research Institute, has expanded the repertoire of hydrophobic bases. Starting with molecules such as benzene and naphthalene, his team built “every imaginable derivative”, he says. “It drove us very much away from anything that looked like a natural base pair at all.” But while testing steps in the replication process, the researchers found two contradictory requirements. A crucial position in the base had to be hydrophobic for enzymes to insert the base into DNA, yet it also had to accept hydrogen bonds if enzymes were to continue with copying the strand.

Romesberg’s team screened 3,600 combinations of 60 bases for the pair that was copied the most efficiently and accurately⁸. The two that won, MMO2 and SICS, “walk a thin line” between being hydrophobic and hydrophilic at the key position, Romesberg says.

A major challenge remained, however: researchers had to show that DNA would retain the unnatural base pairs while billions of copies are made. If enzymes pair unnatural with natural bases too often, the new letters could eventually disappear.

BASE JUMPING

Ichiro Hirao, a chemist at the RIKEN Systems and Structural Biology Center in Yokohama, Japan, had been intrigued by the idea of creating unnatural bases ever since reading James Watson’s 1968 book *The Double Helix* as a teenager. Hirao and his colleagues found that they could reduce mispairing by designing shapes that fit awkwardly with natural bases, and by adding negatively charged or electron-rich chemical groups that repel the natural bases’ corresponding parts. In 2011, Hirao’s team reported that DNA containing an unnatural hydrophobic base pair, called Ds and Diol1-Px, could be copied with 99.77–99.92% fidelity per replication⁹. The

same year, Benner and his colleagues showed that another unnatural base pair — P and Z, which join using hydrogen bonds — achieved fidelity of 99.8% per replication¹⁰. And in July, Romesberg’s team reported rates of 99.66–99.99% for optimized versions of his bases, called NaM and 5SICS (ref. 11), overlapping with the sloppiest rate for natural DNA. “Our best case is now approaching nature’s worst case,” says Romesberg.

Unnatural bases still have a lot to prove, however. Researchers haven’t shown that polymerases can copy more than four of the paired bases in a row¹⁰. The polymerase is “the hard nut to crack”, says Benner. And the solution may be to re-engineer it, too.

Philipp Holliger, a chemical biologist at the Medical Research Council Laboratory of Molecular Biology in Cambridge, UK, and his colleagues demonstrated this approach earlier this year — using nucleic acids called XNA, in which the sugars normally present in DNA or RNA had been replaced by other ring structures¹². The team generated billions of mutants of a natural polymerase and let them evolve by putting selective pressure on them to convert DNA to XNA (see *Nature* <http://doi.org/jrh; 2012>). The researchers then compared the most effective mutants to identify the best one. The polymerase is shaped roughly like a hand, and it turns out that the ‘thumb’ was the key region that needed to change, says Hol-

liger. This region makes contact with the DNA as it exits the enzyme and might act as a final checkpoint to ensure correct synthesis. The team also engineered an enzyme that could convert XNA back into DNA.

Much of the tinkering so far has been done *in vitro*, but researchers hope to show that organisms can read and process the information. Perhaps the closest they have come to incorporating unnatural bases into a living system is an engineered bacterium reported last year¹³ by Philippe Marlière, co-founder of the microbial fluidics company Heurisko in Newark, Delaware. He and his team replaced most of the organism’s T bases with chlorouracil, a form of the RNA base uracil in which a hydrogen atom is replaced with chlorine. The team developed an automated system to introduce the base gradually to a strain of *Escherichia coli* that couldn’t make thymine on its own. After about five months, some of the bacteria couldn’t survive without chlorouracil and they had expunged roughly 90% of the thymine from their genomes.

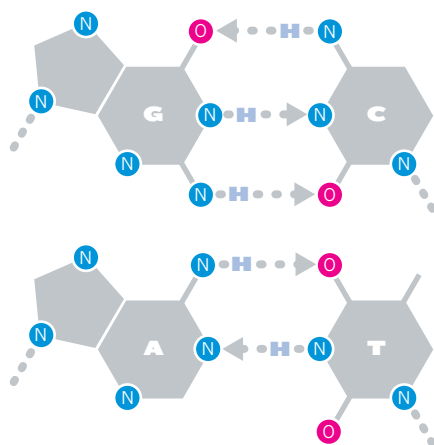
“IF YOU WERE A
CHEMIST
SETTING OUT
TO DESIGN
THIS THING,
YOU WOULDN’T
DO IT THIS WAY
AT ALL.”

DESIGNER DNA

Chemists have designed a slew of new genetic bases, and use various biochemical tricks to help to them pair up and replicate effectively.

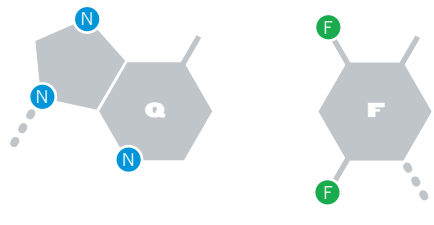
Natural bases

In the canonical guanine-to-cytosine and adenine-to-thymine pairings, bases are held together by two or three hydrogen bonds. Dashed lines show where bases join sugars in the backbone.



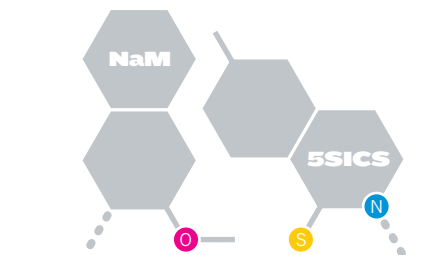
Shedding the bonds

Q, an analogue of A, and F, an analogue of T with fluorine in place of oxygen, do not use hydrogen bonding.



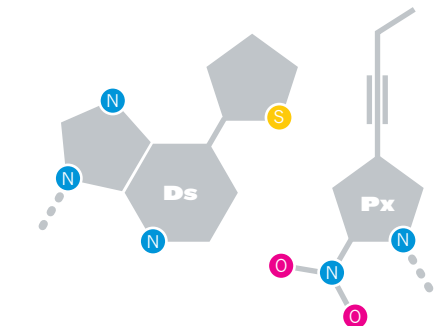
Stable substitutes

NaM and 5SICS contain chemical groups with qualities somewhere between hydrophobic and hydrophilic, which is key to proper replication.



No going back

Ds and Px were designed to pair poorly with canonical bases, so that they won't revert during replication.



Benner, Romesberg and Hirao are also working to coax cells to accept their base pairs. But even if the cells accept the pairs, they might have trouble carrying out processes such as recombination — a highly orchestrated reshuffling of genetic material. “It’s not just a matter of getting these darn things in,” says Andrew Ellington, a biochemist at the University of Texas at Austin and a former graduate student of Benner. “I think this is going to be a modestly Herculean task from here on out.”

Just how far researchers will get is unclear. Marlière’s team aims to replace all four natural bases with unnatural ones. But Romesberg says that developing an organism with only hydrophobic bases will be close to impossible, because cells contain too many components that have adapted to work with natural bases. As for combining an unnatural backbone and unnatural bases in one organism, “our theory is not good enough for us to go in and do both at the same time”, says Benner.

Even if unnatural base pairs don’t yet function in cells, they can still be put to practical use. Siemens Healthcare Diagnostics in Tarrytown, New York, and Luminex in Austin, Texas, already use Benner’s *iso-C* and *iso-G* pair to improve detection and monitoring of viral infections. Siemens, for example, uses a series of linked DNA sequences that bind to HIV-1 RNA in a patient’s blood sample. Inserting unnatural bases into some of the sequences discourages the sequences from binding to random DNA sequences in the sample and makes the HIV-1 RNA easier to detect at low levels.

DNA and RNA molecules can also catalyse reactions and be used as drugs. Developers can improve the performance of a sequence by attaching chemical groups to the bases, and unnatural bases make it easier to target a specific site in a sequence rather than saturating every C or G. Romesberg’s team has added ‘linker’ groups to unnatural bases in DNA that allow precise attachment of a variety of molecules. The team is now trying to engineer sequences that will catalyse reactions more efficiently than their natural counterparts.

Hirao says that his team has generated DNA sequences containing the Ds base that bind much better than natural sequences to interferon- γ , an immune-system protein, and to vascular endothelial growth factor (VEGF), a therapeutic target in cancer and eye disease.

Practical applications aside, researchers are still driven by what Kool calls the “science-fiction appeal” of designing or even improving on living systems. Earth’s early life forms may have settled on their genetic alphabet simply because they were constrained by the chemicals available. Adenine, for example, is easy to make from hydrogen cyanide, which was probably present when life first emerged. Once organisms had a working set of bases, perhaps they got locked into that system. “If you start dabbling too much with your fundamental biochemistry, you’re going to get eaten,” says Benner. Although RNA — generally thought to have preceded DNA — might not be the best possible solution for supporting life, it might be the best solution that could have emerged on prebiotic Earth, Benner suggests.

So if nucleic acids arose independently on another planet, would they have the same bases? Benner thinks not, unless the organisms were subjected to the same constraints. Some universal rules might apply, however. For example, Benner says that backbones with repeating charges — which initially seemed to him like a liability — actually discourage folding and ensure that strands with different base sequences behave similarly during processes such as replication. Although some researchers have had success with alternative backbones, many attempts have resulted in molecules that are too stiff or too loose to form a helix. “I think there is a limit to the chemical variation that can be introduced,” says Holliger (see *Nature* **483**, 528–530; 2012).

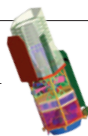
But that isn’t going to stop researchers from pushing the limits. “Why is the chemistry of living things the way it is? Is it because it’s the only possible answer?” asks Kool. “I believe the answer to that question is no. And the only way to prove it conclusively is to do it.” ■

Roberta Kwok is a freelance writer in the San Francisco Bay Area, California.

1. Richert, C., Roughton, A. L. & Benner, S. A. *J. Am. Chem. Soc.* **118**, 4518–4531 (1996).
2. Switzer, C., Moroney, S. E. & Benner, S. A. *J. Am. Chem. Soc.* **111**, 8322–8323 (1989).
3. Piccirilli, J. A. *et al. Nature* **343**, 33–37 (1990).
4. Bain, J. D., Switzer, C., Chamberlin, A. R. & Benner, S. A. *Nature* **356**, 537–539 (1992).
5. Schweitzer, B. A. & Kool, E. T. *J. Am. Chem. Soc.* **117**, 1863–1872 (1995).
6. Moran, S., Ren, R. X.-F., Rummey, S. & Kool, E. T. *J. Am. Chem. Soc.* **119**, 2056–2057 (1997).
7. Moran, S., Ren, R. X.-F. & Kool, E. T. *Proc. Natl Acad. Sci. USA* **94**, 10506–10511 (1997).
8. Leconte, A. M. *et al. J. Am. Chem. Soc.* **130**, 2336–2343 (2008).
9. Yamashige, R. *et al. Nucl. Acids Res.* **40**, 2793–2806 (2012).
10. Yang, Z., Chen, F., Alvarado, J. B. & Benner, S. A. *J. Am. Chem. Soc.* **133**, 15105–15112 (2011).
11. Malyshev, D. A. *et al. Proc. Natl Acad. Sci. USA* **109**, 12005–12010 (2012).
12. Pinheiro, V. B. *et al. Science* **336**, 341–344 (2012).
13. Marlière, P. *et al. Angew. Chem. Int. Edn* **50**, 7109–7114 (2011).

COMMENT

PHYSICS Reliable funding would bring back mega-scale US facilities **p.522**

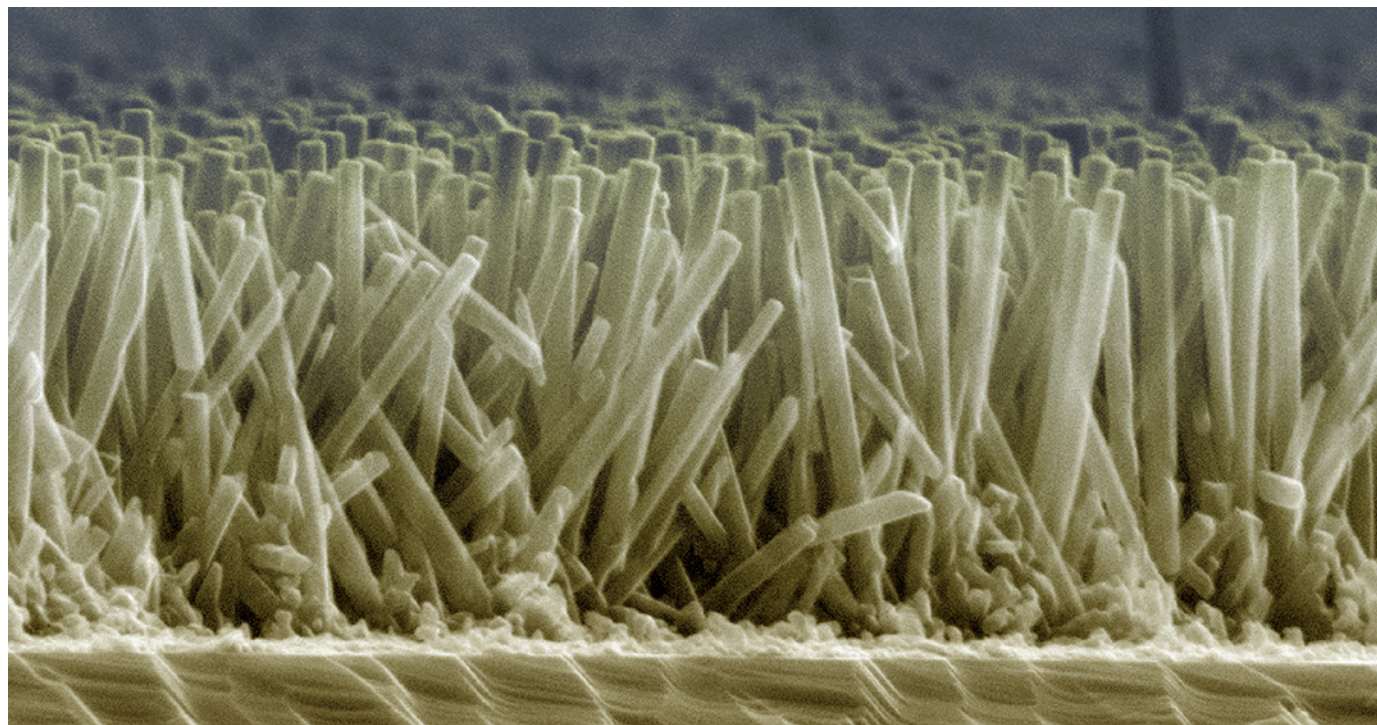


PHILOSOPHY Why random events are often not unexpected in hindsight **p.523**

IN RETROSPECT Biochemist Alexander Oparin's treatise on life's beginnings **p.524**

CLIMATE CHANGE Protect low-lying coastal cities from sea-level rise **p.527**

PEDONG YANG/UNIV. CALIFORNIA BERKELEY/SPL



Artificially grown zinc oxide nanowires, as seen under a scanning electron microscope, measure only a few nanometres in diameter.

Make nanotechnology research open-source

To drive innovation at the nanoscale, the patent thicket must be chopped down, argues **Joshua M. Pearce**.

Any innovator wishing to work on or sell products based on single-walled carbon nanotubes in the United States must wade through more than 1,600 US patents that mention them¹. He or she must obtain a fistful of licences just to use this tubular form of naturally occurring graphite rolled from a one-atom-thick sheet. This is because many patents lay broad claims: one nanotube example covers “a composition of matter comprising at least about 99% by weight of single-wall carbon molecules”. Tens of others make overlapping claims.

This thicket of patents, including entire

classes of nanotechnologies, basic methods and science, is hindering nanotechnology. Excessive patenting is increasing costs, slowing technical development and removing from the public domain fundamental knowledge about the understanding and control of matter on the atomic or molecular scale (1–100 nanometres).

Patent thickets occur in other high-tech fields, but the consequences for nanotechnology are dire because of the potential power

and immaturity of the field. Advances are being stifled at birth because downstream innovation almost always infringes some early broad patents. By contrast, computing, lasers and software grew up without overzealous patenting at the outset².

Nanotechnology offers the promise of enabling matter to be manipulated as easily as software. I believe that those working with it should adopt the open-source approach³ that has proved so successful for software development. All publicly funded nanotechnology research and innovation should be made available ▶

► **NATURE.COM**
More on the impact of nanotechnology investment:
go.nature.com/inicdx

► to everyone for free. A moratorium should be placed on patenting fundamental nanotechnologies and basic quantum-science applications, from which most developments stem.

INTELLECTUAL-PROPERTY SHACKLES

Nanotechnology is big business. According to a 2011 report by technology consultants Cientifica, governments around the world have invested more than US\$65 billion in nanotechnology in the past 11 years. The sector contributed more than \$250 billion to the global economy in 2009 and is expected to reach \$2.4 trillion a year by 2015, according to business analysts Lux Research. Since 2001, the United States has invested \$18 billion in the National Nanotechnology Initiative; the 2013 US federal budget will add \$1.8 billion more.

This investment is spurring intense patent filing by industry and academia. The number of nanotechnology patent applications to the US Patent and Trademark Office (USPTO) is rising each year and is projected to exceed 4,000 in 2012. Anyone who discovers a new and useful process, machine, manufacture or composition of matter, or any new and useful improvement thereof, may obtain a patent that prevents others from using that development unless they have the patent owner's permission.

With universities increasingly operating like corporations, faculty members are pressured into locking away their results as intellectual property (IP), even though their research is largely funded by taxpayers. In the United States, the passage of the 1980 Bayh–Dole Act enabled US universities to retain ownership of the products of federally funded research that had previously been non-exclusively licensed to anyone on request⁴.

Broad patents covering the 'building blocks' of nanotechnology — such as quantum dots, nanowires and fullerenes, carbon nanotubes and methods for making them — hamper conscientious innovators, who must spend time and money to acquire all the necessary licences to avoid lawsuits⁵.

Examples of patents that cover basic components include one owned by the multinational chip manufacturer Intel, which covers a method for making almost any nanostructure with a diameter less than 50 nm; another, held by nanotechnology company NanoSys of Palo Alto, California, covers composites consisting of a matrix and any form of nanostructure. And Rice University in Houston, Texas, has a patent covering "composition of matter comprising at least about 99% by weight of fullerene nanotubes".

The vast majority of publicly announced IP licence agreements are now exclusive, meaning that only a single person or entity may use the technology or any other

technology dependent on it⁶. This cripples competition and technological development, because all other would-be innovators are shut out of the market. Exclusive licence agreements for building-block patents can restrict entire swathes of future innovation.

An evaluation of the carbon-nanotube patent thicket in 2006 found that of 446 carbon-nanotube patents issued in the United States, in which 8,557 claims were made, 420 of those claims were of a building-block type⁷. Imagine how

"Stopping patents on basic nanotechnology will create much more innovation."

equivalent patenting of the idea of a semiconductor or basic programming would have stifled electronics and computing. These dense webs of overlapping rights are created partly as a result of the complex nature of the underlying science. Beating into this patent thicket is made difficult for innovators and patent examiners alike because of the field's interdisciplinary nature and its span across a range of industries. Nanoscience uses a rich and fast-evolving lexicon of technical language — carbon nanotubes can, for example, be described as nanofibres, fibrils, shells, nanocylinders, buckytubes or nanowires. For nanotechnology patent examiners at the USPTO, incomplete availability of information and inadequate training are recognized problems⁸.

Licences can be costly, but the potential expense of litigation for not acquiring them is often much greater. Multimillion-dollar legal fees have overwhelmed nanotechnology companies such as Evident Technologies (legal fees of \$1 million compared with \$4 million in assets) and Luna Innovations (ordered by a jury to pay \$36 million despite assets of \$20 million). Such risks dissuade other companies from working in the nanotechnology field.

THE OPEN-SOURCE ALTERNATIVE

This IP rush assumes that a financial incentive is necessary to innovate, and that without the market exclusivity (monopoly) offered by a patent, development of commercially viable products will be hampered. But there is another way, as decades of innovation for free and open-source software show. Large Internet-based companies such as Google and Facebook use this type of software. Others, such as Red Hat, make more than \$1 billion a year from selling services for products that they give away for free, like Red Hat's version of the computer operating system Linux.

An open-source model would leave nanotechnology companies free to use the best tools, materials and devices available. Costs would be cut because most licence fees would no longer be necessary. Without

the shelter of an IP monopoly, innovation would be a necessity for a company to survive. Openness reduces the barrier for small, nimble entities entering the market.

The field of nanotechnology is a combination of information (such as chemical formulae), software (for example, modelling tools) and hardware (such as atomic force microscopes). All three areas can adopt open-source principles, and some steps have already been taken towards this.

The nanoHUB.org website — established in 2002 by the Network for Computational Nanotechnology with funding from the US National Science Foundation (NSF) — shares simulation programs based on open-source software for nanotechnology research as well as educational materials. Its content is used by hundreds of universities worldwide. Other types of free and open-source software, from microscope-control programs to molecular modelling tools, are proliferating.

Also following an open-source approach are programmes to share construction plans for large and expensive proprietary items of scientific equipment. For example, the SXM team at the University of Münster, Germany, provides free instructions for building a scanning tunnelling microscope. The team has reserved the right to sell the machine, but the list of materials, circuit diagrams and full instructions are posted online (sxm4.uni-muenster.de) so that anyone can build one. The university hosts a spin-off company that makes money by providing add-on services including analytics and workshops.

Critics might counter that the hardware and materials on which most nanotechnology companies base their products are fundamentally different from software, so an open nanotechnology industry would have difficulty attracting the capital needed to scale up. They argue that leading open-source hardware companies — Adafruit, BeagleBoard, Chumby, Liquidware, Seed Studio and SparkFun Electronics — are small, new firms testing unproven business models.

Yet these and dozens of other companies, including Arduino, MakerShed and Solarbotics, earn millions of dollars in revenue each year through providing and

SUMMARY

- Basic nanotechnology is widely patented.
- Many licences are needed to use 'building block' technologies.
- Downstream development of ideas may be stifled as a result.
- Publicly funded nanotechnology research should be open access.
- There should be a moratorium on patenting basic nanoscience.



A nanotechnology researcher at a diffusion furnace handles silicon wafers used in integrated circuits.

supporting open-source hardware in other technological areas. Arduino's open-source microcontroller, for example, has been adopted by thousands of projects, including three-dimensional printing and additive layer manufacturing. These printers are in turn used to fabricate research tools in nanotechnology and other disciplines⁹, spearheading a cascade of innovation that *The Economist* has identified as leading to the "third industrial revolution".

A PATH FORWARD

Stopping patents on basic nanotechnology will create much more innovation than there is now. Three steps are needed. First, the NSF and funding agencies in other countries must insist that the taxpaying public pays only once. Published results from all publicly funded nanotechnology research should be made freely available on the Internet, following established open-access protocols and using databases such as arXiv.

For nanotechnology research in the United States, the NSF should adopt a public-access policy similar to that of the National Institutes of Health (NIH), which stipulates that all NIH-funded research is made freely and openly available on acceptance for publication. The foundation should also support funding for author-pays publishing. In the longer term, Congress should alter the Bayh–Dole Act to exclude private IP lockdown of publicly funded innovations.

Open access to the documentation for publicly funded nanotechnology research

would reduce overly broad patenting by ensuring that patent examiners and innovators have access to more of the literature. It would also expand commercial activity by providing more academics and companies with up-to-date information. Bringing more public oversight to nanotechnology projects could also help to allay fears of the potential negative effects of nanotechnology¹⁰.

Second, all publicly funded ideas and innovations in the nanotechnology sector should not be patented; instead, they should stay in the public domain. These ideas could be deposited in journals or on sites such as nanoHUB.

Third, the USPTO should issue a moratorium on patenting nanotechnology-related fundamental science, materials and concepts. Simply identifying a new behaviour of a material at the nanoscale should not be enough to claim a patent that stops others from working with that material. The current US patent law must be enforced much more strictly.

Companies and universities could still patent applied nanotechnology innovations for which they can garner private investment. Even if universities' licence revenue for fundamental science disappeared, it is far outweighed by the payments for research overheads that come from federally funded grants, often at rates of more than 50% of grant income. For example, at my own institution, which attracts one-and-a-half times the national average of licence agreements per dollar of research, the total grant

income exceeds that from licensing by more than 100 times. Individual researchers rarely benefit in any significant way from licence royalties.

These three changes to the requirements of publicly funded research and patent interpretations in nanotechnology would ensure an innovative market, and leverage the best value for taxpayers from their research investments. ■

Joshua M. Pearce is associate professor in the Open Sustainability Technology Lab, Departments of Materials Science & Engineering and of Electrical & Computer Engineering, Michigan Technological University, Houghton, Michigan 49931-1295, USA.
e-mail: pearce@mtu.edu

1. Miller, J. C., Serrato, R. M., Represas-Cardenas, J. M. & Kundahl, G. A. *The Handbook Of Nanotechnology: Business, Policy, and Intellectual Property Law* (John Wiley & Sons, 2005).
2. Lemley, M. A. *Stanford Law Review* **58**, 601–630 (2005).
3. Mushtaq, U. & Pearce, J. M. in *Nanotechnology and Global Sustainability* (eds Maclurcan, D. & Radywyl, N.) 191–213 (CRC, 2011).
4. Makker, A. *Southern California Law Review* **84**, 1163–1203 (2011).
5. Heller, M. A. & Eisenberg, R. S. *Science* **280**, 698–701 (1998).
6. Tullis, T. K. *Nanotechnology Review* **1**, 189–205 (2012).
7. Harris, D. L. in *Nanotechnology & Society* (eds Allhoff, F. & Lin, P.) 163–184 (Springer, 2009).
8. Stiles, A. R. *Drexel Law Review* **4**, 555–592 (2012).
9. Pearce, J. M. *Science* **337**, 1303–1304 (2012).
10. Tourney, C. *Nature Nanotechnol.* **4**, 136–137 (2009).

Let US physics commit to collaboration

A joined-up funding system is needed to enable the United States to make long-term pledges to major international projects, says **Barry Barish**.

Giant colliders, vast telescope arrays and challenging space missions are now essential for addressing problems at the forefront of physics and astrophysics. But the extent to which the United States is hosting or taking a leadership role in such large facilities is in decline.

This year, one of the most exciting physics discoveries of modern times — the evidence for a Higgs-like boson — was made at CERN, a European particle-physics laboratory. That discovery had been one of the main goals of a US supercollider that was never completed after its funding was cancelled almost two decades ago.

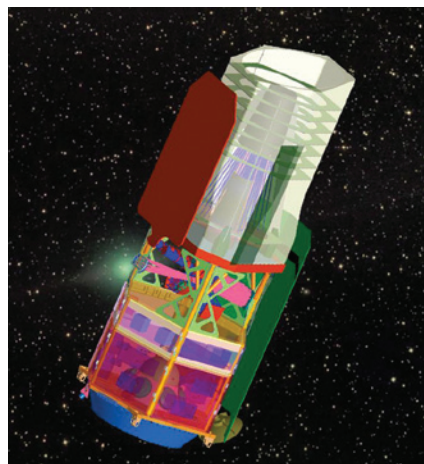
If the United States is to retain its lead in fundamental physics and astronomy, the government needs to devise new mechanisms for supporting international partnerships. This will not necessarily entail more investment or a shift in the size of the projects funded, but it does require a coordinated process that will allow US scientists to make more stable commitments to collaborations.

POOL RESOURCES

For much of the twentieth century, the rich United States did not need to partner with other countries to achieve its science goals. Its scientists made groundbreaking discoveries, including the first detection of cosmic radio waves by Karl Jansky at Bell Telephone Labs in New Jersey in 1933, and evidence for quarks at the Stanford Linear Accelerator Center in California in 1968. US researchers have won or shared 15 of the past 20 physics Nobel prizes, and 60% of the top 50 universities are located in the United States, according to the 2012 *Times Higher Education* World University Rankings.

But physics research has changed. Important breakthroughs increasingly require multibillion-dollar instruments that are too expensive for one country to build alone. For example, the Higgs boson discovery at the Large Hadron Collider (LHC) at CERN near Geneva, Switzerland, is estimated to have cost US\$13 billion in total, an expense shared mainly among CERN's 20 European member states.

Big physics projects such as ITER — an experimental fusion-energy reactor being built in Cadarache, France — are only feasible if the global science community pools its resources. International partnerships



NASA's WFIRST mission has been deferred, giving Europe the chance to lead on dark energy.

leverage the investments of individual countries, enabling their scientists to participate in a wider range of forefront science. And the researchers take skills and innovations back to their home nations.

Scientists in the United States have a strong tradition of international collaboration. The country contributed more than \$500 million to the LHC facility, and it is a 9% partner in ITER. Nevertheless, these projects are hosted and led by other countries. US participation in the Square Kilometre Array (SKA) radio telescope, the proposed International Linear Collider (of which I am director) and a planned dark-energy mission is currently uncertain. Even though these projects have been given the highest priority by their respective international science communities, there is no mechanism to prioritize them within the United States.

SHORT-TERM THINKING

The United States has gained a reputation overseas as an unreliable partner. Unpredictable funding is one reason why other governments are reluctant to collaborate with it. Countries that participate in large projects must make multi-year commitments to design, construct and exploit the facilities. But US budgets are determined one year at a time, so funding streams can suddenly disappear.

For example, after investments of nearly \$2 billion, the US Superconducting Super Collider was cancelled by Congress in 1993 with no regard for the partner countries. They

had been encouraged to contribute half of the projected budget, which had grown to more than \$10 billion (in 1993 dollars). In a more recent example, in 2011 NASA decided not to fund LISA, a proposed US–European space mission to study gravitational waves. Because of other funding commitments, the agency has also deferred its Wide Field of View Survey Telescope (WFIRST), which aimed to detect dark energy; the move leaves Europe to take the lead with its own dark-energy mission, Euclid. These NASA missions were given the highest scientific priorities in the National Academy of Sciences' 2010 decadal survey of astronomy and astrophysics.

US agencies understandably want to keep a close eye on the projects that they fund, and have well-established procedures for doing so. This can result in an extra layer of oversight and reporting for large international projects, on top of the complex governance systems set up by partner countries. Decision-making and priority-setting for such projects need to be accomplished through joint procedures, and should not be skewed by one member.

In my opinion, the United States needs to bid aggressively in the coming decade to host or take lead roles in next-generation mega-scale international projects, such as the International Linear Collider, WFIRST or the SKA. To accomplish this, it must be in a position to make multi-year billion-dollar commitments across several US agencies.

Better defined and more central mechanisms are needed to evaluate and prioritize proposals for ambitious international facilities, perhaps through the White House Office for Science and Technology Policy and the National Academy of Sciences. These mechanisms could also consider the broader impacts of a proposed project on society, such as employment, skills, education and budget considerations.

There is no silver-bullet solution. However, the first steps are to recognize that there is a problem, and then to begin to make the necessary changes. ■

Barry Barish is Linde professor of physics (emeritus) at the California Institute of Technology, Pasadena, California 91125, USA, and director of the Global Design Effort for the International Linear Collider. e-mail: barish@ligo.caltech.edu

NASA



Crises that catch many people unawares are often predictable.

PHILOSOPHY

Creative resilience

Michael Shermer sifts through a study of the science of randomness and our responses to it.

Unexpected events have brought down civilizations, economies, markets and corporations. Nassim Nicholas Taleb, who fleshed out such rare, random 'black swan' effects theoretically in *Fooled by Randomness* (Texere, 2001) and *The Black Swan* (Allan Lane, 2007), offers a solution to the challenge they pose in *Antifragile*.

In more than 400 pages of stream-of-consciousness-style writing, Taleb aims to tell us how to live in a world that is unpredictable and chaotic — how to become 'antifragile'. Antifragility, Taleb stresses, is not the same as robustness, which relates to how well a system can resist change. To be antifragile is to have the capacity to prosper from randomness, uncertainty and disorder, and to benefit from a variety of shocks, especially black-swan events. It is a kind of creative resiliency that Taleb discusses in relation to evolution, politics, business innovation, medicine, economics, ethics and epistemology.

So what are the attributes of antifragility? Take size. You might think that being big — as a nation or corporation — would serve as a buffer to black-swan events. Business schools teach the virtues of 'economies of scale', but Taleb warns that "size hurts you at times of stress". Large entities cannot respond as quickly to rapid change as smaller ones, which tend to be freer to shift strategies. Taleb notes that mergers of major corporations can fail to foster efficiency.

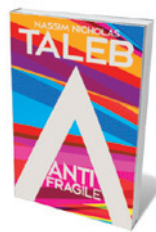
Mergers typically show "at best, no gain from such increase in size". The AOL-Time Warner merger of 2000 and the subsequent split in 2009 is a case in point. Taleb conjectures, too, that big species such as mammoths have become extinct fairly rapidly.

I offer two caveats: the hindsight bias and the confirmation bias.

It is easy to pluck out examples from the historical record of animals and corporations that failed to cope with black-swan events (dinosaurs and mammoths, Blockbuster and Borders). But boa constrictors and many large mammals are holding their own, and the Brobdingnagian Apple and Google are flourishing.

Taleb is aware of these exceptions, but none of us is above bias. While reading *Antifragile*, I found myself thinking more of the exceptions than the rule. The book does not fully explain how to make a system antifragile. Nowhere does Taleb offer, for example, a checklist of things companies or countries can do to prepare for black-swan events.

I have long appreciated Taleb's insistence



Antifragile: Things That Gain From Disorder

NASSIM NICHOLAS TALEB
Random House: 2012.
544 pp. \$30, £25

that we recognize the power of chance and randomness to rule our lives. This is because, by a quirk of our cognition — a process I call 'patternicity' — we tend to find patterns in random noise and concoct probable causal narratives to connect the dots where no connections actually exist. The conspiracy theory is a classic example. For pointing out this tendency alone, Taleb's work commands attention. But much of life is not ruled by randomness and black-swan events, and it is good to bear that in mind when considering what drives change.

The 2008 economic collapse, for example, is cited by Taleb as quintessentially black swanish, but the recovery since has been driven by predictable economic forces implemented judiciously by, in the United States, the federal government and its numerous financial regulators. Moreover, the collapse of the housing and banking industries that triggered the crisis was neither random nor unpredictable. Indeed, Taleb predicted it, on the basis of the long, slow, bubble build-up from easy credit, government policy, Wall Street avarice and other unsurprising forces.

Or take another long-term trend, the decline of violence, documented by psychologist Steven Pinker in *The Better Angels of Our Nature* (Viking, 2011). This has been so slow and steady across so many domains — from wars and homicide to rape, child abuse and beyond — that Pinker needed more than 800 pages to document it. And throughout, no single black-swan-like event emerged to trigger anything but a minor wrinkle in the centuries-long trend.

Most of the time, in most areas of life, the laws of nature and society grind glacially along, oblivious to the occasional blip that may look devastating in the short term, but in the long becomes absorbed in the trend-line. On a graph, such events appear black swanish, but on examination are the result of known forces that may have seemed unpredictable at the time, but in hindsight reveal cause-and-effect relationships in complex systems.

Perhaps this is Taleb's message in *Antifragile*. His heavy emphasis on randomness occasionally obfuscates the power of the predictable, and emphasizing the former over the latter in a narrative of this sweep may distract from this larger point. That aside, there is much to learn from a mind this adroit. If nothing else, it makes you see the world in a new light and that is, possibly, the best way to be antifragile. ■

Michael Shermer is an adjunct professor at Claremont Graduate University and Chapman University, California, and the publisher of *Skeptic* magazine. His latest book is *The Believing Brain*.
e-mail: mshermer@skeptic.com



Aleksandr Oparin (seated) posited that life emerged from compounds in the atmosphere of early Earth.

IN RETROSPECT

The Origin of Life

Clifford P. Brangwynne and Anthony A. Hyman celebrate the first book to plausibly suggest how life began.

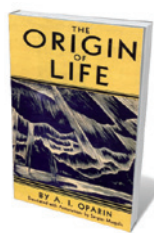
“No religious or philosophical system, no outstanding thinker ever failed to give this question serious consideration.” So wrote Aleksandr Oparin more than 75 years ago, about the quintessential conundrum of how life self-assembled from inanimate components. The Soviet biochemist’s answer is his book *The Origin of Life* (1936). Roughly based on a pamphlet he published in 1924, this book is an enormous contribution to our understanding of life’s improbable beginnings. In it, Oparin argues that conditions on early Earth nurtured the synthesis of amino acids and their assembly into protocells.

Although he trained as a biochemist, Oparin studied the chemical make-up of Earth’s crust, as well as other planets in the Solar System and the Sun. He realized that Earth’s early atmosphere was a strongly reducing environment, rich in methane, water and ammonia. He posited that, with time and a supply of energy such as lightning or geothermal

activity, these simple components would form the complex building blocks of life. And after an English translation was published in 1938, Oparin’s ideas became well known in the West.

Nearly 20 years after the book’s publication — and 60 years ago this year — Stanley Miller and Harold Urey tested Oparin’s hypothesis in a lab at the University of Chicago in Illinois. They sent a continuous electric current through a glass vial containing water, hydrogen, methane and ammonia. Within a week, a substantial amount of the carbon had been converted into complex macromolecules, including many amino acids. This ‘Miller–Urey’ experiment confirmed the significance of Oparin’s ideas, and Miller duly referenced *The Origin of Life*.

Oparin’s work thus played a seminal part in the formulation of our modern ideas of



The Origin of Life
A. I. OPARIN;
TRANSL. SERGIUS
MORGULIS
Macmillan: 1938.

life’s conception. His ideas on the organization of cells and first stirrings of life continued to attract an important audience. In 1957, a large international meeting (attended by Miller) was held in Moscow to discuss the origin of life, the proceedings of which make it clear that Oparin’s book had had a profound influence. And yet, despite his towering achievement, Oparin is today largely forgotten by the broader science community, particularly in the United States. Why?

SOCIAL STRUGGLE

There are two reasons. The first is that after the Second World War, biology in the West moved away from thinking of the cell in physicochemical terms, towards a reductionist molecular-biology approach, with a DNA-centric viewpoint.

The second lies in the cold-war collision between science and politics. Oparin graduated from Moscow State University in 1917, the year of Russia’s October Revolution, and his ideas were forged within that radical context. He explains, for instance, that the question of life’s origin “was always the focal point of a sharp philosophical struggle which reflected the underlying struggle of social classes”. As a prominent Soviet scientist with the full backing of the state, Oparin’s thinking was rooted and framed in the Marxist philosophy that the origin of life is “merely one step in the course of its historical development”.

Not surprisingly, cold-war divisions led many US scientists to dismiss Oparin. The Nobel laureate Hermann Muller, who thought that life originated as a gene, criticized the poor status of DNA within Oparin’s picture of early life. (Oparin apparently stated: “DNA is the end product of metabolism and the nucleus is the dustbin of the cell.”) The proceedings of the 1957 conference point to a growing split between US and Soviet perspectives. With less scientific interchange, the ideas in *The Origin of Life* became marginalized in the West.

After Stalin’s death in 1953 — the year the Miller–Urey experiment was published — Oparin faced criticism within the Soviet Union. He was later forced to resign from the secretaryship of the academy of science because he, along with the rest of the country’s scientific establishment, had supported the discredited agricultural pseudoscientist Trofim Lysenko. Oparin was later forgiven and, in 1979, shortly before his death, received the Lomonosov Gold Medal from the Soviet science academy for outstanding achievement in the natural sciences. His book retained a small but dedicated following.

Today, the primary legacy of *The Origin of Life* is the Miller–Urey experiment, but the synthesis of amino acids took up just part of the book. Oparin went on to describe a mechanism by which macromolecules would self-assemble into large liquid-like structures

➔ **NATURE.COM**
For more on the
Miller–Urey
experiment, see:
go.nature.com/q4f4pa

that he called “complex coacervates” — what today might be called colloidal assemblies. He suggested that these protocells were a key step in the origin of life. However, given the uncertainty at that time about the nature of biological macromolecules, it was unclear exactly how these colloids might form.

This hypothesis of colloidal assembly has largely been displaced by other concepts of life's origins. For example, some hold that membranes must have come first, arguing that the prebiotic soup contained molecules with water-attracting and water-repelling ends capable of self-assembling into cell-like structures (liposomes). Interestingly, later in life, Oparin himself expressed regret at having focused on colloids instead of liposomes.

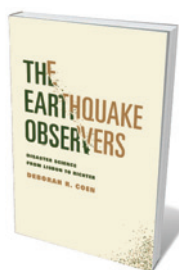
However, current cell and molecular biology provides a new perspective on the feasibility of life beginning from liquid-like macromolecular assemblies, suggesting that Oparin might have been more correct than he thought. Many macromolecules have weak multivalent interactions with other macromolecules, which means they have several sites at which interaction can occur. RNA itself is a flexible, extended, dynamic molecular chain; the interactions between it and other molecules are typically numerous and weak. These properties are sufficient for macromolecules to self-assemble into liquid-phase droplets, like Oparin's coacervates. Recent work on RNA compartmentalization and catalysis in liquid droplets provides additional support for Oparin's concept of primitive protocells in a primordial ‘RNA world’.

Oparin belongs in the pantheon of the twentieth century's greatest scientists for providing a foundation for understanding early molecular evolution. He believed that natural selection had “completely wiped off the face of the Earth all the intermediate forms of organization of primary colloidal systems and of the simplest living things”. Three-quarters of a century before Oparin, Charles Darwin noted that such primitive life forms would be a poor match for contemporary, highly evolved ones. But Darwin also wrote that relatively less-evolved species — “anomalous forms ... living fossils” — often come down through the ages, against all the odds.

Like the ancient mitochondrial organisms found in each of our cells, intracellular RNA droplets could reflect a still more ancient lineage in the assembly of complex cellular structure. Oparin's coacervates may still be alive and well, safe within our cells, like flies in life's evolving amber. ■

Tony Hyman is a cell biologist and director of the Max Planck Institute of Molecular Biology and Genetics in Dresden. **Cliff Brangwynne** is a biophysicist and assistant professor at Princeton University.
e-mails: hyman@mpi-cbg.de;
cbrangwy@Princeton.edu

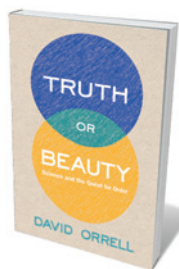
Books in brief



The Earthquake Observers: Disaster Science from Lisbon to Richter

Deborah R. Coen UNIV. CHICAGO PRESS 360 pp. \$35 (2012)

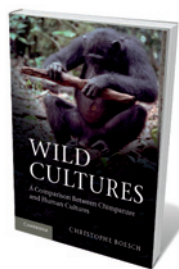
Crowd-sourced science has rarely been so thrilling. As Deborah R. Coen reveals, the rumbustious history of seismology began with roving scientists gathering locals' accounts of shocks, shudders and thumps. Luminaries from Charles Darwin to Alexander von Humboldt reported, too; Charles Dickens likened a quake to a great beast “shaking itself and trying to rise”. Coen argues for a hybridized ‘disaster science’, factoring in such responses from “human seismographs” with geology and instrumental data.



Truth or Beauty: Science and the Quest for Order

David Orrell YALE UNIV. PRESS 356 pp. \$30 (2012)

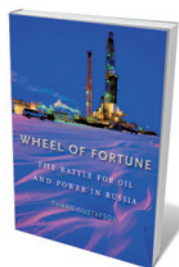
The philosopher Bertrand Russell averred that mathematics has a beauty “sublimely pure, and capable of a stern perfection”. But is science inextricably allied to aesthetic beauty? In applied mathematician David Orrell's exploration of the Pythagorean quest to realise the cosmos mathematically, the cracks in that paradigm show. Orrell swings from the ancient preoccupation with musical harmony and numerical ratios to Renaissance nature studies, the mechanistic approach and the physical sciences of today. Imperfect as it is, ‘messy’ science, he argues, has a novel beauty of its own.



Wild Cultures: A Comparison between Chimpanzee and Human Cultures

Christophe Boesch CAMBRIDGE UNIV. PRESS 288 pp. £60 (2012)

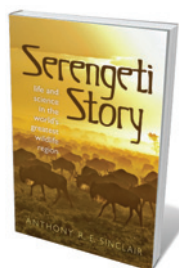
For a third of a century, primatologist Christophe Boesch has hiked in the wilds of Côte d'Ivoire and Gabon in Africa to probe the ‘culture question’ in chimpanzees. Boesch presents systematic evidence for material, social and symbolic culture in wild chimpanzees, drawing too on studies of humans and captive chimps. Comparing the species, he focuses on the teaching and acquisition of cultural traits, and the link between cognition and culture. What makes us human? This book could force a rethink.



Wheel of Fortune: The Battle for Oil and Power in Russia

Thane Gustafson HARVARD UNIV. PRESS 672 pp. \$39.95 (2012)

Russian oil has had a bumpy ride. The world leader in the 1980s, the industry went into steep decline with the Soviet Union's dismantling in 1991. When the Iron Curtain rose, the state's oilmen — mostly geologists and engineers — were shocked by a global industry rife with lawyers and traders. Now oil and roubles shunt through the pipelines of new Russia, but the relationship between state and industry is often explosive. Energy-policy analyst Thane Gustafson reveals Vladimir Putin's pivotal role, the effects of the 2008 crash, and the complex currents and uncertain future of regional oil.

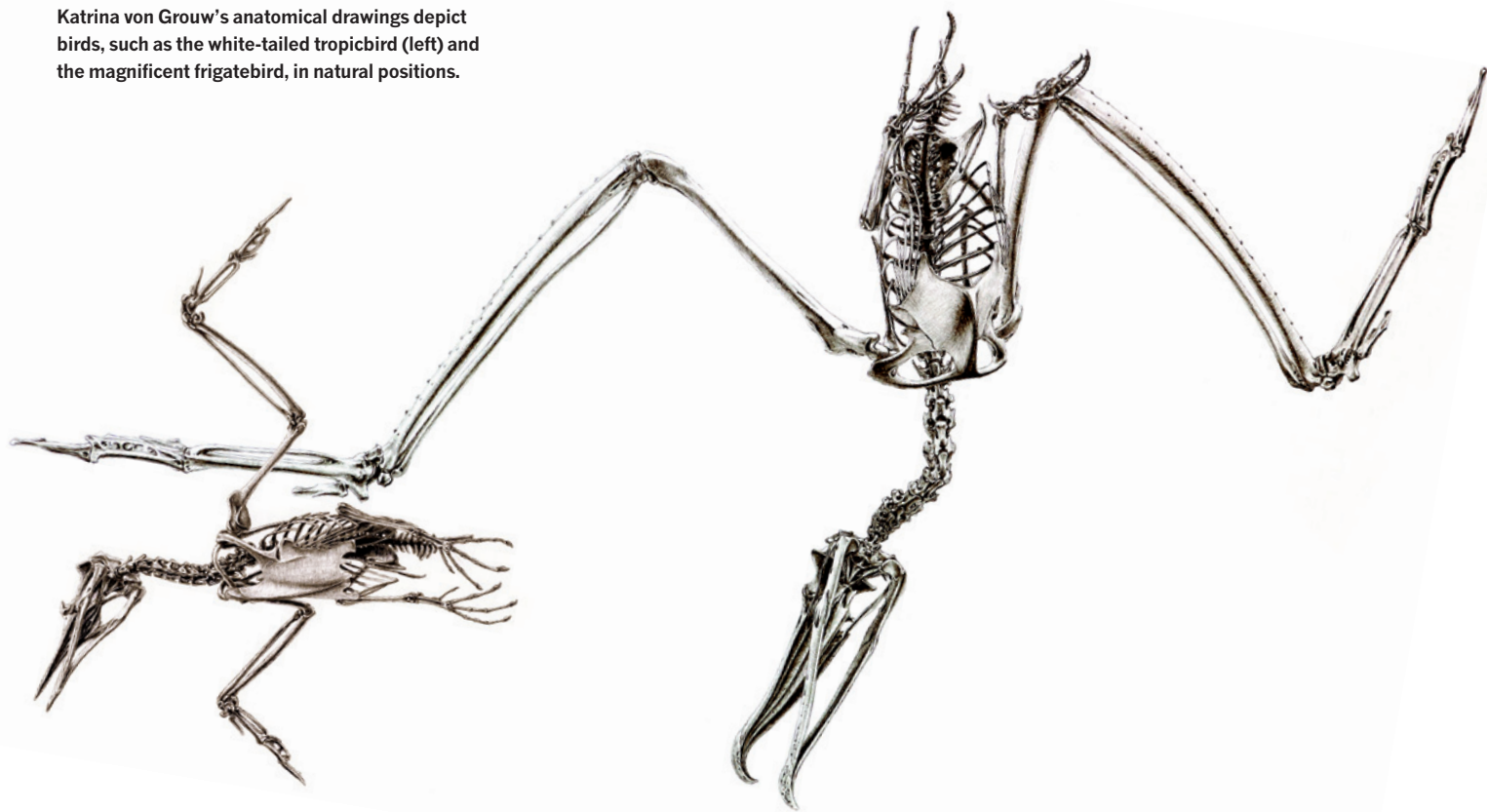


Serengeti Story: Life and Science in the World's Greatest Wildlife Region

Anthony R. E. Sinclair OXFORD UNIV. PRESS 288 pp. £18.99 (2012)

Like some stupendous open-air stage, East Africa's Serengeti ecosystem hosts some of the world's great faunal dramas. Zoologist Anthony Sinclair has been observing them for nearly 50 years. This is a rich interweaving of natural and human history, covering everything from the rinderpest pandemic and ivory exploitation to today's looming threats. Glinting throughout are stories from the field, such as his wife's inadvertent sleep-in with a leopard.

Katrina von Grouw's anatomical drawings depict birds, such as the white-tailed tropicbird (left) and the magnificent frigatebird, in natural positions.



ANATOMY

The bird stripped bare

Alison Abbott enjoys an exquisite tour of skeletal ornithology.

“A convergence of art and science; accessibility and erudition; old and new — without compromise and without apology.” This is how neo-Renaissance ‘birdwoman’ Katrina van Grouw introduces her coffee-table book *The Unfeathered Bird*. And that is exactly what you get.

The book displays van Grouw’s detailed anatomical drawings of bird skeletons and musculature — nearly 400 of them, representing 200 species — alongside her witty and informative text describing each specimen’s adaptation to its environment. A bird’s appearance and behaviour, she explains, influence and are influenced by its skeleton — such as the bony spurs that some have on their wings, used for fighting.

Van Grouw, a qualified natural history illustrator, spent a number of years as a curator of bird specimens at London’s Natural History Museum and taught herself the necessary science to understand her subjects thoroughly. Within a few sentences she can chastise professional ornithologists for their slack terminology, forgive them and deliver her own jargon-free texts that

make concepts such as flight mechanics and evolution appear obvious. For example, she cleverly explains bird anatomy with reference to human anatomy. It is easier to visualize the three major wing sections as evolutionarily equivalent to our upper arm, forearm and hand; a bird’s highly manoeuvrable ‘thumb’ prevents stalling at low flying speeds.

The Unfeathered Bird may be too unsystematic to suit everyone, but that is part of its charm. We learn that genetic analysis unexpectedly confirmed suspicions that New World and Old World vultures may not be related, even though they look and behave similarly — an example of convergent evolution. Carrion birds need to cover large distances with minimum energy expenditure because the carcasses on which



The Unfeathered Bird

KATRINA VAN GROW
Princeton University
Press: 2012. 304 pp.
£34.95, \$49.95

they feed are often scattered. From different starting material on different continents, evolution solved the problem with the same large, highly specialized wing structure. Van Grouw’s focus on the skeleton rather than on external appearance gives the book a special power.

We also learn that not all kingfishers fish, but that hummingbirds do indeed hum. We learn how woodpeckers seemingly defy gravity while boring holes in vertical tree trunks, why there is no reason to pity penguins and that petrels projectile vomit spectacularly onto predators — and nosy ornithologists.

Van Grouw’s book was 25 years in the making: surprisingly quick, considering the work involved. An international list of friends, colleagues, farmers, conservationists — and the occasional taxidermist — donated dead birds for her (and her taxidermist husband) to pluck, skin and boil down to their skeletons. And draw — exquisitely. ■

Alison Abbott is Nature’s senior European correspondent.

K. VAN GROW

Correspondence

Flood defence for financial hubs

Hurricane Sandy is likely to have been a heart-stopping event for officials in many coastal cities around the world — particularly in Shanghai, given its low elevation and complementary status to New York as the financial hub of China.

Shanghai's flood barrier was built more than 20 years ago to protect the old city in Puxi along the Huangpu River waterfront. It could be inadequate against a sea-level rise resulting from this century's predicted 2°C temperature increase due to climate change.

The new financial district across the river in Pudong was constructed at a higher elevation, but its defences could be breached if temperature rises are larger, such as the potential 6°C increase identified as an upper threshold by the PricewaterhouseCoopers Low Carbon Economy Index (see go.nature.com/jvv38l).

Officials in other low-lying coastal cities that are principal economic centres, including Tokyo, Hong Kong, Mumbai and Sydney, need to work out how best to enhance their own protection.

James H. Vance *Taylor, Texas, USA.*

jhv@compuserve.com

Tightening up on tree carbon estimates

During a recent fieldwork campaign with a logging operation in the southwestern Amazon, we weighed a single shihuahuaco tree (*Dipteryx micrantha*) at 76.1 tonnes dry mass, making it the most massive tropical tree ever recorded. Yet its diameter (158 centimetres) and its height (44 metres) were unexceptional. Marked variations in the biomass and species identity of large trees have significant implications

for carbon accounting and the future of tropical forests.

Forest biomass is usually quantified using equations that include parameters such as trunk diameter, height and wood density. However, for this tree, commonly used indirect methods yielded a wide range of estimates, from 17% to 98% of its true mass. Although the biomass of large trees is notoriously difficult to predict, this sixfold range demonstrates the scale of the problem.

Carbon stocks can vary greatly among different species. *Dipteryx* trees have dense wood, slow growth and long lives (up to 1,000 years; J. Q. Chambers *et al.* *Nature* **391**, 135–136; 1998). This is not true of other tree species in the same area. For example, a 115-cm diameter *Cavanillesia umbellata* weighed a mere 2.3 tonnes, which is 12 times lighter than a second *D. micrantha* of comparable size.

This enormous difference in the biomass of two trees of similar dimensions demonstrates the urgent need to improve our understanding of large-tree allometry.

Rosa C. Goodman, Oliver L. Phillips, Timothy R. Baker *School of Geography, University of Leeds, UK.*

rosa.goodman@gmail.com

Global science can bolster diplomacy

The globalization of scientific research (see, for example, *Nature* **490**, 325–329; 2012) has helped to strengthen diplomatic relations between countries around the world, complementing foreign-policy agendas (*Nature* **470**, 425–427; 2011). This underscores the far-reaching impact of governments' investment in science.

As microbiologist Louis Pasteur (1822–95) aptly remarked, “Science knows no country, because knowledge belongs to humanity, and is the

torch which illuminates the world.”

Lindsay Chura *University of Cambridge, UK.*

lrc36@cam.ac.uk

Medicalization of sleep may be needed

As noted by Meredith Wadman in her review of Matthew Wolf-Meyer's book on US sleep medicine, *The Slumbering Masses* (*Nature* **490**, 173–174; 2012), the sweeping generalization that sleep is unnecessarily “medicalized” ignores the drastic consequences of insufficient sleep. Sleep-medicine physicians, like all doctors, have an ethical responsibility to diagnose patients who have a suspected health disorder and to provide them with the most effective treatment.

Chronic sleep deprivation increases the risk of illness and accidents and curtails productivity. Insomnia, the most common complaint, is also associated with a host of morbidities, including psychiatric disorders such as severe depression and the associated risk of suicide. Left untreated, insomnia will seriously damage an individual's health and quality of life.

Sleep medications approved by the US Food and Drug Administration can safely provide relief from insomnia when used properly under the supervision of a physician. Clinical guidelines from my institution, the American Academy of Sleep Medicine, recommend that sedative-hypnotic drugs should be supplemented with behavioural and cognitive therapies, that the lowest effective dose should be prescribed and that medication should be tapered when conditions allow.

Sam Fleishman *American Academy of Sleep Medicine, Darien, Illinois, USA.*
sfleishman@aasmnet.org

Real skin shedding meets mythology

The African spiny mouse represents the first instance of skin shedding in a mammal in which molecular science and the imagination of our ancestors find a common home (A. W. Seifert *et al.* *Nature* **489**, 561–565; 2012).

Stories abound of mammals that can shed and regrow their skins. A letter from the British scholar C. J. Grece to Charles Darwin in 1866 discusses the tale of a large black pig, reported in London's *Morning Star* newspaper (see go.nature.com/szb5df). Grece wrote that the pig “cast its entire skin from the snout to the tail, together with subcutaneous fat of from one to three inches in thickness, leaving a second skin now exposed to the external air. ... The former skin was black and bristly, the new one was, at first, entirely flesh coloured but is changing to black by degrees. ... [The pig] has now naught the matter with it.”

In mythology, a creature known as a selkie, for example, was supposed to shed its skin as it morphed from seal to human. In his *Just So Stories*, Rudyard Kipling in 1902 described a rhinoceros that “took off his skin and carried it over his shoulder as he came down to the beach to bathe”. His neighbour, the Parsee, rubbed that skin with “tickly cake-crumbs and some burned currants” so that, unlike the insouciant pig described to Darwin, the rhinoceros was left “from that day to this” with “a very bad temper”.

Andrew C. Walls *University of Massachusetts Medical School, Worcester, Massachusetts, USA.*
andrew.walls@umassmed.edu

Vanessa E. Johnson *Vanderbilt University School of Medicine, Nashville, Tennessee, USA.*

Scott A. Norton *Children's National Medical Center, Washington DC, USA.*

Synchronized tumbling particles

Magnetic particles have been made that undergo synchronized oscillations when suspended in liquid in a rotating magnetic field. This discovery links the fields of nonlinear dynamics and materials science. [SEE LETTER P.578](#)

SABINE H. L. KLAPP

In 1665, the Dutch scientist Christiaan Huygens discovered that two pendulum clocks mounted on the same wall synchronize with one another — their pendulums swing with the same frequency but exactly out of phase. The origin of this effect is weak coupling of the clocks mediated through the wall's vibrations. Since then, the seemingly old topic of synchronization has developed into one of the most actively studied phenomena, in such diverse contexts as coupled lasers in optics, firing neurons in the brain and people applauding at concerts. So far, however, it has mostly been of conceptual interest to scientists in the fields of applied mathematics, nonlinear dynamics and statistical physics. But with Yan and colleagues' report¹ on page 578 of this issue, the topic now enters the field of materials science. They describe the use of synchronization as a design principle for making micrometre-scale structures.

Yan *et al.* demonstrate their approach in a colloid — a liquid suspension of micrometre-sized particles. The authors' particles are capped on one side with nickel, a magnetically sensitive material, and so are described as magnetic Janus particles; the term Janus alludes to the Roman god who had two different faces on opposite sides of his head (Fig. 1), just as the colloidal particles have a magnetic and a non-magnetic side.

So how can magnetic Janus colloid particles synchronize their behaviour? One key feature of synchronizing dynamic systems is that each unit performs self-sustained oscillations². Yan and colleagues induced oscillations of their Janus particles by placing them in a precessing magnetic field (in which the vector defining the field rotates about the field's directional axis). In this situation, a conventional (paramagnetic) colloidal sphere would acquire a magnetic dipole moment that slavishly follows the motion of the field. The authors' particles, however, are different, because their geometry induces a direction-dependent magnetic response to the field. This causes the axis of symmetry of each particle to undergo a



Figure 1 | Two-faced deity. The Roman god Janus has inspired materials scientists to prepare particles that have two distinct faces — such as the magnetic particles reported by Yan *et al.*¹ that exhibit synchronized behaviour.

persistent, oscillating motion that resembles the 'nutation' movement of a gyroscope¹. Both the phase and the frequency of this oscillation are free (they are not determined by the field), so that the oscillation has adaptable degrees of freedom.

Consider now two magnetic Janus particles in a precessing field. Yan *et al.* observed that, if the spheres are far apart, their oscillations are essentially independent. But at closer distances, each particle is affected by the other's magnetic field. This leads to a dipole–dipole interaction between the particles; the presence of an interaction is the second main ingredient needed for synchronization. Moreover, unlike the oscillatory units in many conventional networks, the authors' magnetic particles can adjust their spatial positions, and so the coupling strength between them. As a consequence, not only do they synchronize their oscillatory phase and frequency, but they also arrange into a dimer-like cluster with 'phase-locked' motion of the magnetic caps — the caps move in such a way that the relative orientation between them does not change (see Fig. 1c of the paper¹).

Yan *et al.* went on to investigate suspensions of many Janus particles, using a combination of

state-of-the-art experimental techniques, computer simulations and theory. They consistently found that synchronization causes the particles to assemble into stable tubular structures (see Fig. 2b of the paper¹), in such a way that the dynamics of particles inside the tubes is coherent and nutation-like. The phase dynamics of the entire tube can be described by the Adler equation of synchronization (which was first suggested by the Japanese physicist Yoshiki Kuramoto in one of the earliest theoretical descriptions of synchronized oscillators³). This is remarkable, because it implies that the complicated tumbling of all the particles in the tube can effectively be considered as a single-particle problem that involves only one phase.

Perhaps not surprisingly, however, Yan and colleagues' colloidal system is far more complex than conventional oscillators. For example, when the authors induced loss of synchronization by changing the field angle (the angle at which the magnetic field precesses about its directional axis), the tubes dissociated into loosely packed zigzag chains. Moreover, they observed that, by slightly varying the parameters of their system, they could select which of several different possible tubular structures forms.

It has long been recognized by materials scientists that complex colloids, such as Janus spheres, form excellent building blocks for nano- and microscale structures, including tubes⁴. However, such structures are traditionally generated by self-assembly processes at equilibrium — that is, the particles form ordered structures because of static particle–particle or particle–field interactions⁵. In these equilibrium systems, different self-assembled structures correspond to different configurations that simultaneously minimize the total energy of the system and maximize the entropy. By contrast, Yan and colleagues' tubular structures are generated by a self-organization process that is not at equilibrium. Their discovery forges a link between synchronization and self-assembly, and will certainly stimulate investigations of other condensed soft-matter systems, from the molecular to the microscale.

There has been enormous recent progress

PHOTO: SCALA, FLORENCE — COURTESY MINISTERO BENI E ATT. CULTURALI

in creating new colloidal building blocks⁶, and it seems likely that many of these could be synchronized when placed in time-dependent fields or exposed to forces that dissipate energy (shear flow). This could open the way to colloidal assemblies relevant to materials science and engineering, including structures that are useful for fluid transport. Such behaviour can be seen in biophysical contexts — for example, the synchronous motion of oscillating organs such as flagella is known to be crucial for the self-propulsion of cells⁷.

Another innovative possibility arising from Yan and colleagues' work is the idea that the dynamics of a colloidal system could be manipulated to form specific assemblies at will. This deliberate selection could perhaps be facilitated using ideas from control theory — a well-established framework in mathematics and engineering for manipulating the dynamics of nonlinear systems to obtain desired outputs or to stabilize specific states.

Finally, it would be interesting to explore

how studies of nonlinear systems could profit from the development of analogous physical systems by materials scientists. For instance, Yan and collaborators' magnetic suspension can be broadly viewed as a network involving non-local coupling of particles. Such networks have been predicted⁸ to spontaneously form 'chimaera' states (which contain domains exhibiting synchronized dynamics and others that have desynchronized dynamics). These states have been experimentally realized only recently in optical⁹ and chemical systems¹⁰. An intriguing question, therefore, is whether Yan and co-workers' magnetic Janus colloids also form chimaera states. If such routes of research are productive, colloidal magnetic suspensions could become model systems for nonlinear behaviour, similar to their well-established role for proving concepts from equilibrium statistical physics¹¹. ■

Sabine H. L. Klapp is at the *Institut für Theoretische Physik, Technische Universität*

Berlin, 10623 Berlin, Germany.
e-mail: klapp@physik.tu-berlin.de

1. Yan, J., Bloom, M., Bae, S.-C., Luijten, E. & Granick, S. *Nature* **491**, 578–581 (2012).
2. Pikovsky, A., Rosenblum, M. & Kurths, J. *Synchronization: A Universal Concept in Nonlinear Science* (Cambridge Univ. Press, 2001).
3. Kuramoto, Y. in *International Symposium on Mathematical Problems in Theoretical Physics* (ed. Arakai, H.) 420 (Springer, 1975).
4. Zerrouki, D., Baudry, J., Pine, D., Chaikin, P. & Bibette, J. *Nature* **455**, 380–382 (2008).
5. Velez, O. D. & Gupta, S. *Adv. Mater.* **21**, 1897–1905 (2009).
6. Damasceno, P. F., Engel, M. & Glotzer, S. C. *Science* **337**, 453–457 (2012).
7. Uchida, N. & Golestanian, R. *Phys. Rev. Lett.* **106**, 058104 (2011).
8. Abrams, D. M. & Strogatz, S. H. *Phys. Rev. Lett.* **93**, 174102 (2004).
9. Hagerstrom, A. M. *et al. Nature Phys.* **8**, 658–661 (2012).
10. Tinsley, M. R., Nkomo, S. & Showalter, K. *Nature Phys.* **8**, 662–665 (2012).
11. Gasser, U., Eisenmann, C., Maret, G. & Keim, P. *ChemPhysChem* **11**, 963–970 (2010).

PALAEOANTHROPOLOGY

Sharpening the mind

The discovery of stone tools dating to 71,000 years ago at a site in South Africa suggests that the humans making them had developed the capacity for complex thought, and passed this knowledge down the generations. SEE LETTER P.590

SALLY MCBREARTY

The origin of human consciousness has historically been of interest to philosophers, clerics, linguists, psychologists and anthropologists. In the past decade, it has also become a key issue for archaeologists. Did the modern manner of human thinking emerge early or late in our species' history, and did it evolve gradually or suddenly? On page 590 of this issue, Brown *et al.*¹ report the discovery of minute stone artefacts that indicate that the bow and arrow was used by people in Africa as early as 71,000 years ago. The manufacture and use of this weaponry system strongly suggest that *Homo sapiens* had by this time already attained mastery of complex technology and ideas*.

Some researchers maintain that there is a disconnect between the appearance of modern human anatomy, which the fossil record shows was present in Africa by 200,000 years (200 kyr) ago², and the emergence of modern human behaviour, which they argue arose as late as 40 kyr ago³. A proposed explanation for this time lag is that a genetic mutation that affected cognitive capability occurred sometime between 50 and 40 kyr ago, and persisted

thereafter³. However, I believe that modern cognitive capacity emerged at the same time as modern anatomy, and that various aspects of human culture arose gradually over the course of subsequent millennia⁴. Brown and colleagues' findings go some way to supporting this hypothesis.

Africa is vast and has been populated by humans and their hominin ancestors for more than 5 million years, yet only a small fraction of the continent has been explored systematically by archaeologists. The vagaries of the preservation of artefacts and fossils also affect what we can know about the past. So it is not surprising that a complete, continuous record of human activities has not been documented.

Even if the record were more complete, it would still be likely that many aspects of past behaviour would be represented patchily or not at all. But some scientists suggest that the gaps in the record are meaningful, reflecting the incomplete development of human cultural capacity³, the isolation of small dispersed prehistoric populations, or the inherent variability of human adaptation. Certain types of evidence believed to represent modern thought are found repeatedly, but at sites scattered across Africa and dating to disparate times. Whether the discontinuities observed in the current record are simply a manifestation

of an incomplete record or a real reflection of early *H. sapiens*' inability to maintain innovations and communicate them to others remains a topic of debate.

Another consideration is that the date for the appearance of modern human behaviour will, of course, depend on the criteria used to recognize it⁵. Researchers have employed a variety of measures for this purpose, but most recent discussions⁶ have opted for artefacts with symbolic content, such as art or ornaments, as the defining benchmark for modern cognitive capacity. The reasoning behind this is that the production of such objects requires the ability to manipulate symbols, and this, by extension, indicates the presence of language. Some researchers include the use of pigment as a signal of symbolic thought^{4,6,7}, and the record shows that colouring materials may have been used as early as 200 or 300 kyr ago^{4,8} (Fig. 1). Body ornaments, such as beads^{9–12}, and carved decorations on everyday objects^{13,14} are almost universally accepted as evidence of symbolic thought, and such items appear in the African record between 100 and 60 kyr ago. But critics of these claims contend that the link between the material objects and the mode of thought is not well established¹⁵, or that the dating of the objects or the context in which they have been found is suspect.

Brown and co-authors take a different approach. They argue that complex technology demonstrates the capacity for complex ideas and for transmission of these ideas, and hence for language. This reasoning stems from the authors' finding of small stone 'bladelets' (microliths) at Pinnacle Point Site 5–6 (PP5–6) in South Africa. The authors provide superb

➔ **NATURE.COM**
For more on
technology and
early humans, see:
go.nature.com/rrfvzg

*This article and the paper under discussion¹ were published online on 7 November 2012.

in creating new colloidal building blocks⁶, and it seems likely that many of these could be synchronized when placed in time-dependent fields or exposed to forces that dissipate energy (shear flow). This could open the way to colloidal assemblies relevant to materials science and engineering, including structures that are useful for fluid transport. Such behaviour can be seen in biophysical contexts — for example, the synchronous motion of oscillating organs such as flagella is known to be crucial for the self-propulsion of cells⁷.

Another innovative possibility arising from Yan and colleagues' work is the idea that the dynamics of a colloidal system could be manipulated to form specific assemblies at will. This deliberate selection could perhaps be facilitated using ideas from control theory — a well-established framework in mathematics and engineering for manipulating the dynamics of nonlinear systems to obtain desired outputs or to stabilize specific states.

Finally, it would be interesting to explore

how studies of nonlinear systems could profit from the development of analogous physical systems by materials scientists. For instance, Yan and collaborators' magnetic suspension can be broadly viewed as a network involving non-local coupling of particles. Such networks have been predicted⁸ to spontaneously form 'chimaera' states (which contain domains exhibiting synchronized dynamics and others that have desynchronized dynamics). These states have been experimentally realized only recently in optical⁹ and chemical systems¹⁰. An intriguing question, therefore, is whether Yan and co-workers' magnetic Janus colloids also form chimaera states. If such routes of research are productive, colloidal magnetic suspensions could become model systems for nonlinear behaviour, similar to their well-established role for proving concepts from equilibrium statistical physics¹¹. ■

Sabine H. L. Klapp is at the *Institut für Theoretische Physik, Technische Universität*

Berlin, 10623 Berlin, Germany.
e-mail: klapp@physik.tu-berlin.de

1. Yan, J., Bloom, M., Bae, S.-C., Luijten, E. & Granick, S. *Nature* **491**, 578–581 (2012).
2. Pikovsky, A., Rosenblum, M. & Kurths, J. *Synchronization: A Universal Concept in Nonlinear Science* (Cambridge Univ. Press, 2001).
3. Kuramoto, Y. in *International Symposium on Mathematical Problems in Theoretical Physics* (ed. Arakai, H.) 420 (Springer, 1975).
4. Zerrouki, D., Baudry, J., Pine, D., Chaikin, P. & Bibette, J. *Nature* **455**, 380–382 (2008).
5. Velez, O. D. & Gupta, S. *Adv. Mater.* **21**, 1897–1905 (2009).
6. Damasceno, P. F., Engel, M. & Glotzer, S. C. *Science* **337**, 453–457 (2012).
7. Uchida, N. & Golestanian, R. *Phys. Rev. Lett.* **106**, 058104 (2011).
8. Abrams, D. M. & Strogatz, S. H. *Phys. Rev. Lett.* **93**, 174102 (2004).
9. Hagerstrom, A. M. *et al. Nature Phys.* **8**, 658–661 (2012).
10. Tinsley, M. R., Nkomo, S. & Showalter, K. *Nature Phys.* **8**, 662–665 (2012).
11. Gasser, U., Eisenmann, C., Maret, G. & Keim, P. *ChemPhysChem* **11**, 963–970 (2010).

PALAEOANTHROPOLOGY

Sharpening the mind

The discovery of stone tools dating to 71,000 years ago at a site in South Africa suggests that the humans making them had developed the capacity for complex thought, and passed this knowledge down the generations. SEE LETTER P.590

SALLY MCBREARTY

The origin of human consciousness has historically been of interest to philosophers, clerics, linguists, psychologists and anthropologists. In the past decade, it has also become a key issue for archaeologists. Did the modern manner of human thinking emerge early or late in our species' history, and did it evolve gradually or suddenly? On page 590 of this issue, Brown *et al.*¹ report the discovery of minute stone artefacts that indicate that the bow and arrow was used by people in Africa as early as 71,000 years ago. The manufacture and use of this weaponry system strongly suggest that *Homo sapiens* had by this time already attained mastery of complex technology and ideas*.

Some researchers maintain that there is a disconnect between the appearance of modern human anatomy, which the fossil record shows was present in Africa by 200,000 years (200 kyr) ago², and the emergence of modern human behaviour, which they argue arose as late as 40 kyr ago³. A proposed explanation for this time lag is that a genetic mutation that affected cognitive capability occurred sometime between 50 and 40 kyr ago, and persisted

thereafter³. However, I believe that modern cognitive capacity emerged at the same time as modern anatomy, and that various aspects of human culture arose gradually over the course of subsequent millennia⁴. Brown and colleagues' findings go some way to supporting this hypothesis.

Africa is vast and has been populated by humans and their hominin ancestors for more than 5 million years, yet only a small fraction of the continent has been explored systematically by archaeologists. The vagaries of the preservation of artefacts and fossils also affect what we can know about the past. So it is not surprising that a complete, continuous record of human activities has not been documented.

Even if the record were more complete, it would still be likely that many aspects of past behaviour would be represented patchily or not at all. But some scientists suggest that the gaps in the record are meaningful, reflecting the incomplete development of human cultural capacity³, the isolation of small dispersed prehistoric populations, or the inherent variability of human adaptation. Certain types of evidence believed to represent modern thought are found repeatedly, but at sites scattered across Africa and dating to disparate times. Whether the discontinuities observed in the current record are simply a manifestation

of an incomplete record or a real reflection of early *H. sapiens*' inability to maintain innovations and communicate them to others remains a topic of debate.

Another consideration is that the date for the appearance of modern human behaviour will, of course, depend on the criteria used to recognize it⁵. Researchers have employed a variety of measures for this purpose, but most recent discussions⁶ have opted for artefacts with symbolic content, such as art or ornaments, as the defining benchmark for modern cognitive capacity. The reasoning behind this is that the production of such objects requires the ability to manipulate symbols, and this, by extension, indicates the presence of language. Some researchers include the use of pigment as a signal of symbolic thought^{4,6,7}, and the record shows that colouring materials may have been used as early as 200 or 300 kyr ago^{4,8} (Fig. 1). Body ornaments, such as beads^{9–12}, and carved decorations on everyday objects^{13,14} are almost universally accepted as evidence of symbolic thought, and such items appear in the African record between 100 and 60 kyr ago. But critics of these claims contend that the link between the material objects and the mode of thought is not well established¹⁵, or that the dating of the objects or the context in which they have been found is suspect.

Brown and co-authors take a different approach. They argue that complex technology demonstrates the capacity for complex ideas and for transmission of these ideas, and hence for language. This reasoning stems from the authors' finding of small stone 'bladelets' (microliths) at Pinnacle Point Site 5–6 (PP5–6) in South Africa. The authors provide superb

➔ **NATURE.COM**
For more on
technology and
early humans, see:
go.nature.com/rrfvzg

*This article and the paper under discussion¹ were published online on 7 November 2012.

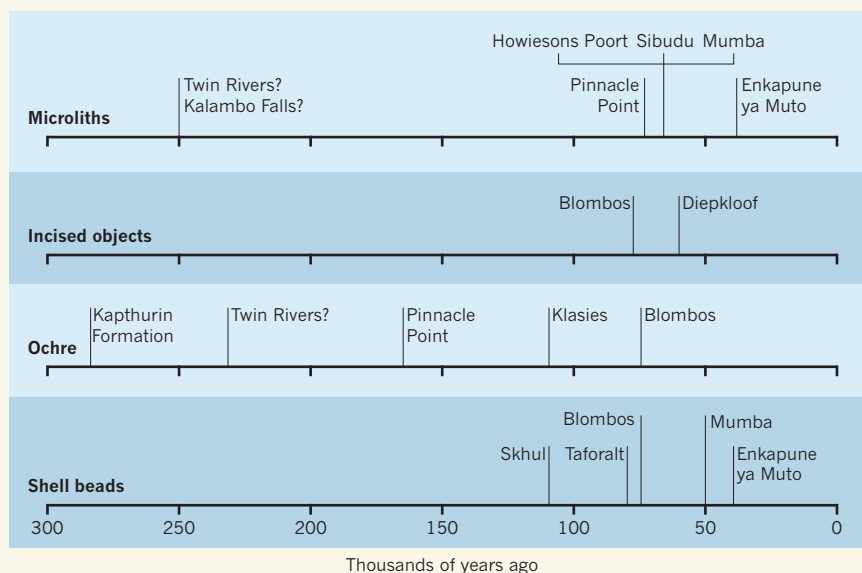


Figure 1 | Archaeological evidence for modern behaviour in early *Homo sapiens*. According to the fossil record, modern human anatomy dates to approximately 200,000 years ago². The archaeological evidence that is used to determine the time and pattern of the emergence of modern human thought and behaviour comes in the form of the production of microliths (small stone tools); the use of ochre (haematite) as a pigment; the decoration of objects with incised motifs; and the creation of shell beads. The coastal site of Pinnacle Point in South Africa contains colouring materials⁴, and Brown *et al.*¹ now describe microliths from this site. Other site locations are: Twin Rivers, Zambia; Kalambo Falls, Zambia; Howiesons Poort, South Africa; Sibudu, South Africa; Mumba, Tanzania; Enkapune ya Muto, Kenya; Klasies, South Africa; Kaphurin Formation, Kenya; Blombos, South Africa; Diepkloof, South Africa; Skhul, Israel; and Taforalt, Morocco.

contextual information in the form of detailed stratigraphic description and finely controlled spatial locations for all objects. Dating using the technique of optically stimulated luminescence indicates an age for this material of approximately 70 kyr ago, showing that humans inhabiting the area at this time had the advanced skills required to produce these tools. Notably, it has been suggested¹⁶ that microlithic technology was present in central Africa much earlier, 200–300 kyr ago, but the context and dating of those finds are uncertain.

Humans making the PP5–6 microliths would have chipped small bladelets from stone that had been carefully selected for its textural properties and heat-treated to improve its workability; they would then have retouched the bladelets into small geometric shapes. When such geometric microliths are found in exceptional prehistoric contexts in which wood is preserved, they are part of arrows¹⁷ (Fig. 2). Microliths are also associated with

the technology of the South African Howiesons Poort industry, which is dated to 60–65 kyr ago (Fig. 1), and analysis of the impact-damage marks and organic residues on Howiesons Poort microliths from the site of Sibudu supports the idea that they are part of complex projectiles¹⁸. The presence of microliths at PP5–6 therefore strongly suggests that the inhabitants of this site used the bow and arrow, although similar damage and residue analysis of the PP5–6 artefacts would enhance our understanding of their use.

Brown and colleagues spell out the six steps that would have been involved in the manufacture of the PP5–6 microliths: collecting and transporting the lithic raw material; gathering wood fuel; heat treating the stone; preparing the stone core; producing the bladelets; and trimming the bladelets into their final shape. The incorporation of these stone tools into arrow armatures and the manufacture of the bow and arrow would have required several

additional steps involving the collection and modification of a variety of materials, including wood, fibre and mastic, and possibly also feathers, bone and sinew. These operations would no doubt have taken place over the course of days, weeks or months, and would have been interrupted by attention to unrelated, more urgent tasks.

The ability to hold and manipulate operations and images of objects in memory, and to execute goal-directed procedures over space and time, is termed executive function¹⁵ and is an essential component of the modern mind. Brown and colleagues' report indicates that this capacity was present in South Africa by 71 kyr ago. Furthermore, their data show that microlithic technology persisted at Pinnacle Point for more than 10 kyr, suggesting that the details of the process were communicated among individuals over many generations.

Brown and colleagues' study may also help us to understand other aspects of the development and spread of modern humans. Users of the bow and arrow have a significant advantage over people limited to hand-delivered weapons in both hunting and interpersonal conflict¹⁹. Human populations are thought to have started migrating from Africa shortly after 100 kyr ago²⁰. If they were armed with the bow and arrow, they would have been more than a match for anything or anyone they met. ■

Sally McBrearty is in the Department of Anthropology, University of Connecticut, Storrs, Connecticut 06269-2176, USA.
e-mail: mcbrearty@uconn.edu

1. Brown, K. S. *et al.* *Nature* **491**, 590–593 (2012).
2. McDougall, I., Brown, F. H. & Fleagle, J. G. *J. Hum. Evol.* **55**, 409–420 (2008).
3. Klein, R. G. & Edgar, B. *The Dawn of Human Culture* (Wiley, 2002).
4. McBrearty, S. & Brooks, A. S. *J. Hum. Evol.* **39**, 453–563 (2000).
5. Wynn, T. & Coolidge, F. L. in *Cognitive Archaeology and Human Evolution* (eds de Beaune, S., Coolidge, F. L. & Wynn, T.) 117–127 (Cambridge, 2009).
6. Henshilwood, C. S. & Marean, C. W. *Curr. Anthropol.* **44**, 627–651 (2003).
7. McBrearty, S. & Stringer, C. *Nature* **449**, 793–794 (2007).
8. Barham, L. S. *Curr. Anthropol.* **43**, 181–190 (2002).
9. Henshilwood, C., d'Errico, F., Vanhaeren, M., van Niekerk, K. & Jacobs, Z. *Science* **304**, 404 (2004).
10. Vanhaeren, M. *et al.* *Science* **312**, 1785–1788 (2006).
11. Bouzouggar, A. *et al.* *Proc. Natl Acad. Sci. USA* **104**, 9964–9969 (2007).
12. d'Errico, F. *et al.* *Proc. Natl Acad. Sci. USA* **106**, 16051–16056 (2009).
13. Henshilwood, C. S., d'Errico, F. & Watts, I. *J. Hum. Evol.* **57**, 27–47 (2009).
14. Texier, P.-J. *Proc. Natl Acad. Sci. USA* **107**, 6180–6185 (2010).
15. Wynn, T. & Coolidge, F. L. *Curr. Anthropol.* **51**, S5–S16 (2010).
16. Barham, L. J. *J. Hum. Evol.* **43**, 585–603 (2002).
17. Rozoy, J.-G. in *The Mesolithic in Europe* (ed. Bonsall, C.) 13–28 (Donald, 1989).
18. Lombard, M. J. *Archaeol. Sci.* **38**, 1918–1930 (2011).
19. Cattelain, P. in *Projectile Technology* (ed. Knecht, H.) 213–240 (Plenum, 1997).
20. Forster, P. *Phil. Trans. R. Soc. Lond. B* **359**, 255–264 (2004).

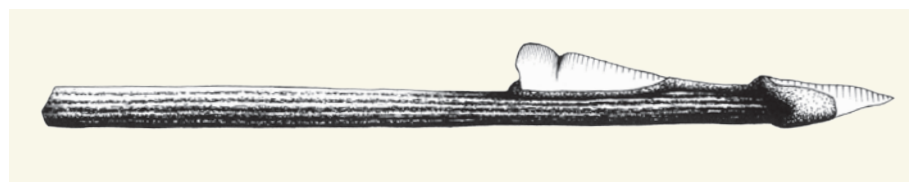


Figure 2 | A complex point. This intact arrow from Rönneholm, Sweden, dating to approximately 9,000 years ago¹⁷, shows a method of hafting microliths onto a wooden shaft. A similar function is proposed for the 71,000-year-old microliths from South Africa, described by Brown *et al.*¹. (Image adapted from ref. 17.)

PHYSICAL CHEMISTRY

Water's response to the fear of water

Spectroscopic analysis reveals that, at low temperatures, hydrophobic molecules dissolved in water strengthen the hydrogen bonding between nearby water molecules. But at high temperatures, the reverse can be true. [SEE LETTER P.582](#)

HUIB J. BAKKER

Water-repellent molecules are said to be hydrophobic — which, literally translated, means they have a fear of water. But unlike human phobias, the effects of the molecular fear of water are difficult to predict. For example, if a nanometre-scale hydrophobic ball is inserted into liquid water, one might expect it to break up the hydrogen bonds between water molecules, thus strongly increasing disorder. The actual outcome, however, is much more complex, and so the effects of hydrophobic solutes on the structure of their hydration shells — the layers of water molecules that surround the solutes — have been a topic of debate for almost 70 years. On page 582 of this issue, Davis *et al.*¹ present an invaluable contribution to the discussion by showing that hydrophobic groups in molecules in fact enhance the ordering of the surrounding hydrogen-bond network of water.

The debate about the effect of hydrophobic molecular groups on water goes back to the work of Frank and Evans² in the 1940s. They discovered that the hydration of such groups is associated with a decrease of entropy. In addition, they observed that the heat capacity of the resulting solutions becomes anomalously high. Both these effects suggest that a hydrophobic solute induces a strong ordering of the surrounding water. On the basis of these findings, Frank and Evans formulated the 'iceberg' model for hydrophobic hydration². In this model, hydrophobic solute molecules create ice-like 'clathrate' structures in the surrounding water. The high local order of these structures could explain the observed entropy decreases associated with the hydration of hydrophobic molecules, whereas 'melting' of ice-like hydration shells could account for the large increases in heat capacity.

During the subsequent decades, the iceberg model has been severely challenged, in particular by neutron-diffraction studies. In these studies, the distance between water molecules near hydrophobic solutes was found to be quite similar to that in bulk liquid water, thereby casting serious doubts on the existence of any local ice-like structures^{3,4}. Moreover, theoretical studies have shown that the thermodynamics of hydrophobic-molecule hydration do not

require the surrounding water to be different from bulk water — the observed entropy decrease can be explained as the effect of the exclusion of water from the volume taken up by the molecule⁵. The water around a solute can maintain the same amount of hydrogen bonding as in the bulk liquid, at least for small hydrophobic solutes (less than 1 nanometre in diameter), in the same way that one can create a hole in a loosely woven fabric without breaking the threads.

Davis and colleagues' experiments shed fresh light on the structure of water surrounding hydrophobic solutes, using a spectroscopic method called Raman multivariate curve resolution. This method allows spectral features associated with the vibrational modes of water molecules hydrating the solute to be selectively extracted. Specifically, the authors obtained the spectra of water molecules that were locally hydrating alcohol molecules, for a variety of alcohols bearing hydrophobic groups of different lengths. By focusing on the spectral features corresponding to vibrations of water's hydroxyl (OH) groups, they obtained information about the strength and the distribution of hydrogen bonds around the alcohols' hydrophobic groups. The authors observed that the hydrogen-bond network in this region is significantly enhanced — that is, more ordered than in bulk liquid water.

How should one envisage this enhanced hydrogen-bond structure? It cannot be truly ice-like, because this would contradict the previous neutron-scattering data. The picture that emerges is that the methyl (CH₃) and methylene (CH₂) groups of the alcohols' hydrophobic groups form ideal templates around which the water network can fold, leading to locally enhanced, tetrahedral order. This network will consist of ridges approximately 0.3 nm in height (the intermolecular distance of the water molecules), with ridge angles of 104.5° (the intramolecular bond angle of the water molecule), as is generally the case for hydrogen-bond networks in water.

Davis *et al.* further found that the enhanced hydrogen-bond structure vanishes when the temperature of the solution is increased. For instance, they observed that the hydrogen bonding of the hydration shell of *n*-pentanol (C₅H₁₁OH) at 60 °C is similar to that of bulk



50 Years Ago

During September 1961, immediately following the resumption of nuclear testing, when there was widespread public concern that the amount of iodine-131 in human thyroids might reach significant proportions, it was decided to make regular measurements of thyroid radioactivity on a few members of the staff at the Radiological Protection Service ... During the peak period a total of 20 members of the staff were measured and the average amount of iodine-131 in their thyroids was 0.25 μmc ... the average amount of iodine-131 actually measured in the thyroids of the group could be predicted from a knowledge of the iodine uptake into the thyroid and the known concentration of iodine-131 in milk during this period. This adds weight to the belief, now widely accepted, that fresh milk is the principal vehicle whereby iodine-131 from nuclear test explosions enters humans.

From *Nature* 24 November 1962

100 Years Ago

The Vulgate Version of the French Arthurian Romances. Edited from manuscripts in the British Museum by H. Oskar Sommer — These sumptuous volumes are priceless gifts to the world of scholarship by the Carnegie Institution of Washington ... In his introduction the editor gives an outline of his studies of the vulgate cycle, as the French version of the Arthurian prose-romances is called ... The core of the typical tale of the conception and birth of an illustrious child of unknown father and a king's wife or daughter appears in the Welsh and Irish versions as something separate from any moral considerations ... We must come down to the vulgate cycle to find in such legends the element of sin.

From *Nature* 21 November 1912

water. This finding is in line with the original ideas of Frank and Evans: the ordered water structures surrounding hydrophobic groups 'melt' upon an increase in temperature.

The enhanced hydrogen-bond structure of the hydration shell and its disappearance upon heating have counterparts in the shells' dynamics. The molecular reorientation of water primarily proceeds through the transient formation of defects in its hydrogen-bond network — particularly the formation of bifurcated hydrogen bonds⁶, in which a single hydrogen atom contributes to two hydrogen bonds. The fact that water is excluded from the volume filled by a solute reduces the rate of formation of defects in hydration shells⁷, an effect that is amplified by the enhancement of the hydrogen-bond network. So, water molecules hydrating a hydrophobic group should undergo slower reorientations than those in the bulk, as is indeed observed in spectroscopic studies^{8–10}. As temperature increases, the enhanced hydrogen-bond structure gradually vanishes, which means that the density of weak and/or defective hydrogen bonds also increases. On heating, therefore, the orientational dynamics of water in hydration shells ought to speed up more than the dynamics of bulk water. Again, this effect has been observed^{8–10}.

Davis *et al.* report another interesting effect for alcohols that have hydrophobic chains longer than 1 nm — at temperatures above 80 °C, the water surrounding the hydrophobic chains acquires a structure that is less ordered than bulk liquid water at the same temperature. This phenomenon has been predicted by theory⁵, and brings us back to the effect of inserting a hydrophobic ball into water: for a large ball with a diameter greater than 1 nm, the curvature of its surface does not fit into the three-dimensional arrangement of the hydrogen bonds of water, and so causes hydrogen bonds near the ball's surface to break up⁵. There is thus a striking difference between small hydrophobic structures of about 0.5 nm in diameter, which enhance the surrounding hydrogen-bond network, and large hydrophobic structures greater than 1 nm in diameter, which break the hydrogen bonds of nearby water molecules.

These findings contribute to our understanding of the hydrophobic interaction — the tendency of hydrophobic groups to cluster together in liquid water. The hydrophobic interaction is one of the most important driving forces in nature, and is key to processes such as protein folding and the self-assembly of lipid membranes. The present study shows that the interaction of a solute with surrounding water is more than just the sum of local chemical interactions; the water's structure strongly depends on how well the solute fits into the water network. The structure of water surrounding a biomolecular solute will thus be the result of a complex interplay of the sizes and

relative positions of the solute's hydrophobic and hydrophilic regions. It is to be hoped that future studies will shed light on these combined effects, and thereby pave the way to a full understanding of the conformational dynamics and aggregation of biomolecules in liquid water. ■

Huib J. Bakker is in the Department of Molecular Nanophysics, FOM Institute AMOLF, Science Park 104, 1098 XG Amsterdam, the Netherlands. e-mail: bakker@amolf.nl

1. Davis, J. G., Gierszal, K. P., Wang, P. & Ben-Amotz, D.

REPRODUCTIVE BIOLOGY

Stem cells bear eggs

Researchers have coaxed cultured embryonic stem cells to develop into eggs that then give rise to normal offspring. The discovery should help to decode the molecular basis of gamete formation and might lead to treatments for infertility.

SIHEM CHELOUFI & KONRAD HOCHEDLINGER

Unlike testes, ovaries do not make gametes throughout life: female mammals are born with a limited supply of oocytes (eggs), which progressively decrease in number until the menopause. This biological barrier has complicated the study both of oocyte development in mammals and of the mechanisms underlying female infertility. Reporting in the latest issue of *Science*, Hayashi *et al.*¹ have induced embryonic stem cells to develop into mature oocytes that, when fertilized, give rise to apparently normal, fertile animals. Together with another report² by the same group on the generation of functional sperm cells from embryonic stem cells, these findings provide the first efficient and accessible protocols to recapitulate male and female gametogenesis from cultured stem cells.

Pluripotency denotes the capacity of cells to give rise to essentially all cell types of the body, including oocytes and sperm. Pluripotent cells normally reside in the early embryo, before and shortly after it implants in the uterus wall. The pluripotent state can be stably captured *in vitro* through the culture of pre-implantation-stage embryos called blastocysts to generate embryonic stem (ES) cells. Moreover, induced pluripotent stem (iPS) cells can be derived from differentiated cell types by introducing a cocktail of transcription factors³. Despite their different origins, iPS cells are highly similar to ES cells at molecular and functional levels.

Because of the developmental plasticity of ES and iPS cells, and the ease with which they can be derived from both mice and humans, stem-cell researchers have focused much

- Nature* **491**, 582–585 (2012).
- Frank, H. S. & Evans, M. W. *J. Chem. Phys.* **13**, 507–532 (1945).
 - Soper, A. K. & Finney, J. L. *Phys. Rev. Lett.* **71**, 4346–4349 (1993).
 - Dixit, S., Crain, S. J., Poon, W. C. K., Finney, J. L. & Soper, A. K. *Nature* **416**, 829–832 (2002).
 - Chandler, D. *Nature* **437**, 640–647 (2005).
 - Laage, D. & Hynes, J. T. *Science* **311**, 832–835 (2006).
 - Laage, D., Stirnemann, G. & Hynes, J. T. *J. Phys. Chem. B* **113**, 2428–2435 (2009).
 - Ishihara, Y., Okouchi, S. & Uedaira, H. *J. Chem. Soc. Faraday Trans.* **93**, 3337–3342 (1997).
 - Yoshida, K., Ibuki, K. & Ueno, M. *J. Chem. Phys.* **108**, 1360–1367 (1998).
 - Petersen, C., Tielrooij, K.-J. & Bakker, H. J. *J. Chem. Phys.* **130**, 214511 (2009).

of their attention on understanding how to instruct the cells to become therapeutically relevant, differentiated cell types *in vitro*. Indeed, scientists have been able to produce nerve cells, heart-muscle cells and gut cells, among others, from cultured pluripotent cells. However, it has been notoriously difficult to derive functional gametes from ES cells⁴. This is not surprising, because germ-cell maturation is a complex process of cellular, chromosomal and molecular changes that endow mature sperm and oocytes with the unique potential to give rise to an entire organism after fertilization.

In an experimental tour de force, Hayashi and co-workers¹ generated oocytes from ES and iPS cells by devising a multi-step procedure that mimics the events occurring in developing embryos (Fig. 1). Shortly after implantation, early gamete precursors, called primordial germ cells (PGCs), are specified within a layer of advanced-stage pluripotent cells called the epiblast, which is poised for differentiation⁵. In a first step, the authors identified a combination of growth factors that could efficiently generate epiblast-like cells from ES cells. The epiblast-like cells were then exposed to the growth factors that induce germ-cell formation *in vivo*, and so gave rise to PGC-like cells *in vitro*.

To reset the genome of germ cells for the next generation, PGCs have to lose certain genome-wide chemical modifications that control gene activity⁵. These epigenetic marks include DNA methylation of imprinted genes, which are expressed in a sex-specific manner from the maternal or paternal chromosomes, and have crucial roles in fetal growth. In developing oocytes and sperm, these marks are

water. This finding is in line with the original ideas of Frank and Evans: the ordered water structures surrounding hydrophobic groups 'melt' upon an increase in temperature.

The enhanced hydrogen-bond structure of the hydration shell and its disappearance upon heating have counterparts in the shells' dynamics. The molecular reorientation of water primarily proceeds through the transient formation of defects in its hydrogen-bond network — particularly the formation of bifurcated hydrogen bonds⁶, in which a single hydrogen atom contributes to two hydrogen bonds. The fact that water is excluded from the volume filled by a solute reduces the rate of formation of defects in hydration shells⁷, an effect that is amplified by the enhancement of the hydrogen-bond network. So, water molecules hydrating a hydrophobic group should undergo slower reorientations than those in the bulk, as is indeed observed in spectroscopic studies^{8–10}. As temperature increases, the enhanced hydrogen-bond structure gradually vanishes, which means that the density of weak and/or defective hydrogen bonds also increases. On heating, therefore, the orientational dynamics of water in hydration shells ought to speed up more than the dynamics of bulk water. Again, this effect has been observed^{8–10}.

Davis *et al.* report another interesting effect for alcohols that have hydrophobic chains longer than 1 nm — at temperatures above 80 °C, the water surrounding the hydrophobic chains acquires a structure that is less ordered than bulk liquid water at the same temperature. This phenomenon has been predicted by theory⁵, and brings us back to the effect of inserting a hydrophobic ball into water: for a large ball with a diameter greater than 1 nm, the curvature of its surface does not fit into the three-dimensional arrangement of the hydrogen bonds of water, and so causes hydrogen bonds near the ball's surface to break up⁵. There is thus a striking difference between small hydrophobic structures of about 0.5 nm in diameter, which enhance the surrounding hydrogen-bond network, and large hydrophobic structures greater than 1 nm in diameter, which break the hydrogen bonds of nearby water molecules.

These findings contribute to our understanding of the hydrophobic interaction — the tendency of hydrophobic groups to cluster together in liquid water. The hydrophobic interaction is one of the most important driving forces in nature, and is key to processes such as protein folding and the self-assembly of lipid membranes. The present study shows that the interaction of a solute with surrounding water is more than just the sum of local chemical interactions; the water's structure strongly depends on how well the solute fits into the water network. The structure of water surrounding a biomolecular solute will thus be the result of a complex interplay of the sizes and

relative positions of the solute's hydrophobic and hydrophilic regions. It is to be hoped that future studies will shed light on these combined effects, and thereby pave the way to a full understanding of the conformational dynamics and aggregation of biomolecules in liquid water. ■

Huib J. Bakker is in the Department of Molecular Nanophysics, FOM Institute AMOLF, Science Park 104, 1098 XG Amsterdam, the Netherlands. e-mail: bakker@amolf.nl

1. Davis, J. G., Gierszal, K. P., Wang, P. & Ben-Amotz, D.

REPRODUCTIVE BIOLOGY

Stem cells bear eggs

Researchers have coaxed cultured embryonic stem cells to develop into eggs that then give rise to normal offspring. The discovery should help to decode the molecular basis of gamete formation and might lead to treatments for infertility.

SIHEM CHELOUFI & KONRAD HOCHEDLINGER

Unlike testes, ovaries do not make gametes throughout life: female mammals are born with a limited supply of oocytes (eggs), which progressively decrease in number until the menopause. This biological barrier has complicated the study both of oocyte development in mammals and of the mechanisms underlying female infertility. Reporting in the latest issue of *Science*, Hayashi *et al.*¹ have induced embryonic stem cells to develop into mature oocytes that, when fertilized, give rise to apparently normal, fertile animals. Together with another report² by the same group on the generation of functional sperm cells from embryonic stem cells, these findings provide the first efficient and accessible protocols to recapitulate male and female gametogenesis from cultured stem cells.

Pluripotency denotes the capacity of cells to give rise to essentially all cell types of the body, including oocytes and sperm. Pluripotent cells normally reside in the early embryo, before and shortly after it implants in the uterus wall. The pluripotent state can be stably captured *in vitro* through the culture of pre-implantation-stage embryos called blastocysts to generate embryonic stem (ES) cells. Moreover, induced pluripotent stem (iPS) cells can be derived from differentiated cell types by introducing a cocktail of transcription factors³. Despite their different origins, iPS cells are highly similar to ES cells at molecular and functional levels.

Because of the developmental plasticity of ES and iPS cells, and the ease with which they can be derived from both mice and humans, stem-cell researchers have focused much

- Nature* **491**, 582–585 (2012).
- Frank, H. S. & Evans, M. W. *J. Chem. Phys.* **13**, 507–532 (1945).
 - Soper, A. K. & Finney, J. L. *Phys. Rev. Lett.* **71**, 4346–4349 (1993).
 - Dixit, S., Crain, S. J., Poon, W. C. K., Finney, J. L. & Soper, A. K. *Nature* **416**, 829–832 (2002).
 - Chandler, D. *Nature* **437**, 640–647 (2005).
 - Laage, D. & Hynes, J. T. *Science* **311**, 832–835 (2006).
 - Laage, D., Stirnemann, G. & Hynes, J. T. *J. Phys. Chem. B* **113**, 2428–2435 (2009).
 - Ishihara, Y., Okouchi, S. & Uedaira, H. *J. Chem. Soc. Faraday Trans.* **93**, 3337–3342 (1997).
 - Yoshida, K., Ibuki, K. & Ueno, M. *J. Chem. Phys.* **108**, 1360–1367 (1998).
 - Petersen, C., Tielrooij, K.-J. & Bakker, H. J. *J. Chem. Phys.* **130**, 214511 (2009).

of their attention on understanding how to instruct the cells to become therapeutically relevant, differentiated cell types *in vitro*. Indeed, scientists have been able to produce nerve cells, heart-muscle cells and gut cells, among others, from cultured pluripotent cells. However, it has been notoriously difficult to derive functional gametes from ES cells⁴. This is not surprising, because germ-cell maturation is a complex process of cellular, chromosomal and molecular changes that endow mature sperm and oocytes with the unique potential to give rise to an entire organism after fertilization.

In an experimental tour de force, Hayashi and co-workers¹ generated oocytes from ES and iPS cells by devising a multi-step procedure that mimics the events occurring in developing embryos (Fig. 1). Shortly after implantation, early gamete precursors, called primordial germ cells (PGCs), are specified within a layer of advanced-stage pluripotent cells called the epiblast, which is poised for differentiation⁵. In a first step, the authors identified a combination of growth factors that could efficiently generate epiblast-like cells from ES cells. The epiblast-like cells were then exposed to the growth factors that induce germ-cell formation *in vivo*, and so gave rise to PGC-like cells *in vitro*.

To reset the genome of germ cells for the next generation, PGCs have to lose certain genome-wide chemical modifications that control gene activity⁵. These epigenetic marks include DNA methylation of imprinted genes, which are expressed in a sex-specific manner from the maternal or paternal chromosomes, and have crucial roles in fetal growth. In developing oocytes and sperm, these marks are

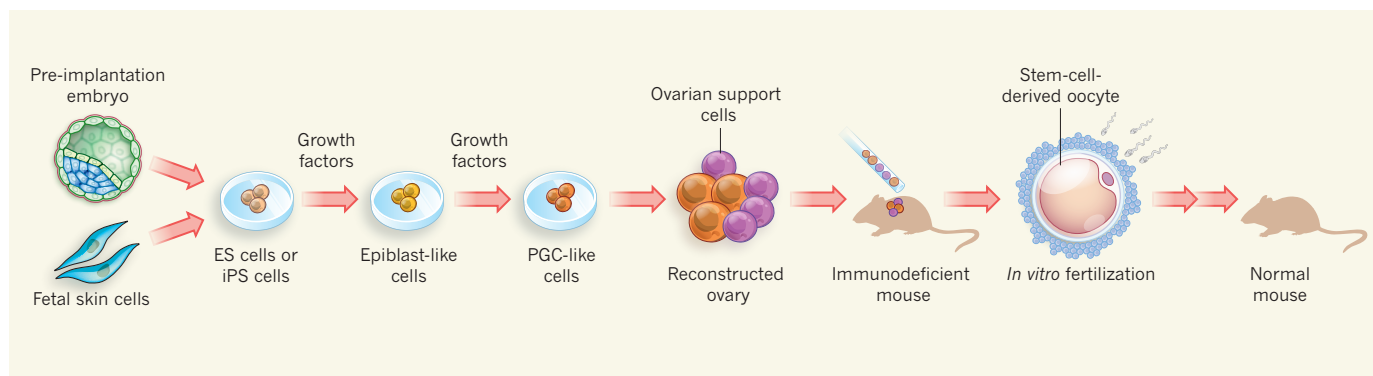


Figure 1 | Oogenesis from cultured stem cells. Hayashi *et al.*¹ exposed embryonic stem (ES) cells derived from pre-implantation embryos, or from induced pluripotent stem (iPS) cells obtained from fetal skin cells, to a combination of growth factors to generate epiblast-like cells. Exposure of these cells to a different set of growth factors then led to formation of primordial germ cell (PGC)-like cells. To induce maturation of the latter, the

authors combined them with ovarian support cells. They then transplanted these 'primed' PGC-like cells under the ovarian bursa of immunodeficient mice, where the cells proceeded through meiotic cell division. The resultant oocytes were fertilized *in vitro* with naturally derived sperm and gave rise to normal mice. Using a similar strategy, Hayashi *et al.* have also generated mature sperm cells from ES and iPS cells².

re-established in a female- or male-specific fashion and are complemented with their non-imprinted equivalent on fertilization.

After the imprints have been erased, PGCs need to go through rounds of meiotic cell division to generate functional gametes. Like any other embryonic or adult cell, PGCs carry the full set of maternal and paternal chromosomes. During meiosis, however, this parental diploid genome is reduced by half to a haploid state through random allocation of chromosomes between the resultant gametes.

To push PGC-like cells towards resetting of the genome and entry into meiosis, Hayashi *et al.* grew artificial ovaries *in vitro*. To do so, they aggregated the support cells that typically surround oocytes in embryonic ovaries, called granulosa and theca cells, with the ES-cell-derived PGCs. Remarkably, the PGC-like cells within these aggregates underwent the same imprint erasure as is normally seen in development.

A greater challenge, however, was to drive the primed PGC-like cells into oocytes that would undergo meiosis. Hayashi *et al.* accomplished this feat by transplanting the ovary-like aggregates into a site under the ovarian bursa (a sac of connective tissue surrounding the ovary) of immunodeficient recipient mice. The PGC-like cells within the transplants then progressed into early-stage oocytes.

In a final step, the authors re-isolated these oocytes, allowed them to mature *in vitro*, and then fertilized them with sperm. Whereas some of the fertilized oocytes stopped developing as a result of genomic abnormalities, others gave rise to healthy pups that grew into adulthood and passed on their genome to the next generation. In a complementary set of experiments, Hayashi and colleagues showed that iPS cells derived from fetal skin cells could be manipulated similarly to generate functional oocytes¹.

This study¹ and the authors' previous report² are proof-of-principle demonstrations that

pluripotent stem cells can be programmed in a step-wise manner into functional gametes. Despite this impressive advance, however, several tasks lie ahead. For instance, a way needs to be found to avoid the production of oocytes with genomic abnormalities that would compromise development. Also, researchers need to determine whether ES and iPS cells of human origin can differentiate into oocytes and sperm in culture. Compared with mouse ES cells, human ES and iPS cells are thought to be in a more advanced state that already resembles the post-implantation epiblast prone to differentiation. Because of this fundamental difference, it may be easier to coax human ES cells into germ cells.

Can the requirement for embryonic ovarian tissue and the transplantation of ovary-tissue aggregates into recipient animals be bypassed and, instead, be recapitulated *in vitro*? Achieving this would be particularly relevant in therapeutic settings such as the restoration of oocyte development after chemotherapy. It might be feasible to derive ovarian support cells through *in vitro* differentiation from ES or iPS cells, or through transdifferentiation of skin or blood cells. (Transdifferentiation is the conversion of one mature cell type into another by forced activation of regulatory genes, and has recently been accomplished⁶ for Sertoli cells, which support spermatogenesis.) The development of such culture systems is also key to understanding the complex molecular and cellular events that enable male and female support cells to induce germ-line maturation and meiosis *in vivo*.

Another puzzle is whether the oocytes that gave rise to offspring in this study were truly equivalent to those that are obtained directly from ovaries. Although the newborn pups were apparently normal, abnormalities such as behavioural deficits and tumour formation — caused by, for example, incomplete imprint erasure or re-establishment — might not manifest themselves until later in life. So

a careful examination of the mice as they age will be needed.

Nonetheless, this discovery is a milestone in basic research in the way it has recapitulated all key steps of gametogenesis in cultured stem cells. The resulting insights, for example, might help researchers to identify the enzymatic activity that is responsible for the erasure of genomic imprints and other marks during PGC development.

These findings also have practical implications. Women who cannot produce oocytes because of injury, disease or age might one day be able to conceive children through *in vitro* fertilization from oocytes derived from their own iPS cells. However, the prospect of transplanting such oocytes into women raises major safety and ethical concerns that will need to be discussed carefully if the findings are repeated in humans. Nevertheless, gametes derived from iPS cells might provide a valuable culture model to study the epigenetic and environmental factors leading to infertility. This technology might also help to rescue endangered or extinct species by producing oocytes and sperm from iPS cells generated from frozen blood or skin samples. ■

Sihem Cheloufi and Konrad Hochedlinger

are at the Howard Hughes Medical Institute, Massachusetts General Hospital, Boston, Massachusetts 02114, USA. They are also at the Harvard Stem Cell Institute and in the Department of Stem Cell and Regenerative Biology, Harvard University, Cambridge. e-mail: khochedlinger@helix.mgh.harvard.edu

- Hayashi, K. *et al.* *Science* **338**, 971–975 (2012).
- Hayashi, K., Ohta, H., Kurimoto, K., Aramaki, S. & Saitou, M. *Cell* **146**, 519–532 (2011).
- Takahashi, K. & Yamanaka, S. *Cell* **126**, 663–676 (2006).
- Daley, G. Q. *Science* **316**, 409–410 (2007).
- Surani, M. A. & Hajkova, P. *Cold Spring Harb. Symp. Quant. Biol.* **75**, 211–218 (2010).
- Buganim, Y. *et al.* *Cell Stem Cell* **11**, 373–386 (2012).

CIRCADIAN RHYTHMS

Depression brought to light

Exposure to abnormal light–dark cycles causes depression–like behaviour and learning deficits in mice. The defects seem to occur independently of disturbances to sleep and other processes regulated by the biological clock. [SEE LETTER P.594](#)

LISA M. MONTEGGIA & EGE T. KAVALALI

Changes in environmental light can alter mood and adversely affect cognitive function¹. Nonetheless, the identity of the neuronal circuitry involved in light-mediated regulation of mood and cognition, and how it functions, are poorly understood. A prevailing hypothesis is that, because alterations in light disrupt circadian rhythms (processes that are controlled by our in-built 24-hour ‘biological clock’), including sleep, they then indirectly alter mood and impair learning. On page 594 of this issue, LeGates *et al.*² explore the link between the effects of light on the circadian system and dysfunctional mood regulation, and begin to delineate the underlying neural circuitry. They provide convincing evidence that abnormal light exposure can directly affect mood and learning*.

LeGates and colleagues exposed mice to 3.5 hours of light followed by 3.5 hours of dark (T7 light cycle), instead of the normal 12-hour light and 12-hour dark cycle. They then examined the effects of this abnormal light cycle on depression-like behaviour, and on learning and memory. The T7 cycle did not alter the total amount of sleep the mice had, suggesting that any physiological effects were independent of sleep deprivation. Moreover, it did not cause significant disruption to circadian rhythms; that is, the biological clocks, which regulate physiological activities in relation to circadian environmental cycles, remained intact and in phase with one another.

Nevertheless, mice experiencing the T7 cycle showed increased depression-related behaviour, along with increased levels of the hormone corticosterone, a potential link to depression. The mice were also impaired in some forms of learning and memory, as indicated by alterations in the extent of long-term potentiation (LTP) — an increase in the strength of synaptic connections between neurons that correlates with learning and memory — in the brain’s hippocampus region. However, long-term synaptic depression (a decrease in strength) was unaffected, suggesting that light-induced changes are specific to synaptic strengthening.

*This article and the paper under discussion² were published online on 14 November 2012.

Physiological functions such as sleep and metabolism are tightly regulated by circadian rhythms that are entrained by ambient light exposure³. Light is classically detected by photon-sensitive neurons — rods and cones in the retina of the eye — which relay information to retinal ganglion cells (RGCs) that, in turn, project to higher brain regions for image formation. However, a population of intrinsically photosensitive RGCs (ipRGCs), which express the photopigment melanopsin and are distinct both from other RGCs and from rods and cones, mediate non-image-forming processes in response to light^{4,5}. The light sensitivity of melanopsin matches that of non-image-forming, but light-dependent, physiological

“This investigation provides a detailed road map by which to pursue understanding of the impact of light on mood and cognitive function.”

processes that are regulated in a circadian manner, including locomotion and the pupillary light reflex^{6,7}.

To examine whether the traits seen with the T7 light cycle were due to direct effects of light — independent of image-forming processes — LeGates and colleagues exposed mice that lacked ipRGCs to this light cycle. The ipRGC-deficient animals did not show alterations in depression-like behaviour, learning or LTP. The authors therefore conclude that light acting on ipRGCs directly contributes to mood regulation and learning.

These findings support the use of the T7-light-cycle paradigm as an animal model of depression, and particularly for evaluating antidepressant treatments. Existing paradigms tend to rely on the behavioural-despair model, which assesses how quickly an animal ‘gives up’ in an inhospitable situation and evaluates antidepressants by whether they can improve performance. Diversification of behavioural paradigms may help to uncover clinically applicable drug targets that could not be identified by these traditional approaches, and which may lead to more reliable and faster-acting antidepressants.

The study raises intriguing questions regarding the mechanisms and specific neuronal

targets of ipRGCs in mediating the effects of light on the regulation of mood and cognitive function. For instance, it suggests that not only activation of ipRGCs but also changes in the long-term pattern of ipRGC exposure to light lead to synaptic plasticity (modification of the strength of neuronal synapses, which may underlie changes in behaviour). It remains unclear whether this effect is caused by changes in the synaptic strengths of ipRGCs themselves or by regulation of their downstream neuronal targets. LTP deficits seen in hippocampal synapses point to more general changes in plasticity, beyond the immediate synaptic projections of ipRGCs. The direct targets of ipRGC projections⁸ (including, but not limited to, the suprachiasmatic nucleus, the intergeniculate leaflet and the olivary pretectal nucleus) that mediate these synaptic abnormalities should be identified.

Interestingly, LeGates *et al.* report that long-term treatment with the antidepressant drugs fluoxetine and desipramine reverses some of the behavioural effects of the T7 cycle, as well as the associated LTP deficit. This indicates that the same neuronal-circuit elements, and possibly neurotrophic factors (which mediate neuronal growth), that, according to traditional models, mediate depressive-like behaviour, are involved in the depressive response to abnormal light exposure.

However, sensitivity to long-term antidepressant administration is a hallmark of behavioural paradigms that depend on chronic stress induction, such as social defeat⁹ (in which an animal repeatedly loses confrontations with another animal of the same species). Consequently, it should be further explored whether some of the more general synaptic plasticity reported by LeGates *et al.* is associated with stress due to exposure to the T7 cycle. It would also be of interest to test whether depressive-like behaviours respond to faster-acting antidepressants such as ketamine, which alleviate symptoms within hours¹⁰. Response to ketamine administration would help to determine whether these light-induced abnormal behaviours are as reversible in the short term as are depressive-like traits elicited during behavioural despair.

LeGates and co-workers’ thorough investigation provides a detailed road map by which to pursue understanding of the impact of light on mood and cognitive function. Dissecting the direct effect of ipRGC synaptic projections on mood and cognition will not only elucidate a rather enigmatic neuromodulatory pathway, but may also provide new neuronal targets for treatments for mood and cognitive disorders. ■

Lisa M. Monteggia is in the Department of Psychiatry and **Ege T. Kavalali** is in the Department of Neuroscience, University of Texas Southwestern Medical Center, Dallas, Texas 75390-9111, USA.
e-mail: lisa.monteggia@utsouthwestern.edu

1. Foster, R. G. & Wulff, K. *Nature Rev. Neurosci.* **6**, 407–414 (2005).
2. LeGates, T. *et al. Nature* **491**, 594–598 (2012).
3. Mohawk, J. A., Green, C. B. & Takahashi, J. S. *Annu. Rev. Neurosci.* **35**, 445–462 (2012).
4. Berson, D. M., Dunn, F. A. & Takao, M. *Science* **295**, 1070–1073 (2002).
5. Hattar, S., Liao, H.-W., Takao, M., Berson, D. M. & Yao, K.-W. *Science* **295**, 1065–1070 (2002).
6. Do, M. T. H. *et al. Nature* **457**, 281–287 (2009).
7. Chen, S.-K., Badea, T. C. & Hattar, S. *Nature* **476**, 92–95 (2011).
8. Hattar, S. *et al. J. Comp. Neurol.* **497**, 326–349 (2006).
9. Berton, O. *et al. Science* **311**, 864–868 (2006).
10. Autry, A. E. *et al. Nature* **475**, 91–95 (2011).

MICROBIOLOGY

A piece of the methane puzzle

The identification of a sea-floor microorganism that single-handedly conducts anaerobic oxidation of methane changes our picture of how the flux of this greenhouse gas from the ocean to the atmosphere is regulated. [SEE ARTICLE P.541](#)

SAMANTHA B. JOYE

Methane is a potent greenhouse gas¹ that exists in immense amounts in sea-floor sediments across the globe². The flux of this methane to the atmosphere can profoundly affect global climate, and previous episodes of rapid climate warming have been ascribed to oceanic methane emissions³. Marine microorganisms that perform anaerobic oxidation of methane (AOM) act as gatekeepers of these sea-floor reservoirs, moderating gas flux from the ocean to the atmosphere. However, despite a strong research effort aimed at understanding its regulation, the process of AOM has mystified biogeochemists and microbiologists for decades. On page 541 of this issue, Milucka *et al.*⁴ describe a single microorganism that can mediate both the oxidative and reductive processes of AOM — a finding that transforms our understanding of both methane and sulphur cycling in the present, past and future environments of Earth*.

Sulphate-linked AOM was first proposed as an explanation for the profiles of dissolved sulphate and methane that are trapped within pore spaces in coastal marine sediments⁵. Twenty years later, AOM was suggested to be a cooperative metabolic process⁶, mediated in marine environments by associations between anaerobic methanotrophic archaea (ANMEs) and sulphate-reducing bacteria. (The archaea are a domain of single-celled, but not bacterial, microorganisms.) Together, these microorganisms were thought to oxidize methane to carbon dioxide while reducing sulphate (SO_4^{2-}) to hydrogen sulphide (H_2S), splitting the energy supplied by this coupled process between them (Fig. 1a). More recently, two alternative mechanisms of AOM were

discovered: one involving the coupling of methane oxidation to the reduction of reactive metals, also presumed to be mediated by cooperating microorganisms⁹ (Fig. 1b) and the other mediated by an extremely unusual

bacterium, *Methoxymirabilis oxyfera*, that makes its own oxygen to fuel AOM in anoxic environments without the aid of a metabolic partner¹⁰ (Fig. 1c).

Now, Milucka *et al.* reveal a fourth mechanism for AOM. The authors report that archaea of the ANME-2 clade use an unusual sulphate-reduction strategy to single-handedly mediate both AOM and sulphate reduction, thereby keeping the energy derived from both reactions mostly to themselves and eliminating the need for a microbial partner for the shuttling of electrons or metabolites. Their work hinged on a culture of microorganisms originally obtained from sea-floor sediments from a Mediterranean mud volcano, Isis, which was enriched in microorganisms involved in AOM over eight years of culture¹¹. The previous lack of such microbial isolates has been a major stumbling block in efforts to unravel the mechanisms of AOM.

With this culture in hand, Milucka *et al.* used a dazzling array of geochemical, molecular biological and microbiological techniques, combined with some clever physiological sleuthing using bacterium-specific antibiotics to link the observed sulphate-reduction activity to the archaea, to show that

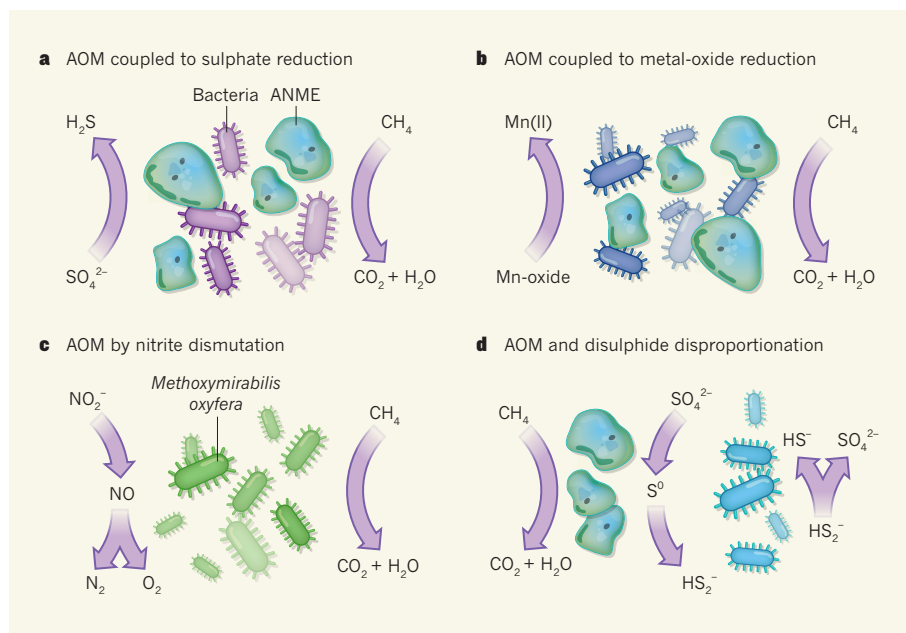


Figure 1 | Modes of microbial anaerobic methane oxidation. There are four known ways in which microorganisms achieve anaerobic oxidation of methane (AOM). Two of these (a, b) are thought to rely on obligate associations between two or more microbial partners, one of which performs oxidation and the other reduction; in the other two cases (c, d), a single microorganism performs both reactions. **a**, Anaerobic methanotrophic archaea (ANMEs) oxidize methane (CH_4) and convert it to carbon dioxide and water, in cooperation with sulphate-reducing bacteria, which convert sulphate (SO_4^{2-}) to hydrogen sulphide (H_2S) (ref. 8). The mechanism of energy exchange between the ANMEs and the sulphate-reducing bacteria is unknown. **b**, The oxidation of methane to CO_2 by ANMEs is coupled to the reduction of metal oxides, whereby metals such as manganese (Mn) or iron (Fe) are reduced to the +2 oxidation state⁹. **c**, The bacterium *Methoxymirabilis oxyfera* converts nitrite (NO_2^-) to nitric oxide (NO) and then dismutates (splits) NO into nitrogen and oxygen as diatomic gases. The bacterium then uses the resulting O_2 to support methane oxidation¹⁰. **d**, Milucka *et al.*⁴ show that some ANMEs oxidize methane (as in a) but also reduce sulphate to zero-valent sulphur (S^0), which they produce in the form of disulphide (HS_2^-). The disulphide can be used by associated bacteria, Deltaproteobacteria, to yield sulphide (HS^-) and sulphate, but this is an association of convenience, rather than necessity.

*This article and the paper under discussion⁴ were published online on 7 November 2012.

1. Foster, R. G. & Wulff, K. *Nature Rev. Neurosci.* **6**, 407–414 (2005).
2. LeGates, T. *et al. Nature* **491**, 594–598 (2012).
3. Mohawk, J. A., Green, C. B. & Takahashi, J. S. *Annu. Rev. Neurosci.* **35**, 445–462 (2012).
4. Berson, D. M., Dunn, F. A. & Takao, M. *Science* **295**, 1070–1073 (2002).
5. Hattar, S., Liao, H.-W., Takao, M., Berson, D. M. & Yao, K.-W. *Science* **295**, 1065–1070 (2002).
6. Do, M. T. H. *et al. Nature* **457**, 281–287 (2009).
7. Chen, S.-K., Badea, T. C. & Hattar, S. *Nature* **476**, 92–95 (2011).
8. Hattar, S. *et al. J. Comp. Neurol.* **497**, 326–349 (2006).
9. Berton, O. *et al. Science* **311**, 864–868 (2006).
10. Autry, A. E. *et al. Nature* **475**, 91–95 (2011).

MICROBIOLOGY

A piece of the methane puzzle

The identification of a sea-floor microorganism that single-handedly conducts anaerobic oxidation of methane changes our picture of how the flux of this greenhouse gas from the ocean to the atmosphere is regulated. [SEE ARTICLE P.541](#)

SAMANTHA B. JOYE

Methane is a potent greenhouse gas¹ that exists in immense amounts in sea-floor sediments across the globe². The flux of this methane to the atmosphere can profoundly affect global climate, and previous episodes of rapid climate warming have been ascribed to oceanic methane emissions³. Marine microorganisms that perform anaerobic oxidation of methane (AOM) act as gatekeepers of these sea-floor reservoirs, moderating gas flux from the ocean to the atmosphere. However, despite a strong research effort aimed at understanding its regulation, the process of AOM has mystified biogeochemists and microbiologists for decades. On page 541 of this issue, Milucka *et al.*⁴ describe a single microorganism that can mediate both the oxidative and reductive processes of AOM — a finding that transforms our understanding of both methane and sulphur cycling in the present, past and future environments of Earth*.

Sulphate-linked AOM was first proposed as an explanation for the profiles of dissolved sulphate and methane that are trapped within pore spaces in coastal marine sediments⁵. Twenty years later, AOM was suggested to be a cooperative metabolic process⁶, mediated in marine environments by associations between anaerobic methanotrophic archaea (ANMEs) and sulphate-reducing bacteria. (The archaea are a domain of single-celled, but not bacterial, microorganisms.) Together, these microorganisms were thought to oxidize methane to carbon dioxide while reducing sulphate (SO_4^{2-}) to hydrogen sulphide (H_2S), splitting the energy supplied by this coupled process between them (Fig. 1a). More recently, two alternative mechanisms of AOM were

discovered: one involving the coupling of methane oxidation to the reduction of reactive metals, also presumed to be mediated by cooperating microorganisms⁹ (Fig. 1b) and the other mediated by an extremely unusual

bacterium, *Methoxymirabilis oxyfera*, that makes its own oxygen to fuel AOM in anoxic environments without the aid of a metabolic partner¹⁰ (Fig. 1c).

Now, Milucka *et al.* reveal a fourth mechanism for AOM. The authors report that archaea of the ANME-2 clade use an unusual sulphate-reduction strategy to single-handedly mediate both AOM and sulphate reduction, thereby keeping the energy derived from both reactions mostly to themselves and eliminating the need for a microbial partner for the shuttling of electrons or metabolites. Their work hinged on a culture of microorganisms originally obtained from sea-floor sediments from a Mediterranean mud volcano, Isis, which was enriched in microorganisms involved in AOM over eight years of culture¹¹. The previous lack of such microbial isolates has been a major stumbling block in efforts to unravel the mechanisms of AOM.

With this culture in hand, Milucka *et al.* used a dazzling array of geochemical, molecular biological and microbiological techniques, combined with some clever physiological sleuthing using bacterium-specific antibiotics to link the observed sulphate-reduction activity to the archaea, to show that

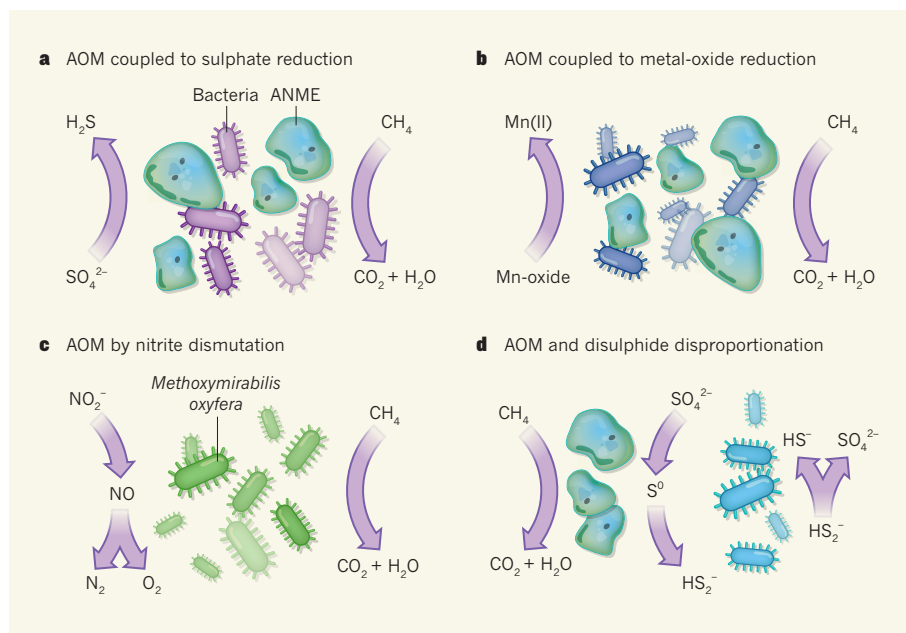


Figure 1 | Modes of microbial anaerobic methane oxidation. There are four known ways in which microorganisms achieve anaerobic oxidation of methane (AOM). Two of these (a, b) are thought to rely on obligate associations between two or more microbial partners, one of which performs oxidation and the other reduction; in the other two cases (c, d), a single microorganism performs both reactions. **a**, Anaerobic methanotrophic archaea (ANMEs) oxidize methane (CH_4) and convert it to carbon dioxide and water, in cooperation with sulphate-reducing bacteria, which convert sulphate (SO_4^{2-}) to hydrogen sulphide (H_2S) (ref. 8). The mechanism of energy exchange between the ANMEs and the sulphate-reducing bacteria is unknown. **b**, The oxidation of methane to CO_2 by ANMEs is coupled to the reduction of metal oxides, whereby metals such as manganese (Mn) or iron (Fe) are reduced to the +2 oxidation state⁹. **c**, The bacterium *Methoxymirabilis oxyfera* converts nitrite (NO_2^-) to nitric oxide (NO) and then dismutates (splits) NO into nitrogen and oxygen as diatomic gases. The bacterium then uses the resulting O_2 to support methane oxidation¹⁰. **d**, Milucka *et al.*⁴ show that some ANMEs oxidize methane (as in a) but also reduce sulphate to zero-valent sulphur (S^0), which they produce in the form of disulphide (HS_2^-). The disulphide can be used by associated bacteria, Deltaproteobacteria, to yield sulphide (HS^-) and sulphate, but this is an association of convenience, rather than necessity.

*This article and the paper under discussion⁴ were published online on 7 November 2012.

ANME-2s can oxidize methane and couple this process directly to sulphate reduction (Fig. 1d). In doing so, the archaea produce an unexpected metabolic end product — zero-valent sulphur (S^0) — which is released from the archaea, probably in the form of disulphide (HS_2^-).

This finding also led the authors to the revelation that the Deltaproteobacteria present in the Isis-sediment culture seem not to be the obligate sulphate-reducing partners they were previously assumed to be. The bacteria are autotrophs, meaning that they use energy from light or from inorganic compounds to convert CO_2 to complex organic compounds. The authors propose that the bacteria obtain this energy through a previously unknown disproportionation reaction (one in which a compound is simultaneously oxidized and reduced to form two different chemical species), by converting the disulphide produced by the ANMEs to hydrogen sulphide and sulphate (Fig. 1d). Thus, instead of obligate cooperative metabolism between the dominant microorganisms in this sea-floor sample, Milucka and colleagues document not one but two novel metabolic processes.

This discovery represents a major event in AOM research, but it also raises several questions that will fuel future research efforts, and offers clues to the metabolic activity of archaea in other environments. For example, Milucka and colleagues show that the ANME-2s in their cultures lack the typical forms of the enzymes responsible for sulphate reduction by microorganisms. However, they offer an intriguing proposal for how the archaea might pull off this process, suggesting that an enzyme usually involved in archaeal methanogenesis, formyl-methanofuran dehydrogenase, might instead support sulphate reduction. This enzyme is a strong candidate, as it has a sufficiently negative midpoint redox potential (−530 millivolts) to allow archaea to do something that even sulphate-reducing bacteria cannot, namely, to reduce sulphate without expending energy in the form of ATP to activate the sulphate. Confirmation of this possibility would address long-standing questions associated with archaeal sulphate reduction across a wide variety of environments.

Milucka and colleagues' demonstration that the association of these ANME-2s and Deltaproteobacteria is one of convenience, rather than necessity, also prompts further consideration. Are other ANMEs, namely, the ANME-1s and ANME-3s, also capable of independent AOM; and if so, do they use a similar metabolic process? Furthermore, the demonstration that archaea can mediate sulphate reduction raises the possibility that they may also do so in situations other than AOM, for example to reduce sulphur in extreme environments — such as in sea-floor hydrothermal vents, or possibly even beyond our planet. Similarly, the discovery of

disulphide disproportionation by bacteria suggests that such metabolic processes may operate in a wide variety of environments.

With this paper, we now have four suggested mechanisms of AOM (Fig. 1). Two of these involve single microorganisms using previously undescribed metabolic pathways that produce either an unexpected intermediate (nitric oxide, by *M. oxyfera*¹⁰) or metabolic products (disulphide production by ANME-2 archaea, as described by Milucka *et al.*). It is still presumed that the other two processes — the coupling of AOM to either sulphate reduction or to metal-oxide reduction — operate through the synergistic interactions of microbial consortia. However, the exact microbial partners in the case of AOM coupled to metal reduction, and the metabolic intermediates involved in either suite of processes, have yet to be determined. But the fact that this story keeps evolving suggests that more fascinating twists on the mode of AOM exist in nature, awaiting discovery. ■

LOW-TEMPERATURE PHYSICS

A chilling effect for molecules

Cold and ultracold molecules provide fertile grounds for scientific discoveries. A method of cooling polyatomic molecules has been demonstrated that will allow researchers to explore the vast potential of these entities. [SEE LETTER P.570](#)

JOHN F. BARRY & DAVID DEMILLE

The ability to trap atomic gases and cool them to ultracold temperatures (about 1 millikelvin or below) has led to revolutionary advances across a range of areas — including atomic clocks, quantum information processing and simulation of condensed-matter systems. The production of ultracold molecular gases is anticipated to have a similarly broad scientific impact. In this issue, Zeppenfeld *et al.*¹ (page 570) demonstrate a novel method for cooling a trapped gas of polyatomic molecules. Their work substantially broadens the range of molecular species for which cooling is possible. It also demonstrates a powerful and generalizable method that may allow the production of even colder molecular gases, as required for most proposed applications*.

Compared with atoms, molecules have additional types of internal motion (such as vibration and rotation) that provide new features to study and manipulate². For example, the long-range, strong electric forces between polar

*This article and the paper under discussion¹ were published online on 14 November 2012.

Samantha B. Joye is in the Department of Marine Sciences, University of Georgia, Athens, Georgia 30602-3636, USA. e-mail: mjoye@uga.edu

1. Denman, K. L. *et al.* *Climate Change 2007: The Physical Science Basis. Contribution of Working Group I to the Fourth Assessment Report of the Intergovernmental Panel on Climate Change* (Cambridge Univ. Press, 2007).
2. Kvenvolden, K. A. *Rev. Geophys.* **31**, 173–187 (1993).
3. Dickens, G. R., O'Neil, J. R., Rea, D. K. & Owen, R. M. *Paleoceanography* **10**, 965–971 (1995).
4. Milucka, J. *et al.* *Nature* **491**, 541–546 (2012).
5. Martens, C. S. & Berner, R. A. *Science* **185**, 1167–1169 (1974).
6. Hoehler, T. M., Alperin, M. J., Albert, D. B. & Martens, C. S. *Glob. Biogeochem. Cycles* **8**, 451–463 (1994).
7. Hinrichs, K.-U., Hayes, J. M., Sylva, S. P., Brewer, P. G. & DeLong, E. F. *Nature* **398**, 802–805 (1999).
8. Boetius, A. *et al.* *Nature* **407**, 623–626 (2000).
9. Beal, E. J., House, C. H. & Orphan, V. J. *Science* **325**, 184–187 (2009).
10. Ettwig, K. F. *et al.* *Nature* **464**, 543–548 (2010).
11. Holler, T. *et al.* *Environ. Microbiol. Rep.* **1**, 370–376 (2009).

molecules make them attractive for use as bits of information in a quantum computer, where conditional logic operations require strong interactions between the constituent bits, or as building blocks for creating exotic phases of matter involving high degrees of quantum entanglement among the particles. Tuning the energy levels of ultracold molecules using electromagnetic fields — which produces particularly significant effects at low temperatures — could allow precise control over chemical-reaction rates, and enable characterization of molecular interactions with unprecedented precision. Furthermore, minute shifts in molecular energies could be observed at these temperatures; for instance, a small difference in the energies of left- and right-handed chiral molecules has been predicted, owing to the intrinsic handedness of the electroweak force that arises from the exchange of particles (Z^0 bosons) between electrons and nuclei. These applications require molecules to have the low kinetic energy associated with ultracold temperatures: this low energy allows the molecules to be trapped and/or to be observed for long times, as is typically necessary for precision spectroscopic measurements.

ANME-2s can oxidize methane and couple this process directly to sulphate reduction (Fig. 1d). In doing so, the archaea produce an unexpected metabolic end product — zero-valent sulphur (S^0) — which is released from the archaea, probably in the form of disulphide (HS_2^-).

This finding also led the authors to the revelation that the Deltaproteobacteria present in the Isis-sediment culture seem not to be the obligate sulphate-reducing partners they were previously assumed to be. The bacteria are autotrophs, meaning that they use energy from light or from inorganic compounds to convert CO_2 to complex organic compounds. The authors propose that the bacteria obtain this energy through a previously unknown disproportionation reaction (one in which a compound is simultaneously oxidized and reduced to form two different chemical species), by converting the disulphide produced by the ANMEs to hydrogen sulphide and sulphate (Fig. 1d). Thus, instead of obligate cooperative metabolism between the dominant microorganisms in this sea-floor sample, Milucka and colleagues document not one but two novel metabolic processes.

This discovery represents a major event in AOM research, but it also raises several questions that will fuel future research efforts, and offers clues to the metabolic activity of archaea in other environments. For example, Milucka and colleagues show that the ANME-2s in their cultures lack the typical forms of the enzymes responsible for sulphate reduction by microorganisms. However, they offer an intriguing proposal for how the archaea might pull off this process, suggesting that an enzyme usually involved in archaeal methanogenesis, formyl-methanofuran dehydrogenase, might instead support sulphate reduction. This enzyme is a strong candidate, as it has a sufficiently negative midpoint redox potential (−530 millivolts) to allow archaea to do something that even sulphate-reducing bacteria cannot, namely, to reduce sulphate without expending energy in the form of ATP to activate the sulphate. Confirmation of this possibility would address long-standing questions associated with archaeal sulphate reduction across a wide variety of environments.

Milucka and colleagues' demonstration that the association of these ANME-2s and Deltaproteobacteria is one of convenience, rather than necessity, also prompts further consideration. Are other ANMEs, namely, the ANME-1s and ANME-3s, also capable of independent AOM; and if so, do they use a similar metabolic process? Furthermore, the demonstration that archaea can mediate sulphate reduction raises the possibility that they may also do so in situations other than AOM, for example to reduce sulphur in extreme environments — such as in sea-floor hydrothermal vents, or possibly even beyond our planet. Similarly, the discovery of

disulphide disproportionation by bacteria suggests that such metabolic processes may operate in a wide variety of environments.

With this paper, we now have four suggested mechanisms of AOM (Fig. 1). Two of these involve single microorganisms using previously undescribed metabolic pathways that produce either an unexpected intermediate (nitric oxide, by *M. oxyfera*¹⁰) or metabolic products (disulphide production by ANME-2 archaea, as described by Milucka *et al.*). It is still presumed that the other two processes — the coupling of AOM to either sulphate reduction or to metal-oxide reduction — operate through the synergistic interactions of microbial consortia. However, the exact microbial partners in the case of AOM coupled to metal reduction, and the metabolic intermediates involved in either suite of processes, have yet to be determined. But the fact that this story keeps evolving suggests that more fascinating twists on the mode of AOM exist in nature, awaiting discovery. ■

LOW-TEMPERATURE PHYSICS

A chilling effect for molecules

Cold and ultracold molecules provide fertile grounds for scientific discoveries. A method of cooling polyatomic molecules has been demonstrated that will allow researchers to explore the vast potential of these entities. [SEE LETTER P.570](#)

JOHN F. BARRY & DAVID DEMILLE

The ability to trap atomic gases and cool them to ultracold temperatures (about 1 millikelvin or below) has led to revolutionary advances across a range of areas — including atomic clocks, quantum information processing and simulation of condensed-matter systems. The production of ultracold molecular gases is anticipated to have a similarly broad scientific impact. In this issue, Zeppenfeld *et al.*¹ (page 570) demonstrate a novel method for cooling a trapped gas of polyatomic molecules. Their work substantially broadens the range of molecular species for which cooling is possible. It also demonstrates a powerful and generalizable method that may allow the production of even colder molecular gases, as required for most proposed applications*.

Compared with atoms, molecules have additional types of internal motion (such as vibration and rotation) that provide new features to study and manipulate². For example, the long-range, strong electric forces between polar

*This article and the paper under discussion¹ were published online on 14 November 2012.

Samantha B. Joye is in the Department of Marine Sciences, University of Georgia, Athens, Georgia 30602-3636, USA. e-mail: mjoye@uga.edu

1. Denman, K. L. *et al.* *Climate Change 2007: The Physical Science Basis. Contribution of Working Group I to the Fourth Assessment Report of the Intergovernmental Panel on Climate Change* (Cambridge Univ. Press, 2007).
2. Kvenvolden, K. A. *Rev. Geophys.* **31**, 173–187 (1993).
3. Dickens, G. R., O'Neil, J. R., Rea, D. K. & Owen, R. M. *Paleoceanography* **10**, 965–971 (1995).
4. Milucka, J. *et al.* *Nature* **491**, 541–546 (2012).
5. Martens, C. S. & Berner, R. A. *Science* **185**, 1167–1169 (1974).
6. Hoehler, T. M., Alperin, M. J., Albert, D. B. & Martens, C. S. *Glob. Biogeochem. Cycles* **8**, 451–463 (1994).
7. Hinrichs, K.-U., Hayes, J. M., Sylva, S. P., Brewer, P. G. & DeLong, E. F. *Nature* **398**, 802–805 (1999).
8. Boetius, A. *et al.* *Nature* **407**, 623–626 (2000).
9. Beal, E. J., House, C. H. & Orphan, V. J. *Science* **325**, 184–187 (2009).
10. Ettwig, K. F. *et al.* *Nature* **464**, 543–548 (2010).
11. Holler, T. *et al.* *Environ. Microbiol. Rep.* **1**, 370–376 (2009).

molecules make them attractive for use as bits of information in a quantum computer, where conditional logic operations require strong interactions between the constituent bits, or as building blocks for creating exotic phases of matter involving high degrees of quantum entanglement among the particles. Tuning the energy levels of ultracold molecules using electromagnetic fields — which produces particularly significant effects at low temperatures — could allow precise control over chemical-reaction rates, and enable characterization of molecular interactions with unprecedented precision. Furthermore, minute shifts in molecular energies could be observed at these temperatures; for instance, a small difference in the energies of left- and right-handed chiral molecules has been predicted, owing to the intrinsic handedness of the electroweak force that arises from the exchange of particles (Z^0 bosons) between electrons and nuclei. These applications require molecules to have the low kinetic energy associated with ultracold temperatures: this low energy allows the molecules to be trapped and/or to be observed for long times, as is typically necessary for precision spectroscopic measurements.

The number of potential applications of ultracold molecular gases has created an intense demand for methods to trap and cool molecules. Standard methods for cooling atoms are not easily extended to molecules, because of their more complex internal structures. For example, laser cooling typically requires that about 10^4 photons be scattered off each particle in the gas, without permanently changing the internal quantum state of the particle. This is difficult with molecules, because photon scattering often excites unwanted rotational and vibrational motions. Only recently have the methods of laser cooling³ and evaporative cooling⁴ been applied to simple (diatomic) molecules.

By contrast, the cooling method demonstrated by Zeppenfeld and colleagues uses the complex structure of molecules to its advantage. It relies on the fact that rotational–vibrational states of a polar molecule, when exposed to an electric field, experience energy shifts that are large, but that vary in size between different states⁵.

Zeppenfeld *et al.* used a spatially varying electric field to trap fluoromethane (CH_3F) molecules, then combined the effect of the trap with a one-way cycle of photon emissions and absorptions to reduce the kinetic energy of the molecules — that is, to cool them (Fig. 1). Molecules are loaded into the trap from a source cooled to cryogenic temperatures. Once in the trapping region, a single cycle of cooling is sufficient to reduce the kinetic energy of the incoming molecules so that they cannot simply slosh back out, enabling the accumulation of molecules in the trap⁶. While still trapped, further cooling then proceeds through more iterations of the cycle (Fig. 1). The cooling is quantified in terms of the phase-space density of the sample (a measure of the total range of velocities and positions of molecules in the gas), which, in this work, increases substantially as the molecules are progressively slowed and confined.

A remarkable feature of the optoelectrical cooling method of Zeppenfeld *et al.* is that the energy removed per cycle is large, so that only a few cycles are required for substantial cooling — they achieved cooling by a factor of 13.5

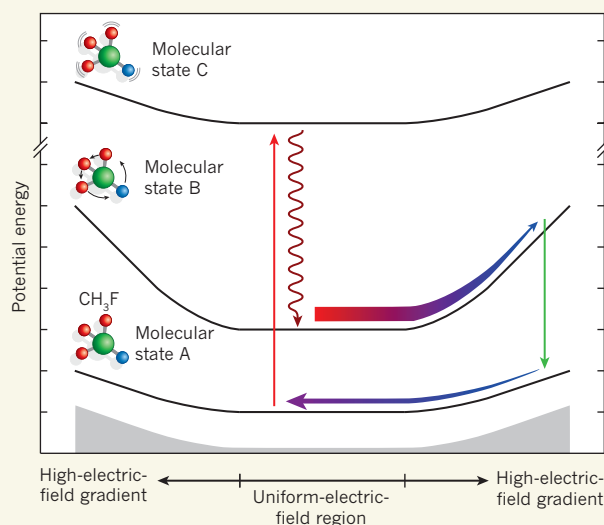


Figure 1 | Optoelectrical molecular cooling scheme. A fluoromethane (CH_3F) molecule begins in a state A, where its interaction with a spatially varying electric field (grey shaded area) creates a shallow potential-energy ‘bowl’ in which the molecule is trapped. A laser stimulates (red straight arrow) the molecule to a vibrationally excited state C, which is in a similarly shallow potential-energy bowl. After about 0.1 seconds, this state spontaneously decays (red wavy arrow) to a long-lived, rotationally excited state B, chosen such that it interacts more strongly with the electric field: the molecule is now trapped in a steeper potential-energy bowl. The molecule is stimulated (green arrow) from state B back to state A by a microwave photon, after moving from the uniform-electric-field region to the edge of a high-electric-field region (thickest arrow, with thickness proportional to the molecule’s velocity), where the molecule moves more slowly because its kinetic energy has been converted to potential energy. This transfer leaves the molecule’s (now small) kinetic energy unchanged. Once in state A again, the molecule ‘rolls’ down the shallow-potential bowl (thin arrow, with thickness proportional to velocity), picking up a smaller amount of kinetic energy than it expended climbing the steep bowl in state B. The potential-energy difference between the B and A states at the location where the molecule is transferred is thereby removed from the system. This cycle can occur in only one direction owing to the spontaneous decay step, and each iteration of the cycle results in removal of kinetic energy (cooling).

to around 29 mK. The low number of cycles necessary allows this method to be effective even as some molecules are lost. For example, about 10% of molecules are lost per cycle because of transitions to unwanted rotational–vibrational states. This loss is much larger than in typical atomic cooling methods; however, the reduction of energy per cycle is also much larger, so that the total phase-space density increases substantially in each cycle. Although the basic concept for this type of cooling cycle was proposed long ago for atomic gases⁷, it never proved very useful for them because losses are rarely a problem; by contrast, this approach seems well suited to the demands of cooling molecules, in which such losses are hard to avoid — particularly for polyatomic species such as CH_3F .

The time required to complete a cooling cycle also matters, primarily because molecules are continually being lost from the trapping region; this is mainly because they occasionally collide with residual room-temperature background gas in the vacuum chamber in which they reside. With this method,

the period for a cooling cycle is quite long, limited by the long time (about 0.1 seconds) before spontaneous decay of the vibrationally excited state in the cycle (Fig. 1) and the fact that molecules spend most of their time in ‘useless’ rotational sublevels⁸. Nevertheless, the optoelectrical cooling method performs comparably to the well-established method of atomic evaporative cooling, in the sense that both have similar fractional particle loss per fractional decrease in temperature⁹. And optoelectrical cooling can be performed at any temperature at which the molecules can be trapped, whereas evaporative cooling requires a large initial phase-space density in order to proceed at a substantial rate.

As for all cooling methods, the rate of change of the temperature will slow as the temperature drops. Hence, reaching ultracold temperatures in a molecular gas would probably require the combination of optoelectrical cooling with additional techniques such as evaporative or ‘sympathetic’ cooling (equilibration with a co-trapped gas of ultracold atoms). Nevertheless, Zeppenfeld and colleagues’ work removes a substantial

obstacle to producing ultracold molecular gases: it represents a beautiful demonstration of new cooling and trapping methods, and their surprising application to a gas of polyatomic molecules. ■

John F. Barry and David DeMille are in the Department of Physics, Yale University, New Haven, Connecticut 06520, USA. e-mails: john.barry@yale.edu; david.demille@yale.edu

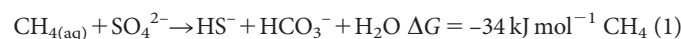
1. Zeppenfeld, M. *et al.* *Nature* **491**, 570–573 (2012).
2. Carr, L. D., DeMille, D., Kreams, R. V. & Ye, J. *New J. Phys.* **11**, 055049 (2009).
3. Shuman, E. S., Barry, J. F. & DeMille, D. *Nature* **467**, 820–823 (2010).
4. Stuhl, B. K. *et al.* Preprint at <http://arxiv.org/abs/1209.6343> (2012).
5. Zeppenfeld, M., Motsch, M., Pinkse, P. W. H. & Rempe, G. *Phys. Rev. A* **80**, 041401 (2009).
6. Ooi, C. H. R., Marzlin, K.-P. & Audretsch, J. *Eur. Phys. J. D* **22**, 259–267 (2003).
7. Pritchard, D. E. *Phys. Rev. Lett.* **51**, 1336–1339 (1983).
8. Shuman, E. S., Barry, J. F., Glenn, D. R. & DeMille, D. *Phys. Rev. Lett.* **103**, 223001 (2009).
9. Ketterle, W. & Van Druten, N. J. *Adv. Atomic Molec. Opt. Phys.* **37**, 181–236 (1996).

Zero-valent sulphur is a key intermediate in marine methane oxidation

Jana Milucka¹, Timothy G. Ferdelman¹, Lubos Polerecky¹, Daniela Franzke¹, Gunter Wegener^{1,2}, Markus Schmid³, Ingo Lieberwirth⁴, Michael Wagner³, Friedrich Widdel¹ & Marcel M. M. Kuypers¹

Emissions of methane, a potent greenhouse gas, from marine sediments are controlled by anaerobic oxidation of methane coupled primarily to sulphate reduction (AOM). Sulphate-coupled AOM is believed to be mediated by a consortium of methanotrophic archaea (ANME) and sulphate-reducing Deltaproteobacteria but the underlying mechanism has not yet been resolved. Here we show that zero-valent sulphur compounds (S⁰) are formed during AOM through a new pathway for dissimilatory sulphate reduction performed by the methanotrophic archaea. Hence, AOM might not be an obligate syntrophic process but may be carried out by the ANME alone. Furthermore, we show that the produced S⁰—in the form of disulphide—is disproportionated by the Deltaproteobacteria associated with the ANME. Our observations expand the diversity of known microbially mediated sulphur transformations and have significant implications for our understanding of the biogeochemical carbon and sulphur cycles.

Anaerobic oxidation of methane coupled to sulphate reduction (AOM), according to equation (1), has a crucial role in the carbon and sulphur cycling in marine environments.



At most investigated AOM sites and in sulphate-reducing enrichment cultures, anaerobic methanotrophic archaea (ANME; groups ANME-1, -2 and -3) and Deltaproteobacteria have been found to co-occur¹. Therefore, it has been proposed that the two organisms mediate AOM, presumably in a syntrophic manner^{2–4}, and thus share the extremely low energy yield of the net reaction (equation (1)). However, the biological basis for AOM has persistently eluded clarification and remains a geomicrobiological puzzle⁵.

We have obtained through continuous cultivation over 8 years a highly enriched AOM culture from sediments of the Mediterranean mud volcano Isis, which is particularly suitable for physiological investigations. As shown by catalysed reporter deposition fluorescence *in situ* hybridization (CARD-FISH), the large and irregularly-shaped

ANME-2 and their smaller, rod- to vibrio-shaped partner bacteria (*Desulfosarcina/Desulfococcus* cluster; DSS) together account for up to 95% of all cells⁶. The culture grows by oxidation of methane, the sole added organic carbon substrate, to CO₂ with concomitant reduction of sulphate to sulphide (Fig. 1a, b). Single-cell analyses by nano-metre-scale secondary ion mass spectrometry (nanoSIMS) show that both microbial groups primarily (>90% of cellular C) derive their biomass carbon from dissolved inorganic carbon (DIC) assimilation and have similar doubling times of 130–160 days (Supplementary Table 1). These values are in agreement with the doubling times deduced previously from bulk measurements in AOM enrichment cultures^{7,8}. The preferential assimilation of DIC by DSS bacteria indicates that these organisms are lithoautotrophs⁸, and do not directly assimilate methane. ANME assimilate both methane-derived and inorganic carbon (Supplementary Table 1).

Immunodetection of canonical sulphate-reducing enzymes (ATP sulphurylase (Sat) and dissimilatory sulphite reductase (Dsr)) and methyl-coenzyme M reductase (Mcr; an archaeal enzyme involved in methane oxidation) in the two abundant cell populations (Fig. 1c) is

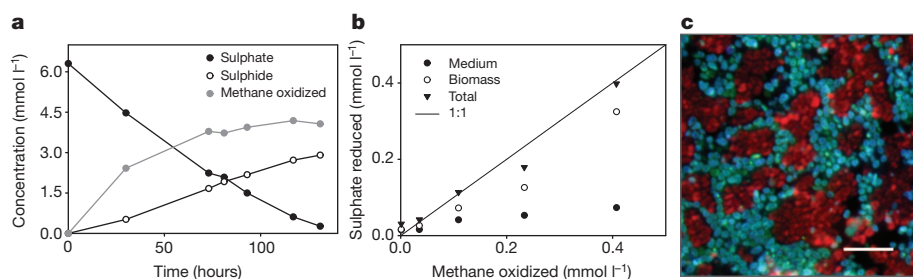


Figure 1 | Microbial activity and composition of the Isis enrichment culture. **a**, Anaerobic oxidation of methane determined from ¹³CO₂ production, decrease in sulphate concentration and increase in sulphide concentration versus time (hours) in incubations with added ¹³CH₄ (*n* = 3). **b**, Total sulphate-derived reduced sulphur species (a sum of reduced sulphur in medium and reduced sulphur in biomass) as determined from ³⁵S accumulation versus methane oxidation as determined from ¹⁴CO₂ production

in incubations with added [³⁵S]sulphate and ¹⁴CH₄ during the first 11 h of a batch incubation (*n* = 1; this experiment was repeated twice). **c**, AOM aggregate labelled with anti-Sat (ATP sulphurylase, green), anti-Dsr (dissimilatory sulphite reductase, blue) and anti-Mcr (methyl-CoM reductase, red) antibodies. Mcr is localized in the larger, irregularly shaped ANME-2 (red), whereas Sat and Dsr co-localize in the rod-shaped DSS bacteria (turquoise). Scale bar, 5 μm.

¹Max Planck Institute for Marine Microbiology, Celsiusstrasse 1, 28359 Bremen, Germany. ²Alfred Wegener Institute, Am Handelshafen 12, 27570 Bremerhaven, Germany. ³University of Vienna, Althanstrasse 14, A-1090 Vienna, Austria. ⁴Max Planck Institute for Polymer Research, Ackermannweg 10, 55128 Mainz, Germany.

consistent with the hypothesis that, in AOM consortia, methane oxidation and (canonical) dissimilatory sulphate reduction are catalysed by ANME and DSS bacteria, respectively. Moreover, the high abundance of DSS bacteria and their similar doubling times with the ANME serve as a support for involvement of both organisms in AOM. Several hypotheses propose a syntrophic mechanism of these consortia, all of which assume a flow of electrons from the ANME to the bacteria. Available experimental evidence^{9,10} as well as most current modelling studies^{11–13}, however, show that putative syntrophic intermediates (that is, hydrogen, formate, acetate or methanol) are not used as electron donors for sulphate reduction during AOM. Other theories suggest a role for methanethiol¹⁴, use of extracellular nanowires^{15,16} or a direct cell-to-cell contact for direct electron transfer. Yet evidence for these hypotheses is still lacking.

Zero-valent sulphur as an intermediate

If the syntrophy is based on extracellular diffusion of a chemical compound, this is expected to be formed from the substrate or from a compound readily available in the environment. We therefore considered involvement of sulphur in oxidation states other than the abundant sulphate or sulphide as a syntrophic intermediate in AOM. Zero-valent sulphur (S^0), in the form of elemental sulphur and dissolved polysulphide sulphur, is commonly measured in the highly reducing, sulphidic environments that characterize AOM ecosystems¹⁷, indicating that not all sulphate is reduced to the $-II$ oxidation state. As the reduction of one sulphate to S^0 only requires six of the eight electrons obtained from methane oxidation, the measured sulphate reduction rates determined from decrease in sulphate would exceed those of anaerobic oxidation of methane. This would result in AOM and sulphate reduction rates that are not coupled exactly in the 1:1 stoichiometry given by equation (1)^{18,19}. Interestingly, in our enrichment culture less sulphide was produced than expected from the decrease in sulphate (Fig. 1a), indicating that reduced sulphur other than sulphide is formed during AOM-coupled sulphate reduction.

The presence of S^0 in wet biomass of our AOM enrichment culture was confirmed by anaerobic extraction with methanol and subsequent analysis of S_8 by high-performance liquid chromatography (HPLC), which revealed elemental sulphur content of up to approximately 5 mmol S per gram of dry biomass ($\sim 15\%$ w/w). Wet biomass was also anaerobically extracted in the presence of methyl trifluoromethanesulphonate, a strong methylating agent that prevents oxidation of labile polysulphides into elemental sulphur by converting them into stable dimethylpolysulphides, which are HPLC- and gas-chromatography-amenable²⁰. HPLC analysis of the methyl trifluoromethanesulphonate-treated methanol extracts showed that the sample contained, besides colloidal sulphur, substantial (up to 0.5 mmol l^{-1}) amounts of all measurable inorganic polysulphides (S_3^{2-} to S_8^{2-} ; Supplementary Fig. 1). The presence of polysulphides in the AOM biomass was confirmed by gas chromatography-mass spectrometry. In contrast, biomass-free medium from the same active culture contained little to no detectable S^0 .

By using confocal micro-Raman spectroscopy with approximately $1 \mu\text{m}$ resolution we detected elemental sulphur in ANME cells identified by FISH (Fig. 2a and Supplementary Fig. 2a–c). Characteristic and strong Raman peaks for elemental sulphur^{21,22} were also recorded in untreated ANME cells (Supplementary Fig. 2d), indicating intracellular accumulation of substantial amounts of elemental sulphur in living cells. NanoSIMS analyses of fixed and sectioned cells showed that ANME cells (Fig. 2b–e), identified by antibodies against Mcr (Fig. 2e), have substantially higher sulphur content than DSS cells ($\sim 30\%$ higher $^{32}\text{S}/^{12}\text{C}$ ratio on average, Supplementary Fig. 3). Although the ANME and the DSS are present in equal abundance (for example, Fig. 1c), most of the AOM biomass is composed of ANME ($\sim 75\%$) due to their substantially larger size (ANME/DSS volume ratio = 3:1; Fig. 2b, c). Therefore, we assume that the bulk of the intracellular S^0 in the biomass is present in the ANME cells. Interestingly, the sulphur content of the ANME correlated ($R^2 = 0.8$; $P < 0.0001$) with the rate of methane assimilation (and thus methane oxidation; Fig. 2f and Supplementary Fig. 4), indicating

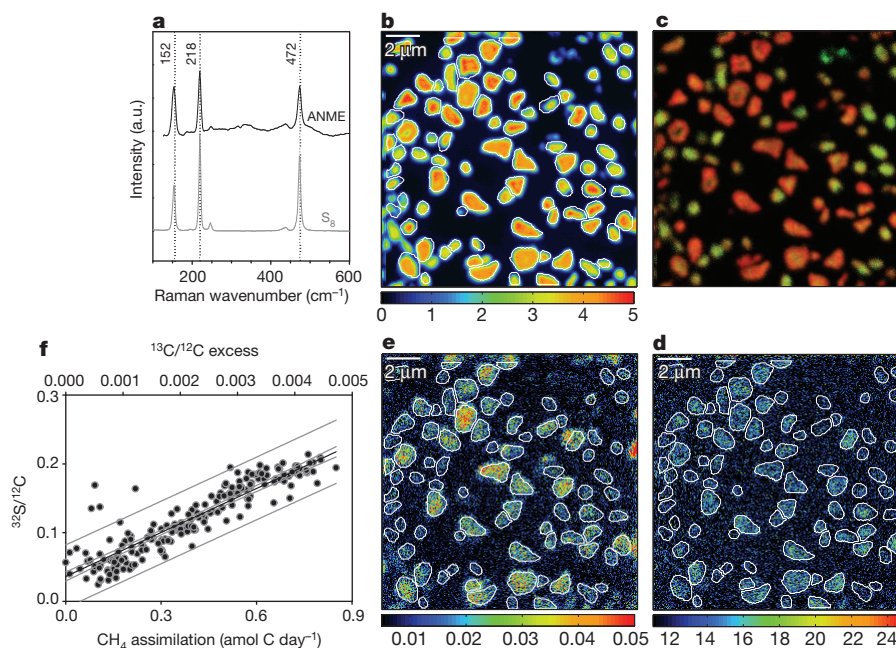


Figure 2 | Zero-valent S in ANME cells in the Isis enrichment culture.

a, Representative Raman spectrum of an ANME cell, identified by FISH ($n = 1$; 30 additional ANME-2 spectra were measured; see also Supplementary Fig. 2), containing prominent peaks at 152, 218 and 472 cm^{-1} characteristic for elemental sulphur (see our reference spectrum of S_8 and refs 21 and 22). a.u., Arbitrary units. **b–e**, NanoSIMS images of Isis enrichment aggregates incubated with ^{13}C -labelled methane. **b**, Individual cells in an AOM aggregate visualized by $^{13}\text{C}/^{12}\text{C}$ ion image. **c**, Composite image showing

sulphur-rich ANME cells (red) and phosphorus-rich DSS cells (green), raw data for this image are provided in Supplementary Fig. 13. **d**, $^{13}\text{CH}_4$ -derived ^{13}C assimilation by ANME shown by a $^{13}\text{C}/^{12}\text{C}$ image (values were multiplied by 1,000). **e**, $^{197}\text{Au}/^{12}\text{C}$ image showing ANME cells targeted by gold-labelled antibodies against Mcr. Coloured scale below panels **b**, **d** and **e** shows ratio of the respective ions. **f**, $^{13}\text{C}/^{12}\text{C}$ excess and the respective methane assimilation determined from $^{13}\text{CH}_4$ -incubations versus $^{32}\text{S}/^{12}\text{C}$ ratio for ANME cells ($n = 198$). Scale bars, $2 \mu\text{m}$.

that intracellular sulphur in the ANME cells is turned over in relation to AOM.

To identify the source of the S^0 , our enrichment culture was incubated under AOM conditions for up to 24 h with $^{34}SO_4^{2-}$ and $^{35}SO_4^{2-}$. The accumulation of sulphate-derived reduced sulphur species in the medium and in the biomass was followed over time. In incubations with a small ($<50 \mu\text{mol l}^{-1}$) added non-labelled sulphide pool, ^{35}S -label from sulphate was detectable in the AOM biomass within 1 h and preceded the release of detectable ^{35}S sulphide into the medium (Supplementary Fig. 5). It is unlikely that the biomass S is a result of assimilatory metabolism because the rate of sulphur accumulation (μmol to mmol per litre per day) by far exceeds the sulphur requirements of these ultra-slow-growing organisms (pmol to nmol per litre per day). Moreover, the rate of sulphur accumulation exceeds the rate of carbon assimilation by the ANME by two orders of magnitude, indicating that the sulphur present in ANME biomass is not used for growth (Supplementary Fig. 6). The rates of overall sulphur turnover (calculated as a sum of both biomass sulphur and reduced sulphur in the medium) were proportional to the measured methane oxidation rates (Fig. 1b). Moreover, the total amount of sulphate reduced (that is, biomass sulphur and sulphide) and methane oxidized approximately follows the 1:1 ratio predicted from the overall stoichiometry of the AOM reaction (equation (1)). This agrees well with the approximately 1:1 ratio for methane oxidation coupled to sulphate reduction previously reported for this and other sulphate-reducing AOM enrichment cultures (for example, refs 10 and 23).

Accumulation of ^{35}S label from sulphate in the AOM biomass before its appearance in the sulphide pool strongly indicates that sulphide oxidation is not the source of biomass sulphur. Indeed, our enrichment culture is maintained under strongly reducing conditions, with no detectable potential oxidants for sulphide other than sulphate. Moreover, incubation of the culture in the presence of ^{35}S sulphide did not lead to a sustainable increase in the ^{35}S content of the biomass with time (Supplementary Fig. 7) as observed during the ^{35}S sulphate addition experiment (Supplementary Fig. 5). This shows that the accumulation of $^{35}S^0$ in the biomass is neither a result of isotope exchange, nor sulphide oxidation, but rather results directly from the reduction of ^{35}S sulphate (Supplementary Discussion). To the best of our knowledge, this is the first evidence for direct S^0 formation during sulphate reduction. Our results indicate that zero-valent sulphur formation in strongly reducing environments can occur even when no potential oxidants other than sulphate (for example, Fe III-containing minerals) are available.

Archaeal sulphate reduction

The AOM-dependent accumulation and turnover of sulphate-derived S^0 in the ANME leads us to conclude that ANME are capable of reducing sulphate to S^0 and, potentially, to sulphide. Accordingly, the addition of bacterial inhibitors (tetracycline and streptomycin) had no detectable effect on the rate of sulphate reduction in the enrichment culture (Supplementary Fig. 8). The enzymatic mechanism of this archaeal sulphate reduction is unclear. All genes and proteins for dissimilatory sulphate reduction that have been so far retrieved from AOM environments and cultures have been shown to be of bacterial origin (for example, refs 6 and 24). Protein immunodetection showed that the ANME did not contain detectable amounts of the canonical enzymes for sulphate reduction (for example, Fig. 1c). Therefore, we propose that sulphate reduction in the ANME might proceed via an enzymatic pathway other than the canonical one (that is, involving Sat, Apr and Dsr). Notably, the formylmethanofuran (MFR)/ CO_2 + MFR redox couple in methanotrophic archaea has a sufficiently low standard midpoint potential (-530 mV) to serve as an electron donor for direct reduction of sulphate to sulphite without the use of ATP²⁵, which is needed to activate sulphate in all known dissimilatory sulphate-reducing microorganisms. Although experimental evidence for such mechanism is not yet available, this could explain

why the non-thermophilic archaeal sulphate reduction has so far remained undetected despite being proposed numerous times^{26–30}.

Bacterial disulphide disproportionation

Direct coupling of methane oxidation to dissimilatory sulphate reduction in the ANME indicates that we must reconsider the role of the Deltaproteobacteria in AOM. The abundant expression of Sat and Dsr enzymes by the DSS in our enrichment culture (Fig. 1c) does not necessarily mean that they perform canonical sulphate reduction. Other pathways, such as sulphide oxidation and disproportionation of intermediate oxidation state sulphur compounds (elemental sulphur, thiosulphate and sulphite), also use Sat, Apr and Dsr^{31,32}. Our incubation experiments with ^{35}S -labelled sulphide render sulphide oxidation unlikely (Supplementary Fig. 7). To test whether the DSS have the capacity to disproportionate, we added colloidal sulphur (approximately 7 mmol l^{-1}) to the Isis enrichment culture in the absence of methane or any other electron donors. Immediately, linear production of sulphide and sulphate was observed (Supplementary Fig. 9) that reached a stoichiometric ratio of 7:1 (Fig. 3a) that was maintained until all added sulphur was consumed. The stoichiometric ratio for elemental sulphur disproportionation is 3:1, significantly lower than the 7:1 ratio observed in our experiment, but under sulphidic conditions that prevail in our incubations, elemental sulphur would react with dissolved sulphide to form soluble inorganic polysulphides that can also be disproportionated. Indeed, the theoretical ratio of sulphide to sulphate production during disulphide disproportionation is exactly 7:1 (equation (2), Supplementary Table 2)

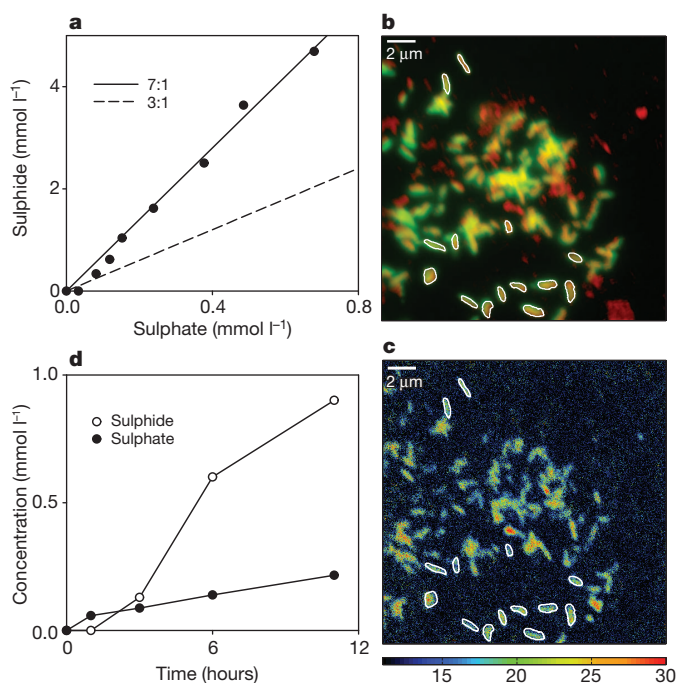


Figure 3 | Disulphide disproportionation by Isis enrichment culture.

a, Linear correlation between sulphate and sulphide production in the Isis enrichment culture incubated with $^{13}CO_2$ and colloidal sulphur in the absence of methane over the course of 70 days ($n = 1$) follows the 7:1 ratio inferred for disulphide disproportionation. **b**, Overlay of nanoSIMS $^{12}C/^{14}N$ image (red) and fluorescence image of microorganisms from the enrichment culture stained with the DSS-658 probe (green). **c**, The $^{13}C/^{12}C$ image shows that the DSS cells (several of which are shown by white outlines) are enriched in ^{13}C . Coloured scale below panel c shows ratio of the respective ions. **d**, Production of sulphide and sulphate (based on ^{35}S accumulation in sulphate after the addition of ^{35}S -sulphide) under AOM conditions ($n = 1$; this experiment was repeated twice).

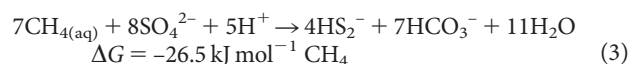
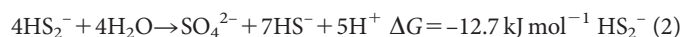
indicating that the organisms in our AOM enrichment disproportionate this most simple of all inorganic polysulphides. The rates of disulphide disproportionation remained constant over a wide range of sulphide concentrations (at least 5 mmol l^{-1}), indicating that disproportionation of disulphide is less sensitive to sulphide than disproportionation of elemental sulphur, and can thus occur in sulphidic environments. To confirm that disulphide disproportionation can support growth, autotrophic carbon assimilation in the biomass was followed by the addition of $\text{H}^{14}\text{CO}_3^-$ and $\text{H}^{13}\text{CO}_3^-$ to the medium. The amount of ^{14}C in the bulk AOM biomass increased with time (Supplementary Fig. 9), indicating that the observed disproportionation is coupled to energy generation and growth. Indeed, single-cell nanoSIMS analysis revealed that DSS-class Deltaproteobacteria, identified by CARD-FISH, were capable of autotrophic growth under disproportionating conditions (Fig. 3b, c). Interestingly, ANME-2 were no longer detectable in the enrichment culture after 70 days of incubation in the presence of colloidal sulphur (Supplementary Fig. 10).

The evidence that disulphide disproportionation also occurs under AOM conditions was provided by the H^{35}S^- -addition experiment. A substantial part of the ^{35}S from ^{35}S -labelled sulphide was recovered in the sulphate pool, although no net sulphate production was observed (Fig. 3d and Supplementary Fig. 11). The rates of sulphide production to tracer-derived sulphate production were approximately 6:1, similar to the 7:1 ratio observed during disulphide disproportionation. In a comparable experiment with the same culture²³, a ratio of produced sulphide to sulphate of approximately 8:1 was obtained. Our combined results indicate that the high transfer rate of ^{35}S sulphide to the sulphate pool ($\sim 12\%$ of AOM rate) can be primarily attributed to the disproportionation of disulphide or S^0 .

Model for sulphate-dependent AOM

On the basis of our observations and thermodynamic considerations, we propose the following model for sulphur cycling between ANME-2 and Deltaproteobacteria involved in AOM (Fig. 4). ANME-2 perform anaerobic oxidation of methane and reduction of sulphate to disulphide (or another S^0 compound, and possibly partly even all the way to sulphide). Disulphide is taken up by the DSS and disproportionated

to sulphide and sulphate in a 7:1 ratio. Sulphate formed during disproportionation is partly re-used by the ANME-2 to oxidize methane and thus no net sulphate production occurs. The overall stoichiometry of AOM coupled to disproportionation (one mole sulphate reduced per one mole methane oxidized) remains 1:1 (that is, sum of equations (2) and (3) gives equation (1)).



Thermodynamic calculations show that the energy gain of the ANME-2:DSS cell abundance ratio in our cultures is maintained close to 1:1 while their size and presumably also biomass ratio is 3:1.

Although the phylogenetically distinct ANME-1 and -3 clusters may have different physiologies, our model could explain the occurrence of single active ANME-2 cells in *in vitro* incubations³³ and in marine environments^{30,34}. The ANME-2 might not depend directly on the activity of bacterial partners because in environments rich in sulphate and methane, sulphate reduction to disulphide is exergonic over a wide range of disulphide concentrations (Supplementary Fig. 12 and Supplementary Discussion). Interestingly, disulphide in its partly protonated form (HS_2^-) is particularly stable at around neutral pH and low Eh³⁵, conditions typical for AOM zones. Although disulphide has largely eluded detection in natural environments, it should be abundant in marine sediments that are undersaturated with respect to S^0 (ref. 17). Thermodynamic calculations also show that AOM coupled to sulphate reduction becomes energetically more favourable if the disulphide produced is scavenged (Supplementary Fig. 12). In principle, ANME-2 can associate with any bacteria that possess the capacity to scavenge the disulphide produced. In several studies ANME-2 and -3 were found to co-exist with bacteria of the order Desulfobulbaceae^{36–38}. Notably, bacteria belonging to this order have been shown to be capable of disproportionation^{39,40}. Thus, a model whereby archaea reduce sulphate to zero-valent sulphur while mediating methane oxidation, and the bacteria gain energy from disproportionation, is consistent with known distributions of archaea and bacteria in AOM habitats.

Biogeochemical implications

Our model could also explain why sulphate reduction has been detected in deeply-buried, methane- and sulphide-rich sediments⁴¹ inhabited by archaea^{42,43}. The deep subsurface is dominated by a large number of different archaeal groups such as the miscellaneous crenarchaeotal group⁴⁴ and marine benthic group B that lack cultured representatives and whose physiology is largely unexplored. It is possible that these archaea might have also adopted a unique pathway for sulphate reduction that might not be necessarily coupled to methanotrophy. The revised model for AOM (Fig. 4), by necessity, should lead to a re-evaluation of the biogeochemistry of methane oxidation and sulphur cycling in marine environments. Current diagenetic models for deep marine sediments are deficient, or 'leaky' with respect to their redox balance⁴⁵. Although methane is oxidized to CO_2 (8 e^-), the ultimate end-product of sulphate reduction in deep marine sediments takes the form of buried iron disulphide, pyrite, in which S has an oxidation state of -1 . Archaeal sulphate reduction to S^0 provides a source of zero-valent sulphur for the formation of pyrite and would therefore mitigate the need to provide an external oxidant (for example, Fe III; ref. 46).

Overall, to our knowledge our observations provide for the first time strong evidence that intercellular sulphur cycling occurs between ANME-2 and DSS Deltaproteobacteria during AOM, which involves new pathways of sulphate reduction and disulphide disproportionation.

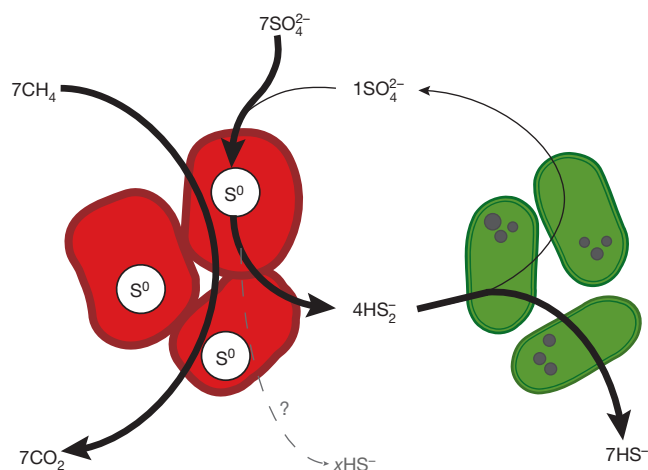


Figure 4 | Revised model of anaerobic oxidation of methane coupled to sulphate reduction. ANME-2 oxidize methane with a concomitant reduction of sulphate to zero-valent sulphur (S^0 , elemental sulphur) that is partially deposited or bound intracellularly. Produced S^0 is exported or diffuses outside the cell where it reacts with sulphide to form polysulphides (disulphide, among others). Disulphide is taken up by the associated Deltaproteobacteria and is disproportionated to sulphate and sulphide. Sulphate produced during disproportionation might be re-used by the ANME and the ANME may also reduce some of the sulphate all the way to sulphide (grey dotted line). Dark circles in the bacteria represent intracellular precipitates rich in iron and phosphorus (Fig. 2c and Supplementary Fig. 14).

These results also greatly expand the range of conditions under which sulphur disproportionation is likely to occur⁴⁷, and, in a large picture, encourage the re-evaluation of the role of sulphate-reducing archaea and sulphur-disproportionating bacteria in present-day and early Earth environments.

METHODS SUMMARY

In all AOM experiments, the Isis enrichment culture was incubated anaerobically in artificial seawater medium with methane as sole electron donor and sulphate as sole electron acceptor. To determine the potential for S^0 disproportionation, colloidal sulphur was added to the medium and the culture was incubated without methane and sulphate.

Methane oxidation rates were determined from $^{13}CO_2$ production in $^{13}CH_4$ incubations by gas chromatography-isotope ratio mass spectrometry or from $^{14}CO_2$ production in $^{14}CH_4$ incubations by scintillation counting. Sulphate reduction rates were determined as changes in sulphate and sulphide concentrations determined by ion chromatography and photometrically, respectively, and from $[^{35}S]$ sulphide production in $[^{35}S]$ sulphate incubations. Sulphate production was determined by ion chromatography in the disproportionation experiments. The sulphate production under AOM conditions was determined from $[^{35}S]$ sulphate production in $[^{35}S]$ sulphide incubations. Elemental S and polysulphide concentrations in biomass and medium were determined by liquid chromatography.

Microbial aggregates from the AOM experiments were collected for immunolabelling, fixed with formaldehyde and cryosectioned. Subsequently, the sections were labelled with primary antibodies targeting either key enzyme(s) for anaerobic oxidation of methane (Mcr) or the canonical sulphate reduction pathway (Apr and Dsr) and fluorochrome- or gold-coupled secondary antibodies. Samples from the disproportionation experiment were collected for halogen *in situ* hybridization. Assimilation of $[^{13}C]DIC$ and $[^{14}C]DIC$ in the biomass in the various experiments was followed by bulk ^{13}C measurements, with nanometre-scale secondary ion mass spectrometry (nanoSIMS) and by scintillation counting, respectively. Doubling times and carbon assimilation of single cells were determined from $[^{13}C]$ methane or $[^{13}C]DIC$ incubations by using nanoSIMS. The presence of S^0 in single cells was determined by Raman-FISH.

Thermodynamic calculations were made for the concentrations and activity coefficients typical for the start of a batch enrichment culture and are listed in Supplementary Information (Supplementary Tables 3, 4 and 5).

Full Methods and any associated references are available in the online version of the paper.

Received 12 April; accepted 3 October 2012.

Published online 7 November 2012.

- Knittel, K. & Boetius, A. Anaerobic oxidation of methane: progress with an unknown process. *Annu. Rev. Microbiol.* **63**, 311–334 (2009).
- Hoehler, T. M., Alperin, M. J., Albert, D. B. & Martens, C. S. Field and laboratory studies of methane oxidation in an anoxic marine sediment: evidence for a methanogen-sulfate reducer consortium. *Glob. Biogeochem. Cycles* **8**, 451–463 (1994).
- Boetius, A. *et al.* A marine microbial consortium apparently mediating anaerobic oxidation of methane. *Nature* **407**, 623–626 (2000).
- Orphan, V. J., House, C. H., Hinrichs, K. U., McKeegan, K. D. & DeLong, E. F. Methane-consuming archaea revealed by directly coupled isotopic and phylogenetic analysis. *Science* **293**, 484–487 (2001).
- Alperin, M. & Hoehler, T. The ongoing mystery of sea-floor methane. *Science* **329**, 288–289 (2010).
- Schreiber, L., Holler, T., Knittel, K., Meyerdierks, A. & Amann, R. Identification of the dominant sulfate-reducing bacterial partner of anaerobic methanotrophs of the ANME-2 clade. *Environ. Microbiol.* **12**, 2327–2340 (2010).
- Nauhaus, K., Albrecht, M., Elvert, M., Boetius, A. & Widdel, F. *In vitro* cell growth of marine archaeal-bacterial consortia during anaerobic oxidation of methane with sulfate. *Environ. Microbiol.* **9**, 187–196 (2007).
- Wegener, G., Niemann, H., Elvert, M., Hinrichs, K. U. & Boetius, A. Assimilation of methane and inorganic carbon by microbial communities mediating the anaerobic oxidation of methane. *Environ. Microbiol.* **10**, 2287–2298 (2008).
- Meulepas, R. J. W., Jagersma, C. G., Khadem, A. F., Stams, A. J. M. & Lens, P. N. L. Effect of methanogenic substrates on anaerobic oxidation of methane and sulfate reduction by an anaerobic methanotrophic enrichment. *Appl. Microbiol. Biotechnol.* **87**, 1499–1506 (2010).
- Nauhaus, K., Boetius, A., Kruger, M. & Widdel, F. *In vitro* demonstration of anaerobic oxidation of methane coupled to sulphate reduction in sediment from a marine gas hydrate area. *Environ. Microbiol.* **4**, 296–305 (2002).
- Sørensen, K. B., Finster, K. & Ramsing, N. B. Thermodynamic and kinetic requirements in anaerobic methane oxidizing consortia exclude hydrogen, acetate, and methanol as possible electron shuttles. *Microb. Ecol.* **42**, 1–10 (2001).
- Orcutt, B. & Meile, C. Constraints on mechanisms and rates of anaerobic oxidation of methane by microbial consortia: process-based modeling of ANME-2 archaea and sulfate reducing bacteria interactions. *Biogeosciences* **5**, 1587–1599 (2008).
- Alperin, M. J. & Hoehler, T. M. Anaerobic methane oxidation by archaea/sulfate-reducing bacteria aggregates: 1. Thermodynamic and physical constraints. *Am. J. Sci.* **309**, 869–957 (2009).
- Moran, J. J. *et al.* Methyl sulfides as intermediates in the anaerobic oxidation of methane. *Environ. Microbiol.* **10**, 162–173 (2008).
- Meyerdierks, A. *et al.* Metagenome and mRNA expression analyses of anaerobic methanotrophic archaea of the ANME-1 group. *Environ. Microbiol.* **12**, 422–439 (2010).
- Shima, S. & Thauer, R. K. Methyl-coenzyme M reductase and the anaerobic oxidation of methane in methanotrophic Archaea. *Curr. Opin. Microbiol.* **8**, 643–648 (2005).
- Holmkvist, L. *et al.* Sulfate reduction below the sulfate-methane transition in Black Sea sediments. *Deep Sea Res. Part I Oceanogr. Res. Pap.* **58**, 493–504 (2011).
- Joye, S. B. *et al.* The anaerobic oxidation of methane and sulfate reduction in sediments from Gulf of Mexico cold seeps. *Chem. Geol.* **205**, 219–238 (2004).
- Hansen, L. B., Finster, K., Fossing, H. & Iversen, N. Anaerobic methane oxidation in sulfate depleted sediments: effects of sulfate and molybdate additions. *Aquat. Microb. Ecol.* **14**, 195–204 (1998).
- Kamysny, A., Ekelchik, I., Gun, J. & Lev, O. Method for the determination of inorganic polysulfide distribution in aquatic systems. *Anal. Chem.* **78**, 2631–2639 (2006).
- Pasteris, J. D., Freeman, J. J., Goffredi, S. K. & Buck, K. R. Raman spectroscopic and laser scanning confocal microscopic analysis of sulfur in living sulfur-precipitating marine bacteria. *Chem. Geol.* **180**, 3–18 (2001).
- Trofimov, B. A., Sinegovskaya, L. M. & Gusarova, N. K. Vibrations of the S-S bond in elemental sulfur and organic polysulfides: a structural guide. *J. Sulfur Chem.* **30**, 518–554 (2009).
- Holler, T. *et al.* Carbon and sulfur back flux during anaerobic microbial oxidation of methane and coupled sulfate reduction. *Proc. Natl Acad. Sci. USA* **108**, E1484–E1490 (2011).
- Basen, M. *et al.* Bacterial enzymes for dissimilatory sulfate reduction in a marine microbial mat (Black Sea) mediating anaerobic oxidation of methane. *Environ. Microbiol.* **13**, 1370–1379 (2011).
- Thauer, R. K. Biochemistry of methanogenesis: a tribute to Marjory Stephenson. *Microbiology* **144**, 2377–2406 (1998).
- Widdel, F., Musat, F., Knittel, K. & Galushko, A. in *Sulphate-Reducing Bacteria: Environmental and Engineered Systems* (eds Barton, L. *et al.*) 265–303 (Cambridge Univ. Press, 2007).
- Johnson, E. F. & Mukhopadhyay, B. in *Microbial Sulfur Metabolism*. (eds Dahl, C. *et al.*) 202–216 (Springer, 2008).
- Thauer, R. K. & Shima, S. in *Incredible Anaerobes: from Physiology to Genomics to Fuels* Vol. 1125 158–170 (Wiley-Blackwell, 2008).
- Thauer, R. K. Anaerobic oxidation of methane with sulfate: on the reversibility of the reactions that are catalyzed by enzymes also involved in methanogenesis from CO_2 . *Curr. Opin. Microbiol.* **14**, 292–299 (2011).
- Orphan, V. J., House, C. H., Hinrichs, K. U., McKeegan, K. D. & DeLong, E. F. Multiple archaeal groups mediate methane oxidation in anoxic cold seep sediments. *Proc. Natl Acad. Sci. USA* **99**, 7663–7668 (2002).
- Krämer, M. & Cypionka, H. Sulfate formation via ATP sulfurylase in thiosulfate-disproportionating and sulfite-disproportionating bacteria. *Arch. Microbiol.* **151**, 232–237 (1989).
- Trüper, H. G. & Fischer, U. Anaerobic oxidation of sulfur compounds as electron donors for bacterial photosynthesis. *Phil. Trans. R. Soc. Lond. B* **298**, 529–542 (1982).
- House, C. H., Beal, E. J. & Orphan, V. J. The apparent involvement of ANMEs in mineral dependent methane oxidation, as an analog for possible Martian methanotrophy. *Life* **1**, 19–33 (2011).
- Treude, T. *et al.* Consumption of methane and CO_2 by methanotrophic microbial mats from gas seeps of the anoxic Black Sea. *Appl. Environ. Microbiol.* **73**, 2271–2283 (2007).
- Rickard, D. & Luther, G. W. Chemistry of iron sulfides. *Chem. Rev.* **107**, 514–562 (2007).
- Niemann, H. *et al.* Novel microbial communities of the Haakon Mosby mud volcano and their role as a methane sink. *Nature* **443**, 854–858 (2006).
- Lösekann, T. *et al.* Diversity and abundance of aerobic and anaerobic methane oxidizers at the Haakon Mosby mud volcano, Barents Sea. *Appl. Environ. Microbiol.* **73**, 3348–3362 (2007).
- Pernthaler, A. *et al.* Diverse syntrophic partnerships from deep-sea methane vents revealed by direct cell capture and metagenomics. *Proc. Natl Acad. Sci. USA* **105**, 7052–7057 (2008).
- Lovley, D. R. & Phillips, E. J. P. Novel processes for anaerobic sulfate production from elemental sulfur by sulfate-reducing bacteria. *Appl. Environ. Microbiol.* **60**, 2394–2399 (1994).
- Fuseler, K. & Cypionka, H. Elemental sulfur as an intermediate of sulfide oxidation with oxygen by *Desulfobulbus propionicus*. *Arch. Microbiol.* **164**, 104–109 (1995).
- Parkes, R. J. *et al.* Deep sub-seafloor prokaryotes stimulated at interfaces over geological time. *Nature* **436**, 390–394 (2005).
- Lipp, J. S., Morono, Y., Inagaki, F. & Hinrichs, K. U. Significant contribution of Archaea to extant biomass in marine subsurface sediments. *Nature* **454**, 991–994 (2008).
- Teske, A. & Sørensen, K. B. Uncultured archaea in deep marine subsurface sediments: have we caught them all? *ISME J.* **2**, 3–18 (2008).
- Kubo, K. *et al.* Archaea of the Miscellaneous Crenarchaeotal Group are abundant, diverse and widespread in marine sediments. *ISME J.* **6**, 1949–1965 (2012).

45. Meysman, F. J. R. & Middelburg, J. J. Acid-volatile sulfide (AVS) — a comment. *Mar. Chem.* **97**, 206–212 (2005).
46. Holmkvist, L., Ferdelman, T. G. & Jørgensen, B. B. A cryptic sulfur cycle driven by iron in the methane zone of marine sediment (Aarhus Bay, Denmark). *Geochim. Cosmochim. Acta* **75**, 3581–3599 (2011).
47. Philippot, P. *et al.* Early Archaean microorganisms preferred elemental sulfur, not sulfate. *Science* **317**, 1534–1537 (2007).

Supplementary Information is available in the online version of the paper.

Acknowledgements We want to thank G. Klockgether, K. Imhoff, S. Littmann and T. Vagner for technical support, G. Lavik and M. Formolo for analytical support and discussions, M. Schüler and T. Keil for assistance with cryosectioning, A. Boetius for providing samples, and T. Holler for the initial enrichment and maintenance of the *Isis*

culture. This work was financially supported by the Max Planck Society and the ERC Advanced Grant 294343 (to M.W.).

Author Contributions J.M., T.G.F., F.W. and M.M.M.K. designed experiments. J.M., T.G.F. and M.M.M.K. performed experiments and analysed data. J.M. performed immunolabeling and microscopy. D.F. performed CARD-FISH and nanoSIMS. L.P. analysed nanoSIMS data. M.S. and M.W. performed Raman measurements, I.L. performed energy-dispersive X-ray spectroscopy analyses, and G.W. contributed new analytical tools. J.M., T.G.F. and M.M.M.K. wrote the manuscript with contributions of all co-authors.

Author Information Reprints and permissions information is available at www.nature.com/reprints. The authors declare no competing financial interests. Readers are welcome to comment on the online version of the paper. Correspondence and requests for materials should be addressed to J.M. (jmilucka@mpi-bremen.de).

METHODS

Cultivation and incubation experiments. The enrichment culture 'Isis' was obtained through continuous (>8 years) incubation from a sediment sample collected on a cruise of RV *L'Atalante* in September 2003 in the eastern Mediterranean Sea (depth ~990 m, *in situ* temperature ~14 °C⁵⁰). The culture was incubated in artificial seawater medium (pH 7.5; salt composition: 0.76 mmol l⁻¹ KBr, 8.05 mmol l⁻¹ KCl, 10 mmol l⁻¹ CaCl₂·2H₂O, 27.9 mmol l⁻¹ MgCl₂·6H₂O, 27.6 mmol l⁻¹ MgSO₄·7H₂O, 451 mmol l⁻¹ NaCl, 4.67 mmol l⁻¹ NH₄Cl, 1.47 mmol l⁻¹ KH₂PO₄; buffer: 30 mmol l⁻¹ HCO₃⁻; trace elements and vitamins prepared and added according to ref. 51; reducing agent ~0.5 mmol l⁻¹ Na₂S) in closed culture vials with CH₄:N₂:CO₂ (75:22.5:2.5) headspace. Methane (Air Liquide) was added to 3 bar overpressure unless indicated otherwise. AOM activity was followed by quantification of methane-dependent sulphide formation using spectrophotometry⁵². When sulphide concentrations in the medium reached ~10 mmol l⁻¹ used medium was replaced by fresh medium. All experiments were performed at room temperature and during all incubations the vials were continuously shaken (40 r.p.m.) to facilitate gas transport.

Maintenance and handling of the culture was performed in an anoxic glove box (Mecaplex) under N₂:CO₂ (90:10) atmosphere. For all experiments an active preculture with high AOM rates (0.24 mmol HS⁻ per gram (dry weight) per day) was used but the culture was diluted into aliquots with different activities for individual experiments.

For the inhibition experiments with selected antibiotics, active Isis culture was aliquoted into three 70 ml serum bottles (25 ml medium + biomass and 45 ml headspace) and pre-incubated for 72 h under AOM conditions (3 bar CH₄ overpressure, ~30 atom % ¹³C; ISOTEC, Sigma-Aldrich) until linear sulphide production was observed. Then, without releasing methane overpressure, streptomycin and tetracycline were added (anoxically and in sterile conditions) to two of the serum bottles, respectively, from a sterile anoxic stock solution (5 g l⁻¹ each) to a final concentration of 25 mg l⁻¹. This concentration has been reported to have inhibitory effect on sulphate-reducing bacteria⁵³. The third bottle was untreated with antibiotics and served as a control. The bottles were incubated on a shaker (40 r.p.m.) at room temperature in the dark. Subsamples were taken anoxically with needles at regular time intervals to monitor the methane oxidation as well as changes in the concentration of total sulphate and sulphide. The sampling involved following: 0.3 ml culture was filtered through a 0.2-µm filter into 50% ZnCl₂ for sulphide measurements; 0.3 ml culture was filtered through a 0.2-µm filter into 0.01 M HCl for sulphate measurements and 0.5 ml culture was filtered onto a 0.22-µm GTTP filter for ³⁵S-scintillation counting. Sulphide was measured using colorimetry⁵⁴, sulphate was measured as described below. Methane oxidation rates were calculated from the measured production of ¹³CO₂. For ¹³CO₂ measurements, 1 ml of sample was filtered through a 0.22-µm filter into a sterile Exetainer. The headspace of the Exetainer was then exchanged with Helium and the sample was acidified by the addition of 100 µl 85% phosphoric acid through the Exetainer septum. The samples were stored upside down at room temperature until measured with gas chromatography-isotope ratio mass spectrometry (GC-IRMS; Fisons VG Optima).

To test for the disproportionation potential of the AOM culture, colloidal sulphur, prepared according to ref. 55, was cleaned through repeated cycles (8–10×) of peptization. To bring it into the anoxic glove box, we precipitated ('salted out') the sol one last time with a saturated NaCl solution and removed the supernatant. In the glove box the pelleted colloid was brought back into solution in sulphate-free artificial seawater medium. Sulphate-free artificial seawater medium was prepared as described above with following modifications: trace elements solution did not contain FeSO₄·7H₂O, MgSO₄·7H₂O was replaced by MgCl₂·6H₂O (55.5 mmol l⁻¹ final concentration), and NaCl concentration was changed correspondingly to 423 mmol l⁻¹. Then, active AOM culture (washed with sulphate-free artificial seawater medium) was added to the bottle containing medium with colloidal sulphur. The final sulphur concentration in the incubation was approximately 8 mmol l⁻¹. The culture (in a 118 ml serum bottle; 50 ml medium + biomass and 68 ml headspace) was then supplemented with ¹³C-bicarbonate (~5 mmol l⁻¹; ISOTEC, Sigma-Aldrich) and ¹⁴C-bicarbonate (10 MBq; Hartmann Analytics) and the pH of the medium was adjusted with 4 M HCl to 7.5. The culture was incubated with an N₂:CO₂ headspace (no added methane, no overpressure) on a shaker (40 r.p.m.) in the dark. During first 70 days, subsamples were regularly taken to monitor sulphate and sulphide production and ¹⁴C-incorporation into biomass. The sampling involved following: 0.4 ml culture was filtered through a 0.2-µm filter into 50% ZnCl₂ for sulphide measurements, 0.3 ml culture was filtered through a 0.2-µm filter into 0.01 M HCl for sulphate measurements, and 0.5 ml culture was filtered onto a 0.22-µm GTTP filter for ¹⁴C-scintillation counting. Sulphide was measured using colorimetry⁵⁴, sulphate was measured as described below. The ¹⁴C content of the biomass was determined by filtering an aliquot of the culture onto a 0.22-µm filter, washing it

with 20 ml sterile anoxic artificial seawater medium and twice with 20 ml 1 M HCl. The filters obtained were subsequently decalcified overnight, in a desiccator with fuming 37% HCl. After decalcification the filter was dried and the radioactivity was measured by scintillation counting (scintillation cocktail: PermaFluorTM; scintillation counter: 2900TR LSA, Packard). At each sampling point small (undefined) amounts of biomass were also fixed with 4% formaldehyde for nanoSIMS analyses. These highly enriched consortia with their inherently slow growth were available only in limited quantities and, therefore, only several biomass flocs (that is, no fixed volumes) were collected from each incubation for fixation in formaldehyde. NanoSIMS analyses were performed with samples taken at 70 and 270 days (Fig. 3b, c and Supplementary Fig. 10).

CARD/halogen *in situ* hybridization coupled to laser marking and nanoSIMS. Aliquots of the Isis enrichment culture grown under disproportionating conditions were taken at regular intervals and fixed in 2% (final concentration) formaldehyde in 50 mM phosphate buffer (pH 7.4). CARD/Halogen *in situ* hybridization was performed as described previously⁵⁶. Briefly, the sample was filtered onto a Au/Pd-coated polycarbonate filter and embedded in 0.1% low melting point agarose. To permeabilize cells for hybridization, filtered samples were treated with lysozyme (10 g l⁻¹) for 40 min at 37 °C. Subsequently, the filter was washed with water and pre-hybridized for 30 min at 46 °C in a hybridization buffer (50% formamide). After adding the oligonucleotide probe (50 ng DSS-658 coupled to horseradish peroxidase; Biomers) to the hybridization mixture the filter was hybridized for another 4 h at 46 °C. After hybridization the filter was washed with a pre-heated washing buffer (15 min at 48 °C) and transferred into amplification buffer containing 0.15% H₂O₂ and 20 µg Oregon Green-labelled tyramides. The amplification step was performed for 20 min at 46 °C. The filter was then washed with PBS and stained with DAPI (1 ng ml⁻¹) for 10 min at 4 °C in the dark. After washing with water and drying, small circles (5-mm diameter) were cut out of the filter and placed on support glasses to be viewed in a Laser Microdissection microscope (DM 6000 B, Leica). Individual fields of view containing labelled cells were marked with a laser. Subsequently, the filter was embedded in a mixture of Citifluor/Vectashield and fluorescent images of the individual fields of view were obtained with an epifluorescent microscope (Zeiss AxioPlan Microscope). The cover glass was removed and the filter was briefly washed in 96% ethanol and water and left to dry. The cut-out filter pieces were subsequently mounted into a suitable holder and used for nanoSIMS imaging.

Preparation of cryosections. Immunolabelling and nanoSIMS: the sample was fixed in 2% formaldehyde in 50 mmol l⁻¹ phosphate buffer (pH 7.4). Fixation was performed for at least 2 h at room temperature. The sample was then briefly washed with cold phosphate buffer to remove precipitates and salt from the medium and stored in fresh 2% formaldehyde in 50 mM phosphate buffer (pH 7.4) at 4 °C until processed further. Biomass flocs were transferred into 2.3 M sucrose and infiltrated overnight at 4 °C on a rotational shaker. Semi-thin cryosections (300–500 nm) prepared as described previously⁵⁷ with a Leica Ultracut EM FCS (Leica Microsystems) and were transferred on poly-L-lysine-coated coverslips in a 1:1 mixture of 2.3 M sucrose:methylcellulose, and dried. The sections were stored at -20 °C until further processing.

Confocal Raman microscopy: Isis biomass was fixed in 4% formaldehyde in 50 mM phosphate buffer, washed with PBS, embedded in OCT compound embedding medium and frozen. Frozen sample was mounted on a metal pin of the Leica CM-3050-S cryotome (Leica Microsystems) and sectioned (2–5 µm thickness). The sections were collected with a brush and placed on a support glass slide to thaw.

Immunolabelling on cryosections. Immunofluorescent labelling: immunolabelling with anti-Mcr, anti-Sat and anti-Dsr antibodies as markers for ANME and DSS, respectively, was performed as described in ref. 58. Briefly, thawed cryosections were washed in PBS and then incubated with primary anti-Mcr (rabbit) and anti-Dsr (guinea-pig) antibodies (at 1:200 dilution). After a wash in PBS + 0.01% Tween the sections were further incubated with the following secondary antibodies: goat anti-rabbit IgG coupled to Cy5 (1:200 dilution; Invitrogen) and goat anti-guinea-pig IgG coupled to rhodamine (1:200 dilution; Santa Cruz Biotechnology). Afterwards the sections were thoroughly washed in PBS + 0.01% Tween and incubated with anti-Sat antibodies, which were pre-conjugated to FITC (fluorescein isothiocyanate; Sigma-Aldrich) according to the manufacturer's instructions. The conjugated anti-Sat-FITC antibody was then used at 1:10 dilution. After final wash in water the sections were embedded in Mowiol/DABCO (1,4-diazobicyclo-[2,2,2]-octane; Sigma; 2% w/v)/DAPI (4',6'-diamidino-2-phenylindole; Sigma; final concentration 1 µg ml⁻¹) mixture, sealed with nail polish and stored at 4 °C.

Immunogold labelling: immunolabelling with anti-Mcr antibody was performed as follows. Cryosections on glass coverslips were washed by positioning the glass 'section-down' on a drop of PBS. Subsequent incubation and washing steps were performed in the same manner. During incubation and washing steps

great care was taken to keep the glass surface with the sections hydrated to prevent cells from drying which would lead to their detachment from the glass support. Immunolabelling was performed with unlabelled primary antibodies raised against methyl-CoM reductase (described in ref. 58). After incubation with primary antibodies the sections were washed three times with PBS + 0.01% Tween. Subsequently, the sections were incubated with secondary antibodies. These secondary antibodies were double-labelled, carrying a fluorochrome (FITC) and a 1.4 nm cluster of NanoGold (Nanoprobes). This double detection system allowed assessment and verification of the specificity of the antibody binding by fluorescence microscopy before nanoSIMS analysis (see Supplementary Fig. 15a). The primary and secondary antibodies were used at 1:200 and 1:20 dilutions, respectively. For epifluorescence microscopy, at this stage the sections were washed, embedded in Mowiol/DABCO/DAPI mixture, sealed with nail polish and stored at 4 °C. Alternatively, for nanoSIMS analysis the sections were washed in water and afterwards incubated for 10 min in 2% methylcellulose in water. Methylcellulose fills the spaces between individual cells and connects them to the glass support underneath. Excess methylcellulose was carefully adsorbed with a filter paper and the glass slide was left to dry. Methylcellulose is stable in high vacuum and is thus compatible with nanoSIMS analysis. In fact, the methylcellulose coating of the sections was found to be essential for a successful nanoSIMS analysis (see further). When dry, the glass was sputter-coated by a thin (~100 nm) platinum layer to avoid charging during nanoSIMS imaging. For handling reasons the sample was metal-coated after methylcellulose coating (the metal layer tends to displace from glass but sticks to methylcellulose). Subsequently, the round coverslip (10-mm diameter) was placed into the standard sample holder of the CAMECA NanoSIMS 50 instrument and analysed.

Image acquisition and processing. The immunolabelled cryosections and CARD-FISH-labelled cells on filters were examined with a Zeiss AxioCam MRc attached to a Zeiss Axioplan Microscope (Zeiss) equipped with an oil immersion planapochromat lens ($\times 100$ 1.3 numerical aperture; Zeiss). The appropriate filter sets for DAPI, FITC/fluorescein, Cy3/rhodamine and Cy5 were used. The exposure times were <20 ms for DAPI and <300 ms for FITC, rhodamine and Cy5, respectively. The images obtained were processed with Adobe Photoshop.

Combination of fluorescence *in situ* hybridization (FISH) and Raman spectroscopy. Biomass (1 ml) of the *Isis* enrichment was collected through the septum of an anoxic Hungate tube with a hypodermic needle (Sterican, size 1, 0.90 \times 40 mm, B. Braun Melsungen AG) connected to a 1 ml syringe (Injekt-F, B. Braun Melsungen AG). Subsequently, the culture was homogenized by shearing it 10 times through the syringe. Then the biomass was centrifuged, the supernatant was removed and the samples were incubated with 1 ml of 0.01 mmol l⁻¹ HCl for 3 h at room temperature to reduce autofluorescence. HCl was removed after another centrifugation step (10,000g, 5 min) and the biomass was resuspended in 1 ml 50% ethanol in phosphate buffered saline (PBS; 10 mmol l⁻¹ sodium phosphate buffer pH 7.4, 130 mmol l⁻¹ NaCl) for fixation. After 3 min the ethanol was removed by pipetting after centrifugation (10,000g, 2 min) and FISH in liquid was performed according to ref. 59 with probes Arch915 (specific for *Archaea*)⁶⁰ and EUBmix (targeting most bacteria)⁶¹ double-labelled with Fluos and Cy5, respectively⁶². Details on oligonucleotide probes are available at probeBase⁶³. After FISH the biomass was dried onto CaF₂ slides, briefly dipped into ice-cold H₂O to wash off residual salts, air-dried with compressed air and transferred to a confocal LabRAM HR800 Raman microspectrometer (Horiba) equipped with a 50 mW 532 nm laser. Before Raman spectroscopy bright field and fluorescence images of biomass particles were acquired with the epifluorescence module of the Raman spectrometer. These images were imported into the LabSpec software package (version 5, Horiba) and cells for Raman analysis were chosen according to their positive FISH signals. Raman spectra of these cells were acquired with about 10% laser power. For most measurements, the pinhole was set to 200- μ m diameter, which results together with the applied $\times 100$ objective in an optical slice thickness of about 1.7 μ m. The acquisition time was 150 s. The Raman spectra were recorded between ~120 and 1,800 cm⁻¹ (with a spectral centre of 1,020 cm⁻¹), which covers most biologically significant signature peaks, including sulphur. Subsequently, CaF₂ peaks (at ~320 cm⁻¹) were subtracted, the spectra were baselined (polynomial 4), mean normalized and transferred to a file format readable by Excel (Microsoft). Spectra of hybridized DSS cells could not be obtained as all cells were destroyed due to heating during Raman measurements. Solid standards, like iron phosphates and S₈ were measured directly on CaF₂ slides.

Transmission electron microscopy (TEM). TEM imaging was performed on the microbial mat sample from Black Sea. The mat was fixed in 4% formaldehyde in phosphate buffer (pH 7.4), washed and embedded in 2% agarose. The sample was then cut with a scalpel into small cubes (approximately 1 mm³). Subsequently, the sample was embedded in EPON resin, contrasted by 1% aqueous osmium tetroxide

and negatively stained with uranyl acetate using an automated microwave tissue processor (Leica Microsystems). The embedded sample was sectioned into ~70-nm sections using an ultramicrotome (Leica Microsystems). The sections were transferred on a formvar-coated copper grid, embedded in 2% methylcellulose and air-dried. Subsequently, the sections were carbon-coated and eventually analysed by electron energy-dispersive X-ray analysis (EDX) using transmission electron microscope (Tecnai G2 F20; FEI/Philips) equipped with an EDX detector.

NanoSIMS analysis of single cells. Image acquisition. All samples (immunogold-labelled thin sections and filter pieces containing hybridized cells from the disproportionation experiment) were analysed using a NanoSIMS 50L (Cameca). Secondary ions ¹²C⁻, ¹³C⁻, ¹²C¹⁴N⁻, ³¹P⁻, ³²S⁻, ³⁴S⁻ and ¹²C⁻, ¹²C¹⁴N⁻, ¹⁹⁴Pt⁻, ¹⁹⁷Au⁻ were recorded in subsequent runs, using 6 electron multipliers. To prevent charging, the samples were sputter-coated with platinum (gold-labelled sections) or gold-palladium (hybridized cells) before nanoSIMS analysis. All samples were pre-sputtered with a Cs⁺ beam of ~500 pA to remove surface contaminations and to implant Cs⁺ ions. For analysis, the samples were sputtered with a 0.3–1.3 pA Cs⁺ primary ion beam focused into a spot of ~100-nm diameter that was scanned over the sample in a 256 \times 256 pixel (gold-labelled sections) or 512 \times 512 pixel (hybridized cells) raster with a counting time of 1 ms per pixel. The instrument was tuned for high mass resolution (5,000–6,000) of individual masses. The respective mass peaks were tuned directly on the sample (¹²C⁻, ¹³C⁻, ¹²C¹⁴N⁻, ³¹P⁻, ³²S⁻, ³⁴S⁻) or using a standard (platinum coating of the glass for ¹⁹⁴Pt⁻ and gold TEM grid for ¹⁹⁷Au⁻). For measurement of isotopes, *t*₀ samples from the respective experiments were analysed for natural abundance. Up to 150 planes were recorded for individual fields of view (15 μ m \times 15 μ m).

Data processing. Ion-count images were processed using Look@NanoSIMS software⁶⁴. For each field of view, the scanned planes were first aligned and accumulated. Subsequently, regions of interest (corresponding to individual cells) were defined by interactive thresholding⁶⁴, using images of ¹²C¹⁴N⁻, ³¹P⁻ and ³²S⁻ as masks. For each region of interest, ¹³C/¹²C, ¹²C¹⁴N/¹²C, ³¹P/¹²C, ³²S/¹²C, ³²S/¹²C¹⁴N and (³¹P/¹²C)/(³²S/¹²C) ratios were calculated. None of the ratios exhibited a significant trend with depth, which justified the use of accumulated ion images for the calculation of ratios in the defined regions of interest. All parameters for determining regions of interest, ratio calculations and further image processing are in detail described in ref. 64 and the software is freely available at <http://www.microsen-wiki.net/lans>.

On the basis of cell morphology, P, S and Au content, cells were automatically (based on a defined cut-off value of ³¹P/³²S) or manually (via visual inspection) identified as ANME or DSS (Supplementary Fig. 15b). The average doublings per day for ANME and DSS cells were calculated by subtracting the average ¹³C/¹²C ratio determined for the cells without label (that is, controls) from those incubated with added labelled DIC, and by subsequently dividing the difference with the ¹³C-labelling percentage of DIC in the incubation medium divided by two and the incubation time (days).

Size calculation, biomass conversion and cellular activity calculations. For the methane carbon assimilation rates for ANME, a mean (*n* = 10) cell size was calculated assuming a cylindrical cell shape. The cellular length (1 μ m) and width (0.5 μ m) used for the size calculation was determined from TEM images and validated against nanoSIMS images. For the size-to-biomass conversion a calibration factor of 6.4 fmol C μ m⁻³ was used^{56,65}. Subsequently, the cellular methane carbon assimilation rates were calculated as the ¹³C/¹²C enrichment of the ANME cells incubated with ¹³CH₄ multiplied by the average cellular biomass divided by ¹³C-labelling % of the dissolved methane and incubation time (that is, 28 or 44 days).

Analysis of sulphur compounds. Sulphate was analysed on a 761 Compact ion chromatograph (Metrohm) with a Metrosep A SUPP 5 column. Carbonate buffer (3.2 mmol l⁻¹ Na₂CO₃ and 1 mmol l⁻¹ NaHCO₃) was used as eluent. The duration of a run was 14 min, with sulphate eluting at ~11.5 min.

Sulphite and thiosulphate in the medium were derivatized at room temperature in the dark with monobromobimane and analysed by HPLC according to the methods described in ref. 66.

Polysulphides were analysed by a modified method from ref. 20. Briefly, dissolved polysulphides were methylated using methyl trifluoromethanesulphonate (methyl triflate) to form methyl polysulphanes that can be separated and quantified using HPLC. Forty ml of anoxic methanol were vigorously stirred in a closed serum vial. Two liquids were rapidly injected into the stirred methanol from syringes: 10 ml of anoxic AOM biomass and/or medium followed immediately by 300 μ l methyl triflate. The additional phosphate buffer used in ref. 20 was not used, because the medium was already strongly buffered. Eighty ml of sodium sulphate solution (375 mM) were added to the reaction mixture and transferred to a 250 ml separatory funnel. Subsequently, the solution was extracted with 2 \times 1 ml *n*-dodecane. Elemental cyclosulphur compounds, such as S₆, S₇ and S₈, can also be extracted into the *n*-dodecane, but not in a quantitative manner⁶⁷.

The obtained extract was analysed by liquid chromatography (GP50 Gradient Pump, equipped with a C18 reverse phase column and a UVD340S Diode Array Detector; all by Dionex). Methanol was used as mobile phase and spectrophotometric detection was performed at 220 and 230 nm wavelengths. Detection limits were 600 nmol l^{-1} , 400 nmol l^{-1} , 300 nmol l^{-1} , 120 nmol l^{-1} , 100 nmol l^{-1} and 60 nmol l^{-1} for S_3^{2-} , S_4^{2-} , S_5^{2-} , S_6^{2-} , S_7^{2-} and S_8^{2-} , respectively. The identification of methylated polysulphides S_4^{2-} to S_6^{2-} was confirmed by gas chromatography-mass spectrometry (Trace GC-MS; ThermoFinnigan) according to ref. 49.

A standard series of polysulphides saturated with respect to elemental sulphur was prepared by dissolving excess elemental sulphur (S_8) in a solution containing $\sim 10 \text{ mmol l}^{-1}$ total dissolved sulphide in an anoxic solution buffered to pH 8.8 (50 mmol l^{-1} phosphate buffer). The resulting yellow polysulphide solution was left to stand overnight to equilibrate and was then methylated as described above. Equilibrium concentrations were calculated using the equilibrium constants from refs 49 and 68. The detection limit for total polysulphide zero-valent sulphur (based on resolved peaks of S_4^{2-} , S_5^{2-} and S_6^{2-}) was $3 \mu\text{mol l}^{-1}$. The average relative standard deviation for the detection of inorganic polysulphide S^0 by the methyl triflate derivatization-based method is 8%⁶⁹.

It should be noted that the method for reaction of the methyl triflate with polysulphides is for solutions. The reaction depends on the very rapid methylation of the dianionic polysulphide compounds before they have the opportunity to disproportionate. The reaction of the methyl triflate with the biomass involves a solid phase. Thus, transport and diffusion of the methyl triflate to polysulphide species in the cell will be hindered. The determination of the precise speciation of polysulphides as in ref. 49 is therefore not possible. Moreover, methyl triflate is one of the most powerful methylating compounds known and is likely to react with other polysulphane-containing compounds or displace other capping groups on the ends of organic polysulphane compounds. In spite of these caveats, the formation of the dimethyl polysulphane compounds provides an unequivocal indication of zero-valent sulphur in the biomass and medium.

Elemental sulphur was measured by methanol and/or chloroform extraction following the methods described in ref. 69 and modified for small volumes. We also measured zero-valent sulphur in biomass by reacting biomass samples preserved in zinc chloride solution (50% w/v) with sulphite solution to form thiosulphate. This is similar to the cyanolysis reaction for zero-valent sulphur described in ref. 69. To 0.65 ml of sample in a 2 ml capped Eppendorf tube 0.25 ml of 100 mmol l^{-1} sodium sulphite solution was added and the samples were allowed to react for 12 h (overnight) at 70°C . Samples were then filtered through a $0.45\text{-}\mu\text{m}$ filter, diluted to 10 ml with water and analysed for thiosulphate using a 761 Compact ion chromatograph (Metrohm). The same column and the eluent were used as for the sulphate measurements. A pre-column was used that served as a zinc trap. The duration of a run was 22 min, with thiosulphate eluting at ~ 19 min.

Preparation of ^{35}S -labelled sulphide. ^{35}S -labelled sulphide was prepared by reduction of radiolabelled sulphate by the method from ref. 70 as modified by G. L. Arnold (personal communication). Briefly, $\sim 5 \text{ MBq}$ of ^{35}S -sulphate (18 GBq mol^{-1} ; Hartmann Analytics) was added to 0.5 ml of 100 mmol l^{-1} sodium sulphate solution and gently dried (80°C) in the bottom of a 250 ml round-bottom flask. The flask with dried sulphate salt and additional flask with boiling stones was connected to a reduction/distillation assembly consisting of a condenser, gas washing trap containing water and a 0.01 mol l^{-1} AgNO_3 trap. A reducing agent containing 163 ml of concentrated HCl, 100 ml of hydriodic acid, 50 ml of 50% hypophosphorous acid was prepared and boiled gently for about 1 h to remove sulphur contamination. Approximately 30 ml of the reducing agent was added to the reaction flask and gently boiled for 3 h. The collected Ag_2S was subsequently converted to ZnS using Cr II reduction method described below and the released sulphide was trapped in 10 ml of ZnCl_2 solution. Measured specific activity of the Zn^{35}S suspension at the time of the experiment was $84.1 \text{ kBq } \mu\text{mol}^{-1} \text{ ZnS}$.

Incubation experiments with isotope-labelled substrates. Three different sets of incubation experiments were performed with the Isis enrichment culture under undisturbed AOM conditions.

(1) To test whether the biomass S originates from sulphate, the enrichment culture (12 ml liquid + biomass and 10 ml headspace) was incubated under AOM conditions (3 bar CH_4 overpressure) with $^{35}\text{SO}_4^{2-}$ tracer ($\sim 2.5 \text{ MBq}$; 18 GBq mol^{-1} ; Hartmann Analytics) and $50 \mu\text{mol l}^{-1}$ sulphide in 22 ml Hungate tubes at room temperature on a shaker (40 r.p.m.) for up to 24 h. Subsamples (1 ml) were taken anoxically through the butyl rubber stopper with a needle after 1, 3, 6, 11 and 24 h and directly filtered through a $0.22\text{-}\mu\text{m}$ GTTP filter into zinc acetate solution (0.9 M) to stop the reaction and fix sulphide. The filter containing biomass flocks was immediately washed once with anoxic artificial seawater medium and twice with 20 ml of 1 M HCl solution to dissolve precipitated iron sulphides and subsequently analysed for ^{35}S by scintillation counting (scintillation cocktail:

LumaSafeTM Plus; scintillation counter: 2900TR LSA, both Packard). At 0 and 24 h subsamples (0.3 ml culture in 50% ZnCl_2) were taken for total sulphide measurements. Sulphide was measured according to ref. 54.

This experiment was repeated and extended as follows: the Isis enrichment culture (10 ml liquid + biomass and 12 ml headspace) was incubated with ^{14}C -labelled methane (8.6 MBq; American Radiolabelled Chemicals), ^{13}C -labelled bicarbonate (50 atom percent ^{13}C), ^{34}S -labelled sulphate (50 atom percent ^{34}S ; Icon Isotopes), ^{35}S -labelled sulphate (2.6 MBq) and $50 \mu\text{mol l}^{-1}$ sulphide in 22 ml Hungate tubes at room temperature for up to 144 h. At 0 and 24 h subsamples (0.3 ml) were taken for total sulphide measurements using colorimetry⁵⁴. Two parallel subsamples (0.5 ml) were taken after 1, 3, 6, 11 and 24 h, which were directly filtered through $0.22\text{-}\mu\text{m}$ GTTP filters either into zinc acetate solution (0.9 M) to fix sulphide or into NaOH (0.6 M) to fix bicarbonate. One filter containing biomass flocks was immediately washed with anaerobic artificial seawater medium and 20 ml of 1 M HCl solution to dissolve precipitated iron sulphides and subsequently analysed by scintillation counting. The other biomass filter was transferred into 4% formaldehyde for subsequent nanoSIMS analysis.

(2) To test whether the biomass S originates from sulphide, ^{35}S -sulphide addition experiment was performed as follows: 5 ml of the Zn^{35}S suspension was placed in a 50 ml serum vial and degassed with nitrogen. Subsequently, 1 ml of nitrogen-degassed phosphoric acid was added and the Zn^{35}S dissolved, releasing H_2^{35}S in the headspace. Approximately 2 ml of headspace gas containing H_2^{35}S ($\sim 21 \text{ kBq}$) were then anoxically transferred with a syringe into a 22 ml Hungate tube with Isis enrichment culture (10 ml medium + biomass and 12 ml headspace) containing $\sim 200 \mu\text{mol l}^{-1}$ sulphide. The Hungate tube was then supplemented with methane overpressure (3 bar) and incubated at room temperature in the dark on a shaker (40 r.p.m.) for up to 24 h. Subsamples (1 ml) were taken after 1, 3, 6, 11 and 24 h and directly filtered through a $0.22\text{-}\mu\text{m}$ GTTP filter into zinc acetate solution (0.9 M) to stop the reaction and fix sulphide. Total sulphide production was measured using colorimetry⁵⁴. The filter containing biomass flocks was immediately washed once with anaerobic artificial seawater medium and twice with 20 ml of 1 M HCl solution to dissolve precipitated iron sulphides and subsequently analysed by scintillation counting. To determine the ^{35}S -sulphate production, 5 ml of the ZnAc-fixed sample was filtered through a $0.02\text{-}\mu\text{m}$ filter to remove ZnS and the flow-through was analysed by scintillation counting.

(3) To measure ^{13}C assimilation from methane and CO_2 by ANME and DSS, a following experiment was performed: Isis enrichment culture (100 ml medium + biomass and 56 ml headspace) was incubated in 156 ml serum bottles with either ^{13}C -labelled methane (50 atom % ^{13}C) or ^{13}C -labelled bicarbonate (4.6 atom % ^{13}C) in the dark at room temperature on a shaker (40 r.p.m.). In both bottles the sulphide concentrations were regularly monitored (according to ref. 52) and the medium was exchanged as soon as 2 mmol l^{-1} sulphide was produced to prevent accumulation of dissolved ^{13}C -intermediates and products (for example, $^{13}\text{CO}_2$ in the $^{13}\text{CH}_4$ incubations). At two time points (28 and 44 days) subsamples (0.5 ml) were taken for bulk ^{13}C measurements and for nanoSIMS analyses of single cells. For bulk ^{13}C measurements, 0.5 ml of the sample was filtered onto baked glass-fibre filters, washed and air-dried before analysis. Abundances of ^{13}C were measured using CO_2 released by flash combustion in excess oxygen at $1,050^\circ\text{C}$ in an automated elemental analyser (Thermo Flash EA, 1112 Series) coupled to a Deltaplus Advantage mass spectrometer (ThermoFinnigan). For nanoSIMS, biomass samples (0.5 ml) were fixed in 4% formaldehyde for 2 h at room temperature. Then, the supernatant containing medium salts and precipitates was removed and the biomass flocs were washed and stored in fresh 4% formaldehyde in 50 mmol l^{-1} phosphate buffer at 4°C until further processing.

Determination of sulphate reduction and methane oxidation rates. In the first set of incubation experiments, radiolabelled reactants and products ($^{35}\text{SO}_4^{2-}$ and total reduced inorganic sulphur, respectively) were separated by cold chromium distillation⁷¹.

In the incubation experiments with ^{14}C and ^{35}S , radiolabelled reactants ($^{14}\text{CH}_4$ and $^{35}\text{SO}_4^{2-}$) and products ($^{14}\text{CO}_2$ and total reduced inorganic sulphur) were separated as follows: ^{14}C -radiolabelled carbonate and reduced ^{35}S species were released from the NaOH-fixed sample by acidification with HCl and subsequent reducing Cr II addition. The mobilized species were separately trapped by bubbling through a series of chemical traps: (1) 7 ml of a 0.1 M, pH 4 citrate buffer; (2) a 5% zinc acetate trap adjusted to pH 6.2 with HCl; (3) a second zinc acetate trap with pH 2; (4) a trap containing 7 ml of Carbosorb E (a CO_2 absorber for scintillation counting; Perkin Elmer); and (5) a second Carbosorb E trap. The first trap (1) was designed to trap extraneous aerosols and drops from the acid solution, the second and third traps (2 and 3) were designed to catch ^{35}S , whereas $^{14}\text{CO}_2$, which passed through traps 2 and 3, was fully trapped in the final two traps (4 and 5). The separation method (for the ^{14}C DIC and ^{35}S - H_2S) represents a novel method which is a combination and adaptation of two well-established methods. We have optimized pH in the traps, as well as the number of traps

required. The efficiency and recovery of the method was checked by tests with ^{35}S -sulphide and ^{14}C -bicarbonate standards.

The radioactivity of biomass, total dissolved reduced inorganic sulphur, dissolved inorganic carbon as well as dissolved sulphate was quantified by scintillation counting (scintillation cocktail: LumaSafe™ Plus; scintillation counter: 2900TR LSA, Packard). Sulphate reduction rates were determined as described in ref. 72. Methane oxidation rates were calculated as described in ref. 73. Due to the fact that the biomass from the third set of experiments contained both ^{14}C - and ^{35}S -label, methane carbon assimilation rates and biomass sulphur accumulation rates could not be directly measured. However, the individual contributions of ^{14}C and ^{35}S to the total recorded radioactivity could be determined due to their different half-lives of 5,730 years and 87 days, respectively. We recorded daily changes in the radioactivity of the biomass via regular scintillation counting over a period of ~3 weeks and based on the assumption that the activity of ^{14}C stays constant over the measuring period. We used following equation to calculate the ^{35}S and ^{14}C in the biomass

$$A^{14}\text{C} = \text{TA}_t + A^{35}\text{S}(t=0)e^{-\lambda t}$$

where TA_t = total measured activity at any time point, t = time in days, A = activity of ^{35}S or ^{14}C , λ = decay constant for ^{35}S .

Free energy calculations. The free energies of sulphate reduction to hydrodisulphide (equation (3) and Supplementary Fig. 12) and hydrodisulphide disproportionation reactions (equation (2)) were calculated using the following equation: $\Delta G = \Delta G^0 + RT \ln Q$ where ΔG^0 is the free energy of reaction at standard state calculated from the free energies of formation from the elements (G_f^0 values taken from ref. 48, except for hydrodisulphide, which was obtained from ref. 49). R is the gas constant ($8.314 \text{ J mol}^{-1} \text{ K}^{-1}$), T is the temperature (K) and Q is the reaction quotient, $Q = ([\text{HS}_2^-]^4 [\text{HCO}_3^-]^7 [\text{H}_2\text{O}]^{11}) / ([\text{CH}_4]^7 [\text{SO}_4^{2-}]^8) ([\text{H}^+]^5)$ for equation (3) and $Q = ([\text{HS}_2^-]^7 [\text{SO}_4^{2-}]^8) ([\text{H}^+]^5) / ([\text{HS}_2^-]^4 [\text{H}_2\text{O}]^4)$ for equation (2).

Calculations of free energies of reactions (ΔG_{rxn}) were made using the concentrations and activity coefficients typical for the start of a batch enrichment culture listed in Supplementary Table 3 at 23 °C. Thermodynamic calculations for colder temperatures (5 to 14 °C) yield Gibbs free energies that are 10 to 15 kJ mol^{-1} less favourable (compared to room temperature) for all disproportionation reactions in Supplementary Table 2. Equilibrium speciation and activity coefficients were calculated using the software The Geochemist's Workbench V. 9.0 (Aqueous Solutions LLC). The exception was for hydrodisulphide that was calculated using a spreadsheet provided by A. Kamyshny, using the values from ref. 49 and assuming that the polysulphide system is saturated with respect to elemental sulphur. Activity coefficients were calculated using the extended Debye–Hückel model and an estimated ionic strength of 0.662 and at 25 °C. The activity of water was calculated to be 0.982. The ionic strength of this seawater medium is slightly above the value of 0.5 to which the extended Debye–Hückel model is deemed to be accurate. The Harvie–Møller–Weare (HMW) model using virial coefficients is more accurate, but the database does not contain virial coefficients for reduced sulphur components. For comparison, calculation of the free sulphate and bicarbonate anion activities is about 10% greater using the HMW thermodynamic database. Given the stoichiometries of the reactions 1 and 2 (Supplementary Table 4), these differences nearly cancel out one another.

48. Stumm, W. & Morgan, J. J. in *Aquatic Chemistry: Chemical Equilibria and Rates in Natural Waters* 3rd edn, 990–1003 (Wiley-Interscience, 1996).

49. Kamyshny, A., Goifma, A., Gun, J., Rizkov, D. & Lev, O. Equilibrium distribution of polysulfide ions in aqueous solutions at 25 °C: a new approach for the study of polysulfide's equilibrium. *Environ. Sci. Technol.* **38**, 6633–6644 (2004).
50. Mastalerz, V., de Lange, G. J., Dählmann, A. & Feseker, T. Active venting at the Isis mud volcano, offshore Egypt: origin and migration of hydrocarbons. *Chem. Geol.* **246**, 87–106 (2007).
51. Widdel, F. & Bak, F. in *The Prokaryotes* (eds. Balows A. T. et al.) Vol. 4, 3352–3378 (Springer, 1992).
52. Cord-Ruwisch, R. A quick method for the determination of dissolved and precipitated sulfides in cultures of sulfate-reducing bacteria. *J. Microbiol. Methods* **4**, 33–36 (1985).
53. Saleh, A. M., Macpherson, R. & Miller, J. D. A. The effect of inhibitors on sulphate reducing bacteria: a compilation. *J. Appl. Bacteriol.* **27**, 281–293 (1964).
54. Cline, J. D. Spectrophotometric determination of hydrogen sulfide in natural waters. *Limnol. Oceanogr.* **14**, 454–458 (1969).
55. Steudel, R., Göbel, T. & Holdt, G. The molecular composition of hydrophilic sulfur sols prepared by acid decomposition of thiosulfate. *Z. Naturforsch.* **43b**, 203–218 (1988).
56. Musat, N. et al. A single-cell view on the ecophysiology of anaerobic phototrophic bacteria. *Proc. Natl Acad. Sci. USA* **105**, 17861–17866 (2008).
57. Tokuyasu, K. T. Technique for ultracytometry of cell suspensions and tissues. *J. Cell Biol.* **57**, 551–565 (1973).
58. Milucka, J., Widdel, F. & Shima, S. Immunological detection of enzymes for sulfate reduction in anaerobic methane-oxidizing consortia. *Environ. Microbiol.* <http://dx.doi.org/10.1111/1462-2920.12003> (28 September 2012).
59. Huang, W. E. et al. Raman-FISH: combining stable-isotope Raman spectroscopy and fluorescence *in situ* hybridization for the single cell analysis of identity and function. *Environ. Microbiol.* **9**, 1878–1889 (2007).
60. Stahl, D. A. & Amann, R. in *Nucleic Acid Techniques in Bacterial Systematics* (eds. Stackebrandt, E. & Goodfellow, M.) 205–248 (John Wiley, 1991).
61. Daims, H., Brühl, A., Amann, R., Schleifer, K. H. & Wagner, M. Probe EUB338 is insufficient for the detection of all Bacteria: development and evaluation of a more comprehensive probe set. *Syst. Appl. Microbiol.* **22**, 434–444 (1999).
62. Stoecker, K., Dorninger, C., Daims, H. & Wagner, M. Double-labeling of oligonucleotide probes for fluorescence *in situ* hybridization (DOPE-FISH) improves signal intensity and increases rRNA accessibility. *Appl. Environ. Microbiol.* **76**, 922–926 (2010).
63. Loy, A., Maixner, F., Wagner, M. & Horn, M. probeBase—an online resource for rRNA-targeted oligonucleotide probes: new features 2007. *Nucleic Acids Res.* **35**, D800–D804 (2007).
64. Polerecky, L. et al. Look@NanoSIMS – a tool for the analysis of nanoSIMS data in environmental microbiology. *Environ. Microbiol.* **14**, 1009–1023 (2012).
65. Ploug, H. et al. Carbon and nitrogen fluxes associated with the cyanobacterium *Aphanizomenon* sp. in the Baltic Sea. *ISME J.* **4**, 1215–1223 (2010).
66. Zopfi, J., Ferdelman, T. G. & Fossing, H. in *Sulfur Biogeochemistry - Past and Present* (eds. Amend, J., Edwards, K. J. & Lyons, T. W.) Vol. 379, 97–116 (The Geological Society of America Special Paper, 2004).
67. Kamyshny, A. Solubility of cyclooctasulfur in pure water and sea water at different temperatures. *Geochim. Cosmochim. Acta* **73**, 6022–6028 (2009).
68. Kamyshny, A., Gun, J., Rizkov, D., Voitsekovski, T. & Lev, O. Equilibrium distributions of polysulfide ions in aqueous solutions at different temperatures by rapid phase derivitization. *Environ. Sci. Technol.* **41**, 2395–2400 (2007).
69. Kamyshny, A., Borkenstein, C. G. & Ferdelman, T. G. Protocol for quantitative detection of elemental sulfur and polysulfide zero-valent sulfur distribution in natural aquatic samples. *Geostand. Geoanal. Res.* **33**, 415–435 (2009).
70. Thode, H. G., Monster, J. & Dunford, H. B. Sulphur isotope geochemistry. *Geochim. Cosmochim. Acta* **25**, 159–174 (1961).
71. Kallmeyer, J., Ferdelman, T. G., Weber, A., Fossing, H. & Jørgensen, B. B. A cold chromium distillation procedure for radiolabeled sulfide applied to sulfate reduction measurements. *Limnol. Oceanogr. Methods* **2**, 171–180 (2004).
72. Jørgensen, B. B. & Fenchel, T. Sulfur cycle of a marine sediment model system. *Mar. Biol.* **24**, 189–201 (1974).
73. Treude, T., Boetius, A., Knittel, K., Wallmann, K. & Jørgensen, B. B. Anaerobic oxidation of methane above gas hydrates at Hydrate Ridge, NE Pacific Ocean. *Mar. Ecol. Prog. Ser.* **264**, 1–14 (2003).

Hippocampal–cortical interaction during periods of subcortical silence

N. K. Logothetis^{1,2}, O. Eschenko¹, Y. Murayama¹, M. Augath¹, T. Steudel¹, H. C. Evrard¹, M. Besserve^{1,3} & A. Oeltermann¹

Hippocampal ripples, episodic high-frequency field-potential oscillations primarily occurring during sleep and calmness, have been described in mice, rats, rabbits, monkeys and humans, and so far they have been associated with retention of previously acquired awake experience. Although hippocampal ripples have been studied in detail using neurophysiological methods, the global effects of ripples on the entire brain remain elusive, primarily owing to a lack of methodologies permitting concurrent hippocampal recordings and whole-brain activity mapping. By combining electrophysiological recordings in hippocampus with ripple-triggered functional magnetic resonance imaging, here we show that most of the cerebral cortex is selectively activated during the ripples, whereas most diencephalic, midbrain and brainstem regions are strongly and consistently inhibited. Analysis of regional temporal response patterns indicates that thalamic activity suppression precedes the hippocampal population burst, which itself is temporally bounded by massive activations of association and primary cortical areas. These findings suggest that during off-line memory consolidation, synergistic thalamocortical activity may be orchestrating a privileged interaction state between hippocampus and cortex by silencing the output of subcortical centres involved in sensory processing or potentially mediating procedural learning. Such a mechanism would cause minimal interference, enabling consolidation of hippocampus-dependent memory.

Episodic memory—that is, memory of places, specific events and their contexts—depends on a synergistic interaction between anatomically related structures within the medial temporal lobe and the neocortex^{1–3}. The process of consolidating such memories occurs in two consecutive steps that both involve an interplay between hippocampus and cortex^{4–7}. During the encoding phase, hippocampus rapidly binds neocortical representations to local memory traces, while during subsequent ‘off-line’ periods of calmness or slow wave sleep (SWS) the new labile traces are concurrently reactivated in hippocampus and cortex to potentiate the corticocortical connections underlying stored representations^{5,8}.

An increasing number of studies support the view that the memory reactivation phase may be partly instantiated in the occurrences of so-called sharp wave-ripple (SPW-R) complexes^{9,10}, which are prominent during the off-line states. SPW-Rs are aperiodic, recurrent instances of large deflections (sharp waves) in the hippocampal local-field potential, and they are associated with synchronous fast-field oscillations (ripples), whose frequency depends on anatomical site (for example, CA1, CA3 or entorhinal cortex), animal state (alert or anaesthetized) and animal species^{9–13}. Many of the ripple properties support the idea that SPW-Rs may indeed be involved in off-line memory consolidation^{5,14}. Their intrinsic frequency and temporal structure are optimal for inducing synaptic plasticity in downstream neurons. Moreover, SPW-Rs have a global nature, reflecting the activation of hippocampal subnetworks and a behaviourally relevant spike content. For example, reactivation of neuronal ensembles that were active during awake experience occurs primarily during ripples^{15–18}, the number of ripples increases after learning, and the increase seems to predict memory recall both in rats^{19–21} and in humans¹². Conversely, elimination of ripples by the electrical stimulation of hippocampus during the post-learning SWS interferes with memory consolidation^{22,23}.

It is worth noting that SPW-Rs are not idiosyncratic hippocampal episodes, but part of a large-scale complex system of many oscillatory networks, the coupling of which coordinates specific information transfer between neocortical and hippocampal cell assemblies^{24–27}. One prominent self-organized oscillatory network involves thalamic and cortical structures, and generates the pattern of slow oscillation^{28,29}. During this slow (0.5–1.5 Hz) oscillation, the membrane potential of both excitatory and inhibitory cells alternates between depolarized (up) and hyperpolarized (down) states, and these excitability phases and their transitions strongly affect the frequency of occurrence of other cortical^{30,31} and hippocampal^{27,32,33} oscillatory patterns. Specifically, SPW-Rs are temporally linked to cortical spindles^{24,34,35}, and therefore their frequency of occurrence also correlates with slow oscillations^{27,33}. It has been suggested that the slow-oscillation network mentioned above underlies off-line information processing and that it has properties that are affected by learning^{36,37}.

Clearly, such organization suggests that memory consolidation is a complex system property emerging from the concerted, context-dependent operations of micro- and macro-networks of the brain. In such systems, the organization and operational principles of complex systems may be better investigated by using multimodal approaches, including concurrent measurements on multiple spatio-temporal scales. Here we used a novel multimodal methodology, which we call neural-event-triggered functional magnetic resonance imaging (NET-fMRI), to record ripples physiologically in the rhesus monkey (*Macaca mulatta*) and use them as events to align and average the time courses of brain activations (see Supplementary Methods). Concurrent multi-site hippocampal recordings and whole-brain fMRI were conducted during epochs of spontaneous activity or electrical stimulation of the CA1 and CA3 hippocampal fields to investigate the full extent of brain regions whose activity is modulated at times of ripple occurrence.

¹Max Planck Institute for Biological Cybernetics, Spemannstraße 38, 72076 Tübingen, Germany. ²Centre for Imaging Sciences, Biomedical Imaging Institute, The University of Manchester, Manchester M13 9PT, UK. ³Max Planck Institute for Intelligent Systems, Spemannstraße 38, 72076 Tübingen, Germany.

Identification of SPW-R complexes in monkeys

Recording electrodes were positioned on the basis of individual, high-resolution structural MRI scans and online observation of neural response profiles (Supplementary Methods and Supplementary Fig. 1). Further classification of electrode contacts in pyramidal-layer and stratum radiatum was based on visual detection of oscillations and inspection of synchronous activity (Supplementary Fig. 2).

Figure 1a shows two typical examples of SPW-R complexes. The upper traces depict the denoised broadband (0.05–500 Hz) field-potential signals, each showing at least one characteristic sharp wave. Consistent with previous studies^{9,11,38}, the duration of the ripple events was found to be less than 100 ms, and the sharp wave deflections had an amplitude of 1–3 mV. The lower traces show the bandpass (80–180 Hz)-filtered derivative of the signal with the fast ripple oscillations associated with sharp waves. The amplitude of ripples was approximately one order of magnitude smaller than that of concurrent sharp waves. SPW-Rs were always synchronous in most recorded sites, with maximum SPW amplitude mainly within the stratum radiatum and clear oscillations within the pyramidal cell layers (Supplementary Fig. 2).

In a large number of previous studies, ripples were commonly detected by first bandpass filtering (for example, 100–250 Hz) the field potential, then rectifying, smoothing and normalizing the derivative signal, and finally detecting suprathreshold signal increases. But this methodology does not discern ripple-related increases in the high-frequency domain from those that may occur in a broader frequency band. In fact, it was recently shown that fast field-potential oscillations of rat hippocampus during sleep or immobility may be split into quantitatively distinct oscillatory patterns, high-gamma-frequency oscillations and ripple oscillations, reflecting the activity of distinct subnetworks³⁸. To better understand the relationship of ripples to whole-brain activity, candidate oscillatory events were first detected by examining the smoothed envelope of the broadband (10–180 Hz) local-field potential (LFP) (see Supplementary Methods). To identify potentially distinct neural events, we next computed the

wavelet spectra of peri-event segments of this signal in a window of –200 to 200 ms and separated them into clusters using an un-supervised feature-extraction algorithm (see Supplementary Methods), permitting decomposition of multivariate data into a user-defined cluster number. Applying the algorithm to all data for different cluster numbers (between two and five) disclosed that the best factorization is obtained with a cluster number of three, yielding three distinct event categories in the frequency domains of 8–22 Hz, 25–75 Hz and 80–180 Hz, referred to here as hpsigma (the range of hippocampal sigma waves), gamma and ripple bands, respectively. The average time–frequency representation of these clusters are shown in Fig. 1b for all sessions with anaesthetized animals. The average peak frequencies of the hpsigma, gamma and ripple spectra were 13.5 ± 1 Hz (mean \pm s.d.), 40.1 ± 13 Hz and 106.5 ± 23 Hz, respectively. The average event durations (full width at half maximum, FWHM) were 226 ± 12 ms, 93 ± 22 ms and 44 ± 4 ms. The corresponding frequency peaks in drug-free experiments (Supplementary Fig. 3a) were 16 ± 3 Hz (mean \pm s.d.), 40.5 ± 18 Hz and 106.8 ± 17.8 Hz, and the event durations were 199 ± 28 ms, 89 ± 26 ms and 40 ± 15.3 ms. Frequency ranges and time durations were determined by calculating the time–frequency decomposition of the suprathreshold (>1 s.d. of event-free intervals) signals and subsequently computing the FWHM. Consistent with previous studies, the oscillation frequency of monkeys and human ripples was lower than in rats, and the event duration was shorter^{9–13}.

To assess further the distinctiveness of the three event types, we examined their relationship to hippocampal slower oscillations such as the delta band. The relationship of each of the three identified events to the delta phase are shown in Fig. 1c (see also Supplementary Methods), with data displayed in the form of polar plots and histograms to assist visualization. A statistically highly significant phase locking was specific to the ripple events (Rayleigh test; $Z = 7.5$, $P < 0.0004$). The orange histograms in the background show the phase distribution of random events (defined by the permutation of inter-event intervals) with their respective Rayleigh values of $Z = 0.5$ and $P < 0.519$, indicating a random distribution of

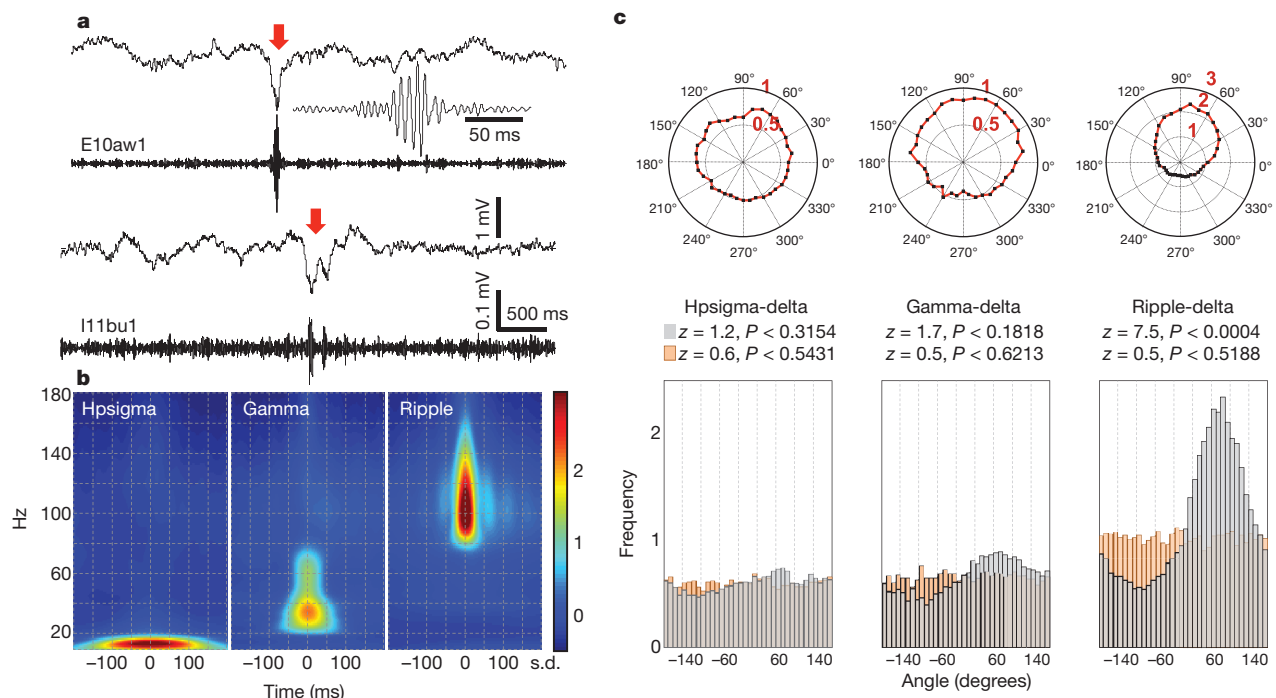


Figure 1 | Sharp wave-ripple complexes. **a**, SPW-Rs from two monkeys (i11, E10). Broadband (0.05–500 Hz) LFP signal (top panel) with (MRI) noise removed, together with their bandpassed (80–180 Hz) derivatives (bottom panel). Arrows show SPW-R. The ripple in the E10aw1 trace is magnified in the inset. **b**, Overall average of complex Morlet-wavelet spectrograms, showing the time–frequency distribution of hpsigma, gamma and ripple events.

c, Cross-frequency coupling of hippocampal events and hippocampal delta-band activity. Results are shown as polar plots (top row; red, frequency of occurrence) and standard histograms (bottom row). Dark histograms are from event-triggered data. The orange histograms in the background reflect phase distribution from random events.

phases. The mean delta-phase value at which ripples occurred was close to 90° (84°), that is, preceding but close to the positive–negative transition of the hippocampal delta wave (see also the average peri-ripple field potential changes in Supplementary Fig. 4a). Similar results were obtained in the awake monkey experiments (Supplementary Figs 3b and 5a).

We then examined the ripple-associated whole-brain activation patterns using NET-fMRI. Based on the detection and classification criteria described above, we observed overall more than 5,000 hpsigma and gamma events, and more than 11,000 ripple events. However, given the slow nature of the blood-oxygen-level-dependent (BOLD) fMRI signal, we excluded short (<1 s) inter-event intervals and instead used 3,966 hpsigma, 4,191 gamma and 9,482 ripple events from all the anaesthetized animal sessions to align and average the fMRI time series. The average LFP time course for the events used for NET-fMRI are shown in Supplementary Figs 4 and 5, together with the distribution of their inter-event intervals for anaesthetized and awake animal experiments. In addition, Supplementary Fig. 6 shows the distinct nature of individual events by showing selective increases in one frequency range but not in the others.

Neural-event-triggered BOLD MRI

The aforementioned events were used to map brain response patterns associated with signal increases in each frequency band. Neural and fMRI time courses were aligned to the time of each event, and their averages were convolved with a haemodynamic response function (HRF) and subsequently used as regressors in a standard event-related design (see Supplementary Methods and Supplementary Fig. 6c, d).

Statistical parametric mapping was then carried out to identify regions whose activity was modulated by the occurrence of the episodic events. To simplify the localization of different brain regions we grouped the detailed structure names of the monkey brain (Supplementary Fig. 10a–c) into group regions of interest (ROIs), taking into account both the functional specificity of structures and the spatiotemporal MRI resolution. For example, the visual area 4 (V4) complex includes the cortical regions V4, V4A, V4D, V4V, the juxtastriate area, the prostriate area and V4T of a standard monkey atlas³⁹.

Results from one fMRI session, under our standard remifentanyl anaesthesia, show that there are widespread, strong increases in the BOLD signal within the hippocampal formation, occipital, sensorimotor, temporal and parietal cortical areas, and in prefrontal cortex (Fig. 2a, b). In contrast, subcortical structures, including basal ganglia, cerebellum, tectum, lateral geniculate nucleus (LGN) and other thalamic nuclei, showed highly significant and robust signal decreases (Fig. 2b). The patterns of activation and deactivation were highly consistent from subject to subject, and from session to session. Similar results were obtained with an un-anaesthetized animal (Figs 2c, d). Typically, the state of the monkey alternated between drowsy or asleep, and awake, with only infrequent mobility periods (for example, moving hands or licking the juice tube). The average ripple-triggered BOLD time courses for all sessions are displayed in Supplementary Figs 7b and 8b for the anaesthetized and awake animal, respectively.

Overall, ripples were related to both positive and negative BOLD responses (PBRs, NBRs). Unexpectedly, closer examination of these ripple-associated BOLD responses revealed that structures exhibiting PBR and NBR were grouped according to a specific anatomical

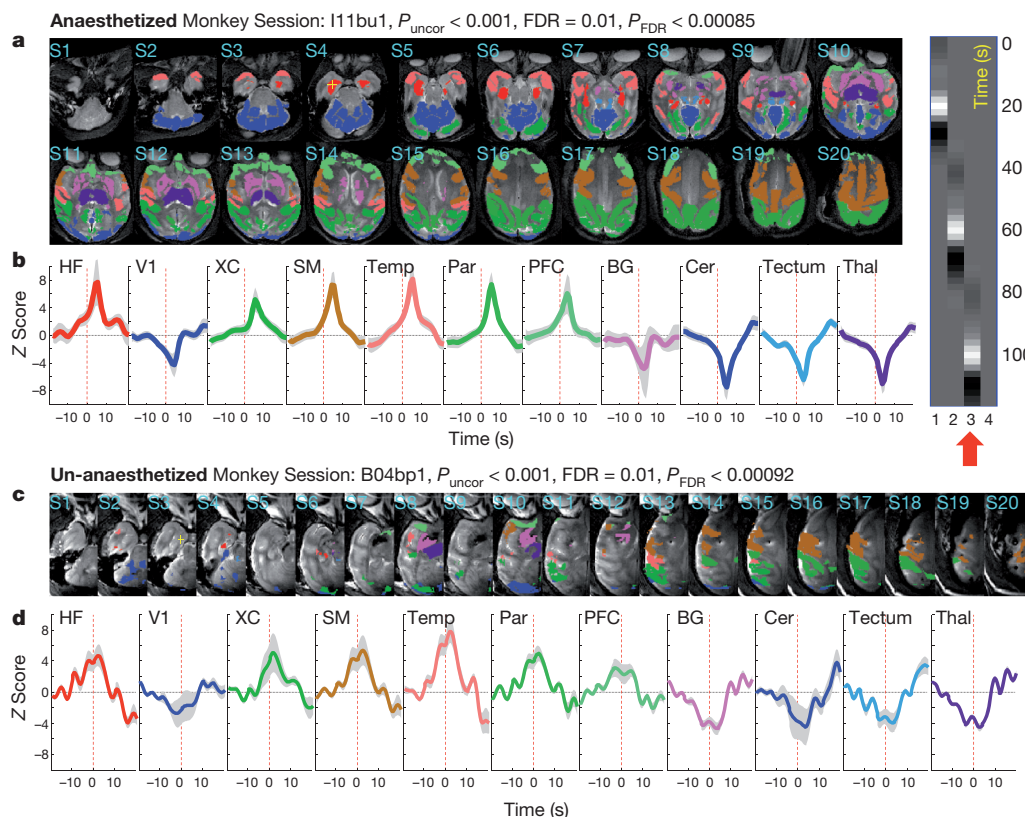


Figure 2 | Examples of ripple-triggered BOLD maps in anaesthetized and awake monkeys. **a**, BOLD maps obtained using NET-fMRI. Colours encode the selected group ROIs. Widespread activations were found in hippocampal formation (HF), extrastriate occipital areas (XC), sensorimotor cortex (SM), temporal (Temp) and parietal (Par) cortical areas, as well as in the prefrontal cortex (PFC). In contrast, subcortical structures, including basal ganglia (BG), cerebellum (Cer), tectum and thalamus (Thal), as well as the primary visual cortex (V1), showed robust signal decreases (see Supplementary Fig. 10 for ROI

names). **b**, Average response in each of the aforementioned ROIs. Thick lines denote the mean of the BOLD time series and shaded areas show ± 1 s.d. The inset (far right panel) shows the design matrix used in all experiments. The red arrow indicates the results obtained using the third regressor. **c**, **d**, Maps and time courses as in **a** and **b**, but for the un-anaesthetized animal (descriptions and conventions as in **a** and **b**). S, slice number. See Supplementary Methods for uncorrected (P_{uncor}) and corrected (P_{FDR}) statistical significance.

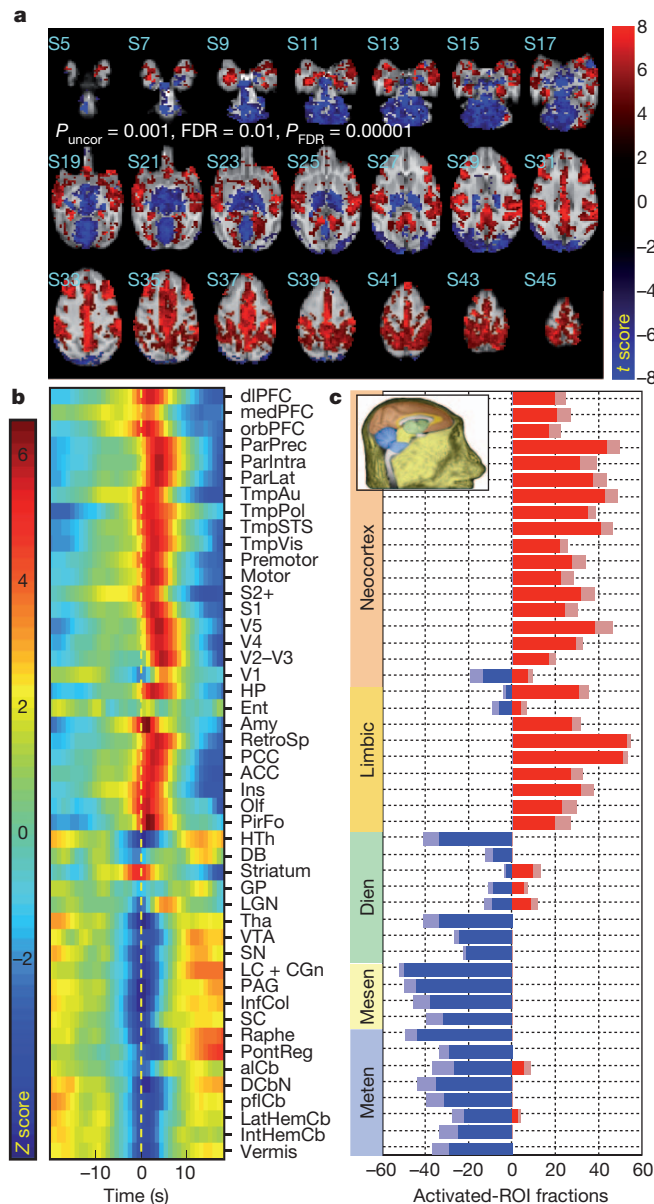


Figure 3 | Average ripple-triggered maps, signal dynamics and activation fractions. **a**, Average activation maps from all sessions. PBRs are observed in neocortex and limbic cortex, whereas activity suppression is seen in the diencephalon, mesencephalon and metencephalon. **b**, Time courses of each group ROI. In the stacked-bar plot, the lighter colour indicates +1 standard deviation. Note the sign change in the transition from cortical to subcortical areas and the difference in response onset. Dien, diencephalon; mesen, mesencephalon; meten, metencephalon. **c**, Fractions of activated voxels for each group ROI. ROIs are listed according to their location within the subdivisions of the standard developmental anatomical brain characterization, namely from the metencephalon (bottom) to the neocortex (top) (see Supplementary Fig. 10 for ROI names).

organization (Fig. 3a displays population data from all sessions, Supplementary Fig. 9 shows the averages of activation maps for each subject (see processing of population data in Supplementary Methods)). Similar to the maps of individual sessions, the population data showed that ripple-related PBRs occurred mainly in neocortex and limbic cortex, whereas activity suppression was observed in the diencephalon, mesencephalon and metencephalon. An almost unique exception to this selective activation–deactivation pattern was the primary visual cortex, V1, the activity of which was either unaffected by ripples or was suppressed (Supplementary Fig. 8e). The time courses of each group ROI (Fig. 3b) and the fractions of activated

voxels for each group ROI (Fig. 3c) indicate that there is a dichotomy of response sign separating neocortex and limbic cortex from the other anatomical subdivisions.

Notably, this characteristic pattern of excitation–inhibition was entirely specific to ripple events. Gamma-associated modulations of brain areas were primarily increases in the BOLD signal (Fig. 4a, b) and of somewhat lesser extent, as can be seen in both the activation maps (Fig. 4a) and the activation fractions (Fig. 4c). Similarly, hpsigma-triggered fMRI gave primarily PBRs, albeit to a significantly lesser extent than those obtained with ripples (average gamma and hpsigma-triggered BOLD time courses for all sessions are displayed in Supplementary Figs 7c, d and 8c, d for anaesthetized and awake animals, respectively).

Timing analysis of ripple-triggered averages

The ripple-triggered average (RTA) responses, such as those shown in Fig. 3b, seemed to have an area-related onset time. We quantified this

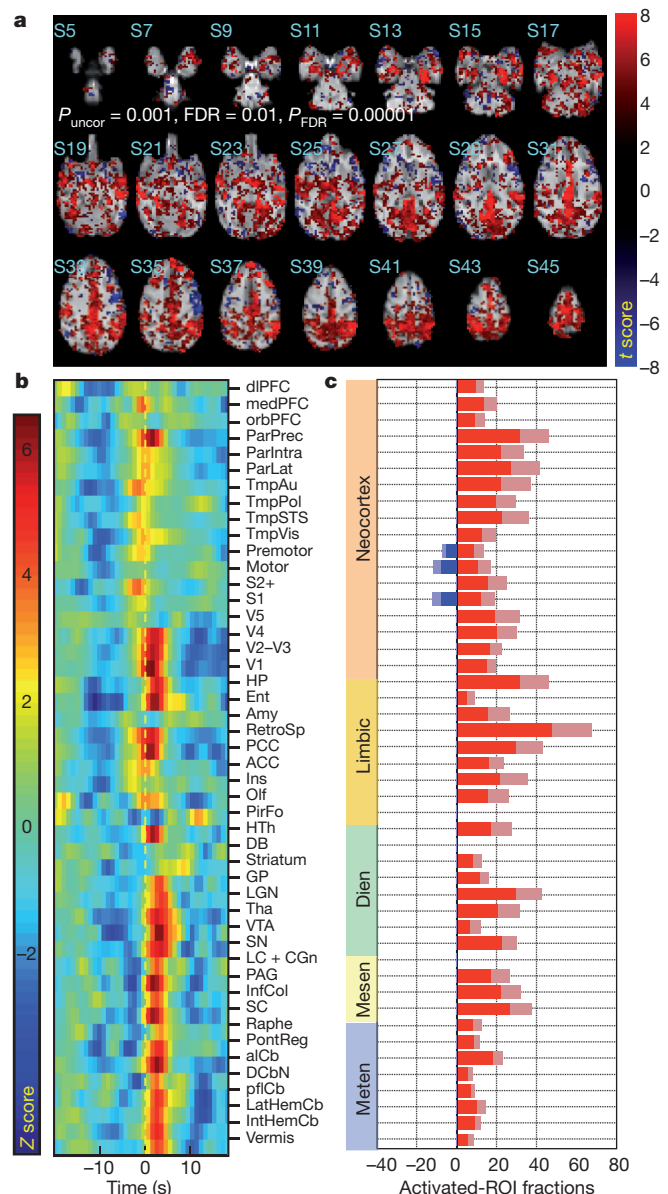


Figure 4 | Gamma-triggered population BOLD responses. Population results from NET-fMRI using gamma events to align physiological and fMRI responses. **a**, Average maps showing activations associated with gamma events. **b**, Time courses of the gamma-triggered BOLD response. Locations and names of ROIs are shown in Supplementary Fig. 10. **c**, Fractions of activated voxels for each group ROI. Conventions as in Fig. 3.

observation by calculating RTA responses for each ROI, clustering the responses and labelling the cluster according to the timing of their maximum (Supplementary Methods). This analysis revealed a robust clustering of responses across sessions: an early RTA response (cluster 1) was characteristic of the frontal and prefrontal cortices, whereas a late RTA response (cluster 2) was mainly observed in sensory areas (Fig. 5a, b). The comparison of cortical RTA responses with hippocampal and thalamic responses revealed a sequential organization of activation and deactivation patterns for these group ROIs. Figure 5c shows the distribution of time points of maximum signal modulations across sessions. According to a pairwise *t*-test, thalamic deactivation seems to be the leading process and is followed by signal increases in temporal, prefrontal and other association cortices, then in hippocampus, and finally in parietal and early sensory cortices.

NET-fMRI seems to be an excellent tool for the study of dynamic and potentially effective connectivity. Other methods that could—in principle—be used to examine network topologies are direct electrical stimulation of the brain combined with fMRI or the non-invasive seed-based resting-state fMRI. To compare the outcomes of such methods with the NET-fMRI results presented here, we also conducted fMRI experiments during direct electrical stimulation (DES) of the CA1 or CA3 hippocampal field and studied the correlation maps obtained by resting-state fMRI using hippocampal seeds.

Connectivity with DES and resting-state fMRI

In the present DES studies, we chose stimulation parameters, such as current strength, burst amplitude and frequency, as well as the frequency of burst occurrence, similar to those calculated from ripple events (Supplementary Information and Supplementary Fig. 11). Typical activation maps obtained by electrical stimulation of the CA1 field are shown in Supplementary Fig. 12. Both activations and deactivations were observed in a number of different cortical and subcortical regions. However, the distribution of PBRs and NBRs

was unrelated to that observed in the case of ripples, probably reflecting either the sustained negative BOLD⁴⁰ or synaptic distance and micro-circuit organization⁴¹ in the target structures (Supplementary Methods). Stimulation of the primate entorhinal cortex (Supplementary Fig. 12) with higher currents and stimulation frequencies entirely failed to induce trans-synaptic activations beyond hippocampus and entorhinal cortex itself.

Finally, the ongoing functional relationship of hippocampus to other cortical and subcortical brain regions was examined using standard seed-based resting-state fMRI. The left panel of Fig. 6 shows the average maps and the right panel shows the average fraction of activated ROI voxels for all sessions ($n = 7$) with hippocampus CA-field seeds. All significantly modulated ROIs, again barring V1 but also orbitofrontal cortex, exhibited strong positive BOLD responses that had a consistent spatial coverage across all sessions. Activated areas were the hippocampal formation, entorhinal cortex, the temporal, posterior cingulate and retrosplenial, prefrontal, olfactory and piriform cortices, as well as regions in thalamus and cerebellum. The cortical activations were similar to those reported in human studies⁴², and were once again unaffected by anaesthesia.

Discussion

Using NET-fMRI in anaesthetized and alert monkeys, we characterized here the brain areas that consistently increased or decreased their activity in relation to electrophysiologically detected and identified SPW-Rs. We show for the first time that the short periods of aperiodic, recurrent fast hippocampal oscillations (ripples) are tightly associated with robust cortical activations that occur concurrently with extensive activity suppression in subcortical thalamic, associational (for example, basal ganglia and cerebellum) and midbrain–brainstem neuromodulatory structures. The observed deactivations and activations were separated well spatially, so that previously described vascular steal phenomena or lateral and feedback interactions⁴⁰ can be safely excluded (see also Supplementary Information). This finding is specific to the ripple events and is not encountered in fMRI triggered by transient increases in the power of other frequency bands such as gamma and hpsigma. Moreover, the cortical–subcortical dichotomy of BOLD responses is observed neither during direct electrical stimulation of hippocampal fields, nor in resting-state fMRI using hippocampal seeds.

Markedly, during ripple episodes there seems to be a suppression of thalamic activity that might be related to sensory processing; a strategy

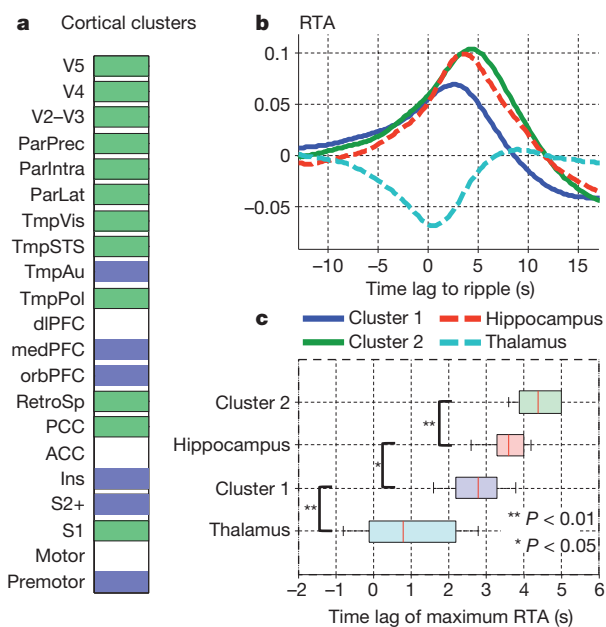


Figure 5 | BOLD response dynamics. **a**, Separation of the ripple-triggered average (RTA) responses in neocortical ROIs in two clusters. ROIs that do not belong significantly to either cluster are in white. **b**, Average RTA across all nine sessions for each cluster, superimposed on average hippocampal and thalamus responses. **c**, Box plot of the time lag until the maximum RTA is reached, for each cluster. On each box, the central mark is the median, the edges of the box are the 25th and 75th percentiles, and the whiskers indicate the most extreme data points. Asterisks, significant differences (P -values are given in the figure) between lags according to a one sided paired *t*-test (see Supplementary Fig. 10 for ROI names).

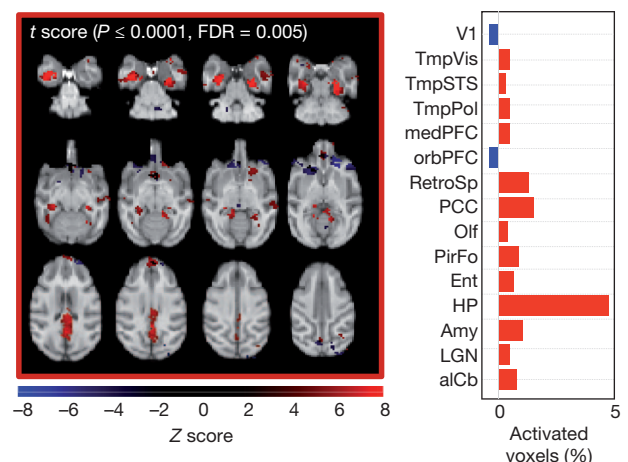


Figure 6 | Resting-state fMRI. BOLD maps (left panel) and the fraction of modulated ROIs (right panel). Resting-state fMRI with the hippocampus proper as the seed. Hippocampal formation, entorhinal cortex, temporal, parietal, prefrontal, olfactory and piriform cortices, as well as regions in thalamus and cerebellum are correlated with the ongoing hippocampus activity (see Supplementary Fig. 10 for ROI names).

that could increase the signal-to-noise ratio of hippocampal–cortical communication. In addition, there is a strong inhibition of large portions of the associational subcortical brain structures that are closely involved in the mechanisms of neural plasticity. For example, the deactivation of the basal ganglia, the pontine region and the cerebellar cortex seems to be consistent with prior evidence of competition between the fundamentally distinct declarative and non-declarative memory systems (see ref. 43 and discussion in Supplementary Information).

The majority of previous studies report competition between memory systems during the execution of various learning tasks, but evidence of post-learning antagonistic interactions between memory systems has also been reported in animal lesion and intra-hippocampal inactivation studies^{44,45}. These findings suggested that competitive interference between multiple memory systems may in part occur during the memory consolidation period⁴⁶. Such ‘competition’ may reflect an adaptive mechanism for optimizing behaviour that is dependent on learning demands, and its physiological basis is of paramount importance for both basic research and clinical applications. Evidently, the actual neuroanatomical interaction nodes between various memory systems that may underlie the deactivations observed here remain to be elucidated in future experiments involving further imaging and multi-site electrophysiological recordings. Nevertheless, we show here for the first time that some form of competition between various memory systems may exist at the time of occurrence of SPW-Rs, during the off-line states. If competitive or even mutually exclusive dynamic connectivity does actually exist it could provide low interference during the consolidation of multiple memory traces.

Another observation is the selective suppression of V1 activity during SPW-Rs, despite the overall positive BOLD responses in the other primary sensory and associational cortices. Such distinct deactivation of V1 may be the result of brief, selective suppression of the brain sites related to so-called ponto-geniculo-occipital (PGO) waves, that is, the phasic field potentials recorded from the pons, LGN, and V1 (ref. 47) during the hippocampal–cortical dialogue (see Supplementary Information).

The dynamics of regional fMRI responses suggest that an initial thalamic activity suppression is followed by signal increases in association cortices, then in hippocampus, and finally in parietal and early sensory cortices. Ripples were the only events that were significantly locked to the positive–negative transition phase of the local slow oscillation, at least in the delta-band cycles. This temporal structure may well reflect the systematic relationship between thalamocortical and hippocampal oscillations that is well known from several electrophysiological studies in animal and humans. As briefly mentioned above, neocortical slow wave oscillations were shown to temporally organize other cortical and hippocampal patterns^{26,27,30–33}, which themselves are temporally linked to spindles^{24,34,35}. In addition, human SPW-Rs seem to be phase locked to hippocampal delta oscillations, indicating that the coupling between neocortical slow oscillations and SPW-Rs may be accomplished by the intermediate phase locking of ripples to the local, hippocampal delta-band activity, which is itself phase locked to neocortical slow oscillations^{48,49}. Our current findings further support the idea that hippocampal delta provides an intermediate synchronization mechanism between cortex and hippocampus. However, it is surprising that such a synchronization occurs concurrently with the interruption of activity in a large number of other structures.

It is worth noting again here that both gamma and hpsigma events correlated with widespread (albeit of lesser spatial extent) modulations of brain areas, and that these modulations were primarily increases in the BOLD signal. As BOLD is known to be particularly sensitive to increase in gamma power⁵⁰, such widespread gamma-related activations may be indicative of episodic synchronous increases of subcortical and cortical regional gamma power that occur during the off-line states. Hippocampal transient high-gamma

episodes have already been described in rats³⁸, but their functional significance is yet to be studied.

In summary, the present study demonstrates the advantage of using multimodal methodologies for the study of emerging properties of a complex system such as the brain. Ripples are characteristic hippocampal events, and their use as a ‘trigger’ has revealed up- and down-regulation of widespread network activity. Yet, a note of caution may be necessary to avoid misinterpretation of the functional importance of such events. Neither the activation maps nor the sequences of up- and down-regulation should be thought of indicating a causal relationship between the trigger event and the network activity changes. The state of widespread networks probably depends on a large number of variables (for example, activity changes in individual structures, or changes in inter-structure correlations), a subset of which may be eventually characterized following intensive future experimentation. The outcome of each experimental session may be conceived as a partially ordered sequence of system states, and such a sequence may indeed provide information related to memory. However, events in isolation are likely to be indicators rather than effectors of any cognitive capacity.

METHODS SUMMARY

All surgical and experimental procedures were approved by the local authorities (Regierungspraesidium, Tübingen Referat 35, Veterinärwesen) and were in full compliance with the guidelines of the European Community (EUVD 86/609/EEC) for the care and use of laboratory animals.

Received 3 June; accepted 24 September 2012.

1. Squire, L. R. Memory and the hippocampus: a synthesis from findings with rats, monkeys, and humans. *Psychol. Rev.* **99**, 195–231 (1992).
2. Eichenbaum, H. Declarative memory: insights from cognitive neurobiology. *Annu. Rev. Psychol.* **48**, 547–572 (1997).
3. Nadel, L. & Hardt, O. Update on memory systems and processes. *Neuropsychopharmacology* **36**, 251–273 (2011).
4. Buzsáki, G. Two-stage model of memory trace formation: a role for “noisy” brain states. *Neuroscience* **31**, 551–570 (1989).
5. Buzsáki, G. The hippocampo–neocortical dialogue. *Cereb. Cortex* **6**, 81–92 (1996).
6. Hasselmo, M. E. Neuromodulation and the hippocampus: memory function and dysfunction in a network simulation. *Prog. Brain Res.* **121**, 3–18 (1999).
7. Pennartz, C. M. A., Uylings, H. B. M., Barnes, C. A. & McNaughton, B. L. Memory reactivation and consolidation during sleep: from cellular mechanisms to human performance. *Prog. Brain Res.* **138**, 143–166 (2002).
8. Eichenbaum, H. A cortical–hippocampal system for declarative memory. *Nature Rev. Neurosci.* **1**, 41–50 (2000).
9. Buzsáki, G., Horvath, Z., Urioste, R., Hetke, J. & Wise, K. High-frequency network oscillation in the hippocampus. *Science* **256**, 1025–1027 (1992).
10. O’Keefe, J. & Nadel, L. *The Hippocampus as a Cognitive Map* 114–152 (Oxford Univ. Press, 1978).
11. Skaggs, W. E. *et al.* EEG sharp waves and sparse ensemble unit activity in the macaque hippocampus. *J. Neurophysiol.* **98**, 898–910 (2007).
12. Axmacher, N., Elger, C. E. & Fell, J. Ripples in the medial temporal lobe are relevant for human memory consolidation. *Brain* **131**, 1806–1817 (2008).
13. Ylinen, A. *et al.* Sharp wave-associated high-frequency oscillation (200 Hz) in the intact hippocampus: network and intracellular mechanisms. *J. Neurosci.* **15**, 30–46 (1995).
14. Girardeau, G. & Zugaro, M. Hippocampal ripples and memory consolidation. *Curr. Opin. Neurobiol.* **21**, 452–459 (2011).
15. Wilson, M. A. & McNaughton, B. L. Reactivation of hippocampal ensemble memories during sleep. *Science* **265**, 676–679 (1994).
16. Kudrimoti, H. S., Barnes, C. A. & McNaughton, B. L. Reactivation of hippocampal cell assemblies: effects of behavioral state, experience, and EEG dynamics. *J. Neurosci.* **19**, 4090–4101 (1999).
17. Nádasdy, Z., Hirase, H., Czurko, A., Csicsvari, J. & Buzsáki, G. Replay and time compression of recurring spike sequences in the hippocampus. *J. Neurosci.* **19**, 9497–9507 (1999).
18. Skaggs, W. E. & McNaughton, B. L. Replay of neuronal firing sequences in rat hippocampus during sleep following spatial experience. *Science* **271**, 1870–1873 (1996).
19. Eschenko, O., Ramadan, W., Molle, M., Born, J. & Sara, S. J. Sustained increase in hippocampal sharp-wave ripple activity during slow-wave sleep after learning. *Learn. Mem.* **15**, 222–228 (2008).
20. O’Neill, J., Senior, T. J., Allen, K., Huxter, J. R. & Csicsvari, J. Reactivation of experience-dependent cell assembly patterns in the hippocampus. *Nature Neurosci.* **11**, 209–215 (2008).
21. Ramadan, W., Eschenko, O. & Sara, S. J. Hippocampal sharp wave/ripples during sleep for consolidation of associative memory. *PLoS ONE* **4**, e6697 (2009).

22. Girardeau, G., Benchenane, K., Wiener, S. I., Buzsaki, G. & Zugaro, M. B. Selective suppression of hippocampal ripples impairs spatial memory. *Nature Neurosci.* **12**, 1222–1223 (2009).
23. Ego-Stengel, V. & Wilson, M. A. Disruption of ripple-associated hippocampal activity during rest impairs spatial learning in the rat. *Hippocampus* **20**, 1–10 (2010).
24. Siapas, A. G. & Wilson, M. A. Coordinated interactions between hippocampal ripples and cortical spindles during slow-wave sleep. *Neuron* **21**, 1123–1128 (1998).
25. Wierzyński, C. M., Lubenov, E. V., Gu, M. & Siapas, A. G. State-dependent spike-timing relationships between hippocampal and prefrontal circuits during sleep. *Neuron* **61**, 587–596 (2009).
26. Isomura, Y. *et al.* Integration and segregation of activity in entorhinal–hippocampal subregions by neocortical slow oscillations. *Neuron* **52**, 871–882 (2006).
27. Sirota, A., Csicsvari, J., Buhl, D. & Buzsaki, G. Communication between neocortex and hippocampus during sleep in rodents. *Proc. Natl Acad. Sci. USA* **100**, 2065–2069 (2003).
28. Steriade, M., Nunez, A. & Amzica, F. A novel slow (1 Hz) oscillation of neocortical neurons *in vivo*: depolarizing and hyperpolarizing components. *J. Neurosci.* **13**, 3252–3265 (1993).
29. McCormick, D. A. & Bal, T. Sleep and arousal—thalamocortical mechanisms. *Annu. Rev. Neurosci.* **20**, 185–215 (1997).
30. Mölle, M., Marshall, L., Gais, S. & Born, J. Grouping of spindle activity during slow oscillations in human non-rapid eye movement sleep. *J. Neurosci.* **22**, 10941–10947 (2002).
31. Amzica, F. & Steriade, M. The K-complex: its slow (1-Hz) rhythmicity and relation to delta waves. *Neurology* **49**, 952–959 (1997).
32. Battaglia, F. P., Sutherland, G. R. & McNaughton, B. L. Hippocampal sharp wave bursts coincide with neocortical “up-state” transitions. *Learn. Mem.* **11**, 697–704 (2004).
33. Mölle, M., Yeshenko, O., Marshall, L., Sara, S. J. & Born, J. Hippocampal sharp wave-ripples linked to slow oscillations in rat slow-wave sleep. *J. Neurophysiol.* **96**, 62–70 (2006).
34. Clemens, Z. *et al.* Temporal coupling of parahippocampal ripples, sleep spindles and slow oscillations in humans. *Brain* **130**, 2868–2878 (2007).
35. Axmacher, N., Mormann, F., Fernandez, G., Elger, C. E. & Fell, J. Memory formation by neuronal synchronization. *Brain Res. Rev.* **52**, 170–182 (2006).
36. Born, J. Slow-wave sleep and the consolidation of long-term memory. *World J. Biol. Psychiatry* **11**, 16–21 (2010).
37. Steriade, M. The corticothalamic system in sleep. *Front. Biosci.* **8**, d878–d899 (2003).
38. Sullivan, D. *et al.* Relationships between hippocampal sharp waves, ripples, and fast gamma oscillation: influence of dentate and entorhinal cortical activity. *J. Neurosci.* **31**, 8605–8616 (2011).
39. Paxinos, G., Huang, X. F., Petrides, M. & Toga, A. W. *The Rhesus Monkey Brain in Stereotactic Coordinates* (Elsevier, 2008).
40. Shmuel, A., Augath, M. A., Oeltermann, A. & Logothetis, N. K. Negative functional MRI response correlates with decreases in neuronal activity in monkey visual area V1. *Nature Neurosci.* **9**, 569–577 (2006).
41. Logothetis, N. K. *et al.* The effects of electrical microstimulation on cortical signal propagation. *Nature Neurosci.* **13**, 1283–1291 (2010).
42. Vincent, J. L. *et al.* Coherent spontaneous activity identifies a hippocampal–parietal mnemonic network. *J. Neurophysiol.* **96**, 3517–3531 (2006).
43. Poldrack, R. A. & Packard, M. G. Competition among multiple memory systems: converging evidence from animal and human brain studies. *Neuropsychologia* **41**, 245–251 (2003).
44. Schroeder, J. P., Wingard, J. C. & Packard, M. G. Post-training reversible inactivation of hippocampus reveals interference between memory systems. *Hippocampus* **12**, 280–284 (2002).
45. Oliveira, A. M., Hawk, J. D., Abel, T. & Havekes, R. Post-training reversible inactivation of the hippocampus enhances novel object recognition memory. *Learn. Mem.* **17**, 155–160 (2010).
46. Poldrack, R. A. & Rodriguez, P. How do memory systems interact? Evidence from human classification learning. *Neurobiol. Learn. Mem.* **82**, 324–332 (2004).
47. Mouret, J., Jeannero, M. & Jouvet, M. L’activité électrique du système visuel au cours de la phase paradoxale du sommeil chez le chat. *J. Physiol. (Paris)* **55**, 305–306 (1963).
48. Wolansky, T., Clement, E. A., Peters, S. R., Palczak, M. A. & Dickson, C. T. Hippocampal slow oscillation: a novel EEG state and its coordination with ongoing neocortical activity. *J. Neurosci.* **26**, 6213–6229 (2006).
49. Axmacher, N., Elger, C. E. & Fell, J. Memory formation by refinement of neural representations: the inhibition hypothesis. *Behav. Brain Res.* **189**, 1–8 (2008).
50. Logothetis, N. K. What we can do and what we cannot do with fMRI. *Nature* **453**, 869–878 (2008).

Supplementary Information is available in the online version of the paper.

Acknowledgements We thank D. Omer and M. Munk for reading the manuscript and for useful suggestions, D. Blaurock for English language corrections and editing, and P. Douay for help with the alert monkey experiments. This research was supported by the Max Planck Society. We apologize to those whose work we have not been able to cite for reasons of space.

Author Contributions N.K.L. and O.E. designed the experiments and carried out research. N.K.L. analysed the data, wrote the manuscript and supervised the research. Y.M. carried out research and, together with M.B., contributed data analysis. M.A. and T.S. collected the physiology fMRI data, H.C.E. helped with all anatomical details required to define ROIs and enable three-dimensional registration of functional images to standard anatomical scans, and A.O. designed and developed all electronics and electrodes permitting concurrent multiple-contact electrophysiological recordings and fMRI.

Author Information Reprints and permissions information is available at www.nature.com/reprints. The authors declare no competing financial interests. Readers are welcome to comment on the online version of the paper. Correspondence and requests for materials should be addressed to N.K.L. (Nikos.Logothetis@tuebingen.mpg.de).

Novel Foxo1-dependent transcriptional programs control T_{reg} cell function

Weiming Ouyang¹, Will Liao^{2,3}, Chong T. Luo^{1,4}, Na Yin¹, Morgan Huse¹, Myoungjoo V. Kim¹, Min Peng¹, Pamela Chan¹, Qian Ma¹, Yifan Mo^{2,3}, Dies Meijer⁵, Keji Zhao⁶, Alexander Y. Rudensky^{1,7}, Gurinder Atwal², Michael Q. Zhang^{8,9} & Ming O. Li¹

Regulatory T (T_{reg}) cells, characterized by expression of the transcription factor forkhead box P3 (Foxp3), maintain immune homeostasis by suppressing self-destructive immune responses^{1–4}. Foxp3 operates as a late-acting differentiation factor controlling T_{reg} cell homeostasis and function⁵, whereas the early T_{reg}-cell-lineage commitment is regulated by the Akt kinase and the forkhead box O (Foxo) family of transcription factors^{6–10}. However, whether Foxo proteins act beyond the T_{reg}-cell-commitment stage to control T_{reg} cell homeostasis and function remains largely unexplored. Here we show that Foxo1 is a pivotal regulator of T_{reg} cell function. T_{reg} cells express high amounts of Foxo1 and display reduced T-cell-receptor-induced Akt activation, Foxo1 phosphorylation and Foxo1 nuclear exclusion. Mice with T_{reg}-cell-specific deletion of *Foxo1* develop a fatal inflammatory disorder similar in severity to that seen in Foxp3-deficient mice, but without the loss of T_{reg} cells. Genome-wide analysis of Foxo1 binding sites reveals ~300 Foxo1-bound target genes, including the pro-inflammatory cytokine *Ifng*, that do not seem to be directly regulated by Foxp3. These findings show that the evolutionarily ancient Akt–Foxo1 signalling module controls a novel genetic program indispensable for T_{reg} cell function.

Among the three *Foxo* genes expressed in T cells, the transcript of *Foxo1* is specifically upregulated in mature thymocytes⁸. To genetically mark cells expressing Foxo1, we engineered a *Foxo1* allele (*Foxo1*^{tag}) encoding an in-frame fusion protein tag containing green fluorescent protein (GFP), Flag and a biotin-labelling peptide that enables Foxo1 biotinylation in *birA*-transgenic mice that express the bacterial biotin ligase BirA (Fig. 1a and Supplementary Fig. 1). T-cell expression of CD127 (also known as IL7r), the product of a previously identified Foxo1 target gene^{11,12}, was unaffected in *Foxo1*^{tag/tag} mice (Supplementary Fig. 1d), indicating that the protein tag does not alter Foxo1 function. Using GFP as a reporter, we found that immature thymocytes expressed low amounts of Foxo1 (Fig. 1a). Foxo1 was more strongly upregulated in T_{reg} cells than in conventional CD4⁺ T cells in the thymus, whereas the peripheral T cells expressed similar amounts of Foxo1 (Fig. 1a).

Foxo1 resides in the nucleus of quiescent T cells, and relocates to the cytosol after T-cell receptor (TCR) stimulation. To investigate the kinetics of Foxo1 translocation, we performed live-imaging experiments on CD4⁺ T cells from *Foxo1*^{tag/tag} mice on a *Foxp3*-internal ribosome entry site (IRES)-red fluorescent protein (RFP)-transgenic background in which T_{reg} cells are marked by the expression of RFP. Whereas high-dose CD3 antibody induced Foxo1 nuclear clearance in all T cells (Fig. 1b, c and Supplementary Video 1), low-dose CD3 antibody triggered Foxo1 translocation in conventional T cells but not in T_{reg} cells (Fig. 1b, c and Supplementary Video 2). Attenuated Foxo1 nuclear clearance in T_{reg} cells was further revealed by the immunostaining of T cells from wild-type mice (Supplementary Fig. 2a, b). Foxo1 nuclear export is regulated by Akt-induced Foxo1 phosphorylation. Low-dose anti-CD3 induced robust Akt and Foxo1 phosphorylation in conventional T cells, which was markedly decreased in T_{reg} cells (Fig. 1d). The phosphorylation defects of Foxo1 and Akt

were less profound in T cells stimulated with high-dose CD3 antibody (Supplementary Fig. 2c). Anti-CD3-induced Erk1 and Erk2 (also known as Mapk3 and Mapk1, respectively) phosphorylation was not compromised at the late time points in T_{reg} cells (Fig. 1d and Supplementary Fig. 2c), suggesting that the Akt pathway might be specifically modulated, probably through high expression of the Akt phosphatase Phlpp1 (ref. 13). Thus, compared to conventional T cells, T_{reg} cells are resistant to TCR-induced Akt activation and Foxo1 nuclear clearance.

To investigate the function of Foxo1 in T_{reg} cells, we crossed mice carrying floxed *Foxo1* alleles (*Foxo1*^{fl/fl}) with *Foxp3*^{cre} mice¹⁴. Foxo1 protein was barely detectable in T_{reg} cells from *Foxp3*^{cre} *Foxo1*^{fl/fl} mice, whereas conventional CD4⁺ T cells from *Foxp3*^{cre} *Foxo1*^{fl/fl} mice expressed comparable amounts of Foxo1 to wild-type T cells (Fig. 2a). In the absence of Foxo1 in T_{reg} cells, mice developed a hunched posture associated with lack of mobility, in addition to crusting of the ears, eyelids and tail (Fig. 2b) before they became moribund within 35 days of birth. Such a fulminant phenotype was comparable in severity to that of mice with the scurfy mutation of the *Foxp3* gene (*Foxp3*^{scf}; Fig. 2b), or mice depleted of T_{reg} cells^{15,16}. In addition, *Foxp3*^{cre} *Foxo1*^{fl/fl} mice showed splenomegaly and lymphadenopathy (Fig. 2c), and had a dense infiltrate of leukocytes in the salivary glands, lung interstitia, liver sinusoids, pancreas acini, stomach, and colon mucosa (Fig. 2d).

The severe immunopathology was associated with the expansion of T-cell populations expressing high amounts of the cell-proliferation marker Ki67 (Fig. 2e and Supplementary Fig. 3). T cells displayed an effector/memory phenotype (Fig. 2f and Supplementary Fig. 4a) and produced increased amounts of the pro-inflammatory cytokine interferon (IFN)- γ (Fig. 2g and supplementary Fig. 4b). Deletion of *Foxo1* from CD4⁺CD8⁺ immature T cells results in compromised

¹Immunology Program, Memorial Sloan-Kettering Cancer Center, New York, New York 10065, USA. ²Cold Spring Harbor Laboratory, Cold Spring Harbor, New York 11724, USA. ³Department of Applied Mathematics & Statistics, Stony Brook University, Stony Brook, New York 11794, USA. ⁴Louis V. Gerstner, Jr Graduate School of Biomedical Sciences, Memorial Sloan-Kettering Cancer Center, New York, New York 10065, USA. ⁵Department of Cell Biology and Genetics, Erasmus University Medical Center, 3000 DR Rotterdam, The Netherlands. ⁶Systems Biology Center, NHLBI, National Institute of Health, Bethesda, Maryland 20892, USA. ⁷Howard Hughes Medical Institute, Memorial Sloan-Kettering Cancer Center, New York, New York 10065, USA. ⁸Department of Molecular and Cell Biology, Center for Systems Biology, The University of Texas at Dallas, Richardson, Texas 75080, USA. ⁹Bioinformatics Division, Center for Synthetic and Systems Biology, TNLIS, Tsinghua University, Beijing 100084, China.

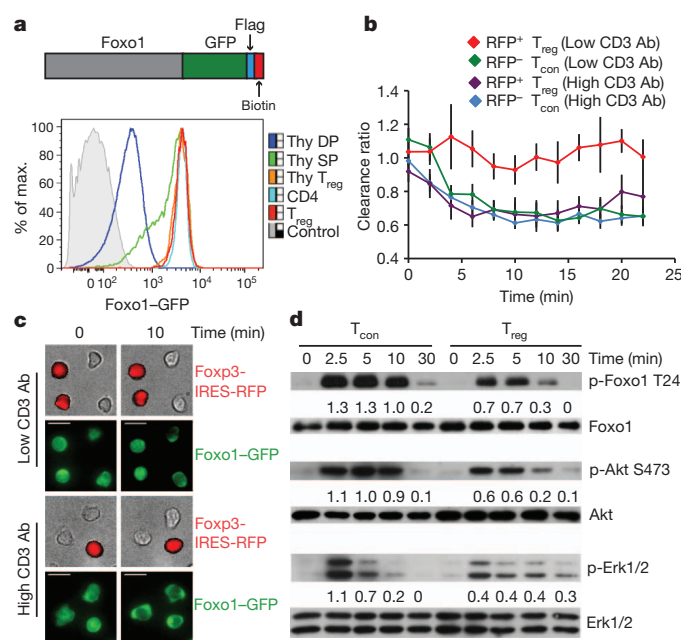


Figure 1 | Foxo1 expression and TCR-induced Foxo1 nuclear exclusion in T_{reg} cells. **a**, Foxo1 fusion protein with a tag containing GFP, Flag and a biotin-labelling peptide (top). Flow cytometric analysis of Foxo1-GFP expression in thymic $CD4^+CD8^+$ double-positive T cells (Thy DP), $CD4^+Foxp3^-$ single-positive T cells (Thy SP) and $CD4^+Foxp3^+$ T_{reg} cells (Thy T_{reg}), and splenic $CD4^+Foxp3^-$ conventional T cells (CD4) and $CD4^+Foxp3^+$ T_{reg} cells from $Foxo1^{tag/tag}$ mice (T_{reg}) (bottom). Cells from wild-type mice were used as a control. **b**, **c**, TCR-induced Foxo1 nuclear clearance in $CD4^+RFP^-$ conventional (T_{con}) and $CD4^+RFP^+$ T_{reg} cells from $Foxo1^{tag/tag}$ mice. Cells were stimulated with $0.01 \mu g ml^{-1}$ (low) or $0.1 \mu g ml^{-1}$ (high) anti-CD3 antibody (Ab) in the presence of $1.0 \mu g ml^{-1}$ anti-CD28. **b**, Quantification of Foxo1 nuclear clearance. Nuclear exclusion leads to a decrease in clearance ratio. **c**, Representative images of Foxo1 nuclear clearance of T_{con} and T_{reg} cells. **d**, Phosphorylated (p)-Foxo1 Thr 24, total Foxo1, p-Akt Ser 473, total Akt, p-Erk1/2 and total Erk1/2 proteins in T_{con} and T_{reg} cells stimulated with low anti-CD3 and anti-CD28 were determined by immunoblotting. The relative amounts of p-Foxo1, p-Akt and p-Erk1/2 proteins normalized to total Foxo1, Akt and Erk1/2 proteins are shown. Error bars represent s.d.; all experiments were repeated at least three times with similar results.

T_{reg} cell differentiation^{8,10}. However, thymic and splenic T_{reg} cell numbers were unaffected in 12-day-old $Foxp3^{cre} Foxo1^{fl/fl}$ mice (Supplementary Fig. 5). By the age of day 20, T_{reg} cell numbers in the peripheral lymphoid tissues were increased in $Foxp3^{cre} Foxo1^{fl/fl}$ mice (Fig. 2h and Supplementary Fig. 4c). These findings imply that the lymphoproliferative disease is caused by a loss of T_{reg} cell function rather than a loss of T_{reg} cells.

The observation that T_{reg} cells were less sensitive to TCR-induced Foxo1 nuclear exclusion implies that Foxo1-dependent transcriptional regulation is crucial for T_{reg} cell function. However, cytosolic Foxo1 regulates autophagy through transcription-independent mechanisms¹⁷. To differentiate the activities of nuclear Foxo1 and cytosolic Foxo1 induced by Akt activation, we inserted a complementary DNA fragment coding for a haemagglutinin (HA)-tagged human Foxo1 mutant in which amino acids at the Akt phosphorylation sites were substituted with alanines¹⁸ (HA-hFoxo1(AAA)), preceded by a loxP-flanked 'neo-STOP' cassette into the *Rosa26* locus (Supplementary Fig. 6). Mice carrying the mutant allele ($Foxo1^{AAA}$) were crossed with oestrogen receptor-Cre (*creER*) mice. Wild-type T cells or T cells from *creER Foxo1^{AAA/+}* mice previously treated with tamoxifen to induce HA-hFoxo1(AAA) expression were stimulated with CD3 and CD28 antibodies. As expected, whereas wild-type Foxo1 translocated from the nucleus to the cytosol, the HA-hFoxo1(AAA)-expressing mutant was defective in nuclear export (Supplementary Fig. 6c). We

further crossed $Foxo1^{AAA/+}$ mice with $Foxp3^{cre}$ mice, and confirmed specific HA-hFoxo1(AAA) expression in T_{reg} cells (Fig. 3a). Ectopic expression of HA-hFoxo1(AAA) did not affect T_{reg} cell differentiation or homeostasis (Supplementary Fig. 7a). Upon breeding the $Foxo1^{AAA}$ allele to $Foxp3^{cre} Foxo1^{fl/fl}$ mice, the lethal inflammatory phenotype was completely rescued (Fig. 3b and supplementary Fig. 7), indicating that the T_{reg} cell defects are caused by a loss of nuclear Foxo1 activity.

For global identification of Foxo1 DNA-binding sites in T_{reg} cells, we performed chromatin immunoprecipitation coupled to high-throughput sequencing (ChIP-seq) experiments using Foxo1 antibody precipitation of chromatin purified from $CD4^+CD25^+$ T cells from C57BL/6 mice, or streptavidin pull-down of chromatin from T_{reg} cells of $Foxo1^{tag/tag} birA$ mice. To define a ChIP-seq peak as significant, we used the model-based analysis of ChIP-seq (MACS) peak calling software and applied an empirical false-discovery rate of 0.01 at which the noise ratio of peak detection was less than 0.005 (Supplementary Fig. 8a). Using this criterion, we identified 3,431 enriched genomic loci that were shared between the antibody and the biotinylated Foxo1 samples (Supplementary Fig. 8b), and were designated as putative Foxo1 binding sites (Supplementary Table 1). Among the Foxo1 binding peaks, we could identify previously characterized binding sites of Foxo1 target genes, including an intronic binding site in the *Foxp3* locus⁸, an *Il7r* enhancer element^{11,12}, as well as binding sites in the proximal promoter regions of the *Fbxo32* and *Bcl2l1* genes^{19,20} (Supplementary Fig. 9).

Foxo1 binding sites were mostly enriched in the promoters and the 5' untranslated regions (UTRs), whereas peaks mapped to the intergenic regions and 3' UTRs were substantially under-represented (Fig. 3c). Further analysis of the peaks showed that Foxo1 preferentially bound to regions within 500 base pairs of the transcription start sites (Supplementary Fig. 8c). Foxo1 binding peaks were enriched for the high-affinity Foxo1 binding motifs, and *de novo* motif prediction from the top 500 ranked binding peaks revealed a conserved Foxo1 recognition site (Supplementary Fig. 8d, e). In addition, approximately 73% of Foxo1 binding sites were mapped to the conserved genomic regions of mammalian species (Supplementary Table 1). These observations support an evolutionarily conserved function for Foxo1 in classical transcriptional regulation of target-gene expression.

To identify the cellular functions directly regulated by Foxo1 transcriptional control, we performed gene-expression profiling on T_{reg} cells from wild-type, $Foxp3^{cre} Foxo1^{fl/fl}$, $Foxp3^{cre} Foxo1^{AAA/+}$ and $Foxp3^{cre} Foxo1^{fl/fl} Foxo1^{AAA/+}$ mice. Comparison of data from wild-type and $Foxp3^{cre} Foxo1^{fl/fl}$ T_{reg} cells revealed 942 and 1,155 genes downregulated or upregulated, respectively, by more than 1.5 fold, ~80% of which were corrected in $Foxp3^{cre} Foxo1^{fl/fl} Foxo1^{AAA/+}$ T_{reg} cells (Supplementary Table 2). By cross-referencing this data set with the data set of Foxo1-bound genes, we identified 310 putative Foxo1 direct target genes, among which 240 and 70 genes were activated or repressed, respectively, by Foxo1 (Fig. 3d and Supplementary Table 3).

T_{reg} cell homeostasis and function are dependent on the T_{reg} -cell-specific transcription factor Foxp3 (ref. 5). ChIP and genome tiling array studies have revealed Foxp3-bound genes in murine T cells^{21,22}. Approximately 6.8% or 9.6% of Foxo1-bound genes were occupied by Foxp3 in T_{reg} cells or in a T-cell line that overexpressed Foxp3 (Supplementary Fig. 10a). Comparison of the putative direct target genes of Foxo1 and Foxp3 revealed that ~90% of activated genes and ~99% of repressed genes were specifically regulated by Foxo1 or Foxp3 (Supplementary Fig. 10b, c and Supplementary Table 3). Indeed, expression of the Foxp3 target gene *Il2ra* (coding for CD25) was decreased in T cells transcribing a *Foxp3* null allele that encodes a GFP reporter²³, but not in Foxo1-deficient T_{reg} cells (Fig. 4a and Supplementary Fig. 10d). A recent study showed that Foxo1 binds to the promoter region of the Foxp3 target gene *Ctla4* (ref. 10). ChIP-seq experiments revealed weak *Ctla4*-promoter binding of Foxo1 in antibody but not biotin samples (data not shown). In the absence of Foxo1, CTLA4 was marginally downregulated, whereas the amount

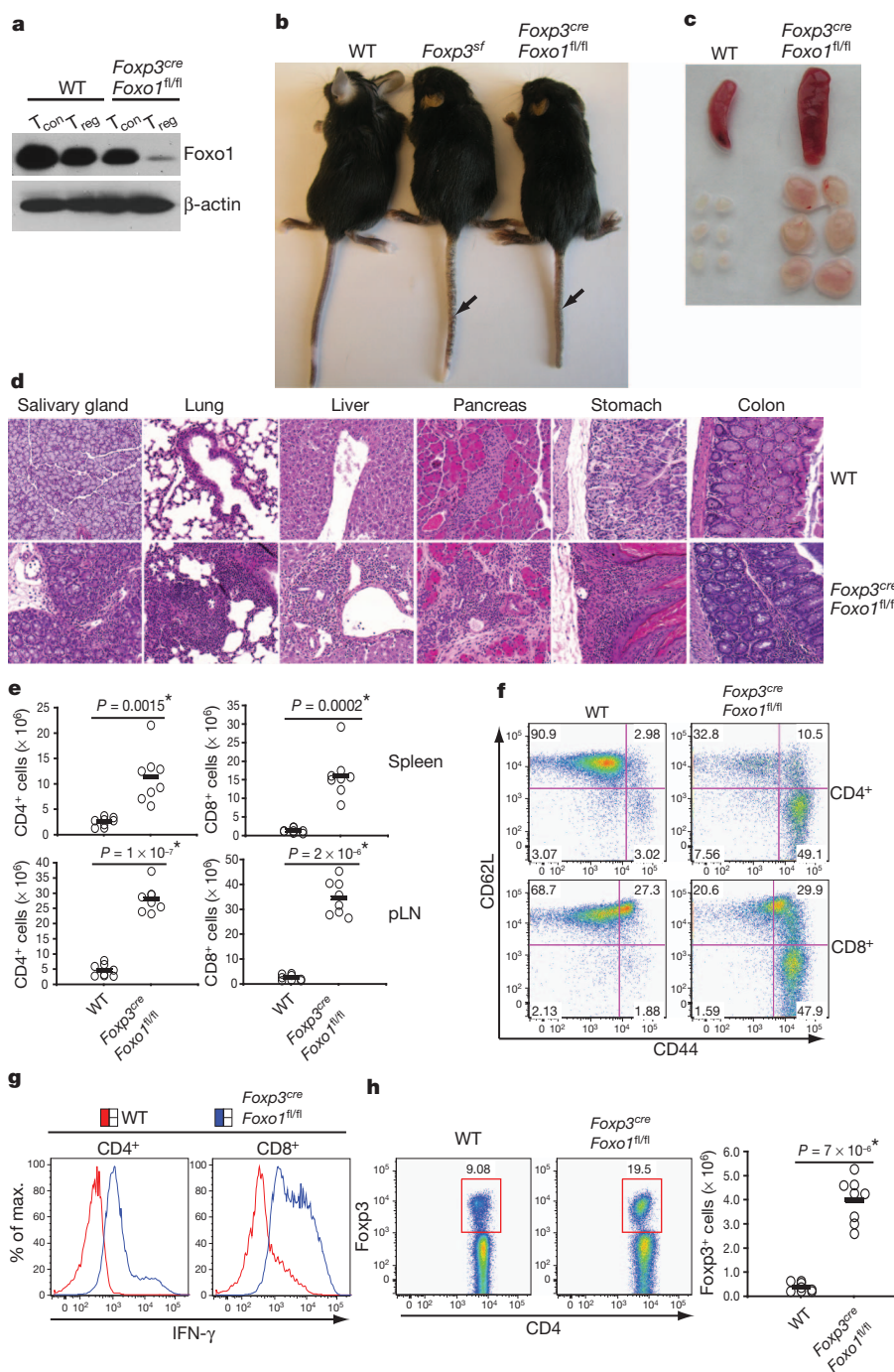


Figure 2 | An essential role for Foxo1 in the control of T_{reg} cell function.

a, Foxo1 protein in CD4⁺ Foxp3[−] conventional (T_{con}) and T_{reg} cells from wild-type (WT) and $Foxp3^{cre} Foxo1^{fl/fl}$ mice was determined by immunoblotting. β -actin was used as a loading control. **b**, Images of 21-day-old wild-type, $Foxp3^{sf}$ and $Foxp3^{cre} Foxo1^{fl/fl}$ mice. Arrows indicate the scurfy tails of $Foxp3^{sf}$ and $Foxp3^{cre} Foxo1^{fl/fl}$ mice. **c**, A representative picture of spleens and peripheral lymph nodes from 20-day-old wild-type and $Foxp3^{cre} Foxo1^{fl/fl}$ mice. **d**, Haematoxylin and eosin staining of salivary gland, lung, liver, pancreas, stomach and colon sections from 21-day-old wild-type and $Foxp3^{cre} Foxo1^{fl/fl}$ mice. **e**, CD4⁺ and CD8⁺ T-cell numbers from spleens and peripheral lymph nodes (pLN) of 17–21-day-old wild-type and $Foxp3^{cre} Foxo1^{fl/fl}$ mice ($n = 8$ per genotype). **f**, Flow cytometric analysis of CD44 and CD62L expression in

peripheral lymph node CD4⁺ and CD8⁺ T cells from 20-day-old wild-type and $Foxp3^{cre} Foxo1^{fl/fl}$ mice. **g**, Peripheral lymph node T cells from 20-day-old wild-type and $Foxp3^{cre} Foxo1^{fl/fl}$ mice were stimulated with phorbol myristate acetate (PMA) and ionomycin for 4 h. The expression of IFN- γ in CD4⁺ and CD8⁺ T cells was determined by intracellular staining. **h**, Flow cytometric analysis of Foxp3 expression in peripheral lymph node CD4⁺ T cells from 20-day-old wild-type and $Foxp3^{cre} Foxo1^{fl/fl}$ mice (left). Peripheral lymph node T_{reg} cell numbers from 17–21-day-old wild-type and $Foxp3^{cre} Foxo1^{fl/fl}$ mice (right; $n = 8$ per genotype). The P values between the two groups are shown. Asterisk indicates a statistically significant difference. Results represent at least three independent experiments.

of *Ctla4* transcript was approximately fourfold lower in the absence of Foxp3 (Fig. 4a and Supplementary Fig. 10e). Foxp3 and CTLA4 are essential for T_{reg} cell inhibition of conventional T-cell proliferation *in vitro*^{23,24}. By contrast, as previously reported in ref. 11, Foxo1-deficient

T_{reg} cells had normal suppressive activity in such assays (Fig. 4b). These observations imply that the Foxp3-dependent program is largely intact in the absence of Foxo1, and the loss of suppressive activity of Foxo1-deficient T_{reg} cells is probably independent of CTLA4.

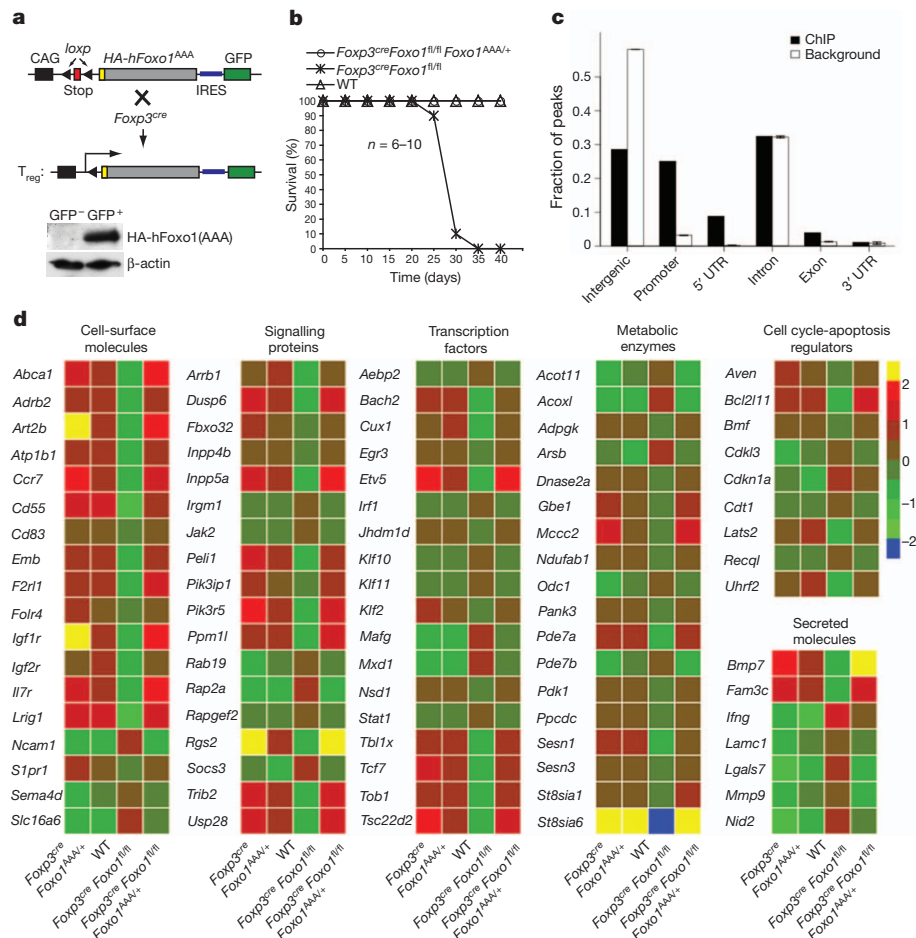


Figure 3 | Foxo1-dependent transcriptional programs in T_{reg} cells. **a**, A schematic representation of the mouse line expressing HA-hFoxo1(AAA) specifically in T_{reg} cells. A cassette containing a floxed stop sequence, a cDNA coding for a HA-tagged human Foxo1(AAA) mutant, and IRES-GFP proteins was inserted into the *Rosa26* locus. Mice with the knock-in allele were crossed with *Foxp3^{cre}* mice (top). The expression of HA-FOXO1(AAA) was determined by immunoblotting with anti-HA. β -actin was used as a loading control (bottom). **b**, Survival of wild-type, *Foxp3^{cre} Foxo1^{fl/fl}* and

Foxp3^{cre} Foxo1^{fl/fl} Foxo1^{AAA/+} mice ($n = 6$ to 10 per genotype). **c**, The overlapping set of peaks shared between antibody and biotin ChIP-seq samples was associated with functional annotations based on the genomic location of the summits within each peak, which revealed enrichment in gene promoters ($P = 0.04$) and 5' UTRs ($P < 1 \times 10^{-10}$) above the background rate using randomly generated peaks. **d**, Foxo1-bound target genes differentially expressed between wild-type and *Foxp3^{cre} Foxo1^{fl/fl}* T_{reg} cells, and whose expression was corrected in *Foxp3^{cre} Foxo1^{fl/fl} Foxo1^{AAA/+}* T_{reg} cells.

To gain insights into the general functional features of the Foxo1-regulated program, we analysed the Gene Ontology and BioCarta pathway association of Foxo1 target genes²⁵. The putative Foxo1 direct target genes were strongly associated with cell communication, signal transduction, transcription and metabolism, and were specifically enriched for genes involved in the Jak-STAT, TCR and insulin-signalling pathways (Supplementary Table 4). A salient characteristic of T_{reg} cells is their inability to produce pro-inflammatory cytokines such as IFN- γ . Foxo1 was recruited to a regulatory element located 22 kilobases upstream from the transcriptional start site of the *Ifng* gene²⁶ in T_{reg} cells (Fig. 4c, d). In the absence of Foxo1, IFN- γ messenger RNA and protein were highly induced in T_{reg} cells (Fig. 4e, f and Supplementary Fig. 11a). However, similar to wild-type T_{reg} cells, Foxo1-deficient T_{reg} cells were unable to produce interleukin (IL)-2 (Supplementary Fig. 11b), which is probably regulated by Foxp3 (ref. 22). To determine whether Foxo1 had a cell-intrinsic role in inhibiting IFN- γ expression, we co-cultured wild-type T_{reg} cells and T_{reg} cells from the disease-free *creER Foxo1^{fl/fl}* mice previously treated with tamoxifen to acutely delete *Foxo1*. A sizable fraction of Foxo1-deficient but not wild-type T_{reg} cells produced IFN- γ under the condition of IL-12 and IFN- γ stimulation (Supplementary Fig. 12a). Importantly, wild-type and Foxo1-deficient conventional CD4⁺ T cells produced similar amounts of IFN- γ (Supplementary Fig. 12b), revealing a specific function for Foxo1 in repressing IFN- γ expression in T_{reg} cells.

To investigate whether IFN- γ production by Foxo1-deficient T_{reg} cells contributed to their loss of suppressive function, we crossed *Foxp3^{cre} Foxo1^{fl/fl}* mice to the IFN- γ -deficient background. Ablation of IFN- γ partially corrected the lethal inflammatory phenotype as well as the lymphoproliferative disease of *Foxp3^{cre} Foxo1^{fl/fl}* mice (Supplementary Fig. 13). To assess the specific function of IFN- γ produced by Foxo1-deficient T_{reg} cells, we used a transfer model of colitis. Recipient mice deficient in recombination-activating gene 1 (*Rag1^{-/-}*) did not develop colitis upon receipt of wild-type, *Foxo1^{-/-}* or *Foxo1^{-/-} Ifng^{-/-}* T_{reg} cells (Supplementary Fig. 14). However, recipients of naive T cells developed a wasting disease and colitis within 4 weeks, which was prevented by wild-type but not Foxo1-deficient T_{reg} cells (Fig. 4g, h and Supplementary Fig. 14b). Importantly, the suppressive activity was largely restored in *Foxo1^{-/-} Ifng^{-/-}* T_{reg} cells (Fig. 4g, h and Supplementary Fig. 14b), supporting *Ifng* as a critical Foxo1 target gene in the control of T_{reg} cell function.

Foxo proteins control Foxp3 expression and T_{reg} cell differentiation^{8–10}. Our new data reveal that the Akt–Foxo1 signalling pathway is modulated in mature T_{reg} cells to maintain high nuclear Foxo1 activity; this is crucial for T_{reg} cell function, in part through Foxo1 inhibition of IFN- γ expression. IFN- γ produced by T_{reg} cells may activate conventional T cells or antigen-presenting cells compromising T_{reg} cell function, but the precise mechanisms remain to be determined. Diminished TCR-induced Akt activation has been

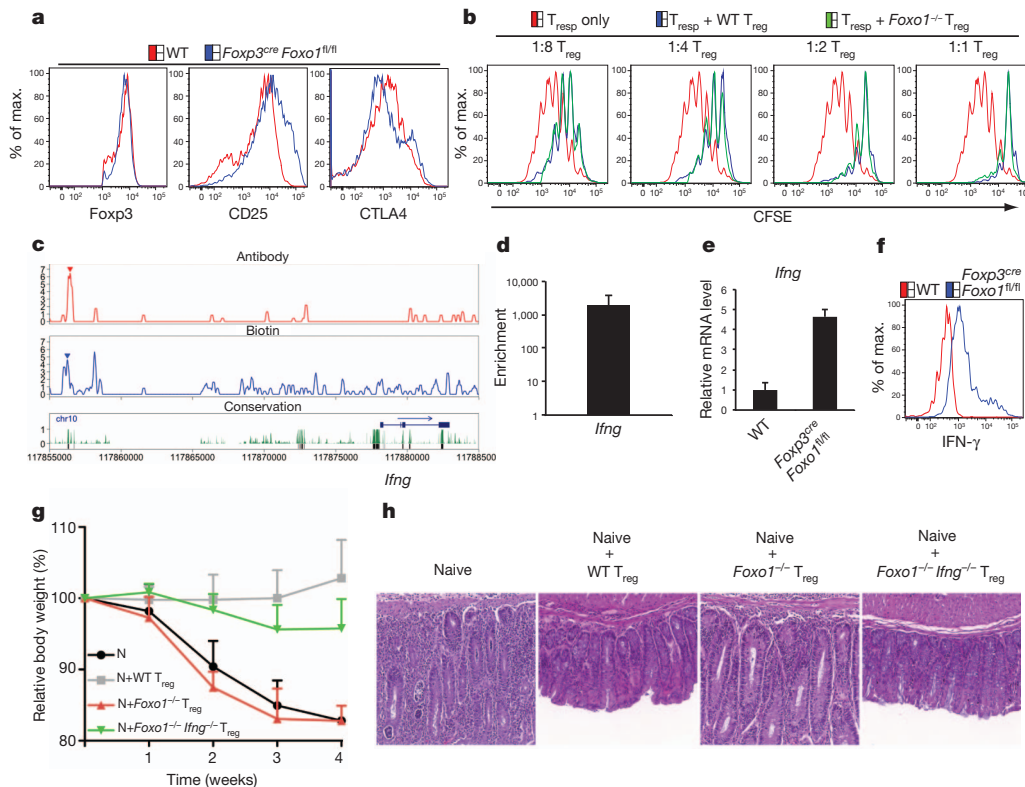


Figure 4 | Restoration of Foxo1-deficient T_{reg} cell function in the absence of IFN-γ. **a**, Flow cytometric analysis of Foxp3, CD25 and CTLA4 expression in lymph node T_{reg} cells from 20-day-old wild-type and *Foxp3^{cre} Foxo1^{fl/fl}* mice. **b**, Suppression of wild-type naive CD4⁺ T cells, labelled with the cytosolic dye carboxyfluorescein diacetate succinimidyl ester (CFSE) (responding T cells (T_{resp})), by wild-type and Foxo1-deficient (*Foxo1^{-/-}*) T_{reg} cells. T_{resp} cell division was assessed by CFSE dilution at the indicated ratios of cell numbers between T_{reg} cell and T_{resp} cells. **c**, Foxo1-bound regions in the *Ifng* locus. **d**, Foxo1 binding to the ChIP-seq peak was confirmed by ChIP-quantitative (q)PCR, and is presented relative to enrichment by immunoprecipitation with isotype-matched control antibody. **e**, Expression of IFN-γ mRNA in T_{reg} cells

from wild-type and *Foxp3^{cre} Foxo1^{fl/fl}* mice was determined by qPCR. **f**, Peripheral lymph node T cells from 20-day-old wild-type and *Foxp3^{cre} Foxo1^{fl/fl}* mice were stimulated with PMA and ionomycin for 4 h. The expression of IFN-γ in T_{reg} cells was determined by intracellular staining. **g**, Naive T cells (N) were transferred to *Rag1^{-/-}* mice alone or in combination with wild-type, *Foxo1^{-/-}* or *Foxo1^{-/-} Ifng^{-/-}* T_{reg} cells. Changes in body weight of *Rag1^{-/-}* recipients over time are shown ($n = 4$) (**g**). Haematoxylin and eosin staining of colon sections from *Rag1^{-/-}* mice at 4 weeks after the transfer (**h**). Error bars represent s.d.; results are representative of at least three independent experiments.

observed in human T_{reg} cells²⁷, suggesting that Foxo1 controls human T_{reg} cell function. Under conditions of strong TCR stimulation, nuclear Foxo1 is translocated to the cytosol in T_{reg} cells, raising the possibility that the Foxo1-dependent program is subject to regulation. Intriguingly, T_{reg} cells from mice infected with *Toxoplasma gondii* produce IFN-γ²⁸. Increased frequencies of IFN-γ-secreting T_{reg} cells are also present in multiple sclerosis and diabetes patients^{29,30}. Future studies will determine whether the loss of Foxo1 function accounts for T_{reg} cell plasticity under these pathological conditions, and whether the Akt–Foxo1 signalling pathway can be manipulated for the treatment of T_{reg}-cell-associated immunological disorders.

METHODS SUMMARY

Mice. The *Foxo1^{tag}* and *Foxo1^{AAA}* knock-in mouse models were generated by homologous recombination. Mice containing floxed *Foxo1*, *Foxp3-IRES-RFP*, *Foxp3^{cre}* and *Foxp3^{gfpko}* (*Foxp3* null allele coding for a GFP reporter) alleles were previously described^{11,14,23}. C57BL/6, *Foxp3^{gfp}*, *Ifng^{-/-}*, *Rag1^{-/-}* and *UBC-cre-ERT2 (creER)* mice were purchased from the Jackson Laboratory. All mice were maintained under specific pathogen-free conditions, and animal experimentation was conducted in accordance with institutional guidelines.

Flow cytometry. Thymic, splenic and lymph node cells were stained with fluorescent-dye-labelled antibodies, acquired and analysed with a LSR II flow cytometer (Becton Dickinson) and FlowJo software (TreeStar). Intracellular staining was carried out with kits from eBiosciences.

ChIP-seq. CD4⁺CD25⁺ T_{reg} cells were purified from C57BL/6 mice by fluorescence-activated cell sorting (FACS), and were used to isolate Foxo1-bound chromatin by immunoprecipitation with anti-Foxo1 (no. ab39670, Abcam).

CD4⁺RFP⁺ T_{reg} cells were purified from *Foxo1^{tag/tag} birA Foxp3-IRES-RFP* mice by FACS, and were used to isolate Foxo1-bound chromatin with streptavidin. The libraries of Foxo1-bound chromatin were prepared and used for sequencing. SR-36 sequencing was done at the Genome Center of Cold Spring Harbor Laboratory.

Expression microarray. Lymph node and splenic T_{reg} cells were isolated from wild-type, *Foxp3^{cre} Foxo1^{fl/fl}*, *Foxp3^{cre} Foxo1^{AAA/+}* and *Foxp3^{cre} Foxo1^{fl/fl} Foxo1^{AAA/+}* mice. RNA was prepared with the miRNeasy Mini Kit (Qiagen). RNA amplification, labelling and hybridization to M430 2.0 chips (Affymetrix) were done at the core facility of Memorial Sloan-Kettering Cancer Center.

Transfer model of colitis. Naive T cells (4×10^5) and T_{reg} cells (2×10^5) were transferred alone or in combination to *Rag1^{-/-}* mice. After T-cell reconstitution, mice were weighed weekly and monitored for signs of disease. Mice were euthanized at 4 weeks after T-cell transfer and their colons were used for histopathological analysis.

Full Methods and any associated references are available in the online version of the paper.

Received 5 December 2011; accepted 12 September 2012.

Published online 7 November 2012.

1. Sakaguchi, S., Yamaguchi, T., Nomura, T. & Ono, M. Regulatory T cells and immune tolerance. *Cell* **133**, 775–787 (2008).
2. Tang, Q. & Bluestone, J. A. The Foxp3⁺ regulatory T cell: a jack of all trades, master of regulation. *Nature Immunol.* **9**, 239–244 (2008).
3. Feuerer, M., Hill, J. A., Mathis, D. & Benoist, C. Foxp3⁺ regulatory T cells: differentiation, specification, subphenotypes. *Nature Immunol.* **10**, 689–695 (2009).
4. Shevach, E. M. Mechanisms of foxp3⁺ T regulatory cell-mediated suppression. *Immunity* **30**, 636–645 (2009).

5. Rudensky, A. Y. Regulatory T cells and Foxp3. *Immunol. Rev.* **241**, 260–268 (2011).
6. Haxhinasto, S., Mathis, D. & Benoist, C. The AKT–mTOR axis regulates *de novo* differentiation of CD4⁺Foxp3⁺ cells. *J. Exp. Med.* **205**, 565–574 (2008).
7. Sauer, S. *et al.* T cell receptor signaling controls Foxp3 expression via PI3K, Akt, and mTOR. *Proc. Natl Acad. Sci. USA* **105**, 7797–7802 (2008).
8. Ouyang, W. *et al.* Foxo proteins cooperatively control the differentiation of Foxp3⁺ regulatory T cells. *Nature Immunol.* **11**, 618–627 (2010).
9. Harada, Y. *et al.* Transcription factors Foxo3a and Foxo1 couple the E3 ligase Cbl-b to the induction of Foxp3 expression in induced regulatory T cells. *J. Exp. Med.* **207**, 1381–1391 (2010).
10. Kerdiles, Y. M. *et al.* Foxo transcription factors control regulatory T cell development and function. *Immunity* **33**, 890–904 (2010).
11. Ouyang, W., Beckett, O., Flavell, R. A. & Li, M. O. An essential role of the forkhead-box transcription factor Foxo1 in control of T cell homeostasis and tolerance. *Immunity* **30**, 358–371 (2009).
12. Kerdiles, Y. M. *et al.* Foxo1 links homing and survival of naive T cells by regulating L-selectin, CCR7 and interleukin 7 receptor. *Nature Immunol.* **10**, 176–184 (2009).
13. Patterson, S. J. *et al.* Cutting edge: PHLPP regulates the development, function, and molecular signaling pathways of regulatory T cells. *J. Immunol.* **186**, 5533–5537 (2011).
14. Rubtsov, Y. P. *et al.* Regulatory T cell-derived interleukin-10 limits inflammation at environmental interfaces. *Immunity* **28**, 546–558 (2008).
15. Kim, J. M., Rasmussen, J. P. & Rudensky, A. Y. Regulatory T cells prevent catastrophic autoimmunity throughout the lifespan of mice. *Nature Immunol.* **8**, 191–197 (2007).
16. Lahl, K. *et al.* Selective depletion of Foxp3⁺ regulatory T cells induces a scurfy-like disease. *J. Exp. Med.* **204**, 57–63 (2007).
17. Zhao, Y. *et al.* Cytosolic FoxO1 is essential for the induction of autophagy and tumour suppressor activity. *Nature Cell Biol.* **12**, 665–675 (2010).
18. Zhang, X. *et al.* Phosphorylation of serine 256 suppresses transactivation by FKHR (FOXO1) by multiple mechanisms. Direct and indirect effects on nuclear/cytoplasmic shuttling and DNA binding. *J. Biol. Chem.* **277**, 45276–45284 (2002).
19. Sandri, M. *et al.* Foxo transcription factors induce the atrophy-related ubiquitin ligase atrogin-1 and cause skeletal muscle atrophy. *Cell* **117**, 399–412 (2004).
20. Gilley, J., Coffey, P. J. & Ham, J. FOXO transcription factors directly activate *bim* gene expression and promote apoptosis in sympathetic neurons. *J. Cell Biol.* **162**, 613–622 (2003).
21. Zheng, Y. *et al.* Genome-wide analysis of Foxp3 target genes in developing and mature regulatory T cells. *Nature* **445**, 936–940 (2007).
22. Marson, A. *et al.* Foxp3 occupancy and regulation of key target genes during T-cell stimulation. *Nature* **445**, 931–935 (2007).
23. Gavin, M. A. *et al.* Foxp3-dependent programme of regulatory T-cell differentiation. *Nature* **445**, 771–775 (2007).
24. Wing, K. *et al.* CTLA-4 control over Foxp3⁺ regulatory T cell function. *Science* **322**, 271–275 (2008).
25. Medina, I. *et al.* Babelomics: an integrative platform for the analysis of transcriptomics, proteomics and genomic data with advanced functional profiling. *Nucleic Acids Res.* **38**, W210–W213 (2010).
26. Hatton, R. D. *et al.* A distal conserved sequence element controls *Ifng* gene expression by T cells and NK cells. *Immunity* **25**, 717–729 (2006).
27. Crellin, N. K., Garcia, R. V. & Levings, M. K. Altered activation of AKT is required for the suppressive function of human CD4⁺CD25⁺ T regulatory cells. *Blood* **109**, 2014–2022 (2007).
28. Oldenhove, G. *et al.* Decrease of Foxp3⁺ Treg cell number and acquisition of effector cell phenotype during lethal infection. *Immunity* **31**, 772–786 (2009).
29. Dominguez-Villar, M., Baecher-Allan, C. M. & Hafler, D. A. Identification of T helper type 1-like, Foxp3⁺ regulatory T cells in human autoimmune disease. *Nature Med.* **17**, 673–675 (2011).
30. McClymont, S. A. *et al.* Plasticity of human regulatory T cells in healthy subjects and patients with type 1 diabetes. *J. Immunol.* **186**, 3918–3926 (2011).

Supplementary Information is available in the online version of the paper.

Acknowledgements We thank R. Flavell for the Foxp3-IRES-RFP mouse strain, K. Rajewsky and C. Xiao for the Rosa26 targeting vector and T. Unterman for the HA-hFoxo1(AAA) construct. This work was supported by the Starr Cancer Consortium (13-A123 to M.O.L., M.Q.Z. and G.A.), the Rita Allen Foundation (M.O.L.), National Bio Resource Project (NBRPC) (2012CB316503 to M.Q.Z.) and National Institutes of Health (HG001696 to M.Q.Z.).

Author Contributions W.O., W.L., C.T.L., N.Y., M.H., G.A., M.Q.Z. and M.O.L. designed the research and analysed the data; W.O., W.L., C.T.L., N.Y., M.H., M.V.K., M.P., P.C., Q.M. and Y.M. did the experiments; D.M. and A.Y.R. provided *birA* and *Foxp3^{Cre}* mouse strains; K.Z. supervised the ChIP-seq experiment; and W.O., W.L. and M.O.L. wrote the manuscript.

Author Information The expression and ChIP-seq data have been deposited in the NCBI GEO database under accession number GSE40657. Reprints and permissions information is available at www.nature.com/reprints. The authors declare no competing financial interests. Readers are welcome to comment on the online version of the paper. Correspondence and requests for materials should be addressed to M.O.L. (lim@mskcc.org) or M.Q.Z. (mzhang@cshl.edu) for computational questions.

METHODS

Mice. To generate a *Foxo1* knock-in mouse model (*Foxo1*^{tag}), two genomic DNA fragments of the *Foxo1* gene were isolated from a C57BL/6 bacterial artificial chromosome library (Genome Systems). A cDNA coding for GFP, Flag and biotin-labelling peptide was inserted into the genomic DNA fragment containing the second exon of *Foxo1* before the stop codon. Targeting vector was constructed by cloning the fragments into pEasy-Flox plasmid. To generate a *Rosa26-hFoxo1*^{AAA} knock-in mouse model (*Foxo1*^{AAA}), the cDNA coding for a HA-tagged human Foxo1 (AAA) mutant was inserted into a *Rosa26* targeting vector. Linearized targeting vectors were transfected into embryonic stem cells derived from the C57BL/6 strain. Homologous recombinants were identified by Southern blotting analysis, and were implanted into foster mothers. Chimaeric mice were bred to C57BL/6 mice, and the F₁ generation was screened for germline transmission. The *neo* gene in *Foxo1*^{tag} mice was removed by breeding F₁ mice with a strain of *cytomegalovirus*-promoter-driven *cre*-transgenic mice (The Jackson Laboratory). Mice containing floxed *Foxo1*, *Foxp3*-IRES-RFP, *Foxp3*^{Cre}, *Foxp3*^{gfpko} (*Foxp3* null allele coding for a GFP reporter) and *birA* alleles were previously described^{11,14,23,31,32}. C57BL/6, *Foxp3*^{sf}, *Ifng*^{-/-}, *Rag1*^{-/-} and UBC-*cre*-ERT2 (*creER*) mice were purchased from the Jackson Laboratory. Mice with intact or floxed *Foxo1* alleles were used as wild-type controls. Mice with T_{reg}-cell-specific deletion of *Foxo1* were generated by crossing *Foxo1* floxed mice with *Foxp3*^{Cre} mice. To mark T_{reg} cells with RFP, mice were bred with *Foxp3*-IRES-RFP mice. To label Foxo1 with biotin, *Foxo1*^{tag} mice were bred with *birA*-transgenic mice. All mice were maintained under specific pathogen-free conditions, and animal experimentation was conducted in accordance with institutional guidelines.

Antibodies and immunoblotting. Anti-p-Foxo1 Thr 24 (no. 9464), anti-Foxo1 (C29H4), anti-p-Akt Ser 473 (D9E), anti-Akt (C67E7), anti-p-Erk1/2, anti-Erk1/2 and anti-HA (6E2) were purchased from Cell Signaling. Anti-β-actin (AC-15) was obtained from Sigma. To determine Foxo1 expression in T_{reg} cells, CD4⁺Foxp3⁺ T_{reg} cells were purified by FACS. Total protein extracts were dissolved in SDS sample buffer. To assess Foxo1 translocation, T cells were stimulated with anti-CD3 and anti-CD28, and the cytosolic and nuclear extracts were prepared. To analyse Akt, Foxo1 and Erk phosphorylation, conventional CD4⁺ T cells and CD4⁺Foxp3⁺ T_{reg} cells were purified by FACS. T cells were stimulated with anti-CD3 and anti-CD28, and the total protein extracts were prepared. Protein extracts were separated on 8% SDS-PAGE gels and transferred to polyvinylidene difluoride membrane (Millipore). The membranes were probed with antibodies and visualized with the Immobilon Western Chemiluminescent HRP Substrate (Millipore).

Live imaging of Foxo1 translocation. CD4⁺ cells were isolated from *Foxo1*^{tag/tag} *Foxp3*-IRES-RFP mice, and stimulated with plate-bound anti-CD3 and anti-CD28 on glass surfaces. GFP, RFP and bright-field images were acquired every 2 min after addition of cells using a fluorescence videomicroscope (Olympus IX-81) fitted with a 40X objective lens. Nuclear Foxo1 clearance was quantified by analysing two orthogonal linescans through each cell. For each linescan, the average intensity of three equally spaced pixels inside the cell was divided by the average intensity of the cell edge on each side to determine a 'clearance ratio'. Nuclear exclusion leads to a decrease in clearance ratio.

Immunofluorescence microscopy. CD4⁺ T cells were isolated from spleen and peripheral lymph nodes of C57BL/6 mice with anti-CD4 microbeads (Miltenyi Biotec Inc.), stimulated with plate-bound anti-CD3 (low dose, 0.01 μg ml⁻¹; high dose, 0.1 μg ml⁻¹) and anti-CD28 (1 μg ml⁻¹) on chamber slides at 37 °C for 20 min. After fixation with 4% paraformaldehyde, cells were permeabilized with Foxp3 Fixation/Permeabilization buffer (eBioscience) according to the manufacturer's instructions. After blocking with Permeabilization buffer and 3% BSA, cells were incubated with 1:250 diluted rabbit anti-Foxo1 (C29H4, Cell Signaling) and rat anti-Foxp3 (FJK-16 s, eBioscience), followed by allophycocyanin (APC)-anti-rabbit and fluorescein isothiocyanate (FITC)-anti-rat secondary antibodies in Permeabilization buffer and 1% BSA. Slides were mounted with gold anti-fading mounting buffer (Invitrogen). Images were acquired with a Leica TCS SP5-II confocal microscope. For quantitative analysis, five fields were selected randomly and total cells in the field were manually counted and grouped with Volocity software (PerkinElmer Inc.), on the basis of their Foxo1 nuclear or cytosolic localization and Foxp3 expression.

Flow cytometry. Fluorescent-dye-labelled antibodies against cell-surface markers CD4, CD8, TCR-β, CD44, CD62L, CTLA4 and CD25 were purchased from eBiosciences. Thymic, splenic and lymph node cells were depleted of erythrocytes by hypotonic lysis. Cells were incubated with specific antibodies for 30 min on ice in the presence of 2.4G2 monoclonal antibody to block FcγR binding. All samples were acquired and analysed with an LSR II flow cytometer (Becton, Dickinson) and FlowJo software (TreeStar). Intracellular Foxp3, CTLA4 and Ki67 stainings were carried out with kits from eBiosciences. To determine cytokine expression, splenic and lymph node T cells were stimulated with 50 ng ml⁻¹ phorbol

12-myristate 13-acetate (Sigma), 1 μM ionomycin (Sigma) and GolgiStop (BD Biosciences) for 4 h. After stimulation, cells were stained with cell-surface marker antibodies, fixed and permeabilized, and stained with anti-Foxp3 in combination with specific antibodies against IFN-γ and IL-2 (eBiosciences).

ELISA. T_{reg} cells were purified from wild-type and *Foxp3*^{Cre} *Foxo1*^{fl/fl} mice by FACS and stimulated with CD3 and CD28 antibodies in the presence of IL-2 for 24 h. Cytokine amounts in tissue-culture supernatants were assayed with ELISA antibody pair for IFN-γ (eBioscience, 88-8312) in accordance with the manufacturer's recommendations.

In vitro T-cell differentiation. CreER-mediated deletion of floxed *Foxo1* alleles was induced by intraperitoneal injection of 2 mg of tamoxifen (Sigma) emulsified in 200 μl of corn oil (Sigma) every day for 5 days. CD4⁺Foxp3⁺ T_{reg} cells or CD44^{lo}CD4⁺Foxp3⁻ conventional T cells from CD45.1⁺ wild-type and CD45.2⁺ tamoxifen-treated *creER* *Foxo1*^{fl/fl} (*Foxo1*^{-/-}) mice were isolated by FACS and were co-cultured at 1:1 ratio with irradiated splenocytes, anti-CD3 (1 μg ml⁻¹), anti-CD28 (2 μg ml⁻¹) and IL-2 (200 U ml⁻¹) in the presence or absence of IL-12 (5 ng ml⁻¹) and IFN-γ (10 ng ml⁻¹) for 3 days.

In vitro T_{reg} cell suppression. CD44^{lo}CD4⁺Foxp3⁻ conventional T cells labelled with CFSE were used as responder cells. Responder T cells (5 × 10⁴) were cultured for 72 h with irradiated splenocytes (1 × 10⁵) and anti-CD3 (2 μg ml⁻¹) in the presence or absence of various numbers of T_{reg} cells. The division of responder T cells was assessed by dilution of CFSE.

Transfer model of colitis. Naive T cells sorted by FACS (CD4⁺CD44^{lo}CD62L^{hi}, 4 × 10⁵) from CD45.1⁺ C57BL/6 mice were transferred into *Rag1*^{-/-} mice alone or in combination with CD45.2⁺ T_{reg} cells (CD4⁺Foxp3⁺, 2 × 10⁵). After T-cell reconstitution, mice were weighed weekly and monitored for signs of disease. Mice were killed at 4 weeks after T-cell transfer and their colons were used for histopathological analysis. The following grades were used to evaluate their disease severity: 0, normal colonic crypt architecture; 1, mild inflammation: slight epithelial cell hyperplasia and increased numbers of leukocytes in the mucosa; 2, moderate colitis: pronounced epithelial hyperplasia, significant leukocyte infiltration, and decreased numbers of goblet cells; 3, severe colitis: marked epithelial hyperplasia with extensive leukocyte infiltration, significant depletion of goblet cells, occasional ulceration, or cryptic abscesses; 4, very severe colitis: marked epithelial hyperplasia with extensive transmural leukocyte infiltration, severe depletion of goblet cells, many crypt abscesses and severe ulceration.

Histopathology. Tissues from killed animals were fixed in Safefix II (Protocol) and embedded in paraffin. 5-μm sections were stained with haematoxylin and eosin.

ChIP-seq. T_{reg} cells were fixed for 10 min at 25 °C with 10% formaldehyde. After incubation, glycine was added to a final concentration of 0.125 M to 'quench' the formaldehyde. Cells were pelleted, washed twice with ice-cold PBS and lysed. The lysates were pelleted, re-suspended and sonicated to reduce DNA length to 300–500 base pairs (bp). The chromatin prepared from T_{reg} cells of C57BL/6 mice was incubated with protein-A-anti-Foxo1 (ab39670, Abcam) or an isotype control antibody overnight. The chromatin prepared from T_{reg} cells of *Foxo1*^{tag/tag} *birA* *Foxp3*-IRES-RFP or control *birA* mice was incubated with streptavidin overnight. The immune complexes were washed, and eluted in 500 μl of elution buffer containing 50 mM Tris, 10 mM EDTA and 1.0% SDS. Precipitated ChIP DNA and input DNA were incubated at 65 °C to reverse the crosslinking. After digestion with RNase and proteinase K, the ChIP and input DNA were purified with phenol/chloroform extraction and ethanol precipitation. The purified DNA was repaired, ligated with an adaptor, and amplified by PCR for 15–20 cycles. The amplified DNA was purified by gel extraction and used for sequencing. SR-36 sequencing was done at the Genome Center of Cold Spring Harbor Laboratory.

Visualizing read densities and identifying binding sites. Uniquely mapped sequencing reads (36 bp) were aligned to the mouse genome (July 2007, NCBI37/mm9) using the Bowtie³³ short-read alignment software (version 0.12.7). Candidate binding sites were predicted using the MACS³⁴ peak detection software (version 1.4.1). In brief, MACS determines regions of enrichment by building sequencing-density profiles for sense and antisense reads, with respect to the reference, and pairing them such that the average distance between pairings can be used to model the approximate library fragment length (*d*). Reads from both strands were then repositioned by shifting a distance half the estimated fragment length, ½*d*, downstream to capture the most likely binding location at the fragment midpoint rather than skewing to the 5' or 3' ends. Enrichment was then determined by scanning the shifted, genome-wide read profile with a window twice the size of the estimated fragment length, where the number of shifted reads falling within this 2 × *d* window was assumed to follow a Poisson distribution, with a mean parameter determined from the local background in the input sample. The empirical false-discovery rate (eFDR) was fine-tuned using the noise ratio to maximize the effectiveness of the peak-calling strategy. The noise

ratio was defined as the number control IgG peaks overlapping control BirA peaks (control overlaps) divided by the number of Foxo1 antibody peaks overlapping Foxo1 biotin peaks (ChIP overlaps). A noise ratio threshold of 0.005 was chosen as it corresponded to a large reduction in noise. To achieve this ratio, peak-calling was performed at an eFDR of 0.01. As defined in ref. 34, false background peaks were enumerated as the number of peaks called when swapping the input and ChIP sample. The eFDR was then calculated as the number of peaks detected divided by the number of background peaks detected. We, thus, determined a suitable threshold of $P < 2.5 \times 10^{-9}$ and $P < 5.0 \times 10^{-6}$, yielding 19,904 and 61,180 significantly enriched loci for antibody- and biotin-based ChIP-seq of Foxo1, respectively. To visualize read-density profiles, we aggregated counts at each genomic position for uniquely mapped reads that were extended to the estimate d . Counts were then smoothed with a moving average within a 200-bp sliding window across the genome. Smoothed average counts were visualized near to genes of interest using the R software package (<http://www.R-project.org>).

Associating peaks with gene features. To further refine our enriched loci, we corroborated peaks detected in antibody-based ChIP-seq with those from our biotinylated-Foxo1 tag-based method. To accomplish this, we distinguished high-confidence peaks by selecting for all 'antibody' peaks overlapped by one or more 'biotin' peaks and extending the 3' and 5' most coordinates to encompass all overlaps, so as to reduce any redundancies. The merged coordinates yielded 3,431 high-confidence, unique, merged regions, which we deemed putative Foxo1 binding sites. To associate peaks with functional regions at high precision and resolution, we intersected antibody peak summits (position of highest read density within a candidate peak region) falling within high-confidence corroborated regions with the set of genomic features (for example, 5' UTR, 3' UTR, exons, introns, 5-kilobase promoter, intergenic space) obtained from the UCSC Table Browser³⁵ (<http://genome.ucsc.edu/>). We also compared our regions with conserved phastCons scores and elements (Euarchontoglires subset)³⁶. Over-representation of these features was estimated empirically by generating 1,000 background sets each containing 3,431 random peaks, maintaining the same distribution of chromosomes and widths as our high-confidence set. Peaks from each background set were assigned to appropriate functional categories. The significance of the observed number of each annotation from our high-confidence summits was then inferred using a Z-test with respect to these randomly generated background counts.

DNA motif analysis. We first extracted nucleotide sequences ± 250 bp flanking all antibody-based ChIP-seq summits associated with peaks corroborated by biotinylated-Foxo1 tag-based ChIP-seq enrichment. These DNA sequences were screened for over-representation of known consensus motifs, using both the JASPAR³⁷ and TRANSFAC³⁸ databases, and the most enriched known motifs were noted. To examine to what extent the consensus Foxo1 TRANSFAC motifs, M00473 and M00474 were enriched, we ranked our putative binding site candidates by P value and assessed the cumulative occurrence rate one peak at a time, from most to least enriched. This was done to illustrate the expectation that the cumulative motif occurrence rate approaches the number of peaks with a motif divided by the total number of peaks but would be significantly increased in more enriched subset of binding candidates. Occurrence was determined using the STORM motif analysis tool available in the CREAD software package³⁹ at a threshold of $P < 1 \times 10^{-4}$. We further substantiated the over-representation of consensus Foxo1 motifs by performing *de novo* motif prediction from the top 500 ranked candidate binding site sequences using the GADEM⁴⁰ motif-discovery algorithm, compared to shuffled sequences with similar di-nucleotide composition as background. Statistical similarity of predicted *de novo* motifs was estimated using the Tomtom⁴¹ motif comparison software available as part of the MEME software suite.

Gene-expression profiling. T_{reg} cells were isolated from the spleens and peripheral lymph nodes of *Foxp3^{cre} Foxo1^{fl/fl}*, *Foxp3^{cre} Foxo1^{AAA/+}*, *Foxp3^{cre} Foxo1^{fl/fl} Foxo1^{AAA/+}* and wild-type mice by FACS. RNA was prepared with the miRNeasy Mini Kit according to the manufacturer's instructions (Qiagen). Two rounds of RNA amplification, labelling and hybridization to M430 2.0 chips (Affymetrix) were done at the Core Facility of Memorial Sloan-Kettering Cancer Center.

Microarray data analysis. Microarray data was analysed using the R statistical software package. To reduce technical variations from array to array, chip

normalization was performed using robust multi-array analysis available via the affy BioConductor package and differential gene expression defined by 1.5-fold change with a false-discovery rate of < 0.01 was determined using the *limma* package^{42,43}. When multiple probes for a given gene were significantly differentially expressed, their log₂-fold changes were averaged.

qPCR. mRNA amounts of *Ifng*, *Il2ra*, *Ctla4* and *Actb* were determined by qPCR with the following primers: *Ifng*, 5'-gcgtcattgaatcacactg-3' and 5'-tgagctcattgaatgcttg-3'; *Il2ra*, 5'-gagactctgccccataac-3' and 5'-gccactgctacctatactcc-3'; *Ctla4*, 5'-tggaactccggaggtacaaag-3' and 5'-aaacggccttcattgatg-3'; *Actb*, 5'-ttgtgacaggatgcagaag-3' and 5'-acatctgctggaaggtggac-3'. The mRNA amounts were normalized to those of *Actb*. Chromatin amounts of the Foxo1 binding site in the *Ifng* locus were determined by qPCR with the following primers: 5'-gacctg-cactctgtgagca-3' and 5'-tctctctctgtggatacc-3'.

Heat-map. To effectively visualize Foxo1-dependent gene expression, we gated relative expression values on wild-type versus *Foxp3^{cre} Foxo1^{AAA/+}* values; that is, the log₂-fold change between wild-type versus *Foxp3^{cre} Foxo1^{AAA/+}* was used to define a wild-type value equal to $\frac{1}{2}$ log₂-fold-change and a *Foxp3^{cre} Foxo1^{AAA/+}* value equal to $\frac{1}{2}$ log₂-fold change. The remaining *Foxp3^{cre} Foxo1^{fl/fl}* and *Foxp3^{cre} Foxo1^{fl/fl}/Foxp3^{cre} Foxo1^{AAA/+}* fold-change values were then similarly normalized with respect to this new wild-type value. We focused on the range of genes within ± 2 log₂-fold change; values exceeding this range at the extremes were coloured blue or yellow. A selection of genes was depicted in which the *Foxp3^{cre} Foxo1^{fl/fl}* phenotype was partially or completely rescued by *Foxp3^{cre} Foxo1^{AAA/+}*, and putative Foxo1 binding sites, as determined by ChIP-seq experiments, resided nearby.

Gene-set enrichment analysis. Gene set and pathway analysis was performed using the FatiGO⁴⁴ tool via the Babelomics²⁵ software suite (<http://babelomics.bioinfo.cipf.es>) on Foxo1-bound target genes showing differential gene expression rescued by *Foxp3^{cre} Foxo1^{AAA/+}*. Significantly over-represented categories were defined by an adjusted P value of 0.05 or less. We highlighted a selection of Gene Ontology categories and BioCarta pathways made available on the Babelomics web-based tool in our analysis.

Statistical analysis. Student's t -test was used to calculate statistical significance for difference in a particular measurement between groups. A P value of < 0.05 was considered statistically significant.

- Wan, Y. Y. & Flavell, R. A. Identifying Foxp3-expressing suppressor T cells with a bicistronic reporter. *Proc. Natl Acad. Sci. USA* **102**, 5126–5131 (2005).
- Driegen, S. et al. A generic tool for biotinylation of tagged proteins in transgenic mice. *Transgenic Res.* **14**, 477–482 (2005).
- Langmead, B., Trapnell, C., Pop, M. & Salzberg, S. L. Ultrafast and memory-efficient alignment of short DNA sequences to the human genome. *Genome Biol.* **10**, R25 (2009).
- Zhang, Y. et al. Model-based analysis of ChIP-Seq (MACS). *Genome Biol.* **9**, R137 (2008).
- Karolchik, D. et al. The UCSC Table Browser data retrieval tool. *Nucleic Acids Res.* **32**, D493–D496 (2004).
- Siepel, A. et al. Evolutionarily conserved elements in vertebrate, insect, worm, and yeast genomes. *Genome Res.* **15**, 1034–1050 (2005).
- Portales-Casamar, E. et al. JASPAR 2010: the greatly expanded open-access database of transcription factor binding profiles. *Nucleic Acids Res.* **38**, D105–D110 (2010).
- Matys, V. et al. TRANSFAC: transcriptional regulation, from patterns to profiles. *Nucleic Acids Res.* **31**, 374–378 (2003).
- Smith, A. D., Sumazin, P., Xuan, Z. & Zhang, M. Q. DNA motifs in human and mouse proximal promoters predict tissue-specific expression. *Proc. Natl Acad. Sci. USA* **103**, 6275–6280 (2006).
- Li, L. GADEM: a genetic algorithm guided formation of spaced dyads coupled with an EM algorithm for motif discovery. *J. Comput. Biol.* **16**, 317–329 (2009).
- Gupta, S., Stamatoyannopoulos, J. A., Bailey, T. L. & Noble, W. S. Quantifying similarity between motifs. *Genome Biol.* **8**, R24 (2007).
- Irizarry, R. A. et al. Summaries of Affymetrix GeneChip probe level data. *Nucleic Acids Res.* **31**, e15 (2003).
- López-Romero, P. Pre-processing and differential expression analysis of Agilent microRNA arrays using the AgiMicroRNA Bioconductor library. *BMC Genomics* **12**, 64 (2011).
- Al-Shahrour, F., Diaz-Uriarte, R. & Dopazo, J. FatiGO: a web tool for finding significant associations of Gene Ontology terms with groups of genes. *Bioinformatics* **20**, 578–580 (2004).

DAXX envelops a histone H3.3–H4 dimer for H3.3-specific recognition

Simon J. Elsässer^{1,2*}, Hongda Huang^{3*}, Peter W. Lewis¹, Jason W. Chin², C. David Allis¹ & Dinshaw J. Patel³

Histone chaperones represent a structurally and functionally diverse family of histone-binding proteins that prevent promiscuous interactions of histones before their assembly into chromatin. DAXX is a metazoan histone chaperone specific to the evolutionarily conserved histone variant H3.3. Here we report the crystal structures of the DAXX histone-binding domain with a histone H3.3–H4 dimer, including mutants within DAXX and H3.3, together with *in vitro* and *in vivo* functional studies that elucidate the principles underlying H3.3 recognition specificity. Occupying 40% of the histone surface-accessible area, DAXX wraps around the H3.3–H4 dimer, with complex formation accompanied by structural transitions in the H3.3–H4 histone fold. DAXX uses an extended α -helical conformation to compete with major inter-histone, DNA and ASF1 interaction sites. Our structural studies identify recognition elements that read out H3.3-specific residues, and functional studies address the contributions of Gly 90 in H3.3 and Glu 225 in DAXX to chaperone-mediated H3.3 variant recognition specificity.

The biology of histone proteins encompasses their synthesis in the cytosol, nuclear import and incorporation into nucleosomes, as well as subsequent eviction from chromatin, redeposition, storage or degradation^{1,2}. Exchange of relatively minor histone variants into distinct, nonrandom genomic locations represents a long-standing mechanism for introducing variation into the chromatin polymer. One compelling example of this mechanism is provided by the mammalian histone H3 family, wherein specialized H3 proteins exist at centromeric (CENPA) and noncentromeric (H3.1, H3.2, H3.3) locations with important distinct functional consequences³. H3.3, for example, has long been correlated with ‘active’ chromatin, but recently has been found associated with other genomic loci, including telomeres^{4,5}. H3.3 enrichment at telomeres and other genomic loci is achieved by specialized chaperone assembly systems, one of which, DAXX, is highlighted in this study.

DAXX is a histone chaperone specific to the evolutionarily conserved histone replacement variant H3.3 (refs 6, 7) that has been shown to deposit H3.3 at heterochromatic loci *in vivo* in cooperation with the ATP-dependent chromatin remodeller ATRX^{4,5}. Although direct mechanistic links are missing, ATRX/DAXX-mediated heterochromatin maintenance has been implicated in telomere stability, and the suppression of pancreatic neuroendocrine tumours (panNET)^{8,9} and paediatric glioblastomas¹⁰, underscoring the importance of gaining more structural and functional insights into DAXX–H3.3 biology.

Our understanding of the mechanism of histone shuttling, hand-over between different chaperone systems, and histone transfer onto and off DNA has been hampered by the as-yet-limited number of co-structures of histone–chaperone complexes^{1,11}. Here we report on the crystal structure of the histone-binding domain (HBD) of the histone chaperone DAXX bound to H3.3–H4 dimer, wherein the DAXX HBD wraps around the H3.3–H4 dimer, as well as *in vitro* and *in vivo* functional studies to account for the specificity of DAXX for histone variant H3.3.

Structure of the DAXX–H3.3–H4 complex

On the basis of previous biochemical studies⁷, we identified the minimal HBD of DAXX (residues 178–389) that formed a biochemically stable

complex with H3.3–H4. We found that introducing a small number of rigidifying substitutions from the centromeric H3 variant CENPA^{12,13} into the H3.3 sequence enabled crystallization of this complex. Distinct crystal forms of DAXX–H3.3–H4 complexes with either five (S96A, Y99F, G102A, A111T and M120F) or seven (additional A75C and F84W) rigidifying substitutions in H3.3 (in magenta background, Fig. 1a) yielded structures refined to 1.95 Å and 2.60 Å resolution, respectively (X-ray statistics in Supplementary Table 1). The five- and seven-substituent structures of the DAXX–H3.3–H4 complexes superpose quite well (stereo view in Supplementary Fig. 1b) with a root mean squared deviation of 0.65 Å. Notably, these rigidifying substitutions do not abrogate the formation of a complex with DAXX *in vivo* (Supplementary Fig. 2a, b, d).

The DAXX HBD adopts an all α -helical fold and wraps around the H3.3–H4 dimer through formation of a 1:1:1 ternary complex, thereby burying 4,500 Å² of surface area (measured using ArealMol in CCP4 program; 40% of the histone surface) in the process (Fig. 1b). The unique variant-specific Ala 87–Ala 88–Ile 89–Gly 90 segment located on α 2 helix of H3.3 (in blue background, Fig. 1a) is positioned at the junctional core of H3.3–H4 (boxed segment in red in Fig. 1b) and is surrounded by loop and helical segments in the complex (expanded view in Fig. 1c). Helices α 1 and α 2 of DAXX form a coiled-coil (hereafter designated as ‘tower’) that packs against a hydrophobic patch of the H3.3 α N helix (Supplementary Fig. 3a, d). The tower helices of DAXX bury a contiguous 1,800 Å² surface-accessible area spanning α N, α 1 and α 2 helices and loops of H3.3 (Fig. 1b, c and Supplementary Fig. 1a). The tower helices are followed by a fully ordered 20-residue linker, threading along the DAXX α 5 helix and connecting to a helix bundle of α 3, α 4 and the base of α 5. The α 5 helix of DAXX is kinked and aligned antiparallel to the α 2 helix of H3.3 in the complex (Fig. 1b), thereby tracking another hydrophobic patch on H3.3 (Supplementary Fig. 3b, e). Finally, the α 6 helix of DAXX forms an antiparallel coiled-coil pair with the α 2 helix of H4 (Fig. 1b) and spans H4 along its amino-terminal half and the interface between H3.3 and H4 along its carboxy-terminal half (Fig. 1b and Supplementary Fig. 3c, f).

¹Laboratory of Chromatin Biology and Epigenetics, The Rockefeller University, New York, New York 10065, USA. ²MRC Laboratory of Molecular Biology, Cambridge CB2 0QH, UK. ³Structural Biology Program, Memorial Sloan-Kettering Cancer Center, New York, New York 10065, USA.

*These authors contributed equally to this work.

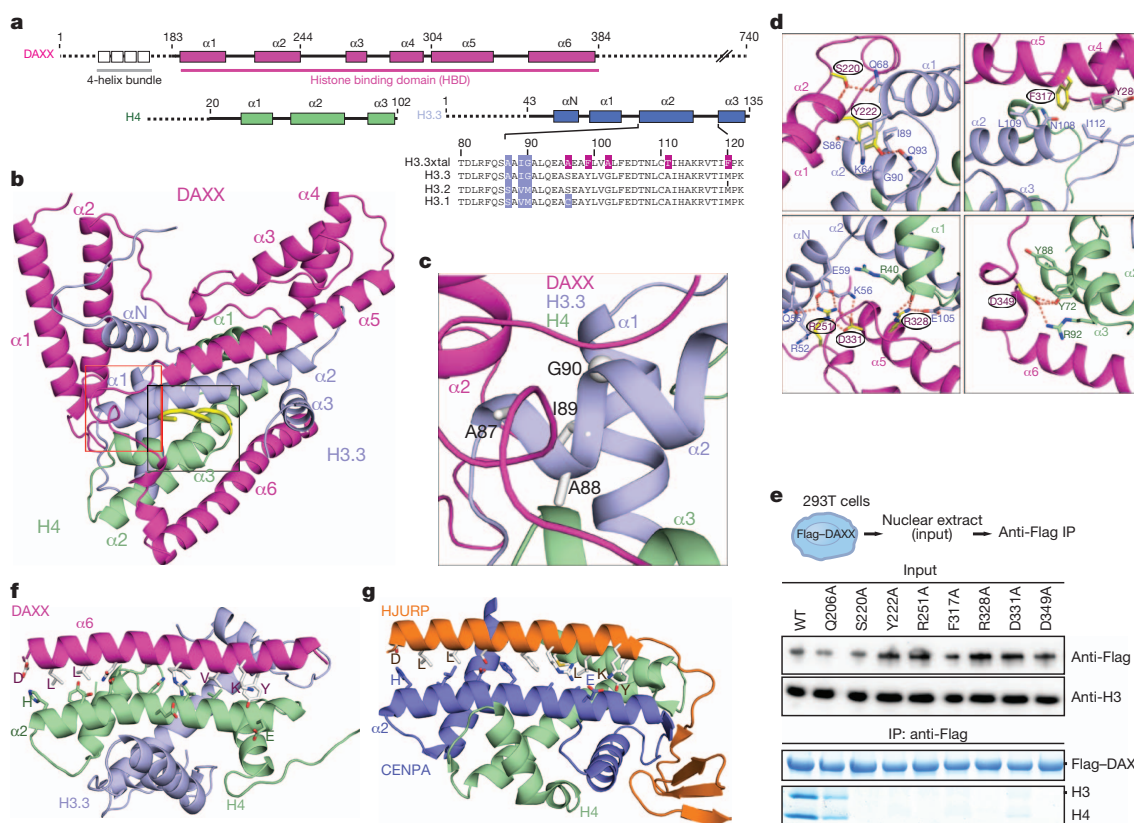


Figure 1 | Structure of the ternary complex of DAXX histone-binding domain (HBD, 178–389) bound to histones H3.3 and H4, and comparison with the ternary HJURP–CENPA–H4 complex. **a**, Schematics of domain architecture of DAXX, H3.3 and H4. **b**, A ribbon view of the crystal structure of the DAXX–H3.3–H4 ternary complex, with the segment containing the variant-specific Ala 87–Ala 88–Ile 89–Gly 90 sequence boxed in red and the C-terminal tail of H4 (in yellow) boxed in black. **c**, A blown-up view of the variant-specific segment. **d**, Close-up views of interactions made by DAXX

residues Ser 220, Tyr 222, Phe 317, Arg 251, Arg 328 and Asp 331 in the complex; see also Supplementary Fig. 5. **e**, DAXX mutants in the H3.3–H4 interface abrogate binding to endogenous histones in 293T cells. Bottom panels show immunoprecipitated DAXX and histones on the same Coomassie-stained gel. **f**, **g**, Striking similarities in coiled-coil interactions between α -helices of the chaperone (contain common interfacial DXXLXXXL(X)₁₃VIXKY segment) and histone in DAXX (**f**) and HJURP (**g**) complexes.

Highlighting the evolution of DAXX as a histone chaperone, highly conserved residues among metazoan species in the DAXX histone-binding domain cluster along the histone interface (Supplementary Fig. 4a, b). Formation of a DAXX–H3.3–H4 complex seems to require both hydrogen bonding, electrostatic and hydrophobic interactions and is sensitive to single-point Ala mutations of conserved DAXX residues Ser 220, Tyr 222, Arg 251, Phe 317, Arg 328, Asp 331 and Asp 349 (Fig. 1d and Supplementary Fig. 5), as monitored *in vivo* (Fig. 1e).

We note that there is a marked similarity between the antiparallel coiled-coil formed by the α 6 helix of DAXX (in magenta) and the α 2 helix of H4 (in green) in the DAXX–H3.3–H4 complex (Fig. 1f) with that formed by the sole helix of HJURP (in orange) and α 2 helix of CENPA (in dark blue) in the HJURP–CENPA–H4 complex^{14–16} (Fig. 1g). Remarkably, the observed coiled-coil interactions are mediated by the interfacial DXXLXXXL(X)₁₃VIXKY helical segment common to both chaperones (Fig. 1f, g and Supplementary Fig. 6a, b). Mutations of interfacial H4 residues abrogate *in vitro* binding of the isolated DAXX α 6 helix to H3.3–H4 (Supplementary Fig. 6c), revealing that the α 6 helix of DAXX has intrinsic propensity to bind H4 (Fig. 1f), and not H3, as the corresponding helix does in the HJURP complex (Fig. 1g). Although functionally distinct, we therefore conclude that DAXX and HJURP histone chaperones have evolved a common mode of contacting the histone core.

DAXX competes with histone–DNA contacts

Overlay of the DAXX HBD bound to a H3.3–H4 dimer with that of the histone dimer in the context of the nucleosome (Fig. 2a, b and

Supplementary Fig. 7a, b) suggests that the DAXX HBD competes with major histone–DNA contacts. It is readily apparent that α 1 and α 2 helices of the tower segment of DAXX in the DAXX–H3.3–H4 ternary complex would severely clash with the DNA wrapped around the H3–H4 core (Fig. 2a). Six acidic residues in the L1 loop of DAXX HBD track a basic patch on H3.3 that contacts the DNA within the nucleosome.

Furthermore, a shift in the positioning of the α N helix by three residues and an unwinding of the C terminus of the α 2 helix in the DAXX complex is apparent (Fig. 2c). The α N helix of H3.3, which forms extensive contacts with the DNA at its entry and exit sites on the nucleosome¹⁷, flips over in the DAXX complex by 180°, and is covered by α 1 and α 2 helices of DAXX in the complex (α N helix in yellow and conformational transition indicated by red arrow in Fig. 2b). The DAXX HBD–H3.3–H4 complex shows no detectable tetrasome assembly activity (Fig. 2d), indicating that other parts of DAXX probably help to mediate the unwrapping of the HBD and release of histone dimer to facilitate chromatin assembly, as previously reported for full-length DAXX *in vitro*⁷.

In the nucleosome structure, α 2 and α 3 helices of H3 from opposing H3–H4 dimers constitute the central four-helix bundle formed in the (H3–H4)₂ tetramer. At the H3–H3' interface (coloured in blue for H3 and dark blue for H3' in Fig. 2e), hydrogen bonds between His 113' of H3' and Arg 116 and Asp 123 of H3 (red box, Fig. 2e) stabilize the four-helix bundle. In the DAXX–H3.3–H4 complex, H3.3 undergoes a conformational change (Supplementary Fig. 8a), such that His 113 is retracted by 7 Å without forming new hydrogen-bonding contacts (black boxes, Fig. 2e, f), whereas Arg 116 of H3.3

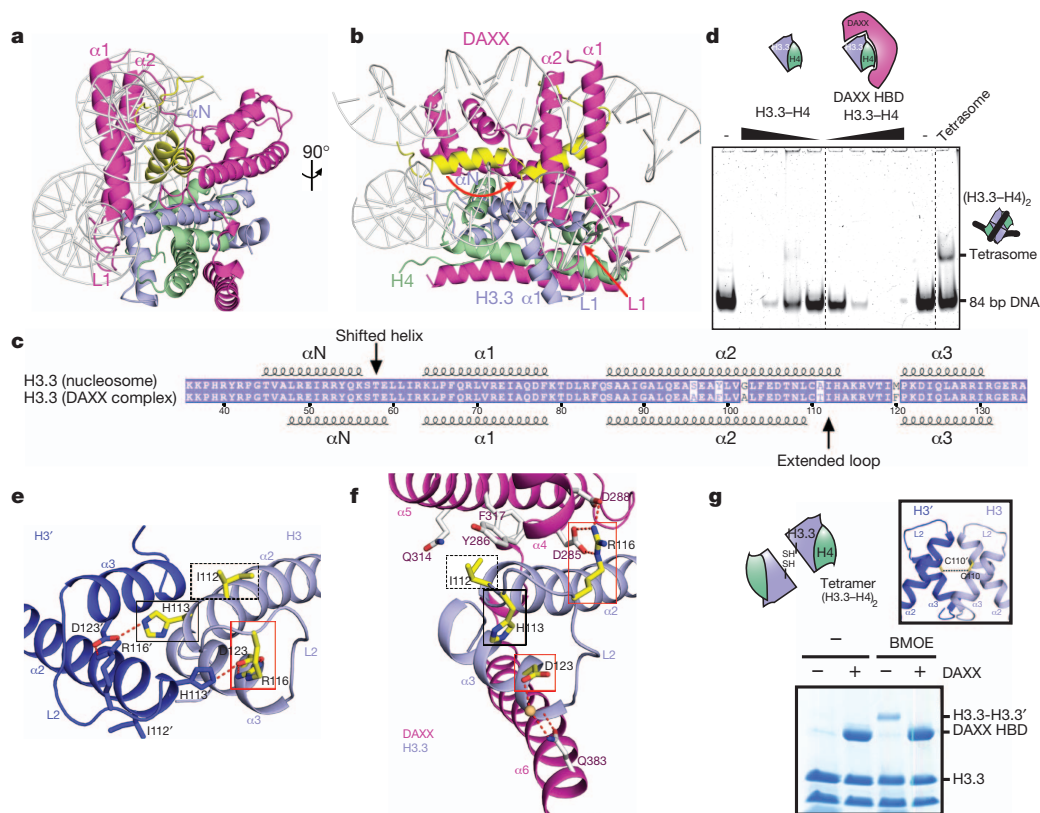


Figure 2 | DAXX competes with major DNA interactions sites and prevents histone tetramer formation through conformational changes in H3.3.

a, b, Alternative views of a model involving replacement of the histone H3–H4 tetramer (in the nucleosomal context) by the DAXX–H3.3–H4 complex. **c,** Schematic comparing α -helical alignments for H3.3 in the nucleosome with that in the DAXX–H3.3–H4 complex. **d,** Tetrasome assembly does not occur from a DAXX HBD–H3.3–H4 complex. A (H3.3–H4)₂ tetrasome can be assembled on an 84-bp DNA fragment by salt dialysis (right-most lane), but not

undergoes 5 Å movement and flips by 180°, whereby it forms a new hydrogen-bonding network with conserved Asp 285 and Asp 288 of DAXX (red box in Fig. 2f; for conserved alignment of Asp residues, see Supplementary Fig. 9). Ile 112 undergoes a small movement and packs against Tyr 286, Gln 314 and Phe 317 of DAXX in the complex (dashed-line black boxes, Fig. 2e, f; see also Supplementary Fig. 8b).

The stabilization of the novel conformation of the C-terminal α 2-helix segment of H3.3 in the DAXX complex suggests that a H3–H3' contact in the form of a four-helix bundle is no longer possible on formation of the ternary DAXX–H3.3–H4 complex. Indeed, the central H3–H3' Cys 110 residues can be crosslinked in the H3.3–H4 tetramer, but not in the presence of DAXX HBD (Fig. 2g). Thus, DAXX, on binding to H3.3–H4, prevents histone tetramer formation.

DAXX and ASF1 compete for H3.3–H4 dimer

The universal H3–H4 dimer chaperone, ASF1/CIA, binds to the H3–H3' interface through formation of an extended β -sheet alignment (Fig. 3a)^{18,19}. As apparent from a comparison of their complexes with H3–H4, both DAXX and ASF1 chaperones compete for the C-terminal α 2-helix segment of H3.3 as well as clashing with adjacent structural elements. In addition, DAXX and ASF1 sequester the C-terminal tail of H4 in distinct conformations (Figs 1b and 3a; C-terminal tail in yellow in black boxed region). In the DAXX complex, the C-terminal tail is buried in a groove formed by the α 5 helix of DAXX, α 2 helix of H3.3 and α 3 helix of H4, and is anchored through a network of hydrogen-bonding interactions (Fig. 3b). Notably, in both

from free H3.3–H4 dimers or DAXX HBD–H3.3–H4 trimers by mixing at physiological conditions. **e,** Interactions between α 2 and α 3 helices of H3 across the dimeric H3–H3' interface in the H3–H4 tetramer (Protein Data Bank accession 1AOI). **f,** Intermolecular hydrogen bonding interactions in the DAXX–H3.3–H4 complex. Side chains that undergo conformational changes on formation of the ternary complex with DAXX are highlighted in yellow and boxed in **e** and **f**. **g,** Test for H3–H3' homodimerization in H3.3–H4 and DAXX–H3.3–H4 complexes by cysteine (Cys 110) crosslinking.

DAXX and ASF1 complexes (Fig. 1b and 3a, respectively), Phe 100 of H4 is buried in a hydrophobic pocket (Supplementary Fig. 10a, b, respectively).

In accordance with these structural incompatibilities, pull-down experiments *in vitro* show that ASF1 binds free H3.3–H4, as well as H3.3–H4 from a preformed DAXX–H3.3–H4 complex, but does not pull down the intact DAXX–H3.3–H4 complex (Supplementary Fig. 11). Biochemical purification from HeLa nuclear extract indicates that ASF1 and DAXX do not exist in a common complex with histones *in vivo* (Supplementary Fig. 12a, b). We therefore wondered if direct competition between histone chaperones contributes to the partitioning of histone H3.3 into distinct histone chaperone complexes. Indeed, reduction of the protein levels of ASF1A and ASF1B by combined RNA interference (RNAi) increased the amount of DAXX that associated with H3.3 *in vivo* (Fig. 3c, left column). Similarly, a C110E mutation of H3.3 that selectively disrupts ASF1 binding increased the association with DAXX *in vivo* (Fig. 3d). Conversely, overexpression of ASF1B and, to a marginal extent, ASF1A reduced the levels of DAXX pulled down with H3.3 *in vivo* (Fig. 3c, right column). In conclusion, formation of DAXX and ASF1 complexes represents concurrent events *in vivo*.

Structural basis of H3.3 specificity

The major histone types H3.1/2 differ from variant H3.3 at no more than five positions, with three of them clustered within one short segment at the base of the α 2 helix of H3.3, namely Ala 87–Ala–Ile–Gly 90 in H3.3 replaced by Ser 87–Ala–Val–Met 90 in H3.1/2 (Fig. 4a,

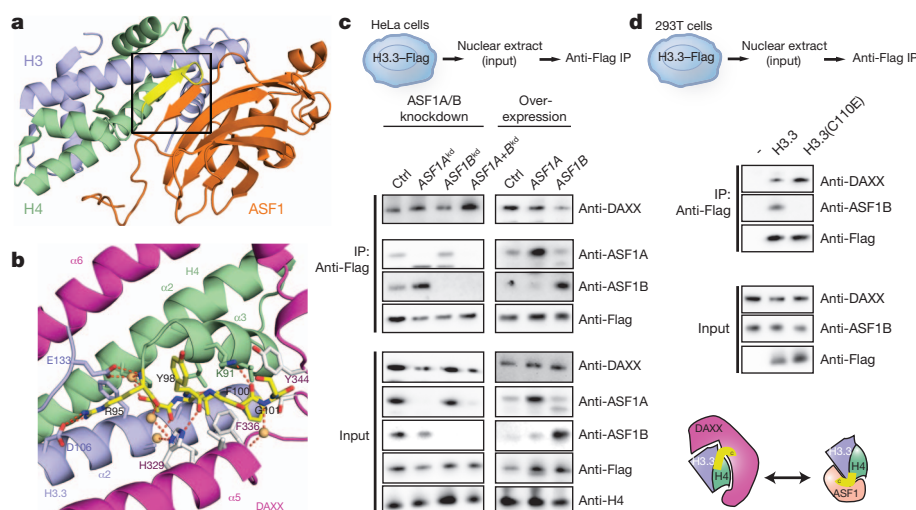


Figure 3 | DAXX uses an extended α -helical conformation to compete with ASF1 interaction sites. **a**, Structure of the ASF1-H3-H4 complex (Protein Data Bank 2HUE), with the C-terminal tail of H4 shown in yellow and boxed in black. **b**, Relocation of the flexible C terminus of H4 and its anchoring through hydrogen-bonding and hydrophobic interactions in the DAXX-H3.3-H4 complex. **c**, Co-immunoprecipitation from HeLa cells shows competition of ASF1A/ASF1B and DAXX for H3.3-H4 dimers *in vivo*. Knockdown (left

bottom). We analysed the effect of single point mutations in the N-terminal H3.3 tail (S31A) and the 'AAIG' motif (A87S, I89V and G90M) on association with DAXX *in vivo*; although A87S and I89V had little effect by themselves, G90M reduced DAXX binding by ~50% and concomitantly pulled down CAF1 subunit p150 (Fig. 4a), which normally is exclusively associated with H3.2 (ref. 20). Conversely, H3.2 was not found to pull down detectable amounts of DAXX, but the reciprocal M90G mutation in H3.2 rescued DAXX

panels) or overexpression (right panels) of ASF1A and/or ASF1B modulate ASF1A and ASF1B protein levels in nuclear extracts (bottom).

Immunoprecipitation of tagged H3.3 shows increased association with DAXX upon co-depletion of ASF1A and ASF1B and, vice versa, decreased association upon ASF1B overexpression. **d**, Co-immunoprecipitation from 293T cells with transiently transfected wild-type H3.3 and mutant incapable of binding ASF1B shows direct competition by ASF1B and DAXX.

binding to ~50% of H3.3 levels *in vivo* (Fig. 4a). Therefore, it seems that Gly 90 is a dominant contributor to chaperone specificity *in vivo*, with positions Ile 87 and Ser 89 having potentially a synergistic effect with Gly 90.

The local environment of the H3.3 AAIG segment in the DAXX HBD-H3.3-H4 complex is shown in Fig. 4b and highlights an extensive hydrogen-bonding network with inclusion of crystallographic water molecules in the vicinity of Gly 90 (Supplementary Fig. 13). Charged or polar side chains from the DAXX tower helices (Gln 206, Tyr 222, Glu 225, Lys 229), as well as residues Gly 337 and Cys 338 from the DAXX L5 linker, were found to line a solvent-filled cavity that is confined by the H3.3 α N and α 2 helices. We identify ten bound water molecules that form a total of 26 hydrogen bonds with the main and side chains of DAXX and H3.3 (Fig. 4b).

Relying again on the five stabilizing H3.3 substitutions, we solved the crystal structure of DAXX bound to H3.3(G90M)-H4 and refined it to 2.05 Å resolution (X-ray statistics in Supplementary Table 2) and compared alignment of side chains in the vicinity of the H3-variant-specific segment (Fig. 4c). The structure of the G90M-substituted H3.3 complex shows only four bound water molecules and a total of eight hydrogen bonds (Fig. 4c and Supplementary Figs 13b and 14). Importantly, the structure of the G90A-substituted H3.3 complex refined to 2.20 Å resolution (X-ray statistics in Supplementary Table 2) also shows fewer water molecules and hydrogen bonds (Supplementary Fig. 15a). Thus, it is not simply an issue of the larger Met 90 displacing the remaining solvent molecules, as essentially the same effect is observed with the smaller Ala 90 side chain. In conclusion, the integrity of the hydrogen bond network in the vicinity of position 90 seems to favour Gly (in H3.3) over Met (in H3.1/2) or Ala in its ternary complex with H4 and DAXX.

The DAXX tower provides specificity to Gly 90

To rationalize how the local perturbation by the H3 variant substitutions affects overall complex stability, we dissected the role of structural elements and individual residues lining the solvent-filled pocket surrounding the H3.3 AAIG motif. Notably, the H3.3 α N helix that packs against both H3.3 α 1 and α 2 helices and the DAXX tower helices in the DAXX-H3.3-H4 complex (Fig. 5a) is disordered in other known histone chaperone complexes^{13,17–19}, indicating that it is positioned and stabilized by hydrogen-bonding and hydrophobic

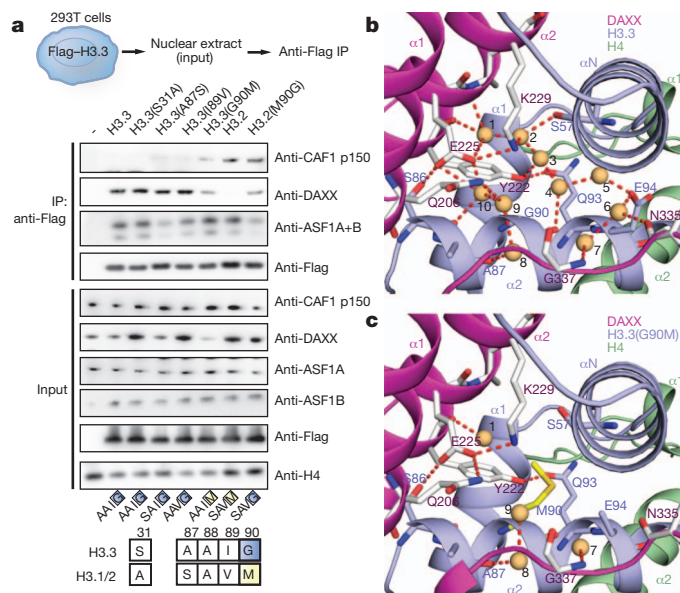


Figure 4 | A structural role for H3.3 G90 as the major determinant for H3.3 variant specificity of DAXX *in vivo*. **a**, Mutagenesis of the H3.3 AAIG motif *in vivo* reveals a dominant role of G90 in directing variant-specific histone chaperones DAXX and CAF-1. Co-immunoprecipitation (top panels) of transiently transfected H3.3 and H3.2 mutants in 293T cells. **b**, **c**, Expanded views of the specificity-determining core segment of the DAXX-H3.3-H4 complex for wild-type (panel b) and H3.3(G90M) mutant (panel c, mutant in yellow). Water molecules are shown as orange balls and labelled from 1 to 10, with hydrogen-bonding network in dashed red lines.

packing interactions with the DAXX tower (Fig. 5a). The side chains of Ser 57 and Glu 59 of the α N helix of H3.3 participate in a hydrogen bond network with Tyr 222, Glu 225, Lys 229 and Arg 251 of DAXX in the vicinity of key variant residues of H3.3 in the complex (Fig. 5a). The tower helices make important contacts with the H3.3 α N helix, as deletion of residues 1–60 of H3.3, but not 1–43, abrogates binding of the DAXX tower (residues 183–251) and full-length DAXX *in vitro* (Fig. 5b and Supplementary Fig. 16a, respectively). *In vitro* binding experiments also show that H3.3 Gln 93 and Glu 94, which appear to anchor the H3.3 α 1 and α N helices relative to the central α 2 helix (Fig. 4b), are required for tower binding (Supplementary 16b). The tower extends several polar side chains—namely Gln 206, Glu 225 and Lys 229—towards the H3.3 α 2 helix that are fully solvated in the wild-type complex (Fig. 4b) but less so in the G90M (Fig. 4c) and G90A (Supplementary Fig. 15a) mutant complexes. Replacement of these side chains with aliphatic side chains disrupts tower binding *in vitro* (Supplementary Fig. 17), corroborating the importance of hydrogen bonds and polar contacts in this region.

In vitro, the DAXX tower alone recapitulates (Fig. 5c) the *in vivo* pull-down data for H3.3 Gly 90 (Fig. 4a), indicating that it confers at least part of the H3.3 variant specificity to the entire protein. Intriguingly, tower binding to H3.2 could be rescued with a M90G mutation, but not a M90A mutation *in vitro* (Fig. 5c), suggesting that insertion of any side chain at position 90 and concomitant loss of water molecules can be discriminated by the DAXX tower.

Discrimination of G90A/M by DAXX(E225A)

In the process of systematically mutating DAXX tower residues coordinating water molecules, we found that K229A and Q206A reduced binding of the tower, whereas E225A did not (Supplementary Fig. 17). Notably, when tested against a set of H3.3 Gly 90 mutants (Fig. 5d and Supplementary Fig. 18), the E225A DAXX tower tolerated various side chains at position 90. Importantly, H3.2 with a single M90G substitution was bound by wild-type, E225A and Y222F DAXX tower (Fig. 5d). The more stringent H3.2 M90A mutant was only bound by the E225A mutant, but not by the K229A and Y222F mutants

(Fig. 5d). This unique gain-of-function effect of the E225A mutant suggested a special role for E225A in discriminating side-chain insertions at H3.3 position 90. In the wild-type crystals of the ternary complex, residue Glu 225 of the DAXX tower positions a water molecule (number 10) close to Gly 90 (3.4 Å and 3.5 Å to the backbone C α and N atoms, respectively) (Fig. 4b), which is evicted in the structures of the ternary complexes of G90M (Fig. 4c) and G90A (Supplementary Fig. 15a) mutants, providing evidence that the coordinated water contributes to the discrimination of the side chain insertions at H3.3 position 90 by DAXX Glu 225.

From our *in vitro* studies on the DAXX tower, we proposed that an E225A mutation would also alleviate the constraints of full-length DAXX for H3.3 Gly 90 *in vivo*. Indeed, when co-expressed with H3.3 or H3.2 *in vivo*, the DAXX(E225A) mutant associated with both, although more weakly with H3.2, whereas wild-type DAXX binding was markedly reduced for H3.2 (Fig. 5e). Therefore, removal of the Glu 225 side chain of DAXX induced a gain-of-function effect on binding H3.2 *in vivo*.

To follow up on this hypothesis, we have also solved structures of five-substituent complexes containing the DAXX(E225A) mutant and the dual DAXX(E225A)–H3.3(G90A) mutants refined to 1.95 and 2.20 Å resolution, respectively (Fig. 5f and Supplementary Fig. 15b, respectively; X-ray statistics in Supplementary Table 2). In the E225A mutant structure, the hydration network is minimally perturbed, with a new water, number 11, occupying the same position as that of the Glu 225 carboxylate group (Fig. 5f and Supplementary Fig. 13c, compare with Fig. 4b). Similarly, the hydration network is retained in the structure of the dual E225A/G90A mutant (Supplementary Fig. 15b) relative to the E225A mutant (Fig. 5f). These observations highlight the contribution of water-mediated interactions in molecular recognition and discrimination²¹ of histone variants by the H3.3–H4 chaperone DAXX.

The implications of the structure–function studies reported here promise to be far-reaching in understanding how variation in histone sequence allows functional diversification of histone deposition pathways in maintaining specialized chromatin structure at a wide range of genomic loci, including telomeres.

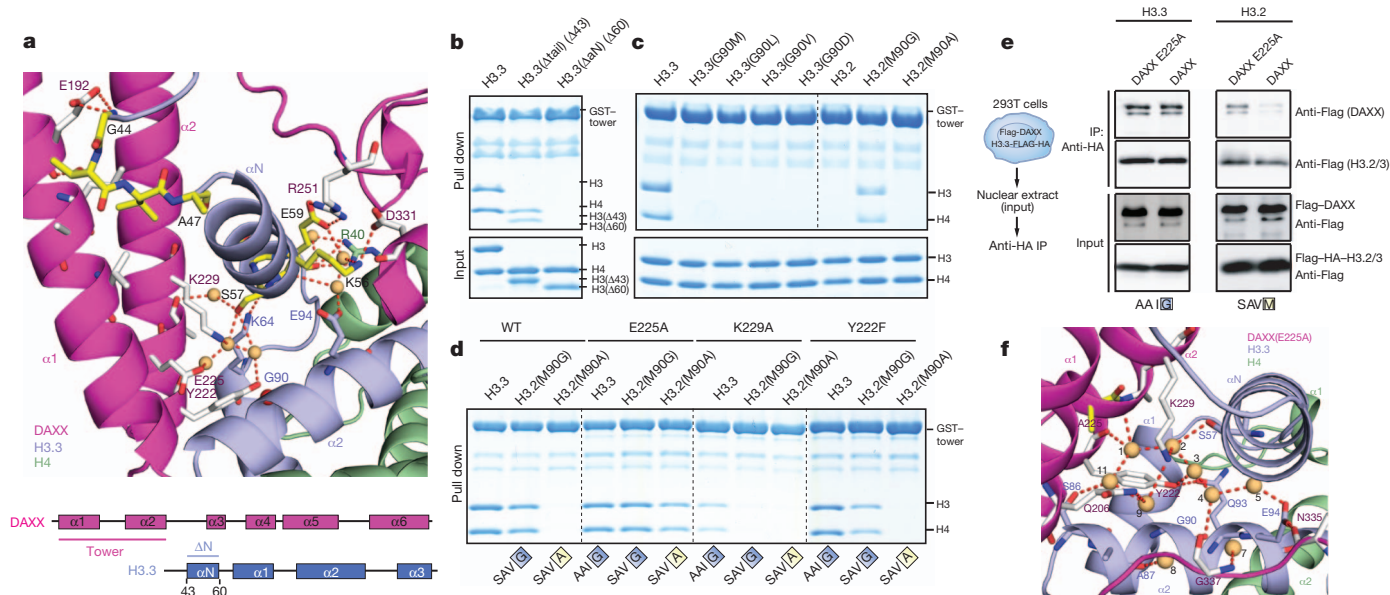


Figure 5 | The DAXX tower provides H3.3 G90 specificity through direct and water-mediated contacts with H3.3 α N, α 1 and α 2 helices. **a**, Hydrogen-bonding interactions at either end of the shifted α N helix of H3.3 in the DAXX–H3.3–H4 complex. **b**, *In vitro* pull-down experiment with the DAXX tower helices (α 1 and α 2) and H3.3 tail deletion showing the importance of its α N helix. **c**, *In vitro* pull down with immobilized DAXX tower and mutants of H3.3 Gly 90 or H3.2 Met 90. **d**, *In vitro* pull down with mutant DAXX tower showing the role

of DAXX E225 in discriminating H3.3 G90. **e**, *In vivo* transient transfection and pull down of combinations of DAXX and histone H3.3 mutants. DAXX(E225A) allows binding of H3.2 *in vivo*. Transient expression (bottom panels) and co-immunoprecipitation (top panels) of DAXX mutants and H3.3 or H3.2. E225A confers on DAXX the propensity to bind H3.2 next to H3.3 (top panel). **f**, Expanded view of the specificity-determining core segment of the DAXX–H3.3–H4 complex containing a DAXX E225A mutant (in yellow).

METHODS SUMMARY

DAXX HBD–H3.3–H4 complexes for crystallization were co-expressed and purified natively or mixed and refolded *in vitro*. The crystals grew in 1.8 M Na/K-phosphate, pH 6.8 or 7.0 at 4 °C with or without micro-seeding and took 1–2 months to grow to suitable size for data collection. The initial model was solved by molecular replacement (MR) program BALBES and subsequent structures were solved by MR in PHASER. All the refinements were done using Coot, Refmac5 and PHENIX.

In vitro experiments were carried out with recombinant proteins expressed in *Escherichia coli* (or insect cells for full-length DAXX). Histones, including all mutants, were purified under denaturing conditions, refolded by dialysis and purified over a Superdex 200 column. Pull downs were carried out with immobilized GST-tagged DAXX fragments and analysed by SDS-PAGE (polyacrylamide gel electrophoresis) and Coomassie staining.

For co-immunoprecipitation experiments, HeLa or 293T cells were transiently transfected. Immunoprecipitations were performed from nuclear extracts with magnetic affinity resin. Elutions were analysed on SDS-PAGE by Coomassie stain or western blotting.

Full Methods and any associated references are available in the online version of the paper.

Received 13 March; accepted 27 September 2012.

Published online 17 October 2012.

- Hondele, M. & Ladurner, A. G. The chaperon-histone partnership: for the greater good of histone traffic and chromatin plasticity. *Curr. Opin. Struct. Biol.* **21**, 698–708 (2011).
- Das, C., Tyler, J. K. & Churchill, M. A. The histone shuffle: histone chaperones in an energetic dance. *Trends Biochem. Sci.* **35**, 476–489 (2010).
- Hamiche, A. & Shuaib, M. Chaperoning the histone H3 family. *Biochim. Biophys. Acta* **1819**, 230–237 (2012).
- Goldberg, A. D. *et al.* Distinct factors control histone variant H3.3 localization at specific genomic regions. *Cell* **140**, 678–691 (2010).
- Wong, L. H. *et al.* ATRX interacts with H3.3 in maintaining telomere structural integrity in pluripotent embryonic stem cells. *Genome Res.* **20**, 351–360 (2010).
- Drane, P. *et al.* The death-associated protein DAXX is a novel histone chaperone involved in the replication-independent deposition of H3.3. *Genes Dev.* **24**, 1253–1265 (2010).
- Lewis, P. W. *et al.* Daxx is an H3.3-specific histone chaperone and cooperates with ATRX in replication-independent chromatin assembly at telomeres. *Proc. Natl Acad. Sci. USA* **107**, 14075–14080 (2010).
- Jiao, Y. *et al.* DAXX/ATRX, MEN1 and mTOR pathway genes are frequently altered in pancreatic neuroendocrine tumors. *Science* **331**, 1199–1223 (2011).
- Heaphy, C. M. *et al.* Altered telomeres in tumors with ATRX and DAXX mutations. *Science* **333**, 425 (2011).
- Schwartzentruber, J. *et al.* Driver mutations in histone H3.3 and chromatin remodeling genes in pediatric glioblastoma. *Nature* **482**, 226–231 (2012).
- Elsässer, S. J. & D'Arcy, S. Towards a mechanism for histone chaperones. *Biochim. Biophys. Acta* **1819**, 211–221 (2012).
- Black, B. E. *et al.* Structural determinants for generating centromeric chromatin. *Nature* **430**, 578–582 (2004).
- Sekulic, N., Bassett, E. A., Rodgers, D. J. & Black, B. E. The structure of (CENP-A-H4)₂ reveals physical features that mark centromeres. *Nature* **467**, 347–351 (2010).
- Hu, H. *et al.* Structure of CENP-A-histone H4 heterodimer in complex with chaperone HJURP. *Genes Dev.* **25**, 901–906 (2011).
- Cho, U.-S. & Harrison, S. C. Recognition of the centromere-specific histone Cse4 by the chaperone Scm3. *Proc. Natl Acad. Sci. USA* **108**, 9367–9371 (2011).
- Zhou, Z. *et al.* Structural basis for recognition of centromere histone variant CenH3 by the chaperone Scm3. *Nature* **472**, 234–237 (2011).
- Luger, K. *et al.* Crystal structure of the nucleosome core particle at 2.8 Å resolution. *Nature* **389**, 251–260 (1997).
- Natsume, R. *et al.* Structure and function of the histone chaperone CIA/ASF1 complexed with histones H3 and H4. *Nature* **446**, 338–341 (2007).
- English, C. M. *et al.* Structural basis for the histone chaperone activity of Asf1. *Cell* **127**, 495–508 (2006).
- Tagami, H., Ray-Gallet, D., Almouzni, G. & Nakatani, Y. Histone H3.1 and H3.3 complexes mediate nucleosome assembly pathways dependent or independent of DNA synthesis. *Cell* **116**, 51–61 (2004).
- Levy, Y. & Onuchic, J. N. Water mediation in protein folding and molecular recognition. *Annu. Rev. Biophys. Biomol. Struct.* **35**, 389–415 (2006).

Supplementary Information is available in the online version of the paper.

Acknowledgements We thank the personnel of synchrotron beam lines 24-ID-C/E at the Advanced Photon Source (Argonne National Laboratory) and beam line X29 at the Brookhaven National Laboratory for their assistance, and the Center for Synchrotron Biosciences grant, P30-EB-009998, from the National Institute of Biomedical Imaging and Bioengineering (NIBIB) for funding. The use of the Rigaku/MSC microMax 007HF and Formulatrix in the Rockefeller University Structural Biology Resource Center was made possible by grant numbers 1S10RR022321-01 and 1S10RR027037-01 from the National Center for Research Resources of the NIH. We thank B. Black for sharing data before publication, A. Ruthenburg, J. Song and Z. Cheng for advice and discussions, and E. Datan for help in expressing DAXX protein. D.J.P. was supported by funds from the Abby Rockefeller Mauze Trust, and the Maloris and STARR Foundations. C.D.A. also acknowledges support from the STARR Foundation and The Rockefeller University. J.W.C. acknowledges support from UK Medical Research Council (MRC) (grants U105181009 and UD99999908). S.J.E. was supported by a Boehringer Ingelheim Funds fellowship and the David Rockefeller Graduate Program and holds an EMBO ALTF 1232-2011.

Author Contributions S.J.E. conceived and led the use of rigidifying mutants to crystallize the complex. Crystals of the seven- and five-substituent complexes were grown by S.J.E. and H.H., respectively. H.H. solved all the crystal structures of the complexes, including mutant complexes, under the supervision of D.J.P. S.J.E. performed biochemical and most cell-based experiments under the supervision of C.D.A. and J.W.C. P.W.L. carried out cell-based experiments and contributed reagents. All authors discussed the results and commented on the manuscript during its preparation.

Author Information Atomic structures of the DAXX–H3.3–H4 complex have been deposited in the RCSB Protein Data Bank with accession codes 4H9N (five-substituent native complex at 1.95 Å), 4H9S (seven-substituent native complex at 2.60 Å), 4H9O (five-substituent H3.3(G90M) mutant complex at 2.05 Å), 4H9P (five-substituent H3.3(G90A) mutant complex at 2.20 Å), 4H9Q (five-substituent DAXX(E225A) mutant complex at 1.95 Å) and 4H9R (five-substituent DAXX(E225A)–H3.3(G90A) mutant complex at 2.20 Å). Supplementary Video 1 shows the ternary five-substituent native complex of DAXX–H3.3–H4. Reprints and permissions information is available at www.nature.com/reprints. The authors declare no competing financial interests. Readers are welcome to comment on the online version of the paper. Correspondence and requests for materials should be addressed to C.D.A. (alliscd@mail.rockefeller.edu) or D.J.P. (pated@mskcc.org).

METHODS

Protein expression and purification. For preparation of histone H3.3–H4 tetramers and DAXX HBD–H3.3–H4 complexes *in vitro*, human DAXX fragment 183–398 or 183–417, human histone H3.3 and codon-optimized H4 (gift from S. Yokoyama) was cloned into pRUTH5 to yield an N-terminal His₆-TEV tag (courtesy of A. Ruthenburg). Single or multiple point mutations were introduced by standard mutagenesis PCR procedures. Histones and DAXX HBD were individually expressed in BL21 Star(DE3) cells (Invitrogen) into inclusion bodies for 4–6 h at 37 °C. Inclusion bodies were resolubilized in 6 M guanidine-HCl, 1 M NaCl, 50 mM Tris-HCl pH 8, and purified on a Ni-NTA affinity column. To prepare H3–H4 tetramers, equimolar ratios of H3 and H4 were mixed in refolding buffer (4 M guanidine, 50 mM MOPS pH 7, 1 M NaCl, 5 mM EDTA, 15% glycerol) and dialysed against 50 mM MOPS pH 7, 1 M NaCl, 1 mM EDTA, 10% glycerol.

For purification of the native DAXX HBD–H3.3–H4 complex, DAXX (178–389) was cloned into a modified RSFDuet-1 vector (Novagen), with an N-terminal His₆-SUMO tag and human histone H3.3 and H4 were cloned into pETDuet-1 vector (Novagen). Either five (S96A, Y99F, G102A, A111T and M120F) or seven (additional A75C and F84W) rigidifying substitutions in H3.3 were introduced by standard mutagenesis PCR procedure. These two plasmids were transformed into BL21 (DE3) RIL cell strain (Stratagene) for co-expression. The cells were grown in LB medium at 37 °C to an OD_{600 nm} value about 1.0 and induced with 1 mM isopropyl β-D-1-thiogalactopyranoside (IPTG) for another 4 h. The DAXX–H3.3–H4 protein complex was purified first on a Ni-NTA affinity column. After removing the SUMO tag, the resulting complex was loaded on a cation exchange HiTrap SP FF column and further purified by gel filtration with a HiLoad 16/600 Superdex 200 column (GE Healthcare). The final high-purity complex was concentrated to 50–100 mg ml^{−1} in a pH 7.5 buffer containing 20 mM Tris-HCl, 1 M NaCl and 2 mM DTT. The DAXX–H3.3(G90M)–H4, DAXX–H3.3(G90A)–H4, DAXX(E225A)–H3.3–H4 and DAXX(E225A)–H3.3(G90A)–H4 complexes were purified as described above.

Crystallization. To yield initial crystals for structure determination, DAXX HBD–H3.3–H4 was refolded *in vitro* from equimolar amounts of DAXX HBD (residues 183–398), H3 containing seven substituents (A75C, F84W, S96A, Y99F, G102A, A111T and M120F) and H4 (residues 20–100), mixed in refolding buffer, by dialysis against 50 mM MOPS pH 7, 1 M NaCl, 1 mM EDTA, 10% glycerol. After insoluble precipitate was removed by centrifugation, the complex was treated with TEV protease (1% w/w), concentrated to 20 mg ml^{−1} and purified on a 16/60 Superdex 200 size exclusion column, equilibrated and run in crystal screening buffer (10 mM MOPS pH 7, 500 mM NaCl, 0.1 mM EDTA, 0.1 mM PMSF, 1 mM TCEP). Peak fractions were pooled and concentrated to 50 mg ml^{−1} in spin concentrators (Amicon Ultra, Millipore).

The 2.6 Å diffracting crystal of the DAXX–H3.3–H4 containing seven substituents formed in sitting-drop vapour-diffusion setups with 2.5 M NaCl, 150 mM Na/K-phosphate pH 6.2, 5% glycerol after a few days at 20 °C.

For crystals of the five substituent (S96A, Y99F, G102A, A111T and M120F) H3.3 and all additional mutants, the respective DAXX–H3.3–H4 complex at a concentration of 52 mg ml^{−1} was used for sparse-matrix and grid-search screens (Hampton Research and Qiagen) and an initial condition (1.8 M Na/K-phosphate, pH 6.9) was identified. The crystals were subsequently reproduced and improved in 1.8 M Na/K-phosphate, pH 7.0 using the hanging-drop vapour-diffusion method at 4 °C. It took more than 1 month for the crystals to grow to a suitable size. The crystals of DAXX–H3.3(G90M)–H4, DAXX–H3.3(G90A)–H4, DAXX(E225A)–H3.3–H4 and DAXX(E225A)–H3.3(G90A)–H4 were microseeded with crystals from the DAXX–H3.3–H4 complex and grown in 1.8 M Na/K-phosphate, pH 6.8 or 7.0, at 4 °C. It took more than two months for the crystals to grow to suitable size for data collection. All the crystals were soaked in a cryoprotectant made from mother liquor supplemented with 20% glycerol, before flash freezing in liquid nitrogen.

Structure determination. The data sets for DAXX–H3.3–H4 were collected at 1.075 Å on beamline X29 (Brookhaven NSLS), whereas the data sets for DAXX–H3.3(G90M)–H4, DAXX–H3.3(G90A)–H4, DAXX(E225A)–H3.3–H4 and DAXX(E225A)–H3.3(G90A)–H4 were collected at 0.979 Å on 24-ID-C/E NE-CAT beamline (Advanced Photo Source, Argonne National Laboratory). All the data sets were processed by using the HKL 2000 program. The initial structure for DAXX–H3.3–H4 was solved by molecular replacement program BALBES²² with a final search model based on Protein Data Bank 2HUE and manually refined and built using Coot²³ and Refmac5²⁴ in CCP4 program suite²⁵. The final structures of the five-substituent and seven-substituent ternary complexes were refined to 1.95 Å and 2.60 Å resolution respectively using PHENIX²⁶. Supplementary Table 1 summarizes the statistics for data collection and structural refinement. The structure of

DAXX–H3.3(G90M)–H4, DAXX–H3.3(G90A)–H4, DAXX(E225A)–H3.3–H4 and DAXX(E225A)–H3.3(G90A)–H4 were solved by molecular replacement in PHASER²⁷ using the structure of DAXX–H3.3–H4 as a search model. Supplementary Table 2 summarizes the statistics for data collection and structural refinement for the mutant ternary complexes.

Mononucleosome assembly assay. Twofold dilutions of 8 pmol of H3.3–H4 or DAXX HBD–H3.3–H4 was mixed with 2 pmol 84-bp DNA (derived from the Widom 601 sequence) in 20 µl assembly buffer AB1 (10 mM HEPES pH 7.5, 40 mM KCl, 60 mM NaCl, 2 mM MgCl₂, 0.5 mM EGTA). Reaction was incubated for 3 h at room temperature and an aliquot analysed on a 6% PAGE in 0.5× TBE.

GST pull downs. Full-length ASF1A, a DAXX fragment spanning the tower helices (residues 183–251), and the α6 helix (residues 349–384) were cloned into a pET-based vector with N-terminal GST-tag (pRUTH2, courtesy of A. Ruthenburg). GST fusion proteins were expressed in Rosetta2(DE3)pLysS cells (Novagen) at 25 °C for 6 h, purified using BugBuster protein extraction reagent (Novagen) and magnetic glutathione resin (Pierce). Pull downs were carried out on 2 µl of magnetic bead slurry saturated with GST-fusion proteins and washed in binding buffer (20 mM phosphate buffer pH 7.4, 1 M NaCl, 10% glycerol, 0.01% Triton X-100, 0.01% CHAPS, 1 mM DTT). Wild-type histone H3.3–H4 and H3.2–H4 tetramers, as well as all mutants, were prepared and purified as described above. 20 µg (at least tenfold excess) of H3–H4 tetramers in 500 µl binding buffer was added to the immobilized DAXX fusion proteins and incubated for 10 min. Beads were separated from solution and washed quickly with three times 1 ml of binding buffer before eluting in 20 µl of binding buffer supplemented with 25 mM fresh glutathione.

Cysteine chemical crosslinking. Bismaleimidoethane (BMOE, Pierce 22323) was dissolved at 20 mM concentration in DMSO. In each reaction, 10 µM H3.3–H4 dimers or DAXX HBD–H3.3–H4 trimeric complex were present in 100 µl reaction volume. The reaction buffer was 20 mM MOPS pH 7, 150 mM NaCl, 1 mM EDTA, 0.5 mM TCEP. BMOE was rapidly added from stock solution to 50 µM concentration. Reactions were incubated for 30 min at room temperature, and stopped by adding 6× laemmli sample buffer including 1% DTT, boiled and run on a SDS-PAGE.

Transient transfection of 293T and HeLa cells and co-immunoprecipitation. Human histone H3.3 and mutants, as well as ASF1A and ASF1B, were cloned into a pCDH vector. Full-length human DAXX was cloned into pRK5 with an N-terminal Flag epitope tag. For transfection, 293T cells were seeded in 6-well plates at 2 × 10⁵ cells per well in DMEM supplemented with 10% FBS, 1× penicillin/streptomycin. After 12–24 h, cells were transfected with 2.5 µg plasmid with Transit LT1 reagent (Mirus) according to the manufacturers manual. Cell were collected after 48 h by scraping and titration in warm DMEM medium and pelleted. Cell pellet was washed with PBS and subsequently with hypotonic buffer (15 mM HEPES pH 7.5, 30 mM KCl, 5 mM MgCl₂). For lysis, cell pellet was re-suspended in 250 µl hypotonic buffer supplemented with 0.02% Nonidet P-40, 0.8 mM PMSF, 1× EDTA-free Protease Inhibitor Cocktail (Roche), 10 µg ml^{−1} RNase I. Lysis was allowed to proceed for 15 min with rotation at 4 °C. 22 µl 5 M NaCl was added (final 400 mM NaCl) under agitation to extract nuclear proteins. Extract was rotated for 15 min at 4 °C and spun 30 min at 4 °C at 20,000g. Supernatant was incubated with 25 µl anti-Flag Affinity gel (Sigma-Aldrich) for 4 h at 4 °C. Beads were washed 2× 5 min with hypotonic buffer plus 400 mM NaCl. Bound proteins were eluted with 1× laemmli SDS sample buffer (63 mM Tris-HCl pH 6.8, 10% glycerol, 2% SDS). DTT was added to eluate to 1% before boiling and running on an SDS PAGE.

RNAi. HeLa cells stably expressing Flag-HA-tagged H3.3 and H3.1 were a gift from G. Almouzni²⁰ siRNAs against ASF1A/B were ordered from Dharmacon, from published sequences (ASF1A, 5′-AAGUGAAGAAUACGAUCAAGU(dTdT)-3′, ASF1B, 5′-AACAACGAGUACCUCAACCCU(dTdT)-3′, (refs 28, 29). HeLa cells were transfected in 6-well plates with Oligofectamin (Invitrogen) according to the manufacturer's protocol and collected after 72 h as described for transient transfections above.

Co-transfection of DAXX and histone mutants. Wild-type pRK5-Flag-hDAXX or hDAXX point mutants were transiently transfected into 293T cells for 48 h (30 µg DNA per 2.0 × 10⁷ cells). Cells were collected and lysed (20 mM HEPES, pH 7.9, 1 mM EDTA, 0.1% Triton X-100, 500 mM KCl, 2 mM 2-mercaptoethanol, 0.8 mM PMSF, 2× Protease inhibitor cocktail (Roche)) before Flag-M2 immunoprecipitation. Immunoprecipitated material was washed extensively (6× 1 ml of 20 mM HEPES, pH 7.9, 1 mM EDTA, 0.1% Triton X-100, 1 M KCl, 2 mM 2-mercaptoethanol, 0.4 mM PMSF) before elution (70 mM glycine, pH 2.5, 150 mM NaCl). pRK5-Flag-hDAXX(E225A) (8 µg DNA per 2.0 × 10⁷ cells) and pCDH-HA–H3.3 or pCDH-HA–H3.2 (2 µg

DNA per 2.0×10^7) were co-transfected into 293T cells for DAXX–H3,3–H4 co-immunoprecipitations.

22. Long, F., Vagin, A. A., Young, P. & Murshudov, G. N. BALBES: a molecular replacement pipeline. *Acta Crystallogr. D* **64**, 125–132 (2008).
23. Emsley, P. & Cowtan, K. Coot: model-building tools for molecular graphics. *Acta Crystallogr. D* **60**, 2126–2132 (2004).
24. Murshudov, G. N., Vagin, A. A. & Dodson, E. J. Refinement of macromolecular structures by the maximum-likelihood method. *Acta Crystallogr. D* **53**, 240–255 (1997).
25. Collaborative Computational Project. The CCP4 suite: programs for protein crystallography. *Acta Crystallogr. D* **50**, 760–763 (1994).
26. Adams, P. D. *et al.* PHENIX: building new software for automated crystallographic structure determination. *Acta Crystallogr. D* **58**, 1948–1954 (2002).
27. McCoy, A. J. *et al.* Phaser crystallographic software. *J. Appl. Crystallogr.* **40**, 658–674 (2007).
28. Groth, A. *et al.* Human Asf1 regulates the flow of S phase histones during replicational stress. *Mol. Cell* **17**, 301–311 (2005).
29. Das, C., Lucia, M. S., Hansen, K. C. & Tyler, J. K. CBP/p300-mediated acetylation of histone H3 on lysine 56. *Nature* **459**, 113–117 (2009).

Albedo and atmospheric constraints of dwarf planet Makemake from a stellar occultation

J. L. Ortiz¹, B. Sicardy^{2,3,4}, F. Braga-Ribas^{2,5}, A. Alvarez-Candal^{6,1}, E. Lellouch², R. Duffard¹, N. Pinilla-Alonso^{1,7}, V. D. Ivanov⁶, S. P. Littlefair⁸, J. I. B. Camargo⁵, M. Assafin⁹, E. Unda-Sanzana¹⁰, E. Jehin¹¹, N. Morales¹, G. Tancredi¹², R. Gil-Hutton¹³, I. de la Cueva¹⁴, J. P. Colque¹⁰, D. N. Da Silva Neto⁵, J. Manfroid¹¹, A. Thirouin¹, P. J. Gutiérrez¹, J. Lecacheux², M. Gillon¹¹, A. Maury¹⁵, F. Colas¹⁶, J. Licandro¹⁷, T. Mueller¹⁸, C. Jacques¹⁹, D. Weaver²⁰, A. Milone²¹, R. Salvo¹², S. Bruzzone¹², F. Organero²², R. Behrend²³, S. Roland¹², R. Vieira-Martins^{9,5,16}, T. Widemann², F. Roques², P. Santos-Sanz^{1,2}, D. Hestroffer¹⁶, V. S. Dhillon⁸, T. R. Marsh²⁴, C. Harlinton²⁵, A. Campo Bagatin²⁶, M. L. Alonso²⁷, M. Ortiz²⁸, C. Colazo²⁹, H. J. F. Lima³⁰, A. S. Oliveira³⁰, L. O. Kerber³¹, R. Smiljanic³², E. Pimentel¹⁹, B. Giacchini¹⁹, P. Cacella³³ & M. Emilio³⁴

Pluto and Eris are icy dwarf planets with nearly identical sizes, comparable densities and similar surface compositions as revealed by spectroscopic studies^{1,2}. Pluto possesses an atmosphere whereas Eris does not; the difference probably arises from their differing distances from the Sun, and explains their different albedos³. Makemake is another icy dwarf planet with a spectrum similar to Eris and Pluto⁴, and is currently at a distance to the Sun intermediate between the two. Although Makemake's size ($1,420 \pm 60$ km) and albedo are roughly known^{5,6}, there has been no constraint on its density and there were expectations that it could have a Pluto-like atmosphere^{4,7,8}. Here we report the results from a stellar occultation by Makemake on 2011 April 23. Our preferred solution that fits the occultation chords corresponds to a body with projected axes of $1,430 \pm 9$ km (1σ) and $1,502 \pm 45$ km, implying a V-band geometric albedo $p_V = 0.77 \pm 0.03$. This albedo is larger than that of Pluto, but smaller than that of Eris. The disappearances and reappearances of the star were abrupt, showing that Makemake has no global Pluto-like atmosphere at an upper limit of 4–12 nanobar (1σ) for the surface pressure, although a localized atmosphere is possible. A density of 1.7 ± 0.3 g cm⁻³ is inferred from the data.

Stellar occultations allow detection of very tenuous atmospheres and can provide accurate sizes and albedos^{9,10,11,3,12}, so we embarked on a programme of predicting and observing occultations by (136472) Makemake, also known as 2005 FY₉. The occultation of the faint star NOMAD 1181-0235723 (with magnitude $m_R = 18.22$, where NOMAD is the Naval Observatory Merged Astronomic Dataset) was predicted in 2010 by methods similar to those used to predict occultations by several large bodies¹³, but refined as shown in Supplementary Information section 1. We arranged a campaign involving 16 telescopes, listed in Supplementary Table 1. The occultation was successfully recorded from seven telescopes, listed in Table 1, at

five sites. From the images obtained, we made photometric measurements as a function of time (light curves).

The light curves of the occultation are shown in Fig. 1. Fitting synthetic square-well models to the light curves yielded the disappearance and reappearance times of the star (Table 1), from which we calculate one chord in the plane of the sky for each site (see Supplementary Information section 3). On the basis of analyses of the light curves, taking into account the cycle time between the images and the dispersion of the data, we deduce that there were no secondary occultations, so we can reject the existence of a satellite larger than about 200 km in diameter in the areas sampled by the chords. The result is consistent with a deep-image survey that did not find any satellites¹⁶. The chords can be fitted with two shape models (Fig. 2). Our preferred shape, which is compatible with our own and other observations (see Supplementary Information section 8), corresponds to an elliptical object with projected axes of $1,430 \pm 9$ km and $1,502 \pm 45$ km. By combining this result with visible photometry at various phase angles¹⁷, we calculated that Makemake has a V-band geometric albedo of $p_V = 0.77 \pm 0.03$ (see Supplementary Information section 4). This is considerably high compared to albedos of other trans-Neptunian objects (TNOs)⁵, and is larger than that of Pluto ($p_V = 0.52$)¹⁸ but smaller than that of Eris ($p_V = 0.96$)³.

The object is large enough to be in hydrostatic equilibrium, so it is possible to use the figures of equilibrium formalism, as done for Haumea¹⁹, to analyse the shape of a body that rotates with Makemake's period of 7.77 h (refs 20, 21). The object could only be a tri-axial Jacobi ellipsoid for densities in the range 0.66–0.86 g cm⁻³ (for example, ref. 22). Such low densities are unrealistic for a body as large as Makemake (see Supplementary Fig. 7). Thus, Makemake must be an oblate Maclaurin spheroid for plausible densities between 1.4 and 2.0 g cm⁻³ (see discussion in Supplementary Information section 8).

¹Instituto de Astrofísica de Andalucía, CSIC, Apartado 3004, 18080 Granada, Spain. ²LESIA—Observatoire de Paris, CNRS, UPMC Univ. Paris 6, Univ. Paris-Diderot, 5 Place J. Janssen, 92195 Meudon Cedex, France. ³Université Pierre et Marie Curie, 4 Place Jussieu, 75252 Paris Cedex 5, France. ⁴Institut Universitaire de France, 103 Boulevard Saint Michel, 75005 Paris, France. ⁵Observatório Nacional/MCTI, Rua General José Cristino 77, CEP20921-400 Rio de Janeiro, Brazil. ⁶European Southern Observatory, Alonso de Córdova 3107, Vitacura, Casilla 19001, Santiago 19, Chile. ⁷SETI Institute, 189 Bernardo Ave., Mountain View, California 94043, USA. ⁸Department of Physics and Astronomy, University of Sheffield, Sheffield S3 7RH, UK. ⁹Observatório do Valongo, Universidade Federal do Rio de Janeiro, Ladeira Pedro Antonio 43, CEP 20.080-090 Rio de Janeiro, Brazil. ¹⁰Unidad de Astronomía, Facultad de Ciencias Básicas, Universidad de Antofagasta, Avenida Angamos 601, Antofagasta, Chile. ¹¹Institut d'Astrophysique de l'Université de Liège, Allée du 6 Août 17, B-4000 Liège, Belgium. ¹²Observatorio Astronómico Los Molinos DICYT-MEC Cno. de los Molinos 5769, 12400 Montevideo, Uruguay. ¹³Complejo Astronómico El Leoncito (CASLEO) and San Juan National University, Avenida España 1512 sur, J5402DSP, San Juan, Argentina. ¹⁴Astroimagen, Abad y Sierra 58Bis, 07800 Ibiza, Spain. ¹⁵San Pedro de Atacama Celestial Explorations, Casilla 21, San Pedro de Atacama, Chile. ¹⁶IMCCE, Observatoire de Paris, UPMC, Univ. Lille 1, CNRS, 77 Av. Denfert-Rochereau, 75014 Paris, France. ¹⁷Instituto de Astrofísica de Canarias, Vía Láctea s/n 38250 La Laguna, Tenerife, Spain. ¹⁸Max-Planck-Institut für Extraterrestrische Physik, Giessenbachstraße, 85748 Garching, Germany. ¹⁹Observatório CEAMIG-REA, Rua Radialista João Sposito 183, Belo Horizonte, Minas Gerais, CEP31545-120, Brazil. ²⁰Observatório Astronômico Christus, Universidade de Fortaleza, Rua João Carvalho, 630, Aldeota, Fortaleza, Brazil. ²¹Instituto Nacional de Pesquisas Espaciais/MCTI, Divisão de Astrofísica, Av. dos Astronautas 1758, São José dos Campos-SP, 12227-010, Brazil. ²²Observatorio astronómico de La Hita, 45840 La Puebla de Almoradiel, Toledo, Spain. ²³Observatoire de Genève, CH-1290 Sauverny, Switzerland. ²⁴Department of Physics, University of Warwick, Coventry CV4 7AL, UK. ²⁵Caisey Harlinton Observatory, The Grange, Scarrow Beck Road, Erpingham, Norfolk NR11 7QX, UK. ²⁶Departamento de Física, Ingeniería de Sistemas y teoría de la Señal and Instituto de Física Aplicada a las Ciencias y la Tecnología, Universidad de Alicante P.O. Box 99, 03080 Alicante, Spain. ²⁷Instituut voor Sterrenkunde, K. U. Leuven, Celestijnenlaan 200B, B-3001 Leuven, Belgium. ²⁸Pontificia Universidad Católica de Chile Vicuña Mackenna 4860 7820436 Macul, Santiago, Chile. ²⁹Observatorio Astronómico el Gato Gris, S. Luis 145, Tanti, Córdoba, Argentina. ³⁰IP&D, Universidade do Vale do Paraíba, Av. Shishima Hifumi, 2911, CEP 12244-000, São José dos Campos, Brazil. ³¹Laboratório de Astrofísica Teórica e Observacional, Departamento de Ciências Exatas e Tecnológicas, Universidade Estadual de Santa Cruz, 45662-00 Rodovia Ilhéus-Itabuna, km 16, Brazil. ³²European Southern Observatory, Karl-Schwarzschild-Str. 2, 85748 Garching bei München, Germany. ³³Rede de Astronomia Observacional, Brasília, SMPW Q25 CJ1-10B, 71745-501, Brazil. ³⁴Universidade Estadual de Ponta Grossa, O.A. — DEGE, Avenida Carlos Cavalcanti 4748, Ponta Grossa 84030-900, Brazil.

Table 1 | Details of the successful observations on 2011 April 23

Site and telescope	Pixel scale (")	Integration time (s)	Filter name	Dead time (s)	Instrument name/ detector	Immersion time (ut)	Emersion time (ut)	Longitude/Latitude/Height
La Silla, 3.5 m NTT	0.35	0.272	r'	0.0036	ULTRACAM channel r'	1:35:44.59 ± 0.07	1:36:43.51 ± 0.08	289° 15' 58.5"E/ 29° 15' 31.8" S/2,345.4 m
La Silla, 3.5 m NTT	0.35	0.272	g'	0.0036	ULTRACAM channel g'	1:35:44.64 ± 0.04	1:36:43.66 ± 0.07	289° 15' 58.5"E/ 29° 15' 31.8" S/2,345.4 m
La Silla, 0.6 m TRAPPIST	0.64	5	Clear	1.435	FLI- PL3041BB	1:35:46.82 ± 1.6	1:36:45.47 ± 1.6	289° 15' 38.2"E/ 29° 15' 16.6" S/2,317.7 m
Paranal, 8 m VLT	0.148	1.521	J	0	ISAAC	1:35:46.00 ± 0.35	1:36:49.60 ± 0.35	289° 35' 50.1"E/ 24° 37' 30.3" S/2,635 m
Armazones, 0.84 m	0.57	10	Clear	3.5	SBIG-STL6303E	1:35:46.30 ± 1.1	1:36:48.52 ± 3	289° 48' 13.6"E/ 24° 35' 51.9" S/2,705.7 m
San Pedro de Atacama, 1.61	5	Clear	1.048	Apogee U42	1:35:37.86 ± 2.7	1:36:43.56 ± 3.1	291° 49' 13.0"E/ 22° 57' 12.2" S/2,305 m	
0.5 m Harlingen	15	Clear	5.966	SBIG-STL11000	1:35:38.66 ± 4	1:36:41.16 ± 2	291° 49' 13.0"E/ 22° 57' 12.2" S/2,305 m	
San Pedro de Atacama, 1.21	0.4 m ASH2	5	Clear	3.851	SITe SI003AB	1:33:57.27 ± 1.6	1:35:01.08 ± 2.2	314° 25' 02.5"E/ 22° 32' 07.8" S/1,810 m
0.4 m ASH2								
Pico Dos Dias, 0.6 m Zeiss	1.98							

Image sequences were obtained with all the telescopes at different image rates and with different dead times, as shown. All the observations were made in the visible, except for the Paranal light curve, which was obtained with ISAAC, a near-infrared instrument¹⁴. The sequences were started typically 20 min before the nominal occultation time, and finished around 20 min later. The images were bias subtracted and flat-field corrected using calibration frames taken before or after the occultation. From the image sequences, fluxes of the combined light source formed by Makemake and the blended star were obtained. The fluxes were obtained by means of synthetic circular-aperture photometry techniques, and the fluxes of other stars in the field of view were extracted using the DAOPHOT package¹⁵. The fluxes as a function of time constitute what we call light curves. These were divided by the fluxes of other stars to compensate for transparency fluctuations in the terrestrial atmosphere. The resulting light curves were divided by the average value of the unocculted part of the light curve to obtain a normalized flux. The uncertainties in the fluxes were obtained from the standard deviation of the data outside the occultation drop. The computers that controlled the cameras were all periodically synchronized with UT time servers, except for ULTRACAM at the 3.5-m NTT, the timing of which was directly synchronized by means of a global positioning system that provided a time accuracy better than 1 ms. We tested the accuracy of the timing of the Internet-synchronized computers by checking the error logs. The maximum deviations of the computer clocks were all less than 10 ms. Thus we adopt this value as a conservative estimate of the error in the times of the images.

Thermal measurements indicate that Makemake must have two terrains with very different albedos^{5,6,23}, and a diameter of $1,420 \pm 60$ km (ref. 6) if assumed to be spherical. This value is in agreement with, but

considerably less precise than, the value of $1,430 \pm 9$ km determined here under the assumption of spherical shape. One of the terrains in the thermal models must be very dark to explain Makemake's thermal

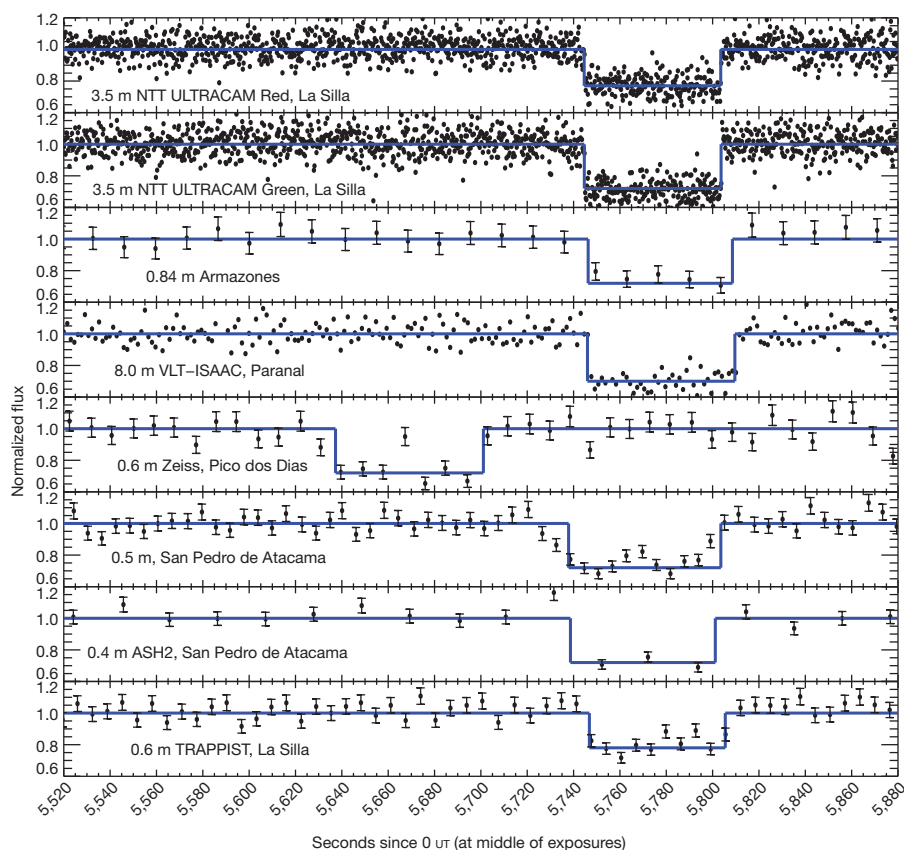


Figure 1 | Light curves of the Makemake event observed from seven telescopes on 2011 April 23. Note that the brightness drop in the Pico dos Dias light curve happens earlier than the rest because the observatory is at a very different longitude (see map in Supplementary Fig. 1). Also note that the ULTRACAM camera provided two channels of useful data (one in the red and the other in the green part of the spectrum). The light curves show the sum of the star and Makemake fluxes, arbitrarily normalized to unity outside the occultation. The R-band star magnitude is about 18.22 according to the

NOMAD catalogue, compared with roughly 17.2 for Makemake. Therefore, the expected brightness drop was around 0.35 in normalized flux, as observed. The error bars are 1σ . The NTT and Very Large Telescope Infrared Spectrometer and Array Camera (VLT-ISAAC) light curves are shown without error bars. The blue lines show square-well models that fit the observations, from which the occultation chords of Fig. 2 are obtained. Possible features in the centre of the occultation light curves are analysed in the Supplementary Information. TRAPPIST, Transiting Planets and Planetesimals Small Telescope.

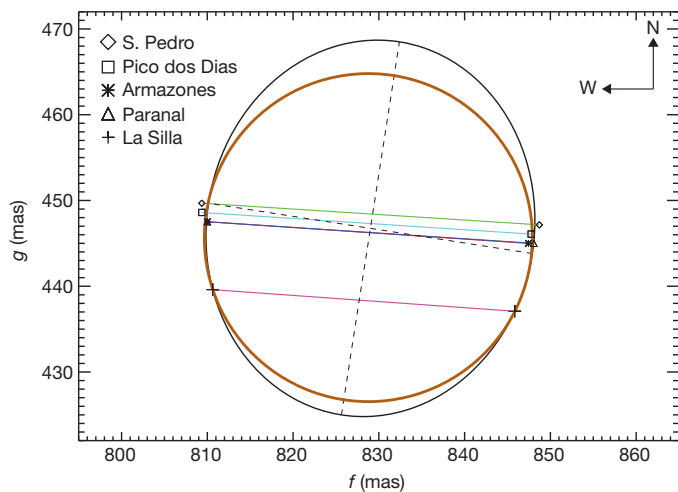


Figure 2 | Occultation chords obtained at five different sites plotted in the projected plane of the sky. The axis marked g indicates the north–south direction in the projected plane of the sky; f indicates the east–west direction. Units are milliarcseconds (mas). Note that the Paranal and Armazones chords almost overlap. The Paranal, Armazones, Pico dos Dias and San Pedro chords sampled the central part of Makemake. The star disappearance takes place on the left. The chord extremities can be fitted by two different models. The first (pictured in brown) is a circle of diameter 38.28 ± 0.22 mas (1σ level), equivalent to $1,430 \pm 9$ km, with a reduced χ^2 of 1.032. The second (pictured in black) is an ellipse with a minor axis of $1,428 \pm 17$ km and an axial ratio of 1.15 ± 0.17 , with the long axis tilted by $9 \pm 24^\circ$ (1σ level) with respect to the local celestial north. The reduced χ^2 of the fit is 1.027. The dashed line shows the axes of the best-fitting ellipse. As discussed in the Supplementary Information, the best shape is between the two models. Makemake was 51.5 AU from Earth and 52.21 AU from the Sun at the time of the occultation.

output at $24\ \mu\text{m}$ (ref. 6), which requires a warm terrain on the order of 50 K (see Supplementary Information section 5). The two terrains and Makemake's low rotational variability^{20,21,24} can be reconciled if the

object is rotating nearly pole-on, if the dark terrain is spread uniformly in longitude (a banded configuration) or by a combination of both conditions.

Makemake is, a priori, a good candidate to have a fully developed atmosphere^{4,7,8}. Its albedo and distance from the Sun lie between those of Pluto (which has a global atmosphere) and Eris (which does not, at least currently). Makemake may also have a similar surface composition to Pluto and Eris, on the basis of spectroscopic observations⁴. At the warm temperatures of about 50 K expected from two-terrain thermal models, methane vapour pressure is on the order of a few microbars, whereas nitrogen vapour pressure is around two orders of magnitude higher (as illustrated in Fig. 32 of a work on vapour pressures²⁵).

However, a global Pluto-like atmosphere is ruled out by our occultation light curves, which have abrupt ingress and egress profiles (Fig. 1). To get an upper limit on a global atmosphere, it is possible to model its effects on occultation profiles and compare them with observations. The profiles from the New Technology Telescope (NTT) imply an upper limit to the surface pressure of a putative methane atmosphere of only 4–12 nbar at a 1σ confidence level, and 20–100 nbar at the 3σ level (see Fig. 3 and Supplementary Information section 6 for a description of the models, which also consider nitrogen).

One possibility that might explain the lack of a global atmosphere is that Makemake has little or no N_2 ice, because N_2 vapour pressure is well above the microbar level even on the cooler terrain. From an update of the results of the models on retention of volatiles⁸, considering new empirical determinations of the vapour pressures of N_2 and CH_4 (ref. 25), Makemake would not have retained N_2 if it were smaller than 1,370 km, which we rule out. With a diameter of 1,430 km, Makemake would have to have a density of less than $1.7\ \text{g cm}^{-3}$, smaller than the adopted nominal value of $1.8\ \text{g cm}^{-3}$ (ref. 8), to result in complete N_2 loss. Considering now that CH_4 is abundant on the surface of Makemake, again from the volatile-retention arguments, its density would have to be greater than $1.4\ \text{g cm}^{-3}$. Other constraints on the density based on the observed shape and the figures of equilibrium are discussed in Supplementary Information section 8. Another

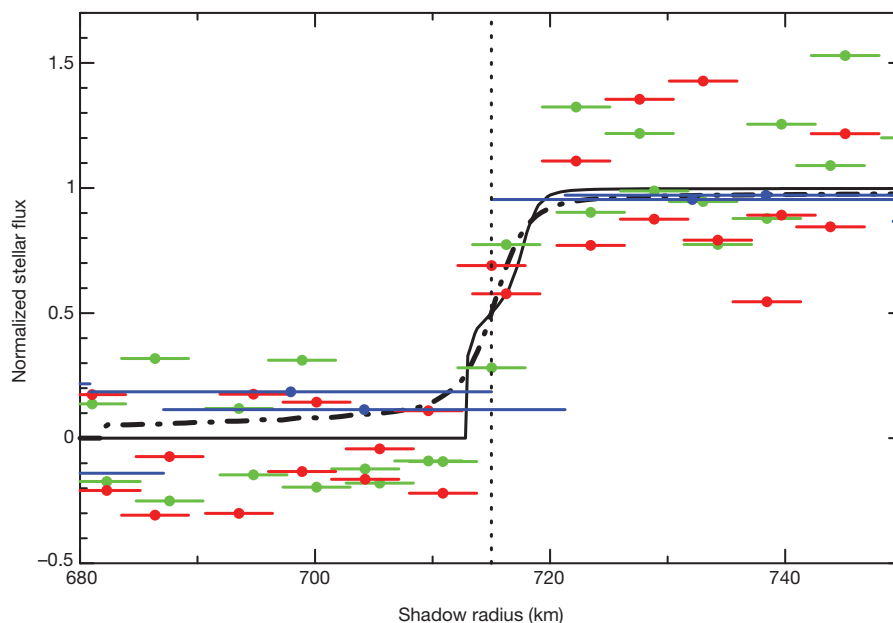


Figure 3 | Observed and synthetic light curves. A comparison of two CH_4 pure atmosphere models with data (ingress and egress profiles: green, NTT g' points; red, NTT r' points; blue, VLT J-band) plotted against the distance to Makemake's shadow centre, assuming a circular limb for simplicity. Bars are the radius intervals corresponding to each integration bin. For better reading, and in contrast to Fig. 1, the fluxes have been normalized between zero (average value of the flux during the occultation) and unity (full stellar flux). The models

correspond to a CH_4 atmosphere with a surface temperature of 30 K, a near-surface temperature gradient of $17\ \text{K km}^{-1}$ followed by an isothermal profile with $T = 100\ \text{K}$ for higher altitudes. Solid line: surface pressure of $P_{\text{surf}} = 8$ nanobar, compatible with the data at 1σ . Dash-dotted line: model with $P_{\text{surf}} = 100$ nanobar (compatible with the data at 3σ). See Supplementary Information for a full description of the models.

possibility to explain the lack of a global atmosphere is a nearly pole-on orientation. From a theoretical study⁷, TNOs with high obliquity are less likely to have globally distributed atmospheres.

The remarkably high albedo of Eris ($p_V = 0.96$) is thought to be the result of a collapsed atmosphere, which coated Eris with bright, fresh ices^{3,26}. A fully condensed atmosphere on Makemake might have resulted in an albedo similar to that of Eris, which is not the case. However, if Makemake had a local rather than a global atmosphere, some parts of the surface could be fully covered with fresh ice from the collapsed part of the atmosphere and be very bright, and others could remain dark. The overall albedo of Makemake could thus be smaller than that of Eris, but larger than that of Pluto. A local atmosphere would also provide a reason for the two-terrain models needed to explain Makemake's thermal data.

Local atmospheres on TNOs are theoretically plausible⁷; they can be confined to a subsolar region or a band at the subsolar latitude. It should be noted that a small drop of only 10 K in surface temperature implies a decrease of three orders of magnitude in the vapour pressure of CH₄ and N₂ at low temperatures.

We can investigate whether the presence of a local atmosphere is consistent with our data. The bottom of the occultation light curves should be flat in an airless body. Flashes in occultations are known to be caused by the focusing effect of an atmosphere when the observer passes near the centre of the shadow²⁷. Thus, the noise level of the light curves at their bottoms can put limits on the local atmosphere that can extend to the limbs. Modelling of central flashes for plausible local atmospheres shows that an atmosphere with surface pressure on the order of several microbars can exist and still be consistent with the data, provided that the atmosphere is confined to specific parts of the limb (see Supplementary Information section 7).

From the information gathered on Pluto, Eris and now Makemake using stellar occultations, we hypothesize that the albedos and other surface properties of the largest TNOs are determined by sublimation and condensation processes. In our picture, the largest albedos would result from atmospheres that have fully condensed (collapsed onto the surface), whereas medium-albedo objects would have local atmospheres and the lower-albedo objects would have global atmospheres from sublimation of the volatiles. Future studies will shed light on this possibility and whether sublimation is fully solar driven or is also driven by other mechanisms. The airborne Stratospheric Observatory For Infrared Astronomy, in combination with large aperture telescopes on the ground, would be an excellent tool for this kind of study.

Received 1 June; accepted 17 September 2012.

- Licandro, J. *et al.* Visible spectroscopy of 2003 UB₃₁₃: evidence for N₂ ice on the surface of the largest TNO? *Astron. Astrophys.* **458**, L5–L8 (2006).
- Tegler, S. C. *et al.* Ice mineralogy across and into the surfaces of Pluto, Triton, and Eris. *Astrophys. J.* **751**, 76 (2012).
- Sicardy, B. *et al.* A Pluto-like radius and a high albedo for the dwarf planet Eris from an occultation. *Nature* **478**, 493–496 (2011).
- Licandro, J. *et al.* The methane ice rich surface of large TNO 2005 FY₉: a Pluto-twin in the trans-Neptunian belt? *Astron. Astrophys.* **445**, L35–L38 (2006).
- Stansberry, J. A. *et al.* in *The Solar System Beyond Neptune*. 161–179 (eds Barucci, M. A., Boehnhardt, H., Cruikshank, D. P., Morbidelli, A. & Dotson, R.) (Univ. Arizona Press, 2008).
- Lim, T. *et al.* "TNOs are Cool": A survey of the trans-Neptunian region. III. Thermophysical properties of (90482) Orcus and (136472) Makemake. *Astron. Astrophys.* **518**, L148 (2010).
- Stern, S. A. & Trafton, L. M. in *The Solar System Beyond Neptune* (eds Barucci, M. A., Boehnhardt, H., Cruikshank, D. P., Morbidelli, A. & Dotson, R.) 365–380 (Univ. Arizona Press, 2008).
- Schaller, E. L. & Brown, M. E. Volatile loss and retention on Kuiper belt objects. *Astron. J.* **659**, L61–L64 (2007).
- Hubbard, W. B., Hunten, D. M., Dieters, S. W., Hill, K. M. & Watson, R. D. Occultation evidence for an atmosphere on Pluto. *Nature* **336**, 452–454 (1988).
- Young, E. F. *et al.* Vertical structure in Pluto's atmosphere from the 2006 June 12 stellar occultation. *Astron. J.* **136**, 1757–1769 (2008).

- Sicardy, B. *et al.* Charon's size and an upper limit on its atmosphere from a stellar occultation. *Nature* **439**, 52–54 (2006).
- Elliot, J. L. *et al.* Size and albedo of Kuiper belt object 55636 from a stellar occultation. *Nature* **465**, 897–900 (2010).
- Assafin, M. *et al.* Candidate stellar occultations by large trans-Neptunian objects up to 2015. *Astron. Astrophys.* **541**, A142 (2012).
- Moorwood, A. *et al.* ISAAC at the VLT. *Messenger* **95**, 1–5 (1999).
- Stetson, P. B. DAOPHOT — a computer program for crowded-field stellar photometry. *Publ. Astron. Soc. Pacif.* **99**, 191–222 (1987).
- Brown, M. E. *et al.* Satellites of the largest Kuiper belt objects. *Astrophys. J.* **639**, L43–L46 (2006).
- Rabinowitz, D. L., Schaefer, B. E. & Tourtellotte, S. W. The diverse solar phase curves of distant icy bodies. I. Photometric observations of 18 trans-Neptunian objects, 7 centaurs, and Nereid. *Astron. J.* **133**, 26–43 (2007).
- Buratti, B. *et al.* Photometry of Pluto in the last decade and before: evidence for volatile transport? *Icarus* **162**, 171–182 (2003).
- Rabinowitz, D. *et al.* Photometric observations constraining the size, shape, and albedo of 2003 EL₆₁, a rapidly rotating, Pluto-sized object in the Kuiper belt. *Astrophys. J.* **639**, 1238–1251 (2006).
- Heine, A. N. & de Lahunta, D. The rotation period and light-curve amplitude of Kuiper belt dwarf planet 136472 Makemake (2005 FY₉). *Astron. J.* **138**, 428–438 (2009).
- Thirouin, A. *et al.* Short-term variability of a sample of 29 trans-Neptunian objects and centaurs. *Astron. Astrophys.* **522**, A93 (2010).
- Tancredi, G. & Favre, S. Which are the dwarfs in the Solar System? *Icarus* **195**, 851–862 (2008).
- Müller, T. *et al.* Makemake: A truly exotic TNO! *EPSC-DPS Joint Meeting, Nantes, France* 1416 (2011).
- Ortiz, J. *et al.* Short-term rotational variability in the large TNO 2005 FY₉. *Astron. Astrophys.* **468**, L13–L16 (2007).
- Fray, N. & Schmitt, B. Sublimation of ices of astrophysical interest: a bibliographic review. *Planet. Space Sci.* **57**, 2053–2080 (2009).
- Alvarez-Candal, A. *et al.* The spectrum of (136199) Eris between 350 and 2350 nm: results with X-Shooter. *Astron. Astrophys.* **532**, A130 (2011).
- Elliot, J. L. *et al.* Occultation of Epsilon Geminorum by Mars. II — The structure and extinction of the Martian upper atmosphere. *Astrophys. J.* **217**, 661–679 (1977).

Supplementary Information is available in the online version of the paper.

Acknowledgements These results were based partially on observations made with European Southern Observatory Telescopes at the La Silla and Paranal Observatories under programme 287C-5013. J.L.O. acknowledges funding from Spanish and Andalusian grants and the European Regional Development Fund (FEDER). B.S. acknowledges support from French National Research Agency (ANR) grant 'Beyond Neptune', and from the Institut Universitaire de France. E.U.-S. acknowledges the support from the Chilean National Commission for Scientific and Technical Research (Gemini-CONICYT funds), and from the North Catholic University of Chile Vicerectorate of Research and Technology Development (UCN-VRIDT). TRAPPIST is a project funded by the Belgian Fund for Scientific Research (FRS-FNRS) with the participation of the Swiss National Science Foundation (SNF). J.I.B.C. acknowledges grants by the Brazilian National Council for the Development of Science and Technology (CNPq), and the Foundation for Research Support of the State of Rio de Janeiro (FAPERJ). P.S.-S. acknowledges financial support by the Centre National de la Recherche Scientifique (CNRS). R.G.-H. acknowledges partial financial support by the Argentinian National Scientific and Technical Research Council (CONICET). F.B.-R. acknowledges the support of the French-Brazilian Doctoral College Coordination of Improvement of Graduated Personnel programme (CDFB/CAPES). A.A.-C. acknowledges support from the Marie Curie Actions of the European Commission (FP7-COFUND). S.P.L., V.S.D. and T.R.M. acknowledge funding for ULTRACAM from the UK Science and Technology Facilities Council. R.D. acknowledges support from Spanish Ministry of Economics and Competitiveness through a Ramón y Cajal contract.

Author Contributions J.L.O. helped to plan the campaign, analysed data for the prediction, made the prediction, participated in the observations, obtained and analysed data, interpreted data and wrote part of the paper. B.S. helped to plan the campaign, participated in the observations, analysed data, interpreted data, wrote and ran the diffraction and ray-tracing codes and wrote part of the paper. F.B.-R. and A.A.-C. helped to plan the campaign, participated in the observations and analysed and interpreted data. E.L. analysed the implications of the results for Makemake's thermal model and putative atmospheric structure and wrote part of the paper. R.D. and V.D.I. helped to plan the observations and analysed data. J.I.B.C., S.P.L., E.U.-S., J.P.C., E.J. and J.M. participated in the observations and analysed data. M.A., F.B.-R., J.I.B.C., R.V.-M., D.N.d.S.N. and R.B. discovered the star candidate and analysed data. P.J.G. and T.M. made thermal models and participated in the interpretation. All other authors participated in the planning of the campaign and/or the observations and/or the interpretations. All authors were given the opportunity to review the results and comment on the manuscript.

Author Information Reprints and permissions information is available at www.nature.com/reprints. The authors declare no competing financial interests. Readers are welcome to comment on the online version of the paper. Correspondence and requests for materials should be addressed to J.L.O. (ortiz@iaa.es).

Sisyphus cooling of electrically trapped polyatomic molecules

Martin Zeppenfeld¹, Barbara G. U. Englert¹, Rosa Glöckner¹, Alexander Pohn¹, Manuel Mielenz¹†, Christian Sommer¹‡, Laurens D. van Buuren¹†, Michael Motsch¹† & Gerhard Rempe¹

Polar molecules have a rich internal structure and long-range dipole–dipole interactions, making them useful for quantum-controlled applications and fundamental investigations. Their potential fully unfolds at ultracold temperatures, where various effects are predicted in many-body physics^{1,2}, quantum information science^{3,4}, ultracold chemistry^{5,6} and physics beyond the standard model^{7,8}. Whereas a wide range of methods to produce cold molecular ensembles have been developed^{9–13}, the cooling of polyatomic molecules (that is, with three or more atoms) to ultracold temperatures has seemed intractable. Here we report the experimental realization of optoelectrical cooling¹⁴, a recently proposed cooling and accumulation method for polar molecules. Its key attribute is the removal of a large fraction of a molecule's kinetic energy in each cycle of the cooling sequence via a Sisyphus effect, allowing cooling with only a few repetitions of the dissipative decay process. We demonstrate the potential of optoelectrical cooling by reducing the temperature of about one million CH₃F molecules by a factor of 13.5, with the phase-space density increased by a factor of 29 (or a factor of 70 discounting trap losses). In contrast to other cooling mechanisms, our scheme proceeds in a trap, cools in all three dimensions and should work for a large variety of polar molecules. With no fundamental temperature limit anticipated down to the photon-recoil temperature in the nanokelvin range, we expect our method to be able to produce ultracold polyatomic molecules. The low temperatures, large molecule numbers and long trapping times of up to 27 seconds should allow an interaction-dominated regime to be attained, enabling collision studies and investigation of evaporative cooling towards a Bose–Einstein condensate of polyatomic molecules.

The ability to prepare ultracold molecular ensembles has an application potential akin to that of ultracold atoms some decades ago. In fact, the association of KRb dimers¹⁵ as well as the laser cooling of SrF (ref. 16) has brought fascinating physics within reach. However, both approaches are restricted to a highly specialized set of purely diatomic molecule species. In order to investigate fundamental physics based on relativistic effects near heavy nuclei^{7,8} or parity violation effects in chiral molecules¹⁷, or to study molecules of chemical interest¹⁸, a more general approach to preparing ultracold molecular ensembles is imperative. This holds in particular for the rich chemical variety of carbon-, nitrogen- or oxygen-based molecules for which the constituent atoms have not even been laser cooled. Devising a dissipative process to cool such molecules into the ultracold regime has been an exceedingly challenging problem. The standard approach for atoms, laser cooling, is in general impossible for molecules owing to the lack of suitable cycling transitions. Creating an artificial cycling transition via cavity cooling¹⁹ has not been demonstrated despite substantial experimental²⁰ and theoretical^{21–23} effort. Likewise, evaporative or sympathetic cooling to ultracold temperatures²⁴ has not been realized owing to lack of density or losses from inelastic collisions.

A particularly promising general framework for cooling is to replace the weak photon recoil in laser cooling with sufficiently strong forces to remove a particle's entire kinetic energy in a single cycle^{14,25,26}. For molecules, a first step towards this approach is the recent achievement of accumulation of NH using a single-photon transition²⁷. Here we present a full implementation of optoelectrical cooling¹⁴ for molecules stored in an electric trap, featuring both accumulation and cooling. Energy is extracted by allowing molecules to move up and down an electric field gradient in different states with differing Stark energies while dissipation to remove entropy is provided by a spontaneous vibrational decay. The scheme is applicable to all molecules with strong electric field interaction and pure rotational–vibrational states, and thus constitutes a general method for cooling molecules to ultracold temperatures.

Reducing the temperature by a large factor requires the cooling cycle to be repeated, and consequently, control being maintained over the internal molecular state. This is achieved using the level scheme shown in Fig. 1a. An electric trap as depicted in Fig. 1b with a homogeneous electric field in the trap centre and strongly increasing fields near the trap boundary²⁸ leads to a position-dependent potential energy for the relevant molecular states as shown. We label states with vibrational quantum number v and symmetric-top rotational quantum numbers J, K, M as $|v; J, \mp K, \pm M\rangle$ with $\mp K$ chosen positive. For a parallel vibrational transition with $\Delta K = 0$, the state $|1; 3, 3, 3\rangle$ decays to the four rotational $v = 0$ states shown in Fig. 1a, with decay to the $|0; 4, 3, 2\rangle$ state ignored due to the small Clebsch–Gordan coefficient of $1/144$. Coupling the more weakly trapped $|0; 3, 3, 2\rangle$ and $|0; 4, 3, 3\rangle$ states with microwave radiation and driving the $|0; 3, 3, 2\rangle$ to $|1; 3, 3, 3\rangle$ transition with an infrared laser results in optical pumping to the strongly trapped $|0; 3, 3, 3\rangle$ and $|0; 4, 3, 4\rangle$ states. Adding a radio-frequency to couple neighbouring M -sublevels in strong electric fields completes the optoelectrical cooling cycle. Losses to the untrapped $M = 0$ states are avoided by coupling the neighbouring M -sublevels with the radio frequency at a rate which is slow compared to the optical pumping (Supplementary Information, sections 1–3). Note that Stark detuning due to the electric fields plays a key role in selectively addressing only the desired infrared and microwave transitions (Supplementary Information section 5).

The experimental sequence to prepare and detect a sample of cooled molecules is shown and explained in Fig. 1c. In addition to cooling, we apply the following two experimental sequences. First, a reference no-cooling measurement with the infrared, microwave and radio-frequency fields left off and the storage time shortened by 20 s results in an uncooled molecular ensemble. Second, reintroduction of the infrared and microwave fields results in accumulation of molecules, also without cooling. Here, molecules entering the trap in the weakly trapped states $|0; 3, 3, M\rangle$ and $|0; 4, 3, M\rangle$ with $1 \leq M \leq J - 1$ are pumped to the strongly trapped $|0; 3, 3, 3\rangle$ and $|0; 4, 3, 4\rangle$ states.

¹Max-Planck-Institut für Quantenoptik, Hans-Kopfermann-Straße 1, 85748 Garching, Germany. †Present addresses: Albert-Ludwigs-Universität Freiburg, Physikalisches Institut, Hermann-Herder-Straße 3, 79104 Freiburg, Germany (M. Mielenz); Institute for Molecular Science, National Institutes of Natural Sciences, Myodaiji, Okazaki 444-8585, Japan (C.S.); Department of Radiation Oncology, The Netherlands Cancer Institute – Antoni van Leeuwenhoek Hospital, 1066 CX Amsterdam, The Netherlands (L.D.v.B.); Laboratorium für Physikalische Chemie, ETH Zürich, CH-8093 Zürich, Switzerland (M. Motsch).

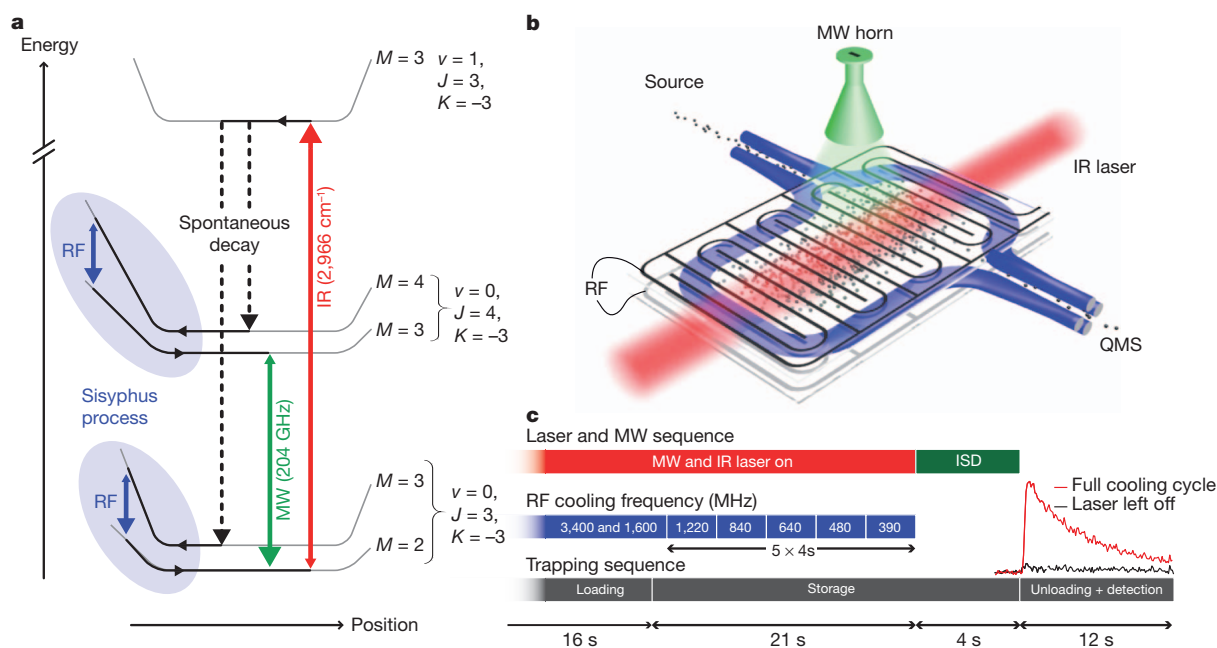


Figure 1 | Implementation of molecule cooling. **a**, Radiation couples molecular states which experience a position-dependent potential energy in an electric trap as indicated. Molecules following the emphasized route lose more kinetic energy when entering the strong-field edge region of the trap than they regain when returning to the trap centre in a more weakly trapped state. Combined with the unidirectionality of the optical pumping back to the strongly trapped states, this leads to cooling. See main text for state nomenclature. **b**, During cooling the molecules are confined in a

microstructured electric trap²⁸, with the infrared (IR), microwave (MW) and radio-frequency (RF) fields applied as indicated. **c**, Experimental sequence for cooling: warm molecules are loaded into the trap for 16 s with the infrared, microwave and two radio-frequency fields (at 3.4 GHz and 1.6 GHz) already applied. The trap is then electrically closed²⁸ and the radio-frequency is decreased stepwise to 390 MHz over the next 21 s. Before unloading the molecules for detection, an internal-state-discrimination (ISD) technique is applied for an additional 4 s (see Methods).

All experimental sequences end by unloading the molecules from the trap and guiding them to the ionization volume of a quadrupole mass spectrometer (QMS) for detection. This results in signals as shown in the inset in Fig. 1c; we show the case for the full cooling sequence to 390 MHz, as well as for the same sequence but with the infrared laser left off. Remarkably, the sequence with the laser switched on results in a strong molecule signal whereas leaving the laser switched off eliminates the signal almost entirely. Thus, the excitation by the laser and the subsequent spontaneous decay clearly plays a key role in keeping molecules in the trap, indicating that a key element of the cooling cycle is working. Note that state-discriminating measurements (see Methods) show that 80% of the molecules with laser

switched on are in the states $|0; 3, 3, M\rangle$ and $|0; 4, 3, M\rangle$ potentially involved in the cooling. Most of these are in the top M -sublevels (Supplementary Information, sections 2–4), establishing our experiment as a practically state-selected source of molecules. This compares to about 20% of molecules initially entering the trap in these states.

For proof of cooling, we now present four complementary measurements. First, we examine the effect of the trap electric field strength on the molecules during unloading. The field strength during this time is particularly important, because it determines both the confining potential for the molecules and the molecule transport efficiency to the detection QMS. In particular, a lower electric field strength reduces the trap depth so that hotter molecules are lost, and a higher electric

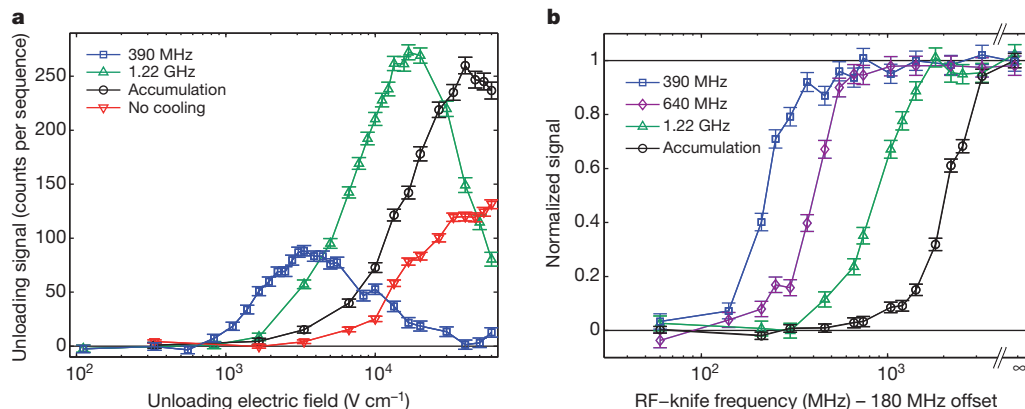


Figure 2 | Demonstration of optoelectrical cooling. **a**, Detected molecule signal versus trap electric field strength during unloading. In addition to results for the no-cooling measurement, the accumulation, and the full cooling sequence to 390 MHz, we show results for cooling to the intermediate frequency of 1.22 GHz. Cooling results in a more than tenfold decrease in the optimal unloading voltage and, together with the accumulation, in a multifold

signal increase at low unloading voltages. **b**, Relative unloading signal with radio frequencies applied as a knife-edge filter. The key shows the radio frequency applied for cooling (except in the case of accumulation) after which the much stronger radio-frequency knife is applied. We subtract 180 MHz from the knife frequency to account for the offset electric field at the centre of the trap (Supplementary Information, section 5). Data show mean $\pm 1\sigma$.

field strength during unloading inhibits colder molecules from finding the trap exit hole to the QMS. We thus expect the molecule signal to fall off in both directions from a maximum at a confining electric field strength which is proportional to the temperature of the molecules, depending on the molecule Stark shifts. Figure 2a shows the measured molecule signal versus unloading electric field strength for four different experimental sequences. The two curves with the cooling sequence applied show a strong decrease in the optimal unloading electric field strength, from about 45 kV cm^{-1} to 16 kV cm^{-1} and 3.3 kV cm^{-1} . Because the plotted signal is mainly from molecules in the states $|0; 3, 3, 3\rangle$ and $|0; 4, 3, 4\rangle$ (Supplementary Information, sections 2–4) which have a similar Stark shift, our data clearly show that a large amount of cooling takes place. The relatively low signal for the full cooling sequence is in large part due to trap losses during the additional 20 s of storage compared to accumulation and no-cooling, accounting for a 2.4 times smaller signal (see below). Note that the accumulation alone results in a molecule signal approximately twofold larger, thus proving an increase in the phase-space density.

As a second measurement, we use a strong radio-frequency field to drive transitions to untrapped states and thus eliminate hotter molecules from the trap (the energy distribution of the molecules is therefore being truncated or ‘cut’, so we refer to this field as a radio-frequency knife). Results are shown in Fig. 2b. For all three measurements with cooling, the cooling sequence is completed to 390 MHz. However, two additional seconds of storage are introduced immediately after the indicated cooling frequency so the radio-frequency knife can be applied. This allows for practically identical experimental sequences. The molecules are unloaded directly only for accumulation. The molecule signal versus knife frequency shows a steep flank at a position which strongly depends on the frequency of the cooling step just before application of the knife. The position of the flank is shifted by approximately a factor of 10, similar to the shift observed in Fig. 2a. Again, the dramatic shift can only be explained by a large amount of cooling. Note that the flanks of the four measurements are well separated, indicating that the energy distributions of the molecules in the four measurements hardly overlap.

Both the previous measurements are sensitive to the internal molecular state, because Stark shift and Stark splitting directly determine the effect of the trap voltages and radio frequencies, respectively. To avoid this effect, we perform a third experiment and directly measure the velocities of the molecules via a time-of-flight technique. Specifically, we switch the 55-cm-long quadrupole guide segment leading to the QMS on and off and measure the arrival time of the molecules. Note that the unloading voltages affect the distribution of molecules arriving at the QMS, with colder (hotter) molecules being preferentially detected at lower (higher) voltages (Supplementary Information, section 6). However, by measuring at the optimal unloading voltages, the effect will be the same for all measurements relative to the ensemble in the trap. We use the same four experimental sequences as for Fig. 2a with the results shown in Fig. 3. Calculating the mean longitudinal velocity $\langle v_z \rangle$ from the data and deriving the molecular temperature T via $k_B T/2 = m \langle v_z^2 \rangle / 2$ (m being the mass of CH_3F), we arrive at the central result: the molecules have been cooled by a factor of 13.5, from 390 mK to 29 mK. Together with the estimated molecule density, this corresponds to a factor 29 increase in phase-space density. In fact, cooling and accumulation by themselves increase the phase-space density by a factor of 70, but this is reduced by trap losses during cooling.

As a fourth and final measurement, Fig. 4 shows the lifetime of molecules in the trap as a function of the final cooling frequency. As expected for cooling²⁸, the lifetime increases from about 10 s without cooling to about 27 s with maximal cooling. This change confirms once more that cooling takes place. By integrating the measured loss rate over time, we find that the additional 20 s of storage for cooling to 390 MHz compared to no-cooling or accumulation leads to a loss of about 60% of the molecules, as has been used above in the discussion of

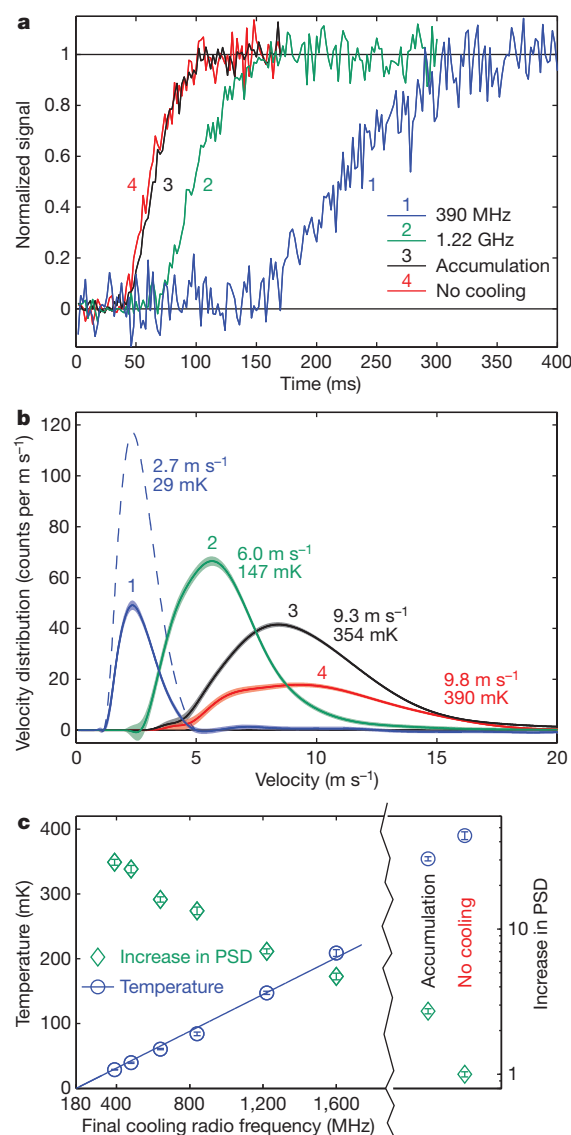


Figure 3 | Time-of-flight measurements to determine molecule velocities.

a, Rising edge of the normalized trap unloading signal for the same variations of the experimental sequence as in Fig. 2a. For cooled molecules one needs to wait more than three times longer before molecules arrive at the QMS. **b**, Molecular velocity distributions 1–4 derived from the rising-edge signals shown in **a** taking into account the number of detected molecules. The dashed blue curve shows the hypothetical result if trap losses (shown in Fig. 4) could be eliminated. The smooth appearance of the data is due to convolution with a Gaussian. Labels on curves show the mean velocity and temperature calculated from the data sets. **c**, Measured molecule temperature (left-hand vertical axis) and total change in phase-space density (PSD; right-hand vertical axis) after each intermediate radio frequency as well as for no-cooling and accumulation. All quoted errors are $\pm 1\sigma$, including the shaded regions in **b**.

Fig. 2a and in Fig. 3b. This loss could be reduced by using better trapping or faster cooling.

In principle, optoelectrical cooling can be continued to much lower temperatures. However, losses during cooling and the low detection efficiency make further cooling increasingly difficult with the present set-up. An improved trap design could increase the trap lifetime, and higher detection efficiencies would make losses more tolerable. Varying the cooling sequence or choosing a molecule species with a faster spontaneous decay would allow faster cooling.

Even without these improvements, the present experiment brings key applications of cold polar molecules within reach. First, the increased phase-space density will improve the sensitivity of high-resolution

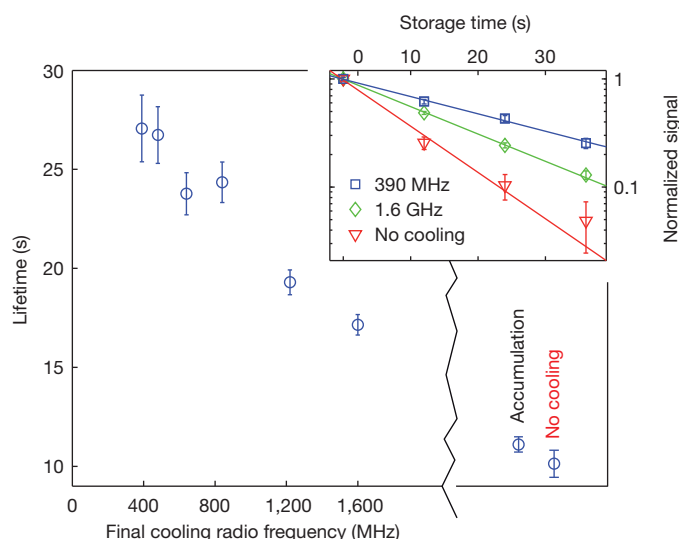


Figure 4 | Trap lifetime for cooled and uncooled molecules. Cooling substantially increases the trap lifetime. Inset, raw data for three of the lifetime measurements. Data show mean $\pm 1\sigma$.

spectroscopy and collision experiments. Second, the temperature obtained will allow molecules to be loaded into more-weakly-confining microwave²⁹ or optical traps that can hold molecules in their rotational ground state, a prerequisite for achieving quantum degeneracy. Last, our chip-like trap and guide architecture matches the demands on hybrid quantum systems to be used for quantum information processing with cold and ultracold molecules⁴.

METHODS SUMMARY

The initial sample of molecules is generated by velocity filtering¹² from a liquid-nitrogen-cooled source and loaded into the electric trap²⁸ via a quadrupole guide. Detection is performed by guiding the molecules to the QMS via a second guide. The selection of CH₃F as the molecule species is based on its favourable properties for trap loading and detection. Large rotational constants and sufficient vapour pressure down to almost 100 K allow efficient velocity filtering with an adequate fraction (~20%) of molecules in the rotational states used for cooling. Low contributions from other molecules at the atomic mass 34 of CH₃F results in very low background for the QMS detection. For dissipation, the spontaneous decay rate (approximately 15 Hz) of the most suited parallel vibrational ν_1 symmetric C–H stretch mode is sufficient. The infrared and microwave radiation sources required for CH₃F (ref. 30) are described in Supplementary Information, section 5.

All quoted errors are obtained from counting statistics of the time-binned QMS signal as the square root of the total number of counts. For each data set, the number n of repetitions of the experimental sequence (see Fig. 1c) was chosen according to signal strength as follows: Fig. 2a $n = 15$ to 72, Fig. 2b $n = 39$, Fig. 3a and b $n = 600$ to 1,140, Fig. 3c $n = 360$ to 1,140, Fig. 4 $n = 23$ to 79.

For internal-state discrimination, a microwave depletion pulse consisting of various microwave frequencies near 204 GHz is applied to mix all M -sublevels of the $J = 3$ and $J = 4$ states, inducing trap losses and leaving only the unaffected background of molecules in other states in the trap. The difference in the unload signal with and without the MWD constitutes the state-discriminated signal.

Received 23 July; accepted 12 September 2012.

Published online 14 November 2012.

- Góral, K., Santos, L. & Lewenstein, M. Quantum phases of dipolar bosons in optical lattices. *Phys. Rev. Lett.* **88**, 170406 (2002).
- Micheli, A., Brennen, G. K. & Zoller, P. A toolbox for lattice-spin models with polar molecules. *Nature Phys.* **2**, 341–347 (2006).

- DeMille, D. Quantum computation with trapped polar molecules. *Phys. Rev. Lett.* **88**, 067901 (2002).
- André, A. *et al.* A coherent all-electrical interface between polar molecules and mesoscopic superconducting resonators. *Nature Phys.* **2**, 636–642 (2006).
- Krems, R. V. Cold controlled chemistry. *Phys. Chem. Chem. Phys.* **10**, 4079–4092 (2008).
- Zuchowski, P. S. & Hutson, J. M. Low-energy collisions of NH₃ and ND₃ with ultracold Rb atoms. *Phys. Rev. A* **79**, 062708 (2009).
- Hinds, E. A. Testing time reversal symmetry using molecules. *Phys. Scr. T* **70**, 34–41 (1997).
- Hudson, J. J. *et al.* Improved measurement of the shape of the electron. *Nature* **473**, 493–496 (2011).
- Weinstein, J. D., DeCarvalho, R., Guillet, T., Friedrich, B. & Doyle, J. M. Magnetic trapping of calcium monohydride molecules at millikelvin temperatures. *Nature* **395**, 148–150 (1998).
- Gupta, M. & Herschbach, D. A mechanical means to produce intense beams of slow molecules. *J. Phys. Chem. A* **103**, 10670–10673 (1999).
- Bethlem, H. L., Berden, G. & Meijer, G. Decelerating neutral dipolar molecules. *Phys. Rev. Lett.* **83**, 1558–1561 (1999).
- Junglen, T., Rieger, T., Rangwala, S. A., Pinkse, P. W. H. & Rempe, G. Slow ammonia molecules in an electrostatic quadrupole guide. *Eur. Phys. J. D* **31**, 365–373 (2004).
- Fulton, R., Bishop, A. I. & Barker, P. F. Optical Stark decelerator for molecules. *Phys. Rev. Lett.* **93**, 243004 (2004).
- Zeppenfeld, M., Motsch, M., Pinkse, P. W. H. & Rempe, G. Optoelectrical cooling of polar molecules. *Phys. Rev. A* **80**, 041401(R) (2009).
- Ni, K.-K. *et al.* A high phase-space-density gas of polar molecules. *Science* **322**, 231–235 (2008).
- Shuman, E. S., Barry, J. F. & DeMille, D. Laser cooling of a diatomic molecule. *Nature* **467**, 820–823 (2010).
- Dassay, Ch. *et al.* Limit on the parity nonconserving energy difference between the enantiomers of a chiral molecule by laser spectroscopy. *Phys. Rev. Lett.* **83**, 1554–1557 (1999).
- Hudson, E. R. *et al.* Production of cold formaldehyde molecules for study and control of chemical reaction dynamics with hydroxyl radicals. *Phys. Rev. A* **73**, 063404 (2006).
- Vuletić, V. & Chu, S. Laser cooling of atoms, ions, or molecules by coherent scattering. *Phys. Rev. Lett.* **84**, 3787–3790 (2000).
- Motsch, M., Zeppenfeld, M., Pinkse, P. W. H. & Rempe, G. Cavity-enhanced Rayleigh scattering. *N. J. Phys.* **12**, 063022 (2010).
- Nagy, D., Asbóth, J. K., Domokos, P. & Ritsch, H. Self-organization of a laser-driven cold gas in a ring cavity. *Europhys. Lett.* **74**, 254–260 (2006).
- Zeppenfeld, M. & Pinkse, P. W. H. Calculating the fine structure of a Fabry–Perot resonator using spheroidal wave functions. *Opt. Express* **18**, 9580–9591 (2010).
- Xuereb, A., Domokos, P., Horak, P. & Freegarde, T. Cavity cooling of atoms: within and without a cavity. *Eur. Phys. J. D* **65**, 273–278 (2011).
- Lara, M., Bohn, J. L., Potter, D., Soldán, P. & Hutson, J. M. Ultracold Rb–OH collisions and prospects for sympathetic cooling. *Phys. Rev. Lett.* **97**, 183201 (2006).
- Pritchard, D. E. Cooling neutral atoms in a magnetic trap for precision spectroscopy. *Phys. Rev. Lett.* **51**, 1336–1339 (1983).
- Narevicius, E., Bannerman, S. T. & Raizen, M. G. Single-photon molecular cooling. *N. J. Phys.* **11**, 055046 (2009).
- Riedel, J. *et al.* Accumulation of Stark-decelerated NH molecules in a magnetic trap. *Eur. Phys. J. D* **65**, 161–166 (2011).
- Englert, B. G. U. *et al.* Storage and adiabatic cooling of polar molecules in a microstructured trap. *Phys. Rev. Lett.* **107**, 263003 (2011).
- DeMille, D., Glenn, D. R. & Petricka, J. Microwave traps for cold polar molecules. *Eur. Phys. J. D* **31**, 375–384 (2004).
- Graner, G. & Guelachvili, G. Extensive high-resolution study of the crowded rovibrational CH₃F spectrum around 3000 cm⁻¹. *J. Mol. Spectrosc.* **89**, 19–41 (1981).

Supplementary Information is available in the online version of the paper.

Acknowledgements We thank P. W. H. Pinkse for help during the early stages of this experiment. Support by the Deutsche Forschungsgemeinschaft via the excellence cluster “Munich Centre for Advanced Photonics” is acknowledged.

Author Contributions All authors contributed to the design, experimental set-up, data collection, analysis, and/or writing of the manuscript.

Author Information Reprints and permissions information is available at www.nature.com/reprints. The authors declare no competing financial interests. Readers are welcome to comment on the online version of the paper. Correspondence and requests for materials should be addressed to M.Z. (martin.zeppenfeld@mpq.mpg.de).

Revealing the quantum regime in tunnelling plasmonics

Kevin J. Savage¹, Matthew M. Hawkeye¹, Rubén Esteban², Andrei G. Borisov^{2,3}, Javier Aizpurua² & Jeremy J. Baumberg¹

When two metal nanostructures are placed nanometres apart, their optically driven free electrons couple electrically across the gap. The resulting plasmons have enhanced optical fields of a specific colour tightly confined inside the gap. Many emerging nanophotonic technologies depend on the careful control of this plasmonic coupling, including optical nanoantennas for high-sensitivity chemical and biological sensors¹, nanoscale control of active devices^{2–4}, and improved photovoltaic devices⁵. But for subnanometre gaps, coherent quantum tunnelling becomes possible and the system enters a regime of extreme non-locality in which previous classical treatments^{6–14} fail. Electron correlations across the gap that are driven by quantum tunnelling require a new description of non-local transport, which is crucial in nanoscale optoelectronics and single-molecule electronics. Here, by simultaneously measuring both the electrical and optical properties of two gold nanostructures with controllable subnanometre separation, we reveal the quantum regime of tunnelling plasmonics in unprecedented detail. All observed phenomena are in good agreement with recent quantum-based models of plasmonic systems¹⁵, which eliminate the singularities predicted by classical theories. These findings imply that tunnelling establishes a quantum limit for plasmonic field confinement of about $10^{-8} \lambda^3$ for visible light (of wavelength λ). Our work thus prompts new theoretical and experimental investigations into quantum-domain plasmonic systems, and will affect the future of nanoplasmonic device engineering and nanoscale photochemistry.

Subwavelength metallic structures can concentrate light into nanoscale dimensions well below the diffraction limit¹⁶ owing to reduced field penetration through a dense electron sea. Nanocavities formed inside a nanogap control the coupling of localized plasmons, thus allowing cavity-tuning^{6–8} targeted to desirable applications that exploit the enhanced optical fields. But as the cavity gaps shrink to atomic length scales, quantum effects emerge and standard classical approaches to describe the optics of these systems fail. One effect of confining electronic wavefunctions to small metallic nanoparticles is to slightly modify the screening that tunes the plasmons¹⁷. However, tunnelling plasmonics in the quantum regime has more profound effects that cannot be explained through hydrodynamic models that account for quantum effects through smearing of the electronic localization¹⁸. Recent theories show that quantum tunnelling across the cavity strongly modifies the optical response^{19,20}, but computational limits restrict these quantum simulations to very small systems below a few nanometres in size. Furthermore, the extreme difficulty of creating and probing subnanometre cavities has limited experimental investigations of plasmonics in the quantum regime. Top-down and self-assembly nanofabrication achieves gaps as small as 0.5 nm between plasmonic nanoparticles^{21,22}, but these fail to reach the quantum tunnelling regime. Small cavities are also accessed in scanning tunnelling microscopes and electro-migrated break-junctions which show optical mixing, emission and rectification phenomena^{23–26}, but the effect of quantum tunnelling on optical plasmon coupling across subnanometre cavities remains unexplored. Here we present broadband optical spectra that

probe dynamically controlled plasmonic cavities and reveal the onset of quantum-tunnelling-induced plasmonics in the subnanometre regime.

Two gold-nanoparticle-terminated atomic force microscope (AFM) tips are oriented tip-to-tip (Fig. 1a). The tip apices define a cavity supporting plasmonic resonances created via strong coupling between localized plasmons on each tip^{7,27}. This dual AFM tip configuration provides multiple advantages. First, independent nanometre-precision movement of both tips is possible with three-axis piezoelectric stages. Second, conductive AFM probes provide direct electrical connection to the tips, enabling simultaneous optical and electrical measurements. Third, the tips are in free space and illuminated from the side in a dark-field configuration (Fig. 1b, c and Supplementary Information). This arrangement provides (for the first time, to our knowledge) background-free broadband spectroscopic characterization of the tip-tip plasmonic nanocavity throughout the subnanometre regime. A super-continuum laser (with polarization parallel to the tip-tip axis) is used as an excitation source, providing high-brightness illumination over a wide wavelength range (450–1,700 nm) and reducing integration times to a few milliseconds. The tips are aligned using a recently developed electrostatic-force technique²⁸. The inter-tip separation d is initially set to 50 nm and then reduced while recording dark field scattering spectra and direct currents simultaneously.

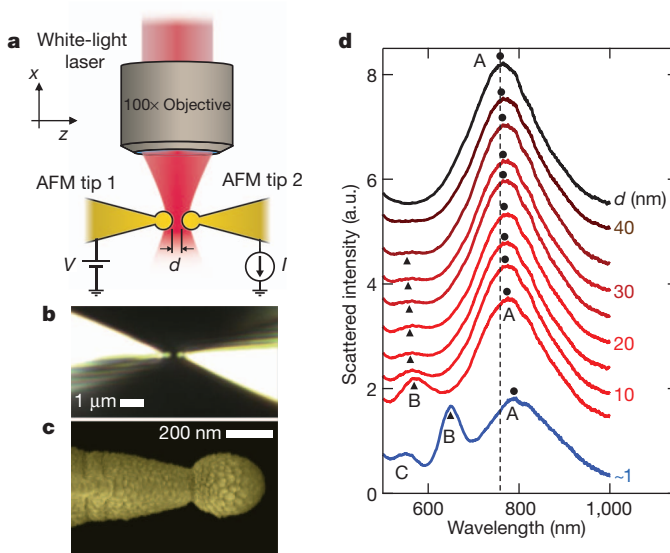


Figure 1 | Formation and characterization of a nanoscale plasmonic cavity. **a**, Scheme for simultaneous optical and electrical measurements of plasmonic cavity formed between two Au-coated tips, shown in dark-field microscope images (**b**) and false-colour scanning electron microscope image (**c**) of a typical tip, end radius $R = 150$ nm. **d**, Measured dark field scattering spectra from one inter-tip cavity at different cavity widths d . Plasmonic cavity resonances are labelled A–C.

¹Nanophotonics Centre, Cavendish Laboratory, University of Cambridge, Cambridge CB3 0HE, UK. ²Material Physics Center CSIC-UPV/EHU and Donostia International Physics Center DIPC, Paseo Manuel de Lardizabal 5, 20018 Donostia-San Sebastián, Spain. ³Institut des Sciences Moléculaires d'Orsay – UMR 8214, CNRS-Université Paris Sud, Bâtiment 351, 91405 Orsay Cedex, France.

Each piezoelectric scan investigates three interaction regimes: capacitive near-field coupling ($50 \text{ nm} > d > 1 \text{ nm}$), quantum regimes ($1 \text{ nm} > d > 0 \text{ nm}$) and physical contact with conductive coupling ($d \leq 0 \text{ nm}$). Crucially, this set-up allows us to resolve the gradual transition between each regime dynamically. The measured dark-field scattering spectra (Fig. 1d) within the capacitive regime ($d \approx 40 \text{ nm}$) show a single plasmonic scattering peak centred near $\lambda = 750 \text{ nm}$ (mode A). As d is reduced, this peak redshifts owing to increasing near-field interactions between the tip plasmons. As the cavity shrinks below 20 nm , a second scattering peak emerges at shorter wavelengths (mode B, $\lambda = 550 \text{ nm}$) and quickly increases in intensity. Modes A and B smoothly redshift until an estimated separation $d = 5 \text{ nm}$, whereupon attractive inter-tip forces overwhelm the AFM-cantilever restoring force and snap the tips into close proximity²⁹. However no current flow is detectable because this snap-to-contact point does not coincide with conductive contact and the metal surfaces remain separated. Snap-to-contact reduces d to $\sim 1 \text{ nm}$, significantly increasing the plasmonic interaction and dramatically changing the plasmonic scattering resonances (blue curve, Fig. 1d). This increased coupling further redshifts modes A and B and reveals a new higher-order resonance (mode C) at $\lambda = 540 \text{ nm}$. After snap-to-contact, increased piezoelectric displacement applies an additional compressive force (0.1 nN per nm of displacement), pushing the tips into closer proximity. After 11.4 nN of force in this run, current flow is detected through the tips, indicating metal-to-metal surface contact. Detailed calculations confirm that the coupled plasmonic modes observed are tightly confined in the nanocavity (see below, and Supplementary Information).

Simultaneously monitoring the optical and electrical properties during approach reveals in detail the plasmon evolution through the subnanometre regime (Fig. 2a–c). As the applied force increases and d is reduced, all three modes redshift and modes A and B weaken while mode C intensifies. The line widths of modes A and B decrease in concert with this reduced scattering strength while mode C broadens owing to increased scattering loss. These spectral changes are well-reproduced by simulations that include quantum tunnelling (Fig. 2d). The calculations employ the quantum corrected model (QCM), a new approach derived from time-dependent density-functional theory that allows incorporation of quantum coherent electron tunnelling into a classical electromagnetic framework to treat large plasmonic systems (Supplementary Information)¹⁵. For $d \gtrsim 0.4 \text{ nm}$, plasmon interactions are consistent with the classical picture (Fig. 2e), accounting for rapidly increasing redshifts as d decreases and a transfer of oscillator strength from modes A and B to mode C, as observed. Although these higher-order coupled modes have been predicted theoretically^{7,8}, they are clearly revealed here dynamically on approach.

At an applied force greater than 8 nN , a new regime is seen that deviates strongly from the classical predictions; modes A and B are now shifting back to shorter wavelengths instead of redshifting divergently. This crossover is clearly seen in the QCM simulations at $d \approx 0.31 \text{ nm}$ (Fig. 2d). The quantum and classical predictions diverge at this crossover point (d_{QR}) because the plasmon interactions enter the quantum regime (QR) when d is sufficiently small to support a critical electron tunnelling rate between the surfaces. Although electron confinement within each tip is minimally affected at this separation, the quantum tunnelling here dramatically modifies the correlations between electronic fluxes¹⁵. The net result is that quantum-tunnelling charge transfer screens the localized plasmon surface charge, decreasing the enhanced fields and reducing plasmonic coupling. For $d < d_{\text{QR}}$, this quantum tunnelling increases exponentially and quickly dominates, creating charge-transfer plasmon modes that blueshift towards $d = 0$.

The redshift-to-blueshift crossover corresponds to the threshold at which quantum-tunnelling charge reduction starts balancing the near-field capacitive coupling. We can estimate d_{QR} roughly by considering charge tunnelling between the surfaces over an optical half-cycle. In the simplest model of a rectangular barrier, when half the plasmon charge is transferred across the junction for a critical gap (\tilde{d}_{QR}) marking

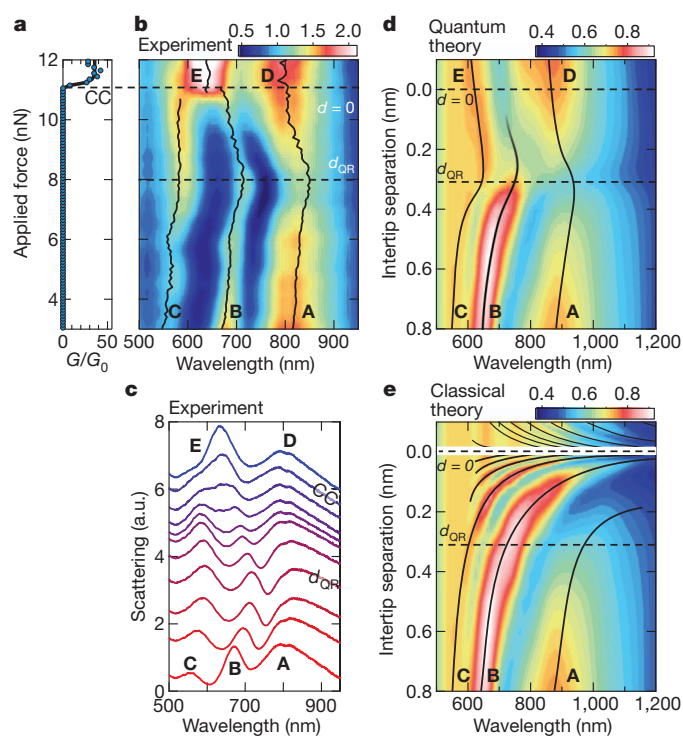


Figure 2 | Onset of quantum tunnelling in sub-nm plasmonic cavities.

a, b, Simultaneously measured electrical conductance (**a**) and dark-field optical back-scattering (**b**) with increasing force applied to the inter-tip cavity after snap-to-contact. Conductive contact (CC) indicates $d = 0$, with onset of quantum regime at d_{QR} . Lines track peak positions. **c**, Selected experimental spectra from the last 1 nm to contact in **b**, shown vertically shifted. **d**, Theoretical total scattering intensity from a tip–tip system incorporating quantum mechanical tunnelling. The threshold (at d_{QR}) indicates where quantum-tunnelling-induced charge screening overcomes the near-field capacitive interaction between plasmons. **e**, Theoretical scattering intensity as in **d** but using purely classical calculations.

the onset of the quantum regime, $\tilde{d}_{\text{QR}} = \ln(3q\lambda\alpha/2\pi)/2q$, where q is the semiclassical electron tunnelling wavenumber, λ is the optical plasmon wavelength and $\alpha \approx 1/137$ is the fine structure constant (see Supplementary Information). At $\lambda = 850 \text{ nm}$, this zeroth-order calculation gives $\tilde{d}_{\text{QR}} = 0.16 \text{ nm}$. Full calculations show that at $d_{\text{QR}} \approx 0.31 \text{ nm}$ sufficient screening has already developed via the quantum transport to overcome the increasing charge build-up, consistent with the estimate for \tilde{d}_{QR} above. Realistically including the coherent quantum transport strongly enhances the tunnelling rate compared to the estimate for the square tunnel barrier used above, increasing the distance at which tunnelling plasmonics takes over, and dictating the emergence of quantum-tunnelling charge-transfer plasmons.

After conductive contact ($d = 0$), when the conductance G first jumps above $G_0 = 2e^2/h$ (here e is the charge on the electron), two scattering peaks are observed—modes D (800 nm) and E (640 nm). Tracking modes A, B and C through the quantum regime as $d \rightarrow 0$ shows the gradual nature of this contact transition, in marked contrast to the singular transition predicted classically (Fig. 2e), where a dense continuum of modes builds up in the touching limit^{7,8}. At d_{QR} mode A weakens sharply, before a new peak appears which blueshifts and intensifies towards conductive contact. While mode B weakens at d_{QR} , mode C strengthens as predicted by the QCM. In both theory and experiment, modes B and C are replaced by mode E at contact. Spectra and conductance change minimally for increasing contact force after conductive contact, indicating a stable final contact. Experiments on a variety of tips show repeatable crossover behaviour at $d < d_{\text{QR}}$ (see Supplementary Information), which forms an optical fingerprint of the new tunnelling plasmonics regime.

To understand plasmon evolution through the quantum regime, the cavity field-distribution is calculated within the QCM accounting for quantum effects (Fig. 3). This allows us to construct a model of tunnelling plasmonics (Fig. 3a). For $d > d_{\text{QR}}$ (I in Fig. 3a), spectra are dominated by the near-field interaction of the cavity-localized surface charges and plasmons couple according to classical models. Once $d \approx d_{\text{QR}}$, the system enters the quantum regime (II in Fig. 3a) and tunnelling opens a conductance channel between the surfaces, modifying the plasmon charge distribution, screening the electric field and reducing the interaction strength. The tunnelling (which is strongly concentrated across the thinnest barrier region) pinches off the field distribution in the centre of the gap, systematically separating the single field lobe into two lobes in the crevices on either side of the neck (Fig. 3b). As d is reduced further (III in Fig. 3a, b), these quantum-tunnelling charge-transfer modes concentrated around the contact crevices blueshift as their apices become blunter. Around d_{QR} , the mode strengths of A and B reach their weakest values because the tunnelling increases sufficiently to screen the charges across the gap, but cannot provide sufficient current to drive the charge-transfer modes into the crevices. Hence at this point the total separated charge localized to the contact region decreases, reducing the optical cross-section.

The onset of quantum tunnelling fundamentally limits optical field confinement in plasmonic nanocavities. The plasmonic surface charge between two spherical surfaces of curvature R is confined laterally to $w \approx \sqrt{Rd}$ (ref. 7), as confirmed by our simulations (Fig. 3c). However, quantum tunnelling limits w to $w_{\text{QL}} \geq \sqrt{Rd_{\text{QR}}}$. Further reducing d rapidly increases the mode spatial width, as the surfaces are quantum-mechanically blurred at this microscopic scale. The tunnelling plasmonics regime thus represents the quantum limit of compression of light that is plasmonically squeezed into a nanogap, as verified in our experiments and QCM calculations. The quantum-limited mode volume can be approximated as $V_{\text{min}} = \pi R d_{\text{QR}}^2 / 4$, which is estimated to be $V_{\text{min}} \approx 1.7 \times 10^{-8} \lambda^3$ in our experiments at $\lambda = 850$ nm (mode A at d_{QR}). As this limit for plasmonics is six orders of magnitude smaller than the tightest field confinement observed in photonic crystal cavities, it still offers unprecedented opportunities for directly visualizing atomic-scale and molecular processes with electronvolt-scale photons.

These experimental and theoretical investigations of plasmonic interactions in subnanometre metal cavities demonstrate that quantum mechanics is already important at the 0.3-nm scale at which tunnelling plasmonics starts to dominate. This understanding is crucial for describing light-matter interactions down to the atomic scale. Stabilizing

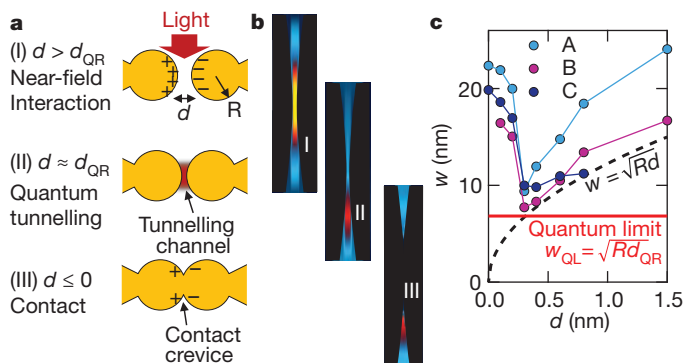


Figure 3 | Evolution of the plasmonic modes through the quantum regime and the quantum limit of plasmonic confinement. **a**, Plasmonic interactions within the three regimes accessed in experiment. **b**, Near-field distributions for modes B \rightarrow E from the QCM theory in each regime. Images are of 40 nm by 5 nm region, same intensity scale. **c**, The lateral confinement width w of each mode, extracted from the simulated near-field distribution, as the cavity width d is reduced. The dashed line marks the classical approximation $w = \sqrt{Rd}$. The onset of quantum tunnelling effects at $d = d_{\text{QR}} = 0.31$ nm sets a quantum limit (w_{QL}) on mode confinement in subnanometre plasmonic cavities.

single-atom contacts or wires will give direct plasmonic access to the quantum transport regime around $1G_0$ (ref. 30). Our work opens up new prospects, such as directing and controlling the chemistry of single molecules within nanogaps (for example, for enhanced photocatalysis), exploiting single-molecule plasmon-assisted transport across nanogaps (for example, for single-molecule electronics), investigating extreme nonlinear interactions and accessing photo-electrochemistry on the subzeptolitre scale.

METHODS SUMMARY

Experimental. Au-coated, ball-type AFM tips (150 nm radius of curvature) were obtained from Nanotools and used as received. Tips were mounted on separate three-axis piezoelectric actuation stages, axially aligned tip-to-tip at long range ($d > 50$ nm) using a nonlinear electrostatic-force technique²⁸, then brought together in 1-nm steps. Plasmons in the nanoscale cavity formed between the tip surfaces were excited with a supercontinuum laser tightly focused by a 0.9NA, 100 \times magnification objective in a dark field configuration. Scattered light was collected with the same objective and spatially filtered with a confocal pinhole to suppress background scattering. Spectral content of the scattered light was measured using a spectrometer with 3-ms integration time. Simultaneous electrical conductance measurements were taken by applying a submillivolt d.c. bias between the tips and measuring the resulting current.

Theoretical. Far-field scattering spectra and local-field distributions were calculated while reducing the inter-tip separation to identify the optical signature of tunnelling plasmonics and understand plasmon mode evolution through the quantum regime. Electron tunnelling effects were incorporated into a classical electrodynamics simulation using the QCM approach¹⁵ to account for the quantum-mechanical tunnelling between particles. The tunnelling gap is described by a quantum-corrected dielectric function constructed from the full quantum-mechanical jellium calculation of the static gap conductivity. The optical response of the structure was then solved using a boundary-element method. Corresponding purely classical simulations were also performed.

Received 21 June; accepted 2 October 2012.

Published online 7 November 2012.

- Xu, H., Bjerneld, E. J., Käll, M. & Börjesson, L. Spectroscopy of single hemoglobin molecules by surface enhanced Raman scattering. *Phys. Rev. Lett.* **83**, 4357–4360 (1999).
- Schuck, P. J., Fromm, D. P., Sundaramurthy, A., Kino, G. S. & Moerner, W. E. Improving the mismatch between light and nanoscale objects with gold bowtie nanoantennas. *Phys. Rev. Lett.* **94**, 017402 (2005).
- Cubukcu, E., Kort, E. A., Crozier, K. B. & Capasso, F. Plasmonic laser antenna. *Appl. Phys. Lett.* **89**, 093120 (2006).
- Curto, A. G. *et al.* Unidirectional emission of a quantum dot coupled to a nanoantenna. *Science* **329**, 930–933 (2010).
- Atwater, H. A. & Polman, A. Plasmonics for improved photovoltaic devices. *Nature Mater.* **9**, 205–213 (2010).
- Nordlander, P., Oubre, C., Prodan, E., Li, K. & Stockman, M. I. Plasmon hybridization in nanoparticle dimers. *Nano Lett.* **4**, 899–903 (2004).
- Romero, I., Aizpurua, J., Bryant, G. W. & de Abajo, F. J. G. Plasmons in nearly touching metallic nanoparticles: singular response in the limit of touching dimers. *Opt. Express* **14**, 9988–9999 (2006).
- Aubry, A., Lei, D. Y., Maier, S. A. & Pendry, J. B. Interaction between plasmonic nanoparticles revisited with transformation optics. *Phys. Rev. Lett.* **105**, 233901 (2010).
- Prodan, E., Radloff, C., Halas, N. J. & Nordlander, P. A hybridization model for the plasmon response of complex nanostructures. *Science* **302**, 419–422 (2003).
- Atay, T., Song, J.-H. & Nurmikko, A. V. Strongly interacting plasmon nanoparticle pairs: from dipole-dipole interaction to conductively coupled regime. *Nano Lett.* **4**, 1627–1631 (2004).
- Jain, P. K., Huang, W. & El-Sayed, M. A. On the universal scaling behavior of the distance decay of plasmon coupling in metal nanoparticle pairs: a plasmon ruler equation. *Nano Lett.* **7**, 2080–2088 (2007).
- Danckwerts, M. & Novotny, L. Optical frequency mixing at coupled gold nanoparticles. *Phys. Rev. Lett.* **98**, 026104 (2007).
- Lassiter, J. B. *et al.* Close encounters between two nanoshells. *Nano Lett.* **8**, 1212–1218 (2008).
- Taylor, R. W. *et al.* Precise subnanometer plasmonic junctions for SERS within gold nanoparticle assemblies using cucurbit[*n*]uril glue. *ACS Nano* **5**, 3878–3887 (2011).
- Esteban, R., Borisov, A. G., Nordlander, P. & Aizpurua, J. Bridging quantum and classical plasmonics. *Nature Commun.* **3**, 825 (2012).
- Novotny, L. & van Hulst, N. Antennas for light. *Nature Photon.* **5**, 83–90 (2011).
- Scholl, J. A., Koh, A. L. & Dionne, J. A. Quantum plasmon resonances of individual metallic nanoparticles. *Nature* **483**, 421–427 (2012).
- Ciraci, C. *et al.* Probing the ultimate limits of plasmonic enhancement. *Science* **337**, 1072–1074 (2012).

19. Zuloaga, J., Prodan, E. & Nordlander, P. Quantum description of the plasmon resonances of a nanoparticle dimer. *Nano Lett.* **9**, 887–891 (2009).
20. Song, P., Nordlander, P. & Gao, S. Quantum mechanical study of the coupling of plasmon excitations to atomic-scale electron transport. *J. Chem. Phys.* **134**, 074701 (2011).
21. Kern, J. *et al.* Atomic-scale confinement of resonant optical fields. *Nano Lett.* <http://dx.doi.org/10.1021/nl302315g> (published online 17 September 2012).
22. Duan, H., Fernández-Domínguez, A. I., Bosman, M., Maier, S. A. & Yang, J. K. W. Nanoplasmonics: classical down to the nanometer scale. *Nano Lett.* **12**, 1683–1689 (2012).
23. Bragas, A. V., Landi, S. M. & Martínez, O. E. Laser field enhancement at the scanning tunneling microscope junction measured by optical rectification. *Appl. Phys. Lett.* **72**, 2075–2077 (1998).
24. Schneider, N. L., Schull, G. & Berndt, R. Optical probe of quantum shot-noise reduction at a single-atom contact. *Phys. Rev. Lett.* **105**, 026601 (2010).
25. Chen, C., Bobisch, C. A. & Ho, W. Visualization of Fermi's golden rule through imaging of light emission from atomic silver chains. *Science* **325**, 981–985 (2009).
26. Ward, D. R., Hüser, F., Pauly, F., Cuevas, J. C. & Natelson, D. Optical rectification and field enhancement in a plasmonic nanogap. *Nature Nanotechnol.* **5**, 732–736 (2010).
27. Johansson, P. Light emission from a scanning tunneling microscope: fully retarded calculation. *Phys. Rev. B* **58**, 10823–10834 (1998).
28. Savage, K. J., Hawkeye, M. M., Soares, B. F. & Baumberg, J. J. From microns to kissing contact: dynamic positioning of two nano-systems. *Appl. Phys. Lett.* **99**, 053110 (2011).
29. Cappella, B. & Dietler, G. Force distance curves by atomic force microscopy. *Surf. Sci. Rep.* **34**, 1–104 (1999).
30. Ittah, N. & Selzer, Y. Electrical detection of surface plasmon polaritons by 1G₀ gold quantum point contacts. *Nano Lett.* **11**, 529–534 (2011).

Supplementary Information is available in the online version of the paper.

Acknowledgements This work was supported by EPSRC grants EP/G060649/1 and EP/H007024/1, EU grant CUBi-HOLE, and projects FIS2010-19609-C02-01 and EUI200803816 from the Spanish Ministry of Science and Innovation. J.J.B. also acknowledges support from the Ikerbasque Foundation, Jesus College Cambridge and the University of Cambridge, and M.M.H. acknowledges support from a Canadian NSERC post-doctoral fellowship.

Author Contributions J.J.B. conceived of and planned the experiments. K.J.S. and M.M.H. designed, constructed and performed the experiments. J.A., A.G.B. and R.E. conceived of the theoretical approach, and carried out the calculations. All the authors contributed to analysing the results and writing the paper.

Author Information Reprints and permissions information is available at www.nature.com/reprints. The authors declare no competing financial interests. Readers are welcome to comment on the online version of the paper. Correspondence and requests for materials should be addressed to J.J.B. (jjb12@cam.ac.uk).

Linking synchronization to self-assembly using magnetic Janus colloids

Jing Yan¹, Moses Bloom², Sung Chul Bae¹, Erik Luijten^{2,3} & Steve Granick^{1,4,5}

Synchronization occurs widely in the natural and technological worlds, from the rhythm of applause and neuron firing¹ to the quantum mechanics of coupled Josephson junctions², but has not been used to produce new spatial structures. Our understanding of self-assembly has evolved independently in the fields of chemistry and materials, and with a few notable exceptions^{3,4} has focused on equilibrium rather than dynamical systems. Here we combine these two phenomena to create synchronization-selected microtubes of Janus colloids, micron-sized spherical particles with different surface chemistry on their opposing hemispheres, which we study using imaging and computer simulation. A thin nickel film coats one hemisphere of each silica particle to generate a discoid magnetic symmetry, such that in a precessing magnetic field its dynamics retain crucial phase freedom. Synchronizing their motion, these Janus spheres self-organize into micrometre-scale tubes in which the constituent particles rotate and oscillate continuously. In addition, the microtube must be tidally locked to the particles, that is, the particles must maintain their orientation within the rotating microtube. This requirement leads to a synchronization-induced structural transition that offers various applications based on the potential to form, disintegrate and fine-tune self-assembled in-motion structures *in situ*. Furthermore, it offers a generalizable method of controlling structure using dynamic synchronization criteria rather than static energy minimization, and of designing new field-driven microscale devices in which components do not slavishly follow the external field.

Consider applause after a musical performance⁵. After a short period of chaotic clapping, applause often becomes rhythmic—everyone claps with the same phase and tempo. This illustrates fundamental elements of synchronization: the individual units display periodic motion, they display adjustable phase and frequency, and they couple⁶. However, in such classic synchronization problems units lack the freedom to change position in response to their interaction, a spatial adaptability that is essential to self-assembly. Here we considered situations where synchronization and self-assembly are inextricably linked and led to a new type of colloidal assembly. As proof of concept, we examined the example of magnetic Janus spheres.

Thin nickel films (18 nm or 21 nm) were directionally deposited onto one hemisphere of 3- μm spherical silica particles^{7,8}. The magnetic response of these particles is smaller along the Janus director (red arrow in Fig. 1a) and larger in the plane perpendicular to it (Supplementary Fig. 2), yielding a discoid symmetry. Suspended in deionized water, the spheres sedimented close to the chamber bottom. In optical images they appeared like the phases of the moon, owing to the dark metal coating. By applying a precessing magnetic field^{9–11} (Fig. 1a), we produced a torque on each sphere with two orthogonal components, one that drove it to spin around the precession axis with angle φ , and another that drove it to oscillate perpendicular to the rotating plane with angle α (Supplementary Fig. 4 and Supplementary Videos 1 and 2). The resulting dynamics, which

resembled a gyroscope's nutation, are quantitatively captured by the equations of motion (Methods). Notably, the rotation and oscillation frequencies can be controlled by the precession angle θ (Fig. 1b).

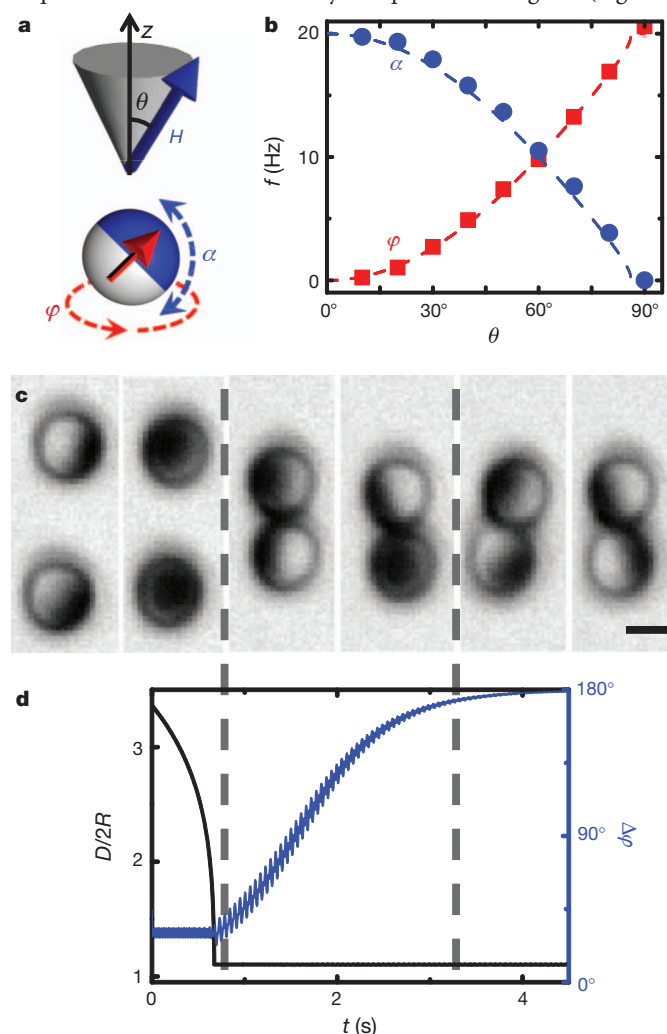


Figure 1 | Single- and two-particle dynamics in precessing fields. **a**, Janus director (red) rotates around precession axis z (angle φ) while oscillating perpendicularly (angle α), in a precessing field H with precession angle θ . **b**, Measured frequencies of φ and α versus θ confirm predictions (dashed lines). Nickel coating, 18 nm. **c**, Images of two approaching particles at $\theta = 25^\circ$ (precession axis is vertical) at successive times. Initially approximately in-phase, the directors end in anti-phase (scale bar, 2 μm). **d**, Centre-to-centre separation D (normalized by diameter $2R$) and phase difference $\Delta\varphi$ versus time t from simulations under the same conditions. After the separation reaches its minimum, $\Delta\varphi$ gradually approaches its steady-state value 180° . Vertical dashed lines mark corresponding parts of panels **c** and **d**.

¹Department of Materials Science and Engineering, University of Illinois, Urbana, Illinois 61801, USA. ²Department of Materials Science and Engineering, Northwestern University, Evanston, Illinois 60208, USA. ³Department of Engineering Sciences and Applied Mathematics, Northwestern University, Evanston, Illinois 60208, USA. ⁴Department of Physics, University of Illinois, Urbana, Illinois 61801, USA. ⁵Department of Chemistry, University of Illinois, Urbana, Illinois 61801, USA.

Hence, for most experiments we employed a fixed frequency f (20 Hz) and field strength (5 mT), leaving θ as the control parameter. Although composed of Brownian particles, the system was deterministic, with interactions around 10^4 times the thermal energy. Therefore, our findings could in principle scale up to macroscopic systems.

Phase freedom¹², a consequence of the discoid magnetic symmetry, allows interacting spheres to adjust their phases. For example, two particles (Fig. 1c) initially attract and approach until stopped by electrostatic repulsion at a separation of about 200 nm. Only at this close separation does the magnetic field created by one particle generate an appreciable torque on the other particle. Although small, this torque gradually drove the two particles to an antiphase steady state in both α and ϕ , regardless of the initial state. Once synchronized, the particles' rotation slowed slightly, while their geometric centres started to rotate around a common central axis. Their spatial positions are staggered head-to-tail owing to the Janus feature, which is captured in simulation by a point dipole moment shifted from the particle's geometric centre¹³. We observed frequency locking even when particles had different coating thicknesses and hence different inherent frequencies.

Next we considered suspensions of these Janus spheres. At low precession angle θ , we observed a family of long, defect-free microtubes forming spontaneously (region I in Fig. 2a). Structurally, unlike the chiral helices observed in amphiphilic self-assembly¹⁴ or magnetic assembly directed by steric hindrance¹⁵, these microtubes were achiral and can be interpreted as staggered stacks of regular polygons with k edges (Fig. 2b). We labelled them $(kk0)$, following classic nomenclature¹⁶. Their formation followed a nucleation-and-growth scheme (Supplementary Video 5). Initially, zigzag chains approached and wrapped around one another randomly, then short ordered $(kk0)$ strands nucleated, and finally nuclei propagated to 'zip up' a corresponding structure. Once formed, these structures rolled on the substrate. Within region I of the dynamic state diagram, the distribution of microtubes changed with θ (Fig. 2c): increasing θ shifted the distribution towards smaller k . On exceeding a threshold θ only zigzag chains were observed (region II) and subsequent increase of θ transformed them in known ways^{9,11} into hexagonal sheets oriented perpendicular to the precession axis (region III, Fig. 2d). The synchronization-induced structural transitions of interest here occurred at relatively low θ where the frequency dependence is small.

Although static tubular packings have long been known¹⁶ and realized recently¹⁷, here the spheres remained in continual motion, exhibiting nutation-like dynamics even within the aggregate. Moreover, they synchronized: for example, Supplementary Video 7 shows three particles within a triangular cross-section of the (330) structure, locked into a 120° phase shift (Fig. 3a).

The most striking synchronization occurred between the rotating microtube and its constituent particles, such that the spheres' metallic faces continually faced inward, reminiscent of the familiar tidal locking of the Moon and Earth. This dynamic requirement is the key to understanding the structural stability. We analysed this system ignoring interactions between microtubes, which is a valid assumption for a broad range of volume fractions. We considered a (330) structure in its lowest-energy configuration in a static field, with each sphere's director pointing to the central axis. Once the precessing field was switched on, the constituent particles rotated with respect to the tube and adopted an average orientation that deviates from inward-pointing by an angle ψ defined in Fig. 3b. Distorting the lowest-energy configuration, this generated a restoring torque $dE/d\psi$ (incorporating all many-body interactions) that rotated the tube while slowing the constituent particles. It was proportional to $\sin\psi$ (Supplementary Fig. 9) with a proportionality coefficient ε that quantifies rotational coupling between the tube and particle and depends on the instantaneous tube configuration. Balancing this magnetic torque with viscous drag, we find (see Supplementary Information for the derivation):

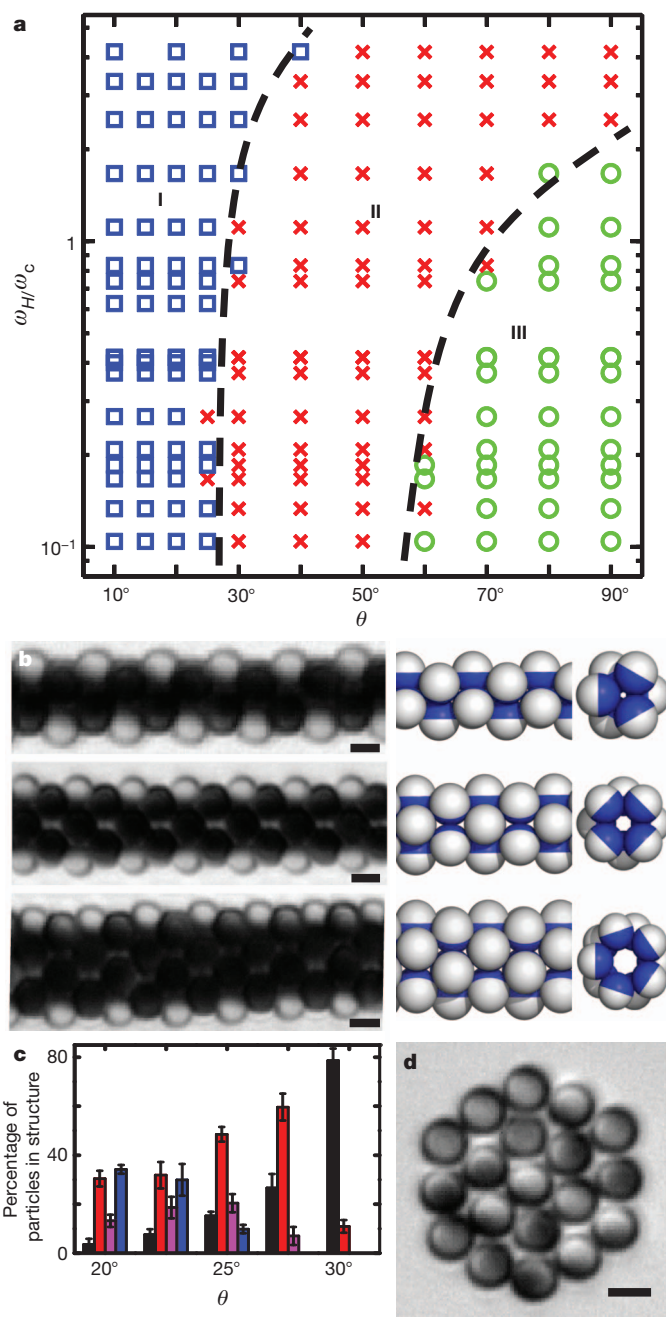


Figure 2 | Synchronized self-assembly. **a**, Measured dynamic state diagram in the ω_H - θ plane. The external field frequency ω_H is normalized by the characteristic frequency ω_c (Methods). Boundaries (black lines) are guides to the eye. Regions I, II and III involve microtubes, zigzag chains and planar sheets, respectively. **b**, Observed images (left) and corresponding models (right, side and end views) of microtubes ($k = 3, 4, 5$) parallel to the precession axis. **c**, Dependence on θ of the distribution of microtubes. Nickel coating, 21 nm. (550), blue; (440), magenta; (330), red; zigzag chain, black. Error bars correspond to one standard deviation. Results are obtained from four independent samples each containing more than 3,000 particles. **d**, Hexagonal sheets perpendicular to the precession axis in region III ($\theta = 70^\circ$). All scale bars are 3 μm .

$$\frac{d\psi}{dt} = \omega_{\text{free}} - \varepsilon(\zeta_r^{-1} + \zeta_{\text{tube}}^{-1}) \sin \psi \quad (1)$$

Here ω_{free} is the angular velocity of free particles under the same condition, and ζ_r and ζ_{tube} are the rotational friction coefficients of the single particle and the entire tube, respectively. Although in principle the hydrodynamic forces^{18,19} should matter, their effect is secondary to

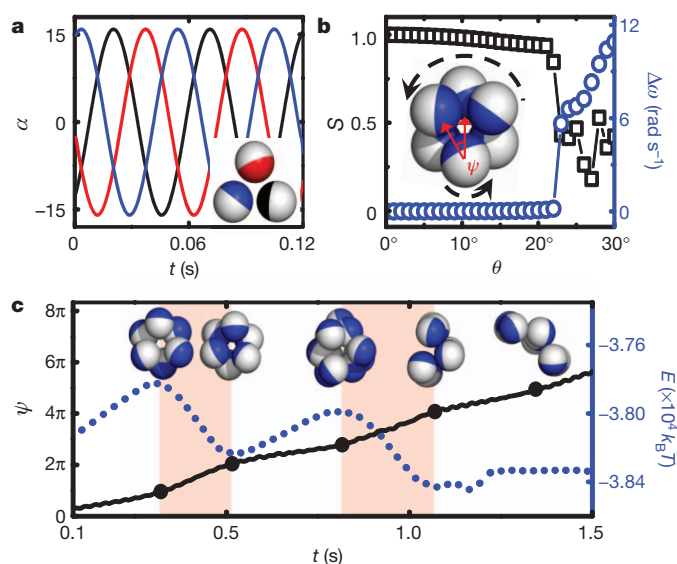


Figure 3 | Synchronization-induced structural transitions. **a**, Illustration of phase locking of the oscillation angle α for cross-sectional particles in a (330) microtube (inset), simulated at $\theta = 18^\circ$. **b**, Order parameter S and difference $\Delta\omega$ in rotation frequency between constituent particle and microtube, plotted versus θ for simulated (330) microtube (inset). Particle directors deviate from centre-pointing by angle ψ . Arrows indicate rotation of tube and individual sphere. **c**, Time evolution of ψ (black) and energy E (blue) during disassembly of an unstable (330) microtube at $\theta = 30^\circ$. Shaded regions highlight phase slip. Snapshots (inset models) along the time axis are shown at times indicated by dots.

the magnetic forces (Supplementary Information). Equation (1) has the same mathematical form as the classical Adler equation for synchronization²⁰, so we can apply all the general analyses of this equation.

A crucial prediction of equation (1) is the existence of a critical frequency above which an assembly cannot track its constituent particles. If $\omega_{\text{free}} > \varepsilon(\zeta_r^{-1} + \zeta_{\text{tube}}^{-1})$, no steady-state solution (that is, $d\psi/dt = 0$) exists. In that case, the time trajectory of ψ displays periodic phase slips²¹ (shaded regions in Fig. 3c), leading to a transient high-energy configuration where the magnetic hemispheres of constituent particles face outward. This unsynchronized state ultimately dissociated into a loose aggregate of zigzag chains with lower average energy. Because ω_{free} depends monotonically on θ , a critical ω_{free} translates into a critical θ_c . Figure 3b confirms the coupling between the loss of synchronization, characterized by the difference $\Delta\omega$ in rotational frequency of the constituent particles and the entire structure, and the structural transition, reflected by the sharp decrease of the positional order parameter S (defined in Methods). This process explains the boundary between regions I and II of Fig. 2a.

This dynamics-induced transition offers interesting possibilities for structural selection (Fig. 2c) that would not be possible with conventional static energy minimization. The large energy barriers between different ($kk0$) tubes preclude thermal equilibration and hence both in static fields and at low θ a broad distribution of k was observed. However, at higher θ , synchronization criteria set in. The larger the tube diameter, the smaller the coupling strength ε and the larger the friction ζ_{tube} , leading to lower dissociation angle θ_c . For example, with increasing θ in Fig. 2c we saw fewer (550) microtubes and none above θ_c (which is about 25° for this structure). The abundance of medium-diameter structures such as (330) thus first increased at the expense of thicker structures and dominated at some angles. This agrees qualitatively with the trend seen in simulation (Supplementary Fig. 13).

Modulation of the magnetic properties allows other types of tubular packing as well. Consistent with simulations from random initial conditions, we also observed ($kk2k$) and chiral structures when we coated the same nickel films onto paramagnetic spheres (Supplementary

Video 9). Such particles are indeed closer to the shifted-dipole model used in simulation, because their magnetic properties are dominated by the bulk rather than the thin film coating, whose magnetic properties are complicated by the coating profile²².

On the basis of their capacity for *in situ* assembly, disassembly and reconfigurability, the structures demonstrated in this study suggest various potential applications, such as selective cargo uptake and transport²³ inside these hollow microtubes and fluid flow control²⁴ with the known high efficiency of synchronized states^{6,19,24}. The path is also clear to extend these approaches using patterned arrays of external driving sources²⁵ to achieve spatially resolved reconfigurable structures.

These synchronization criteria suggest a materials selection method complementary to the conventional equilibrium approach of energy minimization. To dynamically destabilize structures that compete with targeted ones could benefit the current trend of designing self-assembly of anisotropic building blocks^{26–28} (which tend to form multiple possible structures), and may stimulate related consideration of other dynamical systems, both smaller (molecular) and larger (granular) than considered here. This argument applies generally to magnetic, electric, chemical and hydrodynamic fields. The required phase-free dynamics can be achieved by designing shapes more complex than the simple spheres considered here or more generally via a driving frequency so high that building blocks cannot track the field. Such non-slaved responses to external fields have been underappreciated in self-assembly but are shown here to result in structures impossible with classical slaved motion^{3,4,29,30}.

METHODS SUMMARY

Nickel coatings of 18 nm or 21 nm followed by 15–20 nm SiO₂ are deposited vertically onto a planar submonolayer of monodisperse 3-μm silica particles using electron-beam deposition. The particles are washed thoroughly with deionized water and isopropyl alcohol, then sonicated and collected in deionized water. A spatially homogeneous precessing magnetic field generated by three orthogonal pairs of solenoids is applied within a home-built microscope equipped with a 50× long-working-distance objective and a complementary metal–oxide–semiconductor camera. Particle tracking is performed using Matlab with home-written code. Molecular dynamics simulations are performed using spherical particles with excluded-volume interactions (represented by a shifted-truncated Lennard–Jones potential) and magnetic dipole moments computed self-consistently every time step. Magnetic parameters are chosen in accordance with experiment. Simulations involve up to 80 particles and cover 2×10^8 time steps, corresponding to 25.2 s in experiment; doubling the system size confirms the same trends.

Full Methods and any associated references are available in the online version of the paper.

Received 1 June; accepted 25 September 2012.

- Strogatz, S. *Sync: the Emerging Science of Spontaneous Order* Ch. 2 (Hyperion, 2003).
- Ozyuzer, L. *et al.* Emission of coherent THz radiation from superconductors. *Science* **318**, 1291–1293 (2007).
- Grzybowski, B. A., Stone, H. A. & Whitesides, G. M. Dynamic self-assembly of magnetized, millimetre-sized objects rotating at a liquid–air interface. *Nature* **405**, 1033–1036 (2000).
- Snezhko, A. & Aranson, I. S. Magnetic manipulation of self-assembled colloidal asters. *Nature Mater.* **10**, 698–703 (2011).
- Néda, Z., Ravasz, E., Brechet, Y., Vicsek, T. & Barabási, A.-L. The sound of many hands clapping. *Nature* **403**, 849–850 (2000).
- Pikovsky, A., Rosenblum, M. & Kurths, J. *Synchronization: a Universal Concept in Nonlinear Sciences* (Cambridge, 2001).
- Sinn, I. *et al.* Magnetically uniform and tunable Janus particles. *Appl. Phys. Lett.* **98**, 024101 (2011).
- Smoukov, S. K., Gangwal, S., Marquez, M. & Velev, O. D. Reconfigurable responsive structures assembled from magnetic Janus particles. *Soft Matter* **5**, 1285–1292 (2009).
- Osterman, N. *et al.* Field-induced self-assembly of suspended colloidal membranes. *Phys. Rev. Lett.* **103**, 228301 (2009).
- Tierno, P., Claret, J., Sagués, F. & Cèbers, A. Overdamped dynamics of paramagnetic ellipsoids in a precessing magnetic field. *Phys. Rev. E* **79**, 021501 (2009).
- Martin, J. E., Venturini, E., Gulley, G. L. & Williamson, J. Using triaxial magnetic fields to create high susceptibility particle composites. *Phys. Rev. E* **69**, 021508 (2004).

12. Kiss, I. Z., Zhai, Y. & Hudson, J. L. Emerging coherence in a population of chemical oscillators. *Science* **296**, 1676–1678 (2002).
13. Kantorovich, S., Weeber, R., Cerdà, J. J. & Holm, C. Ferrofluids with shifted dipoles: ground state structures. *Soft Matter* **7**, 5217–5227 (2011).
14. Chen, Q. *et al.* Supracolloidal reaction kinetics of Janus spheres. *Science* **331**, 199–202 (2011).
15. Zerrouki, D., Baudry, J., Pine, D., Chaikin, P. & Bibette, J. Chiral colloidal clusters. *Nature* **455**, 380–382 (2008).
16. Erickson, R. O. Tubular packing of spheres in biological fine structures. *Science* **181**, 705–716 (1973).
17. Lohr, M. A. *et al.* Helical packings and phase transformations of soft spheres in cylinders. *Phys. Rev. E* **81**, 040401(R) (2010).
18. Riedel, I. H., Kruse, K. & Howard, J. A self-organized vortex array of hydrodynamically entrained sperm cells. *Science* **309**, 300–303 (2005).
19. Kotar, J. *et al.* Hydrodynamic synchronization of colloidal oscillators. *Proc. Natl Acad. Sci. USA* **107**, 7669–7673 (2010).
20. Adler, R. A study of locking phenomena in oscillators. *Proc. Inst. Radio Engineers* **34**, 351–357 (1946).
21. Polin, M., Tuval, I., Drescher, K., Gollub, J. P. & Goldstein, R. E. *Chlamydomonas* swims with two “gears” in a eukaryotic version of run-and-tumble locomotion. *Science* **325**, 487–490 (2009).
22. Albrecht, M. *et al.* Magnetic multilayers on nanospheres. *Nature Mater.* **4**, 203–206 (2005).
23. Duncanson, W. J. *et al.* Microfluidic synthesis of advanced microparticles for encapsulation and controlled release. *Lab Chip* **12**, 2135–2145 (2012).
24. Vilfan, M. *et al.* Self-assembled artificial cilia. *Proc. Natl Acad. Sci. USA* **107**, 1844–1847 (2010).
25. Yellen, B. B., Hovorka, O. & Friedman, G. Arranging matter by magnetic nanoparticle assemblers. *Proc. Natl Acad. Sci. USA* **102**, 8860–8864 (2005).
26. Damasceno, P. F., Engel, M. & Glotzer, S. C. Predictive self-assembly of polyhedra into complex structures. *Science* **337**, 453–457 (2012).
27. Sacanna, S., Irvine, W. T. M., Chaikin, P. M. & Pine, D. J. Lock and key colloids. *Nature* **464**, 575–578 (2010).
28. Gerbode, S. J. *et al.* Glassy dislocation dynamics in 2D colloidal dimer crystals. *Phys. Rev. Lett.* **105**, 078301 (2010).
29. Vissers, T., van Blaaderen, A. & Imhof, A. Band formation in mixtures of oppositely charged colloids driven by an ac electric field. *Phys. Rev. Lett.* **106**, 228303 (2011).
30. Jäger, S. & Klapp, S. H. L. Pattern formation of dipolar colloids in rotating fields: layering and synchronization. *Soft Matter* **7**, 6606–6616 (2011).

Supplementary Information is available in the online version of the paper.

Acknowledgements This work was supported by the US Army Research Office, grant award number W911NF-10-1-0518 (Y.J., S.C.B. and S.G.) and by the National Science Foundation under award number DMR-1006430 (M.B. and E.L.). The methods of Janus particle fabrication were supported by the US Department of Energy, Division of Materials Science, under award number DE-FG02-07ER46471 through the Frederick Seitz Materials Research Laboratory at the University of Illinois at Urbana-Champaign. We acknowledge support from the National Science Foundation, CBET-0853737 for equipment and from the Quest high-performance computing facility at Northwestern University. We thank J. Whitmer for writing the original version of the simulation code.

Author Contributions J.Y. and S.G. initiated this work. J.Y. and S.C.B. built the set-up; J.Y. performed the experiments; M.B. and E.L. performed the modelling and simulations. J.Y., M.B., E.L. and S.G. wrote the paper.

Author Information Reprints and permissions information is available at www.nature.com/reprints. The authors declare no competing financial interests. Readers are welcome to comment on the online version of the paper. Correspondence and requests for materials should be addressed to E.L. (luijten@northwestern.edu) or S.G. (sgranick@uiuc.edu).

METHODS

Particle synthesis. Onto a planar submonolayer¹⁴ of monodisperse 3- μm silica particles (Tokuyama), an 18-nm or 21-nm nickel coating followed by a SiO_2 coating 15–20 nm thick is deposited vertically using electron-beam deposition. The SiO_2 layer prevents oxidation of nickel and makes the particle chemically isotropic. A control glass slide without particles is coated simultaneously and used to measure the apparent film thickness by ellipsometry (J. A. Woollam VASE ellipsometer). Magnetic hysteresis-loop measurements are performed using a SQUID magnetometer (Quantum Design MPMS-XL) on a dense monolayer of particles ($0.5\text{ cm} \times 0.5\text{ cm}$). The monolayer is washed thoroughly with deionized water and isopropyl alcohol, then sonicated in water to collect the particles. In deionized water, the particles have a ζ potential of $-36 \pm 6\text{ mV}$ (Malvern Zetasizer Nano).

Set-up. A spatially homogeneous precessing magnetic field is generated by three orthogonal pairs of solenoids (Science Source 14835 with iron cores, and custom-designed coils from Teachspin) in a home-built magnetic set-up. Two pairs of solenoids receive two sinusoidal voltages from a function generator (Agilent 33522A), amplified by power amplifiers (Kepco 100-4D), with $\pi/2$ phase difference between each signal to produce the rotating component of the precessing field. The third pair of solenoids is connected to a direct-current power supply (Hewlett-Packard 6266B), to provide the static component of the precessing field. The field strength and frequency response are calibrated using a triaxial Gaussmeter (Alpha Lab Model VGM). The magnetic field is homogeneous within 5% across 1 cm, which greatly exceeds the maximum field of view of $170\text{ }\mu\text{m} \times 128\text{ }\mu\text{m}$. Videos are taken in a home-built microscope using an LED light source (Thorlabs MCWHL2), a $50\times$ long-working-distance objective (Mitutoyo, numerical aperture 0.55) and a CMOS camera (Edmund Optics 5012M GigE).

Single-particle tracking. A dilute suspension ($\sim 10^{-2}\text{ mg ml}^{-1}$) of Janus particles in deionized water is introduced into the imaging chamber (Lab-Tek II chambered cover glass). The particles sediment to the bottom, but negative charges on the silica particles prevent adsorption to the chamber walls as well as irreversible clustering of particles. A precessing magnetic field is applied with precession axis either perpendicular or parallel to the bottom wall; in the parallel case the particles roll on the wall and translate accordingly. By restricting the field of view to a small area, we capture high-speed videos of single-particle dynamics at ~ 600 frames per second. The rotation and oscillation frequencies of the particles are determined using home-written Matlab code. For each θ , at least five particles are analysed. Standard deviations are smaller than the symbols in Fig. 1b.

Equations of motion. The full derivation and discussion are given in the Supplementary Information. In summary, by treating each particle as a paramagnetic sphere with an anisotropic susceptibility tensor, and balancing the magnetic torque by the viscous torque by assuming an overdamped condition¹⁰, we arrive at two coupled differential equations:

$$\frac{d\alpha}{dt} = \omega_c (\sin \alpha \cos \beta \sin \theta - \cos \alpha \cos \theta) (\cos \alpha \cos \beta \sin \theta + \sin \alpha \cos \theta)$$

$$\frac{d\beta}{dt} = \omega_H + \omega_c \frac{\sin \beta \sin \theta}{\cos \alpha} (\cos \alpha \cos \beta \sin \theta + \sin \alpha \cos \theta)$$

in which ω_H is the field frequency and φ and α are the azimuth angle and the complement of the inclination angle of the particle director defined in Supplementary Fig. 4, respectively. The parameter $\beta = \omega_H t - \varphi$ is the phase lag between the azimuth angles of the external field and the particle, and ω_c is defined as $\mu_{\text{water}} V_{\text{Ni}} \Delta \chi H^2 / \zeta_r$, a characteristic frequency arising when magnetic force and viscous force are balanced. μ_{water} is the permeability of the medium, V_{Ni} is the volume of magnetic material on a single particle, ζ_r is the rotational drag coefficient, and $\Delta \chi = \chi_{\perp} - \chi_{\parallel}$, where χ_{\parallel} is the susceptibility parallel to the Janus director \hat{n} and χ_{\perp} is the susceptibility in any direction perpendicular to \hat{n} . For example, the case of 18-nm Ni coating and 5-mT field strength yields $\omega_c = 942\text{ rad s}^{-1}$, corresponding to 150 Hz. We use this value and the equations of motion to predict the rotation/oscillation frequencies presented in Fig. 1b.

Protocol for applying the magnetic field. Before each experiment, particles are concentrated on one side of the cell using a 20-Hz, 5-mT rotating field that drives the particles towards one side of the imaging chamber. Subsequently a precessing field with opposite direction of rotation is applied with the precession axis parallel to the bottom of the sample cell (horizontal or vertical in the images). Videos are taken at rates of up to 300 frames per second for individual structures. Within 5 min, microtubes form and their distribution reaches a steady state within 10 min. We image the middle of the cell, covering a broad range of concentrations where individual tubes exist with minimum mutual interference. The distribution is quantified by visual inspection of the structures; rotation exposes different faces of the tubes, facilitating their determination. Over 3,000 particles are included in each sample. For each θ , at least four independent samples are analysed. Error bars in Fig. 2c correspond to one standard deviation.

Simulation. Molecular dynamics computer simulations are performed with self-consistent magnetic interactions and shifted-truncated Lennard-Jones interactions at field strength and frequency equivalent to 5 mT and 20 Hz, for 2×10^8 time steps. The system has dimensions $40 \times 40 \times 80$ or $40 \times 40 \times 160$ in reduced simulation units and contains up to 80 particles; doubling the system size confirms the same trends. The colloid diameter in these units is 4.3. The time step of 0.001 ($\approx 1.26 \times 10^{-7}\text{ s}$) provides energy stability in the overdamped regime where we operate. Each particle is treated as a sphere with a point dipole shifted from the particle's geometric centre. The anisotropic magnetic susceptibility is scaled by the experimental hysteresis curve and the dipole-moment shift is determined by matching the experimentally observed bond angle of the zigzag chain in a static magnetic field. Magnetic interactions are determined at each time step by solving the linear system of equations for each particle's magnetic moment as a function of the field produced by the other particles and the spatially uniform, time-dependent external field. Simulations to evaluate microtube structure stability begin with particles arranged in the given structure, at the equilibrium pair distance, with particles oriented towards the microtube's central axis. Particles relax into their steady-state configuration provided that the structure is stable for the given parameters. S is defined as $\frac{1}{n} \left| \sum_{j=1}^n \exp(i2k\theta_{jn}) \right|$, where θ_{jn} is the azimuth angle of a particle j 's position vector (Supplementary Fig. 8).

Water structural transformation at molecular hydrophobic interfaces

Joel G. Davis¹, Kamil P. Gierszal¹, Ping Wang¹ & Dor Ben-Amotz¹

Hydrophobic hydration is considered to have a key role in biological processes ranging from membrane formation to protein folding and ligand binding¹. Historically, hydrophobic hydration shells were thought to resemble solid clathrate hydrates^{2–4}, with solutes surrounded by polyhedral cages composed of tetrahedrally hydrogen-bonded water molecules. But more recent experimental^{5–8} and theoretical^{9–16} studies have challenged this view and emphasized the importance of the length scales involved. Here we report combined polarized, isotopic and temperature-dependent Raman scattering measurements with multivariate curve resolution (Raman-MCR)^{17–19} that explore hydrophobic hydration by mapping the vibrational spectroscopic features arising from the hydrophobic hydration shells of linear alcohols ranging from methanol to heptanol. Our data, covering the entire 0–100 °C temperature range, show clear evidence that at low temperatures the hydration shells have a hydrophobically enhanced water structure with greater tetrahedral order and fewer weak hydrogen bonds than the surrounding bulk water. This structure disappears with increasing temperature and is then, for hydrophobic chains longer than ~1 nm, replaced by a more disordered structure with weaker hydrogen bonds than bulk water. These observations support our current understanding of hydrophobic hydration, including the thermally induced water structural transformation that is suggestive of the hydrophobic crossover predicted to occur at lengths of ~1 nm (refs 5, 9, 10, 14).

Raman-MCR measurements yield solute-correlated (SC) spectra that contain features arising from both solute intramolecular vibrations and solute-induced perturbations of water OH stretch vibrations^{17–19}. All the SC spectra described here were extracted from replicate pure water and aqueous alcohol solution spectra using the MCR algorithm self-modelling curve resolution (SMCR)^{19,20}. SC spectra provide unambiguous evidence of water structure changes, because a SC spectrum would not contain any water OH spectral features if the structure of water in the solute's hydration shell were identical with that of bulk water. Because the perturbed OH features of interest underlie water's broad OH stretch band, detecting changes in the hydrophobic hydration-shell structure requires the measurement of solution Raman spectra with signal-to-noise ratios of at least 1,000:1 and little or no interfering background signal. This is achieved by using highly purified samples and a custom-built high-throughput micro-Raman system¹⁹. All experiments were performed at concentrations well below the onset of alcohol aggregation (as explained in Supplementary Discussion).

Figure 1a shows the Raman spectra of pure water and a 0.5 M (~0.01 mole fraction) aqueous n-butanol-d₉ solution at 20 °C; deuterated n-butanol was used to displace the solute CH stretch band from the water OH stretch band. The resulting SC spectrum (red curve in Fig. 1a and expanded inset) reveals a small dangling (non-hydrogen-bonded)^{17,21} water OH peak near 3,660 cm⁻¹ as well as two broad overlapping hydrogen-bonded OH features near 3,200 cm⁻¹ and 3,400 cm⁻¹. All of the OH features seen in the SC spectrum arise predominantly from hydration-shell water molecules (rather than from the alcohol's OH head group or hydrogen bonding between water and the alcohol head group), as confirmed by comparing results

obtained from solutes with different numbers of OH head groups (see Supplementary Methods and Supplementary Discussion). The lower panels in Fig. 1 demonstrate how SC spectra may be used to reveal changes in both tetrahedral ordering and hydrogen-bond strengths in water.

Figure 1b compares aqueous n-butanol-d₉ SC spectra obtained from total (V + H) and depolarized (H) Raman spectra, as well as the OH Raman band of pure water (blue). The red shaded region in Fig. 1b indicates that the hydration shell of n-butanol gives rise to strongly polarized lower-frequency OH stretch Raman scattering. Theoretical predictions of polarized Raman spectra of pure water^{22,23} and ice²⁴ suggest that highly polarized OH Raman scattering near 3,200 cm⁻¹ arises from tetrahedral water structures with strong intermolecular resonance coupling. Moreover, the relative intensity of the Raman

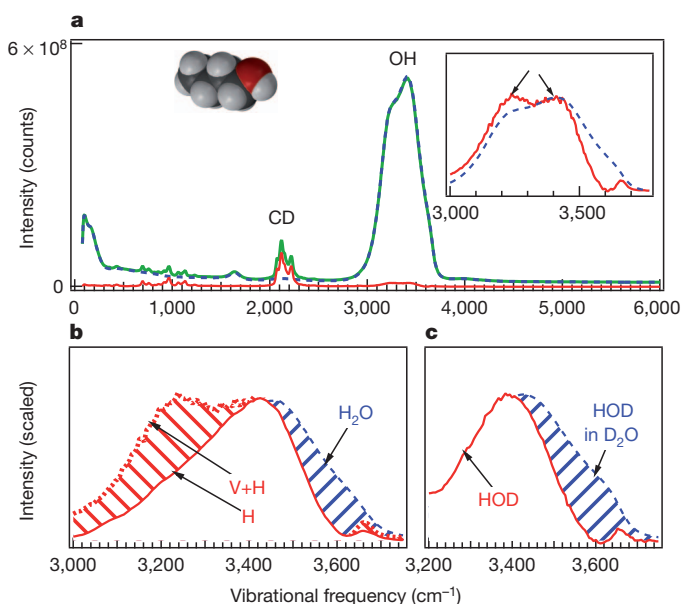


Figure 1 | Raman spectra of aqueous n-butanol-d₉. Shown are isotopic, polarized and SC Raman spectra at 20 °C that reveal differences between hydrophobic hydration-shell and bulk water structures. **a**, Raman spectra of pure water (blue) and a 0.5 M aqueous solution of n-butanol-d₉ (green), and the corresponding SC spectrum (red) with features that arise from solute intramolecular vibrations and from hydration-shell water molecules whose vibrational spectrum is perturbed by the solute. The inset shows an expanded view of the SC OH stretch region, and the OH band of pure water scaled to the same maximum intensity. Arrows indicate hydrogen-bonded OH; the small peak on the right is the dangling OH. **b**, Comparison of total (H + V) and depolarized (H) SC OH spectra, revealing the polarized character of the low-frequency hydration-shell OH Raman scattering (red region) indicative of increased tetrahedral order, and the depletion of the weakly hydrogen-bonded population (blue region). **c**, Isotopically dilute (n-butanol-d₉ in 10% HOD/D₂O) SC OH spectra, confirming the depletion of weak water hydrogen bonds in the hydration shell.

¹Purdue University, Department of Chemistry, West Lafayette, Indiana 47907, USA.

band near $3,200\text{ cm}^{-1}$ increases significantly on the formation of methane clathrate hydrates²⁵. Thus, the red shaded region in Fig. 1b implies that hydration-shell water molecules have greater tetrahedral order than bulk water. The blue shaded region in Fig. 1b implies that the hydrophobic hydration shell has fewer weak hydrogen bonds, as further demonstrated in Fig. 1c.

Figure 1c shows SC spectra obtained from *n*-butanol- d_9 dissolved in isotopically dilute water consisting of 10% HOD in D_2O . Such measurements serve to suppress OH resonance coupling and to ensure that the observed OH stretch Raman scattering arises from isolated OH bonds whose frequencies are better correlated with hydrogen-bond strength²². The difference between the red SC band and the blue bulk water OH band thus confirms that hydrophobic hydration leads to a depletion of the weakest (highest OH frequency) hydrogen-bond population. Although we believe that these are the first experiments to reveal this depletion, our results are consistent with molecular dynamics simulations of argon in water⁴ and of water structure around polypeptide hydrophobic residues¹¹ that found a reduced population of the weakest hydrogen bonds in the hydration shell compared with the bulk.

Figure 2a documents the structural transformation as the solution temperature is increased towards 100°C . Below 60°C , the SC spectra of aqueous *n*-pentanol look somewhat similar in shape to the *n*-butanol SC spectra at 20°C (compare with Fig. 1) and reflects the hydrophobically ordered water in the hydration shell (which is more tetrahedral and has fewer weak hydrogen bonds than bulk water). This population is greatest near 0°C and then decreases as the temperature approaches 60°C , at which point the small amplitude of the SC spectrum indicates that the structure of the hydration shell closely resembles that of bulk water (except for the excess dangling OH bond population at $\sim 3,660\text{ cm}^{-1}$). Above 60°C , a different hydration shell structure emerges: the average hydration-shell OH frequency is clearly higher than the average bulk water OH frequency (at the same temperature), implying a new water structure reminiscent of that at an air–water interface, at which water hydrogen bonds are also slightly weaker than in bulk water²⁶.

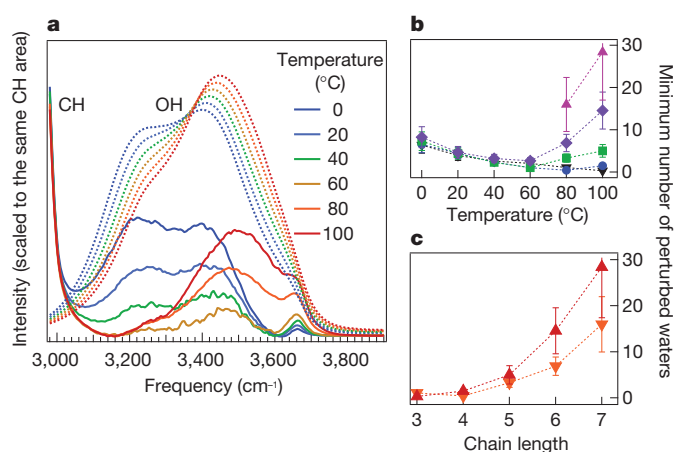


Figure 2 | Effect of temperature and alcohol chain length on water structural transformation. **a**, Temperature-dependent SC spectra of aqueous *n*-pentanol (solid curves) and the corresponding pure water Raman spectra (dashed curves), revealing the disappearance of the low-temperature structure (blue–green) and growth of the high-temperature structure (orange–red). **b**, **c**, Plots of the minimum number of perturbed hydration-shell waters against temperature (**b**; chain lengths: black, 3; blue, 4; green, 5; purple, 6; magenta, 7) and alcohol chain length (**c**; orange, 80°C ; red, 100°C), revealing the strong influence of chain length on the high-temperature hydration shell structural transformation. The points in **b** and **c** each represent mean values of three or more replicate measurement and the $\pm 30\%$ error bars represent typical standard deviations of these replicate measurements (except for the *n*-heptanol results, which have a standard deviation of about $\pm 40\%$).

We obtain the number of water OH groups whose vibrations are perturbed by the hydrophobic interface, and hence differ from bulk water, by integrating the areas of the SC OH bands (see Supplementary Methods). The numbers represent approximate lower bounds, because the observed SC OH spectral features can arise from a small number of strongly perturbed hydration-shell water molecules or from a larger number of less strongly perturbed water molecules. The number of perturbed OH groups changes with temperature (Fig. 2b) and with the number of carbons in the hydrophobic chain of the alcohol (Fig. 2c). At low temperatures this number decreases with increasing temperature, as the more tetrahedral structure gives way to a structure that more closely resembles bulk water. At higher temperatures the number of perturbed waters is strongly dependent on chain length, revealing that the new high-temperature water structure forms more readily around longer hydrophobic chains than around shorter chains (as further demonstrated in Fig. 3). These results indicate that most (and perhaps all) of the water molecules in the first hydration shell participate in the high-temperature structural transformation around *n*-heptanol, whose first hydration shell contains ~ 52 water molecules (determined as described in the Supplementary Methods).

A comparison of the temperature-dependent SC spectra of *n*-propanol and *n*-butanol (Fig. 3a, b) reveals that the new high-temperature structure does not form around linear alcohols with fewer than four carbons: the hydrophobic hydration shell of *n*-propanol in Fig. 3a retains a more tetrahedral structure over the entire liquid temperature range, and it has almost entirely disappeared at 100°C but has not yet been replaced by a more disordered and weakly hydrogen-bonded structure. Similar behaviour has also been obtained for shorter alcohols (see Supplementary Information and Supplementary Figs 2 and 3). The SC spectra of *n*-butanol in Fig. 3b reveal that adding one more carbon to the *n*-propanol chain is sufficient to induce the appearance of the high-temperature structural transformation of the hydration shell. The depolarized and isotopically dilute SC spectra of aqueous *n*-butanol in Fig. 3c and Fig. 3d, respectively, reveal that the temperature-dependent transformation that occurs above $\sim 80^\circ\text{C}$ involves

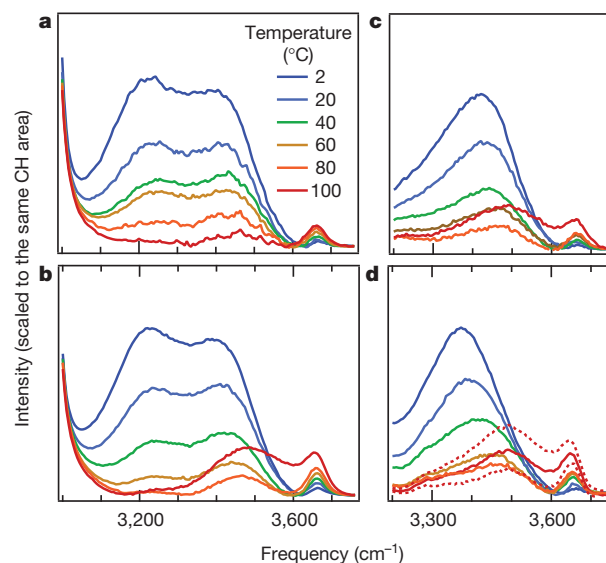


Figure 3 | Critical size for structural transformation of hydration-shell water. **a**, **b**, Temperature-dependent SC spectra showing that whereas the low-temperature hydration-shell structure of aqueous *n*-propanol disappears (**a**), that of aqueous *n*-butanol—which has a hydrocarbon chain length of $\sim 1\text{ nm}$ —transforms into a high-temperature structure distinct from that of bulk water structure (**b**). **c**, **d**, The onset of the high-temperature transformation is evident in both the depolarized (**c**) and isotopically dilute (**d**) SC spectra of aqueous *n*-butanol. The dashed curves in **d** indicate the reproducibility range of the HOD SC spectra at 100°C .

the entire hydration shell, not just the highly tetrahedral and strongly resonant-coupled water subpopulation.

We note that the observed structural transformation in the hydration shells of *n*-alcohols may relate to the two interfacial water structures seen in simulations of hydrated nanoparticles¹⁵ and proteins¹⁶, in which one structure has lower energy and greater tetrahedral order whereas the other is a higher-energy 'surface defect' or 'inverted' structure with greater entropy and faster relaxation dynamics. Our observation that the more tetrahedral interfacial water structure gives way to a structure that increasingly resembles bulk water as the temperature is increased from 0 °C to 60 °C is also in keeping with NMR and optical pump-probe⁶ studies, which indicate the same temperature trend for the reorientation dynamics of water. Above 60 °C and with alcohols longer than ~1 nm, we observe the emergence of a less ordered and more weakly hydrogen-bonded water structure. This transition seems to resemble a transformation between two structural states, but it may well involve a broad range of water structures whose temperature dependence mimics a simpler two-state transformation²⁷. Nevertheless, a two-state thermodynamic analysis can reproduce both the magnitude and temperature dependence of the experimental hydration heat capacity of hydrophobic solutes²⁸ and *n*-pentanol (see Supplementary Discussion).

Regarding the dependence of the observed structural transformation of the hydration shell on the molecular size of the *n*-alcohol solutes, we note that over 0–100 °C the hydration entropies of idealized hydrophobic (hard-sphere) solutes remain negative for small solutes and cross from negative to positive values for nanometre-sized solutes^{29,30}. In other words, the temperature at which hydrophobic hydration entropies change sign decreases with increasing solute size, in much the same way as the temperature at which we observe a water structural transformation decreases with increasing alcohol chain length.

The above spectroscopic observations and thermodynamic considerations are further reminiscent of the theoretically predicted crossover from a more ordered to a less ordered (air–water-interface-like) hydration-shell structure with an increase in either temperature or solute size, with a crossover length scale of the order of 1 nm (refs 9, 10, 14, 29, 30). However, our results imply that the critical length scale associated with the low temperature (more tetrahedral) structure is not the same as that associated with the high-temperature (more disordered) structure: whereas the similar low-temperature hydration-shell spectra of all *n*-alcohols imply a characteristic length scale comparable to the size of a single CH₂ or CH₃ group, the observation of a high-temperature structural transformation only in the hydration shells of *n*-alcohols longer than ~1 nm implies that this transformation is sensitive to the solute's overall hydrocarbon chain length rather than to the size of a single CH₂ or CH₃ group.

METHODS SUMMARY

The solutes methanol, ethanol, 1-propanol and *n*-butanol were distilled in small quantities; 1-pentanol, 1-hexanol and 1-heptanol were used without further purification. Aqueous samples containing short-chain alcohols up to 1-butanol were prepared at a concentration of 0.5 M using ultra-purified water (18.2 mΩ cm resistance). Results for longer-chain alcohols were obtained from the equilibrated water-rich phase in a two-phase system with a small alcohol-rich upper liquid layer. Raman measurements were performed using a home-built, micro-Raman system that included an argon-ion laser (514.5 nm, ~50 mW power at the sample) and a thermoelectrically cooled charge-coupled device detector (1,340 pixels × 400 pixels) mounted on a 300-mm focal length imaging spectrograph with a grating of 300 grooves mm⁻¹, with a dispersion of ~5 cm⁻¹ per CCD pixel. A 20× microscope objective (with a working distance of 20 mm) was used to both focus the laser and collect the backscattered Raman light from the middle of the aqueous solution in a 1-cm glass cuvette contained within a thermoelectric temperature-controlled cell holder. The solution temperature was controlled to within ±0.01 °C over a temperature range of 0–100 °C. A helium lamp was placed behind the sample during data collection, and the He lines were used to monitor and correct subpixel wavelength drifts (resulting from barometric pressure changes and other factors). Two to four sequential measurements accumulated for 5 min each were

collected from each pure water and solution sample (at each temperature) and used as input to the SMCR algorithm. Further details are provided in Supplementary Methods.

Received 22 March; accepted 6 September 2012.

- Ball, P. Water as an active constituent in cell biology. *Chem. Rev.* **108**, 74–108 (2008).
- Frank, H. S. & Evans, J. W. Free volume and entropy in condensed systems. 3. Entropy in binary liquid mixtures; partial molar entropy in dilute solutions; structure and thermodynamics of aqueous electrolytes. *J. Chem. Phys.* **13**, 507–532 (1945).
- Glew, D. N. Aqueous solubility and gas-hydrates—methane–water system. *J. Phys. Chem.* **66**, 605–609 (1962).
- Rosky, P. J. & Zichi, D. A. Molecular librations and solvent orientational correlations in hydrophobic phenomena. *Faraday Symp. Chem. Soc.* **17**, 69–78 (1982).
- Li, I. T. S. & Walker, G. C. Signature of hydrophobic hydration in a single polymer. *Proc. Natl Acad. Sci. USA* **108**, 16527–16532 (2011).
- Petersen, C., Tielrooij, K. J. & Bakker, H. J. Strong temperature dependence of water reorientation in hydrophobic hydration shells. *J. Chem. Phys.* **130**, 214511 (2009).
- Buchanan, P., Aldiwan, N., Soper, A. K., Creek, J. L. & Koh, C. A. Decreased structure on dissolving methane in water. *Chem. Phys. Lett.* **415**, 89–93 (2005).
- Zhang, X. Y., Zhu, Y. X. & Granick, S. Hydrophobicity at a Janus interface. *Science* **295**, 663–666 (2002).
- Lum, K., Chandler, D. & Weeks, J. D. Hydrophobicity at small and large length scales. *J. Phys. Chem. B* **103**, 4570–4577 (1999).
- Chandler, D. Interfaces and the driving force of hydrophobic assembly. *Nature* **437**, 640–647 (2005).
- Matysiak, S., DeBenedetti, P. G. & Rosky, P. J. Dissecting the energetics of hydrophobic hydration of polypeptides. *J. Phys. Chem. B* **115**, 14859–14865 10.1021/jp2079633 (2011).
- Laage, D., Stirnemann, G. & Hynes, J. T. Why water reorientation slows without iceberg formation around hydrophobic solutes. *J. Phys. Chem. B* **113**, 2428–2435 (2009).
- Raschke, T. M. & Levitt, M. Nonpolar solutes enhance water structure within hydration shells while reducing interactions between them. *Proc. Natl Acad. Sci. USA* **102**, 6777–6782 (2005).
- Garde, S. & Patel, A. J. Unraveling the hydrophobic effect, one molecule at a time. *Proc. Natl Acad. Sci. USA* **108**, 16491–16492 (2011).
- Friesen, A. D. & Matyushov, D. V. Non-Gaussian statistics of electrostatic fluctuations of hydration shells. *J. Chem. Phys.* **135**, 104501 (2011).
- Cheng, Y. K. & Rosky, P. J. Surface topography dependence of biomolecular hydrophobic hydration. *Nature* **392**, 696–699 (1998).
- Perera, P. N. *et al.* Observation of water dangling OH bonds around dissolved nonpolar groups. *Proc. Natl Acad. Sci. USA* **106**, 12230–12234 (2009).
- Perera, P., Wyche, M., Loethen, Y. & Ben-Amotz, D. Solute-induced perturbations of solvent-shell molecules observed using multivariate Raman curve resolution. *J. Am. Chem. Soc.* **130**, 4576–4579 (2008).
- Gierszal, K. P. *et al.* Pi-hydrogen bonding in liquid water. *J. Phys. Chem. Lett.* **2**, 2930–2933 (2011).
- Lawton, W. H. & Sylvestre, E. A. Self modeling curve resolution. *Technometrics* **13**, 617–633 (1971).
- Tomlinson-Phillips, J. *et al.* Structure and dynamics of water dangling OH bonds in hydrophobic hydration shells. Comparison of simulation and experiment. *J. Phys. Chem. A* **115**, 6177–6183 10.1021/jp111346s (2011).
- Yang, M. & Skinner, J. L. Signatures of coherent vibrational energy transfer in IR and Raman line shapes for liquid water. *Phys. Chem. Chem. Phys.* **12**, 982–991 (2010).
- Torii, H. Time-domain calculations of the polarized Raman spectra, the transient infrared absorption anisotropy, and the extent of delocalization of the OH stretching mode of liquid water. *J. Phys. Chem. A* **110**, 9469–9477 (2006).
- Li, F. & Skinner, J. L. Infrared and Raman line shapes for ice Ih. II. H₂O and D₂O. *J. Chem. Phys.* **133**, 244504 (2010).
- Liu, C. L., Ye, Y. G., Meng, Q. G., Lu, W. J. & Wang, F. F. *In situ* Raman spectroscopic observation of micro-processes of methane hydrate formation and dissociation. *Spectrosc. Spectr. Anal.* **31**, 1524–1528 (2011).
- Stiopin, I. V. *et al.* Hydrogen bonding at the water surface revealed by isotopic dilution spectroscopy. *Nature* **474**, 192–195 10.1038/nature10173 (2011).
- Smith, J. D. *et al.* Unified description of temperature-dependent hydrogen-bond rearrangements in liquid water. *Proc. Natl Acad. Sci. USA* **102**, 14171–14174 (2005).
- Gill, S. J., Dec, S. F., Olofsson, G. & Wadso, I. Anomalous heat-capacity of hydrophobic solvation. *J. Phys. Chem.* **89**, 3758–3761 10.1021/j100263a034 (1985).
- Garde, S., Hummer, G., Garcia, A. E., Paulaitis, M. E. & Pratt, L. R. Origin of entropy convergence in hydrophobic hydration and protein folding. *Phys. Rev. Lett.* **77**, 4966–4968 10.1103/PhysRevLett.77.4966 (1996).
- Ben-Amotz, D. Global thermodynamics of hydrophobic cavitation, dewetting, and hydration. *J. Chem. Phys.* **123**, 184501–184508 (2005).

Supplementary Information is available in the online version of the paper.

Acknowledgements This work was supported by the National Science Foundation (CHE-0847928). We thank B. Widom, D. Chandler, M. Fayer and S. Granick for comments and suggestions; D. Wilcox for writing the SMCR code used in this work; B. Rankin for performing molecular dynamics simulations to determine the number of

water molecules in the first hydration shells of n-alcohols (as further described in Supplementary Methods); and D. L. McCaffrey, S. Zukowski and C. DeShaw (undergraduate research students) for assistance in collecting experimental results relevant to this work.

Author Contributions J.G.D. and K.P.G. performed experimental measurements and reproducibility validations. J.G.D. further contributed to the SMCR data analysis and manuscript writing. P.W. designed and constructed the high-performance Raman

system that facilitated these studies. D.B.-A. conceived and supervised the work, and contributed to the data analysis and manuscript preparation.

Author Information Reprints and permissions information is available at www.nature.com/reprints. The authors declare no competing financial interests. Readers are welcome to comment on the online version of the paper. Correspondence and requests for materials should be addressed to D.B.-A. (bendor@purdue.edu).

Lower satellite–gravimetry estimates of Antarctic sea-level contribution

Matt A. King^{1,2}, Rory J. Bingham¹, Phil Moore¹, Pippa L. Whitehouse³, Michael J. Bentley³ & Glenn A. Milne⁴

Recent estimates of Antarctica's present-day rate of ice-mass contribution to changes in sea level range from 31 gigatonnes a year (Gt yr^{-1} ; ref. 1) to 246 Gt yr^{-1} (ref. 2), a range that cannot be reconciled within formal errors³. Time-varying rates of mass loss^{2,4–6} contribute to this, but substantial technique-specific systematic errors also exist³. In particular, estimates of secular ice-mass change derived from Gravity Recovery and Climate Experiment (GRACE) satellite data are dominated by significant uncertainty in the accuracy of models of mass change due to glacial isostatic adjustment^{7,8} (GIA). Here we adopt a new model of GIA, developed from geological constraints, which produces GIA rates systematically lower than those of previous models, and an improved fit to independent uplift data⁹. After applying the model to 99 months (from August 2002 to December 2010) of GRACE data, we estimate a continent-wide ice-mass change of $-69 \pm 18 \text{ Gt yr}^{-1}$ ($+0.19 \pm 0.05 \text{ mm yr}^{-1}$ sea-level equivalent). This is about a third to a half of the most recently published GRACE estimates^{2,5}, which cover a similar time period but are based on older GIA models. Plausible GIA model uncertainties, and errors relating to removing longitudinal GRACE artefacts ('destriping'), confine our estimate to the range -126 Gt yr^{-1} to -29 Gt yr^{-1} ($0.08\text{--}0.35 \text{ mm yr}^{-1}$ sea-level equivalent). We resolve 26 independent drainage basins and find that Antarctic mass loss, and its acceleration, is concentrated in basins along the Amundsen Sea coast. Outside this region, we find that West Antarctica is nearly in balance and that East Antarctica is gaining substantial mass.

Attempts to quantify the recent imbalance between water entering the Antarctic continent (in the form of snow) and water leaving it (mainly through ice flow) have yet to reach a consensus^{3,10}, with even the most recent estimates of mass change spanning almost an order of magnitude: -31 Gt yr^{-1} (ref. 1) to -246 Gt yr^{-1} (ref. 2) ($0.09\text{--}0.68 \text{ mm yr}^{-1}$ sea-level equivalent). Until consensus is reached on a more tightly bounded range, it will not be possible to confidently determine individual contributions to the 3.2 mm yr^{-1} globally averaged sea-level change observed for recent decades¹⁰, or fully understand patterns in regional sea-level change that are sensitive to the geographic distribution of meltwater sources^{11,12}. Disparities in Antarctic ice-mass balance estimates are particularly obvious between the different measurement approaches^{1,3}, suggesting that technique-specific errors are non-negligible in most, if not all, studies so far.

Studies based on data from the GRACE mission offer the prospect of comprehensively measuring regional- to continental-scale mass changes. However, estimates of secular ice-mass change may only be obtained indirectly from these data after the removal of mass change signals due to other processes, and in particular glacial isostatic adjustment (GIA)⁸—the response of the solid Earth to ice and ocean loading during the Late Quaternary period. Accurate modelling of GIA requires accurate knowledge of both the spatiotemporal evolution of the ice sheets, especially after the Last Glacial Maximum, and the Earth's response to changing surface loads. A general lack of data from Antarctica with which to constrain GIA model parameters has been a

key limitation in arriving at a well-constrained estimate of Antarctic mass balance from GRACE observations. However, a variety of recent observations^{13–16} now consistently indicate a significantly smaller ice loss from West Antarctica since the Last Glacial Maximum compared to most previous model reconstructions. These observations have not been incorporated into GIA models previously applied to GRACE data. As a consequence, past studies have overestimated the contemporary GIA signal, resulting in a systematic overestimate of ice-mass loss inferred from GRACE observations¹⁴ and bringing into question the conclusion that consensus has been reached with independent mass-balance approaches⁴.

Here we applied a new GIA model¹⁷ (W12a) to GRACE data to estimate the ice-mass balance for 26 independent Antarctic drainage basins from August 2002 to December 2010. The W12a model comprises a glaciologically self-consistent ice history⁹ constrained to fit data that delimit past ice extent and elevation, and an Earth viscosity model chosen such that GIA predictions from W12a best fit a suite of relative sea-level records around Antarctica¹⁷. The advance of W12a on previous models applied to GRACE data^{18,19} is illustrated by the misfit to GPS uplift rates being halved¹⁷. Our use of W12a addresses the dominant GRACE-related error in previous Antarctic analyses^{5,8}. Furthermore, because parameter uncertainty in both the Earth and, uniquely, ice model components, was explicitly considered in developing W12a, we were able to bound the GIA error without resorting to simply differencing two models, as has been done previously⁸. Here we adopted a modified version of W12a with improved performance along the Siple coast (Fig. 1), where data to constrain the model were initially lacking (see Supplementary Information 3).

We used 99 monthly samples of GRACE release-4 (RL04) spherical harmonic solutions produced at the Center for Space Research at the University of Texas, Austin. We added degree-1 and replaced degree-2, order-0 coefficients alongside other now-conventional corrections (see Methods). With data spanning nearly nine years, our solutions allow a more robust separation of transient signals²⁰ from linear trends and accelerations in mass change than earlier studies.

Previous GRACE studies have reported estimates of mass change in up to 16 independent Antarctic drainage basins²¹, although the spatial concentration of errors in previous GIA models¹⁴ means some of those basin estimates may be especially biased. Here we produced simultaneously-resolved mass-change time series for 26 drainage basins using a forward-modelling approach used in an earlier study²² of Greenland ice-mass change (see Methods). To prevent leakage of non-Antarctic signals into the continental basins we also estimated changes over the two major Antarctic ice shelves, the Atlantic, Pacific and Indian sectors of the Southern Ocean to 40°S , and Patagonia. We estimated, and applied, a correction for leakage of signal between basins as described in Supplementary Information 2. For the continental basins we estimated mass change rates, referenced to the time series midpoint (November 2006; Fig. 1; Supplementary Table 1), and accelerations in mass change (Fig. 2b) (see Methods).

¹School of Civil Engineering and Geosciences, Newcastle University, Newcastle upon Tyne NE1 7RU, UK. ²School of Geography and Environmental Studies, University of Tasmania, Hobart 7001, Australia. ³Department of Geography, Durham University, Durham DH1 3LE, UK. ⁴Department of Earth Sciences, University of Ottawa, Ottawa, Ontario K1N 6N5, Canada.

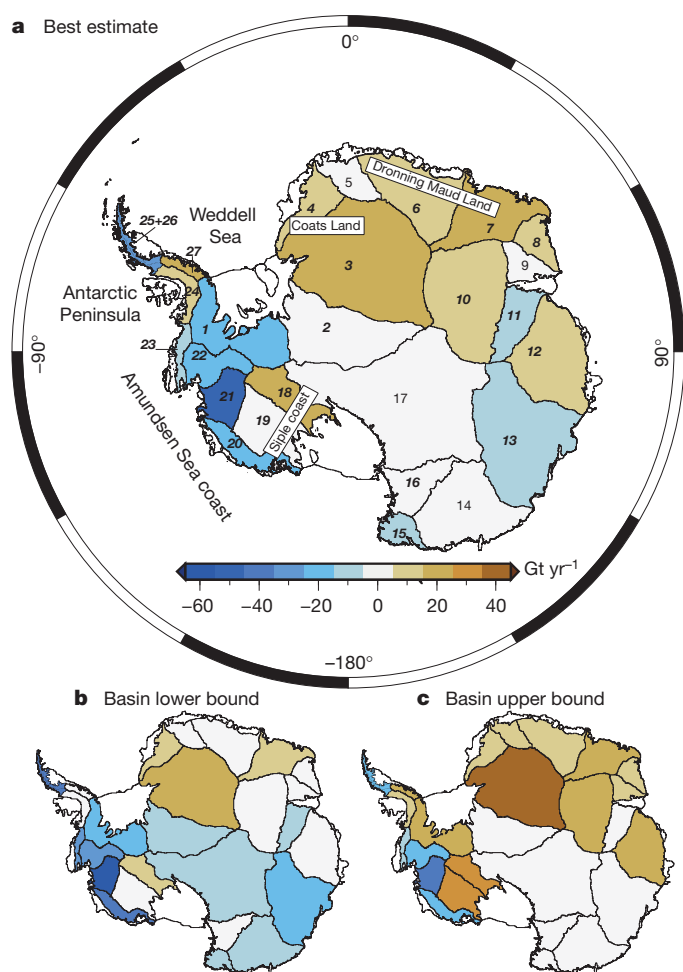


Figure 1 | Mass change rates by drainage basin. **a**, Best estimate of ice-mass change using the modified W12a GIA model, with basins numbered (boldface italics where trends are statistically different to zero with 95% confidence). **b**, **c**, Basin-specific lower and upper bounds on ice-mass change, respectively, reflecting the potential systematic error in our basin estimates. The systematic errors include contributions from GIA uncertainty, destriping and internal leakage. Leakage effects sum towards zero over multiple basins.

Summing over all 26 basins, we found the rate of Antarctica's ice-mass change to be $-69 \pm 18 \text{ Gt yr}^{-1}$ (all uncertainties are for the 95% confidence level) over the observation period, with the West Antarctic (basins 1, 18–27) mass change of $-118 \pm 9 \text{ Gt yr}^{-1}$ being partially compensated by the East Antarctic (basins 2–17) mass change of $+60 \pm 13 \text{ Gt yr}^{-1}$. We also computed corresponding estimates using an alternative GRACE analysis approach⁸ (see Supplementary Information 5), and these confirmed that our mass-change rates are not overly sensitive to our adopted approach (compare Supplementary Tables 1 and 2). For comparison to previous GRACE work that used older GIA models, replacing W12a with ICE-5G¹⁹ produced total rates of estimated Antarctic mass loss that were greater by 90 Gt yr^{-1} .

Our mass rate uncertainties are much smaller than for other studies because we did not include the GIA model uncertainty in terms of a random error. Instead, we partitioned errors into random and systematic components (see Methods), with the latter reflecting the systematic influence of GIA and GRACE destriping errors on the estimated ice-mass changes. We quantified the potential influence of systematic errors on our preferred ice-mass change estimates (based on the modified W12a model) through the definition of conservative upper and lower bounds computed for each basin (Fig. 1b, c and Supplementary Table 1). The bounds for our overall mass change rates were $[-126, -29] \text{ Gt yr}^{-1}$ with a relatively small West Antarctic range of $[-128, -103] \text{ Gt yr}^{-1}$, and a larger East Antarctic range of $[+7, +89] \text{ Gt yr}^{-1}$,

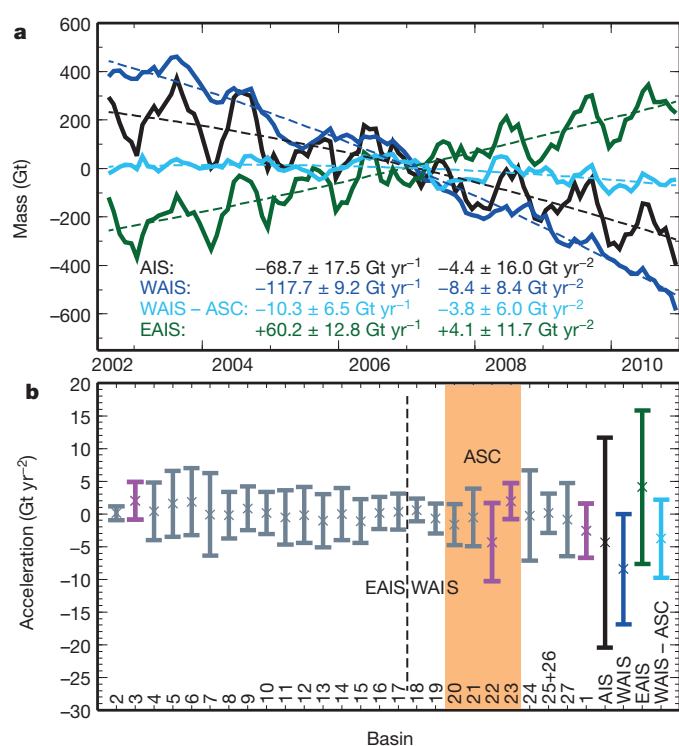


Figure 2 | Mass change time series and accelerations. **a**, Regional mass change time series (solid lines) and best-fit trend and acceleration (dashed line and text). Stated uncertainties are for the 95% confidence interval (2σ) and reflect the random errors on our estimates. **b**, Accelerations by basin and region with 2σ error bars. Basins with ice-mass change accelerations that are statistically different from zero with 68% confidence are shown in pink. Accelerations for regions are colour-coded as in **a**. AIS, Antarctic Ice Sheet; WAIS, West Antarctic Ice Sheet (including the Antarctic Peninsula); EAIS, East Antarctic Ice Sheet; ASC, Amundsen Sea Coast; and WAIS - ASC is the WAIS after subtraction of the total ASC mass change. ASC basins are highlighted in orange.

reflecting the sparser constraints on GIA models in East Antarctica. Within these ranges our preferred estimates are nearer the upper bound.

The spatial pattern of change (Fig. 1) revealed that East Antarctic mass increase is concentrated along coastal regions, notably Dronning Maud Land and Coats Land, with little to no change in the deep interior. A large accumulation event took place in Dronning Maud Land in 2009; considering only the period before this reduces the overall East Antarctic trend negligibly, although with a factor-of-2.5 larger uncertainty. West Antarctic mass loss was mostly concentrated in basins along the Amundsen Sea coast ($-108 \pm 8 \text{ Gt yr}^{-1}$), whereas elsewhere in West Antarctica we found a much smaller net mass loss ($-10 \pm 7 \text{ Gt yr}^{-1}$; Fig. 2a). The Amundsen Sea coast mass loss is in close agreement with the pattern of ice elevation change for 2003–2008 (ref. 23). We estimated the Pine Island Glacier basin (basin 22) to have been losing mass at $-24 \pm 7 \text{ Gt yr}^{-1}$, in agreement with the rate estimated for 2006 using satellite altimetry⁶ ($-21.4 \pm 0.5 \text{ Gt yr}^{-1}$). We estimated that Thwaites Glacier basin (basin 21) has been losing twice as much mass ($-54 \pm 5 \text{ Gt yr}^{-1}$) as the Pine Island Glacier basin over the period 2002–2010.

As with other recent GRACE studies^{2,5}, we found that the rate of mass loss for Antarctica as a whole has increased over the analysis period (Fig. 2a), but our estimate of the acceleration ($-4 \pm 16 \text{ Gt yr}^{-2}$) is only 15% of the estimate from another study², and we do not find it to be statistically different from zero. Considering West Antarctica only, acceleration is significant with 95% confidence, but our basin-by-basin analysis allowed us to identify statistically significant (68% confidence) mass-loss increase in only one basin—the basin containing Pine Island Glacier (basin 22) along the Amundsen Sea coast (Fig. 2b). Basin 1 exhibited accelerated mass loss, but from a negligible

base rate. Other basins exhibited positive accelerations in mass change, presumably owing to accumulation anomalies. We do not find the basin containing Thwaites glacier (basin 21) to be undergoing an overall significant acceleration in mass loss.

Our estimate of the rate of ice-mass change over Antarctica is around 36–48% of the most recent GRACE estimates of $-190 \pm 77 \text{ Gt yr}^{-1}$ (ref. 5) and $-143 \pm 73 \text{ Gt yr}^{-1}$ (ref. 2), which use older GIA models and a data span ending nearly two years earlier. The East Antarctic ice-mass increase we find conflicts with the near-zero change found by differencing modelled snow accumulation and observed mass discharge²⁴, but is in closer agreement with satellite altimetry studies^{1,25} that use data from the decade previous to our study period. Considering two recent attempts to reconcile discrepant measurements of Antarctic mass change^{1,4}, we find that our estimate is closer to the altimetry-based results of ref. 1 (-65 Gt yr^{-1} overall for 1992–2001, if we include our estimate of -34 Gt yr^{-1} for the part of the Antarctic Peninsula missing in their study) and is incompatible with recent input-minus-output results⁴ of -200 Gt yr^{-1} . Our estimate is also more aligned to the results of another altimeter-based study²⁶, which overlaps in time (2003–07) with our own, and determines an estimated mass change in the range $[-84, -103] \text{ Gt yr}^{-1}$. Nevertheless, further work is required to understand the remaining inter-technique differences more fully.

Our results for East Antarctica are heavily reliant on the inference of East Antarctic Ice Sheet growth following the Last Glacial Maximum, as reproduced in the W12a ice history; accumulation increases during this period are well supported by ice-core data⁹ but spatial sampling and knowledge of ice dynamic effects are poor, and so constraints on the time-evolution of ice-sheet volume are weak. Similarly, in West Antarctica, late Holocene ice-sheet changes are poorly known and at present unmodelled, but may be crucial to accurate GIA modelling. Although the W12a GIA model can no doubt be improved, particularly once new data pertinent to these limitations are obtained, the geological and geodetic data we have considered^{9,17} suggest that it is robust, and so our results represent a substantial advance on previous GRACE studies of Antarctic ice-mass change.

Our best estimate of net Antarctic ice-mass discharge into the oceans over 2002–2010 is $69 \pm 18 \text{ Gt yr}^{-1}$, equivalent to $+0.19 \pm 0.05 \text{ mm yr}^{-1}$ global average sea-level rise, with bounded values (see Methods) no higher than $+0.35 \text{ mm yr}^{-1}$ and no lower than $+0.08 \text{ mm yr}^{-1}$. The preferred estimate represents less than 10% of the observed increase of 3.2 mm yr^{-1} in global average sea level during the same period²⁷ and less than half the Antarctic value used in a recent attempt to close the sea-level budget²⁸. Taking a recent GRACE-based estimate of the rise in sea level due to glaciers, ice caps and ice sheets²⁹ and replacing their Antarctic component with ours gives a total contribution of $1.22 \pm 0.17 \text{ mm yr}^{-1}$ to global sea-level change over the period 2002–2010, indicating that glacierized regions account for about 38% of the global signal, with the remainder dominated by ocean warming and continental hydrology. Significant near-monotonic mass-loss increases are currently limited to the basin that contains Pine Island Glacier, along the Amundsen Sea coast, and modelling suggests that this glacier has a maximum plausible contribution to sea level of 7.6 cm this century³⁰; ice-sheet perturbations elsewhere, particularly of oceanic origin, may mean that the total Antarctic contribution will exceed this value by 2100.

METHODS SUMMARY

The Antarctic component of ICE-5G was replaced with the W12a reconstruction to create a global deglaciation model. This was combined with an optimum Earth model to compute geoid rates while considering rotational feedback. We used GRACE fields to spherical harmonic degree and order 60. Pre-processing was similar to previous studies, including replacing $C_{2,0}$ with values from satellite laser ranging³¹, inserting degree-1 harmonics, modelling far-field hydrology, and deriving surface spherical harmonics using load Love numbers to determine the expansion of mass change in terms of equivalent water height. We then subtracted the modelled GIA signal. Stokes coefficients were filtered using empirical

orthogonal functions (EOFs; ref. 22), using only EOFs whose principal components were statistically significant. A forward modelling approach was then adapted to generate time series of mass change for 32 basins, correcting for internal leakage (see Supplementary Information 2). We separated our error estimates into systematic and random components. The former are derived from a suite of plausible Earth and ice models defined in terms of uplift rates and converted into geoid rates. We extended these bounds to reflect differences between destriped and EOF-filtered solutions and internal leakage scenarios. Random errors (2σ) are from fitting a linear + acceleration + harmonic model, degree-1 uncertainties and temporal correlations.

Full Methods and any associated references are available in the online version of the paper.

Received 27 June; accepted 24 September 2012.

Published online 21 October 2012.

- Zwally, H. & Giovinetto, M. B. Overview and assessment of Antarctic ice-sheet mass balance estimates: 1992–2009. *Surv. Geophys.* **32**, 351–376 (2011).
- Velicogna, I. Increasing rates of ice mass loss from the Greenland and Antarctic ice sheets revealed by GRACE. *Geophys. Res. Lett.* **36**, L19503 (2009).
- Shepherd, A. & Wingham, D. Recent sea-level contributions of the Antarctic and Greenland ice sheets. *Science* **315**, 1529–1532 (2007).
- Rignot, E., Velicogna, I., van den Broeke, M. R., Monaghan, A. & Lenaerts, J. Acceleration of the contribution of the Greenland and Antarctic ice sheets to sea level rise. *Geophys. Res. Lett.* **38**, L05503 (2011).
- Chen, J. L., Wilson, C. R., Blankenship, D. & Tapley, B. D. Accelerated Antarctic ice loss from satellite gravity measurements. *Nature Geosci.* **2**, 859–862 (2009).
- Wingham, D. J., Wallis, D. W. & Shepherd, A. Spatial and temporal evolution of Pine Island Glacier thinning, 1995–2006. *Geophys. Res. Lett.* **36**, L17501 (2009).
- Barletta, V. R., Sabadini, R. & Bordon, A. Isolating the PGR signal in the GRACE data: impact on mass balance estimates in Antarctica and Greenland. *Geophys. J. Int.* **172**, 18–30 (2008).
- Velicogna, I. & Wahr, J. Measurements of time-variable gravity show mass loss in Antarctica. *Science* **311**, 1754–1756 (2006).
- Whitehouse, P. L., Bentley, M. J. & Le Brocq, A. M. A deglacial model for Antarctica: geological constraints and glaciological modelling as a basis for a new model of Antarctic glacial isostatic adjustment. *Quat. Sci. Rev.* **32**, 1–24 (2012).
- Solomon, S., et al. (eds) *Contribution of Working Group I to the Fourth Assessment Report of the Intergovernmental Panel on Climate Change* (Cambridge University Press, 2007).
- Tamisieva, M. E., Mitrova, J. X., Milne, G. A. & Davis, J. L. Global geoid and sea level changes due to present-day ice mass fluctuations. *J. Geophys. Res.* **106**, 30849–30863 (2001).
- Stammer, D., Agarwal, N., Herrmann, P., Kohl, A. & Mechoso, C. R. Response of a coupled ocean-atmosphere model to Greenland ice melting. *Surv. Geophys.* **32**, 621–642 (2011).
- Bentley, M. J. et al. Deglacial history of the West Antarctic Ice Sheet in the Weddell Sea embayment: constraints on past ice volume change. *Geology* **38**, 411–414 (2010).
- Thomas, I. D. et al. Widespread low rates of Antarctic glacial isostatic adjustment revealed by GPS observations. *Geophys. Res. Lett.* **38**, L22302 (2011).
- Bevis, M. et al. Geodetic measurements of vertical crustal velocity in West Antarctica and the implications for ice mass balance. *Geochim. Geophys. Geosyst.* **10**, Q10005 (2009).
- Mackintosh, A. et al. Retreat of the East Antarctic ice sheet during the last glacial termination. *Nature Geosci.* **4**, 195–202 (2011).
- Whitehouse, P. L., Bentley, M. J., Milne, G. A., King, M. A. & Thomas, I. D. A new glacial isostatic adjustment model for Antarctica: calibrated and tested using observations of relative sea-level change and present-day uplift rates. *Geophys. J. Int.* **190**, 1464–1482 (2012).
- Ivins, E. R. & James, T. S. Antarctic glacial isostatic adjustment: a new assessment. *Antarct. Sci.* **17**, 541–553 (2005).
- Peltier, W. R. Global glacial isostasy and the surface of the ice-age Earth: the ICE-5G (VM2) model and GRACE. *Annu. Rev. Earth Planet. Sci.* **32**, 111–149 (2004).
- Tregoning, P., Ramillien, G., McQueen, H. & Zwart, D. Glacial isostatic adjustment and nonstationary signals observed by GRACE. *J. Geophys. Res.* **114**, B06406 (2009).
- Horwath, M. & Dietrich, R. Signal and error in mass change inferences from GRACE: the case of Antarctica. *Geophys. J. Int.* **177**, 849–864 (2009).
- Wouters, B., Chambers, D. & Schrama, E. J. O. GRACE observes small-scale mass loss in Greenland. *Geophys. Res. Lett.* **35**, L20501 (2008).
- Pritchard, H. D. et al. Antarctic ice-sheet loss driven by basal melting of ice shelves. *Nature* **484**, 502–505 (2012).
- Rignot, E. et al. Recent Antarctic ice mass loss from radar interferometry and regional climate modelling. *Nature Geosci.* **1**, 106–110 (2008).
- Davis, C. H., Li, Y., McConnell, J. R., Frey, M. M. & Hanna, E. Snowfall-driven growth in East Antarctic Ice Sheet mitigates recent sea-level rise. *Science* **308**, 1898–1901 (2005).
- Gunter, B. et al. A comparison of coincident GRACE and ICESat data over Antarctica. *J. Geodesy* **83**, 1051–1060 (2009).
- Church, J. A. & White, N. J. Sea-level rise from the late 19th to the early 21st century. *Surv. Geophys.* **32**, 585–602 (2011).

28. Church, J. A. *et al.* Revisiting the Earth's sea-level and energy budgets from 1961 to 2008. *Geophys. Res. Lett.* **38**, L18601 (2011).
29. Jacob, T., Wahr, J., Pfeffer, W. T. & Swenson, S. Recent contributions of glaciers and ice caps to sea level rise. *Nature* **482**, 514–518 (2012).
30. Gladstone, R. M. *et al.* Calibrated prediction of Pine Island Glacier retreat during the 21st and 22nd centuries with a coupled flowline model. *Earth Planet. Sci. Lett.* **333–334**, 191–199 (2012).

Supplementary Information is available in the online version of the paper.

Acknowledgements This work was funded by NERC, and an RCUK Academic Fellowship to M.A.K., and partially supported by COST Action ES0701. G.A.M.

acknowledges support from the Natural Sciences and Engineering Research Council of Canada and the Canada Research Chairs programme. We thank E. Ivins for discussions.

Author Contributions M.A.K. and G.A.M. conceived the study. M.A.K. oversaw the work and wrote the paper. P.M. did the GRACE processing and R.J.B. did the forward modelling. R.J.B. and M.A.K. did the leakage analysis. P.L.W., M.J.B. and G.A.M. developed the GIA model. All authors commented on the paper.

Author Information Reprints and permissions information is available at www.nature.com/reprints. The authors declare no competing financial interests. Readers are welcome to comment on the online version of the paper. Correspondence and requests for materials should be addressed to M.A.K. (m.a.king@newcastle.ac.uk).

METHODS

GIA model. The Antarctic component of ICE-5G (ref. 19) was replaced with the W12a deglacial reconstruction⁹ to create a global deglaciation model. This was combined with the optimum Earth model of ref. 17 to create our GIA model for Antarctica. Geoid height rates for this model are calculated, taking care to remove the direct component of rotational feedback³². These are then converted into spherical harmonics. Uncertainties related to the Antarctic ice-sheet reconstruction and the choice of Earth model are included in our bounded error estimates.

GRACE data analysis. We used 99 monthly GRACE (RL04) fields from the Center for Space Research for the period August 2002 to December 2010 inclusive, consisting of spherical harmonics to degree and order 60 with pre-processing similar to previous studies². We replaced $C_{2,0}$ with values from satellite laser ranging³¹ and inserted degree-1 harmonics³³. To reduce signal leakage we used monthly values of total water storage from the Global Land Data Assimilation System model³⁴, with water height represented by surface harmonics up to degree and order 60, and used load Love numbers to represent an elastic Earth. To conserve the total mass $C_{0,0}$ for each month, the ocean mass (as supplied by the GRACE de-aliasing GAD product) was combined with the Global Land Data Assimilation System and a compensatory water layer was applied uniformly across the oceans. The GAD product was used only to conserve total mass and not to restore the a priori ocean signal used in the GRACE gravity field determinations. We subtracted modelled GIA and then derived surface spherical harmonics using load Love numbers to determine the expansion of mass change in terms of equivalent water height³⁵.

Forward modelling. Stokes coefficients were then filtered using an approach²² based on empirical orthogonal functions (EOFs). For the even (C_{lm}) and odd (S_{lm}) coefficients, EOFs were computed for each degree l . Only EOFs whose principal components could be distinguished from white noise using the two-sample Kolmogorov–Smirnov test with 99% confidence were used to reconstruct the time series of the degree l Stokes coefficients. Maps of surface loading were then computed after smoothing using a Gaussian filter with half-weight radius of 250 km applied in the spectral domain. A forward modelling approach adapted from ref. 22 was used to find, for each time step, the mass change in each basin consistent with the smoothed surface loading map obtained directly from the Stokes coefficients. Starting with a set of initial mass changes for each basin, a map of surface loading was obtained by distributing the mass change in each basin uniformly over its surface. Then, working on each basin in turn, a sequence of maps was generated with the mass of the focus basin spanning a range of values about the initial value. These maps were then projected into spherical harmonic space and remapped, discarding the degree 0 and 1 terms, with 250-km Gaussian filtering applied in the spectral domain. The root-mean-square difference, over the entire domain, between the directly obtained surface loading map and the spectrally filtered map of uniform basin values was computed, and the value in the focus basin minimizing the root-mean-square difference was retained. If no minimum was found then the search range was repeatedly doubled until a minimizing value was found. This was repeated for each basin and the cycle through basins repeated until the values for all basins remained unchanged between cycles. The process was initialised with a step size of 100 Gt and then iterated with the step size reducing by an order of magnitude until a resolution of 0.1 Gt was achieved. The final values from the previous time step provided the starting values at the next time step, except for the

first time step where the starting values were found by integrating the directly obtained map of surface loading. Experiments showed that final values were insensitive to the initial values. From these time series we subtracted harmonic signals corresponding to tidal aliasing frequencies for tidal constituents S2, K2 and the K2 sideband (S2: 161 days; K2: 3.8 years; K2 sideband: 4.8 years). The resulting basin time series were subsequently analysed after applying a correction for internal leakage (see Supplementary Information 2).

Error estimates. We separated our error estimates into systematic and random components. The systematic components, which define our lower and upper bounds, are dominated by GIA model uncertainty and were defined by taking a suite of models of present-day GIA-related uplift (computed using 17 plausible Earth models and 16 plausible ice models) and calculating spatially varying differences from the best GIA model uplift estimate on a 0.5° grid. The 17 Earth models, chosen from a suite of 297 models, are those that best fit (95% confidence) relative sea-level data at 14 sites around Antarctica¹⁷. They are combined with the W12a ice model⁹. The 16 ice-sheet model realizations span a realistic parameter space of ice-model inputs and give a reasonable fit to a data set of 62 palaeo-ice-extent observations⁹. They are combined with the preferred Earth model of ref. 17. From this solution space, some Earth/ice model combinations will produce GIA model predictions that give a poor fit to GPS-derived uplift observations, so our approach of summing the errors relating separately to ice model and Earth model uncertainty provides a conservative pair of bounds. Once the bounds were defined in terms of uplift rates, these were converted into geoid height rates following the method of ref. 36. We extended these bounds to reflect differences between destriped³⁷ and EOF filtered solutions (up to 10 Gt yr^{-1} in basins 1, 12, 22 and 25+26; and $<5 \text{ Gt yr}^{-1}$ for other basins). For basin-specific bounds only, we also considered the effect of adopting alternative mass distributions within each basin when correcting for internal leakage (see Supplementary Information 2). The random error components come from fitting a model of mass change (M) with time (t) to the basin time series by solving for unknowns c_i in $(M = c_1 t + 0.5 c_2 t^2 + \sum_{i=3}^4 c_i \sin(2\pi f t) + \sum_{i=5}^6 c_i \cos(2\pi f t) + c_0)$, considering harmonics with periods ($1/f$) of 0.5 and 1.0 years. We scaled 2σ coefficient uncertainties by a factor of two to account for unmodelled temporal correlations²¹, adding degree-1 2σ uncertainties from the misfit of linear, annual and semi-annual terms to the degree-1 time series³³.

31. Cheng, M. K. & Tapley, B. D. Variations in the Earth's oblateness during the past 28 years. *J. Geophys. Res.* **109**, B09402 (2004).
32. Tamisiea, M. E. Ongoing glacial isostatic contributions to observations of sea level change. *Geophys. J. Int.* **186**, 1036–1044 (2011).
33. Swenson, S., Chambers, D. & Wahr, J. Estimating geocenter variations from a combination of GRACE and ocean model output. *J. Geophys. Res.* **113**, B08410 (2008).
34. Rodell, M. *et al.* The global land data assimilation system. *Bull. Am. Meteorol. Soc.* **85**, 381–394 (2004).
35. Wahr, J., Molenaar, M. & Bryan, F. Time variability of the Earth's gravity field: hydrological and oceanic effects and their possible detection using GRACE. *J. Geophys. Res.* **103**, 30205–30229 (1998).
36. Purcell, A. *et al.* Relationship between glacial isostatic adjustment and gravity perturbations observed by GRACE. *Geophys. Res. Lett.* **38**, L18305 (2011).
37. Swenson, S. & Wahr, J. Post-processing removal of correlated errors in GRACE data. *Geophys. Res. Lett.* **33**, L08402 (2006).

An early and enduring advanced technology originating 71,000 years ago in South Africa

Kyle S. Brown^{1,2}, Curtis W. Marean², Zenobia Jacobs³, Benjamin J. Schoville², Simen Oestmo², Erich C. Fisher², Jocelyn Bernatchez², Panagiotis Karkanas⁴ & Thalassa Matthews⁵

There is consensus that the modern human lineage appeared in Africa before 100,000 years ago^{1,2}. But there is debate as to when cultural and cognitive characteristics typical of modern humans first appeared, and the role that these had in the expansion of modern humans out of Africa³. Scientists rely on symbolically specific proxies, such as artistic expression, to document the origins of complex cognition. Advanced technologies with elaborate chains of production are also proxies, as these often demand high-fidelity transmission and thus language. Some argue that advanced technologies in Africa appear and disappear and thus do not indicate complex cognition exclusive to early modern humans in Africa^{3,4}. The origins of composite tools and advanced projectile weapons figure prominently in modern human evolution research, and the latter have been argued to have been in the exclusive possession of modern humans^{5,6}. Here we describe a previously unrecognized advanced stone tool technology from Pinnacle Point Site 5–6 on the south coast of South Africa, originating approximately 71,000 years ago. This technology is dominated by the production of small bladelets (microliths) primarily from heat-treated stone. There is agreement that microlithic technology was used to create composite tool components as part of advanced projectile weapons^{7,8}. Microliths were common worldwide by the mid-Holocene epoch, but have a patchy pattern of first appearance that is rarely earlier than 40,000 years ago^{9,10}, and were thought to appear briefly between 65,000 and 60,000 years ago in South Africa and then disappear. Our research extends this record to ~71,000 years, shows that microlithic technology originated early in South Africa, evolved over a vast time span (~11,000 years), and was typically coupled to complex heat treatment that persisted for nearly 100,000 years. Advanced technologies in Africa were early and enduring; a small sample of excavated sites in Africa is the best explanation for any perceived ‘flickering’ pattern.

Microlithic technology varies worldwide and is often defined regionally⁹. Microlithic is used to describe small stone blades (bladelets) retouched to create highly standardized shapes (backed blades or segments), or assemblages with high frequencies of small tools¹⁰. We follow Clark’s concise technological definition: the process of manufacture (core reduction) is focused on the production of small flakes and bladelets less than 50 mm in maximum length⁷ (Supplementary Discussion). Microlithic technology has been considered more typical of the Later Stone Age (LSA) and Upper Palaeolithic phase postdating 45 kyr in Africa and Eurasia, respectively, atypical for the Middle Stone Age (MSA) in Africa (300–45 kyr), absent in the Middle Palaeolithic in Eurasia, and potentially a universal stage in the evolution of Palaeolithic technologies¹⁰.

Backed blade technology occurs earliest in Africa. The oldest East African sites with microliths are the Naisiusiu Beds at Olduvai Gorge, Enkapune Ya Muto, and Mumba rockshelter. The Naisiusiu Beds have infinite radiocarbon ages of >45 kyr¹¹ and electron spin resonance (ESR)

ages of 59 ± 5 kyr and 62 ± 5 kyr¹². The earliest Enkapune Ya Muto (Endingi) microlithic has a calibrated radiocarbon age of ≥ 45 kyr⁸. The oldest backed blades at Mumba rockshelter (Tanzania) are dated by optically stimulated luminescence (OSL) to 57 ± 5 kyr¹³. Small numbers of backed blades come from Twin Rivers in Zambia¹⁴, but the age is contested^{15,16}. The Howiesons Poort (HP) in southern Africa is well represented by many samples, meets the Clark definition of microlithic technology (Fig. 1), and is well constrained by large numbers of OSL ages to between 60 and 65 kyr¹⁷.

The microlithic technology we report is from Pinnacle Point Site 5–6 (PP5–6) on the south coast of South Africa (Supplementary Fig. 1 and Supplementary Discussion). The deposits we report here come

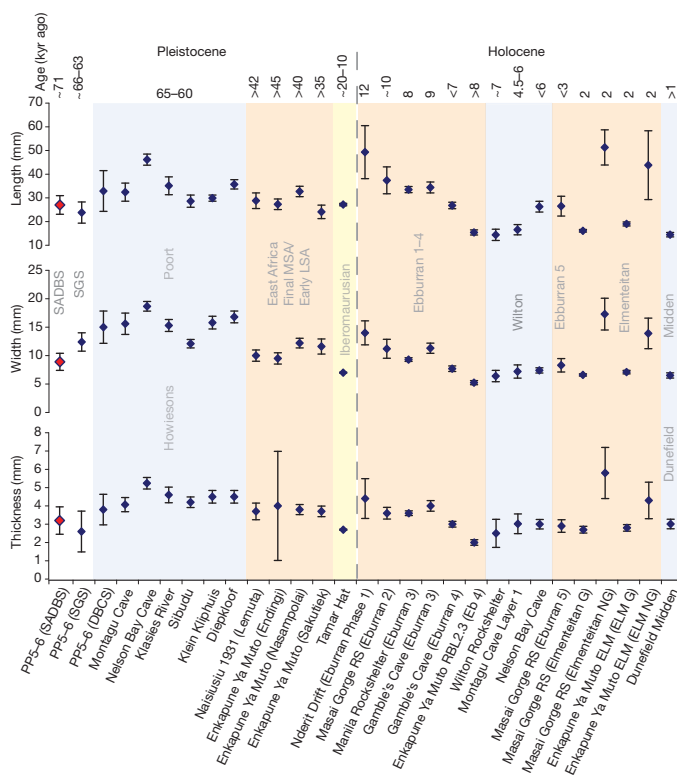


Figure 1 | Segment dimensions from PP5–6 and selected late Pleistocene and Holocene sites. Mean and error bars showing 95% confidence intervals for segment dimensions were calculated for segment length, width and thickness using published sample mean (\bar{x}), standard deviation (s) and sample count (n) values from selected African assemblages. The equation for calculating the 95% confidence interval is: $\bar{x} \pm t_{0.05}(n-1) * s / \sqrt{n}$, in which $t_{0.05}$ is the value at probability 0.05 at $(n-1)$ degrees of freedom from a two-tailed t -table. The values for $t_{0.05}$ were calculated using the TINV function in Microsoft Excel. Sources for data described are in Supplementary Information.

¹Department of Archaeology, University of Cape Town, Rondebosch 7701, South Africa. ²Institute of Human Origins, School of Human Evolution and Social Change, PO Box 872402, Arizona State University, Tempe, Arizona 85287-4101, USA. ³Centre for Archaeological Science, School of Earth and Environmental Sciences, University of Wollongong, Wollongong 2522, Australia. ⁴Ephoreia of Palaeoanthropology-Speleology of Southern Greece, Arditou 34b, 11636 Athens, Greece. ⁵Department of Natural History, Iziko South African Museum, PO Box 61, Cape Town 8000, South Africa.

from the Long Section at PP5–6 (ref. 18), a ~ 14 m (vertical) continuous sediment stack revealed by nine \sim two-month seasons of excavation. Combined with 76 OSL samples and total station piece-plotting, the PP5–6 Long Section provides a high resolution sequence to investigate the age and character of technological change. A brief overview of the major strata and ages surrounding and containing the microlithic strata follows (see Supplementary Discussion). The Shelly Ashy Dark Brown Sand (SADBS) contains the oldest microlithic assemblage (Fig. 2). The SADBS is underlain by the aeolian Ashy Light Brown Sand (ALBS) with a weighted mean OSL age of 71.1 ± 2.3 kyr ($n = 6$). The SADBS has a weighted mean age of 70.6 ± 2.3 kyr ($n = 6$). The top of the SADBS is an eroded surface overlain by the Orange Brown Sand 1 (OBS1) with a weighted mean OSL age of 66.0 ± 2.8 kyr ($n = 3$). The Shelly Gray Sand (SGS) overlies the OBS1 and is beneath the Dark Brown Compact Sand (DBCS) with three OSL ages ranging from 58 ± 4 to 65 ± 4 kyr. The Reddish Brown Sand and Roofspall (RBSR) caps the sequence with seven statistically consistent OSL ages, and a weighted mean age of 53.9 ± 1.7 kyr. Most microliths reported here were plotted directly by total station with millimetre accuracy, whereas the others come from small lenses also constrained by total station measurements. Outstanding contextual control is provided through total station plotting combined with field stratigraphy, three-dimensional geographic information system (GIS) analysis of plotted finds, and soil and sediment micromorphology (Supplementary Discussion).

The HP is present at PP5–6 in the DBCS with a range of backed and notched tool forms (Supplementary Fig. 2), heat-treated silcrete (80%)¹⁸, and an age consistent with other HP occurrences¹⁷. Core reduction focused on the production of small blades (mean length 27 mm); some retouched into backed blade segments (symmetric tools that are backed (blunted) on one side and sharp on the other (Fig. 3)) and notched pieces (Supplementary Table 1). DBCS segments (silcrete = 8, chert = 3) have dimensions (mean length 33 mm) similar to those of other HP sites in southern Africa (Fig. 1). Notched pieces are a common retouched tool form in the HP sample from Klasies

River^{19,20}, are common in the DBCS, and are rare in the underlying SADBS. The DBCS has single and double platform silcrete cores that were reduced to a relatively small size (mean length 30 mm). The SGS stratum has a small but dense sample of lithics with backed pieces (Supplementary Fig. 3) and three irregular notched pieces. The small sample of SGS segments ($n = 5$) has the shortest mean length (24 mm) in comparison to those of the DBCS and SADBS (Fig. 1). There are few diagnostic tools in the OBS1, probably owing to the fragmented assemblage and abundance of quartz. There are two small crescents at the base of the OBS1, similar in form to those of the SADBS (Supplementary Figs 3 and 4).

The SADBS lithic assemblage is dominated by small blade products that are significantly shorter ($t(167) = 2.06$, $P = 0.02$) and narrower ($t(167) = 2.23$, $P = 0.01$) than those of the DBCS (one-tailed Student's t -test). SADBS blade length and width are also statistically different from the Klasies River HP when compared across 95% confidence intervals of the means (Supplementary Fig. 5 and Supplementary Table 2). SADBS blades have plain platforms typically with abrasion on the platform edge adjacent to the flaking surface, and are made almost exclusively on silcrete and other non-quartzite raw materials. Crested blades and small unidirectional and bidirectional blade cores support the characterization of the SADBS as a bladelet-focused assemblage. SADBS formal tools are segments made from small silcrete and chert blades (Supplementary Fig. 4), with mean length/width ratios significantly higher than those of the DBCS (HP) (Mann–Whitney $U = 17$, exact $P = 0.006$). SADBS, SGS and DBCS segments have coefficient of variation values for length that are in the range of segment values for other HP and LSA Wilton (Holocene) tool assemblages (Supplementary Table 3).

We conducted a comparative analysis of segments between the PP5–6 samples, HP assemblages and more recent archaeological sites throughout Africa. SADBS segment dimensions (Supplementary Table 4) are within the 95% confidence intervals for segments at the MSA and LSA boundary in East Africa, the Tamar Hat Iberomaurusian in North Africa

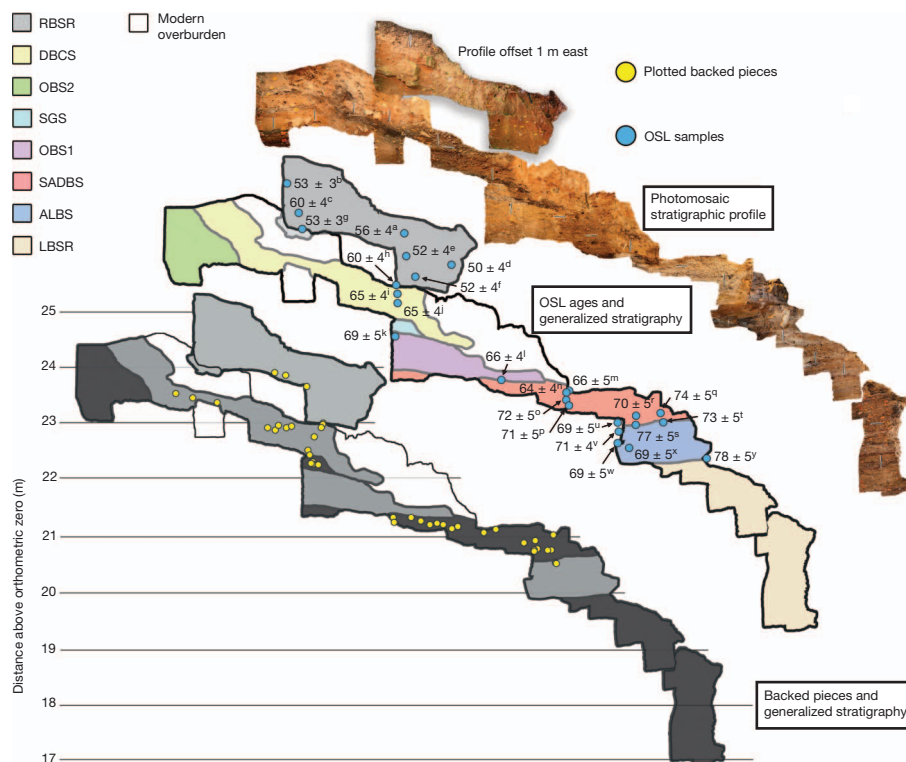


Figure 2 | PP5–6 stratigraphic aggregates. Photomosaic of the upper 8 m of stratigraphy (top), total station plotted OSL sample locations (middle) and locations and association of total station plotted microlithic segments (bottom).

Age superscript corresponds to superscript with sample codes presented in Supplementary Table 5. The excavated archaeological deposit extends below what is depicted in the figure.

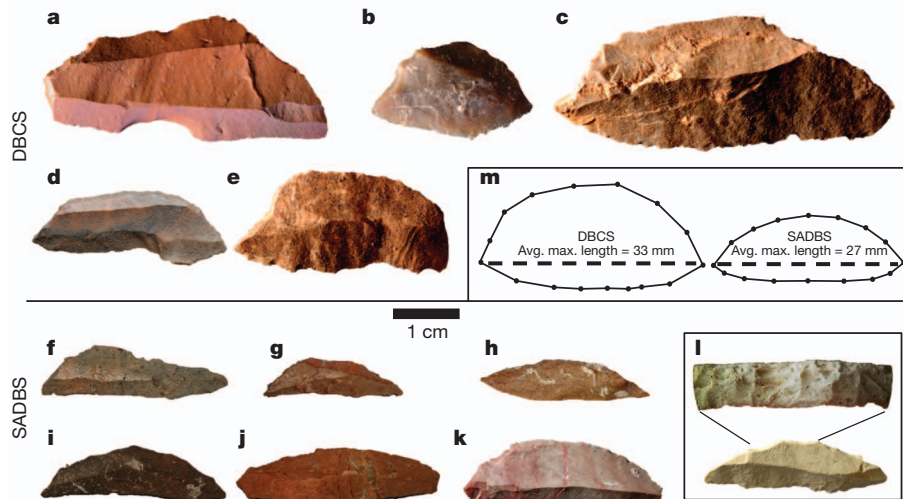


Figure 3 | PP5-6 microlithic tools. a–l, Representative images of PP5-6 segments from the DBCS (HP; a–e) and SADBS (f–k), showing differences in size and shape, and fine flaking of the backed edge (l) on a segment from the OBS1. Backed blades are oriented with the backed edge up and the unmodified edge down. m, The average shape for each stratigraphic aggregate is shown

(~20–10 kyr), and Holocene assemblages in South and East Africa (Fig. 1). More easily flaked obsidian (owing to its lack of crystalline structure) dominates the East African assemblages, so despite a tougher raw material (silcrete) the SADBS knappers produced comparable microliths. SADBS segments are shorter and thinner than HP segments with no overlap in confidence intervals for width; they are more similar to East African LSA assemblages than the HP (Fig. 1). A shape analysis was performed using landmark-based geometric morphometrics (Supplementary Fig. 6), which focuses on complete form more effectively than conventional linear dimension analyses^{21,22}. Shape analysis was performed on a more limited sample of sites because it required direct access to the artefacts or large samples of published segment images. The mean segment shape from the HP at PP5-6 is not significantly different from the Klasies River HP ($P = 0.07$, non-parametric testing, multivariate analysis of variance (MANOVA)). However, SADBS segment shape is significantly different from both PP5-6 HP ($P = 0.035$) and Klasies River HP ($P = 0.026$) (Supplementary Figs 7 and 8). At PP5-6 the SADBS is stratified below and substantially predates the HP, and, despite being older, is even more convergent on later classic microlithic forms than the HP.

The silcrete that dominates the SADBS and HP at PP5-6 was heat treated¹⁸, a technique that is known to date back to ~162 kyr at Pinnacle Point 13B. The technological recipe for microlith production at PP5-6 follows this long complex chain: (1) collection of silcrete at patchily distributed sources; (2) collection and transport of appropriate wood fuel to heat treatment locations; (3) controlled temperature heat treatment of silcrete; (4) preparation of microblade cores on silcrete; (5) controlled production of bladelets; (6) reshaping of bladelets into microliths; (7) production of mounts on wood or bone; and (8) adhesion of microliths to form compound tools. The HP has been considered ‘complex’²³ or ‘exceptional’²⁴ and the disappearance of the HP advanced technology has been argued to reflect a transient pattern of technological complexity in Africa that flickers in and out of existence as a function of demography^{3,4}. The thick high resolution sequence dated by large numbers of OSL ages at PP5-6 allows us to demonstrate technological continuity in the microlith production on heat-treated silcrete from ~71–60 kyr, showing retention of a recipe that requires high fidelity intergenerational transmission across a large region, whereas heat treatment technology persisted for nearly 100,000 years or more¹⁸. Backed blade, microlithic and heat treatment technologies may strengthen and weaken as preferred strategies, but

scaled to the average maximum (avg. max.) length (DBCS on the left, SADBS on the right). The artefact plotted find numbers (project specimen numbers) are 121094 (a), 133878 (b), 266888 (c), 280295 (d), 266287 (e), 107536 (f), 259888 (g), 312237 (h), 151511 (i), 272915 (j), 155127 (k) and 177975 (l).

the temporal span is vast, indicating that the cognitive capacity for culturally embedding and transmitting these complex recipes manifests early and persistently in southern Africa. The perceived transient pattern of advanced technologies probably reflects the very small sample of well-excavated sites in Africa, a sample that is a tiny fraction of the available European Middle Palaeolithic sample, and the need to study materials recovered from the smallest sieve fractions. Each new excavated site in Africa seems to chip away at this flickering pattern of advanced technologies.

SADBS microlithic backed bladelets differ in form from the previously described HP and are similar in linear dimensions to Holocene microlithic segments. The SADBS microliths document a commitment to microlithic technology 6,000 years before the HP, while also showing that the preferred bladelet form changed over time. On the basis of ethnographic analogy, these Holocene microliths were proposed to have tipped arrows^{25,26}. However, microliths could also have been used to tip atlatl (spearthrower) darts^{5,27}. Early modern humans in South Africa had the cognition to design and transmit at high fidelity these complex recipe technologies. This ability facilitated effective weapons grounded in microlithic technology, conferring increased killing distance and power over hand-cast spears²⁸. Microlith-tipped projectile weapons increased hunting success rate, reduced injury from hunting encounters gone wrong, extended the effective range of lethal interpersonal violence²⁹, and would have conferred substantive advantages on modern humans as they left Africa and encountered Neanderthals equipped with only hand-cast spears³⁰.

METHODS SUMMARY

PP5-6 has been excavated from 2006–2012 creating a ~14 m vertical excavated section. To summarize briefly, the site is excavated in 50-cm quadrants, named by their bearing: NE, NW, SE and SW, within 1-m squares. Excavations follow natural stratigraphic units (for example, layers and features), and thus square-quadrant-stratigraphic unit provenience designation is the minimum assigned to any find. All observed finds were plotted directly to total station in three dimensions, and the rest were captured by nested 10–3–1 mm wet-sieving.

OSL dating determines burial ages for sediments based on the increase in the number of trapped electrons in mineral grains with increasing time after burial, in response to the energy supplied by background levels of ionizing radiation from environmental sources. The time elapsed since sediments were last exposed to sufficient heat or sunlight to empty the relevant electron traps can be estimated from measurements of the OSL signal, together with determinations of the radioactivity of the sample and the material surrounding it to a distance of ~50 cm. The

burial dose ('equivalent dose', D_e) can be measured using the OSL signal from a sample of sediment and represents the radiation dose to which sedimentary grains have been exposed in their burial environment. The dose rate (D_r) represents the rate of exposure of these grains to ionizing radiation over the entire period of burial; this dose is mostly derived from the radioactive decay of ^{238}U , ^{235}U , ^{232}Th (and their daughter products) and ^{40}K , with lesser contributions from cosmic rays and from radioactive inclusions internal to the dated mineral grains. The burial age of grains that were well bleached by sunlight at the time of deposition can then be calculated from the D_e divided by the D_r .

Full Methods and any associated references are available in the online version of the paper.

Received 22 August; accepted 5 October 2012.

Published online 7 November 2012.

- Blum, M. G. B. & Jakobsson, M. Deep divergences of human gene trees and models of human origins. *Mol. Biol. Evol.* **28**, 889–898 (2011).
- Endicott, P., Hob, S. Y. W. & Stringer, C. Using genetic evidence to evaluate four palaeoanthropological hypotheses for the timing of Neanderthal and modern human origins. *J. Hum. Evol.* **59**, 87–95 (2010).
- d'Errico, F. & Stringer, C. Evolution, revolution or saltation scenario for the emergence of modern cultures? *Phil. Trans. R. Soc. B* **366**, 1060–1069 (2011).
- Powell, A., Shennan, S. & Thomas, M. Late Pleistocene demography and the appearance of modern human behavior. *Science* **324**, 1298–1301 (2009).
- Sisk, M. L. & Shea, J. J. The African origin of complex projectile technology: an analysis using tip cross-sectional area and perimeter. *Int. J. Evol. Biol.* **2011**, 968012 (2011).
- Brooks, A. S., Nevell, L., Yellen, J. E. & Hartman, G. in *Transitions Before the Transition* (eds Hovers, E. & Kuhn, S. L.) 233–255 (Springer, 2006).
- Clark, J. D. in *Recent Advances in Indo-Pacific Prehistory* (eds Misra, V. N. & Bellwood, P.) 95–101 (E. J. Brill, 1985).
- Ambrose, S. Small things remembered: origins of early microlithic industries in Sub-Saharan Africa. *Archaeol. Papers Am. Anthropol. Assoc.* **12**, 9–29 (2002).
- Kuhn, S. & Elston, R. Introduction: thinking small globally. *Archaeol. Papers Am. Anthropol. Assoc.* **12**, 1–7 (2002).
- Kuhn, S. Pioneers of microlithization: the "proto-Aurignacian" of Southern Europe. *Archaeol. Papers Am. Anthropol. Assoc.* **12**, 83–94 (2002).
- Manega, P. C. *Geochronology, Geochemistry and Isotopic Study of the Plio-Pleistocene Hominid Sites and the Ngorongoro Volcanic Highland in Northern Tanzania*. PhD thesis, Univ. Colorado (1993).
- Skinner, A. R., Hay, R. L., Masao, F. & Blackwell, B. A. B. Dating the Naisiusiu Beds, Olduvai Gorge, by electron spin resonance. *Quat. Sci. Rev.* **22**, 1361–1366 (2003).
- Gliganic, L. A., Jacobs, Z., Roberts, R. G., Domínguez-Rodrigo, M. & Mabulla, A. Z. P. New ages for Middle and Later Stone Age deposits at Mumba rockshelter, Tanzania: optically stimulated luminescence dating of quartz and feldspar grains. *J. Hum. Evol.* **62**, 533–547 (2012).
- Barham, L. Backed tools in Middle Pleistocene central Africa and their evolutionary significance. *J. Hum. Evol.* **43**, 585–603 (2002).
- Herries, A. I. R. A chronological perspective on the Acheulian and its transition to the Middle Stone Age in Southern Africa: the question of the Fauresmith. *Int. J. Evol. Biol.* **2011**, 1–25 (2011).
- Barham, L. Clarifying some fundamental errors in Herries' "a chronological perspective on the Acheulian and its transition to the Middle Stone Age in southern Africa: the question of the Fauresmith". *Int. J. Evol. Biol.* **2012**, 1–5 (2012).
- Jacobs, Z. *et al.* Ages for the Middle Stone Age of Southern Africa: implications for human behavior and dispersal. *Science* **322**, 733–735 (2008).
- Brown, K. S. *et al.* Fire as an engineering tool of early modern humans in coastal South Africa. *Science* **325**, 859–862 (2009).
- Singer, R. & Wymer, J. *The Middle Stone Age at Klasies River Mouth in South Africa* (Univ. of Chicago Press, Chicago, 1982).
- Wurz, S. The Howiesons Poort backed artefacts from Klasies River: an argument for symbolic behavior. *S. Afr. Archaeol. Bul.* **54**, 38–50 (1999).
- Adams, D. C. *et al.* Geometric morphometrics: ten years of progress following the 'revolution'. *Ital. J. Zool. (Modena)* **71**, 5–16 (2004).
- Rohlf, F. J. tpsDig Version 2.10. <http://life.bio.sunysb.edu/morph/index.html> (2006).
- Mellars, P. Major issues in the emergence of modern humans. *Curr. Anthropol.* **30**, 349–385 (1989).
- Bar-Yosef, O. & Kuhn, S. The big deal about blades: laminar technologies and human evolution. *Am. Anthropol.* **101**, 322–338 (1999).
- Clark, J. D., Phillips, J. & Staley, P. S. Interpretations of prehistoric technology from ancient Egyptian and other sources. Part I: ancient Egyptian bows and arrows and their relevance for African prehistory. *Paleorient* **2**, 323–388 (1974).
- Clark, J. D. Interpretations of prehistoric technology from ancient Egyptian and other sources. Part II: prehistoric arrow forms in Africa as shown by surviving examples of traditional arrows of the San Bushmen. *Paleorient* **3**, 127–150 (1975).
- Pétillon, J.-M. *et al.* Hard core and cutting edge: experimental manufacture and use of Magdalenian composite projectile tips. *J. Archaeol. Sci.* **38**, 1266–1283 (2011).
- Shea, J. The origins of lithic projectile point technology: evidence from Africa, the Levant, and Europe. *J. Archaeol. Sci.* **33**, 823–846 (2006).
- Bingham, P. M. Human evolution and human history: A complete theory. *Evol. Anthropol.* **9**, 248–257 (2000).
- Churchill, S. E., Franciscus, R., McKean-Peraza, H., Daniel, J. & Warren, B. Shanidar 3 Neanderthal rib puncture wound and paleolithic weaponry. *J. Hum. Evol.* **57**, 163–178 (2009).

Supplementary Information is available in the online version of the paper.

Acknowledgements We thank the MAPCRM staff for their assistance, the Dias Museum for field facilities, and SAHRA and HWC for permits. This research was funded by the National Science Foundation (grants BCS-9912465, BCS-0130713, BCS-0524087 and BCS-1138073 to C.W.M.), the Hyde Family Foundation, the Institute of Human Origins (IHO), and the Australian Research Council (DP1092843 to Z.J.).

Author Contributions K.S.B. led the lithic analysis and with C.W.M. took the lead in writing the paper; J.B. contributed to the site analysis; E.C.F. conducted the GIS analysis and photomosaic construction; C.W.M. is the project director and an excavation permit co-holder; S.O. contributed to the lithic analysis; B.J.S. contributed to the lithic analysis and conducted the morphometric analysis; Z.J. conducted the OSL dating; P.K. studied the sedimentology and geology of the site; T.M. is an excavation permit co-holder and contributes to palaeoenvironmental studies; and J.B., K.S.B., E.C.F., C.W.M., S.O. and B.J.S. all contributed substantially to the excavations. All authors contributed to the writing of the paper.

Author Information The data reported in this paper are tabulated in the Supplementary Information and archived at Arizona State University. Reprints and permissions information is available at www.nature.com/reprints. The authors declare no competing financial interests. Readers are welcome to comment on the online version of the paper. Correspondence and requests for materials should be addressed to C.W.M. (curtis.marean@asu.edu).

METHODS

Excavation methods. PP5–6 has been excavated from 2006–2011 as part of the South African Coast Paleoclimate, Paleoenvironment, Paleoecology, Paleoanthropology Project (SACP4), creating a ~14 m vertical excavated section. All excavations are conducted using published protocols^{31–34}. To summarize briefly, the site is excavated in 50-cm quadrants within squares, named by their bearing: NE, NW, SE and SW. Excavations follow natural stratigraphic units (for example, layers and features), and thus square–quadrant–stratigraphic unit provenience designation is the minimum assigned to any find. Sediment volumes were measured during excavation, and bulk samples of sediment were taken from every unique stratigraphic unit. All observed finds were plotted directly to total station in three dimensions, and the rest were captured by nested 10–3–1 mm wet-sieving. Laboratory processing of materials from PP5–6 is still in progress and thus most analyses involving archaeological specimens are limited to piece-plotted artefacts that have been catalogued and analysed up to the date of submission.

OSL dating methods. OSL dating determines burial ages for sediments^{35–40}. The method is based on the increase in number of trapped electrons in mineral grains (such as quartz) with increasing time after burial, in response to the energy supplied by background levels of ionizing radiation from environmental sources. The time elapsed since sediments were last exposed to sufficient heat or sunlight to empty the relevant electron traps can be estimated from measurements of the OSL signal, together with determinations of the radioactivity of the sample and the material surrounding it to a distance of ~50 cm. The burial dose ('equivalent dose', D_e) can be measured using the OSL signal from a sample of sediment, which can be as small as a single sand-sized grain, and represents the radiation dose to which sedimentary grains have been exposed in their burial environment. The dose rate (D_r) represents the rate of exposure of these grains to ionizing radiation over the entire period of burial; this dose is mostly derived from the radioactive decay of ^{238}U , ^{235}U , ^{232}Th (and their daughter products) and ^{40}K , with lesser contributions from cosmic rays and from radioactive inclusions internal to the dated mineral grains. The burial age of grains that were well bleached by sunlight at the time of deposition can then be calculated from D_e divided the D_r .

Shape analysis methods. Dorsal view artefact images were digitized with two landmarks at technologically homologous points where the backed edge intersects the unretouched edge on the proximal and distal ends (Supplementary Fig. 6). Seven sliding semi-landmarks were then placed along both the backed and sharp edges to capture the shape of curves between landmarks⁴¹. Procrustes superimposition analysis was performed and displayed using the thin-plate spline programs available from Rohlf²². This removes differences in size, orientation and image positioning. A relative warps, or principal components, analysis on the shape variables provides an indication of the relationship in shape space of the SADBS segments with those of the DBCS. The average shape is the origin point, and the deformation grids at each axis end illustrate the direction of shape change along those vectors (Supplementary Fig. 7). PC1 along the x axis separates narrower SADBS tools from rounded crescent shaped HP tools.

Stratigraphic photomosaic method. The PP5–6 Long Section photomosaic (Fig. 2) compiles 486 photographs taken in nine-image high definition range (HDR) sets spanning –4 to +4 exposure value (EV) captured with a Nikon D300S camera with flashes arranged to limit shadows and stabilize the lighting conditions. The photos were shot at f11, maintaining a focal distance of 25 cm, and providing an image resolution <0.5 cm. Photo rectification chits placed onto the profile at ~20 cm spacing provided systematic tie points between the overlapping

images. We used the Adobe Lens Calibration Utility to develop a personalized geometric lens distortion and vignetting correction. Corrections were made in Adobe Lightroom 3 and the corrected NEF images were exported as TIFFs. We used Enfuse GUI v2.1 for HDR processing.

Photographic areas not part of the stratigraphic section were digitally masked from each 0EV image using Adobe Photoshop CS5. Removal of these areas was necessary to minimize parallax stitching distortion and did not alter the appearance or morphology of the stratigraphy visible within the images. The masks applied to the 0EV images were then applied to each equivalent HDR image. The masked 0EV images were mosaicked using PTGUI v9.0.4 to interpolate patterns between each image. ECF subsequently refined the image matching using photo chits and other prominent landmarks across images. The geometrically warped image stack was exported to Photoshop and mosaicked using the 'auto-blend' function to create seamless layer masks that were then individually refined and checked. The processing steps were repeated on the HDR images using the 0EV file as a template to provide an exact copy of the geometric warp and mosaic. The 0EV final layer masks were applied to the HDR image layers, thereby creating two identical photomosaic profiles, 0EV and HDR. Linear colour and sharpening enhancements of the final profile were as follows: a high-pass filter (radius = 10 pixels) was applied to the HDR mosaic and overlaid onto the 0EV mosaic image to provide linear sharpening and texture enhancement. Colour and contrast enhancement was accomplished by duplicating the final 0EV mosaic and overlaying it atop itself, adjusting the transparency of the overlay image to 50%.

The final mosaic was georectified in ESRI ArcGIS10 using the image photo rectification chits. The spline method was used to warp image mosaic to the 2D photo chit point locations with a root mean square < 0.01. The full photo mosaic was subdivided into six panels and converted to 2.5 dimensions by texture mapping each panel onto an equivalently-sized polygon in Google Sketchup. The true three-dimensional location of the lower right corner of each panel provided an anchor to project each Sketchup plate within the three-dimensional GIS in its proper spatial position.

31. Marean, C. W. *et al.* Paleoanthropological investigations of Middle Stone Age sites at Pinnacle Point, Mossel Bay (South Africa): Archaeology and hominid remains from the 2000 Field Season. *PaleoAnthropol.* **83**, 14–83 (2004).
32. Dibble, H. L. *et al.* The use of barcodes in excavation projects. *SAA Archaeol. Rec.* **7**, 33–38 (2005).
33. Marean, C. W. *et al.* The stratigraphy of the Middle Stone Age sediments at Pinnacle Point Cave 13B (Mossel Bay, Western Cape Province, South Africa). *J. Hum. Evol.* **59**, 234–255 (2010).
34. Bernatchez, J. & Marean, C. W. Total station archaeology and the use of digital photography. *SAA Archaeol. Rec.* **11**, 16–21 (2011).
35. Huntley, D. J., Godfrey-Smith, D. I. & Thewalt, M. L. W. Optical dating of sediments. *Nature* **313**, 105–107 (1985).
36. Aitken, M. J. *An Introduction to Optical Dating* (Oxford Univ. Press, 1998).
37. Duller, G. A. T. Luminescence dating of Quaternary sediment: recent developments. *J. Quat. Sci.* **19**, 183–192 (2004).
38. Lian, O. B. & Roberts, R. G. Dating the Quaternary: progress in luminescence dating of sediments. *Quat. Sci. Rev.* **25**, 2449–2468 (2006).
39. Jacobs, Z. & Roberts, R. G. Advances in optically stimulated luminescence dating of individual grains of quartz from archeological deposits. *Evol. Anthropol.* **16**, 210–223 (2007).
40. Wintle, A. G. Fifty years of luminescence dating. *Archaeometry* **50**, 276–312 (2008).
41. Bookstein, F. L. Landmark methods for forms without landmarks: morphometrics of group differences in outline shape. *Med. Image Anal.* **1**, 225–243 (1997).

Aberrant light directly impairs mood and learning through melanopsin-expressing neurons

Tara A. LeGates^{1*}, Cara M. Altimus^{1*}, Hui Wang², Hey-Kyoung Lee², Sunggu Yang², Haiqing Zhao¹, Alfredo Kirkwood², E. Todd Weber³ & Samer Hattar^{1,2}

The daily solar cycle allows organisms to synchronize their circadian rhythms and sleep–wake cycles to the correct temporal niche¹. Changes in day-length, shift-work, and transmeridian travel lead to mood alterations and cognitive function deficits². Sleep deprivation and circadian disruption underlie mood and cognitive disorders associated with irregular light schedules². Whether irregular light schedules directly affect mood and cognitive functions in the context of normal sleep and circadian rhythms remains unclear. Here we show, using an aberrant light cycle that neither changes the amount and architecture of sleep nor causes changes in the circadian timing system, that light directly regulates mood-related behaviours and cognitive functions in mice. Animals exposed to the aberrant light cycle maintain daily corticosterone rhythms, but the overall levels of corticosterone are increased. Despite normal circadian and sleep structures, these animals show increased depression-like behaviours and impaired hippocampal long-term potentiation and learning. Administration of the antidepressant drugs fluoxetine or desipramine restores learning in mice exposed to the aberrant light cycle, suggesting that the mood deficit precedes the learning impairments. To determine the retinal circuits underlying this impairment of mood and learning, we examined the behavioural consequences of this light cycle in animals that lack intrinsically photosensitive retinal ganglion cells. In these animals, the aberrant light cycle does not impair mood and learning, despite the presence of the conventional retinal ganglion cells and the ability of these animals to detect light for image formation. These findings demonstrate the ability of light to influence cognitive and mood functions directly through intrinsically photosensitive retinal ganglion cells.

In mammals, all light information for image formation and regulation of behaviour is detected by the retina and signalled to the relevant brain targets through retinal ganglion cells (RGCs). Most RGCs signal light to thalamic relay nuclei and then to the visual cortex for image functions. A population of intrinsically photosensitive RGCs (ipRGCs^{3,4}), which predominantly signal light information for non-image-forming visual functions, expresses the photopigment melanopsin and can be distinguished from most RGCs that support image tracking and detection⁵. ipRGCs project to several hypothalamic and preoptic areas such as the suprachiasmatic nucleus (SCN), subparaventricular nucleus and ventrolateral preoptic area to regulate circadian rhythms and sleep. However, they also project to limbic regions such as the lateral habenula and the medial amygdala^{4,6}, highlighting a possible role in the regulation of cognitive functions.

To determine how aberrant light influences behaviour, we subjected mice to an ultradian cycle consisting of 3.5-h light and 3.5-h dark (T7). Our previous studies showed that this T7 aberrant light cycle does not affect the architecture (Supplementary Fig. 1) or the total sleep levels when compared to a 12 h:12 h light–dark (T24) control cycle⁷. We also determined whether the circadian timing system was disrupted in the

T7 animals by measuring core body temperature and general activity rhythms. The T7 cycle does not cause circadian arrhythmicity in either output rhythm (Fig. 1a, b and Supplementary Fig. 2), although the circadian period is lengthened.

To determine whether the T7 cycle influences the molecular basis of the circadian clock, we measured circadian changes of a molecular clock component (PER2) in central (SCN) and peripheral (liver) tissues. Mice housed in the T7 cycle show similar rhythms and localization of PER2 expression in the SCN as in littermates housed in the T24 cycle (Fig. 1c and Supplementary Fig. 3), indicating no disruption of internal rhythmicity of the SCN pacemaker. Furthermore, *Per2* levels in the liver from mice housed in the T24 or T7 light cycle were intact and showed similar phases (Fig. 1d). Together, these data show that the T7 light cycle does not disrupt sleep or cause circadian arrhythmicity. Although the circadian timing system and sleep remain intact under the T7 light cycle, mice are exposed to light pulses at all circadian phases during the experimental time course owing to the mismatch between the imposed light cycle and the period length. Thus, the T7 cycle will allow us to determine the direct influence of aberrant light exposure on mood and cognitive functions.

The T7 model causes light to appear during the night (active) phase of the animals' cycle. To determine which brain regions respond to light presented at night, we measured expression of the transcription factor c-Fos in response to an acute light pulse. After examination of ipRGC targets that are part of or known to influence the limbic system, we found light-induced c-Fos expression in the amygdala, lateral habenula and subparaventricular nucleus (Supplementary Fig. 4). This suggests that light input particularly when presented at an aberrant time of day may influence regions of the brain involved in mood and cognitive functions.

Shorter day-length during the winter months leads to a seasonal form of depression known as seasonal affective disorder (SAD), and appropriately timed light therapy can alleviate the symptoms of SAD⁸. We thus investigated whether the T7 cycle, which exposes animals to light at inappropriate times, causes depression-like behaviours in mice by evaluating sucrose anhedonia and behavioural despair in the forced swim test (FST). Mice housed in the T7 cycle showed decreased sucrose preference, indicating an increase in depression-like behaviour (Fig. 1e and Supplementary Fig. 5). This was further supported by the FST; mice housed in the T7 cycle spent significantly more time immobile than mice housed in the T24 cycle (Fig. 1f).

An established association with depression is increased serum corticosterone levels⁹. We measured serum corticosterone in animals housed in T24 or T7 cycles at four time points across the day. Although we found an intact circadian rhythm in corticosterone with a similar phase to mice housed in the T24 cycle, the overall levels of corticosterone were increased in mice housed in the T7 light cycle (Fig. 1g).

Increases in corticosterone levels as well as anhedonia are correlated with increased stress and anxiety¹⁰. To assay anxiety-like behaviour, we

¹Department of Biology, Johns Hopkins University, Baltimore, Maryland 21218, USA. ²Department of Neuroscience, Johns Hopkins University, Baltimore, Maryland 21218, USA. ³Department of Biology, Rider University, Lawrenceville, New Jersey 08648, USA.

*These authors contributed equally to the work.

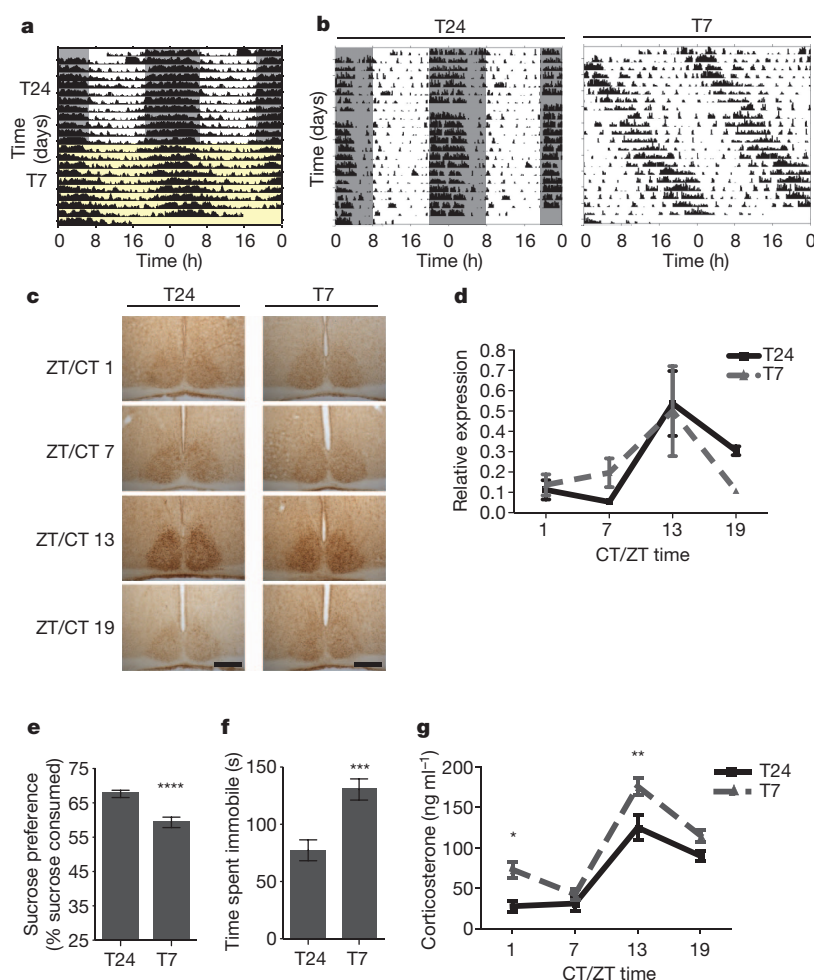


Figure 1 | Aberrant light increases depression-like behaviour and corticosterone levels. **a**, Body temperature rhythms under the T24 (grey/white) and T7 (yellow) cycles. **b**, General activity rhythms under the T24 (left) and T7 (right) cycles. **c**, PER2 expression in the SCN was rhythmic under the T24 and T7 cycles. Scale bars, 200 μ m. **d**, Liver *Per2* expression was rhythmic ($P_{\text{time}} = 0.0072$) ($n = 3$ –4 per time point, $P_{\text{light cycle}} = 0.8482$). CT, circadian

time; ZT, zeitgeber time. **e**, T7 mice showed sucrose anhedonia ($n = 16$ (T24) and $n = 15$ (T7), $P < 0.0001$). **f**, T7 mice showed increased immobility in the FST ($n = 22$ per group, $P = 0.0002$). **g**, Corticosterone levels were rhythmic but increased in T7 mice ($n = 5$ –6 per time point, $P_{\text{time}} < 0.0001$, $P_{\text{light cycle}} < 0.0001$, Bonferroni post-test: $P < 0.05$ ZT/CT 1 and $P < 0.01$ ZT/CT 13). * $P < 0.05$; ** $P < 0.01$; *** $P < 0.001$; **** $P < 0.0001$. Error bars indicate s.e.m.

used three tests: open field test, light–dark box and elevated plus maze. We found no significant difference between animals maintained in the T24 cycle and those in the T7 cycle (Supplementary Fig. 6). These results show that the T7 cycle does not globally influence behaviour but specifically elicits depression- and not anxiety-like behaviours.

Increased serum corticosterone levels and depression have been closely associated with hippocampal learning deficits¹¹. We conducted a hippocampal-dependent task, the Morris water maze (MWM) (Fig. 2a–d). In the MWM, the T7 mice required significantly more trials to achieve the same latency in locating a hidden platform compared with the T24 mice (Fig. 2b), despite similar swim speeds. All our measurements were done during the day in the T24 mice (Supplementary Fig. 7). Previous studies using the MWM have shown that mice use a hippocampal-dependent spatial strategy and a hippocampal-independent non-spatial strategy to locate the platform¹². We sought to determine whether the deficit in learning acquisition in the T7 mice was due to the lack of hippocampal-dependent spatial learning. We therefore conducted a probe trial, in which the platform in the water maze was removed from the target quadrant¹³ (Fig. 2c). We found that mice housed in the T24 cycle showed a significant preference for the target quadrant, whereas mice housed in the T7 cycle showed no preference for the target quadrant (Fig. 2c). Using a reversal assay, mice housed in the T24 cycle required significantly more trials to locate

the platform in the new quadrant, whereas the T7 mice showed no change in the latency to locate the platform (Fig. 2d). This further supports the dependence of T7 mice on a non-spatial escape strategy, highlighting a hippocampal-dependent learning deficit.

Spatial learning deficits are usually associated with long-term potentiation (LTP)¹⁴ decrement in the hippocampus. We found that mice housed in both the T24 and T7 cycles have similar basal synaptic transmission at the Schaffer collaterals in the hippocampus (Fig. 2e, f). However, mice housed in a T7 cycle showed impaired LTP in response to both one and four pulses of theta burst stimulation (TBS; Fig. 2g, h). We found no difference in low-frequency stimulation-induced long-term depression (LTD) between mice housed in the T24 and T7 cycles (Fig. 2i). Impaired LTP with no change in LTD has been previously associated with sleep deprivation¹⁵. The selective LTP deficits observed in mice housed in the T7 aberrant light cycle independent of sleep deprivation indicates that learning impairments due to inappropriate light exposure and sleep deprivation may use similar neural pathways (see model in Supplementary Fig. 13).

To determine whether the learning deficits in the T7 cycle extend to tasks involved in hippocampal-dependent recognition memory, we conducted the novel object recognition test¹⁶. Mice housed in the T24 cycle showed a significant preference for the novel object (Fig. 2j). By contrast, mice housed in the T7 cycle showed no preference for a novel object from a familiar object (Fig. 2j).

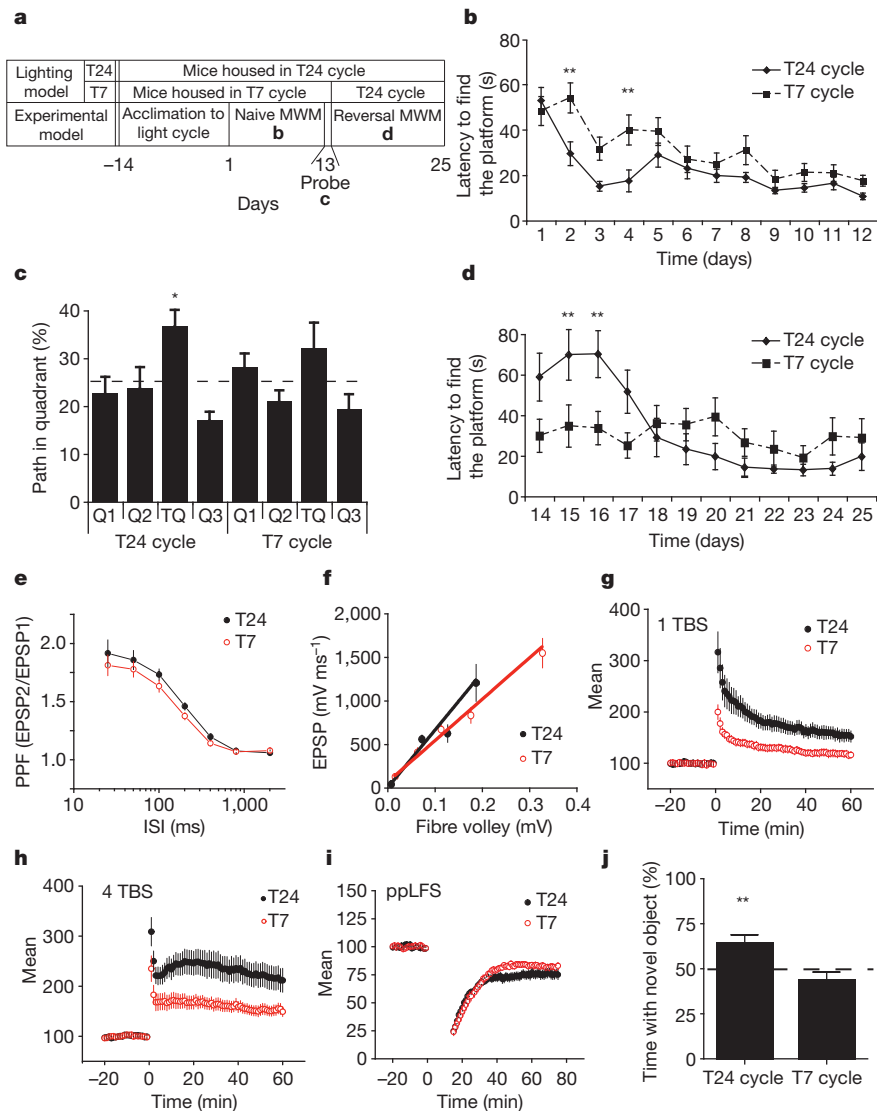


Figure 2 | Aberrant light impairs hippocampal learning, LTP, and recognition memory. **a**, Experimental model for the MWM. **b**, T7 mice showed impaired learning ($n = 21$ per group, $P_{\text{interaction}} = 0.041$, Bonferroni post-test $P < 0.01$ days 2 and 4). **c**, T7 mice show no significant preference for the target quadrant (TQ) (T24: $n = 9$, $P = 0.011$; T7: $n = 9$, $P = 0.25$). Dotted line indicates chance (25%). **d**, Mice housed in the T24 cycle showed an increased latency in a reversal trial, whereas T7-housed mice show a similar latency to the acquisition phase ($n = 9$ per group, $P_{\text{interaction}} < 0.0003$, Bonferroni post-test: $P < 0.01$ days 15 and 16). **e**, **f**, T24 and T7 mice have

similar basal synaptic release properties ($P_{\text{interaction}} = 0.7256$) ($n = 5$ per group) (fibre volley: $P_{\text{interaction}} = 0.984$, slope: $P > 0.1$). EPSP; excitatory postsynaptic potential; ISI, interstimulus intervals; PPF, paired-pulse facilitation. **g–i**, T7 mice showed LTP deficits ($n = 5$ per group, 1 TBS: $P_{\text{interaction}} < 0.01$; 4 TBS: $P_{\text{interaction}} < 0.01$) (**g** and **h**) but no difference in LTD (**i**). ppLFS, paired-pulse low-frequency stimulation. **j**, T7 mice showed deficit in novel object recognition (T24: $n = 24$, $P = 0.0057$; T7: $n = 24$, $P = 0.1773$). * $P < 0.05$; ** $P < 0.01$. Error bars indicate s.e.m.

To investigate whether antidepressants could rescue the learning deficits observed in T7 mice, we chronically administered fluoxetine to T24 and T7 mice (Fig. 3a). Chronic fluoxetine treatment decreased depression-like behaviour in mice housed in the T7 cycle (Fig. 3b). Furthermore, this treatment was able to rescue the learning deficit observed in the novel object recognition test (Fig. 3c). In support of this behavioural rescue of hippocampal function, chronic fluoxetine treatment also rescued the LTP deficit induced by the T7 cycle (Fig. 3d). Subchronic fluoxetine treatment did not rescue the increased depression or learning defect observed in mice housed in the T7 cycle (Supplementary Fig. 8), consistent with published reports¹⁷. We also used desipramine, a tricyclic antidepressant, and found that desipramine restored learning (Supplementary Fig. 9 and Supplementary Information). These results show that the detrimental behavioural changes induced by aberrant light exposure can be alleviated with antidepressant administration.

To determine the mechanism by which fluoxetine restores learning, we measured the circadian period in T7 mice treated with fluoxetine.

Although fluoxetine can phase shift the circadian oscillator¹⁸, chronic administration of fluoxetine did not change the length of the circadian period in mice housed in the T7 cycle (Supplementary Fig. 10). We then examined the corticosterone rhythms in fluoxetine-treated T7 mice and showed that corticosterone rhythms persist with lower overall levels compared with untreated mice (Fig. 3e). These data indicate that fluoxetine treatment does not alter circadian rhythms but instead lowers the level of corticosterone, which could lead to lower depression-like behaviour and better learning.

Studies have suggested that ipRGCs, in addition to affecting reflexive, irradiance-dependent non-image forming visual functions, might directly influence higher cognitive functions and brain processing of emotions^{19–22}. To determine directly whether ipRGCs mediate the effects of the T7 cycle on mood and learning, we tested mice lacking ipRGCs (*Opn4*^{aDTA/aDTA}, herein referred to as aDTA mice). Although most ipRGCs are ablated, these mice still retain more than 95% of RGCs and are capable of image formation⁵. First, we compared wild

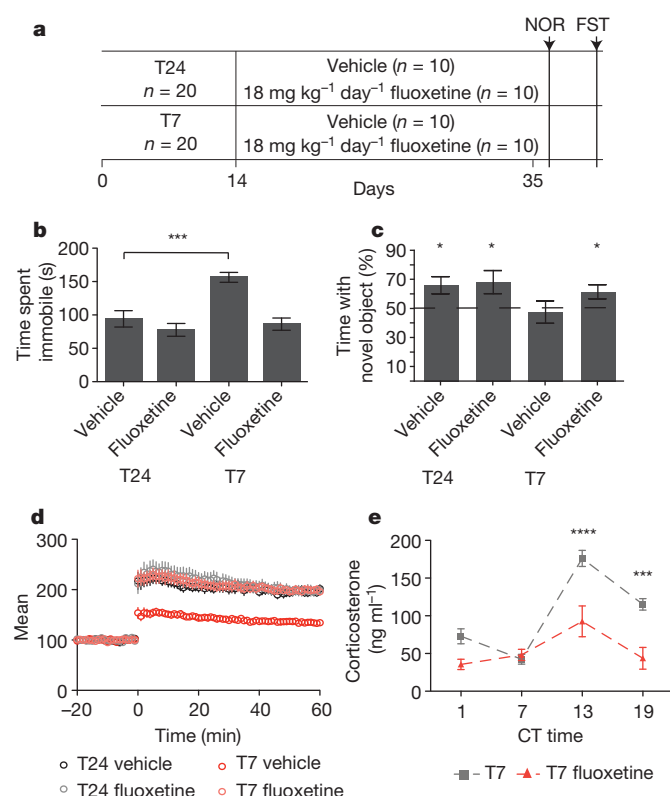


Figure 3 | Chronic antidepressant administration rescues learning.

a, Timeline for fluoxetine administration and testing. NOR, novel object recognition. **b**, Chronic fluoxetine reduced T7 immobility time in the FST ($n = 10$ per group, $P_{\text{interaction}} = 0.0092$, Bonferroni post-test: $P < 0.001$ T24 versus T7 vehicle). **c**, T7 mice treated with fluoxetine showed restored novel object preference (T24_{vehicle}: $n = 9$, $P = 0.03$; T24_{fluoxetine}: $n = 9$, $P = 0.048$; T7_{vehicle}: $n = 10$, $P = 0.77$; T7_{fluoxetine}: $n = 10$, $P = 0.04$). **d**, Chronic fluoxetine rescued the T7-induced LTP deficit ($n = 5$ (T24 vehicle), $n = 5$ (T24 fluoxetine), $n = 5$ (T7 vehicle), and $n = 4$ (T7 fluoxetine); $P_{\text{interaction}} < 0.0001$). **e**, Chronic fluoxetine decreased corticosterone levels in T7 mice ($n = 5$ –8 per time point). T7 corticosterone levels are plotted for comparison. ($P_{\text{interaction}} = 0.0053$, Bonferroni post-test: $P < 0.0001$ CT 13 and $P < 0.001$ CT 19). * $P < 0.05$; *** $P < 0.001$; **** $P < 0.0001$. Error bars indicate s.e.m.

type to aDTA littermates and showed no differences in baseline for the FST and corticosterone levels (Supplementary Fig. 11). We then placed aDTA mice under T24 and T7 cycles and found no difference in anxiety-like behaviours between the two groups (Supplementary Fig. 12). By contrast, the increased depression-like behaviour, learning deficits and hippocampal LTP decrement observed in the T7 cycle in wild-type animals were not observed in aDTA mice exposed to this cycle (Fig. 4). These results indicate that the negative influence of the aberrant light cycles on behaviour requires ipRGCs. Thus, subconscious light detection in humans via ipRGCs may be responsible for the depression and learning deficits observed under disruptive light environments.

Manipulation of the light environment can lead to disruptions in circadian rhythms and sleep and also cause mood and learning defects in mice and humans^{2,23,24}. These studies have led to a model in which light affects cognition exclusively through the modulation of sleep and circadian pathways (Supplementary Fig. 13). Here, we provide a further model in which light directly influences mood leading to learning deficits in the context of an intact circadian timing system and normal sleep distribution and architecture (Supplementary Fig. 13a). Further support that the effects of the T7 cycle are not due to circadian disruptions originate from behavioural comparisons to animals lacking a functional circadian oscillator (for example, circadian mutant- or SCN lesioned- animals), in which reduced depression-like behaviour is observed^{25,26} (Supplementary Fig. 13b). Taken together,

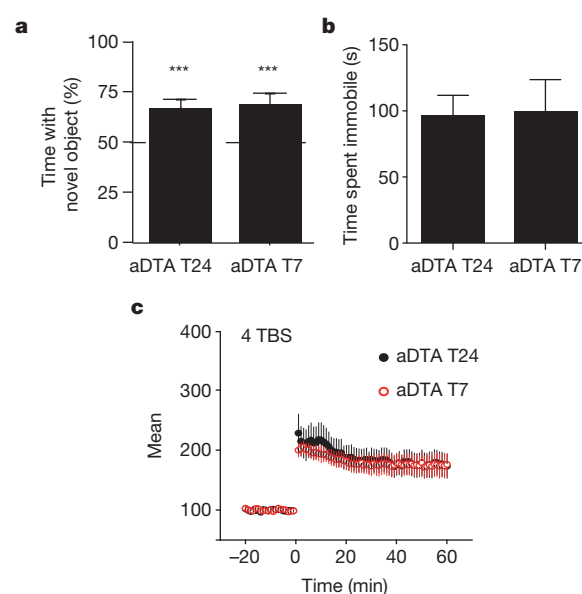


Figure 4 | ipRGCs mediate impairment of mood and learning by aberrant light. **a**, Mice lacking ipRGCs showed a significant preference for the novel object when housed in both the T24 and T7 light cycles ($n = 12$ per group, $P < 0.001$). **b**, aDTA mice housed in the T7 cycle performed similarly to those housed in the T24 cycle in the FST ($n = 6$ (T24) and $n = 5$ (T7), unpaired t -test: $P = 0.93$). **c**, T7 aDTA mice had similar LTP to T24 aDTA mice in response to four-pulse TBS. *** $P < 0.001$. Error bars indicate s.e.m.

these data provide evidence that the aberrant light effects on mood are direct. Furthermore, the depression-like behaviour caused by the T7 aberrant light cycle can serve as an alternative experimental model for depression research in rodents, independent of genetic manipulations or aversive treatments such as repetitive restraint or electric shocks.

METHODS SUMMARY

Adult (4–8 months) male mice (B6/129 F₁ hybrid; Jackson Laboratory) were used for all experiments involving wild-type mice placed under different light environments. Adult littermate aDTA mice placed under different light environments were of B6/129 background (6–8 months) and were raised in our laboratory. aDTA mice could not be used until they were at least 6 months old because elimination of the melanopsin cell population in these mice is not complete until this time⁵. All mice were individually housed in standard animal facility cages with access to food and water *ad libitum*. All mice were initially entrained to a 12 h:12 h light–dark cycle (T24), after which the lights for one group were switched to a 3.5 h:3.5 h light–dark cycle (T7) for 2 weeks. The light intensity during the light portion was ~800 lx, chosen to cause no circadian arrhythmicity. All experiments were done in accordance with the regulations set forth by Johns Hopkins University and Rider University Animal care and use committee.

Behavioural analysis. Mice were maintained in the T24 or T7 light cycle for 2 weeks before testing unless otherwise indicated. Body temperature and general activity were measured to evaluate circadian rhythmicity. Sucrose preference and the FST were used to assess depression-like behaviour. The MWM and novel object recognition test were used to assess hippocampal-dependent learning.

Cellular and molecular analysis. To examine the circadian timing system, immunohistochemistry and qRT–PCR were used to quantify PER2 expression in the SCN and liver, respectively. Serum corticosterone levels were quantified by ELISA. Electrophysiological recordings from the dorsal hippocampus were performed to evaluate hippocampal function including LTP and LTD.

Full Methods and any associated references are available in the online version of the paper.

Received 4 April 2011; accepted 11 October 2012.

Published online 14 November 2012.

- Reppert, S. M. & Weaver, D. R. Coordination of circadian timing in mammals. *Nature* **418**, 935–941 (2002).
- Foster, R. G. & Wulff, K. The rhythm of rest and excess. *Nature Rev. Neurosci.* **6**, 407–414 (2005).

3. Berson, D. M., Dunn, F. A. & Takao, M. Phototransduction by retinal ganglion cells that set the circadian clock. *Science* **295**, 1070–1073 (2002).
4. Hattar, S., Liao, H. W., Takao, M., Berson, D. M. & Yau, K. W. Melanopsin-containing retinal ganglion cells: architecture, projections, and intrinsic photosensitivity. *Science* **295**, 1065–1070 (2002).
5. Güler, A. D. *et al.* Melanopsin cells are the principal conduits for rod–cone input to non-image-forming vision. *Nature* **453**, 102–105 (2008).
6. Hattar, S. *et al.* Central projections of melanopsin-expressing retinal ganglion cells in the mouse. *J. Comp. Neurol.* **497**, 326–349 (2006).
7. Altimus, C. M. *et al.* Rods–cones and melanopsin detect light and dark to modulate sleep independent of image formation. *Proc. Natl Acad. Sci. USA* **105**, 19998–20003 (2008).
8. Lam, R. W. & Levitan, R. D. Pathophysiology of seasonal affective disorder: a review. *J. Psychiatry Neurosci.* **25**, 469–480 (2000).
9. Nestler, E. J. *et al.* Neurobiology of depression. *Neuron* **34**, 13–25 (2002).
10. McEwen, B. S. Protective and damaging effects of stress mediators. *N. Engl. J. Med.* **338**, 171–179 (1998).
11. Cryan, J. F. & Holmes, A. The ascent of mouse: advances in modelling human depression and anxiety. *Nature Rev. Drug Discov.* **4**, 775–790 (2005).
12. Baldi, E., Lorenzini, C. A. & Corrado, B. Task solving by procedural strategies in the Morris water maze. *Physiol. Behav.* **78**, 785–793 (2003).
13. Vorhees, C. V. & Williams, M. T. Morris water maze: procedures for assessing spatial and related forms of learning and memory. *Nature Protocols* **1**, 848–858 (2006).
14. Bliss, T. V. & Collingridge, G. L. A synaptic model of memory: long-term potentiation in the hippocampus. *Nature* **361**, 31–39 (1993).
15. McDermott, C. M. *et al.* Sleep deprivation causes behavioral, synaptic, and membrane excitability alterations in hippocampal neurons. *J. Neurosci.* **23**, 9687–9695 (2003).
16. Honey, R. C., Watt, A. & Good, M. Hippocampal lesions disrupt an associative mismatch process. *J. Neurosci.* **18**, 2226–2230 (1998).
17. Dulawa, S. C., Holick, K. A., Gundersen, B. & Hen, R. Effects of chronic fluoxetine in animal models of anxiety and depression. *Neuropsychopharmacology* **29**, 1321–1330 (2004).
18. Sprouse, J., Braselton, J. & Reynolds, L. Fluoxetine modulates the circadian biological clock via phase advances of suprachiasmatic nucleus neuronal firing. *Biol. Psychiatry* **60**, 896–899 (2006).
19. Lockley, S. W. *et al.* Short-wavelength sensitivity for the direct effects of light on alertness, vigilance, and the waking electroencephalogram in humans. *Sleep* **29**, 161–168 (2006).
20. Vandewalle, G. *et al.* Spectral quality of light modulates emotional brain responses in humans. *Proc. Natl Acad. Sci. USA* **107**, 19549–19554 (2010).
21. İyilikci, O., Aydın, E. & Canbeyli, R. Blue but not red light stimulation in the dark has antidepressant effect in behavioral despair. *Behav. Brain Res.* **203**, 65–68 (2009).
22. Warthen, D. M., Wiltgen, B. J. & Provencio, I. Light enhances learned fear. *Proc. Natl Acad. Sci. USA* **108**, 13788–13793 (2011).
23. Fonken, L. K. *et al.* Influence of light at night on murine anxiety- and depressive-like responses. *Behav. Brain Res.* **205**, 349–354 (2009).
24. Ma, W. P. *et al.* Exposure to chronic constant light impairs spatial memory and influences long-term depression in rats. *Neurosci. Res.* **59**, 224–230 (2007).
25. Roybal, K. *et al.* Mania-like behavior induced by disruption of CLOCK. *Proc. Natl Acad. Sci. USA* **104**, 6406–6411 (2007).
26. Tataroğlu, O., Aksoy, A., Yilmaz, A. & Canbeyli, R. Effect of lesioning the suprachiasmatic nuclei on behavioral despair in rats. *Brain Res.* **1001**, 118–124 (2004).

Supplementary Information is available in the online version of the paper.

Acknowledgements We would like to thank T. Gould, G. Ball and A. Sawa for their expert advice on the behavioural tests. We would like to thank R. Kuruvilla for her critical reading and advice on this manuscript. We would also like to thank the mouse tri-laboratory for suggestions and advice. This work was supported by the David and Lucile Packard Foundation grant to S.H.

Author Contributions T.A.L., C.M.A., H.Z., E.T.W. and S.H. designed experiments. T.A.L. and C.M.A. carried out experiments. H.W., H.-K.L., S.Y. and A.K. designed and performed electrophysiological experiments. T.A.L., C.M.A., H.Z., E.T.W. and S.H. wrote the paper.

Author Information Reprints and permissions information is available at www.nature.com/reprints. The authors declare no competing financial interests. Readers are welcome to comment on the online version of the paper. Correspondence and requests for materials should be addressed to S.H. (shattar@jhu.edu).

METHODS

Animals and housing. Adult (4–8 months) male mice (B6/129 F₁ hybrid; Jackson Laboratory) were used for all experiments involving wild-type mice placed under different light environments. Adult littermate aDTA mice placed under different light environment were of B6/129 background (6–8 months) and were raised in our laboratory. aDTA mice could not be used until they were at least 6 months old because elimination of the melanopsin cell population in these mice is not complete until this time⁵. All mice were individually housed in standard animal facility cages with access to food and water *ad libitum*. All mice were initially entrained to a 12 h:12 h light–dark cycle (T24), after which the lights for one group were switched to 3.5 h:3.5 h light–dark (T7) for 2 weeks. The light intensity during the light portion was ~800 lx, chosen to have no circadian arrhythmicity. All experiments were done in accordance with the regulations set forth by Johns Hopkins University and Rider University Animal care and use committee.

Body temperature measurements. Body temperature measurements were made using G2 E-mitter telemetric probes from Mini Mitter (Respironics). The telemetric probe was implanted into the peritoneum and sutured to the inside of the abdominal wall. Mice were given 1 week to recover from surgery before any recording.

Recordings were obtained using Vitalview software (Respironics), at a rate of 30 measurements per hour. Throughout, experiment mice were maintained in their home cage without perturbation and the light cycles were adjusted to test response to both the T24 and T7 light cycles. Circadian period was determined by fitting a regression line to the onsets of activity over a 7-day period using Clocklab (Actimetrics). Period lengths of mice housed in the T24 and T7 light cycles were compared using an unpaired Student's *t*-test.

General activity measurements. General activity was measured using infrared motion detectors from Mini Mitter (Respironics). Mice were housed individually, and the motion detector was mounted to the top of the cage so that general activity could be monitored throughout the T24 and T7 light cycle. Data were collected in 10-min bins using Vitalview software (Respironics). Circadian period length was determined by fitting a regression line to the onsets of activity over a 7-day period using Clocklab (Actimetrics). Period lengths of mice housed in the T24 and T7 light cycles were compared using an unpaired Student's *t*-test.

Molecular rhythm measurements. Mice were housed in either the T24 ($n = 16$) or the T7 ($n = 16$) light cycle for 2 weeks, during which general activity was monitored in T7 mice to determine their circadian phase. Mice were sampled across four time points. Mice under the T24 cycle were sampled at ZT 1, 7, 13 and 19, and mice under the T7 cycle were sampled at CT 1, 7, 13 and 19, which was determined using their general activity rhythm. Each mouse was removed from its cage, and tail blood was quickly sampled. The mouse was then anaesthetized with 1 ml of avertin (20 mg ml⁻¹). Once anaesthetized, a small sample of liver was isolated. The mouse was then perfused transcardially with 0.9% saline followed by 4% paraformaldehyde. The brain was removed and postfixed overnight in 4% paraformaldehyde followed by cryoprotection and embedding in OCT compound (Sakura Finetek).

Real-time PCR. Liver samples were homogenized and RNA extracted using the RNeasy mini kit (Qiagen). The Retroscript kit (Ambion) was used to reverse transcribe poly(A) RNAs. Real-time quantitative PCR was performed with iQ SYBR Green Supermix and the iCycler iQ real-time PCR detection system (Bio-Rad). Each sample was analysed in triplicate reactions of 50 µl. Primers for *Per2* were forward: 5'-GCCTTCAGACTCATGATGACAGA-3' and reverse: 5'-TTTGTGTGCGTCAGCTTTGG-3'. Primers for 18S rRNA (internal control) were forward: 5'-CGCCGCTAGAGGTGAAATTC-3' and reverse: 5'-TTGGCAAATGCTTTTCGCTC-3'.

Data were analysed using the $\Delta\Delta C_t$ method, normalizing each sample to the internal control, and relative messenger RNA was determined as the percentage of the maximum value observed in the experiment. Data were analysed by two-way analysis of variance (ANOVA) followed by a Bonferroni post-hoc test to examine differences over time as well as potential light cycle effects on *Per2* expression.

PER2 immunohistochemistry. Brains were sectioned (40 µm) by cryostat through the rostral–caudal extent of the SCN, and were stored free floating in 0.1 M phosphate buffer. Free-floating sections were incubate in blocking buffer (0.1 M phosphate buffer, 3% triton, 0.5% bovine serum albumin and 1% goat serum) for 2 h. Sections were then incubated in rabbit anti-Per2 (Alpha Diagnostic International; 1:4,000 in blocking buffer) overnight and visualized with a Vectastain horseradish peroxidase kit (Vector Labs) using 3,3'-diaminobenzidine (DAB; Sigma). Sections were mounted on microscope slides, dehydrated and coverslipped with Permount. Sections were imaged at $\times 10$ magnification with a Zeiss Axio Imager M1 microscope. Optical density was measured using ImageJ. Data were analysed by two-way ANOVA followed by a Bonferroni post-hoc test to examine differences over time as well as potential light cycle effects on PER2 expression.

Corticosterone measurement. Serum was isolated from collected tail blood and assayed for corticosterone by ELISA (Assaypro). Data were analysed by two-way ANOVA followed by a Bonferroni post-hoc test to examine differences over time as well as light cycle effects on corticosterone levels. For fluoxetine experiments, corticosterone levels were analysed by two-way ANOVA followed by a Bonferroni post-hoc to examine differences over time as well as the effect of fluoxetine.

For the experiment comparing wild-type and aDTA mice, serum was sampled from wild-type and aDTA mice at ZT 13/CT 13 based on general activity rhythms (as described above). The samples were processed as described above. Corticosterone levels of wild-type and aDTA mice were analysed by unpaired Student's *t*-test.

Light-induced c-Fos expression. Mice were housed under a 12 h:12 h light–dark cycle and were exposed to a 10-min light pulse at ZT 14 (2 h after light offset), after which they were placed back in the dark for a further 80 min. Control mice remained in the dark until anaesthetization. Ninety minutes after the start of light presentation, mice were deeply anaesthetized with 1 ml of avertin (20 mg ml⁻¹). Once anaesthetized, the mice were perfused transcardially with 0.9% saline followed by 4% paraformaldehyde. Brains were removed, postfixed overnight in 4% paraformaldehyde, and then transferred to 0.1 M phosphate buffer. Brains were sectioned (40 µm) through the rostro–caudal extent of the SCN using a vibrotome (World Precision Instruments). Sections were stored free floating in 0.1 M phosphate buffer. Every other section was stained immunohistochemically for c-Fos. Sections were incubated in blocking buffer (0.1 M phosphate buffer, 3% Triton X-100 and 0.5% bovine serum albumin) for 2 h. Sections were incubated in rabbit anti-c-Fos (Calbiochem Ab-5; 1:20,000) overnight at 4 °C and then visualized with a goat anti-rabbit Vectastain horseradish peroxidase kit (Vector Labs) using DAB (Sigma) as a chromagen. Sections were mounted on microscope slides, dehydrated and coverslipped with Permount. Slides were viewed and imaged on a Zeiss Axio Imager.M1 microscope at $\times 5$ magnification. Photoshop and ImageJ were used to count c-Fos-positive cells and measure the area of region counted from. The number of c-Fos positive cells was normalized to the area of the region, and these values were compared between mice that received a light pulse and dark controls. These data were analysed using an unpaired Student's *t*-test.

Sucrose anhedonia. Mice were housed in the presence of two water bottles 1 day before testing to acclimate them to the bottles. Sucrose preference was assessed over 2 days. Each day, one bottle containing 1% sucrose and one bottle containing water were introduced at the beginning of the active phase. The position of these bottles was switched 6 h later, and the bottles were removed at the end of the active phase. Bottles were weighed at the beginning and end of the active period to measure amount consumed. Sucrose preference was calculated by dividing the amount of sucrose consumed by the total amount consumed (water and sucrose). The percentage of sucrose consumed by mice in the T24 and T7 cycles was compared by a Student's *t*-test.

FST. Mice were individually placed in an inescapable container of water (25 °C) for 6 min. Behaviour was monitored by video cameras positioned in front of the apparatus and scored by a video tracking system (Forced Swim Test, Bioserve). Time spent immobile for the last 4 min of the test was calculated. Increased time spent immobile is indicative of increased depression-related behaviour. The amount of time spent immobile during the last 4 min was analysed by Student's *t*-test. For fluoxetine experiments, the amount of time spent immobile during the last 4 min were analysed by two-way ANOVA followed by a Bonferroni post-hoc to compare light cycle and drug treatment.

Open field. Mice were individually placed in the centre of a large, brightly lit arena (500 lx, 60 \times 60 cm) and allowed to explore for 5 min. Behaviour was monitored from above by a video camera connected to a computerized video tracking system (Anymaze, Stoelting). The apparatus was cleaned thoroughly between each trial. The percentage distance travelled and time in the centre of the arena were measured. These measures were compared between mice housed in the T24 and T7 cycles using an unpaired Student's *t*-test.

Light–dark box. The light–dark box consisted of two compartments equivalent in size (20 \times 20 cm); one area is brightly lit (600 lx) and the other is dimly lit (<1 lx). A small opening joins the two compartments, so the mice could freely move between the two areas. Mice were dark adapted for 1 h before testing. At the beginning of the test, dark-adapted mice were placed in the lit compartment facing away from the opening and allowed to freely explore for 5 min. Behaviour was monitored from above by a video camera connected to a computerized video tracking system (Anymaze). The apparatus was cleaned thoroughly between each trial. The number of transitions between the two compartments as well as the time spent and distance travelled in the lit room were measured as indications of anxiety-related behaviour. These measures were compared between mice housed in the T24 and T7 cycles using an unpaired Student's *t*-test.

Elevated plus maze. The apparatus consisted of two open arms (42 \times 6 cm) opposite to one another and two arms enclosed by walls (42 \times 6 \times 14 cm) opposite

of one another forming a cross. The arms were separated by a central platform (6×6 cm). The maze was elevated (33 cm) such that the open arms convey openness, unfamiliarity and elevation. The light intensity in the open arms was ~ 600 lx, whereas the light intensity in the closed arms was ~ 200 lx. Mice were placed in the centre of the elevated plus maze facing one of the open arms. Behaviour was monitored from above by a video camera connected to a computerized video tracking system (Anymaze). The apparatus was cleaned thoroughly between each trial. The time spent and the distance travelled in the open arms were measured as indications of anxiety-related behaviour. These measures were compared between mice housed in the T24 and T7 cycles using an unpaired Student's *t*-test.

MWM. The water maze consisted of a circular pool (150 cm in diameter) with room temperature water ($26\text{--}28^\circ\text{C}$). The water was made opaque with the addition of non-toxic white tempura paint to hide the escape platform. The platform was made from PVC piping with a top (10 cm in diameter) painted white and submerged in the pool such that 1 cm of water covered the platform hiding it from sight. For visual trials, a flag made from a 50-ml conical tube covered with coloured tape was placed on the platform. During the acquisition, probe and reversal trials, four cues were attached to the side of the pool equidistant from one another, and the entire pool was surrounded by a plain curtain to block any other visual cues. Performance was scored using a video tracking system (Anymaze) with a camera mounted above the pool. The light intensity at the water surface was approximately 500 lx.

Mice were tested in four stages: visual, acquisition, probe and reversal (see Fig. 2a). Before spatial training, mice were trained to escape the pool using the visual flag located on top of the platform to familiarize them with the test. This was performed four times with an inter-trial interval of (30 min), and the platform was moved between each trial. We also used this visual training to screen for and remove animals that show floating behaviour in the water maze. Animals that floated in two or more trials during training were not tested in the spatial task to prevent confounds from floating behaviour. During the acquisition phase, mice were trained (one trial per day for 12 days) to find the hidden platform using the four visual distal cues surrounding the pool. The mouse was randomly placed in a different area of the pool at the start of each trial with the platform maintained in the same quadrant (target quadrant). The platform was removed on day 13 in the probe trial. The swimming in each quadrant and specifically the preference for the target quadrant was measured to evaluate spatial memory using a computerized video tracking system (Anymaze). Reversal training began on day 14 when the platform was moved to the quadrant opposite the original target quadrant. Mice were trained as described for the acquisition phase.

Latency to locate the platform during the acquisition and reversal phases was analysed by two-way ANOVA followed by a Bonferroni post-hoc test to examine changes in latency throughout the course of the experiment as well as the effect of light cycle exposure. Probe trial was analysed by calculating the percentage time spent in the target quadrant and performing a one-sample *t*-test to determine whether this was significantly above 25%.

Novel object recognition. Novel object recognition was composed of three stages: acclimation to the novel object arena, familiar object exposure and finally novel object exposure. Mice were first removed from their home cage, acclimated to the empty testing arena (light intensity of 500 lx) for 10 min, and subsequently returned to their home cage 24 h before including two objects in the arena. The day after acclimation, mice were returned to this arena with two identical objects that they could freely explore for 10 min, after which they were returned to their home cage for 1 h. At the end of the 1-h period, mice were placed back into the arena with one of the objects changed to a novel object, and were allowed to

explore both the familiar and novel objects for 5 min. Behaviour was monitored from above by a video camera connected to a computerized video tracking system (Anymaze), and the percentage of time spent with each object was calculated. Wild-type mice spend more time with the novel object, however, mice with recognition memory deficits will not be able to distinguish the novel from the stable object. Objects had been previously tested to ensure that animals showed no initial preference for a particular object. The identity of the objects (familiar versus novel) was counterbalanced. The objects and arena were thoroughly cleaned between each trial to remove odour cues. Object recognition was analysed by calculating the percentage time spent with the novel object and performing a one sample *t*-test to determine whether this was significantly above 50%.

Slice electrophysiology. Coronal (0.4 mm) hippocampal slices were prepared as described²⁷ in ice-cold dissection buffer (2.6 mM KCl, 1.23 mM NaH_2PO_4 , 26 mM NaHCO_3 , 212.7 mM sucrose, 10 mM dextrose, 3 mM MgCl_2 and 1 mM CaCl_2 , bubbled with 5% CO_2 , 95% O_2). Recordings were done in a similar buffer but with the sucrose replaced by NaCl and the temperature raised to 30°C . Synaptic responses were evoked at 0.33 Hz stimulating the Schaffer collaterals with 0.2-ms pulses (concentric bipolar electrodes, FHC), and recorded extracellularly in CA1 stratum radiatum. LTP was induced by TBS, consisting of one or four theta epochs delivered at 0.1 Hz. Each epoch, in turn, consisted of 10 trains of four pulses (at 100 Hz) delivered at 5 Hz. LTD was induced by low frequency stimulation (1 Hz, 15 min). These protocols were delivered after 20 min of stable baseline transmission. All hippocampal slice electrophysiological recordings were performed and analysed by an experimenter blind to the treatment of the animals. Two-way ANOVA was used to analyse fibre volley differences between the T7 and T24 treatments. The slopes for the linear fit of the fibre-volley-slope relationship were compared by *t*-test.

Fluoxetine administration. Mice were housed in either the T24 or T7 cycle for two weeks ($n = 20$ per group) with food and water *ad libitum*. For chronic treatment, this was followed by a 3-week treatment of $18\text{ mg kg}^{-1}\text{ day}^{-1}$ of fluoxetine (Sigma). For subchronic treatment, this was followed by a 4-day treatment of $18\text{ mg kg}^{-1}\text{ day}^{-1}$. Fluoxetine was administered in the drinking water and control mice received tap water. Dosage was calculated based on the average amount of water consumed per day and mouse weight. Fluoxetine consumption was also measured during treatment to determine the amount consumed per mouse.

Period length measurement with fluoxetine treatment. Mice were housed under infrared motion detectors as described above. Mice were housed in the T7 light cycle for 2 weeks after which fluoxetine ($18\text{ mg kg}^{-1}\text{ day}^{-1}$) was administered in the drinking water for 3 weeks. Circadian period was determined by fitting a regression line to the onsets of activity over a 7-day period. Period lengths before and after 3 weeks of fluoxetine treatment were compared by paired *t*-test.

Desipramine administration. Desipramine (Sigma) was dissolved in sterile water with 5% Tween-20. Each mouse received 16 mg kg^{-1} desipramine intraperitoneally 24- and 1-h before testing in the novel object recognition paradigm. The same volume of vehicle (water with 5% Tween-20) was administered intraperitoneally to control mice.

Statistical analysis. All statistical analysis was performed using GraphPad Prism. Specific tests used to analyse data are described their respective section of the methods.

27. Lee, H. K., Min, S. S., Gallagher, M. & Kirkwood, A. NMDA receptor-independent long-term depression correlates with successful aging in rats. *Nature Neurosci.* **8**, 1657–1659 (2005).

Synaptic amplification by dendritic spines enhances input cooperativity

Mark T. Harnett^{1*}, Judit K. Makara^{1,2*}, Nelson Spruston¹, William L. Kath³ & Jeffrey C. Magee¹

Dendritic spines are the nearly ubiquitous site of excitatory synaptic input onto neurons^{1,2} and as such are critically positioned to influence diverse aspects of neuronal signalling. Decades of theoretical studies have proposed that spines may function as highly effective and modifiable chemical and electrical compartments that regulate synaptic efficacy, integration and plasticity^{3–8}. Experimental studies have confirmed activity-dependent structural dynamics and biochemical compartmentalization by spines^{9–12}. However, there is a longstanding debate over the influence of spines on the electrical aspects of synaptic transmission and dendritic operation^{3–8,13–18}. Here we measure the amplitude ratio of spine head to parent dendrite voltage across a range of dendritic compartments and calculate the associated spine neck resistance (R_{neck}) for spines at apical trunk dendrites in rat hippocampal CA1 pyramidal neurons. We find that R_{neck} is large enough ($\sim 500 \text{ M}\Omega$) to amplify substantially the spine head depolarization associated with a unitary synaptic input by ~ 1.5 - to ~ 45 -fold, depending on parent dendritic impedance. A morphologically realistic compartmental model capable of reproducing the observed spatial profile of the amplitude ratio indicates that spines provide a consistently high-impedance input structure throughout the dendritic arborization. Finally, we demonstrate that the amplification produced by spines encourages electrical interaction among coactive inputs through an R_{neck} -dependent increase in spine head voltage-gated conductance activation. We conclude that the electrical properties of spines promote nonlinear dendritic processing and associated forms of plasticity and storage, thus fundamentally enhancing the computational capabilities of neurons^{19–21}.

To measure the ratio of spine-to-dendrite voltage amplitude and associated R_{neck} , we combined two-photon Ca^{2+} imaging and glutamate uncaging with dual dendritic patch-clamp current injection and voltage recording from hippocampal CA1 pyramidal neurons in acute slices from adult rats. Excitatory input was produced by uncaging onto a single spine of interest located on the apical dendritic trunk. The resulting excitatory postsynaptic potential (EPSP) was measured in the dendritic branch (termed $\text{EPSP}_{\text{branch}}$; see Methods), and laser power was modulated to generate a range of $\text{EPSP}_{\text{branch}}$ amplitudes and associated spine head Ca^{2+} signals (assayed via the calcium indicator dye Oregon Green 488 BAPTA-1 (OGB-1)) that were mediated exclusively by voltage-gated Ca^{2+} channels (Fig. 1b, e, f; 0.5 – $1.0 \mu\text{M}$ tetrodotoxin (TTX) and 50 – $100 \mu\text{M}$ D(-)-2-amino-5-phosphonvaleric acid (AP5) present; Supplementary Figs 2–4). Next, excitatory postsynaptic current (EPSC)-shaped currents were injected into the dendrite to depolarize the spine to a level at which the associated spine Ca^{2+} signals matched those produced by the glutamate uncaging (Fig. 1c–f and Supplementary Fig. 9) ($8.6 \pm 1.0 \mu\text{m}$ between pipettes, $14.2 \pm 1.7 \mu\text{m}$ from spine of interest to voltage-recording electrode). Owing to the lack of voltage attenuation from the dendrite to the spine^{3,4,6}, these dendritic depolarizations provide an accurate estimate of the amplitude of uncaging-evoked spine head potentials (termed $\text{EPSP}_{\text{spine}}$; see Methods). The amount of electrical compartmentalization produced by the spine was

measured as the amplitude ratio (AR) of $\text{EPSP}_{\text{spine}}$ to $\text{EPSP}_{\text{branch}}$. R_{neck} was subsequently calculated from this value and the measured dendritic impedance ($11.0 \pm 1.0 \text{ M}\Omega$, $n = 8$ cells; equation (4) in Methods).

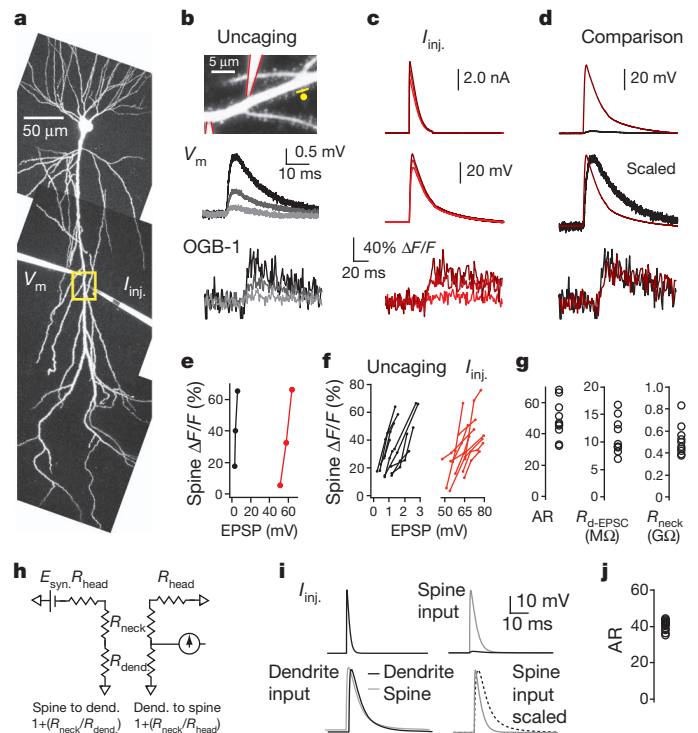


Figure 1 | Measurement of voltage amplitude ratio across apical trunk spine necks. **a**, Two-photon Z-stack image of a CA1 pyramidal neuron patched with two electrodes at the apical trunk $\sim 200 \mu\text{m}$ from the soma. **b**, Top, yellow box from **a** expanded to show spine imaging (yellow line) and two-photon glutamate-uncaging (yellow dot) locations. Electrodes are outlined in red. Middle, averaged voltage traces and bottom, spine Ca^{2+} signals evoked by uncaging at increasing laser powers. **c**, EPSC-shaped waveforms delivered through one electrode (I_{inj} , top) evoked EPSPs recorded at the other electrode (V_m , middle) and spine Ca^{2+} signals (bottom). **d**, Comparison of voltage traces (top, actual amplitude; middle, scaled) corresponding to similar spine Ca^{2+} signals (bottom). **e**, Spine Ca^{2+} signals versus EPSP amplitude evoked by single-spine glutamate uncaging (black) and EPSC injection (red) for the cell shown in **a–d**. **f**, Summary of ten experiments comparing single trunk spine uncaging with current injection during dual dendritic recording. **g**, AR calculated from $\text{EPSP}_{\text{spine}}/\text{EPSP}_{\text{branch}}$ at comparable spine Ca^{2+} signals (left) for experiments shown in **f** and associated peak dendritic input resistance during EPSC injection ($R_{\text{d-EPSC}}$; middle) were used to derive R_{neck} (right). **h**, Circuit diagram for voltage attenuation from dendrite-to-spine versus spine-to-dendrite across spine head, spine neck, and dendritic resistances. **i**, Voltage responses at the dendrite (black) or spine head (grey) in a multi-compartment model of a CA1 neuron for a trunk spine $213 \mu\text{m}$ from the soma with a $500 \text{ M}\Omega$ R_{neck} in response to fast current injection at either the spine head or dendrite. **j**, Summary of AR for 18 model trunk spines located 150 – $300 \mu\text{m}$ from the soma.

¹HMMI Janelia Farm Research Campus, Ashburn, Virginia 20147, USA. ²Institute of Experimental Medicine, Hungarian Academy of Sciences, Budapest 1083, Hungary. ³Departments of Applied Mathematics and Neurobiology, Northwestern University, Evanston, Illinois 60208, USA.

*These authors contributed equally to this work.

For apical trunk spines located $223 \pm 10 \mu\text{m}$ from the soma we measured an AR of 49.0 ± 3.8 and corresponding R_{neck} of $514 \pm 44 \text{ M}\Omega$ ($n = 10$ spines from 8 cells; Fig. 1g). A morphologically realistic multi-compartmental simulation using an R_{neck} of $500 \text{ M}\Omega$ for trunk spines at similar locations supported the above observations (Fig. 1i, j). Under physiological conditions, the mean unitary dendritic EPSP amplitude at these synapses is $\sim 0.5 \text{ mV}$ ²². Together with our measurements above, this reported value suggests spine head depolarizations of $\sim 25 \text{ mV}$ for an average unitary event. These data indicate that spines function as high-impedance input compartments that passively amplify synaptic depolarization locally within the spine head to well over what could be achieved by synapses directly onto dendrites. Thus, unitary synaptic inputs may effectively recruit spine voltage-dependent conductances^{5,8,14,17,23} such as *N*-methyl-D-aspartate receptors (NMDARs) (Supplementary Fig. 1; see also Fig. 4).

We next compared the electrical properties of spines across various dendritic compartments. Owing to the inaccessibility of small-diameter oblique branches, we replaced dendritic current injection with multi-site glutamate-uncaging techniques to estimate $\text{EPSP}_{\text{spine}}$ (see Methods; Fig. 2 and Supplementary Figs 2–4, 6 and 8). We observed that the spine-to-branch AR was much lower in apical oblique dendrites than in the trunk and continued to decline significantly from originating branch points to more distal sites (Fig. 2a–e; AR: 7.8 ± 0.5 , $n = 7$ spines from 7 cells for proximal sites; 3.6 ± 0.3 , $n = 10$ spines from 7 cells for medial sites; and 1.7 ± 0.1 , $n = 9$ spines from 6 cells for distal sites; $P < 0.0001$, one-way analysis of variance (ANOVA)). Similar ratios were found at the terminal ends of oblique dendrites (within $8 \mu\text{m}$ of the end) for EPSPs evoked with a rapid-stimulation paradigm (see Methods; Fig. 2e, red symbols; AR: 1.7 ± 0.2 , $n = 12$ spines from 8 cells). Consistent with this small ratio, input onto a single spine triggered substantial Ca^{2+} signals in other nearby spines at these distal locations (Supplementary Fig. 5a–d). These data indicate that the level of passive synaptic amplification produced by R_{neck} is dependent on dendritic properties with the greatest effect at the largest compartments.

A morphologically realistic computer model was used to examine the factors involved in producing the above spatial patterns of $\text{EPSP}_{\text{spine}}$, $\text{EPSP}_{\text{branch}}$ and AR. A simple model in which the dendritic location of the input was varied while R_{neck} was held constant at $500 \text{ M}\Omega$ completely reproduced all experimental observations (Fig. 3a–c). These results indicate that the spatial profile of passive spine amplification (~ 30 -fold decrease from trunk to branch end) reported in Fig. 2 could result solely from expected changes in local dendritic impedance^{3,4,6}. When the converse simulation was implemented (that is, local dendritic impedance was held constant and R_{neck} was reduced with distance), additional implausible and experimentally unsupported manipulations were required (see Methods). This strongly suggests that R_{neck} does not systematically change across different dendritic compartments (see Supplementary Fig. 6 for intraregional variation in R_{neck}) and that the level of depolarization within the spine head is relatively independent of the local impedance profile of the dendrite (see Supplementary Equations and Supplementary Discussion). However, the size of synaptic depolarization in the parent dendrite will vary considerably (increasing ~ 30 -fold from trunk to branch end) owing to proportional changes in the impedance of different dendritic compartments. This effect could produce the relative location independence of $\text{EPSP}_{\text{branch}}$ observed in Fig. 2f, g (ref. 24). Altogether, the presence of a large, yet modifiable, R_{neck} allows dendritic spines to function as consistent, yet adjustable, high-impedance input structures throughout the apical dendritic arborization of CA1 pyramidal neurons^{14,15,25}.

Of the parameters affecting dendritic impedance (axial resistance, membrane capacitance, membrane resistance) only membrane resistance is readily modulated. We therefore investigated the role of membrane resistance in spine electrical function by blocking a variety of voltage-dependent ion channels (Fig. 3d–h). Bath application of BaCl_2 (250 – $400 \mu\text{M}$) and ZD7288 ($10 \mu\text{M}$) increased steady-state dendritic membrane resistance (measured $262 \pm 33 \mu\text{m}$ from the soma) from

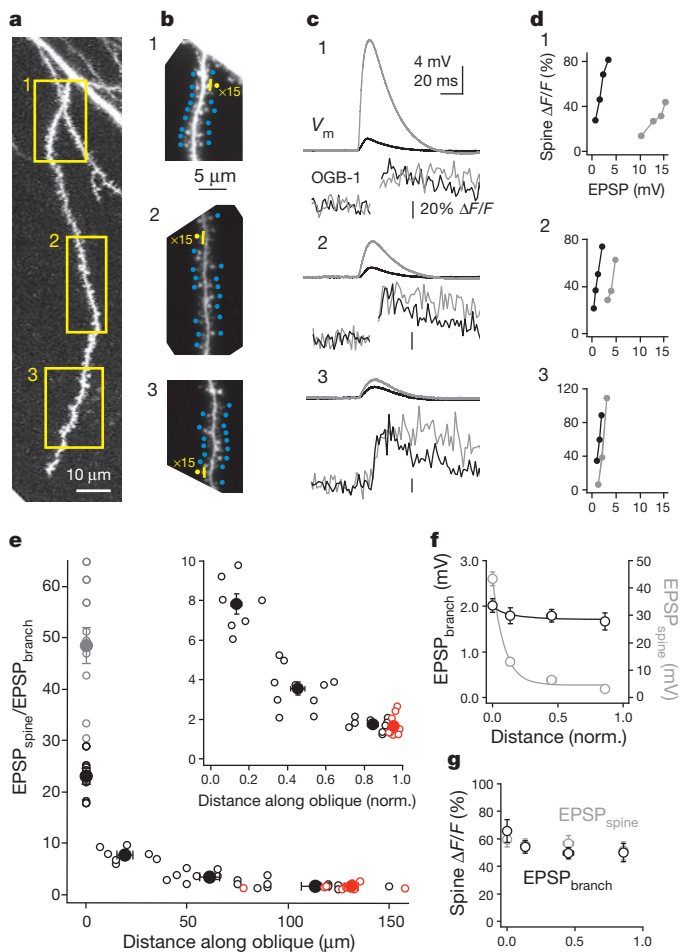


Figure 2 | Spine neck voltage amplitude ratio varies as a function of dendritic compartment. **a**, Z-stack image showing uncaging locations (yellow boxes) along a single apical oblique dendrite that branches from the trunk $250 \mu\text{m}$ from the soma. **b**, Increased magnification of the areas indicated in **a** showing locations for imaging (yellow line) and uncaging (yellow circles) at the spine of interest or at 15 nearby spines (blue circles). **c**, Voltage traces (recorded in the apical trunk, top) corresponding to comparable spine Ca^{2+} signals (bottom) evoked by stimulation of the spine of interest with 15 low-power uncaging pulses (black) or 15 neighbouring spines (grey) at the three input sites indicated in **a** and **b**. Note the similar EPSP kinetics for the two stimulation paradigms. **d**, Relationship between EPSP amplitude and spine head Ca^{2+} signals for single spine (black) versus neighbouring spines (grey) stimulation along the oblique branch. **e**, Spine-to-branch voltage AR as a function of dendritic compartment. Black denotes experiments conducted using uncaging at 15 neighbouring spines for $\text{EPSP}_{\text{spine}}$ (as per **a–d**); red indicates experiments conducted at distal tips of oblique dendrites using single stimulation of the spine of interest compared with only 1–2 neighbouring spines; and grey denotes single uncaging at trunk spines versus EPSC injection during dual dendritic recording (from Fig. 1; see Methods for discussion of different AR measurement paradigms). Inset shows AR along oblique branches as a function of normalized branch length. Open circles are data from individual spines; filled circles represent means for different compartments. **f**, Mean amplitudes of $\text{EPSP}_{\text{branch}}$ (black) and $\text{EPSP}_{\text{spine}}$ (grey) used to calculate AR as a function of normalized (norm.) distance along apical oblique dendrites for experiments conducted as described in **a–d**, from black data points in **e**. **g**, Corresponding mean spine head Ca^{2+} signals for $\text{EPSP}_{\text{branch}}$ (black) and $\text{EPSP}_{\text{spine}}$ (grey) from **f**. Error bars denote s.e.m.

$31.6 \pm 3.2 \text{ M}\Omega$ to $133.2 \pm 7.7 \text{ M}\Omega$ ($P < 0.0001$, paired *t*-test, $n = 6$). As expected from theoretical considerations (see Supplementary Equations and Supplementary Discussion), this large increase in membrane resistance did not significantly alter AR (23.2 ± 1.7 versus 21.1 ± 1.5 , $n = 6$ spines from 6 cells, $P = 0.097$, paired *t*-test, for trunk spines $285 \pm 36 \mu\text{m}$ from soma). Additionally, manipulating resting conductance over several orders of magnitude had essentially no impact on AR

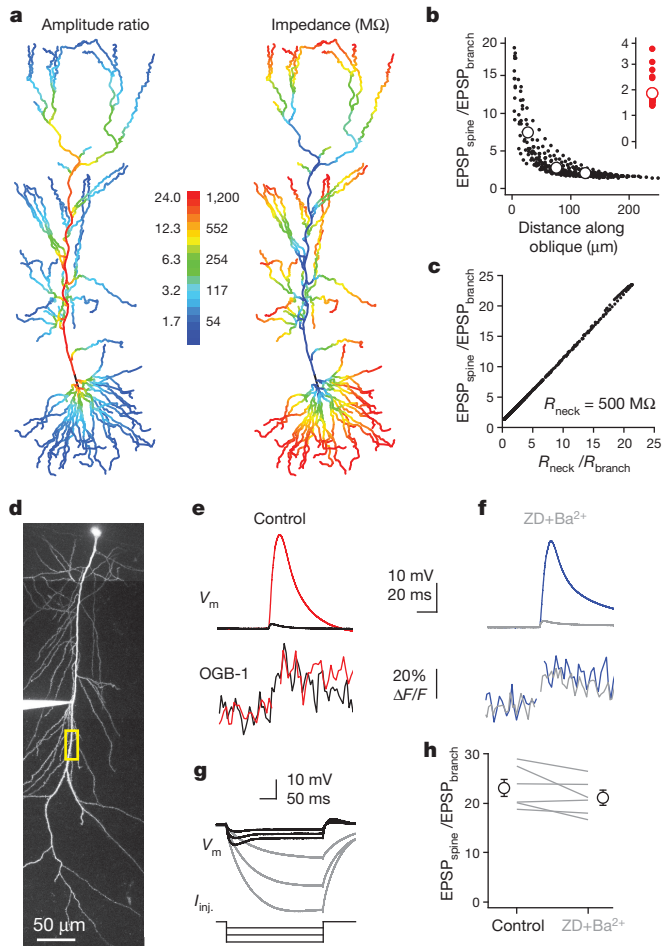


Figure 3 | Spine-to-branch voltage amplitude ratio is mediated by dendritic impedance. **a**, Left, spatial distribution of AR for spines with 500 M Ω R_{neck} in the model CA1 neuron (stimulation conducted as described for Fig. 2a–d). Right, local impedance across all compartments in the model. **b**, Modelling results for 323 spines (black dots) located on apical oblique branches that originated from the trunk 150–400 μ m from the soma. Open circles represent bins of the first, second and third 50 μ m along the obliques. Error bars are within the symbols. Inset shows AR for 26 model spines located within 8 μ m of the tip of an oblique (as per Fig. 2e, red symbols). **c**, The degree of voltage attenuation across spine necks in the model closely matches the R_{neck}/R_{branch} ratio. **d**, Image stack of a CA1 pyramidal cell patched 215 μ m from the soma. Yellow box indicates region of interest for trunk spine imaging and uncaging. **e**, Example voltage traces (top) of EPSP_{spine} (red; evoked by uncaging at 30 neighbouring trunk spines) and EPSP_{branch} (black; evoked by single uncaging at spine of interest) for comparable spine Ca²⁺ signals (bottom) under control conditions. **f**, Example voltage traces of EPSP_{spine} (blue) and EPSP_{branch} (grey) for comparable spine Ca²⁺ signals after application of 10 μ M ZD7288 (ZD) and 400 μ M Ba²⁺ for the same spine in **e**. **g**, Effect of ZD and Ba²⁺ on dendritic voltage responses evoked by 100–300 pA hyperpolarizing step current injections at –65 mV for the cell in **d–f** (control, black; ZD + Ba²⁺, grey). **h**, Summary of the effect of ZD and Ba²⁺ on spine-to-branch AR for six spines from six dendritic recordings. Error bars denote s.e.m.

in the model (see Supplementary Equations and Supplementary Discussion)²⁴. These results illustrate that, in addition to R_{neck} , the most important determinants of passive spine voltage amplification are morphological factors that control the magnitude of axial current (that is, dendritic diameter as well as proximity to branch and end points). Because such factors are not easily modified, changes in R_{neck} would be the most tenable approach to altering the amplifying properties of spines^{14,15}.

The passive amplification capabilities of spines could potentially increase the recruitment of active voltage-dependent conductances at the site of input^{5,8,14,17,23}, thereby enhancing interactions among

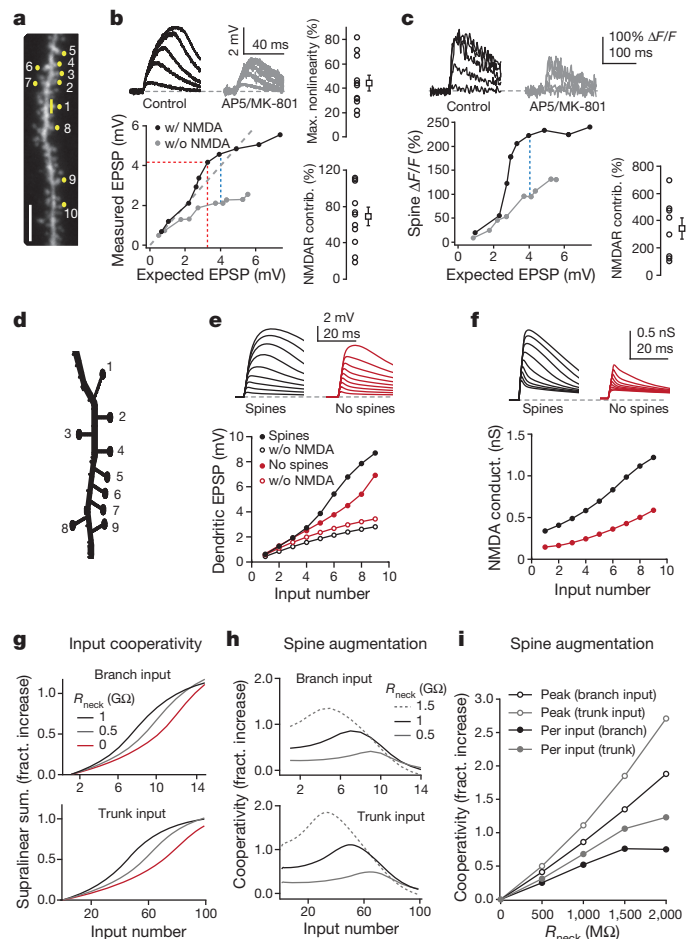


Figure 4 | Spines enhance the cooperative interaction among multiple inputs. **a**, Oblique dendrite with trunk branch point 150 μ m from the soma illustrating linescan profile (yellow line) and uncaging locations (yellow dots with numbers showing sequence). Scale bar, 5 μ m. **b**, Example voltage traces (top; every second trace shown) and expected versus measured EPSP plot (bottom) for uncaging at increasing numbers of spines under control conditions (black) and in the presence of NMDAR antagonists (grey), recorded at trunk. Grey dashed line indicates unity. Red dashed line indicates measurement of maximal nonlinearity (population data shown at top right, $n = 11$) and blue dashed line shows quantification of NMDAR contribution to the input–output relationship (population data shown at bottom right, $n = 11$). **c**, Example fluorescence traces (top; every second trace shown) and plot of peak $\Delta F/F$ versus expected EPSP from spine 1 during recruitment of increasing numbers of neighbouring spines under control conditions (black) and in the presence of NMDAR antagonists (grey). Blue dashed line indicates measurement of NMDAR contribution to spine head Ca²⁺ signals (population data shown at bottom right, $n = 8$). **d**, Schematic of model conditions in an oblique branch. **e**, Dendritic trunk voltage traces (top) and dendritic trunk input–output voltage relationship (bottom) with synapses onto spines (black) and onto collapsed spines (red) for the model oblique branch shown in **d**. Similar curves are shown without NMDARs present (open red and open black circles). **f**, Spine NMDAR conductance traces (top) and spine NMDAR activation versus input number (bottom) with synapses onto spines (black) and onto collapsed spines (red) for the oblique branch shown in **d**. **g**, The greater-than-linear component of input–output curves expressed as the fractional increase over linear summation for inputs ($G_{AMPA} = 0.7$ nS; $G_{NMDAR} = 1.4$ nS) onto a terminal oblique branch or apical trunk near the branch. Input number was increased until the peak of supralinear summation was approached. **h**, Augmentation of input cooperativity by spines expressed as fractional increase in cooperativity over level achieved by no-spine input (fractional difference of $R_{neck} > 0$ and $R_{neck} = 0$ summation curves as in **g**). **i**, Spine augmentation of peak and mean input cooperativity expressed as a function of R_{neck} . Peak and mean cooperativity values are taken from plots in **h**.

multiple synaptic inputs. To test this idea we used multi-site uncaging and simultaneous Ca^{2+} imaging with NMDARs intact to produce voltage and single-spine Ca^{2+} input–output curves at individual apical oblique branches (Fig. 4a–c). Single inputs evoked small but detectable Ca^{2+} influx ($\sim 25\%$ $\Delta F/F$) into activated spines and recruitment of additional inputs increased spine Ca^{2+} signals and membrane depolarization in an NMDAR-dependent nonlinear fashion (maximal EPSP nonlinearity under control: $44 \pm 6\%$, $n = 11$ spines from 11 cells; peak difference of control versus 50–100 μM AP5 and 12.5 μM MK-801 for EPSP: $68 \pm 10\%$, $n = 11$ spines from 11 cells; and spine head $\Delta F/F$: $344 \pm 76\%$, $n = 8$ spines from 8 cells). These data were used to produce a multi-compartmental simulation that compared the level of cooperativity among synaptic inputs placed either onto spine compartments or directly onto dendrites (Fig. 4d–i). The simulations show that passive electrical amplification by spines promotes the recruitment of local active voltage-dependent conductances by multiple inputs, increasing the amount of above-linear summation (Fig. 4e, f). Input cooperativity, quantified as the amount of supralinear depolarization provided by additional synaptic input, increases as a function of R_{neck} (Fig. 4g and Supplementary Fig. 8). In general, this augmentation of input cooperativity by spines (expressed as the fractional increase over the no-spine condition) initially increases then declines with additional inputs (Fig. 4h). The exact relationship of spine augmentation to input number is dependent on R_{neck} , with a saturation effect beginning to occur for spines with $R_{\text{neck}} > 1.5 \text{ G}\Omega$ (dashed line, Fig. 4h). High-impedance spines increase peak cooperativity (up to $\sim 5\times$) and mean cooperativity per input (up to $\sim 2\times$) as a function of R_{neck} in both large apical trunk and small terminal branch dendritic compartments (Fig. 4i; see Supplementary Fig. 7 for model parameter ranges). The presence of high-impedance spines therefore inherently augments input cooperativity by promoting electrical cross-talk between coactive synaptic inputs, providing a mechanism whereby activity-dependent changes in R_{neck} can regulate synaptic efficacy and nonlinear dendritic processing among potentiated synapses^{14,15}.

Our results provide insight into how the intrinsic properties of dendritic spines allow them to fundamentally shape neuronal processing and storage. Spines exhibit a high neck resistance (varying around 500 M Ω) that passively amplifies local synaptic depolarization up to 50-fold. This amplification increases the activation of voltage-dependent processes within the spine head, enhances the interaction among coactive spines, and increases nonlinear dendritic integration (Fig. 4 and Supplementary Figs 1 and 7). Furthermore, spines endow individual synapses with the ability to locally control the amount of passive (ohmic) and active (voltage-dependent conductance-based) amplification they experience through the regulation of R_{neck} ^{5,14,15}. The amplifying and coordinating properties of dendritic spines we have described here will have a profound effect on neuronal input processing²⁶, and will also influence information storage by promoting the induction of clustered forms of synaptic and dendritic plasticity among coactive spines^{27–29}. Thus, spines enhance the ability of neurons to detect, uniquely respond to, and store distinct synaptic input patterns^{26,30}.

METHODS SUMMARY

All animal experimentation was approved by the Janelia Farm Institutional Animal Care and Use Committee and by the Animal Care and Use Committee of the Institute of Experimental Medicine, Hungarian Academy of Sciences, and was in accordance with 86/609/EEC/2 and DIRECTIVE 2010/63/EU Directives of the European Community. Full details of experimental procedures for slice preparation, patch-clamp recording, two-photon calcium imaging and uncaging, data analysis and computational modelling are provided in Methods.

Full Methods and any associated references are available in the online version of the paper.

Received 24 May; accepted 7 September 2012.

Published online 28 October 2012.

1. Ramón y Cajal, S. Estructura de los centros nerviosos de las aves. *Rev. Trim. Histol. Norm. Patol.* **1**, 1–10 (1888).

2. Bourne, J. N. & Harris, K. M. Balancing structure and function at hippocampal dendritic spines. *Annu. Rev. Neurosci.* **31**, 47–67 (2008).
3. Rall, W. Theory of physiological properties of dendrites. *Ann. NY Acad. Sci.* **96**, 1071–1092 (1962).
4. Rall, W. in *Cellular Mechanisms Subservicing Changes in Neuronal Activity* (ed Woody, C. D. et al.) Brain Information Service Report No. 3 (Univ. of California, 1974).
5. Miller, J. P., Rall, W. & Rinzel, J. Synaptic amplification by active membrane in dendritic spines. *Brain Res.* **325**, 325–330 (1985).
6. Koch, C. & Zador, A. The function of dendritic spines: devices subserving biochemical rather than electrical compartmentalization. *J. Neurosci.* **13**, 413–422 (1993).
7. Yuste, R. Dendritic spines and distributed circuits. *Neuron* **71**, 772–781 (2011).
8. Hao, J. & Oertner, T. G. Depolarization gates spine calcium transients and spike-timing-dependent potentiation. *Curr. Opin. Neurobiol.* **22**, 509–515 (2012).
9. Guthrie, P. B., Segal, M. & Kater, S. B. Independent regulation of calcium revealed by imaging dendritic spines. *Nature* **354**, 76–80 (1991).
10. Yuste, R. & Denk, W. Dendritic spines as basic functional units of neuronal integration. *Nature* **375**, 682–684 (1995).
11. Yasuda, R. & Murakoshi, H. The mechanisms underlying the spatial spreading of signaling activity. *Curr. Opin. Neurobiol.* **21**, 313–321 (2011).
12. Chen, Y. & Sabatini, B. L. Signaling in dendritic spines and spine microdomains. *Curr. Opin. Neurobiol.* **22**, 389–396 (2012).
13. Svoboda, K., Tank, D. W. & Denk, W. Direct measurement of coupling between dendritic spines and shaft. *Science* **272**, 716–719 (1996).
14. Grunditz, A., Holbro, N., Tian, L., Zuo, Y. & Oertner, T. G. Spine neck plasticity controls postsynaptic calcium signals through electrical compartmentalization. *J. Neurosci.* **28**, 13457–13466 (2008).
15. Bloodgood, B. L. & Sabatini, B. L. Neuronal activity regulates diffusion across the neck of dendritic spines. *Science* **310**, 866–869 (2005).
16. Palmer, L. M. & Stuart, G. J. Membrane potential changes in dendritic spines during action potentials and synaptic input. *J. Neurosci.* **29**, 6897–6903 (2009).
17. Bloodgood, B. L., Giessel, A. J. & Sabatini, B. L. Biphasic synaptic Ca influx arising from compartmentalized electrical signals in dendritic spines. *PLoS Biol.* **7**, e1000190 (2009).
18. Tsay, D. & Yuste, R. On the electrical function of dendritic spines. *Trends Neurosci.* **27**, 77–83 (2004).
19. London, M. & Häusser, M. Dendritic computation. *Annu. Rev. Neurosci.* **28**, 503–532 (2005).
20. Wu, X. E. & Mel, B. W. Capacity-enhancing synaptic learning rules in a medial temporal lobe online learning model. *Neuron* **62**, 31–41 (2009).
21. Legenstein, R. & Maass, W. Branch-specific plasticity enables self-organization of nonlinear computation in single neurons. *J. Neurosci.* **31**, 10787–10802 (2011).
22. Magee, J. C. & Cook, E. P. Somatic EPSP amplitude is independent of synapse location in hippocampal pyramidal neurons. *Nature Neurosci.* **3**, 895–903 (2000).
23. Bloodgood, B. L. & Sabatini, B. L. Nonlinear regulation of unitary synaptic signals by $\text{CaV}_{2.3}$ voltage-sensitive calcium channels located in dendritic spines. *Neuron* **53**, 249–260 (2007).
24. Jaffe, D. B. & Carnevale, N. T. Passive normalization of synaptic integration influenced by dendritic architecture. *J. Neurophysiol.* **82**, 3268–3285 (1999).
25. Gullledge, A. T., Carnevale, N. T. & Stuart, G. J. Electrical advantages of dendritic spines. *PLoS ONE* **7**, e36007 (2012).
26. Branco, T., Clark, B. A. & Häusser, M. Dendritic discrimination of temporal input sequences in cortical neurons. *Science* **329**, 1671–1675 (2010).
27. Losonczy, A., Makara, J. K. & Magee, J. C. Compartmentalized dendritic plasticity and input feature storage in neurons. *Nature* **452**, 436–441 (2008).
28. Makara, J. K., Losonczy, A., Wen, Q. & Magee, J. C. Experience-dependent compartmentalized dendritic plasticity in rat hippocampal CA1 pyramidal neurons. *Nature Neurosci.* **12**, 1485–1487 (2009).
29. Harvey, C. D. & Svoboda, K. Locally dynamic synaptic learning rules in pyramidal neuron dendrites. *Nature* **450**, 1195–1200 (2007).
30. Gasparini, S. & Magee, J. C. State-dependent dendritic computation in hippocampal CA1 pyramidal neurons. *J. Neurosci.* **26**, 2088–2100 (2006).

Supplementary Information is available in the online version of the paper.

Acknowledgements We thank A. Milstein, S. Gale and R. Chitwood for help in creating analysis tools and G. Murphy, S. Williams and D. Johnston for comments on the manuscript. This work was supported by the Howard Hughes Medical Institute, the National Institutes of Health (NS-046064, NS-077601) and the Wellcome Trust (International Senior Research Fellowship to J.K.M., grant number 090915).

Author Contributions M.T.H., J.K.M. and J.C.M. conceived the project and designed the experiments. M.T.H. and J.K.M. performed all experiments and data analysis. N.S., W.L.K. and J.C.M. performed computer simulations. M.T.H., J.K.M. and J.C.M. wrote the paper with comments from all authors.

Author Information Reprints and permissions information is available at www.nature.com/reprints. The authors declare no competing financial interests. Readers are welcome to comment on the online version of the paper. Correspondence and requests for materials should be addressed to J.C.M. (mageej@janelia.hhmi.org).

METHODS

Hippocampal slice preparation. Acute, transverse hippocampal slices (400 μm) were prepared from 7–12-week-old male Sprague-Dawley and Wistar rats as described previously^{27,28}, according to methods approved by the Janelia Farm Institutional Animal Care and Use Committee and the Animal Care and Use Committee (ACUC) of the Institute of Experimental Medicine, Hungarian Academy of Sciences, and in accordance with 86/609/EEC/2 and DIRECTIVE 2010/63/EU Directives of the EU. In brief, animals were deeply anaesthetized with isoflurane and transcardially perfused with ice-cold cutting solution containing (in mM): sucrose 220, NaHCO_3 28, KCl 2.5, NaH_2PO_4 1.25, CaCl_2 0.5, MgCl_2 7, glucose 7, sodium pyruvate 3, and ascorbic acid 1, saturated with 95% O_2 and 5% CO_2 . The brain was quickly removed and sectioned in cutting solution with a Vibratome (Leica). Slices were incubated in a submerged holding chamber in artificial cerebrospinal fluid (ACSF) at 37 °C for 30–60 min and then stored in the same chamber at 25 °C. For recording, slices were transferred to the submerged recording chamber of the microscope where experiments were performed at 34–37 °C in ACSF containing (in mM): NaCl 125, KCl 3, NaHCO_3 25, NaH_2PO_4 1.25, CaCl_2 1.3, MgCl_2 1, glucose 25, sodium pyruvate 3, and ascorbic acid 1, saturated with 95% O_2 and 5% CO_2 . Except where described, NMDARs and voltage-gated Na^+ channels were blocked by continuous bath application of 50–100 μM AP5 (Tocris) and 0.5–1.0 μM TTX (Tocris), respectively. In some experiments, 10–15 μM MK-801 (Tocris) was also present in the ACSF; no differences were observed, so data were combined. ZD7288, nimodipine, 2-methyl-6-(phenylethynyl)-pyridine hydrochloride (MPEP), 7-(hydroxymino)cyclopropa[b]chromen-1a-carboxylate ethyl ester (CPCCOEt), 1-naphthylacetylspermine (NASPM) (all from Tocris) and BaCl_2 , NiCl_2 , cyclopiazonic acid, philanthotoxin-433 (all from Sigma) were prepared as stock solutions, stored at –20 °C and diluted directly to the extracellular solution on the day of the experiment.

Patch-clamp recording. Cells were visualized using an Olympus BX-61 epifluorescent microscope equipped with infrared Diodo optics and a water-immersion lens (60 \times , 0.9 NA; Olympus). Current-clamp whole-cell recordings from the soma or apical dendrites of hippocampal CA1 pyramidal neurons were performed with Dagan BVC-700 amplifiers in the active 'bridge' mode, filtered at 3 kHz and digitized at 50 kHz. Patch pipettes (2–8 M Ω) were filled with a solution containing (in mM): potassium gluconate 134, KCl 6, HEPES buffer 10, NaCl 4, Mg_2ATP 4, Tris_2GTP 0.3, sodium phosphocreatine 14, 0.05 Alexa 594 and 0.1 OGB-1 (Invitrogen), pH 7.25. In some experiments (Supplementary Figs 3 and 4), OGB-1 was replaced with 0.2 mM Fluo-4 or 0.2 mM Calcium Green-1 dextran conjugate (molecular mass: 70,000; both from Invitrogen). Series resistance, monitored throughout the experiment, was <30 M Ω for perisomatic recordings and ranged from 12 to 40 M Ω for dendritic recordings. All neurons had resting membrane potentials between –62 and –68 mV (dendritic recordings) or –56 and –65 mV (somatic recordings) and were confirmed to have intact somas and tufts. For simulated EPSC injection during dual dendritic trunk recording (Fig. 1) we used a simple compartment model of a spine, spine neck and parent branch implemented in the neuron modelling environment to determine the appropriate kinetics for current injection into the dendrite to mimic synaptic depolarization in the spine head. The resulting waveform is shown in Fig. 1c.

Two-photon imaging and uncaging. A dual galvanometer-based two-photon laser scanning system (Prairie Technologies) was used to image neurons and to focally uncage glutamate at individual dendritic spines^{27,28}. Two ultrafast pulsed laser beams (Chameleon Ultra II; Coherent) were used: one at 880 and 920 nm for imaging Alexa 594 and OGB-1 (Molecular Probes), respectively, and one at 720 nm to photolyse 4-methoxy-7-nitroindolyl-caged-L-glutamate (MNI-glutamate) (Tocris Cookson; 10 mM, dissolved in freshly carbogenated ACSF containing 50–100 μM AP5 and 0.5–1.0 μM TTX unless otherwise noted and applied via pressure ejection through a pipette above the slice). Laser beam intensity was independently controlled with electro-optical modulators (model 350-50; Conoptics). Uncaging dwell time was 0.2 ms; galvo move time intervals varied depending on the experiment (see below). Linescan imaging through spines was performed at 150–500 Hz with dwell times of 8–12 μs for <400 ms.

Particular care was taken to limit photodamage during imaging and uncaging. This included the use of a passive 8 \times pulse splitter in the uncaging path in most experiments to reduce photodamage drastically³¹. Basal fluorescence of both channels was continuously monitored as an immediate indicator of damage to cellular structures. Subtle signs of damage included decreases in or loss of phasic Ca^{2+} signals in spine heads in response to either uncaging or current injection, small but persistent depolarization following uncaging, and changes in the kinetics of voltage responses to uncaging or current injection. Experiments were terminated if neurons exhibited any of these phenomena.

Determination of AR and R_{neck} . Our experimental strategy was based on the biophysical property of asymmetric voltage attenuation across the spine neck due to the high impedance of the spine head relative to the low dendritic branch input

impedance^{4,6,32}. Thus, EPSP-shaped voltage transients substantially attenuate only as they propagate out of the spine and into the dendrite. We exploited this feature to compute an AR for EPSPs initiated in the spine and measured in the dendrite ($\text{EPSP}_{\text{branch}}$; so called because the measured EPSP amplitude reflects the spine potential after it has propagated across the spine neck into the branch) compared to those producing the same level of spine depolarization when initiated and measured in the dendrite ($\text{EPSP}_{\text{spine}}$; representing the EPSP amplitude in the spine head). Our computer model confirmed that AR magnitude is independent of the electrical recording site and that this method is sufficiently accurate to measure spine voltage AR throughout the CA1 dendritic arborization within the stratum radiatum (Supplementary Fig. 8).

For the dual dendritic patch experiments shown in Fig. 1, the EPSPs evoked by uncaging at single spines exhibited an almost identical amplitude at both pipettes (1.41 ± 0.16 versus 1.44 ± 0.15 mV, $n = 9$, $P = 0.3032$, paired t -test), demonstrating that the base of the dendrite at nearby spines is isopotential with the recording electrode. In addition, our morphologically realistic multi-compartmental model suggests that the trunk should be relatively isopotential to ~30 μm proximal (towards the soma) and ~50 μm distal from the electrode.

Calculation of R_{neck} is based on the voltage divider equation^{4,32} (see Fig. 1h). EPSP amplitude at the spine head for a synapse on the spine is given by:

$$V_{\text{head}} = E_{\text{syn}} \cdot \frac{R_{\text{neck}} + R_{\text{dend}}}{1/G_{\text{syn}} + R_{\text{neck}} + R_{\text{dend}}} \quad (1)$$

in which V_{head} is the EPSP amplitude in the spine head and R_{dend} is local dendritic input resistance.

EPSP amplitude at the dendrite for a synapse on the spine is given by:

$$V_{\text{dend}} = E_{\text{syn}} \cdot \frac{R_{\text{dend}}}{1/G_{\text{syn}} + R_{\text{neck}} + R_{\text{dend}}} \quad (2)$$

in which V_{dend} is the EPSP amplitude in the dendrite.

The ratio of the amplitudes (AR) is given by:

$$\text{AR} = \frac{R_{\text{neck}} + R_{\text{dend}}}{R_{\text{dend}}} = 1 + \frac{R_{\text{neck}}}{R_{\text{dend}}} \quad (3)$$

The resistance of the spine neck (R_{neck}) can be calculated from:

$$R_{\text{neck}} = (\text{AR} - 1) \times R_{\text{dend}} \quad (4)$$

Uncaging input paradigms. Because we cannot patch small diameter terminal branches, in order to measure AR in these compartments, local dendritic current injection (as used in Fig. 1) was replaced with rapid multi-site glutamate uncaging onto neighbouring spines near the spine of interest while recording the resultant EPSPs at the apical trunk (Figs 2 and 3e and Supplementary Figs 3, 4 and 6c–f) or soma (Supplementary Figs 2a–c and 6a, b). The speed at which each spine on a dendrite can be stimulated is limited by the uncaging galvanometers (in practice this is 0.3 ms per spine: 0.2 ms dwell time + 0.1 ms move time). Thus, to control for possible confounds in differential dendritic filtering along oblique branches, we matched the shape of depolarizations for $\text{EPSP}_{\text{branch}}$ and $\text{EPSP}_{\text{spine}}$ measured at the voltage-recording electrode by using 15 (low-power) uncaging events at the single spine of interest versus 15 (higher power) uncaging events distributed at 15 neighbouring spines on the same branch (Fig. 2 and Supplementary Figs 3 and 4). The branch uncaging input was performed at the galvanometer speed limit while the galvanometer move time was occasionally increased (up to 0.3 ms) for the 15 uncaging events at the single spine in order to match the kinetics of the two EPSPs. The computer model indicates that the kinetic slowing associated with this method decreased observed AR ~50% at dendritic trunk regions (Supplementary Fig. 8a; thus the AR values of ~22 for the trunk experiments conducted in this manner in Fig. 2e compared to the AR of ~45 measured by comparing a single uncaging event with fast current injection in Fig. 1) and ~15% at terminal branch locations (Supplementary Fig. 8b). However, at the distal tip of oblique branches, where the dendritic impedance is high owing to the sealed end, we were able to conduct experiments comparing a single uncaging event at the spine of interest to uncaging at only 1–2 nearby neighbours (see Supplementary Fig. 5a–d) for the calculation of AR in this compartment (Fig. 2e, red symbols). Thus, we have accurate fast kinetic boundary conditions for AR at the trunk (using current injection, Fig. 1) and the distal dendritic tip (using 1–2 neighbouring spines; Fig. 2e, red symbols) while the exact shape of the distribution of AR along the branch will vary slightly depending on the frequency of the stimulation protocol. For some experiments measuring the relative effects of pharmacology on AR, we compared a single uncaging event at the spine of interest with uncaging at a number of neighbouring spines (Fig. 3e and Supplementary Fig. 2b).

Data analysis. Analysis was performed using custom-written macros in IgorPro and MATLAB. Ca^{2+} and voltage signals were analysed offline using averaged traces of 3–10 trials with no smoothing or background subtraction. Some imaging trials exhibited a light artefact from the uncaging laser, which was excised. Ca^{2+} signal amplitude was measured as the maximum average of three consecutive points within 50 ms after uncaging. For calculation of AR, spine Ca^{2+} signals greater than 25% and less than 125% $\Delta F/F$ (the linear range of OGB-1; Invitrogen) were compared between stimulation paradigms at a range of different intensities. For branch versus spine Ca^{2+} signals exhibiting less than 25% difference (average difference of $3.1 \pm 1.5\%$, $n = 109$ spines from 71 neurons; see also Supplementary Fig. 9) their respective EPSPs (larger than 1 mV for trunk spines recorded at the trunk $< 50 \mu\text{m}$ away, or larger than 0.5 mV for oblique spines recorded at the trunk or soma) were compared. All comparisons that fit these criteria for a given spine were averaged to compute the AR for that paradigm at that spine.

Morphological and distance measurements were performed using ImageJ/FIJI (National Institutes of Health) on two-dimensional maximal intensity projections of 1–2 μm Z-series collected at the end of the experiment. Spines on apical oblique branches were categorized as proximal, middle or distal by division of the overall branch length into thirds.

Owing to the necessity of clearly isolating a single spine for uncaging in order to accurately calculate AR (if multiple spines are activated by a single uncaging event, EPSP_{branch} becomes artifactually large compared to the observed spine head Ca^{2+} signal and distorts the AR), spines chosen for imaging were clearly separated from their parent dendrite (and nearby neighbours). Individual spines were selected to reflect the average phenotype of their neighbours along a branch, and did not exhibit overly large heads or long necks, presumably falling into an intermediate category between or spanning the previously described ‘stubby’ and ‘mushroom’ types. At the beginning of an experiment, Ca^{2+} signals in response to single-spine uncaging at various laser powers were first measured and only those spines in which the Ca^{2+} signal and EPSP amplitude increased incrementally as a function of power were further studied. This criterion was met in most spines of the apical trunk and oblique dendrites. However in a subgroup of spines, primarily on oblique branches, Ca^{2+} signals were either small and unreliable or did not increase proportional to increasing stimulation. These recordings were not included in this study. For the long spine neck experiments in Supplementary Fig. 6a, b, we searched the dendritic arborization for the longest-necked spines we could find (which appeared to constitute $< 1\%$ of the overall spine population).

Computational methods. All simulations were performed using the NEURON simulation environment³³ with the variable time step (CVODE) method. The CA1 pyramidal neuron morphology used in the simulations was reconstructed from a rat hippocampal pyramidal neuron described previously^{34,35}. The model included a membrane capacitance of $1 \mu\text{F cm}^{-2}$ and an axial resistivity of $150 \Omega\text{cm}$. The membrane resistivity was taken to be $20,000 \Omega\text{cm}^2$ at the soma and to drop linearly as a function of distance to $2,500 \Omega\text{cm}^2$ at a distance of $100 \mu\text{m}$ and beyond to reflect, in a simple way, the observed greater density of voltage-gated channels observed experimentally in these cells^{36,37}. As a result, the somatic input resistance was observed to be $27 \text{M}\Omega$, and the input resistance $200 \mu\text{m}$ from the soma along the main apical dendrite was $23 \text{M}\Omega$.

A second model (uniform R_{dend} model) was constructed to produce a relatively constant local dendritic input impedance along apical oblique branches while maintaining the measured amount of amplitude filtering down the branches. This required reductions in both axial and membrane resistivity coordinated with dendritic diameter, implemented through gradients of axial (from 28 to $150 \Omega\text{cm}$; branch tip to trunk) and membrane resistivities (from 28 to $2,500 \Omega\text{cm}^2$; branch tip to trunk) in a specific oblique dendrite (branching from the main apical dendrite approximately $300 \mu\text{m}$ from the soma) according to the following formulae:

$$r_L(x) = r_L(0)[a(x)/a(0)]^\alpha$$

and

$$r_m(x) = r_m(0)[a(x)/a(0)]^\beta$$

in which x is the distance along the oblique branch measured from the main apical dendrite, r_L is axial resistivity, r_m is membrane resistivity, a is dendrite diameter, and $\alpha = 1.5$, $\beta = 4$. The selected branch had an approximately constant input impedance over most of its length (~ 50 – $60 \text{M}\Omega$ over $\sim 200 \mu\text{m}$). This model could reproduce the observed dependence of AR upon distance along the oblique dendrite if R_{neck} was also dependent upon distance. A prediction for the required R_{neck} can be computed from

$$R_{\text{neck}} = (\text{AR} - 1)R_{\text{dend}}$$

in which AR is the desired target amplitude ratio and R_{dend} is the dendritic input impedance. R_{neck} for this condition ranged from 39.7 to $465.1 \text{M}\Omega$ from tip to

trunk. A variable increase in synaptic conductance approaching tenfold (20 to 2.0nS from tip to trunk) was also required to match data shown in Fig. 2d. However, in the uniform R_{D} model several key fundamental electrophysiological properties move far out of reported experimental ranges. First, the membrane time constant becomes very small ($< 100 \mu\text{s}$) because of the large leak conductance. Reported experimental measures are two orders of magnitude larger³⁶. Second, the impedance load of each dendrite branch increases considerably causing enhanced attenuation of signals propagating from dendrite to soma. In the standard model the maximum amount of attenuation from the distal apical trunk to the soma was 6.4, whereas in the uniform R_{dend} model the level of attenuation was 46.9. Finally, the manipulations caused the input resistance at the soma to drop to $6 \text{M}\Omega$. These values are both approximately an order of magnitude out of the range of what has been observed experimentally³⁶. Altogether, the need for coordinated 5 – $10\times$ manipulations of axial resistivity, membrane resistivity, R_{neck} and synaptic conductance contradicts experimental evidence³⁸ and is extremely implausible.

In both models, spines were modelled as a cylindrical compartment representing the spine neck with length $1.58 \mu\text{m}$ and diameter $0.077 \mu\text{m}$ and a spherical head with diameter $0.5 \mu\text{m}$; with an axial resistivity of $150 \Omega\text{cm}$, this produced a R_{neck} of $500 \text{M}\Omega$. Simulations of spines placed directly on the dendrite were modelled by reducing the neck length to $0.01 \mu\text{m}$ and increasing the diameter to $0.5 \mu\text{m}$ (to match the spine head diameter). AMPA synapses were modelled as a double-exponential conductance function with rise time 0.1ms , decay time 1ms and reversal potential 0mV . For simulations involving only AMPA synapses, the peak conductance was adjusted dynamically at each location in the dendritic tree using a root-finding algorithm³⁹ to reach a target depolarization in the spine head of 35mV ; results were not strongly dependent upon the specific target voltage used. Modelling of low-power multi-event or rapid multi-site glutamate uncaging was performed computationally by activating a series of synapses with a 0.3 -ms delay between events. To speed up simulations of single-site multiple events, the series of double-exponential AMPA conductances was replaced with a single, averaged conductance. To do the averaging, one starts with a double-exponential synapse that turns on at the source time s ,

$$g = g_{\text{max}} C(e^{-(t-s)/\tau_2} - e^{-(t-s)/\tau_1}) \text{ for } t > s$$

The constant C is chosen so that the maximum of the right-hand side is g_{max} . Note that here we are assuming that $\tau_1 < \tau_2$. τ_1 is the rise time and τ_2 is the decay time. If we now suppose that synapses are distributed over the time interval $0 < s < T$ with conductance $g_{\text{max}} = g(s)ds$, and we add up these individual contributions,

$$g = \int_0^{\min(t,T)} g(s)C(e^{-(t-s)/\tau_2} - e^{-(t-s)/\tau_1})ds$$

Note the upper limit $\min(t,T)$ is due to causality; for $t < T$ one only has contributions for $0 < s < t$; when $t > T$; however, one gets contributions for the whole range, $0 < s < T$. If one assumes a uniform distribution of synaptic strength over time (that is, each successive uncaging event elicits exactly the same amount of synaptic response), one can take $g(s) = 1$ and evaluate the integral. The result is

$$g/C = \tau_2(1 - e^{-t/\tau_2}) - \tau_1(1 - e^{-t/\tau_1}) \text{ for } t < T,$$

$$g/C = \tau_2(1 - e^{-T/\tau_2})e^{-(t-T)/\tau_2} - \tau_1(1 - e^{-T/\tau_1})e^{-(t-T)/\tau_1} \text{ for } t > T$$

The maximum of this function can be determined and C chosen to normalize the conductance. Because it was found that computational models of rapid multi-site glutamate uncaging depended very weakly upon spine location, as long as spines were within a spatial range of a few tens of μm of one another, the above averaged conductance was also used to simulate multi-site glutamate uncaging. AR can depend strongly on the additional time interval over which synaptic current is distributed. Supplementary Fig. 8 shows the result of simulations for a synapse on a spine located either on the main apical trunk approximately $200 \mu\text{m}$ from the soma, or on an apical oblique dendrite roughly 80% of the distance along the oblique from the trunk to the tip of the oblique. For the case of the spine on the apical trunk, as the time interval T increases from 0 to 6ms , the AR decreases from more than 40 to approximately 20 . Further increases in the time interval cause relatively small further decreases in the AR, as the value asymptotes to the AR for steady-state currents. For the case of the spine on the oblique, the AR is largely independent of the spread time of the synaptic current. In simulations including NMDAR synapses, the AMPA conductance was set at 0.7 – 1nS . NMDAR synapses were modelled as a double-exponential conductance function with rise time 1ms , decay time 75ms , peak 1.4 – 3.0nS and reversal potential 0mV . In addition, for NMDAR synapses a voltage-dependent factor

$$g(V) = \frac{1}{1 + \exp.(-0.062V[\text{Mg}]/3.57)}$$

multiplied the total conductance, in which V is the membrane potential in mV, and $[\text{Mg}]$ is the extracellular magnesium concentration in mM, to model the relief of the voltage-dependent magnesium block of NMDA channels. A magnesium concentration of 1 mM was used in all simulations.

31. Ji, N., Magee, J. C. & Betzig, E. High-speed, low-photodamage nonlinear imaging using passive pulse splitters. *Nature Methods* **5**, 197–202 (2008).
32. Johnston, D. & Wu, S. *Foundations of Cellular Neurophysiology* Ch. 13, 400–411 (MIT Press, 1995).
33. Hines, M. L. & Carnevale, N. T. The neuron simulation environment. *Neural Comput.* **9**, 1179–1209 (1997).
34. Golding, N. L., Kath, W. L. & Spruston, N. Dichotomy of action-potential backpropagation in CA1 pyramidal neuron dendrites. *J. Neurophysiol.* **86**, 2998–3010 (2001).
35. Golding, N. L., Mickus, T. J., Katz, Y., Kath, W. L. & Spruston, N. Factors mediating powerful voltage attenuation along CA1 pyramidal neuron dendrites. *J. Physiol. (Lond.)* **568**, 69–82 (2005).
36. Magee, J. C. Dendritic Ih normalizes temporal summation in hippocampal CA1 neurons. *Nature Neurosci.* **2**, 508–514 (1999).
37. Hoffman, D. A., Magee, J. C., Colbert, C. M. & Johnston, D. K. K^+ channel regulation of signal propagation in dendrites of hippocampal pyramidal neurons. *Nature* **387**, 869–875 (1997).
38. Katz, Y. *et al.* Synapse distribution suggests a two-stage model of dendritic integration in CA1 pyramidal neurons. *Neuron* **63**, 171–177 (2009).
39. Dowell, M. & Jarratt, P. A modified regula falsi method for computing the root of an equation. *Bit Numerical Mathematics* **11**, 168–174 (1971).

Progressive degeneration of human neural stem cells caused by pathogenic LRRK2

Guang-Hui Liu^{1,2*}, Jing Qu^{1,2*}, Keiichiro Suzuki^{2*}, Emmanuel Nivet², Mo Li², Nuria Montserrat³, Fei Yi², Xiuling Xu¹, Sergio Ruiz², Weiqi Zhang¹, Ulrich Wagner⁴, Audrey Kim⁴, Bing Ren⁴, Ying Li¹, April Goebel², Jessica Kim², Rupa Devi Soligalla², Ilir Dubova², James Thompson⁵, John Yates III⁵, Concepcion Rodriguez Esteban², Ignacio Sancho-Martinez² & Juan Carlos Izpisua Belmonte^{2,3}

Nuclear-architecture defects have been shown to correlate with the manifestation of a number of human diseases as well as ageing^{1–4}. It is therefore plausible that diseases whose manifestations correlate with ageing might be connected to the appearance of nuclear aberrations over time. We decided to evaluate nuclear organization in the context of ageing-associated disorders by focusing on a leucine-rich repeat kinase 2 (*LRRK2*) dominant mutation (G2019S; glycine-to-serine substitution at amino acid 2019), which is associated with familial and sporadic Parkinson's disease as well as impairment of adult neurogenesis in mice⁵. Here we report on the generation of induced pluripotent stem cells (iPSCs) derived from Parkinson's disease patients and the implications of *LRRK2* (G2019S) mutation in human neural-stem-cell (NSC) populations. Mutant NSCs showed increased susceptibility to proteasomal stress as well as passage-dependent deficiencies in nuclear-envelope organization, clonal expansion and neuronal differentiation. Disease phenotypes were rescued by targeted correction of the *LRRK2* (G2019S) mutation with its wild-type counterpart in Parkinson's disease iPSCs and were recapitulated after targeted knock-in of the *LRRK2* (G2019S) mutation in human embryonic stem cells. Analysis of human brain tissue showed nuclear-envelope impairment in clinically diagnosed Parkinson's disease patients. Together, our results identify the nucleus as a previously unknown cellular organelle in Parkinson's disease pathology and may help to open new avenues for Parkinson's disease diagnoses as well as for the potential development of therapeutics targeting this fundamental cell structure.

Nuclear-envelope disruption has been correlated recently with ageing as well as a number of pathological manifestations in humans^{4,6–9}. To study the role that the nuclear envelope might have during ageing-related neurodegenerative processes we chose to focus our attention on Parkinson's disease, the second most prevalent neurodegenerative disease among ageing individuals. *LRRK2* is a large multi-domain protein bearing kinase activity¹⁰ whose mutations correlate with inherited and sporadic Parkinson's disease^{10,11}. Specifically, the G2019S mutation leads to an increase in *LRRK2* kinase activity correlating with the manifestation of disease^{3,10–13}. However, the molecular and cellular implications of *LRRK2* (G2019S) mutation during Parkinson's disease manifestation and progression remain elusive.

We decided first to evaluate potential novel interactions. By using a flag-tagged version of *LRRK2* (G2019S) and MudPIT (multi-dimensional protein identification technology) analysis, we identified unreported nuclear components in *LRRK2* (G2019S)-containing protein complexes (Supplementary Fig. 2a, b and Supplementary Table 1). Furthermore, *LRRK2* (G2019S) overexpression resulted in deformed nuclei with a pedal-like structure (Supplementary Fig. 2c, d).

The fact that *LRRK2* (G2019S) leads to impaired adult neurogenesis in mice⁵ led us to take advantage of iPSC technologies and their potential for directed differentiation into specific human cell lineages (Supplementary Figs 3 and 4). Differentiation of iPSCs into neural progenitors and then serial passaging resembling cellular 'ageing'¹⁴ showed progressive deterioration of nuclear architecture in mutant but not in wild-type NSCs (referred to here as ipNSCs-*LRRK2* (G2019S) and ipNSCs-wt, respectively) (Fig. 1a–f and Supplementary Figs 5, 6 and 7). Nuclear aberrations started to manifest by passage 14 and progressively resulted in compartmentalized pedal-like nuclei. Staining for lamin B1 in late-passage (for example, passage 19) ipNSCs-*LRRK2* (G2019S) as well as *LRRK2* (G2019S)-overexpressing wild-type NSCs showed a markedly enlarged nuclear area, accompanied by a decrease in nuclear circularity (Fig. 1c–e, Supplementary Fig. 5c and Supplementary Fig. 8a). Noticeably, late-passage ipNSCs-*LRRK2* (G2019S) showed local loss of lamin B1 and lamin B2 at specific folds of the nuclear envelope (Fig. 1c, f, g and Supplementary Figs 6e and 7), whereas all other examined nuclear components remained correctly localized (Fig. 1f and Supplementary Figs 6e and 7). Co-immunoprecipitation experiments revealed that ectopically expressed *LRRK2* (G2019S) associated in protein complexes with both lamin B1 and lamin B2 (Fig. 1h). Furthermore, increased phosphorylation of lamin B1 and lamin B2 was seen in late-passage ipNSCs-*LRRK2* (G2019S) (Supplementary Fig. 8b), suggesting that excessive *LRRK2* kinase activation may directly or indirectly stimulate phosphorylation of B-type lamins in NSCs. Finally, analysis of the mitochondria, an organelle frequently implicated in Parkinson's disease pathogenesis¹⁰, showed the normal expression of the outer mitochondrial membrane receptor TOM20 as well as the mitochondrial heat-shock protein HSP60 in both NSCs-wt and NSCs-*LRRK2* (G2019S) (Supplementary Fig. 9).

We next examined whether *LRRK2* (G2019S)-elicited nuclear defects contributed to epigenetic alterations such as those observed during cellular ageing^{1,2,15}. Fluorescence *in situ* hybridization revealed a dramatic increase of centromeric signals accompanied by reorganization of centromeric, but not telomeric, heterochromatin in passage 15 ipNSCs-*LRRK2* (G2019S) (Supplementary Fig. 10a). Genome-wide epigenetic analysis showed passage-dependent differences in global H3K4me3 modifications, an epigenetic mark associated with human neuronal ageing¹⁶, at the analysed promoter regions (Fig. 2a and Supplementary Fig. 10b). At passage 15, 437 genes in ipNSCs-*LRRK2* (G2019S) displayed ≥ 5 -fold enrichment for the epigenetic mark H3K4me3 compared to ipNSCs-wt, whereas no significant differences were seen when comparing to undifferentiated iPSCs. Interestingly, most of these genes were associated with neurogenesis and neural function (Supplementary Table 2).

¹National Laboratory of Biomacromolecules, Institute of Biophysics, Chinese Academy of Sciences, Beijing 100101, China. ²Gene Expression Laboratory, Salk Institute for Biological Studies, 10010 North Torrey Pines Road, La Jolla, California 92037, USA. ³Center for Regenerative Medicine in Barcelona, Doctor Aiguader 88, 08003 Barcelona, Spain. ⁴Department of Cellular and Molecular Medicine, Ludwig Institute for Cancer Research, University of California, San Diego School of Medicine, La Jolla, California 92093-0653, USA. ⁵Department of Cell Biology, Scripps Research Institute, La Jolla, California 92037, USA.

*These authors contributed equally to this work.

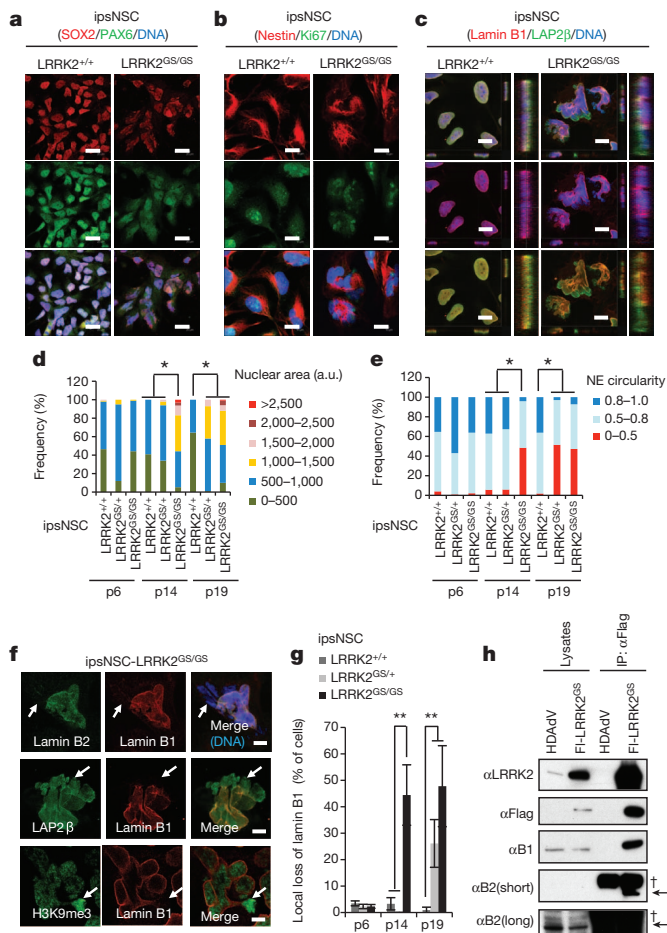


Figure 1 | *LRRK2*(G2019S) mutation results in progressive deterioration of nuclear architecture in ipNSCs. **a, b**, Immunofluorescence analysis of the indicated neural progenitor markers and proliferation markers Ki67 in wild-type (*LRRK2*^{+/+}) and homozygous *LRRK2*(G2019S) mutant (*LRRK2*^{GS/GS}) iPSC-derived NSCs (ipNSCs) at passage 14. Nuclei were stained with Hoechst. Scale bars, 20 μm (**a**) and 10 μm (**b**). **c**, Immunofluorescence of lamin B1 and LAP2β (also known as TMPOβ) at passage 14. Nuclei were stained with Hoechst. Projections on the *y* and *z* planes from representative nuclei are shown on the right of each panel. Scale bars, 10 μm. **d**, Quantifications of nuclear area (**d**) and nuclear envelope (NE) circularity (**e**) in differentiated NSCs at passages 6, 14 and 19. a.u., arbitrary units. At least 100 randomly chosen cells were counted. **P* < 10^{−15}. **f**, Subcellular distributions of lamin B1, lamin B2, LAP2β and H3K9me3 were determined at passage 15. Arrow, nuclear-envelope microdomains deficient for B-type lamins. Scale bars, 5 μm. **g**, Quantifications of local loss of lamin B1 in ipNSCs. Data are shown as mean ± s.d., *n* = 3. ***P* < 0.01. **h**, Extracts from wild-type esNSCs transduced with HDAdV-venus vector (HDAdV) or HDAdV-venus-Flag-*LRRK2*(G2019S) (FL-*LRRK2*^{GS}) were immunoprecipitated (IP) with an anti-Flag antibody, and then by immunoblot analysis for the indicated proteins. Arrow, lamin B2. †, non-specific bands.

These results led us to propose that *LRRK2*(G2019S) might progressively affect other *in vitro* NSC functions such as clonal expansion and neuronal differentiation. Newly generated ipNSCs-wt and ipNSCs-*LRRK2*(G2019S) were similarly capable of both clonal expansion and neuronal differentiation, whereas only ipNSCs-wt retained clonogenic and differentiation capacity after extensive passaging (passage 14 and above) (Fig. 2b–d and Supplementary Fig. 8c). Notably, passage 16 to 17 ipNSCs-*LRRK2*(G2019S) failed to give rise to MAP2⁺ (or Tuj1⁺) cells and resulted in aberrant non-neuronal cellular morphologies upon differentiation (Fig. 2c, d and Supplementary Figs 8c and 11a, b). Injection of proteasome inhibitors into animal brains has been shown to recapitulate Parkinson's disease phenotypes¹⁷. Interestingly, treatment of NSCs with the proteasome inhibitor MG132 resulted

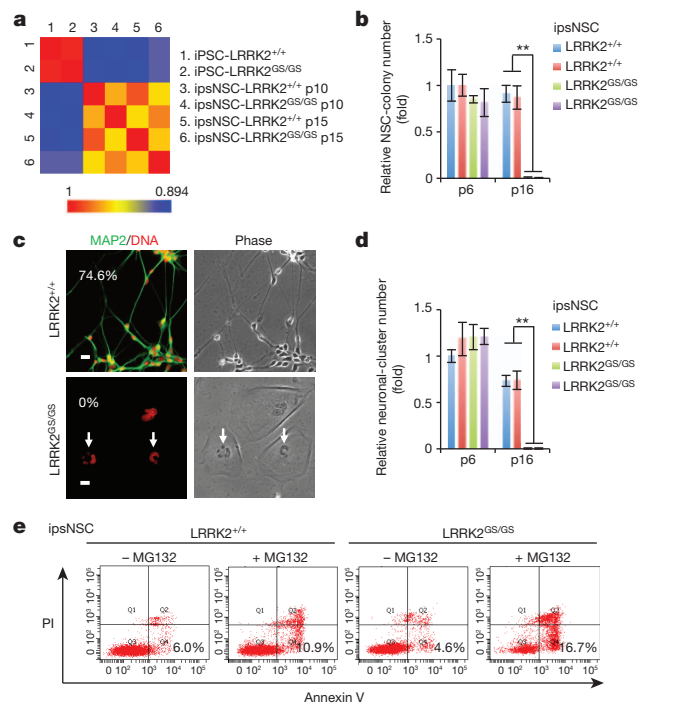


Figure 2 | *LRRK2*(G2019S) mutant ipNSCs show deficiency in clonal expansion, spontaneous neuronal differentiation at the late passages and exhibit enhanced susceptibility to proteasomal stress-induced apoptosis. **a**, Pair-wise comparisons of quantile-normalized log₂-read counts within ±2.5 kb of the transcription start site (TSS) or RefSeq genes. **b**, Passage 16 ipNSCs-*LRRK2*^{GS/GS} showed significantly lower colony-forming capacity. The two *LRRK2*^{+/+} represent the cell derivatives from two independent iPSC-*LRRK2*^{+/+} lines, respectively, and the two *LRRK2*^{GS/GS} represent the cells derived from two independent iPSC-*LRRK2*^{GS/GS} lines, respectively. Data are shown as mean ± s.d., *n* = 3. ***P* < 0.01. **c**, Immunofluorescence analysis of the neuronal marker MAP2 in spontaneous-differentiation experiments. Arrow, deformed nuclei. Percentages of neuronal-differentiation efficiency, indicated by the ratio of MAP2-positive cells to the total number of cell nuclei, are shown in corners. See Supplementary Fig. 11a (left panels) for wide-field images. Scale bar, 20 μm. **d**, Fourteen days after ipNSC seeding, ipNSCs-*LRRK2*^{GS/GS} at passage 16 showed significantly lower neuronal-differentiation capability than their wild-type counterparts. Data are shown as mean ± s.d., *n* = 3. ***P* < 0.01. **e**, Cell-apoptosis assays after MG132 treatment (10 μM, 20 h) in ipNSCs-*LRRK2*^{+/+} and ipNSCs-*LRRK2*^{GS/GS} at passage 15. Representative results from three independent experiments are shown.

in increased apoptosis in ipNSCs-*LRRK2*(G2019S) in a passage-independent manner, compared to their wild-type counterparts (Fig. 2e and Supplementary Fig. 11c, d).

To validate further that the observed cellular phenotypes were related to NSCs carrying the *LRRK2*(G2019S) mutation, we evaluated different somatic cell types and also generated two different unbiased cellular systems, an isogenic control iPSC line by targeted correction of the *LRRK2*(G2019S) mutation as well as the reversal by specific knock-in of *LRRK2*(G2019S) mutation into human Embryonic Stem Cells (hESCs) by helper-dependent adenoviral vector (HDAdV)-mediated gene targeting^{18–21} (Fig. 3a–c and Supplementary Figs 12 and 13). Contrary to *LRRK2*(G2019S) NSCs, long-term *in vitro* culture of differentiated somatic cell populations other than NSCs did not result in misshapen nuclei (Supplementary Fig. 15). Differentiation of *LRRK2*(G2019S)-corrected iPSCs to NSCs (c-ipNSCs-*LRRK2*(G2019S)) resulted in the rescue of aberrant cellular phenotypes, as compared to the respective uncorrected controls (Fig. 3d–g). Conversely, *LRRK2*(G2019S) knock-in in ESCs resulted in the progressive appearance of disrupted nuclear architecture, compromised clonal expansion, impaired neural differentiation and increased susceptibility to proteasomal stress upon differentiation into NSCs (esNSC-*LRRK2*(G2019S))

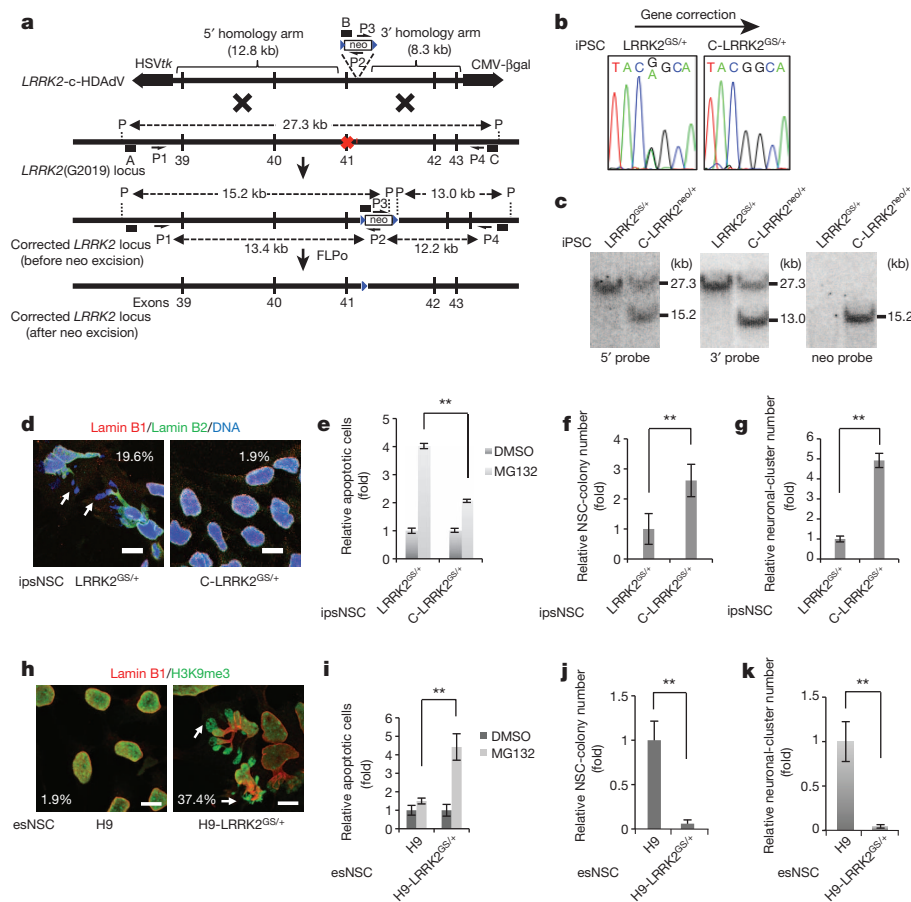


Figure 3 | Phenotypic analyses of isogenic iPSC and ESC lines in the presence or absence of the *LRRK2*(G2019S) mutation. **a**, Schematic representation of HDAdV-based correction of the G2019S mutation in the *LRRK2* gene locus. Upwards and downwards arrows indicate the primer sites for polymerase chain reaction (PCR; P1, P2, P3 and P4). The probes for Southern blot analysis are shown as black bars (A, 5' probe; B, neo probe; C, 3' probe). Blue triangles, FLPO recognition target (FRT) site. Black crosses, homologous recombination between homology arms. HSVtk, herpes simplex virus (HSV) thymidine kinase (*tk*) gene. P, the PflFI restriction enzyme sites. Red cross, mutation site in exon 41. **b**, Sequencing results of the G2019S mutation site in exon 41 of the *LRRK2* gene in *LRRK2*(G2019S) heterozygous mutant iPSCs before (left; *LRRK2*^{G2019S/+}) and after (right; C-*LRRK2*^{G2019S/+}) gene correction. **c**, Southern blot analysis of *LRRK2*(G2019S) heterozygous mutant iPSCs (*LRRK2*^{G2019S/+}) and their gene-corrected counterparts bearing neo cassette (C-*LRRK2*^{neo/+}). **d**, Subcellular distributions of lamin B1 and lamin B2 in

representative ipsNSCs-*LRRK2*^{G2019S/+} and ipsNSCs-C-*LRRK2*^{G2019S/+} at passage 19. Scale bars, 10 μm. **e**, Apoptosis assays after MG132 treatment in corrected and uncorrected ipsNSCs. **f**, **g**, Colony-formation (f) and neuronal-differentiation (g) assays of ipsNSCs at passage 19. **h**, Immunofluorescence analysis for lamin B1 and H3K9me3 in wild-type H9 hESCs derived NSCs (esNSCs-H9) and their mutant counterparts (esNSCs-H9-*LRRK2*^{G2019S/+}) at passage 14. Scale bars, 10 μm. **i**, Apoptosis assays after MG132 treatment in esNSCs-H9 and esNSCs-H9-*LRRK2*^{G2019S/+} at passage 10. **j**, Colony-formation assay on esNSCs-H9 and esNSCs-H9-*LRRK2*^{G2019S/+} at passage 14. **k**, Spontaneous neuronal-differentiation assay of esNSCs-H9 and esNSCs-H9-*LRRK2*^{G2019S/+} at passage 14. For e–g and i–k, data are shown as mean ± s.d., *n* = 3. ***P* < 0.01. For d, nuclei were stained with Hoechst. For d and h, arrows indicate nuclear microdomains deficient for lamin B1. Percentages of lamin B1-deficient nuclei are shown in corners.

(Fig. 3h–k and Supplementary Figs 13 and 14). Together, our results suggested a specific role for *LRRK2*(G2019S) during the manifestation of passage-dependent NSC abnormal phenotypes and highlighted the nucleus as a potential novel organelle affected in Parkinson's disease.

As *LRRK2*(G2019S) displays enhanced Ser/Thr protein kinase activation that correlates with its pathogenic role in Parkinson's disease^{10,11,22–24}, we investigated whether kinase activity correlated with nuclear degeneration (Supplementary Fig. 16). Our results suggested that cell passaging further enhanced *LRRK2*(G2019S)-mediated phosphorylation of a number of different substrates including 4E-BP1, a known *LRRK2* target²⁴ (Fig. 4a and Supplementary Fig. 16a, b). Interestingly, Ser 935 phosphorylation, an indicator for *LRRK2* activation^{12,22,25,26}, was increased in passage 15 ipsNSCs-*LRRK2*(G2019S) relative to total *LRRK2* levels (Fig. 4a and Supplementary Fig. 16c).

Chemical inhibition has been shown previously to protect against *LRRK2*-associated toxicity *in vitro* and *in vivo*^{13,22}. Accordingly, treating late-passage ipsNSCs-*LRRK2*(G2019S) with *LRRK2*-In-1, a potent and selective *LRRK2* inhibitor^{12,22}, resulted in reduced phosphorylation of

LRRK2 downstream targets and marked rescue of the aberrant cellular parameters seen in late-passage ipsNSCs-*LRRK2*(G2019S), (Fig. 4b–f, Supplementary Fig. 6a–c and Supplementary Movie 1). Microarray analysis showed that 5-day treatment of passage 14 esNSCs-*LRRK2*(G2019S) with *LRRK2*-In-1 was sufficient to restore a gene-expression signature similar to that of wild-type esNSCs and significantly different from untreated controls (Fig. 4g and Supplementary Table 3). Further studies on cross-talking signalling pathways suggested that *LRRK2*-In-1 was capable of restoring both nuclear morphology and colony-like growth in late-passage ipsNSCs-*LRRK2*(G2019S), whereas LY294002, a PI3K inhibitor, partially rescued nuclear morphology (Supplementary Fig. 16c and 17).

Finally, we investigated nuclear morphology in post-mortem human brain samples. Lamin B1 immunostaining showed that a high proportion of cells display altered nuclear morphologies within the hippocampal dentate gyrus, but not in non-neurogenic areas such as cortex regions, in all the samples analysed from *LRRK2*(G2019S) Parkinson's disease patients, compared to their respective age-matched

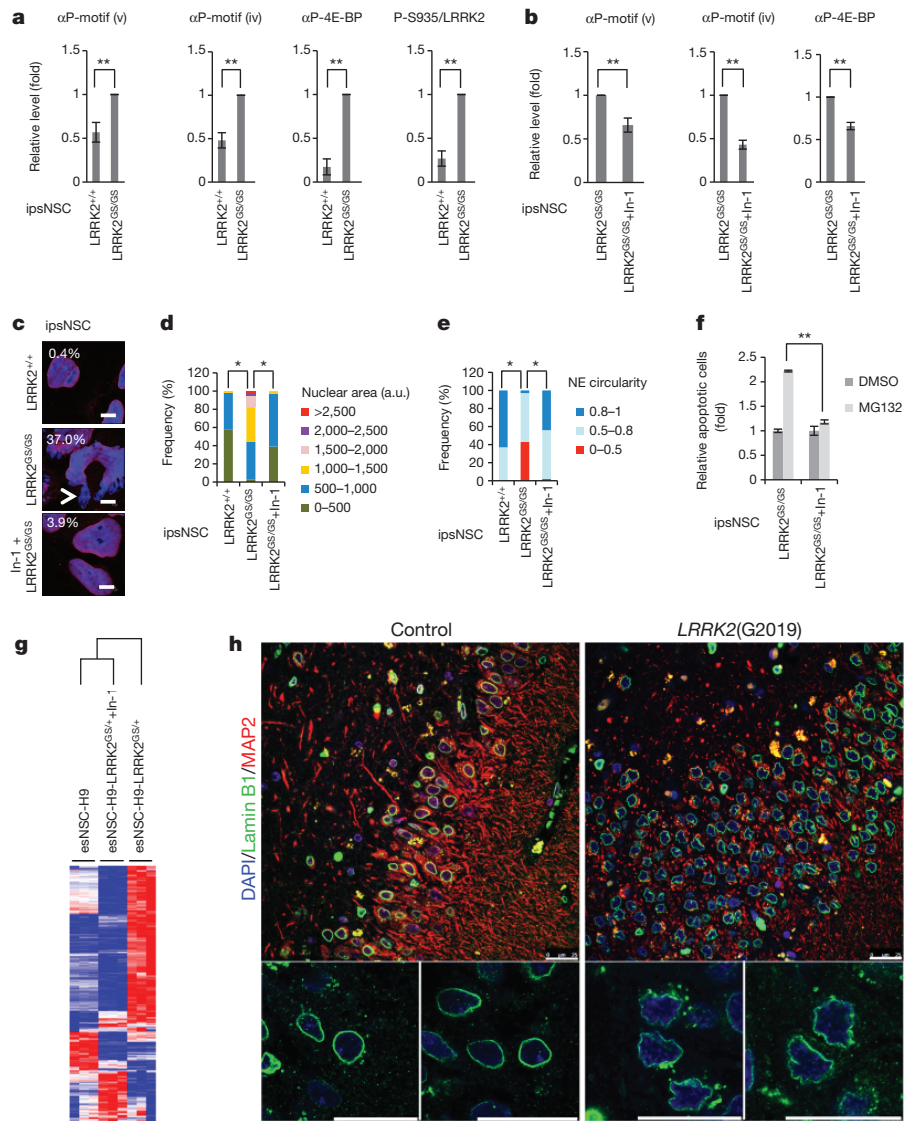


Figure 4 | Rescue of *LRRK2*(G2019S)-associated phenotypic defects in NSCs by inhibition of *LRRK2* kinase activity and morphological analysis of nuclear envelope in Parkinson's disease brain slices. **a**, Immunoblot analysis of passage 15 ipsNSCs-*LRRK2*^{+/+} and ipsNSCs-*LRRK2*^{GS/GS}. Data are shown as mean \pm s.d., $n = 3$. $**P < 0.01$. P-S935/LRRK2 represents the ratio of Ser935-phosphorylated LRRK2 to total LRRK2. **b**, Immunoblot analysis of indicated phosphorylated protein substrates in ipsNSCs. Data are shown as mean \pm s.d., $n = 3$. $**P < 0.01$. α P-motif (v) and α P-motif (iv) refer to the two antibodies recognizing two different phosphorylated motifs (for PKA and PKC substrates), respectively (also see Supplementary Fig. 16a). **c**, Nuclear-morphology analysis in ipsNSCs-*LRRK2*^{GS/GS} at passage 15 treated with *LRRK2*-In-1 for 4 days, compared to untreated controls. Nuclei were stained with Hoechst. Arrowhead, nuclear

microdomains deficient for lamin B1. Scale bars, 5 μ m. **d**, **e**, Quantification of nuclear area (**d**) and nuclear envelope (NE) circularity (**e**) in ipsNSCs at passage 15 treated and untreated with *LRRK2*-In-1 for 4 days. a.u., arbitrary units. $*P < 10^{-15}$. **f**, ipsNSCs-*LRRK2*^{GS/GS} at passage 17 were treated with or without *LRRK2*-In-1 for 8 days, and then with MG132 for 20 h. Data are shown as mean \pm s.d., $n = 3$. $**P < 0.01$. **g**, Hierarchical clustering of gene-expression profiles on the brain slices (hippocampal region) of esNSCs-H9, esNSCs-H9-*LRRK2*^{GS/+} and esNSCs-H9-*LRRK2*^{GS/+} treated with 3 μ M *LRRK2*-In-1 for 5 days at passage 14. Bars show the relative similarities between different groups. **h**, Immunofluorescence analysis on the brain slices (hippocampal region) of Parkinson's disease patients bearing the *LRRK2*(G2019S) mutation (right panel) and age-matched healthy individuals (left panel). Scale bars, 25 μ m.

controls ($78.8\% \pm 3.41$ and $16.49\% \pm 2.41$, respectively (\pm s.e.m.)) (Fig. 4h, Supplementary Table 5 and Supplementary Fig. 18). Interestingly, nuclear aberrations were not only present in *LRRK2*(G2019S) but also in several idiopathic Parkinson's disease human brain samples (mean \pm s.e.m.: $47.28\% \pm 4.28$). Notably, control samples also displayed nuclear disruption to a certain extent, which might be due to the described association of physiological ageing and the nuclear envelope²⁷ (Fig. 4h and Supplementary Fig. 18). Owing to the reduced number of samples ($n = 5$) we cannot conclude that the above-mentioned phenotypes have a 100% penetrance in all Parkinson's disease patients. However, these results indicate the possibility that dysfunctional NSC pools, and/or their respective neuronal derivatives at early stages of maturation, might contribute to the hippocampal and

subventricular zone-related age-dependent non-motor symptoms—including depression, anxiety and hyposmia—associated with *LRRK2*(G2019S)-bearing individuals and Parkinson's disease^{5,28,29}.

Together, our results show that *LRRK2*(G2019S)-elicited aberrant phenotypic manifestations seem to be particularly prominent in human NSC populations and are more noticeable at late passages. Of most relevance, our studies further indicate the suitability of iPSC-based models of disease and ageing not only for the *in vitro* recapitulation of known disease phenotypes, as extensively described, but also as a platform for discovery and study of otherwise novel and elusive cell parameters and populations³⁰ (Supplementary Fig. 1). Furthermore, through the analysis of human brain samples, our study demonstrates that these cellular aberrations can also be found *in vivo*. The fact that this

validation was only possible in human samples once a reliable iPSC *in vitro* system was employed highlights further the potential of patient-specific iPSCs, not only for disease modelling but, most importantly, for the advancement of disease-pathology knowledge.

METHODS SUMMARY

iPSC generation. Parkinson's disease fibroblasts were obtained from Telethon Genetic Biobank Network. Normal fibroblasts were purchased from the Coriell Cell Repository. Fibroblasts were reprogrammed with retroviruses expressing OCT4, SOX2 and KLF4. The generated iPSC lines were maintained in hESC medium on iMEF feeder cells or in mTeSR medium (StemCell Technologies) on Matrigel^{1,18}.

Targeted gene correction in iPSCs-LRRK2(G2019S) and generation of the isogenic hESC line with an LRRK2(G2019S) mutation. Gene targeting in iPSCs-LRRK2(G2019S) and H9 ESCs was carried out using a helper-dependent adenoviral vector (HDAdV)-based method^{18–21}.

Statistical analysis. Results are presented as mean \pm s.d. or mean \pm s.e.m. for at least three independent biological replicates. Comparisons were performed using the student's *t*-test. Distributions of nuclear area and nuclear envelope circularity were analysed with the Kolmogorov–Smirnov test.

Received 25 November 2011; accepted 31 August 2012.

Published online 17 October 2012.

- Liu, G. H. *et al.* Recapitulation of premature ageing with iPSCs from Hutchinson–Gilford progeria syndrome. *Nature* **472**, 221–225 (2011).
- Dechat, T. *et al.* Nuclear lamins: major factors in the structural organization and function of the nucleus and chromatin. *Genes Dev.* **22**, 832–853 (2008).
- Kudlow, B. A., Kennedy, B. K. & Monnat, R. J., Jr. Werner and Hutchinson–Gilford progeria syndromes: mechanistic basis of human progeroid diseases. *Nature Rev. Mol. Cell Biol.* **8**, 394–404 (2007).
- Worman, H. J., Ostlund, C. & Wang, Y. Diseases of the nuclear envelope. *Cold Spring Harb. Perspect. Biol.* **2**, a000760 (2010).
- Winner, B. *et al.* Adult neurogenesis and neurite outgrowth are impaired in LRRK2 G2019S mice. *Neurobiol. Dis.* **41**, 706–716 (2011).
- Chang, K. H. *et al.* Nuclear envelope dispersion triggered by deregulated Cdk5 precedes neuronal death. *Mol. Biol. Cell* **22**, 1452–1462 (2011).
- Tran, D., Chalhoub, A., Schooley, A., Zhang, W. & Ngsee, J. K. A mutation in VAPB that causes amyotrophic lateral sclerosis also causes a nuclear envelope defect. *J. Cell Sci.* **125**, 2831–2836 (2012).
- Padiath, Q. S. *et al.* Lamin B1 duplications cause autosomal dominant leukodystrophy. *Nature Genet.* **38**, 1114–1123 (2006).
- Woulfe, J. M. Abnormalities of the nucleus and nuclear inclusions in neurodegenerative disease: a work in progress. *Neuropathol. Appl. Neurobiol.* **33**, 2–42 (2007).
- Cookson, M. R. The role of leucine-rich repeat kinase 2 (LRRK2) in Parkinson's disease. *Nature Rev. Neurosci.* **11**, 791–797 (2010).
- Cookson, M. R. & Bandmann, O. Parkinson's disease: insights from pathways. *Hum. Mol. Genet.* **19**, R21–R27 (2010).
- Deng, X. *et al.* Characterization of a selective inhibitor of the Parkinson's disease kinase LRRK2. *Nature Chem. Biol.* **7**, 203–205 (2011).
- Lee, B. D. *et al.* Inhibitors of leucine-rich repeat kinase-2 protect against models of Parkinson's disease. *Nature Med.* **16**, 998–1000 (2010).
- Li, W. *et al.* Rapid induction and long-term self-renewal of primitive neural precursors from human embryonic stem cells by small molecule inhibitors. *Proc. Natl Acad. Sci. USA* **108**, 8299–8304 (2011).
- Krishnan, V. *et al.* Histone H4 lysine 16 hypoacetylation is associated with defective DNA repair and premature senescence in Zmpste24-deficient mice. *Proc. Natl Acad. Sci. USA* **108**, 12325–12330 (2011).
- Cheung, I. *et al.* Developmental regulation and individual differences of neuronal H3K4me3 epigenomes in the prefrontal cortex. *Proc. Natl Acad. Sci. USA* **107**, 8824–8829 (2010).
- Xie, W. *et al.* Proteasome inhibition modeling nigral neuron degeneration in Parkinson's disease. *J. Neurochem.* **115**, 188–199 (2010).
- Liu, G. H. *et al.* Targeted gene correction of laminopathy-associated LMNA mutations in patient-specific iPSCs. *Cell Stem Cell* **8**, 688–694 (2011).
- Suzuki, K. *et al.* Highly efficient transient gene expression and gene targeting in primate embryonic stem cells with helper-dependent adenoviral vectors. *Proc. Natl Acad. Sci. USA* **105**, 13781–13786 (2008).
- Li, M. *et al.* Efficient correction of hemoglobinopathy-causing mutations by homologous recombination in integration-free patient iPSCs. *Cell Res.* **21**, 1740–1744 (2011).
- Aizawa, E. *et al.* Efficient and accurate homologous recombination in hESCs and hiPSCs using helper-dependent adenoviral vectors. *Mol. Ther.* **20**, 424–431 (2012).
- Rudenko, I. N., Chia, R. & Cookson, M. R. Is inhibition of kinase activity the only therapeutic strategy for LRRK2-associated Parkinson's disease? *BMC Med.* **10**, 20 (2012).
- Kanao, T. *et al.* Activation of FoxO by LRRK2 induces expression of proapoptotic proteins and alters survival of postmitotic dopaminergic neuron in *Drosophila*. *Hum. Mol. Genet.* **19**, 3747–3758 (2010).
- Gehrke, S., Imai, Y., Sokol, N. & Lu, B. Pathogenic LRRK2 negatively regulates microRNA-mediated translational repression. *Nature* **466**, 637–641 (2010).
- Nichols, R. J. *et al.* 14-3-3 binding to LRRK2 is disrupted by multiple Parkinson's disease-associated mutations and regulates cytoplasmic localization. *Biochem. J.* **430**, 393–404 (2010).
- Dzambo, N. *et al.* Inhibition of LRRK2 kinase activity leads to dephosphorylation of Ser(910)/Ser(935), disruption of 14–3–3 binding and altered cytoplasmic localization. *Biochem. J.* **430**, 405–413 (2010).
- Scaffidi, P. & Misteli, T. Lamin A-dependent nuclear defects in human aging. *Science* **312**, 1059–1063 (2006).
- Poulopoulos, M. *et al.* Clinical and Pathological Characteristics of LRRK2 G2019S Patients with PD. *J. Mol. Neurosci.* **47**, 139–143 (2012).
- Thaler, A., Mirelman, A., Gurevich, T., Simon, E., Orr-Urtreger, A., Marder, K., Bressman, S. & Giladi, N. Lower cognitive performance in healthy G2019S LRRK2 mutation carriers. *Neurology* **79**, 1027–1032 (2012).
- Tiscornia, G., Vivas, E. L. & Belmonte, J. C. Diseases in a dish: modeling human genetic disorders using induced pluripotent cells. *Nature Med.* **17**, 1570–1576 (2011).

Supplementary Information is available in the online version of the paper.

Acknowledgements We would like to thank K. Mitani, P. Ng, A. Lieber, Y. Imai, M. A. Miyawaki, Filocamo, S. Goldwurm, Telethon Genetic Biobank Network for providing constructs and cells (the fibroblast samples were obtained from the “Cell Line and DNA Biobank from patients affected by Genetic Diseases” (G. Gaslini Institute)-Telethon Genetic Biobank Network (project no. GTB07001)); Neurological Tissue Bank of the Biobank-Hospital Clinic-IDIBAPS for providing human brain tissue; F. Gage, M. Hetzer, J. Yao, Y. Mu, D. Yu, E. Gelpi, X. M. Wang, X. Wang, G. Bai and Z. J. Liu for helpful discussions; M. Joens and J. Fitzpatrick of the Waitt Advanced Biophotonics Core Facility for performing TEM analysis; M. Marti for imaging, teratoma and karyotyping analysis; F. Osakada for statistics analysis; and M. Schwarz, P. Schwarz and L. Laricchia-Robbio for administrative help. G.-H.L. is supported by the Thousand Young Talents program of China, the National Laboratory of Biomacromolecules, the Strategic Priority Research Program of the Chinese Academy of Sciences, the National Natural Science Foundation of China (NSFC) (81271266 and 31222039), and the Beijing Municipal Natural Science Foundation. J.Q. was partly supported by an AFAR/Ellison Medical Foundation postdoctoral fellowship. K.S. was partly supported by a Uehara Memorial Foundation research fellowship. E.N. was partly supported by an F.M. Kirby Foundation postdoctoral fellowship. X.X. is supported by NSFC (31201111). B.R. was supported by a US National Institute of Health (NIH) grant (ES017166) and the Ludwig Institute for Cancer Research. J.Y. was supported by an NIH grant (P41 RR011823). J.C.I.B. was supported by grants from the Glenn Foundation, G. Harold and Leila Y. Mathers Charitable Foundation, Sanofi, the California Institute of Regenerative Medicine, the Ellison Medical Foundation, the Helmsley Charitable Trust, ERA-Net Neuron, MINECO and Fundacion Cellex.

Author Contributions G.-H.L., J.Q., K.S. prepared the figures, designed and performed all *in vitro* experiments. E.N. and N.M. designed and performed *in vivo* experiments. A.G., J.K., R.D.S., X.X., W.Z., Y.L., S.R. and C.R.E. provided technical assistance. I.D. performed teratoma studies. F.Y. generated microarray data. M.L. performed FISH and DNA methylation assays. B.R., U.W. and A.K. performed and analysed epigenetic studies. J.T. and J.Y.II performed proteomic studies. G.-H.L., J.Q., K.S., E.N., I.S.-M. and J.C.I.B. wrote the manuscript.

Author Information Reprints and permissions information is available at www.nature.com/reprints. The authors declare no competing financial interests. Readers are welcome to comment on the online version of the paper. Correspondence and requests for materials should be addressed to J.C.I.B. (belmonte@salk.edu) or G.-H.L. (gghliu@ibp.ac.cn).

Mitochondrial Atpif1 regulates haem synthesis in developing erythroblasts

Dhvanit I. Shah¹, Naoko Takahashi-Makise², Jeffrey D. Cooney^{1†}, Liangtao Li², Iman J. Schultz^{1†}, Eric L. Pierce^{1†}, Anupama Narla^{1,3}, Alexandra Seguin², Shilpa M. Hattangadi^{3,4†}, Amy E. Medlock⁵, Nathaniel B. Langer^{1†}, Tamara A. Dailey⁵, Slater N. Hurst¹, Danilo Faccenda⁶, Jessica M. Wiwczar^{7†}, Spencer K. Heggers¹, Guillaume Vogin^{1†}, Wen Chen^{1†}, Caiyong Chen¹, Dean R. Campagna⁸, Carlo Brugnara⁹, Yi Zhou³, Benjamin L. Ebert¹, Nika N. Danial⁷, Mark D. Fleming⁸, Diane M. Ward², Michelangelo Campanella⁶, Harry A. Dailey⁵, Jerry Kaplan² & Barry H. Paw^{1,3}

Defects in the availability of haem substrates or the catalytic activity of the terminal enzyme in haem biosynthesis, ferrochelatase (Fech), impair haem synthesis and thus cause human congenital anaemias^{1,2}. The interdependent functions of regulators of mitochondrial homeostasis and enzymes responsible for haem synthesis are largely unknown. To investigate this we used zebrafish genetic screens and cloned mitochondrial *ATPase inhibitory factor 1* (*atpif1*) from a zebrafish mutant with profound anaemia, *pinotage* (*pnt*^{tg209}). Here we describe a direct mechanism establishing that Atpif1 regulates the catalytic efficiency of vertebrate Fech to synthesize haem. The loss of *Atpif1* impairs haemoglobin synthesis in zebrafish, mouse and human haematopoietic models as a consequence of diminished Fech activity and elevated mitochondrial pH. To understand the relationship between mitochondrial pH, redox potential, [2Fe–2S] clusters and Fech activity, we used genetic complementation studies of Fech constructs with or without [2Fe–2S] clusters in *pnt*, as well as pharmacological agents modulating mitochondrial pH and redox potential. The presence of [2Fe–2S] cluster renders vertebrate Fech vulnerable to perturbations in Atpif1-regulated mitochondrial pH and redox potential. Therefore, *Atpif1* deficiency reduces the efficiency of vertebrate Fech to synthesize haem, resulting in anaemia. The identification of mitochondrial Atpif1 as a regulator of haem synthesis advances our understanding of the mechanisms regulating mitochondrial haem homeostasis and red blood cell development. An *ATP1F1* deficiency may contribute to important human diseases, such as congenital sideroblastic anaemias and mitochondriopathies.

A deficiency in haem, which is used in a wide variety of metabolic and regulatory pathways in cells³, results in pathological conditions that range from mild anaemia to early *in utero* death⁴. As an essential component of haemoglobin, the individual enzymes and substrates of haem biosynthesis have been well studied²; however, key gaps remain in our knowledge of genes that regulate intracellular iron and haem transport and homeostasis. This incomplete understanding prevents researchers from developing targeted therapies for a broad range of disorders, including congenital anaemias and porphyrias, as well as metabolic and neurological disorders.

We recovered *pnt*, a zebrafish (*Danio rerio*) non-lethal recessive mutant, from an unbiased ethyl nitrosourea (ENU) mutagenesis screen⁵ for defects in circulating erythroid cells⁶. *pnt* embryos were anaemic (Fig. 1a) despite normal expression of the erythroid cell markers β -globin

and band-3 (data not shown). On the basis of red cell indices, the erythrocytes from *pnt* embryos that survive to adult stage exhibited hypochromic, microcytic anaemia (Supplementary Fig. 1a). Histological analysis of adult *pnt* haematopoietic tissues showed no gross morphological defects (Supplementary Fig. 1b).

To identify a candidate gene for the *pnt* locus we carried out positional cloning and chromosomal walk, which identified the most

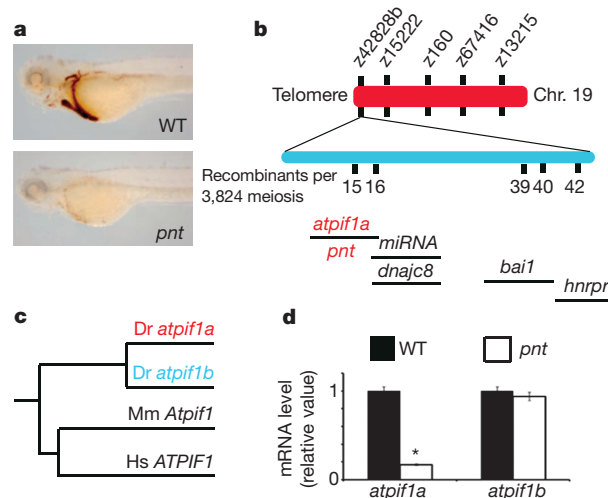


Figure 1 | Disruption of *atpif1* in *pinotage* (*pnt*^{tg209}) produces hypochromic anaemia. **a**, *pnt* embryos are severely anaemic. Wild-type (WT) embryo at 72 h post-fertilization exhibits o-dianisidine-stained (brown) haemoglobinized cells. Original magnification $\times 5$. **b**, The positional cloning of the *pnt* locus on zebrafish chromosome 19. A positional cloning approach using 1,912 diploid *pnt* embryos identified the closest linked genetic marker as z42828b. A chromosomal walk was initiated at a distance of ~ 0.01 centimorgan (cM) from the *pnt* locus. The bacterial artificial chromosome clone, encompassing the *pnt* locus, is shown below, along with the annotated genes within the critical physical contig. **c**, Phylogenetic dendrogram showing the amino acid homology between the various *atpif1* genes. *D. rerio* (Dr) *atpif1a* aligns with its related paralogue, *atpif1b*, on zebrafish chromosome 17. Both *atpif1a* and *atpif1b* are shown clustering with their functional mammalian orthologues from mouse (Mm) and human (Hs). **d**, qRT-PCR analysis of *atpif1a* and *atpif1b* mRNA in *pnt* and wild-type embryos, showing reduced *atpif1a* and normal *atpif1b* mRNA level in *pnt*. * $P < 0.05$ (*t*-test, $n = 3$, error bars indicate standard error of the mean, s.e.m.).

¹Department of Medicine, Division of Hematology, Brigham and Women's Hospital, Harvard Medical School, Boston, Massachusetts 02115, USA. ²Department of Pathology, University of Utah School of Medicine, Salt Lake City, Utah 84312, USA. ³Department of Medicine, Division of Hematology-Oncology, Boston Children's Hospital, Harvard Medical School, Boston, Massachusetts 02115, USA.

⁴Whitehead Institute for Biomedical Research and Massachusetts Institute of Technology, Cambridge, Massachusetts 02142, USA. ⁵Biomedical and Health Sciences Institute, Departments of Microbiology, Biochemistry & Molecular Biology, University of Georgia, Athens, Georgia 30602, USA. ⁶Royal Veterinary College, University of London and University College London Consortium for Mitochondrial Research, London NW1 0TU, UK. ⁷Department of Cancer Biology, Dana-Farber Cancer Institute, Harvard Medical School, Boston, Massachusetts 02115, USA. ⁸Department of Pathology, Boston Children's Hospital, Harvard Medical School, Boston, Massachusetts 02115, USA. ⁹Department of Laboratory Medicine, Boston Children's Hospital, Harvard Medical School, Boston, Massachusetts 02115, USA. [†]Present addresses: University of Texas Health Science Center, San Antonio, Texas 78229, USA (J.D.C.); IntRNA Technologies, 3584 CH Utrecht, The Netherlands (I.J.S.); Georgia Institute of Technology, Atlanta, Georgia 30332, USA (E.L.P.); Yale University, New Haven, Connecticut 06510, USA (S.M.H. and J.M.W.); Columbia University, New York, New York 10032, USA (N.B.L.); Alexis Vautrin Cancer Centre, 54511 Vandoeuvre-Les-Nancy Cedex, France (G.V.); and Texas A&M Health Science Center, Temple, Texas 76504, USA (W.C.).

probable candidate gene to be mitochondrial *ATPase inhibitory factor 1* (zgc:162207; which we refer to hereafter as *atpif1a*) (Fig. 1b). Phylogenetic analysis showed that an *ATPase inhibitory factor 1-like protein* (zgc: 153321; which we refer to hereafter as *atpif1b*) on chromosome 17 is 71% similar to *atpif1a* at the amino acid level (Fig. 1c), and is probably the result of gene duplication in teleosts⁷. Peptide alignments further displayed human (*ATP1F1*, chromosome 1) and mouse (*Atpif1*, chromosome 4) orthologues for *atpif1a* and *atpif1b* (Fig. 1c). Quantitative reverse-transcriptase polymerase chain reaction (qRT-PCR) showed reduced levels of *atpif1a* messenger RNA in *pnt* embryos (Fig. 1d) and *pnt* adult kidney marrow compared to their respective wild-type controls (Supplementary Fig. 1c). The levels of *atpif1b* mRNA were, however, unchanged in *pnt* embryos (Fig. 1d) and elevated two to threefold in *pnt* adult kidney marrow (Supplementary Fig. 1c). Thus, *atpif1a* is probably the gene disrupted in the *pnt* locus. Previous studies have shown that mitochondrial *Atpif1* regulates the proton motive force via mitochondrial influx of H⁺ ions, mitochondrial structure, and ATP synthesis, indicating that *Atpif1* is required in a wide range of metabolically active tissues⁸. The broad requirement for *Atpif1* is reinforced by the ubiquitous expression of both *atpif1a* and *atpif1b* in zebrafish embryos (Supplementary Fig. 1d) and *Atpif1* in various mouse adult and fetal organs (Supplementary Fig. 1e).

To verify the loss-of-function phenotype for *atpif1a*, we injected two *atpif1a* antisense splice-blocking (Fig. 2a) and translational-blocking morpholinos (data not shown) to knock down *atpif1a* expression in zebrafish embryos. The *atpif1a*-silenced embryos (morphants) lacked haemoglobinized cells, as detected by *o*-dianisidine staining, thereby phenocopying the anaemia in *pnt* embryos (Fig. 2a). The anaemic phenotype in the morphant embryos correlates with a reduction of *atpif1a* mRNA levels, verifying that the splice-blocking morpholinos accurately targeted *atpif1a* (Fig. 2b, Supplementary Discussion 1 and Supplementary Fig. 2a–d).

To validate further that *atpif1a* is the gene disrupted in *pnt*, we overexpressed *atpif1a* sense-strand complementary RNA (cRNA) in *pnt* embryos and subsequently evaluated their haemoglobinization. To assess the specificity of our complementation assay, we also injected *pnt* embryos with non-functional *atpif1a* cRNA harbouring a missense mutation (E26A) in the regulatory inhibitory domain⁹. Only functional *atpif1a* complemented the anaemia in *pnt* embryos (Fig. 2c), thereby confirming that *atpif1a* is the gene disrupted in *pnt* embryos. Consistent with a two- to threefold increase in *atpif1b* expression in surviving *pnt* adults (Supplementary Fig. 1c), the ectopic expression of *atpif1b* cRNA also complemented *pnt* anaemia (Fig. 2c), a result of their redundant function. These data indicate that the hypomorphic and viable phenotype of *pnt* could be attributed to the ability of *atpif1b* to partially compensate for the loss of function of *atpif1a* (Supplementary Fig. 1c). This is in contrast to other situations with paralogues, such as the *mitoferrin* (*mfrn*) transporters¹⁰, which do not partially compensate for loss of their other paralogue.

To identify the genetic mutation in the *pnt* locus, we first sequenced the open reading frame and splice junctions of the *atpif1a* gene and did not find a mutation. Instead, we discovered an AC insertional mutation in the 3' untranslated region (3' UTR) of the *atpif1a* gene (Fig. 2d). This mutation was linked to the *pnt* locus following the distinct segregation of wild-type and mutant conformations on single-strand conformational polymorphism (SSCP) analysis (Fig. 2e). To establish the functional consequences of the 3' UTR mutation on the stability of *atpif1a* mRNA, we designed constructs containing the zebrafish *atpif1a* open reading frame fused with either the wild-type or mutant 3' UTR sequences, and transfected mouse erythroleukaemia (MEL) cells with each construct individually for stable selection (Supplementary Fig. 2e). A decrease in steady-state *atpif1a* mRNA levels in cells harbouring mutant 3' UTR constructs as compared to the wild-type construct was shown by qRT-PCR analysis (Fig. 2f and Supplementary Discussion 2). These data demonstrate that the mutation in the 3' UTR of the *atpif1a* gene destabilizes its steady-state mRNA. The observed

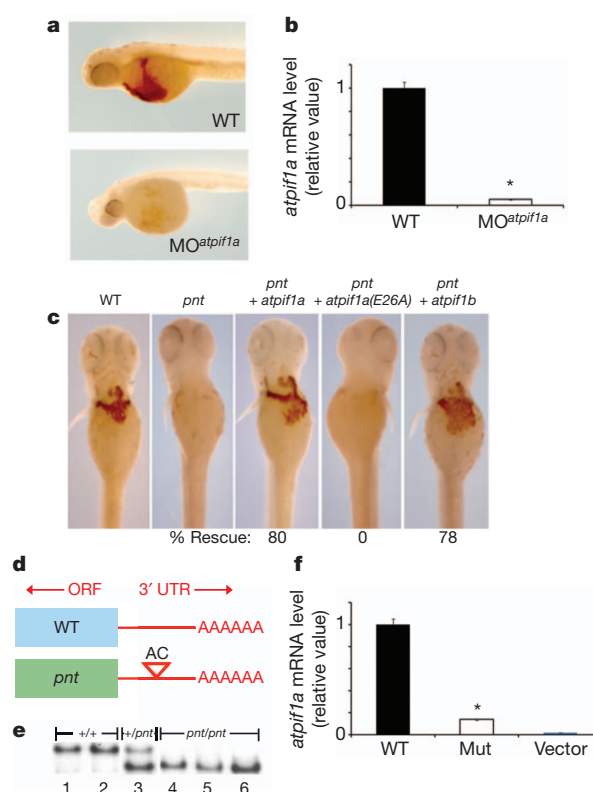


Figure 2 | Functional characterization of the *atpif1a* gene. **a**, Splice blocking morpholino (MO) knockdown of *atpif1a* phenocopies the anaemia observed in *pnt* embryos. Original magnification $\times 5$. **b**, qRT-PCR analysis shows that the anaemic phenotype is due to the accurate knockdown of *atpif1a*. **c**, Ectopic expression of *atpif1a* or *atpif1b* cRNA functionally complements the anaemia in *pnt* embryos at 72 h post-fertilization. Wild-type control, *pnt* and rescued *pnt* embryos complemented with *atpif1a* or *atpif1b* cRNA are stained with *o*-dianisidine. The non-functional *atpif1a*, harbouring the E26A mutation, specifically failed to complement the *pnt* anaemia. Original magnification $\times 5$. **d**, *pnt* embryos have an A to C mutation in the 3' UTR of the *atpif1a* gene. **e**, The 3' UTR mutation co-segregates with the *pnt* phenotype by SSCP analysis. The SSCP segregation pattern for lanes 1–2 (+/+), lane 3 (+/*pnt*) and lanes 4–6 (*pnt/pnt*). **f**, The AC insertional mutation in the 3' UTR of the *atpif1a* cDNA functionally destabilizes its mRNA. The mutant construct (Mut) stably expressed in MEL cells showed reduced *atpif1a* mRNA levels. * $P < 0.05$ (t-test, $n = 3$, error bars indicate standard error of the mean, s.e.m.).

decrease in the *atpif1a* mRNA level in *pnt* embryos (Fig. 1d) is consistent with the ascribed function for the 3' UTR mutation, which destabilizes *atpif1a* steady-state mRNA and leads to its degradation¹¹.

In mammalian cells, *Atpif1* is located in the inner mitochondrial membrane and primarily regulates the function of the F_1F_0 -ATP synthase¹². There is, however, no direct evidence suggesting a role for *Atpif1* in haem synthesis or erythropoiesis. To ascertain the role of *Atpif1* in mammalian haem synthesis, we used short hairpin RNAs (shRNAs) to stably silence *Atpif1* in differentiating mammalian haematopoietic cells: human primary CD34⁺ (hCD34⁺) cells, mouse primary fetal liver (MPFL) cells and MEL cells. The reduced number of haemoglobinized cells in *Atpif1*-silenced hCD34⁺ and MEL cells (Fig. 3a and Supplementary Fig. 3a) and the reduced haemoglobin content in MPFL cells transduced with *Atpif1* shRNAs (Supplementary Fig. 3b, c) demonstrate a conserved haem-specific function of *Atpif1*. Consistent with a high turnover of haem in developing erythroblasts¹³, we observed that the haemoglobinization defect was specific to *Atpif1*-silenced differentiating erythroid cells. Similarly, we observed that during terminal erythroid maturation the expression of *Atpif1* protein increases along with other proteins required for haem synthesis¹⁴, such as *Fech* and *mitoferrin1* (*Mfrn1*, also called *Slc25a37*) (Supplementary Fig. 3d). Analogous *Atpif1*-silencing experiments performed in non-erythroid

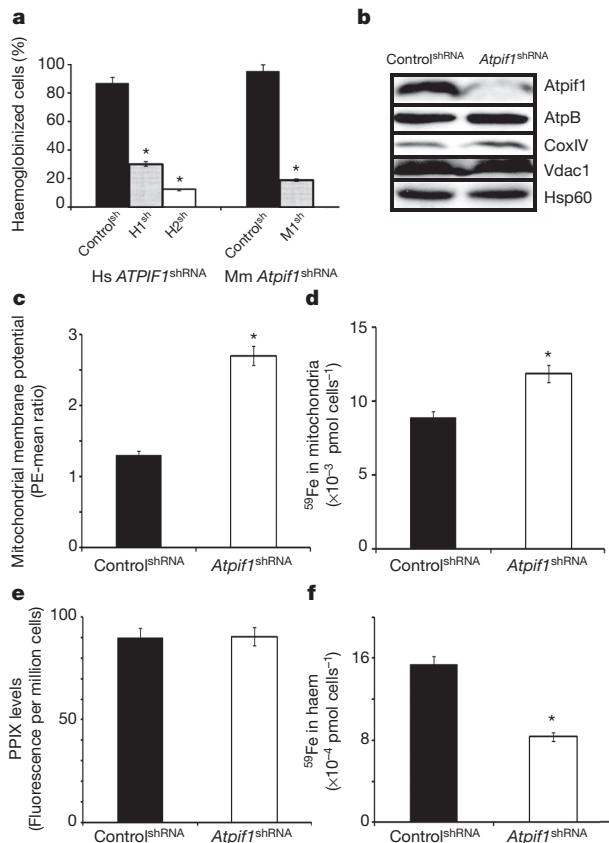


Figure 3 | Loss of *Atp1f1* produces a haemoglobinization defect in mammalian cells. **a**, Silencing of *Atp1f1* in human CD34⁺ (left) and MEL (right) cells with shRNAs (human, H1^{sh} and H2^{sh}; mouse, M1^{sh}) results in a haemoglobinization defect. **b**, Western blot analysis in *Atp1f1* shRNA-silenced MEL cells (mouse, M1^{sh}). *Atp1f1* protein level is reduced in *Atp1f1* shRNA (M1^{sh})-silenced cells; however, the mitochondrial structural proteins AtpB, CoxIV, Vdac1 and Hsp60 are not affected. **c**, Silencing of *Atp1f1* increased the mitochondrial membrane potential ($\Delta\Psi$ m), analysed using a TMRE fluorescence probe in the presence of verapamil and FCCP. **d**, Silencing of *Atp1f1* elevates the import of ⁵⁹Fe in the mitochondria, consistent with the increased mitochondrial $\Delta\Psi$ m. **e**, Silencing of *Atp1f1* does not influence the formation of protoporphyrin IX (PPIX), indicating that PPIX and iron are not limiting for haem synthesis. **f**, The level of ⁵⁹Fe incorporated in haem is greatly reduced in *Atp1f1*-silenced MEL cells, recapitulating the haem synthesis defect in *pnt*. **P* < 0.05 (*t*-test, *n* = 3, error bars indicate standard error of the mean, s.e.m.).

(NIH 3T3) and undifferentiated MEL cells showed no measurable haem defects (Supplementary Fig. 4). This indicates that *Atp1f1* is essential for terminal erythroid maturation and is not critical for haem synthesis in non-erythroid cells and early erythroid progenitors.

Under physiological conditions, the F₁F₀-ATP synthase generates a proton motive force and ATP by transporting H⁺ ions into the mitochondria^{8,15}. Under oxidative stress conditions, the F₁F₀-ATP synthase reverses the direction of H⁺ transport, thus reducing ATP and the proton motive force^{8,15}. *Atp1f1* inhibits the reversal of F₁F₀-ATP synthase to decrease ATP hydrolysis, thereby maintaining the mitochondrial membrane potential and proton motive force⁸. To determine the causal association between the roles of *Atp1f1* in mitochondrial homeostasis and mammalian haem synthesis, we used stable *Atp1f1*-shRNA-silenced MEL cells. Consistent with the silencing of *Atp1f1*, the *Atp1f1* protein levels were reduced (Fig. 3b). To test the possibility of global mitochondrial structural dysfunction we examined several integral mitochondrial proteins, such as the β -subunit of ATP synthase, complex IV, voltage-dependent anionic-selective channel protein 1, and heat shock protein 60 (Fig. 3b), and their protein expression was found to be normal. In addition, electron microscopy and biochemical analysis revealed normal mitochondrial integrity,

indicating that the gross structural architecture of mitochondria in *Atp1f1*-silenced MEL cells was preserved (Fig. 3b and Supplementary Fig. 5). However, we found that the knockdown of *Atp1f1* in differentiating MEL cells caused a depletion of cellular ATP levels (Supplementary Figs 6a, b), an increase in mitochondrial membrane potential ($\Delta\Psi$ m) (Fig. 3c and Supplementary Fig. 6c), and an alkalization of the mitochondria (Supplementary Fig. 6d).

Haem synthesis requires the incorporation of ferrous ion (Fe²⁺) into protoporphyrin IX (PPIX), which is catalysed by Fech on the matrix side of the inner mitochondrial membrane¹⁶. Because the loss of *Atp1f1* primarily results in a haem synthesis defect in differentiating erythroid cells, we analysed the mitochondrial levels of haem, haem substrates and their related enzymes. We have previously shown that Mfrn1, an inner mitochondrial membrane transporter, facilitates the import of iron into erythroid mitochondria¹⁰, which is dependent upon the mitochondrial $\Delta\Psi$ m^{17,18}. Consistent with the increased mitochondrial $\Delta\Psi$ m in *Atp1f1*-silenced MEL cells (Fig. 3c and Supplementary Fig. 6c), the uptake of radioisotope-labelled iron (⁵⁹Fe) into the mitochondria was increased (Fig. 3d), indicating that the loss of *Atp1f1* increases mitochondrial iron load. Iron transported into the mitochondrial matrix is either used to make iron and sulphur [2Fe-2S] clusters or incorporated into PPIX by Fech to generate haem^{1-3,13}. *Atp1f1*-silenced MEL cells had normal levels of mitochondrial PPIX (Fig. 3e), suggesting that the enzymes and substrates necessary to make this haem precursor are not rate-limiting. The incorporation of ⁵⁹Fe into PPIX to generate haem, however, was reduced (Fig. 3f), despite sufficient levels of Fech substrates, iron and PPIX. We predicted that the catalytic efficiency of Fech was compromised, therefore we measured the activity and protein expression levels of Fech. Although normal levels of Fech protein were present, Fech activity was reduced (Fig. 4a), suggesting that the defect in haem synthesis in *pnt* could be attributed to a reduction in Fech activity. We found that the basal mitochondrial pH of control cells was pH 7.4, and for *Atp1f1*-silenced MEL cells it was pH 8.6 (Fig. 4b, Supplementary Discussion 3 and Supplementary Fig. 6d). Because *Atp1f1*-silenced MEL cells have higher basal mitochondrial pH, we predicted that elevated mitochondrial pH might influence Fech's efficiency in making haem, and secondly that the Fech isolated from these cells would be already detrimentally affected by the elevated pH. To test our hypothesis, we preincubated the purified human FECH at pH 7.4, pH 8.0, pH 8.5 and pH 9.0 for 1 h, and then ran the FECH assay at pH 7.4. We found that preincubation at elevated pH decreased human FECH activity and thus reduced its capacity to make haem (Supplementary Fig. 6e). In addition, we found that increasing the mitochondrial pH to pH 8.5 or pH 9.0 would further lower Fech activity in both control and *Atp1f1*-silenced MEL cells (Fig. 4c), indicating that Fech activity is a function of mitochondrial pH (Supplementary Discussion 3). Together, these data indicate that the ability of Fech to generate haem was compromised due to the increase in mitochondrial pH that occurs in *Atp1f1*-silenced differentiating MEL cells.

We further found that lowering mitochondrial membrane potential and thus mitochondrial pH—using pharmacological agents carbonyl cyanide 4-(trifluoromethoxy)phenylhydrazone (FCCP) at 1 mM concentration for 1 h or 2,4-dinitro-phenol (2,4-DNP) at 500 μ M for 1 h¹⁹—could rescue the anaemic phenotype in *Atp1f1*-silenced MEL cells (Fig. 4d). These data reinforce our observation that *Atp1f1* regulates haem synthesis by means of its modulation of the mitochondrial membrane potential ($\Delta\Psi$ m) and mitochondrial pH.

Atp1f1-silenced MEL cells have normal cytosolic and mitochondrial [2Fe-2S] cluster biogenesis because proteins dependent on [2Fe-2S] cluster synthesis, such as cytosolic xanthine oxidase (Supplementary Fig. 7a) and mitochondrial aconitase (Fig. 4e), show normal activity. The post-translational stability of Fech apoprotein depends on iron availability and an intact [2Fe-2S] cluster assembly machinery^{20,21}. However, the functional role of the [2Fe-2S] cluster in Fech activity remains unknown (Supplementary Discussion 4). All vertebrate Fech

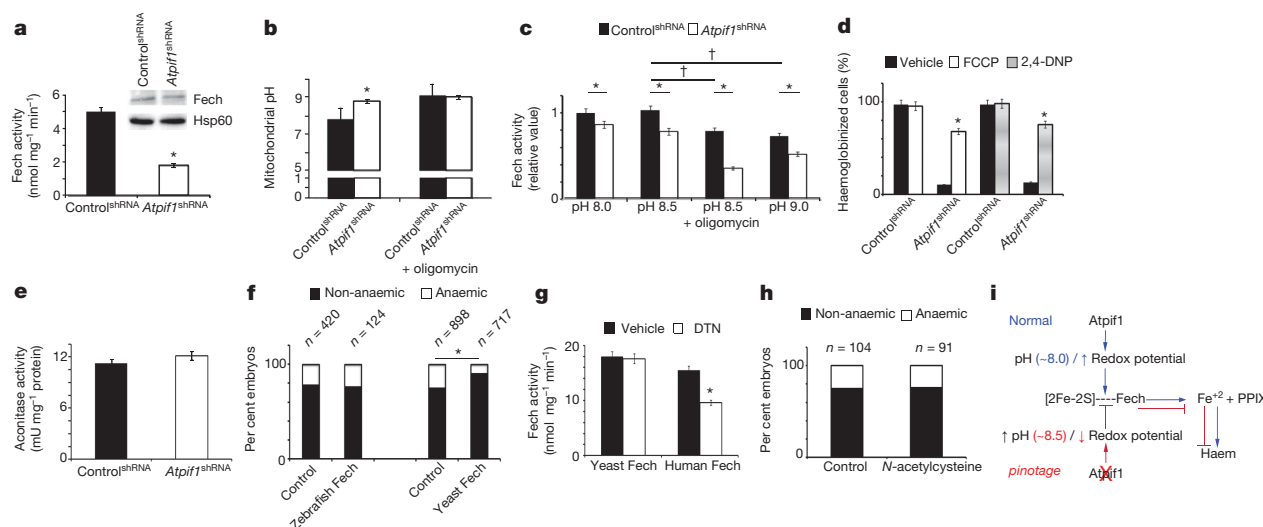


Figure 4 | Atpif1 regulates haem synthesis by modulating Fech activity.

a, Ferrochelatase (Fech) protein levels are normal (top right); however, the FEch activity is reduced in *Atpif1*-silenced MEL cells. **b**, Silencing of *Atpif1* in MEL cells increases the mitochondrial matrix pH to pH 8.6. The left histograms summarize values at resting conditions (– oligomycin), and the right histograms represent challenge with oligomycin (+ oligomycin) that normalizes the initial difference. **c**, Analysis of Fech activity as a function of pH. The elevation of mitochondrial pH to pH 8.5 or pH 9.0 markedly reduced Fech activity in MEL cells. **d**, Drugs lowering mitochondrial membrane potential reverses the anaemic phenotype due to loss of *Atpif1* expression. Treatment of FCCP and 2,4-DNP complements the anaemic phenotype of *Atpif1*-silenced MEL cells. **e**, Aconitase activity, a marker for mitochondrial [2Fe–2S] cluster synthesis, is normal in *Atpif1*-silenced MEL cells. **f**, The presence of an [2Fe–2S] cluster makes Fech susceptible to mitochondrial pH alteration in the absence of *Atpif1*. Validating this prediction, yeast Fech, lacking [2Fe–2S], complements *pnt* anaemia indicating a resistance to pH changes in the absence of *atpif1*. Zebrafish Fech, containing [2Fe–2S], does not complement *pnt* anaemia,

enzymes possess [2Fe–2S] clusters, whereas Fech from the yeast *Saccharomyces cerevisiae* does not have a cluster^{16,21}. On the basis of these data and our current observations, we proposed that the [2Fe–2S] cluster of Fech could influence Fech activity *in situ* by rendering Fech responsive to changes in the mitochondrial proton motive force, and thus mitochondrial pH and redox potential.

To test experimentally whether [2Fe–2S]-cluster-containing Fech responded to the capacity of Atpif1 to regulate mitochondrial proton motive force and thus mitochondrial pH, we designed Fech constructs containing or lacking [2Fe–2S] (zebrafish and yeast Fech, respectively) and also containing a vertebrate mitochondrial targeting propeptide. Both constructs, irrespective of the presence of [2Fe–2S] clusters, functionally complemented a genetic deficiency for zebrafish Fech in *freixenet*^{6,22} (*frx*^{tu271}, Supplementary Fig. 7b). When either the zebrafish or yeast Fech cRNA was injected into *pnt* embryos, the yeast Fech rescued *pnt* anaemia, whereas zebrafish Fech did not (Fig. 4f). These data suggest that it is the [2Fe–2S] cluster of the zebrafish Fech that makes this enzyme vulnerable to pH perturbations of the mitochondrial matrix in *atpif1*-deficient *pnt* embryos. Therefore, Atpif1 has an essential role in stabilizing the activity of [2Fe–2S]-cluster-containing Fech by modulating changes in mitochondrial matrix pH. On the basis of our results, we infer that yeast Fech, lacking the [2Fe–2S] cluster, is resistant to mitochondrial pH changes in *pnt* embryos. Consistent with our observation that the activity of yeast Fech would be unaffected by mitochondrial pH (Fig. 4f), we found that the yeast *inh1* knockout did not produce a defect in haem synthesis (data not shown). These data show that Atpif1 regulates haem synthesis in higher vertebrate erythroid tissues, whereas its counterpart in *S. cerevisiae*, *Inh1*, does not regulate haem synthesis.

The redox potential of mitochondrial matrix at pH 7.4 is –280 mV and it is reduced to –370 mV at pH 8.4²³. As the mitochondrial pH

indicating its susceptibility to mitochondrial alkalization. **g**, The [2Fe–2S] of Fech is sensitive to a decrease of redox potential. DTN, a strong reducing agent, treatment decreases human FECH activity and does not affect yeast Fech activity. **h**, Reactive oxygen species (ROS) are not responsible for *pnt* anaemia. Treatment of *pnt* embryos with *N*-acetylcysteine (NAC) does not reverse *pnt* anaemia. **i**, A proposed mechanistic model of Atpif1 function in the maintenance of mitochondrial pH and regulation of Fech activity for haem synthesis. Mitochondrial haem synthesis requires Fech to incorporate iron into PPIX at physiological pH. Atpif1 normally preserves the mitochondrial pH. Loss of Atpif1 increases the alkalinity of mitochondrial pH, and the presence of [2Fe–2S] cluster makes Fech susceptible to mitochondrial pH and redox potential perturbations, and consequently reduces its catalytic efficiency for the production of haem. * $P < 0.05$ (*t*-test, $n = 3$); † $P < 0.05$ versus control cells at pH 8.5 (*t*-test, $n = 3$); error bars indicate standard error of the mean, s.e.m.; unless n values are otherwise stated, for all data n refers to three independent biological replicates; bars without an asterisk are not statistically significant; all samples were analysed for statistical significance.

is inversely related to mitochondrial redox potential²³, we further analysed the susceptibility of the [2Fe–2S] of Fech to reduction in mitochondrial redox potential. When we treated human FECH (with [2Fe–2S]) and yeast Fech (without [2Fe–2S]) with a strong reducing agent, sodium dithionite (DTN, 10 mM), we found that the DTN treatment could only reduce the activity of human and not yeast Fech (Fig. 4g). This further suggests that [2Fe–2S] of vertebrate Fech is sensitive to the reduction in the redox potential. Thus, Fech activity is reduced in *Atpif1*-silenced MEL cells as its [2Fe–2S] cluster is sensitive to an elevation of mitochondrial pH (Fig. 4b–d, f) and a reduction in redox potential (Fig. 4g), and not because of a defect in [2Fe–2S] cluster biosynthetic assembly (Fig. 4e and Supplementary Fig. 7a).

To exclude an anaemic phenotype in *pnt* as a causal effect of reactive oxygen species (ROS)-induced haem degradation, we treated *pnt* mutant embryos with *N*-acetylcysteine (NAC, 10 μ M for 48 h), a potent antioxidant used for ROS studies in zebrafish embryos^{24,25}, and found that NAC could not rescue *pnt* anaemia (Fig. 4h). This demonstrates that the anaemic phenotype in *pnt* is not due to increased ROS generation. The haem oxygenase 1 enzyme (Hmox1) is a ROS-responsive, cellular enzyme responsible for haem degradation²⁶. We found normal transcript levels of *Hmox1* in control and *Atpif1*-silenced MEL cells (Supplementary Fig. 7c). Consistent with our model, it has been demonstrated that only overexpression of *Atpif1* gene, not loss of Atpif1 activity, induces ROS production, independent of the Hif1 α pathway²⁷, and that the overexpression of *Atpif1* did not affect cellular hydrogen peroxide levels, indicating that the Atpif1-mediated superoxide signal is of mild intensity and localized in mitochondria²⁷. Together, these data suggest that ROS and haem degradation are not responsible for the haem defect we observed in *Atpif1*-deficient erythroid cells.

Atpif1 modulates the mitochondrial pH and redox potential and thus allows Fech to efficiently catalyse the incorporation of iron into PPIX to produce haem. Loss of *Atpif1* allows the mitochondrial pH—and consequently the redox potential—to change to a level that reduces [2Fe–2S] cluster-containing Fech activity, thereby reducing haem synthesis, resulting in hypochromic anaemia in *pnt* (Fig. 4i). Previous human studies have identified *ALAS2*, *FXN*, *ABCB7* and *SLC25A38* as the genetic causes of congenital sideroblastic anaemias^{28,29}. Data presented herein demonstrate that *Atpif1* should now be added to the list of proteins whose native function is required for normal erythropoiesis. This makes *ATP1F1* a candidate gene for the understanding and treatment of human sideroblastic anaemias and mitochondrial disorders.

METHODS SUMMARY

All procedures were approved by the Animal Care and Use Committee of Boston Children's Hospital. We performed complete blood count and Wright-Geimsa analyses on peripheral blood recovered from adult *pnt* mutants. Genetic mapping and positional cloning were used to identify *zgc:162207* (*atpif1a*) as the candidate gene for the *pnt* locus on zebrafish chromosome 19. We used qRT–PCR using TaqMan gene expression assays (Applied Biosystems) to measure levels of *atpif1a* and *atpif1b* mRNA. Morpholinos (Gene Tools) against splice sites of *atpif1a* and *atpif1b* were designed and injected into wild-type embryos to verify a loss-of-function phenotype. The cRNA for *atpif1a*, *atpif1a* (E26A), and *atpif1b* were injected into *pnt* embryos for complementation tests. The cDNA prepared from wild-type and *pnt* embryos was sequenced and the mutation in the 3' UTR of the *atpif1a* sequence was verified using SSCP gels.

We silenced *Atpif1* in hCD34⁺, MPFL and MEL cells using shRNAs. The *Atpif1*-silenced, differentiated hCD34⁺ and MEL cells were stained with *o*-dianisidine to measure haemoglobinized cells, whereas MPFL cells were treated with Drabkin's reagent to measure relative haemoglobin content. The loss of *Atpif1* protein and the state of mitochondrial structural proteins in MEL cells were verified using western blotting and electron microscopic analyses. We analysed the fluorescent intensities of tetramethylrhodamine ethyl ester (TMRE) as a function of mitochondrial membrane potential, magnesium green as a function of ATP levels, and the ratio of carboxy SNARF-1 to Mitotracker green as a function of the mitochondrial matrix pH^{8,12}.

We prepared ⁵⁹Fe-saturated transferrin and measured ⁵⁹Fe incorporated in mitochondria and complexed in haem using a gamma counter. We examined PPIX levels and the catalytic efficiency of Fech in MEL cells using spectrophotometric analysis. The MEL cells were treated with FCCP and 2,4-DNP, followed by analysis for haemoglobinized cells. Human and yeast Fech were treated with DTN and their catalytic efficiency was subsequently measured. Aconitase activity was determined as a measure of [2Fe–2S] cluster levels³⁰. The cRNA for zebrafish *Fech* or yeast *Fech* was injected into *pnt* embryos, and their efficiency in rescuing the anaemia in *pnt* was measured using *o*-dianisidine staining and verified by using SSCP analysis¹⁰. Statistical analyses were performed by paired or un-paired Student's *t*-tests. Significance was set at *P* < 0.05.

Received 20 October 2011; accepted 23 August 2012.

Published online 7 November 2012.

- Schultz, I. J., Chen, C., Paw, B. H. & Hamza, I. Iron and porphyrin trafficking in heme biogenesis. *J. Biol. Chem.* **285**, 26753–26759 (2010).
- Iolascon, A., De Falco, L. & Beaumont, C. Molecular basis of inherited microcytic anemia due to defects in iron acquisition or heme synthesis. *Haematologica* **94**, 395–408 (2009).
- Severance, S. & Hamza, I. Trafficking of heme and porphyrins in metazoa. *Chem. Rev.* **109**, 4596–4616 (2009).
- Anderson, K. E., Sassa, S., Bishop, D. F. & Desnick, R. J. in *The Online Metabolic & Molecular Basis of Inherited Disease* (ed. Bishop, D. F.) 1–153 (The McGraw-Hill Press, 2011).
- Shin, J. T. & Fishman, M. C. From zebrafish to human: modular medical models. *Annu. Rev. Genomics Hum. Genet.* **3**, 311–340 (2002).
- Ransom, D. G. et al. Characterization of zebrafish mutants with defects in embryonic hematopoiesis. *Development* **123**, 311–319 (1996).
- Postlethwait, J. H. et al. Vertebrate genome evolution and the zebrafish gene map. *Nature Genet.* **18**, 345–349 (1998).
- Campanella, M., Parker, N., Tan, C. H., Hall, A. M. & Duchon, M. R. IF₁: setting the pace of the F₁F₀-ATP synthase. *Trends Biochem. Sci.* **34**, 343–350 (2009).
- Ando, C. & Ichikawa, N. Glutamic acid in the inhibitory site of mitochondrial ATPase inhibitor, IF₁, participates in pH sensing in both mammals and yeast. *J. Biochem.* **144**, 547–553 (2008).
- Shaw, G. C. et al. Mitoferrin is essential for erythroid iron assimilation. *Nature* **440**, 96–100 (2006).

- Houseley, J. & Tollervey, D. The many pathways of RNA degradation. *Cell* **136**, 763–776 (2009).
- Campanella, M. et al. Regulation of mitochondrial structure and function by the F₁F₀-ATPase inhibitor protein, IF₁. *Cell Metab.* **8**, 13–25 (2008).
- Richardson, D. R. et al. Mitochondrial iron trafficking and the integration of iron metabolism between the mitochondrion and cytosol. *Proc. Natl Acad. Sci. USA* **107**, 10775–10782 (2010).
- Nilsson, R. et al. Discovery of genes essential for heme biosynthesis through large-scale gene expression analysis. *Cell Metab.* **10**, 119–130 (2009).
- Walker, J. E. The regulation of catalysis in ATP synthase. *Curr. Opin. Struct. Biol.* **4**, 912–918 (1994).
- Lanzilotta, W. N. & Dailey, H. A. Human ferrochelatase. In *Handbook of Metalloproteins* (ed. Messerschmidt, A.) Vol. 4/5: 138–146 (John Wiley & Sons, 2011).
- Lange, H., Kispal, G. & Lill, R. Mechanism of iron transport to the site of heme synthesis inside yeast mitochondria. *J. Biol. Chem.* **274**, 18989–18996 (1999).
- Froschauer, E. M., Schweyen, R. J. & Wiesenberger, G. The yeast mitochondrial carrier proteins Mrs3p/Mrs4p mediate iron transport across the inner mitochondrial membrane. *Biochim. Biophys. Acta* **1788**, 1044–1050 (2009).
- Park, D. et al. Continued clearance of apoptotic cells critically depends on the phagocyte Ucp2 protein. *Nature* **477**, 220–224 (2011).
- Crooks, D. R., Ghosh, M. C., Haller, R. G., Tong, W. H. & Rouault, T. A. Posttranslational stability of the heme biosynthetic enzyme ferrochelatase is dependent on iron availability and intact iron-sulfur cluster assembly machinery. *Blood* **115**, 860–869 (2010).
- Medlock, A. E. & Dailey, H. A. Examination of the activity of carboxyl-terminal chimeric constructs of human and yeast ferrochelatases. *Biochemistry* **39**, 7461–7467 (2000).
- Childs, S. et al. Zebrafish *dracula* encodes ferrochelatase and its mutation provides a model for erythropoietic protoporphyria. *Curr. Biol.* **10**, 1001–1004 (2000).
- Hu, J., Dong, L. & Outten, C. E. The redox environment in the mitochondrial intermembrane space is maintained separately from the cytosol and matrix. *J. Biol. Chem.* **283**, 29126–29134 (2008).
- Yu, D. et al. miR-451 protects against erythroid oxidant stress by repressing 14-3-3 ζ. *Genes Dev.* **24**, 1620–1633 (2010).
- North, T. E. et al. PGE₂-regulated wnt signaling and *N*-acetylcysteine are synergistically hepatoprotective in zebrafish acetaminophen injury. *Proc. Natl Acad. Sci. USA* **107**, 17315–17320 (2010).
- Cao, Y. A. et al. Heme oxygenase-1 deletion affects stress erythropoiesis. *PLOS One* **6**, e20634 (2011).
- Formentini, L., Sanchez-Arago, M., Sanchez-Cenizo, L. & Cuezva, J. M. The mitochondrial ATPase inhibitory factor 1 triggers a ROS-mediated retrograde pro-survival and proliferative response. *Mol. Cell* **45**, 731–742 (2012).
- Sheftel, A. D., Richardson, D. R., Prchal, J. & Ponka, P. Mitochondrial iron metabolism and sideroblastic anemia. *Acta Haematol.* **122**, 120–133 (2009).
- Carnaschella, C. Hereditary sideroblastic anaemias: pathophysiology, diagnosis, and treatment. *Semin. Hematol.* **46**, 371–377 (2009).
- Li, L. & Kaplan, J. A mitochondrial-vacuolar signaling pathway in yeast that affects iron and copper metabolism. *J. Biol. Chem.* **279**, 33653–33661 (2004).

Supplementary Information is available in the online version of the paper.

Acknowledgements We thank members of our laboratory (M. Cassim, A. Kaplan, G. Hildick-Smith and H. Anderson) and colleagues (S. L. Alper, K. Pepper and N. S. Trede) for critical review of the manuscript, T. C. Law for *pnt* adult blood characterization, H. Mulhern for help with the electron microscopy, and Christopher Lawrence and his team for the zebrafish husbandry. This research was supported in part by the Cooley's Anemia Foundation (D.I.S. and C.C.), the March of Dimes Foundation (B.H.P.), the American Heart Association (J.D.C. and A.E.M.), the Dutch National Science Fund (I.J.S.), the *Fondation Soldati pour la Recherche en Cancerologie* (G.V.), the Burroughs Wellcome Fund (N.N.D.), the NIDDK (D.I.S., B.H.P., A.N., J.K., H.A.D. and S.M.H.) and the NHLBI (D.I.S. and B.H.P.).

Author Contributions D.I.S. and B.H.P. originally conceived the project, designed and performed the experiments, analysed data and wrote the manuscript. N.T.-M., A.S., L.L., D.M.W. and J.K. measured ⁵⁹Fe uptake in mitochondria and complexed in haem, PPIX levels, Fech activity, xanthine oxidase and aconitase activities and the haem levels in a yeast knockout for *Inh1* and participated in scientific discussions. J.D.C., I.J.S., E.L.P. and N.B.L. did zebrafish embryo microinjections. S.K.H., G.V., C.C. and W.C. helped with zebrafish colony maintenance and protein experiments. Y.Z. helped with high resolution meiotic mapping. A.N., S.N.H. and B.L.E. helped with silencing *ATP1F1* in human primary CD34⁺ cells. S.M.H. helped with silencing *Atpif1* in MFPL cells. A.E.M., T.A.D. and H.A.D. created Fech constructs for injection, measured Fech activity as a function of pH, analysed Fech structure for [2Fe–2S] clusters and participated in scientific discussions. D.F., J.M.W., M.C. and N.N.D. helped to design and measure mitochondrial physiological parameters. C.B. analysed *pnt* adult blood parameters. D.R.C. and M.D.F. helped with electron microscopic analysis of mitochondrial structure and disease.

Author Information Sequences are available in GenBank/EMBL/DBJ as follows: zebrafish *atpif1a* (NM_001089521.1), zebrafish *atpif1b* (NM_001044859), mouse *Atpif1* (NC_000070.5) and human *ATP1F1* (NC_005104.2). Reprints and permissions information is available at www.nature.com/reprints. The authors declare no competing financial interests. Readers are welcome to comment on the online version of the paper. Correspondence and requests for materials should be addressed to B.H.P. (bpaw@rics.bwh.harvard.edu) or H.A.D. (hdailey@uga.edu) or J.K. (jerry.kaplan@path.utah.edu).

Accelerated disassembly of IgE–receptor complexes by a disruptive macromolecular inhibitor

Beomkyu Kim^{1*}, Alexander Eggel^{2*}, Svetlana S. Tarchevskaya¹, Monique Vogel², Heino Prinz³ & Theodore S. Jardetzky¹

IgE antibodies bind the high-affinity IgE Fc receptor (FcεRI), found primarily on mast cells and basophils, and trigger inflammatory cascades of the allergic response^{1,2}. Inhibitors of IgE–FcεRI binding have been identified and an anti-IgE therapeutic antibody (omalizumab) is used to treat severe allergic asthma^{3,4}. However, preformed IgE–FcεRI complexes that prime cells before allergen exposure dissociate extremely slowly⁵ and cannot be disrupted by strictly competitive inhibitors. IgE–Fc conformational flexibility indicated that inhibition could be mediated by allosteric or other non-classical mechanisms^{6–8}. Here we demonstrate that an engineered protein inhibitor, DARPin E2_79 (refs 9–11), acts through a non-classical inhibition mechanism, not only blocking IgE–FcεRI interactions, but actively stimulating the dissociation of preformed ligand–receptor complexes. The structure of the E2_79–IgE–Fc₃₋₄ complex predicts the presence of two non-equivalent E2_79 sites in the asymmetric IgE–FcεRI complex, with site 1 distant from the receptor and site 2 exhibiting partial steric overlap. Although the structure is indicative of an allosteric inhibition mechanism, mutational studies and quantitative kinetic modelling indicate that E2_79 acts through a facilitated dissociation mechanism at site 2 alone. These results demonstrate that high-affinity IgE–FcεRI complexes can be actively dissociated to block the allergic response and suggest that protein–protein complexes may be more generally amenable to active disruption by macromolecular inhibitors.

The IgE antibody Fc, comprising three domains (Cε2–Cε3–Cε4), binds the α-chain of FcεRI (FcεRIα) with subnanomolar affinity (<1 nM)^{1,2}. The IgE–Fc Cε3 domains contact receptor directly and can adopt multiple conformational states, ranging from closed to open forms^{6–8,12}, which could have an impact on FcεRI binding and potential receptor complex dynamics. In an effort to characterize different IgE ligands and mechanisms of FcεRI inhibition, we developed a fluorescence binding assay that distinguishes IgE ligands using a site-specific reporter fluorophore. A double mutant (C328A/K367C) of the IgE–Fc Cε3–Cε4 protein (IgE–Fc₃₋₄) was labelled with Alexa Fluor 488 at residue 367 (referred to as AF488–Fc), which is adjacent to the FcεRIα binding site (Supplementary Fig. 1). AF488–Fc exhibited systematic fluorescence quenching with increasing concentrations of FcεRIα (Fig. 1a), yielding a dissociation constant (K_d) of ~22 nM (Supplementary Table 1), consistent with the lower affinity of the C328A mutation¹³. FcεRIα-directed inhibitors, such as unlabelled IgE–Fc₃₋₄ and anti-FcεRIα antibody (monoclonal antibody 15.1)^{14,15}, reversed receptor-induced fluorescence quenching (Fig. 1b, c and Supplementary Table 1),

IgE-directed inhibitors, including the anti-IgE antibody omalizumab (Xolair)^{3,4}, a 34-nucleotide DNA aptamer (D17.4)^{16,17}, and DARPin E2_79 (refs 9–11), yielded three inhibition profiles. Omalizumab induced fluorescence quenching comparable to FcεRIα (Fig. 1d and Supplementary Table 1), consistent with its binding an epitope overlapping the FcεRIα site^{18,19}. E2_79 restored the receptor-quenched

fluorescence signal (Fig. 1e and Supplementary Table 1), similar to FcεRIα binding inhibitors (Fig. 1b, c). D17.4 did not quench or compete with FcεRIα, but in an indirect competitive binding experiment with AF488–Fc, FcεRIα and unlabelled wild-type IgE–Fc₃₋₄, D17.4 induced systematic fluorescence quenching (Fig. 1f and Supplementary Table 1),

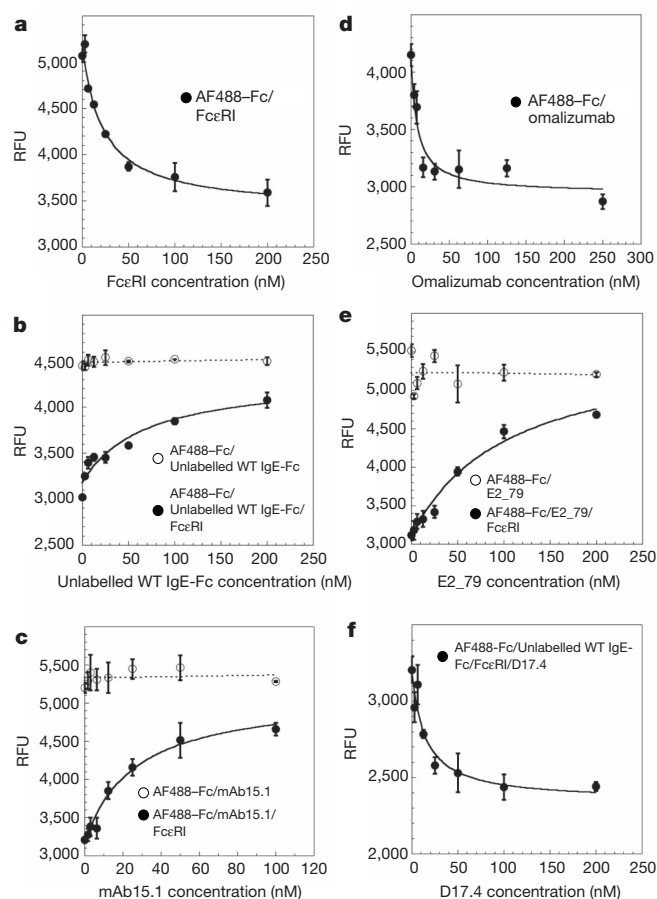


Figure 1 | A fluorescence-quenching assay reveals different classes of IgE-directed inhibitors. **a**, AF488–Fc fluorescence is quenched by FcεRIα. RFU, relative fluorescence units. **b**, Unlabelled IgE–Fc₃₋₄ competes for FcεRIα binding (filled circles, solid line) but has no effect on AF488–Fc alone (open circles, dotted line). **c**, The anti-FcεRIα antibody mAb15.1 competes for FcεRIα binding (filled circles, solid line) but has no effect on AF488–Fc fluorescence (open circles, dotted line). **d**, Omalizumab quenches AF488–Fc fluorescence similar to FcεRIα. **e**, E2_79 competes for FcεRIα binding (filled circles, solid line) but does not affect AF488–Fc fluorescence (open circles, dotted line). **f**, D17.4 competes in assays containing AF488–Fc, FcεRIα and wild-type IgE–Fc₃₋₄, by binding IgE–Fc₃₋₄ competitor (filled circles, solid line). Error bars represent standard deviations of replicate measurements.

¹Department of Structural Biology, Stanford University School of Medicine, Stanford, California 94305, USA. ²Institute of Immunology, University of Bern, CH-3010 Bern, Switzerland. ³Max-Planck-Institut für Molekulare Physiologie, Otto-Hahn-Str. 11, 44227 Dortmund, Germany.

*These authors contributed equally to this work.

consistent with D17.4 binding to wild-type IgE-Fc₃₋₄ but not AF488-Fc. These data indicated that D17.4 and omalizumab act as direct competitive inhibitors, but E2_79 was a candidate allosteric inhibitor.

We determined the 4.3 Å crystal structure of E2_79 bound to IgE-Fc₃₋₄ (Supplementary Table 2) using a cysteine mutant (C335) that locks the Fc into a closed conformational state²⁰. E2_79 binds the IgE Cε3 domain and does not directly engage residues involved in FcεRIα binding (Fig. 2a, b). E2_79 interactions extend throughout the Cε3 domain, including the Cε3-Cε4 domain linker and encroaching on FcεRIα-binding loops (Fig. 2a, c).

To examine the structural basis for E2_79 inhibition, we superimposed the E2_79 structure onto the IgE-Fc-FcεRIα complex using the IgE Cε3 domains. The IgE-Fc-FcεRIα complex is asymmetric, defining two distinct E2_79 sites (Fig. 2b). In the complex, site 1 is entirely exposed, with E2_79 and FcεRIα separated by ~20 Å and no steric overlap (Fig. 2b), indicating the potential for simultaneous E2_79 and FcεRIα binding. For site 2, three E2_79 and five FcεRIα residues make contacts <3.5 Å (Supplementary Table 3), causing partial steric overlap.

We generated three E2_79 double mutants (E20A/R23A, Y45A/W46A and E126A/D127A) to probe the inhibition mechanism (Fig. 2c). E20 and R23 are located adjacent to the Cε3-Cε4 domain linker and could affect the Cε3 domain conformational state, allosterically inhibiting FcεRIα. Y45 and W46 are in the hydrophobic interface with the IgE Fc, and are probably important for binding affinity. E126 and D127 account for most of the predicted steric conflicts with FcεRI

at site 2 (Supplementary Table 3) and could potentially interact with the FcεRI FG binding loop containing R427, contributing to the inhibition. The E20A/R23A and E126A/D127A mutants exhibited similar binding affinity to IgE Fc compared to wild-type E2_79 (Fig. 3a, b), whereas the Y45A/W46A mutant showed significantly reduced binding affinity (Fig. 3c). The inhibition activities of the E20A/R23A and E126A/D127A mutants remained similar compared to that of wild-type E2_79 (Fig. 3d, e), indicative of a non-allosteric model. The Y45A/W46A mutant exhibited no inhibition (Fig. 3f), as expected from its lack of binding (Fig. 3c). The mutants validated the crystal structure, and indicated that E2_79 inhibition is not due to Cε3-Cε4 linker or FcεRI binding loop interactions.

To investigate binding of E2_79 to the IgE-FcεRIα complex, we conducted Biacore experiments that revealed a marked acceleration of complex disassembly. FcεRIα was coupled to the chip, then loaded with either full-length IgE (Sus11) or IgE-Fc₃₋₄ proteins (Supplementary Fig. 2). The monoclonal anti-IgE antibody Le27 recognizes a non-inhibitory epitope in the IgE Cε4 domain, and binding to the preformed IgE-FcεRIα complexes was readily observed (Supplementary Fig. 2a, e). In contrast, E2_79, but not controls, stimulated rapid dissociation of both Sus11 and IgE-Fc₃₋₄ complexes (Supplementary Fig. 2b-d, f-h).

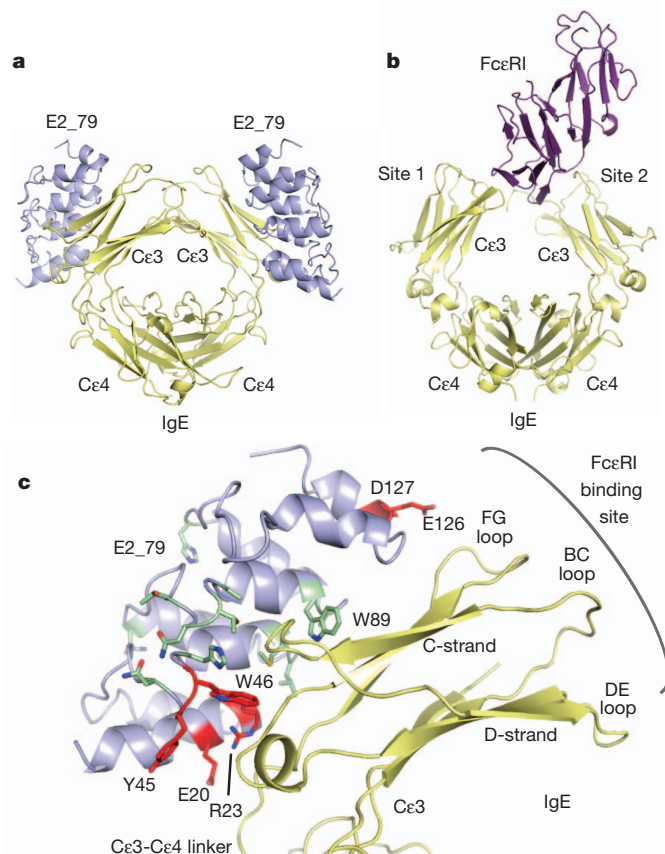


Figure 2 | DARPin E2_79 binds IgE-Cε3 domains outside the FcεRIα binding site. **a**, Crystal structure of the E2_79 (light blue) and C335 IgE-Fc₃₋₄ (pale yellow) complex. **b**, Structure of the IgE-Fc₃₋₄-FcεRIα complex oriented similarly to **a**. FcεRIα (purple) binds asymmetrically, and two non-equivalent E2_79 binding sites (1 and 2) are indicated. **c**, Residues in E2_79 at the interface with the IgE-Fc₃₋₄ are shown as beige sticks. Mutated residues (E20, R23, Y45, W46, E126 and D127) are shown as red sticks. The FcεRIα binding loops (BC, DE and FG) in the Cε3 domain are indicated.

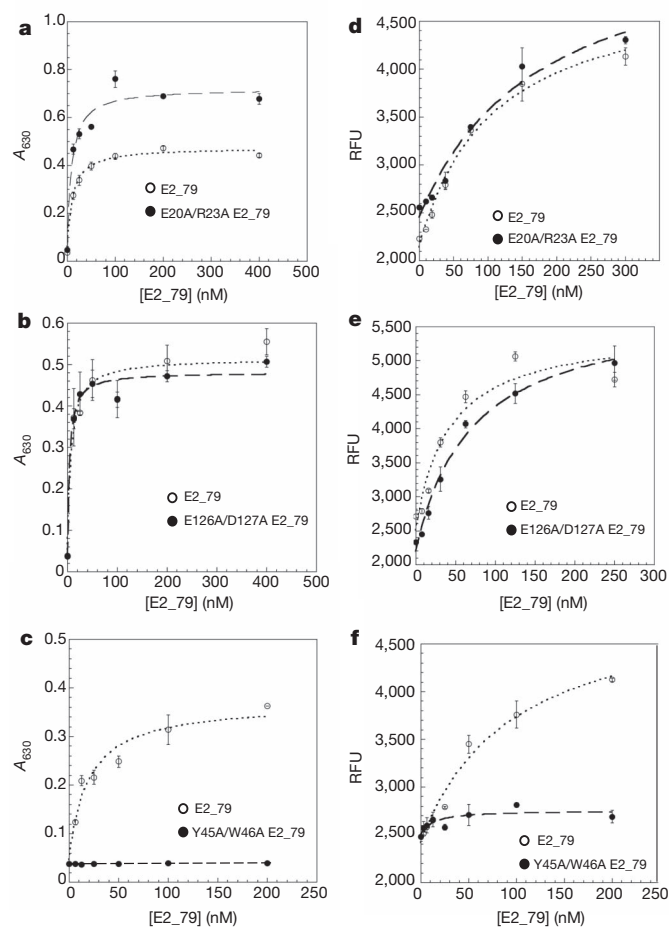


Figure 3 | Binding and inhibition activities of E2_79 mutants. **a**, The E20A/R23A mutant exhibits a binding affinity similar to wild-type E2_79. **b**, The E126A/D127A mutant binds similarly to wild-type E2_79. **c**, The Y45A/W46A mutant exhibits a loss of binding to IgE-Fc₃₋₄. **d**, The E20A/R23A mutant inhibits FcεRIα binding similar to wild-type E2_79. **e**, The E126A/D127A mutant inhibits FcεRIα binding similar to wild-type E2_79. **f**, The Y45A/W46A mutant does not inhibit FcεRIα binding. Direct binding (**a-c**) was measured by ELISA. Inhibition was measured using the fluorescence quenching assay (**d-f**). Error bars represent standard deviations of replicate measurements.

E2_79 and FcεRIα binding to IgE are linked by a six state coupled binding reaction scheme (Fig. 4a, b), in which two E2_79 molecules and one FcεRIα protein can potentially assemble into a quaternary complex with IgE. We considered three potential mechanisms to explain the accelerated complex dissociation: (1) a classic competitive inhibition mechanism operating solely through steric conflicts at site 2; (2) an allosteric mechanism operating through both site 1 and site 2; (3) a facilitated dissociation mechanism in which E2_79 binding to IgE–FcεRIα complexes only at site 2 stimulates complex dissociation. Model 3 represents a competitor-induced dissociation mechanism²¹ in which a subset of ligand attachment points that become exposed during partial complex dissociation can be engaged by an exogenously added competitor, thereby accelerating the intrinsic dissociation rate. This has been named ‘facilitated dissociation’²². To discriminate quantitatively between the three inhibition mechanisms, we developed the complete reaction schemes as COPASI biochemical network models²³, allowing the simulation of the time-dependent evolution of the reaction

pathways and intermediates, as well as global curve fitting and parameter estimation with the surface plasmon resonance (SPR) data.

The classic competitive inhibition mechanism is not consistent with the SPR data, but predicts high-affinity binding of E2_79 to site 1 and no acceleration of IgE release from the chip surface (Supplementary Fig. 3a, b). Simulations for this model are similar to the experimental observations with the Le27 antibody (Supplementary Fig. 2a, e). In this model, E2_79 competition is only mediated by site 2, where steric hindrance prevents E2_79 binding to IgE–FcεRIα complexes. Relaxation to a new equilibrium occurs with the unaccelerated, slow dissociation rate of the complex.

For the allosteric model, we posited that both site 1 and site 2 would contribute to FcεRIα inhibition and the acceleration of complex dissociation. In this model, E2_79 binding to sites 1 and 2 in the IgE–FcεRIα complex should both exhibit reduced affinity associated with the allosteric coupling. Similarly, both site 1 and site 2 binding by E2_79 would induce reduced affinity and increased dissociation rates

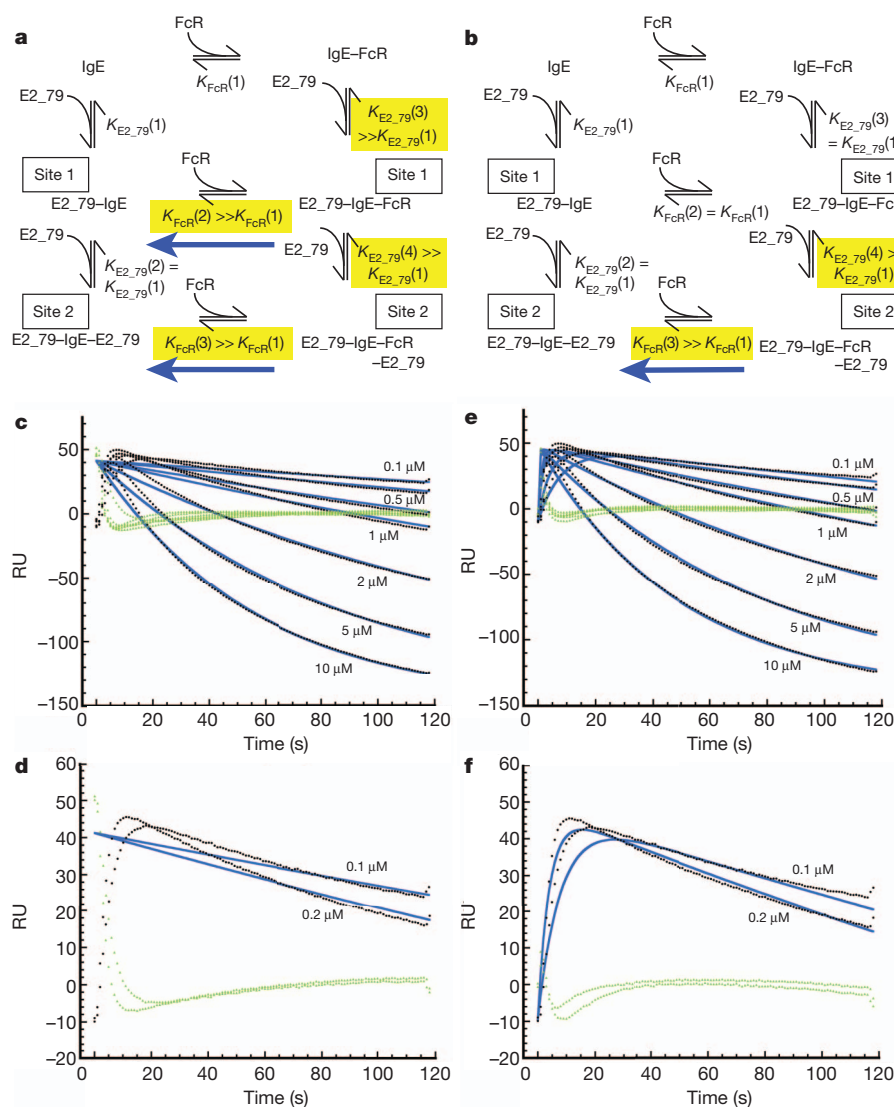


Figure 4 | Kinetic modelling of SPR data points to a facilitated dissociation mechanism for E2_79. **a**, Reaction scheme for the allosteric model. Blue arrows indicate that IgE–FcεRIα complex dissociation is accelerated by E2_79 binding to site 1 and site 2. **b**, Reaction scheme for the facilitated dissociation model. The blue arrow indicates that IgE–FcεRIα complex dissociation is only accelerated by E2_79 binding to site 2. **c**, **d**, Best global curve fitting result for the allosteric model, shown with seven concentrations of E2_79 (**c**), or the 100 nM

and 200 nM E2_79 concentration curves (**d**). **e**, **f**, Best global curve fitting result for the facilitated dissociation model, shown with seven concentrations of E2_79 (**e**), or the 100 nM and 200 nM E2_79 concentration curves (**f**). Rate and equilibrium dissociation constants highlighted in yellow were fit as described in Methods. In panels **c**–**f**, black circles represent SPR data, fitted curves are coloured blue, and green triangles represent residual differences.

for FcεRIα (Fig. 4a). Owing to this allosteric coupling, IgE–FcεRIα complexes should not have any high-affinity binding sites for E2₇₉.

For the facilitated dissociation model, we posited that E2₇₉ binding to site 1 is not affected by FcεRIα binding, consistent with the predicted >20 Å distance between these proteins (Figs 2b and 4b). There is also correspondingly no change in FcεRIα binding affinity associated with E2₇₉ binding to site 1. The rate constants for both of these binding steps were initially set to the experimentally determined rate constants for E2₇₉ and FcεRIα binding in the absence of the other ligand. In this model, only the binding affinity of E2₇₉ at site 2 is reduced by FcεRIα, through this non-classical competition mechanism. Similarly, there must be a corresponding reduction in FcεRIα binding affinity in the quaternary E2₇₉–IgE–FcεRIα–E2₇₉ complex. Importantly, in this model, site 1 retains native high affinity for E2₇₉ in the IgE–FcεRIα complex, whereas only site 2 exhibits reduced E2₇₉ affinity and the ability to accelerate FcεRIα dissociation. This distinguishes it from the allosteric model, which lacks any high-affinity E2₇₉ sites in the complex.

The initial 120 s of SPR data for IgE–Fc₃₋₄ (Supplementary Fig. 2h), covering E2₇₉ concentrations from 100 nM to 10 μM, were simultaneously fit using the allosteric and facilitated dissociation COPASI models. Curve fitting (Fig. 4c–f) demonstrates that only the facilitated dissociation mechanism captures the biphasic behaviour of the SPR traces accurately. The SPR data exhibit a ~50 resonance units (RU), E2₇₉-concentration-dependent association phase within the first 10–20 s that cannot be modelled by the full allosteric mechanism (Fig. 4c, d). Whereas both models fit the later concentration-dependent dissociation rates for the IgE–FcεRIα complexes, the initial 10–20 s demonstrate an association that corresponds to the presence of the high-affinity binding of E2₇₉ to the exposed site 1 within the IgE–FcεRIα complex. Given the robustness of the fitting, we allowed site 1 kinetic constants in the facilitated dissociation model to vary from experimental values for both E2₇₉ and FcεRIα (Supplementary Table 4). This provided slightly improved curve fitting, and the fitted E2₇₉ site 1 kinetic constants remained close to those determined for the independently binding ligand, further validating this model over an allosteric one.

Non-classical or allosteric inhibitors have the general potential to not only block receptor–ligand binding, but to also engage and actively dissociate preformed receptor complexes. For the IgE–FcεRIα interaction, the activated release of receptor-bound antibody on the surface of effector cells might prove beneficial in treating acute allergic reactions. Here we demonstrated that the E2₇₉ DARPIn is a disruptive inhibitor that binds to IgE–FcεRIα complexes, markedly accelerating their dissociation orders of magnitude over the unaccelerated intrinsic rate.

It has been proposed that facilitated dissociation occurs through competition for subsite attachment points within a ligand-binding site, which become partially exposed before full ligand dissociation^{21,22}. In principle, competitor-induced acceleration of ligand dissociation can be explained by multiple mechanisms, such as allosteric or facilitated dissociation mechanisms considered here, but few observations have been fully examined by both structural and kinetic methods. Small-molecule inhibitors of TNF have been shown to accelerate the dissociation of TNF trimers^{24,25}, potentially intercalating into the trimeric interface. It has been suggested, and it is probably commonly assumed, that larger macromolecular inhibitors depend on complete dissociation of protein complexes and would be unlikely to engage partially dissociated intermediates, potentially providing a ‘kinetic advantage’ to small-molecule protein interaction inhibitors²⁵. However, the E2₇₉-induced dissociation of IgE–FcεRIα complexes indicates that macromolecular therapeutics may have untapped potential as disruptive inhibitors. Antibody-induced complex dissociation has been observed, but specific mechanisms and requirements for such accelerated dissociation have not been fully investigated^{26–28}. Facilitated dissociation may also have an unappreciated role in naturally evolved macromolecular complex disassembly processes.

METHODS SUMMARY

IgE and FcεRIα were produced in insect cells, whereas E2₇₉ was produced in *Escherichia coli* as described¹⁰. Other proteins or DNA ligands (omalizumab, Mab15-1, D17.4, Sus11) were purchased or obtained as described in Methods. IgE–Fc₃₋₄ and E2₇₉ mutants were generated by site-directed mutagenesis and confirmed by DNA sequencing. Fluorescence binding experiments and ELISA assays were performed using a Synergy 4 multi-mode plate reader (BioTek), with labelled AF488–Fc produced as described in Methods. Diffraction data for the IgE–Fc₃₋₄–C335–E2₇₉ complex was collected at the Advanced Light Source beamline 8.3.1 and the structure solved by molecular replacement. SPR assays were conducted with a BIAcore X100 machine and evaluated with BIAevaluation and COPASI²³ software.

Full Methods and any associated references are available in the online version of the paper.

Received 14 December 2011; accepted 3 September 2012.

Published online 28 October 2012.

- Kraft, S. & Kinet, J. P. New developments in FcεRI regulation, function and inhibition. *Nature Rev. Immunol.* **7**, 365–378 (2007).
- Gould, H. J. & Sutton, B. J. IgE in allergy and asthma today. *Nature Rev. Immunol.* **8**, 205–217 (2008).
- D’Amato, G., Buccichioni, E., Oldani, V. & Canonica, W. Treating moderate-to-severe allergic asthma with a recombinant humanized anti-IgE monoclonal antibody (Omalizumab). *Treat. Respir. Med.* **5**, 393–398 (2006).
- Chang, T. W. The pharmacological basis of anti-IgE therapy. *Nature Biotechnol.* **18**, 157–162 (2000).
- Holdom, M. D. *et al.* Conformational changes in IgE contribute to its uniquely slow dissociation rate from receptor FcεRI. *Nature Struct. Mol. Biol.* **18**, 571–576 (2011).
- Dhaliwal, B. *et al.* Crystal structure of IgE bound to its B-cell receptor CD23 reveals a mechanism of reciprocal allosteric inhibition with high affinity receptor FcεRI. *Proc. Natl Acad. Sci. USA* **109**, 12686–12691 (2012).
- Wurzberg, B. A. & Jardetzky, T. S. Conformational flexibility in immunoglobulin E–Fc₃₋₄ revealed in multiple crystal forms. *J. Mol. Biol.* **393**, 176–190 (2009).
- Wurzberg, B. A., Garman, S. C. & Jardetzky, T. S. Structure of the human IgE–Fc Cε3–Cε4 reveals conformational flexibility in the antibody effector domains. *Immunity* **13**, 375–385 (2000).
- Eggel, A., Baumann, M. J., Amstutz, P., Stadler, B. M. & Vogel, M. DARPins as bispecific receptor antagonists analyzed for immunoglobulin E receptor blockage. *J. Mol. Biol.* **393**, 598–607 (2009).
- Baumann, M. J., Eggel, A., Amstutz, P., Stadler, B. M. & Vogel, M. DARPins against a functional IgE epitope. *Immunol. Lett.* **133**, 78–84 (2010).
- Eggel, A. *et al.* Inhibition of ongoing allergic reactions using a novel anti-IgE DARPIn–Fc fusion protein. *Allergy* **66**, 961–968 (2011).
- Garman, S. C., Wurzberg, B. A., Tarchevskaya, S. S., Kinet, J. P. & Jardetzky, T. S. Structure of the Fc fragment of human IgE bound to its high-affinity receptor FcεRIα. *Nature* **406**, 259–266 (2000).
- Basu, M. *et al.* Purification and characterization of human recombinant IgE–Fc fragments that bind to the human high affinity IgE receptor. *J. Biol. Chem.* **268**, 13118–13127 (1993).
- Wang, B. *et al.* Epidermal Langerhans cells from normal human skin bind monomeric IgE via FcεRI. *J. Exp. Med.* **175**, 1353–1365 (1992).
- Mirkin, I., Schweighoffer, T. & Kricek, F. Inhibition of human cord blood-derived mast cell responses by anti-FcεRI Mab 15/1 versus anti-IgE Omalizumab. *Immunol. Lett.* **109**, 120–128 (2007).
- Mendonça, S. D. & Bowser, M. T. *In vitro* selection of high-affinity DNA ligands for human IgE using capillary electrophoresis. *Anal. Chem.* **76**, 5387–5392 (2004).
- Wiegand, T. W. *et al.* High-affinity oligonucleotide ligands to human IgE inhibit binding to Fcε receptor I. *J. Immunol.* **157**, 221–230 (1996).
- Zheng, L. *et al.* Fine epitope mapping of humanized anti-IgE monoclonal antibody omalizumab. *Biochem. Biophys. Res. Commun.* **375**, 619–622 (2008).
- Wright, J. D. & Lim, C. Prediction of an anti-IgE binding site on IgE. *Protein Eng.* **11**, 421–427 (1998).
- Wurzberg, B. A. *et al.* An engineered disulfide bond reversibly traps the IgE–Fc₃₋₄ in a closed, non-receptor binding conformation. *J. Biol. Chem.* <http://dx.doi.org/10.1074/jbc.M112.407502> (2012).
- Prinz, H. & Striessnig, J. Ligand-induced accelerated dissociation of (+)-cis-diltiazem from L-type Ca²⁺ channels is simply explained by competition for individual attachment points. *J. Biol. Chem.* **268**, 18580–18585 (1993).
- Gutfreund, H. *Kinetics for the Life Sciences. Receptors, Transmitters and Catalysts* (Cambridge Univ. Press, 1995).
- Hoops, S. *et al.* COPASI—a COMplex Pathway Simulator. *Bioinformatics* **22**, 3067–3074 (2006).
- He, M. M. *et al.* Small-molecule inhibition of TNF-α. *Science* **310**, 1022–1025 (2005).
- Wells, J. A. & McClendon, C. L. Reaching for high-hanging fruit in drug discovery at protein–protein interfaces. *Nature* **450**, 1001–1009 (2007).
- Wang, C. C. *et al.* Negative and positive site-site interactions, and their modulation by pH, insulin analogs, and monoclonal antibodies, are preserved in the purified insulin receptor. *Proc. Natl Acad. Sci. USA* **85**, 8400–8404 (1988).

27. Lowenthal, J. W. *et al.* High and low affinity IL 2 receptors: analysis by IL 2 dissociation rate and reactivity with monoclonal anti-receptor antibody PC61. *J. Immunol.* **135**, 3988–3994 (1985).
28. Boulain, J. C. & Menez, A. Neurotoxin-specific immunoglobulins accelerate dissociation of the neurotoxin-acetylcholine receptor complex. *Science* **217**, 732–733 (1982).

Supplementary Information is available in the online version of the paper.

Acknowledgements We thank B. Wurzburg and other past and present members of the Jardetzky Laboratory. This research was supported in part by an NIH research grant (AI-18939) and an American Asthma Foundation Senior Investigator Award as well as the Swiss National Science Foundation grant number 310030_127350 to T.S.J. We also thank C. A. Dahinden and B. M. Stadler and members of their groups for valuable discussions. Furthermore, we thank M. J. Baumann for technical support and Molecular

Partners AG, especially P. Amstutz, M. T. Stumpp, P. Forrer and D. Steiner, for placing DARPin libraries at our disposal and providing scientific support.

Author Contributions B.K., A.E., S.S.T. and T.S.J. designed and performed experiments. B.K., A.E., S.S.T., H.P. and T.S.J. analysed data. B.K., S.S.T., A.E., M.V. and T.S.J. contributed reagents. B.K., S.S.T., A.E., M.V., H.P. and T.S.J. discussed/commented on results and edited the manuscript. B.K., A.E. and T.S.J. wrote the manuscript and Supplementary Information, and prepared the figures.

Author Information The structure factors and model for the E2_79–C335 IgE complex have been deposited in the Protein Data Bank under accession code 4GRG. Reprints and permissions information is available at www.nature.com/reprints. The authors declare no competing financial interests. Readers are welcome to comment on the online version of the paper. Correspondence and requests for materials should be addressed to T.S.J. (tjardetz@stanford.edu).

METHODS

Mutagenesis. IgE-Fc₃₋₄ mutants for the fluorescence assay (C328A/G335C, C328A/K367C, T369C and R427C) were generated by site-directed mutagenesis (QuickChange kit, Stratagene) or made commercially (Mutagenix) and confirmed by DNA sequencing. We refer to the resulting double C328A/G335C and C328A/K367C IgE-Fc₃₋₄ mutant proteins as C335 IgE-Fc₃₋₄ and C367 IgE-Fc₃₋₄, respectively. E2_79 mutations (E20A/R23A, Y45A/W46A, W89A and E126A/D127A) were introduced into the original E2_79 gene⁹⁻¹¹. The E2_79 mutants for the binding assays were generated by site-directed mutagenesis (QuickChange kit, Stratagene) and confirmed by DNA sequencing.

Expression and purification of proteins. Expression and purification of the soluble FcεRI α-chain ectodomain was carried out as previously described^{12,29}. Omalizumab (Xolair) was purchased from Novartis. MAb15.1 (anti-FcεRIα) was a gift from the Kinet laboratory. Selection and characterization of the DARPin E2_79 has been reported elsewhere¹⁰. Expression and purification of the E2_79 mutants were carried out as previously described¹⁰. The IgE-Fc₃₋₄ cysteine mutants were expressed in insect cells. The wild-type IgE-Fc₃₋₄, C367 and C335 IgE-Fc₃₋₄ proteins were cloned into pENTRIA (Invitrogen) using a KpnI-XhoI fragment and transferred into the BaculoDirect C-term Linear DNA by using LR Clonase II Enzyme Mix (Invitrogen). Recombinant baculoviruses expressing wild-type and C367 IgE-Fc₃₋₄ proteins were generated using BaculoDirect C-term Transfection Kit (Invitrogen). Recombinant virus was selected and amplified following standard protocols. The wild-type and C367 IgE-Fc₃₋₄ proteins include 3 non-native residues (ADP) generated by the construct at the N terminus and 48 non-native residues including a V5 epitope and a histidine affinity tag (His tag) at the C terminus. For protein production, Hi5 insect cells were grown to a density of 1.3–1.5 million cells ml⁻¹ and infected with the recombinant baculovirus stocks coding for wild-type and mutant IgE-Fc₃₋₄ proteins. Cell supernatants were collected 2.5–3 days after infection and filtered through a Durapore 0.45 µm filter (Millipore). The supernatants were incubated with Ni-NTA agarose (Invitrogen) at room temperature for 3 h, and then loaded into a column. The column was rinsed with 4–5 column volumes of the washing buffer (50 mM Tris (pH 8), 50 mM imidazole, and 300 mM NaCl), and IgE-Fc₃₋₄ was eluted directly with the elution buffer (50 mM Tris (pH 8), 200 mM imidazole, and 300 mM NaCl). The samples were dialysed and concentrated in buffer (50 mM Tris (pH 8) and 50 mM NaCl) using an Amicon ultrafiltration device (Millipore) to a protein concentration of 1 mg ml⁻¹. Proteins were quantified using a Nanodrop spectrophotometer using an extinction coefficient of $\epsilon = 1.32 \text{ cm}^{-1} (\text{mg ml}^{-1})^{-1}$ at 280 nm⁸. To remove the C-terminal tag residues, purified IgE-Fc₃₋₄ was concentrated to 2–3 mg ml⁻¹ and treated with 5–10 U recombinant enterokinase (Invitrogen) per 1 mg protein at room temperature overnight. The enzyme was removed using Ekapture agarose (Novagen).

Dye labelling of AF488-Fc. Purified C367 IgE-Fc₃₋₄ was incubated with three molar equivalents of TCEP (Tris(2-Carboxyethyl)phosphine) at room temperature for 1 h. After TCEP treatment, the presence of free thiol groups in the C367 was confirmed using a thiol and sulphide quantification kit (Molecular Probes). Cysteine-reactive Alexa Fluor 488 (maleimide derivative) was purchased from Invitrogen/Molecular Probes and dissolved in DMSO (dimethyl sulphoxide) at a concentration of 1 mg ml⁻¹. The C367 IgE-Fc₃₋₄ was incubated with 5 molar equivalents of Alexa Fluor 488, at 4 °C overnight. Unreacted dye was removed by gel filtration on a Superdex 200 column (GE Healthcare) equilibrated in buffer (50 mM Tris (pH 8) and 50 mM NaCl).

Fluorescence measurements. Fluorescence experiments were performed using a Synergy 4 multi-mode plate reader (BioTek) in black 96-well Costar fluorescence plates (Corning) in assay buffer (50 mM Tris (pH 8), 50 mM NaCl, 0.1% (v/v) Tween-20, and 100 nM BSA (bovine serum albumin)) at room temperature. Fluorescence was measured using an excitation wavelength of 488 nm and emission was monitored at 520 nm. All samples were incubated at room temperature for at least 10 min before measurement. All measurements were recorded in duplicate. Data obtained were analysed and plotted using KaleidaGraph (Synergy). Binding constants (K_d) of FcεRIα and omalizumab, and half-maximal effective concentrations (EC_{50}) of wild-type IgE-Fc₃₋₄, mAb15.1, D17.4 and E2_79 were obtained by fitting the experimental data to a standard Michaelis–Menten model. The oligonucleotide ligand (D17.4)¹⁷ was synthesized by the PAN Facility (Stanford University School of Medicine).

To monitor fluorescence quenching, each well in a black plate contained 1 µg ml⁻¹ AF488-Fc and increasing concentrations of FcεRIα (0–200 nM) or omalizumab (0–250 nM) in the fluorescence buffer in a total volume of 100 µl. For direct competition assays, each well in a black 96-well plate contained 1 µg ml⁻¹ AF488-Fc, 50 nM FcεRIα, and one of the following competitors: unlabelled wild-type IgE-Fc₃₋₄ (0–200 nM), mAb15.1 (0–100 nM) and E2_79 (0–200 nM). FcεRIα and competitors (except for mAb15.1) were mixed together, and AF488-Fc was added

last. For competition assays with mAb 15.1, AF488-Fc and mAb15.1 were mixed together, and FcεRIα was added last.

For the double competition assay with D17.4, each well in a black 96-well plate contained 1 µg ml⁻¹ AF488-Fc, 50 nM unlabelled wild-type IgE-Fc₃₋₄, 50 nM FcεRIα, and increasing concentrations of D17.4 (0–200 nM) in the fluorescence buffer in a final volume of 100 µl. D17.4 ligand was annealed at 70 °C and cooled before use. The AF488-Fc and unlabelled wild-type IgE-Fc₃₋₄ were mixed together, and then 50 nM FcεRIα and D17.4 were added last together.

Biacore binding assays. SPR assays were conducted with a BIAcore X100 machine and evaluated with BIAevaluation Software, as well as the specific COPASI models described below. Recombinant FcεRIα, corresponding to a previously described N- and C-terminal fusion of FcεRIα with human serum albumin¹⁰, was coupled to the CM5 chip surface. The surface of both flow cells on the CM5 chip were activated with EDC + NHS (both flow cells). Target was injected only in flow cell 2 at 10 µg ml⁻¹ until the target response of 2,500 RU or 700 RU was reached. The surfaces of both flow cells were deactivated with ethanolamine. In all experiments the response (nonspecific binding) in flow cell 1 is subtracted from the signal of flow cell 2. 10 nM IgE was injected for 2 min. The maximal response ($t = 360$ s) is set to 0. The off-rate of IgE (buffer flow) was observed for 3 min. As the interaction of IgE with FcεRIα is very high affinity ($\sim 1 \times 10^{-10}$ M), almost no off-rate is observable in this short time. Thus, the baseline is very stable (almost horizontal), providing an ideal condition to test the binding of a third molecule to the FcεRIα–IgE complex. Different concentrations of anti-IgE molecules were tested. For each measurement new IgE was added to the immobilized FcεRIα as the chip surface was regenerated (stripped) after each run (each concentration of every binder) with 50 mM NaOH. The anti-IgE molecules were injected for 2 min. Dissociation was again observed for 3 min. E2_79 as well as control IgG were tested with FcεRIα alone (without IgE) and no binding was observed.

Protein crystallization. The C335 IgE-Fc₃₋₄–E2_79 complex was concentrated to $\sim 10 \text{ mg ml}^{-1}$ in buffer (50 mM Tris (pH 8) and 50 mM NaCl) using Vivaspins 500 (Sartorius) concentrators, and the final concentration was confirmed using a Nanodrop spectrophotometer (Nanodrop Technologies) with a theoretical absorbance of 0.1% of 1.108 at 280 nm. Initial crystallization conditions were found by sitting-drop vapour diffusion at room temperature using Qiagen JCSG Core Suite screens (Qiagen), and optimized by hanging-drop vapour diffusion methods. The best crystals of C335 IgE-Fc₃₋₄–E2_79 were obtained in 1–3 days by mixing 0.5 µl of protein mixed with 0.5 µl of reservoir solution (0.1 M phosphate-citrate (pH 4.2), 5% (w/v) PEG-3000, 25% (v/v) 1,2-propanediol, 10% (v/v) glycerol; final pH of ~ 5) and incubating over 600 µl of reservoir solution. The crystals were transferred into harvest buffer (0.1 M phosphate-citrate (pH 4.2), 8% (w/v) PEG-3000, 25% (v/v) 1,2-propanediol, 10% (v/v) glycerol), and then flash-cooled in liquid nitrogen.

X-ray data collection, molecular replacement and refinement. Data were collected on beamline 8.3.1 at the Advanced Light Source. All data were indexed, integrated, and scaled using the programs Denzo and Scalepack in the HKL2000 suite³⁰. The C335–E2_79 crystal grew in space group $P3_2$, with unit cell dimensions $a = 71.3 \text{ Å}$, $b = 71.3 \text{ Å}$, $c = 178.5 \text{ Å}$ and $\gamma = 120^\circ$. The structure was solved by molecular replacement with Phaser³¹, using high-resolution crystal structures of the C335 IgE-Fc₃₋₄ (ref. 20) and a homologous DARPin (Protein Data Bank accession 3HG0) as the starting models. Iterative rounds of coordinate and B-factor refinement were done with Refmac, interspersed with manual model building in Coot³². The final model was refined to $\sim 4.3 \text{ Å}$ with statistics collected in Supplementary Table 2. The geometry of the complex model was assessed using MolProbity³³ and PROCHECK³⁴.

ELISA binding assays with E2_79 mutants. 100 µl of purified IgE-Fc₃₋₄ was incubated in microtitre plates overnight at 4 °C at a concentration of 1 µg ml⁻¹ in 0.05 M sodium carbonate buffer. Plates were rinsed and blocked by the same procedures used in the FcεRI binding assay. E2_79 mutants (E20A/R23A, Y45A/W46A and E126A/D127A) containing a His-tag were added at concentrations ranging from 0 nM to 200 nM or 400 nM in duplicate to wells coated with the purified IgE-Fc₃₋₄. The binding of E2_79 containing the His-tag to plate-bound IgE-Fc₃₋₄ was monitored using anti-His tag antibody (Novagen, 70796-3) as a primary antibody and anti-mouse IgG HRP conjugated antibody (R&D system, HAF007) as the secondary antibody. The anti-His tag antibody in a 1:1,000 dilution was incubated after washing for 1 h at room temperature, and then, the anti-mouse IgG HRP conjugated antibody was incubated after washing for 1 h at room temperature. Plates were washed and developed using TMB single solution (Invitrogen, 00-2023). Microplates were read using a Synergy 4 multi-mode plate reader (BioTek) at 650 nm.

COPASI modelling. The COPASI software package for quantitative modelling of biochemical networks³⁵ was used to build the full reaction schemes presented in Fig. 4 and Supplementary Fig. 3. The model consists of eight species and seven reactions within a single compartment. Global quantities were defined, corresponding to on/off

rates for the reaction steps associated with each mechanism, a consolidated 'Biacore output' (RU_{calc}) corresponding to reaction intermediates bound to the chip surface, a fractional mass weighting constant (F_{ME}) to account for E2_79 chip-bound species and overall scaling (k_{ov}) and baseline constants (C_0) for fitting the experimental SPR data. The Biacore output (RU_{calc}) represents a combination of the three receptor-bound species affecting the SPR measurements and was defined mathematically as:

$$RU_{calc} = k_{ov} * ([IgE-Fc\epsilon RI]_t + (1 + F_{ME}) * [E2_79-IgE-Fc\epsilon RI]_t + (1 + 2 * F_{ME}) * [E2_79-IgE-Fc\epsilon RI-E2_79]_t) + C_0$$

where $[IgE-Fc\epsilon RI]_t$, $[E2_79-IgE-Fc\epsilon RI]_t$ and $[E2_79-IgE-Fc\epsilon RI-E2_79]_t$ represent the time-dependent evolution of these reaction species as numerically simulated by COPASI, using the specific model restrictions. Biacore data were extracted using the BiaEvaluation software and imported directly into COPASI for parameter estimation. Each kinetic time course includes 120 data points (seconds), corresponding to a total of 840 data points for the simultaneous fitting of the model parameters. Data fitting was carried out with all available convergence methods, with best results obtained with simulated annealing, particle swarm, Hook & Jeeves, and Levenberg-Marquardt algorithms. The stable convergence of these multiple methods to similar end points was taken as an indicator of the robustness of the fitting and the convergence to a common, global minimum. Experimentally determined rate constants for E2_79 and Fc ϵ RI α were determined in independent Biacore experiments and allowed to vary by 2–3-fold during the data fitting. E2_79 concentrations used experimentally were also allowed to vary

up to 25% and F_{ME} was allowed to vary from 0 to 1. For the allosteric model, kinetic rate constants for site 1 and site 2 E2_79-IgE-Fc ϵ RI α complexes were set to be equivalent. These four parameters were allowed to vary freely, along with k_{ov} and C_0 yielding a total of six freely varying parameters. For the initial fitting of the facilitated dissociation model, kinetic rate constants for site 1 were restricted to experimentally determined values for E2_79 binding in the absence of Fc ϵ RI α , and only the four kinetic constants associated with site 2 E2_79-IgE-Fc ϵ RI α -E2_79 complexes were allowed to vary freely, also yielding a total of six freely varying parameters. For the full fitting of the facilitated dissociation model, kinetic rate constants for both site 1 and site 2 complexes were allowed to vary widely, yielding a total of 10 highly varying parameters.

29. Garman, S. C., Kinet, J. P. & Jardetzky, T. S. Crystal structure of the human high-affinity IgE receptor. *Cell* **95**, 951–961 (1998).
30. Otwinowski, Z. & Minor, W. Processing of X-ray diffraction data collected in oscillation mode. in *Methods Enzymol.* Vol. 276 (eds Carter, J. C. W. & Sweet, R. M.) 307–326 (Academic, 1997).
31. McCoy, A. J. *et al.* Phaser crystallographic software. *J. Appl. Crystallogr.* **40**, 658–674 (2007).
32. Emsley, P. & Cowtan, K. Coot: model-building tools for molecular graphics. *Acta Crystallogr. D* **60**, 2126–2132 (2004).
33. Chen, V. B. *et al.* MolProbity: all-atom structure validation for macromolecular crystallography. *Acta Crystallogr. D* **66**, 12–21 (2010).
34. Laskowski, R. A., Rullmann, J. A., MacArthur, M. W., Kaptein, R. & Thornton, J. M. AQUA and PROCHECK-NMR: programs for checking the quality of protein structures solved by NMR. *J. Biomol. NMR* **8**, 477–486 (1996).

BTB-ZF factors recruit the E3 ligase cullin 3 to regulate lymphoid effector programs

Rebecca Mathew¹, Michael P. Seiler¹, Seth T. Scanlon¹, Ai-ping Mao¹, Michael G. Constantinides¹, Clara Bertozzi-Villa¹, Jeffrey D. Singer² & Albert Bendelac¹

The differentiation of several T- and B-cell effector programs in the immune system is directed by signature transcription factors that induce rapid epigenetic remodelling. Here we report that promyelocytic leukaemia zinc finger (PLZF), the BTB-zinc finger (BTB-ZF) transcription factor directing the innate-like effector program of natural killer T-cell thymocytes^{1,2}, is prominently associated with cullin 3 (CUL3), an E3 ubiquitin ligase previously shown to use BTB domain-containing proteins as adaptors for substrate binding^{3–7}. PLZF transports CUL3 to the nucleus, where the two proteins are associated within a chromatin-modifying complex. Furthermore, PLZF expression results in selective ubiquitination changes of several components of this complex. CUL3 was also found associated with the BTB-ZF transcription factor BCL6, which directs the germinal-centre B cell and follicular T-helper cell programs. Conditional CUL3 deletion in mice demonstrated an essential role for CUL3 in the development of PLZF- and BCL6-dependent lineages. We conclude that distinct lineage-specific BTB-ZF transcription factors recruit CUL3 to alter the ubiquitination pattern of their associated chromatin-modifying complex. We propose that this new function is essential to direct the differentiation of several T- and B-cell effector programs, and may also be involved in the oncogenic role of PLZF and BCL6 in leukaemias and lymphomas^{8,9}.

To investigate the molecular mechanisms that PLZF uses to regulate the innate-like natural killer T (NKT)-cell thymocyte differentiation program during development, we examined its protein-interaction partners. NKT-cell thymocytes were purified from V α 14-J α 18-transgenic mice and, after immunoprecipitation with an anti-PLZF antibody, associated proteins were submitted to mass spectrometry analysis (Table 1, column 1, and Supplementary Fig. 1). A major group was composed of nuclear proteins involved in binding and modifying chromatin, including HDAC1 and DNMT1, which were previously reported to interact with PLZF in myeloid cells^{9,10}, as well as special AT-rich binding

protein 1 (SATB1) and lamin B1 (LMNB1), which anchor specific DNA sequences to nuclear compartments associated with gene activation and repression, respectively^{11–14}. We focused on the E3 ubiquitin ligase CUL3 because previous reports had established that the BTB domain of several proteins, including the BTB-ZF protein BAZF, could serve as ‘adaptors’ for CUL3-mediated ubiquitination by binding both CUL3 and its substrates^{3–7,15}. Reciprocal immunoprecipitation of CUL3-associated proteins pulled down PLZF as a major protein along with an overlapping set of proteins (Table 1, column 2, and Supplementary Fig. 1). Furthermore, confocal microscopic analysis of NKT-cell thymocytes demonstrated colocalization of the two proteins in a speckled nuclear pattern (Fig. 1a, top).

By contrast, in the major lineage of CD4 T cells, CUL3 was mainly found in the cytosol with only a faint presence in nuclear speckles (Fig. 1a, middle). However, after expression of a CD4 promoter-driven PLZF transgene, which induces developmental acquisition of the NKT-cell lineage effector program^{1,16}, CUL3 was mostly in the nucleus, colocalizing with PLZF in nuclear speckles (Fig. 1a, bottom). A similar binding and transport of CUL3 from the cytoplasm to the nucleus was previously demonstrated after cotransfection with the nuclear BTB-domain-containing protein speckle-type POZ protein (SPOP) in HeLa cells¹⁷. Mass spectrometric analysis of anti-PLZF and anti-CUL3 immunoprecipitates from PLZF-transgenic thymocytes identified a similar set of proteins as that from NKT-cell thymocytes (Table 1, columns 3 and 4, and Supplementary Fig. 2), including other known partners of PLZF such as NCOR and SIN3A (ref. 9). Western blot analyses confirmed that a fraction of PLZF coprecipitated with CUL3, and that chromatin-binding and -modifying proteins such as HDAC1, SATB1 and lamin B1 were associated with the PLZF–CUL3 complex (Fig. 1b). The specificity of the interaction between PLZF and CUL3 was further tested using *in vitro* translated proteins, and shown to depend on the CUL3 residues Leu 52 and Glu 55 (Supplementary

Table 1 | PLZF–CUL3 interactions

	NKT		PLZF-transgenic	
	Anti-PLZF IP	Anti-CUL3 IP	Anti-PLZF IP	Anti-CUL3 IP
Ubiquitination	CUL3	CUL3	CUL3, CUL4B, CAND1	CUL3
BTB protein	KEAP1, PLZF	PLZF	PLZF, BTBD11	PLZF, BCL6
Chromatin binding/structure	LMNB1, DNMT1, SATB1, HDAC1, HP1BP3	LMNB1, DNMT1, BAZ1B, EZH2, HP1BP3	LMNB1, DNMT1, SATB1, HDAC1, HP1BP3, EPC1, LBR, HAT1, CHD4, EP400, YY1, RBBP4, SIN3A, NCOR2, CXXC1, SMARCA5	LMNB1, DNMT1, SATB1, PCM-1, HP1BP3, EPC1, LBR, CHD4, EP400, BAZ1B, SMARCA4, DMAP1, RCC2, HMGB2
	H4	H1.3	H4 H1.5, H1.2 H2A.1 H2B.1	H4 H2A.1, H1.4, H1.2 H2A.1 H2B.1
RNA Pol II-mediated transcription	TOP2A	TOP2A, EEF2	TOP2A, EIF3B	TOP2A, TOP1
Nuclear transport	NUP153, NUP214, NUP98, NUP88	NUP155		NUP205

Mass spectrometric analysis of proteins immunoprecipitated by anti-PLZF and anti-CUL3 antibodies from indicated thymocyte populations (data from two to three independent experiments). Other proteins that did not belong to the indicated categories are shown with the complete data sets in Supplementary Figs 1 and 2. Analysis of Gene Ontology term enrichment demonstrates *P* values ranging from 10^{–5} to 10^{–8} for nuclear transcriptional and chromatin-organization proteins. IP, immunoprecipitation.

¹Committee on Immunology, Department of Pathology, The Howard Hughes Medical Institute, University of Chicago, Chicago, Illinois 60637, USA. ²Department of Biology, Portland State University, Portland, Oregon 96207, USA.

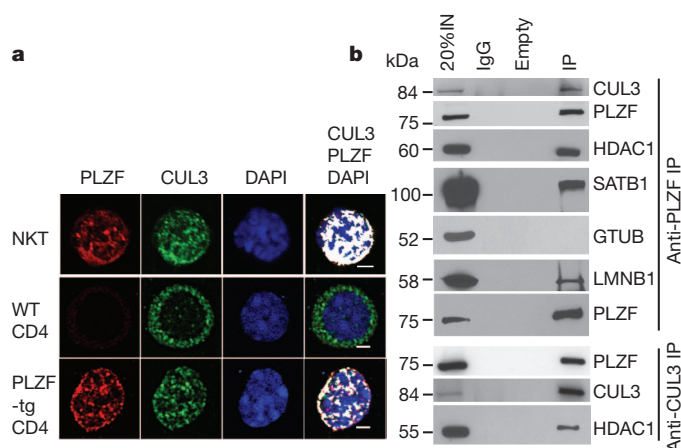


Figure 1 | Interaction and colocalisation of CUL3 with PLZF. **a**, Confocal microscopic analysis of fresh NKT-cell thymocytes and splenic CD4 T cells from wild-type (WT) and PLZF-transgenic (tg) mice, as indicated. White colour indicates colocalization. DAPI, 4',6-diamidino-2-phenylindole. Scale bars, 2 μ m. **b**, Western blot analysis of anti-CUL3 and anti-PLZF immunoprecipitates (IP) from PLZF-transgenic thymocytes. 20% IN refers to 20% of the input lysate before immunoprecipitation. Data are representative of at least three independent experiments.

Fig. 3), as reported for other BTB proteins^{3,18}, although direct binding remains to be formally established¹⁹.

Of note, the BTB-ZF transcription factor BCL6, which characterizes the germinal-centre B cell⁸ and follicular T-helper cell responses²⁰ but is also transiently expressed by cortical thymocytes²¹, was immunoprecipitated by anti-CUL3 in thymocytes (Table 1, column 4). Analysis by western blot in transfected HeLa cells confirmed this association (Supplementary Fig. 4).

Rapid changes in ubiquitination pattern have recently been reported in chromatin-remodelling situations and are thought to regulate gene expression^{22–24}. By bringing CUL3 from the cytosol to chromatin-modifying complexes in the nucleus, PLZF might be expected to induce changes in ubiquitination. This was tested using an unbiased ubiquitination proteomics method comparing whole cell lysates of thymocytes from PLZF-transgenic and wild-type littermates. Independent experiments with different batches of mice identified 48 proteins showing concordant changes, most of which consisted of increased ubiquitination in PLZF-transgenic cells (Fig. 2a and Supplementary Fig. 5). Notably, 14 of these 48 proteins were either components of the CUL3–PLZF complex identified in our previous immunoprecipitation experiments, or were well-known interaction partners of one or several of the proteins identified in the complex. The former included CAND1, LMNB1, DNMT1, SATB1 and H1.2. The latter included UHRF1, which regulates DNMT1 through ubiquitylation²⁵; H2A.1, which is regulated by CUL3 in SPOP–CUL3 complexes²⁶; H2A.Z, which is loaded by EP400 onto chromatin²⁷; the deubiquitinase BRCC3 interacting with H2A, H2B, H2A.X and CAND1 (ref. 28); and the repressor ASXL1 interacting with CBX5 and EZH2 (refs 27, 29). These results are summarized in a protein-interaction diagram in Fig. 2a.

Increased ubiquitination of the key nuclear proteins SATB1 and lamin B1 was directly confirmed by immunoprecipitation and western blot analyses in transfected 293T cells. In these experiments, SATB1 and lamin B1 were overexpressed because technical limitations made it impossible to determine the ubiquitination pattern of endogenous proteins (Fig. 2b). Furthermore, ubiquitination was shown to require the E2-binding domain of CUL3, supporting the conclusion that CUL3 can directly ubiquitinate these PLZF-associated proteins *in vivo*. In confocal microscopy experiments, PLZF and CUL3 were colocalized at lamin B1-positive sites in the nuclear lamina and at SATB1 sites of the nuclear matrix in a typical cage-like pattern (Supplementary Fig. 6). Furthermore, CUL3 was present at PLZF-bound promoters as

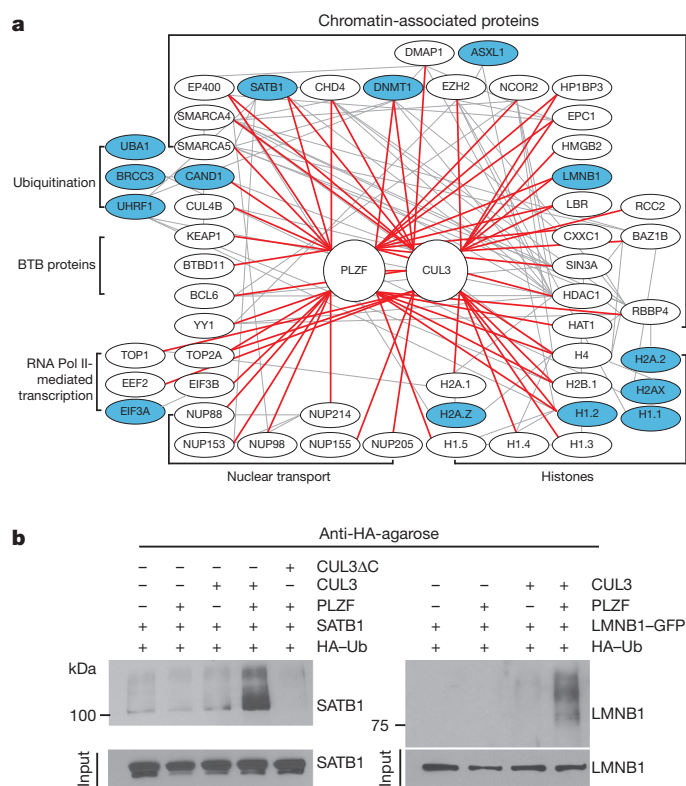


Figure 2 | Ubiquitination changes after PLZF expression. **a**, Mass spectrometric analysis of proteins immunoprecipitated by anti-ubiquitin branch K-GG antibodies (UbiScan) from wild-type and PLZF-transgenic thymocytes showed differential ubiquitination of the proteins depicted in blue-filled ovals in a global diagram of PLZF- and CUL3-interaction partners, with enrichment for proteins involved in chromatin organization ($P < 10^{-6}$). Peptides from two independent experiments are listed in Supplementary Fig. 5. Red lines link proteins identified by coprecipitation in this study; grey lines represent previously established protein interactions (Ingenuity Pathway). **b**, Western blot analysis of anti-haemagglutinin (HA)-ubiquitin (Ub) immunoprecipitates from lysates of 293T cells transfected with indicated plasmids and immunoblotted with anti-SATB1 or anti-lamin B1 (LMNB1). CUL3AC is a mutant CUL3 lacking the E2-binding domain. The molecular mass of the lamin B1–GFP fusion protein is 75 kDa. Data are representative of at least three experiments.

shown by chromatin immunoprecipitation coupled to quantitative PCR (ChIP-qPCR) (Supplementary Fig. 7), suggesting that PLZF–CUL3 complexes associate at PLZF-binding promoters across the genome and in nuclear subcompartments involved in gene expression or repression.

To explore further the functional role of CUL3 in lymphocyte development and function, in which BTB-ZF transcription factors such as PLZF and BCL6 are of major importance, we bred *Cul3^{fl/fl}* mice³⁰ to CD4-Cre and CD19-Cre deleter strains. Mice lacking CUL3 in T cells exhibited a thymus with normal cellularity and representation of CD4 and CD8 T-cell lineages (Fig. 3a). T regulatory (T_{reg}) cells showed a modest but statistically significant twofold increase (Fig. 3a). By contrast, the number of NKT cells was massively decreased, with a sharp developmental block occurring at the CD24^{lo}CD44^{lo}NK1.1[–] stage 1, similar to the block described in mice lacking PLZF^{1,2} (Fig. 3b and Supplementary Fig. 8). These results support the importance of the PLZF–CUL3 interaction in NKT-cell development.

Intriguingly, in older mice lacking CUL3 in T cells, the spleen and lymph nodes became enlarged, the result of a net increase in B-cell numbers with spontaneous formation of germinal centres made of peanut agglutinin (PNA)⁺ B cells (Fig. 3c, d). Whereas thymic CD4⁺CD8[–] T cells exhibited a normal phenotype, a population of splenic CD4 T cells expressing a PD1⁺CXCR5⁺ follicular T-helper

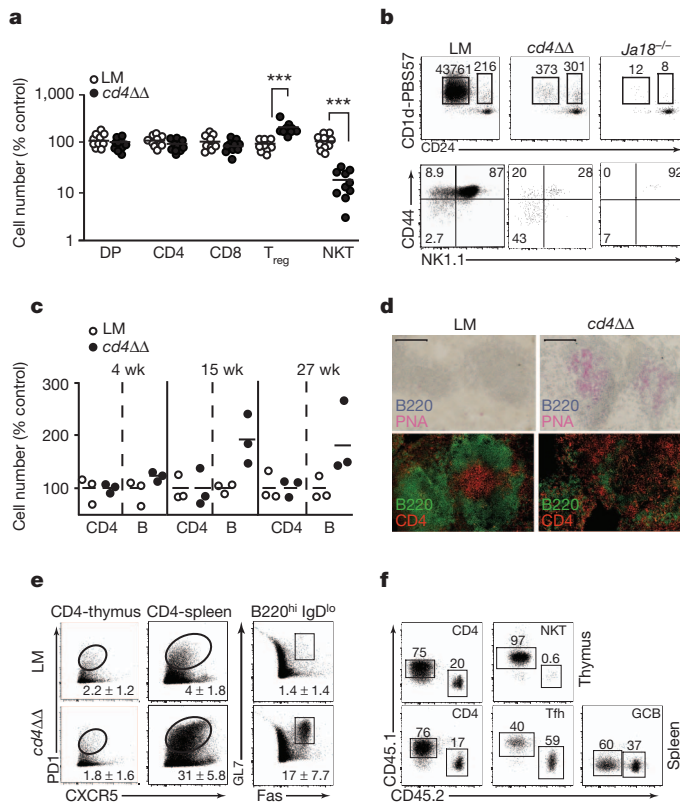


Figure 3 | Lymphocyte development and function in *Cul3^{cd4Δ/Δ}* mice. **a**, Thymic subsets in *Cul3^{cd4Δ/Δ}* and littermate controls. DP, double positive $CD4^+ CD8^+$. **b**, CD1d-PBS57 tetramer magnetic-activated cell sorting (MACS)-enriched NKT-cell thymocytes in *Cul3^{cd4Δ/Δ}*, wild-type littermate (LM) controls and in *Ja18^{-/-}* mice lacking NKT precursors. Top, absolute numbers of early $CD24^{hi}$ stage 0 precursors and maturing $CD24^{lo}$ cells recovered per thymus after MACS. Bottom, percentages of $CD24^{lo}$ stages 1, 2 and 3 based on sequential acquisition of CD44 and NK1.1. **c**, Splenic CD4 T-cell and B-cell counts at different ages. **d**, Immunohistochemical analysis of spleen from 8-week-old mice stained as indicated. Scale bars, 100 μ m. **e**, FACS analysis of splenic subsets, as indicated, in 8-week-old mice. Numbers indicate the mean percentage \pm s.e.m. **f**, Lethally irradiated recipients of a 3:1 mixture of wild-type and *Cul3^{cd4Δ/Δ}* T cells analysed as indicated. GCB denotes $B220^{hi} IgD^{lo} GL7^+ Fas^+$; Tfh denotes $CD4^+ PD1^+ CXCR5^+$. Data are representative of six independent experiments; $n = 18-20$ (**e**, **f**).

cell phenotype progressively accumulated in ageing mice, concomitantly with $GL7^+ Fas^+$ germinal-centre B cells (Fig. 3e). Consistent with these findings, immunohistological analysis demonstrated large germinal centres with penetration of the B-cell follicles by CD4 T cells (Fig. 3d). In radiation chimaeras reconstituted with a 3:1 mixture of wild-type ($CD45.1$) and *Cul3^{cd4Δ/Δ}* ($CD45.2$) T cells, the *CUL3*-deficient compartment showed absence of NKT cells and increased follicular CD4 T-helper cells, demonstrating the cell-intrinsic nature of these defects (Fig. 3f). As expected, germinal-centre B cells of both compartments were indiscriminately expanded. Other effector programs available to CD4 T cells, however, appeared unperturbed as *CUL3*-deficient CD4 cells normally expanded and differentiated towards T-helper 1 (T_H1), T_H2 or T_H17 effector cells *in vitro* (Supplementary Fig. 8).

Mice lacking *CUL3* in B cells showed normal development of follicular B cells but exhibited a selective four- to fivefold reduction of marginal-zone B cells in the spleen and of B1 B cells in the peritoneum (Fig. 4a). These cell-intrinsic defects were considerably amplified in the competitive environment of mixed bone marrow chimaeras (Fig. 4b, c). Whereas the circulating levels of immunoglobulins were normal or modestly decreased (Fig. 4d) and the antibody response to the T cell-independent antigen dinitrophenylated Ficoll (DNP-Ficoll) appeared conserved (Fig. 4e), T-cell-dependent B-cell responses exhibited various

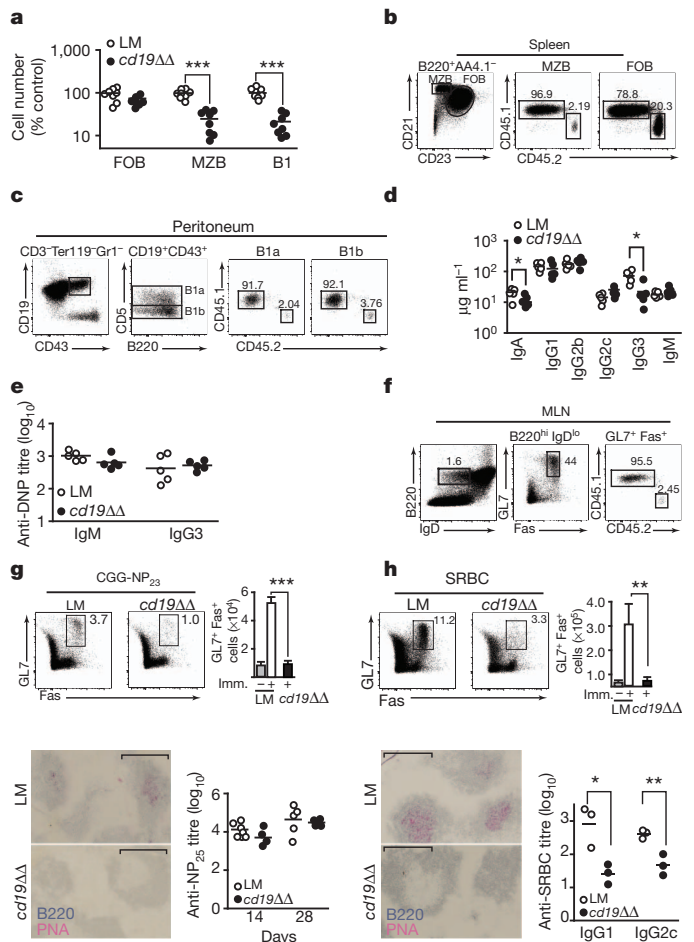


Figure 4 | Lymphocyte development and function in *Cul3^{cd19Δ/Δ}* mice. **a**, Splenic follicular B (FOB) cells, marginal-zone B (MZB) cells and peritoneal B1 B cells in 8-week-old *Cul3^{cd19Δ/Δ}* and littermate controls. **b**, **c**, FACS analysis of splenic follicular B and marginal-zone B cells (**b**) and peritoneal B1a/B1b subsets (**c**), gated as indicated, in the wild-type ($CD45.1$) and *cd19Δ/Δ* ($CD45.2$) compartments of 1:1 mixed bone marrow chimaeras (data representative of $n = 9$). **d**, Serum immunoglobulin isotypes in 10–11-week-old mice ($n = 5$). **e**, Serum antibody response to DNP-Ficoll at day 14. **f**, FACS analysis of spontaneous GCB cells in mesenteric lymph nodes (MLN) of 1:1 mixed bone marrow chimaeras (representative of $n = 9$). **g**, Splenic GCB cells (day 28) after immunization at days 0 and 21 with CGG-NP₂₃. Top panels show FACS staining and summary bar graph (mean and s.e.m., $n = 8$). Bottom panels show immunohistochemical staining of spleen at day 28 and serum anti-NP₂₅ titres at days 14 and 28. Scale bars, 100 μ m. **h**, Similar analysis 7 days after immunization with SRBCs. Summary bar graph (mean and s.e.m., $n = 15$). Scale bars, 100 μ m.

defects. We noted that the germinal-centre B cells that spontaneously develop in the mesenteric lymph nodes of unimmunized mice were reduced, particularly in competitive bone marrow chimaeras (Fig. 4f). The germinal-centre responses observed after immunization against the T-cell-dependent antigens nitrophenyl 23-coupled chicken γ -globulin (CGG-NP₂₃) and sheep red blood cell (SRBC) were markedly impaired, as assessed by immunohistochemical staining of $GL7^+ Fas^+$ B cells (Fig. 4g, h). The antibody response to SRBCs was depressed, whereas the serum antibody response to highly polyvalent nitrophenyl appeared conserved (Fig. 4g, h). These defects are similar to those reported in *BCL6*-deficient mice⁸.

Our study suggests that *CUL3* is an essential partner of key BTB-ZF transcription factors in the lymphoid lineage. The different effect of *CUL3* on the follicular T-helper cell and the germinal-centre B-cell responses suggests that *CUL3* regulates distinct components of these

two BCL6-driven programs²⁰. In addition, the defect in marginal zone B and B1 cells may hint at the existence of as yet unidentified BTB-ZF factors controlling these enigmatic populations.

Although proteomic analysis of ubiquitination was performed at the whole cell level, a considerable proportion of changes induced by PLZF expression was concentrated on the PLZF–CUL3-associated complex itself, including key nuclear matrix proteins such as SATB1 and lamin B1, which target specific DNA sequences for chromatin remodelling and gene regulation, respectively^{11–14}. The precise nature and role of these changes remain to be determined, but the emerging evidence of the importance of ubiquitination in chromatin regulation^{22–24} suggests that they specify key aspects of the transcriptional programs directed by these transcription factors. A similar function of CUL3 may regulate the oncogenic properties of PLZF and BCL6 in leukaemias and lymphomas^{8,9}.

METHODS SUMMARY

Mass spectrometric analysis of PLZF- and CUL3-associated proteins. NKT cells (15×10^6) purified from the thymus of V α 14-J α 18-transgenic mice, or whole thymocytes (50×10^6 – 75×10^6) from PLZF-transgenic mice were subjected to lysis and immunoprecipitation with anti-PLZF or anti-CUL3 antibodies, trypsin-digested and analysed by liquid chromatography–electrospray tandem mass spectrometry on a thermo LTQ Orbitrap Hybrid FT mass spectrometer.

Western blot ubiquitination assay. 293T cells were lipofectamine-transfected with the plasmids pHA-Ub (2 μ g), pSATB1-Myc-His (2 μ g), pLMNB1-GFP (2 μ g), pPLZF-Flag (0.5 μ g), pCUL3-Myc (2 μ g) or pCUL3 Δ C (2 μ g) as indicated. After 24 h, 20 μ M proteasome inhibitor MG132 was added and cells were incubated for another 4–6 h. Ubiquitin conjugates were immunoprecipitated with anti-haemagglutinin agarose beads and analysed by immunoblotting with anti-SATB1 and anti-lamin B1.

Mass spectrometric analysis of ubiquitinated proteins. Total thymocytes (3×10^8) were submitted to lysis, trypsin digestion and immunoprecipitation with the anti-ubiquitin branch antibody (UbiScan, Cell Signaling Technology). Eluted peptides were characterized by tandem mass spectrometry collected with an LTQ-Orbitrap Velos Hybrid mass spectrometer (Thermo). Changes in ubiquitinated peptide levels were measured between PLZF-transgenic and wild-type thymocytes. Fold-changes above 1.45 were considered if confirmed in two independent immunoprecipitation experiments using different batches of mice.

Confocal microscopy. Purified thymocytes or lymphocytes were attached to slides, fixed with 4% paraformaldehyde in PBS and permeabilized with 0.5% Triton in PBS before staining with specific antibodies and analysis on Leica SP10-2-ED-CW super resolution laser scanning confocal or Olympus 1X81 laser scanning microscope using Image J software.

Mice. B6 mice bearing a targeted floxed allele of CUL3 were bred to CD4-Cre and CD19-Cre deleter mice. Controls used in the experiments are littermates with a Cre⁺ CUL3^{WT/WT} or Cre⁺ CUL3^{fl/fl} genotype.

Bone marrow chimaeras. Six-to-eight-week-old lethally irradiated (10 Gy) B6 mice were reconstituted with 2×10^6 – 5×10^6 bone marrow cells and examined 8–10 weeks after irradiation.

Full Methods and any associated references are available in the online version of the paper.

Received 22 August 2011; accepted 5 September 2012.

Published online 21 October 2012.

1. Savage, A. K. *et al.* The transcription factor PLZF directs the effector program of the NKT cell lineage. *Immunity* **29**, 391–403 (2008).
2. Kovalovsky, D. *et al.* The BTB-zinc finger transcriptional regulator PLZF controls the development of invariant natural killer T cell effector functions. *Nature Immunol.* **9**, 1055–1064 (2008).
3. Xu, L. *et al.* BTB proteins are substrate-specific adaptors in an SCF-like modular ubiquitin ligase containing CUL-3. *Nature* **425**, 316–321 (2003).
4. Furukawa, M., He, Y. J., Borchers, C. & Xiong, Y. Targeting of protein ubiquitination by BTB–Cullin 3–Roc1 ubiquitin ligases. *Nature Cell Biol.* **5**, 1001–1007 (2003).
5. Geyer, R., Wee, S., Anderson, S., Yates, J. & Wolf, D. A. BTB/POZ domain proteins are putative substrate adaptors for cullin 3 ubiquitin ligases. *Mol. Cell* **12**, 783–790 (2003).

6. Pintard, L., Willems, A. & Peter, M. Cullin-based ubiquitin ligases: Cul3-BTB complexes join the family. *EMBO J.* **23**, 1681–1687 (2004).
7. Zimmerman, E. S., Schulman, B. A. & Zheng, N. Structural assembly of cullin-RING ubiquitin ligase complexes. *Curr. Opin. Struct. Biol.* **20**, 714–721 (2010).
8. Basso, K. & Dalla-Favera, R. BCL6: master regulator of the germinal center reaction and key oncogene in B cell lymphomagenesis. *Adv. Immunol.* **105**, 193–210 (2010).
9. McConnell, M. J. & Licht, J. D. The PLZF gene of t(11;17)-associated APL. *Curr. Top. Microbiol. Immunol.* **313**, 31–48 (2007).
10. Guidez, F. *et al.* RAR α -PLZF overcomes PLZF-mediated repression of CRABP1, contributing to retinoid resistance in t(11;17) acute promyelocytic leukemia. *Proc. Natl Acad. Sci. USA* **104**, 18694–18699 (2007).
11. Yasui, D., Miyano, M., Cai, S., Varga-Weisz, P. & Kohwi-Shigematsu, T. SATB1 targets chromatin remodelling to regulate genes over long distances. *Nature* **419**, 641–645 (2002).
12. Cai, S., Lee, C. C. & Kohwi-Shigematsu, T. SATB1 packages densely looped, transcriptionally active chromatin for coordinated expression of cytokine genes. *Nature Genet.* **38**, 1278–1288 (2006).
13. Reddy, K. L., Zullo, J. M., Bertolino, E. & Singh, H. Transcriptional repression mediated by repositioning of genes to the nuclear lamina. *Nature* **452**, 243–247 (2008).
14. Zullo, J. M. *et al.* DNA sequence-dependent compartmentalization and silencing of chromatin at the nuclear lamina. *Cell* **149**, 1474–1487 (2012).
15. Ohnuki, H. *et al.* BAZF, a novel component of cullin3-based E3 ligase complex, mediates VEGFR and Notch cross-signaling in angiogenesis. *Blood* **119**, 2688–2698 (2012).
16. Savage, A. K., Constantinides, M. G. & Bendelac, A. Promyelocytic leukemia zinc finger turns on the effector T cell program without requirement for agonist TCR signaling. *J. Immunol.* **186**, 5801–5806 (2011).
17. Kwon, J. E. *et al.* BTB domain-containing speckle-type POZ protein (SPOP) serves as an adaptor of Daxx for ubiquitination by Cul3-based ubiquitin ligase. *J. Biol. Chem.* **281**, 12664–12672 (2006).
18. Wilmutsuk, W. & Singer, J. D. The Cullin3 ubiquitin ligase functions as a Nedd8-bound heterodimer. *Mol. Biol. Cell* **18**, 899–909 (2007).
19. Errington, W. J. *et al.* Adaptor protein self-assembly drives the control of a Cullin-RING ubiquitin ligase. *Structure* **20**, 1141–1153 (2012).
20. Crotty, S. Follicular helper CD4 T cells (TFH). *Annu. Rev. Immunol.* **29**, 621–663 (2011).
21. Hyjek, E., Chadburn, A., Liu, Y. F., Cesarman, E. & Knowles, D. M. BCL-6 protein is expressed in precursor T-cell lymphoblastic lymphoma and in prenatal and postnatal thymus. *Blood* **97**, 270–276 (2001).
22. Braun, S. *et al.* The Cul4-Ddb1^{Cdt2} ubiquitin ligase inhibits invasion of a boundary-associated antisilencing factor into heterochromatin. *Cell* **144**, 41–54 (2011).
23. Wang, H. *et al.* Role of histone H2A ubiquitination in Polycomb silencing. *Nature* **431**, 873–878 (2004).
24. Bosch-Presegué, L. *et al.* Stabilization of Suv39H1 by SirT1 is part of oxidative stress response and ensures genome protection. *Mol. Cell* **42**, 210–223 (2011).
25. Du, Z. *et al.* DNMT1 stability is regulated by proteins coordinating deubiquitination and acetylation-driven ubiquitination. *Sci. Signal.* **3**, ra80 (2010).
26. Hernández-Muñoz, I. *et al.* Stable X chromosome inactivation involves the PRC1 Polycomb complex and requires histone MACROH2A1 and the CULLIN3/SPOP ubiquitin E3 ligase. *Proc. Natl Acad. Sci. USA* **102**, 7635–7640 (2005).
27. Hargreaves, D. C. & Crabtree, G. R. ATP-dependent chromatin remodeling: genetics, genomics and mechanisms. *Cell Res.* **21**, 396–420 (2011).
28. Sowa, M. E., Bennett, E. J., Gygi, S. P. & Harper, J. W. Defining the human deubiquitinating enzyme interaction landscape. *Cell* **138**, 389–403 (2009).
29. Beisel, C. & Paro, R. Silencing chromatin: comparing modes and mechanisms. *Nature Rev. Genet.* **12**, 123–135 (2011).
30. McEvoy, J. D., Kossatz, U., Malek, N. & Singer, J. D. Constitutive turnover of cyclin E by Cul3 maintains quiescence. *Mol. Cell Biol.* **27**, 3651–3666 (2007).

Supplementary Information is available in the online version of the paper.

Acknowledgements We thank A. Dinner, J. Licht, G. Prive, A. Ruthenburg, R. Sciammas, H. Singh and P. Wilson for discussions, J. C. Silva and M. Stokes for UbiScan analysis, C. Labno and V. Bindokas for help with confocal microscopy, and K. Block, L. Roach, D. Zanner, F. Meng and L. Bai for help with experiments. This work was supported by National Institute of Health (NIH) grants 5R01GM082940 (J.D.S.) and R01AI038339 (A.B.), and an Irvington Institute postdoctoral fellowship from the Cancer Research Institute (R.M.). A.B. is a Howard Hughes Medical Institute Investigator.

Author Contributions R.M. designed the research, performed experiments and analysed data. M.P.S., S.T.S., A.M., M.G.C. and C.B.-V. performed experiments and analysed data. J.D.S. helped to design experiments and provided the Cul3^{fl/fl} mice and CUL3 constructs. R.M. and A.B. co-wrote the paper. A.B. supervised the research.

Author Information Reprints and permissions information is available at www.nature.com/reprints. The authors declare no competing financial interests. Readers are welcome to comment on the online version of the paper. Correspondence and requests for materials should be addressed to A.B. (abendela@bsd.uchicago.edu).

METHODS

Mice. C57BL/6, B6.SJL-Ptprca Pep3b/BoyJ (CD45.1), Cd19-Cre (B6.129P2(C)-Cd19^{tm1(cre)Cgn}) and Cd4-Cre (B6.Tg(cd4-cre)1Cwi) mice were obtained from Jackson Laboratories. B6.Cul3^{fl/fl} mice³⁰ and B6.129P2-Cul3^{fl/fl} mice were bred in our colony. Among the littermates of Cul3^{cd4ΔΔ} and Cul3^{cd19ΔΔ} mice, we used both Cre⁺ Cul3^{WT/WT} and Cre⁻ Cul3^{fl/fl} mice as controls. All mice were raised in a specific pathogen-free environment at the University of Chicago and experiments were performed in accordance with the guidelines of the Institutional Animal Care and Use Committee.

Cell culture. HeLa and 293T cells were maintained in DMEM (GIBCO) supplemented with 10% FBS and 1% penicillin/streptomycin. KG1a cells were maintained in IMDM media (GIBCO) supplemented with 10% FBS and 1% penicillin/streptomycin. All cell lines were purchased from the American Type Culture Collection (ATCC).

Plasmids and antibodies. Plasmids used in this study are gifts from investigators or were generated in the laboratory: human pcDNA3-Myc-CUL3 (Y. Xiong); pcDNA3-DN-hCUL3Flag³¹ (Addgene, plasmid 15820) lacking sequences 418–760 at the carboxy terminus and serving as a catalytically inactive mutant (CUL3ΔC); pcDNA3.1-SATB1-Myc-His (R. Grosschedl); pEGFP-C3-LMN1 (Y.-H. Fu); pFlag-CMV2-PLZF (in which PLZF was PCR-amplified from C57BL/6 thymic NKT cDNA and cloned into a SalI site of pFlag-CMV2).

Primary antibodies were: anti-CUL3 (C-0871 from Sigma; A301-109A from Bethyl Laboratories), anti-PLZF (monoclonal 2A9 Calbiochem; polyclonal AF2944 R&D systems), anti-BCL6 (polyclonal ab19011 Abcam; C-19 and N-3 Santa Cruz Biotechnologies; monoclonal G1191E eBioscience), antiSATB1 (L745 Cell Signaling Technology; monoclonal 14 BD Bioscience), anti-lamin B1 (monoclonal 4E4 Sigma; M-20 and S-20 Santa Cruz), anti-HA (TA-150034 Origene), anti-HDAC1 (ab-7028 Abcam). Mouse, goat or rabbit IgG (mIgG2a-ab18413, gIgG-ab37373 or rIgG-ab37415-5 Abcam). Secondary antibodies were anti-rabbit IgG-HRP (GE Healthcare or eBioscience), donkey anti-goat IgG-HRP (Santa Cruz Biotechnologies).

Immunoprecipitation of PLZF- or CUL3-associated proteins. NKT cells (15×10^6) or thymocytes (50×10^6 – 75×10^6) were lysed on ice for 30 min in 0.5–1 ml lysis buffer (50 mM Tris-HCl, pH 8.0, 150 mM NaCl, 5 mM EDTA, pH 8.0), 0.5% (v/v) Nonidet P-40, 1 mM dithiothreitol and 1× protease inhibitor mix (Roche). Lysates were cleared by centrifugation, pre-cleared with Protein A/G sepharose beads (Invitrogen) at 4 °C for 1 h, and incubated at 4 °C for 2 h with anti-PLZF- or anti-CUL3-bound Protein A/G Sepharose (Invitrogen) beads. Beads were washed three times with lysis buffer followed by three washes with PBS plus 0.05% Triton. Bound proteins were eluted by boiling for 5 min and resolved on 10% SDS-PAGE (BioRad). For immunoblot, the gel was transferred to nitrocellulose membrane (Transblot transfer medium, 0.45 mm, Biorad) and blotted using specific antibodies.

Mass spectrometry. For the identification of coimmunoprecipitated proteins, slices of SDS-PAGE gels stained with colloidal blue (NuPAGE, Invitrogen) were destained using 100 mM ammonium bicarbonate, pH 7.5, in 50% acetonitrile. A reduction step was performed by addition of 100 μl 50 mM ammonium bicarbonate, pH 7.5, and 10 μl of 10 mM TCEP (Tris(2-carboxyethyl)phosphine-HCl) at 37 °C for 30 min. The proteins were alkylated by adding 100 μl 50 mM iodoacetamide and allowed to react in the dark at 20 °C for 30 min. Gel slices were washed in water, then in acetonitrile and dried by SpeedVac for 30 min. Trypsin digestion was carried out overnight at 37 °C using sequencing grade modified trypsin (Promega) at a 1:50 enzyme to protein ratio in 50 mM ammonium bicarbonate, pH 7.5, and 20 mM CaCl₂. Peptides were extracted from the gel pieces with 5% formic acid and dried by SpeedVac. The peptide samples were analysed by a liquid chromatography–electrospray tandem mass spectrometry (LC–MS/MS) on a Thermo LTQ Orbitrap Hybrid FT mass spectrometer. Spectra were then analysed with Mascot (Matrix Science, version3, Mascot) and Sequest (ThermoFinnigan, version v.27, rev. 11) set up to search the *mus_musculus* database. Peptide identifications were accepted if they could be established at greater than 95% probability. Protein identifications were accepted if they could be established at greater than 90% probability and contained at least two unique identified peptides.

UbiScan analysis. Thymocytes (3×10^8) were submitted to Cell Signaling Technology for UbiScan analysis using the ubiquitin branch antibody (1990 Cell Signaling Technology) following a method modified from ref. 32. Lysates were sonicated, cleared by centrifugation, reduced and carboxamidomethylated. Total protein for each lysate was normalized before digestion. Lysates were digested with trypsin. Peptides were separated from non-peptide material by solid-phase extraction with Sep-Pak C18 classic cartridges (Waters). Lyophilized peptides were redissolved, and ubiquitinated peptides were isolated using slurries of the ubiquitin branch antibody. Peptides were eluted from antibody-resin into a total volume of 100 μl in 0.15% trifluoroacetic acid. Eluted peptides were concentrated with C18 spin tips immediately before LC–MS analysis. The samples were

run in duplicate to generate analytical replicates and increase the number of MS/MS identifications from each sample. Peptides were loaded directly onto a 10 cm × 75 μm PicoFrit capillary column packed with Magic C18 AQ reversed-phase resin. The column was developed with a 72-min linear gradient of acetonitrile in 0.125% formic acid delivered at 280 nl min⁻¹. Tandem mass spectra were collected with an LTQ-Orbitrap Velos hybrid mass spectrometer (Thermo), a top-20 method, a dynamic exclusion repeat count of 1 and a repeat duration of 30 s. Mass spectrometry spectra were collected in the Orbitrap component of the mass spectrometer, and MS/MS spectra were collected in the LTQ. MS/MS spectra were evaluated using SEQUEST 3G and the SORCERER 2 platform from Sage-N Research (v4.0, Milpitas CA). Peptide assignments were obtained using a 5% false positive discovery rate. Searches were performed against the mouse NCBI database updated on 9 June 2010. Cysteine carboxamidomethylation was specified as a static modification, oxidation of methionine residues was allowed, and ubiquitination was allowed on lysine residues. Each MS/MS spectrum arises from a parent ion observed during a survey mass spectrometry scan and can be linked to the intensity of that parent ion at its chromatographic apex, essentially measuring the abundance of the peptide in the sample. Parent ion intensities were extracted from the ion chromatogram file of each sample using proprietary software and are reported in the quantification tables. Changes in ubiquitinated peptide levels were measured by taking the ratio of raw intensities. Raw intensity values were used to calculate average values and raw ratios between samples. The raw ratios were normalized based on the median ratio found, and normalized ratios and fold-changes are reported.

Flow cytometry. CD1d-PBS57 tetramers were obtained from the NIH tetramer facility. Fluorochrome-labelled monoclonal antibodies (clones indicated in bracket) against CD4 (GK1.5), CD8a (53-6.7), TCRβ (H57-597), CD24 (M1/69), CD25 (PC61), FOXP3 (FJK-16), CD44 (IM7), NK1.1 (PK136), B220 (RA3-6B2), CxCR5, PD1 (29F.1A12), ICOS (C398.4A), IgD (11.26c.2a), Fas (JO2), GL7, CD3e, CD1d (1B1), CD21/35 (7G6), CD23(B3B4), CD45.1 (A20), CD45.2 (104), CD5 (53-7.3), CD43 (S7), CD93 (AA4.1), CD19 (ID3), IgM (11/41), CD69 (H1.2F3) and γδTCR (GL3) were purchased from e-Bioscience, BD Biosciences or Biolegend. For FOXP3 intracellular flow cytometry, cells were fixed using the permeabilization and fixation buffer (Foxp3 staining buffer set) from eBioscience. Samples were analysed on an LSRII (Becton Dickinson), or sorted on a FACS Aria (Becton Dickinson) or MoFlo (Dako Cytomation). Data were analysed using FlowJo (Tree Star).

Confocal microscopy. Purified NKT-cell thymocytes or CD4 splenocytes were attached to slides (Superfrost plus microscope slides, Fisherbrand) by cytospin, and fixed for 15 min with 4% paraformaldehyde in PBS followed by three PBS washes. Cells were permeabilized with 0.5% Triton in PBS for 10 min, washed and blocked with 10% donkey serum and 1% BSA for 1 h at room temperature before staining with anti-PLZF or anti-CUL3 for 2 h at room temperature in a humidifying chamber. After PBS washes, cells were stained with donkey anti-rabbit Alexa 488 (Invitrogen), donkey anti-goat Alexa 555 antibodies (Invitrogen) or donkey anti-mouse 647 (Invitrogen) for 30 min at room temperature. Cells were washed with PBS 0.005% Triton, then PBS, and mounted with prolong gold mounting solution (Invitrogen). Control staining included rabbit IgG and goat IgG followed by corresponding secondary antibody or secondary antibody alone. Images were captured on Leica SP10-2-ED-CW super resolution laser scanning confocal (×100/1.4 oil) and Olympus IX81 laser scanning microscopes and were analysed with ImageJ software.

Immunoprecipitation and western blot detection of ubiquitinated proteins. 293T cells grown in 6-well plates were lipofectamine-transfected with plasmids pHA-Ub (2 μg), pSATB1-Myc-His (2 μg), pLMNB1-GFP (2 μg), pPLZF-Flag (0.5 μg), pCUL3-Myc (2 μg) or pCUL3ΔC (2 μg) as indicated. The plasmid concentration was kept constant by adding pmaxGFP (Amara). After 24 h, 20 μM MG132 was added and cells were incubated for another 4–6 h. Cells were collected with gentle scraping and resuspended in 300 μl RIPA buffer (25 mM Tris-HCl, pH 7.6, 150 mM NaCl, 1% NP-40, 1% sodium deoxycholate, 0.1% SDS and 1× protease inhibitor). Cells were lysed by sonication (Bioruptor, Diagenode) for 12 min, with 30 s on and 30 s off. Lysates were centrifuged at 13,800g at 4 °C for 10 min to remove cell debris. One-hundred microlitres of the lysate was diluted 1:4 with RIPA buffer supplemented with 1× protease inhibitors, and incubated with 25 μl anti-HA-agarose (A2095 clone HA-7, Sigma) for 4 h. The beads were washed four times with RIPA buffer and boiled for 5 min in 50 μl SDS gel-loading buffer containing 50 mM β-mercaptoethanol at 95 °C. Samples were separated by SDS-PAGE and immunoblotted with antibodies against SATB1 or lamin B1.

Immunofluorescence. For immunofluorescence studies, frozen OCT (Tissue-Tek)-embedded 5-μm sections of spleens were dried overnight and stained with biotinylated rat anti-B220 (RA3-6B2 BD Biosciences) and Alexa-Fluor 488-conjugated rat anti-CD4 (RM4-5 Invitrogen) antibodies, followed by Cy3-streptavidin (Invitrogen) and visualized using a SP5 II microscope (Leica). Data were analysed using ImageJ (Bitplane) software.

For immunohistochemical studies, frozen OCT-embedded sections were dried overnight, fixed with ice-cold acetone and incubated with methanol and 0.3% hydrogen peroxide to neutralize endogenous peroxidase activity, and blocked with 5% rat serum, then streptavidin-biotin blocking (Vector Laboratories). Sections were stained with biotinylated PNA (Vector Laboratories), followed by Vectastain ABC-alkaline phosphatase kit (Vector Laboratories) and the Vector Red alkaline phosphatase substrate kit (Vector Laboratories). After treatment with serum and streptavidin-biotin block, sections were stained with biotinylated rat anti-B220 antibody (RA3-6B2 BD Biosciences), followed by reaction with the Vectastain ABC kit (Vector Laboratories) and ImmPACT SG peroxidase substrate kit (Vector Laboratories) according to manufacturer's instructions. Sections were dehydrated, cleared with xylene and mounted using Permount solution (Fischer Scientific). Micrographs were taken with the FSX-100 microscope camera system (Olympus) and data were analysed using ImageJ (Bitplane) software.

Generation of bone marrow chimaeras. Six-to-eight-week-old B6 (CD45.1) mice were subjected to irradiation with 10 Gy using a γ -cell 40 irradiator with a caesium source and were injected intravenously 3–6 h later with 2×10^6 – 5×10^6 bone marrow cells obtained from the femurs of donor mice. Bone marrow-reconstituted mice were analysed 8–10 weeks after irradiation

NKT cell enrichment. NKT cells were labelled with allophycocyanin (APC)-conjugated CD1d-PBS57 tetramers, bound to anti-APC magnetic beads, and enriched on an MACS cell separator (Miltenyi Biotec) as described previously³³.

Mouse immunizations. Six-to-eight-week-old mice were immunized intraperitoneally with 100 μ g of DNP-Ficoll (Biosearch Technologies) in PBS, 50 μ g CGG-NP₂₃ (Biosearch Technologies) mixed 1:1 with alum, or 2×10^8 SRBCs (Lampire Biological Laboratories). Mice injected with CGG-NP₂₃ were boosted on day 21 with the same inoculum and killed on day 28. Levels of anti-DNP and anti-NP antibodies were determined by ELISA against BSA-DNP₇ and BSA-NP₂₅, respectively (Biosearch Technologies) and anti-SRBC antibodies were measured by FACS using an indirect isotype-specific immunofluorescence assay (eBiosciences, Southern Biotech).

Statistical analysis. Unpaired Student's *t*-test was performed with Prism (Graph Pad Software). **P* < 0.05; ***P* < 0.001; ****P* < 0.0001.

31. Jin, J., Ang, X. L., Shirogane, T. & Wade Harper, J. Identification of substrates for F-box proteins. *Methods Enzymol.* **399**, 287–309 (2005).
32. Rush, J. *et al.* Immunoaffinity profiling of tyrosine phosphorylation in cancer cells. *Nature Biotechnol.* **23**, 94–101 (2005).
33. Benlagha, K., Wei, D. G., Veiga, J., Teyton, L. & Bendelac, A. Characterization of the early stages in thymic NKT cell development. *J. Exp. Med.* **202**, 485–492 (2005).

Structure and mechanism of a bacterial sodium-dependent dicarboxylate transporter

Romina Mancusso^{1,2}, G. Glenn Gregorio¹, Qun Liu³ & Da-Neng Wang^{1,4}

In human cells, cytosolic citrate is a chief precursor for the synthesis of fatty acids, triacylglycerols, cholesterol and low-density lipoprotein. Cytosolic citrate further regulates the energy balance of the cell by activating the fatty-acid-synthesis pathway while downregulating both the glycolysis and fatty-acid β -oxidation pathways^{1–4}. The rate of fatty-acid synthesis in liver and adipose cells, the two main tissue types for such synthesis, correlates directly with the concentration of citrate in the cytosol^{2–5}, with the cytosolic citrate concentration partially depending on direct import across the plasma membrane through the Na⁺-dependent citrate transporter (NaCT)^{6,7}. Mutations of the homologous fly gene (*Indy*; *I'm not dead yet*) result in reduced fat storage through calorie restriction⁸. More recently, *Nact* (also known as *Slc13a5*)-knockout mice have been found to have increased hepatic mitochondrial biogenesis, higher lipid oxidation and energy expenditure, and reduced lipogenesis, which taken together protect the mice from obesity and insulin resistance⁹. To understand the transport mechanism of NaCT and INDY proteins, here we report the 3.2 Å crystal structure of a bacterial INDY homologue. One citrate molecule and one sodium ion are bound per protein, and their binding sites are defined by conserved amino acid motifs, forming the structural basis for understanding the specificity of the transporter. Comparison of the structures of the two symmetrical halves of the transporter suggests conformational changes that propel substrate translocation.

NaCT (also known as SLC13A5) is a member of the mammalian solute carrier family 13 (SLC13), which also includes two dicarboxylate transporters (NaDC1 and NaDC3; also known as SLC13A2 and SLC13A3, respectively) (Supplementary Figs 1–3)^{10,11}. Although these three plasma membrane proteins transport both tricarboxylates such as citrate and dicarboxylates such as succinate, malate and fumarate, they also have distinct substrate specificity^{12–17}. Whereas NaCT transports primarily citrate, NaDC1 and NaDC3 have a higher affinity for succinate, with NaDC3 being the high-affinity transporter. Intriguingly, the SLC13 family also contains two additional highly homologous proteins, NaS1 and NaS2 (also known as SLC13A1 and SLC13A4, respectively) (Supplementary Figs 2 and 3), which transport sulphate instead of carboxylates^{10,11}. Transport by SLC13 proteins is Na⁺ driven, with one substrate molecule being co-transported together with three or four Na⁺ ions per cycle¹¹. Along with the homologous fly protein INDY, the mammalian SLC13 proteins belong to the divalent anion/Na⁺ symporter (DASS) family, which also contains numerous bacterial members (Supplementary Figs 2 and 3)^{11,18}. Several of these bacterial DASS proteins have been shown to catalyse Na⁺-coupled dicarboxylate uptake, with two Na⁺ ions being co-transported with one substrate molecule^{19–22}. In turn, the DASS family belongs to the ion transporter superfamily¹⁸, which comprises 16 transporter families, with over 32,000 members identified thus far.

To understand the transport mechanism of INDY proteins, we functionally characterized the INDY homologue from *Vibrio cholerae*

(VcINDY). VcINDY consists of 462 amino acids and shares 26–33% sequence identity with the three human SLC13 transporters (Supplementary Fig. 3). We first tried to verify whether VcINDY was a Na⁺-driven carboxylate transporter and to identify its substrate. In *Escherichia coli* whole cells transformed with the *V. cholerae* gene^{13,22}, VcINDY catalysed the uptake of succinate (Fig. 1a). The transport was driven by a Na⁺ gradient, but K⁺ had no effect. Interestingly, a Li⁺ gradient also drove transport, although at a slightly slower rate. The uptake reached saturation within 3 min, similar to what had been observed for its homologues^{10,11}. The transport of succinate by VcINDY could be inhibited by malate and fumarate, slightly inhibited by glutamate, but not inhibited by sulphate (Fig. 1b). This suggests that malate and fumarate, two other dicarboxylates, are also substrates of VcINDY, as observed in other mammalian and bacterial INDY homologues^{10,11}. Citrate also slightly inhibited succinate transport by VcINDY, presumably in a competitive manner. VcINDY is found to be a dimer in detergent, as judged by size-exclusion chromatography (Supplementary Fig. 4). Although its dimeric state was unaffected by the presence of Na⁺, dicarboxylate or citrate, its peak height at increased temperatures depended on the presence of carboxylate (Supplementary Fig. 5). Although succinate or malate stabilized the protein modestly, the presence of citrate markedly improved the thermostability of the protein, indicating a specific interaction between VcINDY and citrate.

We then crystallized VcINDY in the presence of citrate, Na⁺ and Li⁺, and the crystals diffracted X-rays to 3.2 Å resolution. The crystal structure was determined using single-wavelength anomalous diffraction from data merged from four separate selenomethionyl data sets (Supplementary Fig. 6 and Supplementary Tables 1 and 2)²³. In the crystal structure, the VcINDY protein formed a dimer, which has the shape of the letter 'M' when viewed from within the membrane plane, with a concave aqueous basin (Fig. 1c, d and Supplementary Figs 7 and 8). Each protein protomer comprises 11 transmembrane α -helices, termed TM1–11 (Fig. 2a). As the amino and carboxy terminals of INDY proteins from other species have been shown to be in the cytosol and the extracellular space, respectively²⁴, the extramembraneous extrusions of the protein and the concave aqueous basin are inferred to be the cytosolic side. The interface between the two protein protomers is formed by TM3, TM4a and TM9b, interacting with TM4b, TM8 and TM9a of the neighbouring protomer (Fig. 1d and Supplementary Fig. 7). The interface between the two protomers has an area of $\sim 2,500$ Å², a large interface area in agreement with the observed stable protein dimer in detergent solution (Supplementary Fig. 4).

Among the 11 transmembrane α -helices, TM4, TM5, TM9 and TM10 are each broken into two segments within the membrane, and each pair is named 'a' and 'b', respectively (Fig. 2a and Supplementary Fig. 8). The loops between TM5a and TM5b (L5ab), and between TM10a and TM10b (L10ab) are each eight amino acids long. In addition, VcINDY also contains several other secondary

¹The Helen L. and Martin S. Kimmel Center for Biology and Medicine at the Skirball Institute of Biomolecular Medicine, New York University School of Medicine, 540 First Avenue, New York, New York 10016, USA. ²Molecular Biophysics Graduate Program, New York University School of Medicine, 540 First Avenue, New York, New York 10016, USA. ³New York Structural Biology Center, NSLS X4, Brookhaven National Laboratory, Upton, New York 11973, USA. ⁴Department of Cell Biology, New York University School of Medicine, 540 First Avenue, New York, New York 10016, USA.

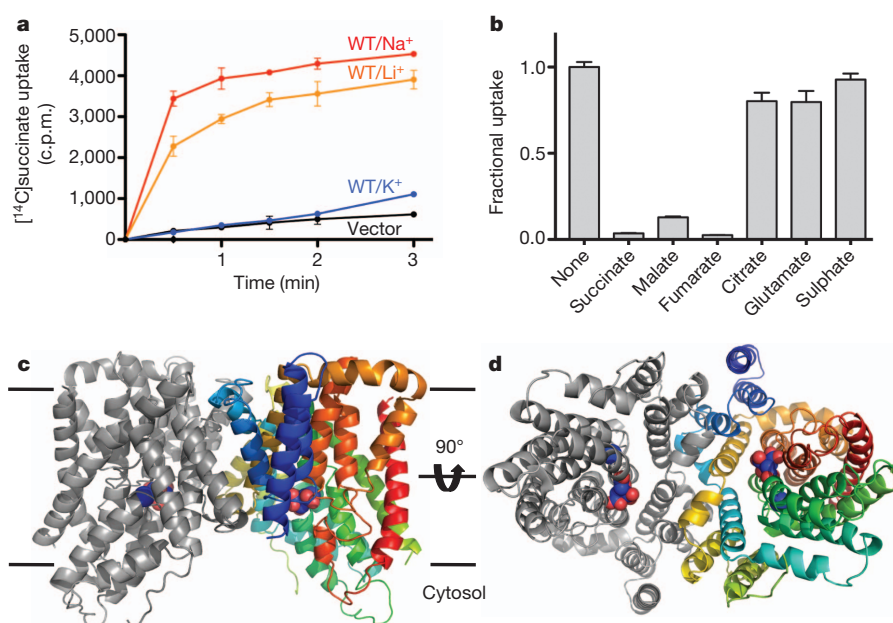


Figure 1 | Functional characterization and structure determination of the Na⁺-dependent dicarboxylate transporter VcINDY from *Vibrio cholerae*. **a**, Na⁺-driven succinate transport by VcINDY measured in whole cells^{13,22}. The succinate uptake was measured in VcINDY-transformed *E. coli* in buffers that contained 5 μ M [¹⁴C]succinate and Na⁺, Li⁺ or K⁺. The control experiment was carried out in Na⁺ buffer using cells that were transformed with empty vector. **b**, Uptake of [¹⁴C]succinate in the presence of various di- and tricarboxylates and sulphate (at 1 mM concentration). For **a** and **b**, $n = 3$.

c, Crystal structure of the VcINDY dimer at 3.2 Å resolution viewed from within the membrane. A citrate molecule and a Na⁺ ion are adjacently bound to each VcINDY protomer at the cytosolic basin of the protein dimer. **d**, Crystal structure of the VcINDY dimer viewed from the cytosol. The bound citrate is exposed to the cytosolic space whereas the Na⁺ ion is buried. In **c** and **d**, the polypeptide in one protomer is coloured using the standard rainbow scheme. c.p.m., counts per minute. WT, wild type.

structure elements. A helical hairpin (HP_{in}) inserts into the membrane from the cytosolic side, which is connected to TM4 through helix H4c on the membrane surface and by a loop to TM5. Similarly, on the opposite side of the membrane, a helical hairpin (HP_{out}) inserts into

the protein from the periplasm and connects to TM9 through helix H9c. Such helical hairpins and intramembrane loops within a broken helix are often found to have a chief mechanistic role in membrane transport proteins^{25–28}.

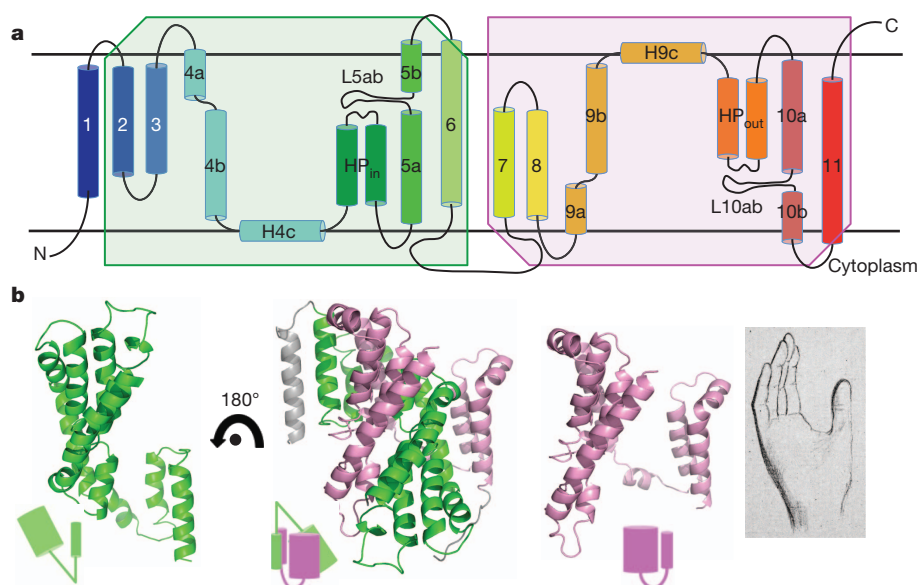


Figure 2 | Structure of the VcINDY protomer. **a**, Transmembrane topology of VcINDY. The two halves of the protein, TM2–6 and TM7–11, are related by a repeat in amino acid sequence, resulting in a transmembrane topology that displays an inverted two-fold symmetry. **b**, The N- and C-terminal halves of the protomer each form a hand-shaped structure, and the two hands are related by an inverted two-fold symmetry. TM2 and TM3 form the thumb, and the helical bundle of TM4b–TM6 takes the shape of the palm in the N-terminal half; in the C-terminal half, the thumb is formed by TM7 and TM8 and the palm by

TM9a–TM11. Note the linker helix between the palm and the thumb in the N-terminal half is at a larger angle from the membrane plane than that of the linker in the C-terminal hand, giving the former a V-shape and the latter a U-shape. The structures of two helical bundles, the palms, are similar and their superposition yields a root mean squared deviation of 2.9 Å for backbone C α atoms. The N- and C-terminal halves of the protein are coloured green and purple, respectively.

The N- and C-terminal halves of VcINDY share a 26.2% identity in amino acid sequence. Closer inspection of its crystal structure reveals that the protein consists of a two-fold repeat (Fig. 2). The N-terminal half of the protein, TM2–TM6, is related to the C-terminal half, TM7–TM11, by an inverted, two-fold symmetry, with the symmetry axis parallel to the membrane plane and the two halves of the protein inserted into the membrane from opposite directions. Each half of the protein has the shape of a hand (Fig. 2b). For the N-terminal half, TM2 and TM3 form a thumb, and the palm is formed by a five-helix bundle that consists of TM4b, TM5 and TM6 as well as the helical hairpin HP_{in}. The thumb and the palm are connected by TM4a, which is at a 45° angle from the membrane plane, yielding a 'V'-shaped hand. The entire N-terminal hand inserts into the membrane from the periplasmic side. Related by the inverted two-fold symmetry, the C-terminal hand—its thumb formed by TM7 and TM8 and its palm formed by TM9b, HP_{out}, TM10 and TM11—inserts from the cytosolic side. The helix that connects the thumb and the palm, TM9a, occurs at an angle to the membrane plane of about 25°. Thus, the angle between the thumb and palm in the C-terminal hand has the shape of a letter 'U'. When superimposed by their thumbs, the two helical bundles are at different heights in the membrane (Supplementary Figs 9 and 10). As expected from the crystallization conditions containing Na⁺ and citrate, we identified a citrate molecule and one Na⁺ ion bound to each of the transporter protomers in the structure (Fig. 1c, d and Supplementary Fig. 8). The citrate molecule and Na⁺ ion are located near to each other in a cleft at the inner end of the dimer basin, directly exposed to the cytosolic space (Fig. 3a). It follows that the crystal structure of VcINDY represents an inward-facing conformation.

The transport of substrates into the cell by VcINDY is driven by the inward sodium gradient (Fig. 1a). In the VcINDY protomer, a Na⁺ ion sits in a clamshell formed by the HP_{in} tip and the L5ab loop, and is separated from the cytosolic space by the bound citrate molecule (Fig. 3a and Supplementary Fig. 11). We named this structural element the 'hairpin tip-capping loop motif' for sodium binding. The Na⁺ ion interacts directly with both the amino acid side chains and backbone carbonyl oxygen atoms of these residues (Fig. 3b). Specifically, the Na⁺ ion is coordinated by the Ser 146 side chain, its backbone oxygen, the Ser 150 backbone oxygen and the Asn 151 side chain, all from HP_{in}, and by the backbone oxygen of Gly 199 from L5ab (Fig. 3b and Supplementary Table 3). When Ser 146 was mutated into an alanine or a leucine, the transport rate of VcINDY decreased markedly (Fig. 3c and Supplementary Fig. 12), supporting the critical role of this residue in the coordination of the Na⁺ ion. We named this Na⁺ ion 'Na1'.

For bacterial INDY proteins, biochemical experiments have shown that, typically, two Na⁺ ions are co-transported with one substrate

molecule^{19,20,22}. In the VcINDY structure, there is a second hairpin tip-capping loop motif, located in the C-terminal half of the protein that is related to the N-terminal site by inverted two-fold symmetry (Fig. 3a). This motif comprises the HP_{out} tip and loop L10ab (Fig. 2a). Both the amino acid sequences for the two motifs and the HP_{in} and HP_{out} segments are highly conserved among various INDY proteins (Supplementary Fig. 3). We therefore proposed that the hairpin tip-capping loop motif in the C-terminal half of VcINDY forms the second Na⁺-binding site (Fig. 3a). However, no electron density for a Na⁺ ion is observed at this region. There are two possible explanations. One is that this 'Na2' site is occupied by a Li⁺ ion, which is too light to visualize at the current resolution. Another possibility, which we favour, is that the Na2 ion has already been released. As this site is directly exposed to the cytosolic space, it is logical to be the first Na⁺ ion to escape before release of the substrate molecule itself. This is further supported by the observation that the distance between the HP_{out} tip and loop L10ab in the empty Na2 clamshell is larger than that of the occupied Na1 clamshell (Supplementary Fig. 13), indicating an open structure after Na⁺ release. Interestingly, when the equivalent glutamate residue of VcINDY Glu 374 at the HP_{out} tip in the Na2 clamshell was mutated in the mammalian NaDC1 (Glu 475), the Michaelis constant (*K_m*) for substrate transport increased markedly¹⁴, in agreement with a Na⁺ site being at this location. Finally, in the L10ab loop, the equivalent residue of VcINDY-Cys 413 in human NaCT, Phe 500, has been shown to be essential for Li⁺ binding and its stimulation of citrate transport²⁹. As the Na1 ion is buried and inaccessible to the cytoplasmic space until the bound substrate is released, the Na1 and the tentative Na2 ions are mechanistically non-equivalent.

Between the Na1 and Na2 sites, a citrate molecule is found to bind in the middle of the VcINDY protomer (Fig. 4 and Supplementary Fig. 14). This binding pocket displays a strong positive electrostatic surface potential (Fig. 4a). It is formed by residues from HP_{in}, TM5, HP_{out} and TM10. Just like the two-fold symmetry of the citrate molecule, the binding pocket is also symmetrical. The 5-carboxyl group of citrate points to Ser 150, Asn 151 and Thr 152 from HP_{in}, whereas the 1-carboxyl group directly interacts with an inverted triangle formed by Ser 377, Asn 378 and Thr 379 from HP_{out} (Fig. 4b). The cytosolic and periplasmic sides of the binding pocket are formed by Thr 421 and Pro 422 from L10ab, and by Pro 201 and Ser 202 from L5ab, respectively. Additional interaction to the citrate is mediated through hydrogen bonding with the side chains of Ser 150, Thr 379 and Thr 421.

As citrate inhibits the transport of succinate (Fig. 1b), it is reasonable to assume that the observed citrate-binding pocket in VcINDY (Fig. 4)

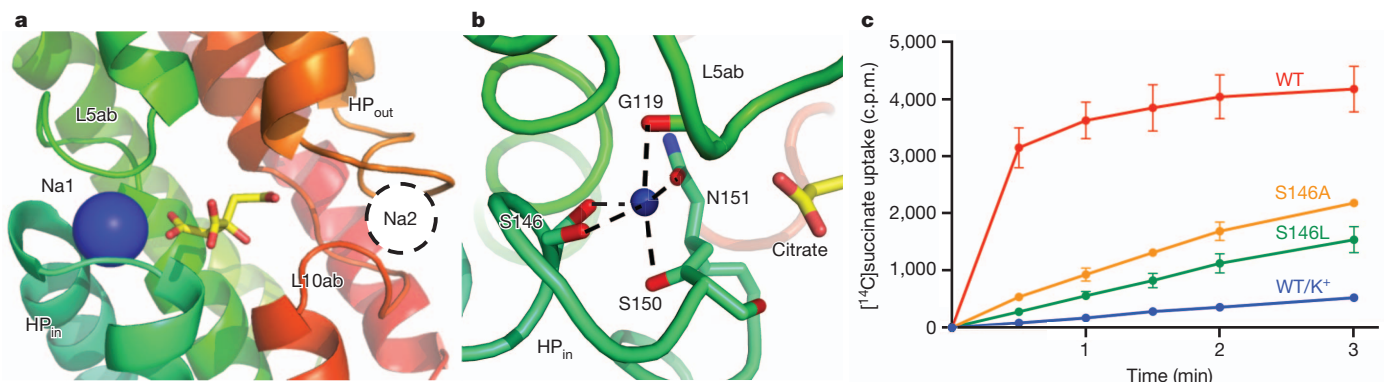


Figure 3 | Na⁺ ion-binding sites in VcINDY. **a**, Structure of the Na⁺-binding site (Na1) formed by the tip of HP_{in} and the L5ab loop. The binding site has the shape of a clamshell, which we named the hairpin tip-capping loop motif for sodium binding. A second, putative Na⁺-binding site (Na2), is suggested to be located between the tip of HP_{out} and the L10ab loop formed by the C-terminal hairpin tip-capping loop motif. However, no electron density for Na⁺ was

found at this site in the crystal structure. In the current inward-facing transporter structure, the Na2 site is directly exposed to the cytosolic space. **b**, Coordination of the Na⁺ ion at the Na1 site. Both side chains of amino acid residues and backbone carboxyl oxygen atoms are involved in the Na⁺ coordination. **c**, Succinate transport activity of Na1-site mutants (*n* = 3).

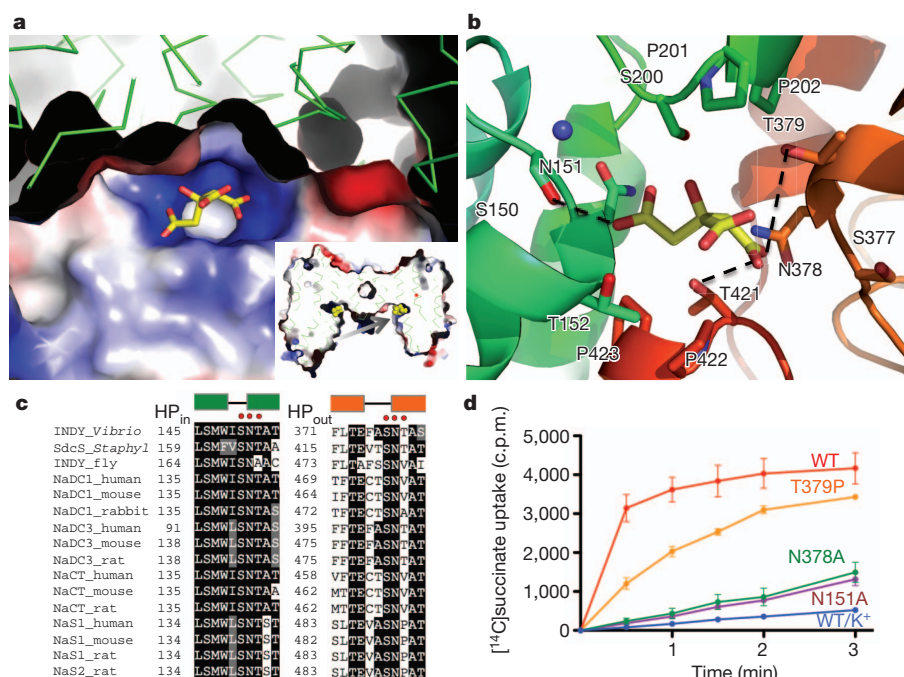


Figure 4 | Substrate-binding site in VcINDY. **a**, Electrostatic surface potential of the substrate-binding site. Inset, cross-section of the electrostatic surface potential of the VcINDY dimer. The plane of this central cross-section is perpendicular to the membrane and is at a small angle from the long axis of the dimer in order to show both citrate molecules bound to the transporter dimer. The arrow points in the direction of the view in **a**. **b**, Structure of the substrate-binding site with a citrate bound, showing the coordination of the substrate analogue. Three hydrogen bonds are indicated by dashed lines. The citrate lies at a small angle to the membrane plane, and its long axis is parallel to

the protomer–protomer interface. The central 6-hydroxyl- and carboxyl groups are exposed to the cytosolic space. Although the side chain of Ser 150 forms a hydrogen bond with the 5-carboxyl group of the citrate, its backbone carbonyl oxygen atom participates in the coordination of the Na⁺ ion. Similarly, the side chain of Asn 151 interacts with both Na⁺ and the bound citrate. **c**, Amino acid sequence alignment of VcINDY and its homologues, showing the two SNT carboxylate-binding motifs. **d**, Succinate transport activity of substrate-binding site mutants ($n = 3$).

is also the binding site for dicarboxylate substrates and that a substrate molecule binds to the transporter in a similar manner. In fact, when either Asn 151 or Asn 378 was mutated to an alanine, the affinity of VcINDY to succinate was found to be markedly reduced and the transport rate decreased (Fig. 4c, d and Supplementary Fig. 12). Just like the amino acid sequence conservation for the Na⁺-binding motifs, the Ser-Asn-Thr (SNT) motif in the N-terminal half is highly conserved among INDY proteins of various species, from bacteria to human, whereas the C-terminal motif allows for variation between a threonine and a valine only in the third position (Fig. 4c). Therefore, these two SNT motifs can be regarded as the signature sequences of Na⁺-dependent tri- and dicarboxylate transporters in the DASS family. In agreement with this notion, it was previously observed that when the serine and asparagine residues in the C-terminal SNT motif were mutated into a cysteine in the rabbit NaDC1 protein, the transport rate for succinate dropped to 25% and 0% of the wild type, respectively¹⁶. Alternatively, when the equivalent of VcINDY-Pro 422 or Pro 423 in rabbit NaDC1 was mutated into a glycine or alanine¹⁷, the protein still transported succinate, further supporting that the determinant for substrate specificity is primarily mediated through 1,5-carboxyl groups of the substrate to the two SNT motifs of the protein. The highly positively charged nature of the substrate-binding site explains why dicarboxylates such as glutamate, which has an HN⁺ group, are not a substrate for mammalian SLC13 proteins¹². Finally, the substrate-binding pocket in the structure also explains the substrate preference between carboxylate and sulphate transporters among SLC13 proteins (Fig. 4c, Supplementary Fig. 15 and Supplementary Discussion)^{10,11}.

Although the bound Na⁺ ion does not directly coordinate the substrate molecule as in some other transporters²⁶, the substrate-binding site shares residues with both the Na⁺- and the putative Na²-binding sites (Fig. 3a). Although the side chain of Ser 150 forms a hydrogen

bond with the 5-carboxyl group of the citrate, its backbone carbonyl oxygen atom participates in the coordination of the Na⁺ ion. Similarly, the side chain of Asn 151 binds to citrate on one side and coordinates Na⁺ on its opposite side. Such close proximity and, especially, the residue-sharing nature of the substrate- and the Na⁺-binding sites immediately suggests an ion-coupling mechanism of substrate transport. As previous biochemical experiments have shown that Na⁺ ions bind to INDY proteins before a substrate can bind^{13,15,19,20,22}, it follows that the binding of Na⁺ ions creates an optimal binding site for the substrate through an induced-fit mechanism. Our mechanism is supported by previous studies on the single-nucleotide polymorphism of human NaDC1 (ref. 30). The change of Val 477, at the third position of the C-terminal SNT motif, to a methionine markedly lowers affinity to Na⁺ and simultaneously abolishes succinate transport.

The core of the VcINDY protomer structure formed by the two helical bundles (the palms) resembles that of the recently determined concentrative nucleoside transporter, CNT²⁸, which has no detectable homology with VcINDY and is not a member of the ion transport superfamily¹⁸. The palms of the VcINDY protein, TM4–TM6 and TM9–TM11, are equivalent to H3–H5 and H6–H8 in CNT, respectively (Supplementary Fig. 16). The substrate-binding sites in the two transporters are also located at approximately the same position. With only one clamshell Na⁺-binding motif, CNT has one Na⁺ ion bound, which is located at the equivalent site of the VcINDY Na⁺. As VcINDY is a dimer and CNT a trimer, the scaffoldings and the manners of expected conformational changes in the two transporters are different (Supplementary Discussion).

Our crystal structure also suggests a model for conformational changes needed in VcINDY to propel substrate across the membrane (Supplementary Fig. 17 and Supplementary Discussion). In the outward-facing (C_o) state, the two halves of a protomer adopt an N(U-shaped)-C(V-shaped) conformation. In response to Na⁺ and

substrate binding, it converts to an N(V-shaped)-C(U-shaped) conformation as observed in our crystal structure (Fig. 2), followed by Na⁺ and substrate release to the cytosol. Such a transport mechanism, along with the structural basis of substrate and ion specificity and ion coupling to substrate transport, provides a direct framework for understanding its mammalian counterpart^{10,11}. As the human NaCT protein may be a particularly attractive drug target for obesity, diabetes and cardiovascular diseases, the identification of the substrate-binding motifs may aid in the development of such agents.

METHODS SUMMARY

The transporter protein from *V. cholerae* (AAF95939; VcINDY) was overexpressed in *E. coli* BL21-AI cells using a modified pET vector. The protein was purified in *N*-decyl- β -maltoside on a cobalt affinity column, followed by preparative size-exclusion chromatography in buffer containing 50 mM Tris, pH 7.5, 100 mM NaCl, 50 mM lithium citrate, 5% glycerol and 0.15% *N*-decyl- β -maltoside. Transport activity of VcINDY at 25 °C was characterized using a whole-cell assay of [¹⁴C]succinate uptake^{13,22}. *E. coli* BL21 p-Lys cells transformed with the gene coding for VcINDY were grown to *D*_{660 nm} 0.7 and collected. Transport was initiated by mixing the cell suspension with concentrated assay buffer to yield a final concentration of 5 mM NaCl, 95 mM Tris, pH 7.5, and 5 μ M [¹⁴C]succinate. Aliquots were taken at various time points and the transport reaction was terminated by collecting the cells on nitrocellulose filters, followed by measuring the radioactivity with a liquid scintillation counter. For the competition assay, the final buffer also included 1 mM of the test compound. For the activity measurements of mutants, their expression levels in *E. coli* cells were verified by western blot. Crystals of VcINDY were grown at 18 °C using hanging-drop vapour diffusion by mixing sizing column-purified samples with 29% (v/v) polyethylene glycol 1000, 50 mM lithium citrate and 50 mM MOPS, pH 6.5. For structure determination, anomalous diffraction data were collected from seleno-L-methionine (SeMet) crystals at a wavelength of 0.9792 Å. Initial phases were obtained through a multi-crystal SeMet single-wavelength anomalous dispersion method²³, using data merged from four crystals. Structure models were built and the final one was refined to 3.2 Å resolution.

Full Methods and any associated references are available in the online version of the paper.

Received 27 April; accepted 30 August 2012.

Published online 21 October 2012.

- Spencer, A. F. & Lowenstein, J. M. Supply of precursors for synthesis of fatty acids. *J. Biol. Chem.* **237**, 3640–3648 (1962).
- Bloch, K. & Vance, D. Control mechanisms in synthesis of saturated fatty-acids. *Annu. Rev. Biochem.* **46**, 263–298 (1977).
- Ruderman, N. B., Saha, A. K., Vavvas, D. & Witters, L. A. Malonyl-CoA, fuel sensing, and insulin resistance. *Am. J. Physiol.* **276**, E1–E18 (1999).
- Sul, H. S. & Smith, S. in *Biochemistry of Lipids, Lipoproteins and Membranes* 5th edn (eds Vance, D. E. & Vance, J. E.) 155–190 (Elsevier, 2008).
- Nishikori, K., Iritani, N. & Numa, S. Levels of acetyl coenzyme A carboxylase and its effectors in rat-liver after short-term fat-free refeeding. *FEBS Lett.* **32**, 19–21 (1973).
- Inoue, K., Zhuang, L., Maddox, D. M., Smith, S. B. & Ganapathy, V. Structure, function, and expression pattern of a novel sodium-coupled citrate transporter (NaCT) cloned from mammalian brain. *J. Biol. Chem.* **277**, 39469–39476 (2002).
- Gopal, E. *et al.* Expression and functional features of NaCT, a sodium-coupled citrate transporter, in human and rat livers and cell lines. *Am. J. Physiol. Gastrointest. Liver Physiol.* **292**, G402–G408 (2007).
- Rogina, B., Reenan, R. A., Nilsen, S. P. & Helfand, S. L. Extended life-span conferred by cotransporter gene mutations in *Drosophila*. *Science* **290**, 2137–2140 (2000).
- Birkenfeld, A. L. *et al.* Deletion of the mammalian *INDY* homolog mimics aspects of dietary restriction and protects against adiposity and insulin resistance in mice. *Cell Metab.* **14**, 184–195 (2011).
- Markovich, D. & Murer, H. The SLC13 gene family of sodium sulphate/carboxylate cotransporters. *Pflügers Arch.* **447**, 594–602 (2004).
- Pajor, A. M. Molecular properties of the SLC13 family of dicarboxylate and sulfate transporters. *Pflügers Arch.* **451**, 597–605 (2006).
- Wright, S. H., Kippen, I., Klinenberg, J. R. & Wright, E. M. Specificity of the transport system for tricarboxylic acid cycle intermediates in renal brush borders. *J. Membr. Biol.* **57**, 73–82 (1980).
- Wright, S. H., Hirayama, B., Kaunitz, J. D., Kippen, I. & Wright, E. M. Kinetics of sodium succinate cotransport across renal brush-border membranes. *J. Biol. Chem.* **258**, 5456–5462 (1983).
- Griffith, D. A. & Pajor, A. M. Acidic residues involved in cation and substrate interactions in the Na⁺/dicarboxylate cotransporter, NaDC-1. *Biochemistry* **38**, 7524–7531 (1999).
- Yao, X. & Pajor, A. M. The transport properties of the human renal Na⁺-dicarboxylate cotransporter under voltage-clamp conditions. *Am. J. Physiol. Renal Physiol.* **279**, F54–F64 (2000).
- Pajor, A. M. Conformationally sensitive residues in transmembrane domain 9 of the Na⁺/dicarboxylate co-transporter. *J. Biol. Chem.* **276**, 29961–29968 (2001).
- Joshi, A. D. & Pajor, A. M. Role of conserved prolines in the structure and function of the Na⁺/dicarboxylate cotransporter 1, NaDC1. *Biochemistry* **45**, 4231–4239 (2006).
- Prakash, S., Cooper, G., Singhi, S. & Saier, M. H. The ion transporter superfamily. *Biochim. Biophys. Acta.* **1618**, 79–92 (2003).
- Hall, J. A. & Pajor, A. M. Functional characterization of a Na⁺-coupled dicarboxylate carrier protein from *Staphylococcus aureus*. *J. Bacteriol.* **187**, 5189–5194 (2005).
- Hall, J. A. & Pajor, A. M. Functional reconstitution of SdcS, a Na⁺-coupled dicarboxylate carrier protein from *Staphylococcus aureus*. *J. Bacteriol.* **189**, 880–885 (2007).
- Youn, J. W., Jolkver, E., Kramer, R., Marin, K. & Wendisch, V. F. Identification and characterization of the dicarboxylate uptake system DccT in *Corynebacterium glutamicum*. *J. Bacteriol.* **190**, 6458–6466 (2008).
- Strickler, M. A., Hall, J. A., Gaiko, O. & Pajor, A. M. Functional characterization of a Na⁺-coupled dicarboxylate transporter from *Bacillus licheniformis*. *Biochim. Biophys. Acta* **1788**, 2489–2496 (2009).
- Liu, Q., Zhang, Z. & Hendrickson, W. A. Multi-crystal anomalous diffraction for low-resolution macromolecular phasing. *Acta Crystallogr. D* **67**, 45–59 (2011).
- Zhang, F. F. & Pajor, A. M. Topology of the Na⁺/dicarboxylate cotransporter: the N-terminus and hydrophilic loop 4 are located intracellularly. *Biochim. Biophys. Acta* **1511**, 80–89 (2001).
- Hunte, C. *et al.* Structure of a Na⁺/H⁺ antiporter and insights into mechanism of action and regulation by pH. *Nature* **435**, 1197–1202 (2005).
- Yamashita, A., Singh, S. K., Kawate, T., Jin, Y. & Gouaux, E. Crystal structure of a bacterial homologue of Na⁺/Cl[−]-dependent neurotransmitter transporters. *Nature* **437**, 215–223 (2005).
- Faham, S. *et al.* The crystal structure of a sodium galactose transporter reveals mechanistic insights into Na⁺/sugar symport. *Science* **321**, 810–814 (2008).
- Johnson, Z. L., Cheong, C. G. & Lee, S. Y. Crystal structure of a concentrative nucleoside transporter from *Vibrio cholerae* at 2.4 Å. *Nature* **483**, 489–493 (2012).
- Inoue, K., Zhuang, L., Maddox, D. M., Smith, S. B. & Ganapathy, V. Human sodium-coupled citrate transporter, the orthologue of *Drosophila Indy*, as a novel target for lithium action. *Biochem. J.* **374**, 21–26 (2003).
- Pajor, A. M. & Sun, N. N. Single nucleotide polymorphisms in the human Na⁺-dicarboxylate cotransporter affect transport activity and protein expression. *Am. J. Physiol. Renal Physiol.* **299**, F704–F711 (2010).

Supplementary Information is available in the online version of the paper.

Acknowledgements We are grateful to M. Punta and B. Rost for bioinformatics analysis of membrane transporters, to J. Love and B. Kloss for assistance in cloning, and to the staff at beamlines X4, X25 and X29 of the National Synchrotron Light Source in the Brookhaven National Laboratory and at the 23ID at the Advanced Photon Source at the Argonne National Laboratory for assistance in X-ray diffraction experiments, and to J. Llodra for help with artwork. We thank B. K. Czyzewski, W. A. Hendrickson, N. K. Karpowich, F. Mancina and J. J. Marden for discussions and for participating in synchrotron trips. This work was financially supported by National Institutes of Health grants U54-GM075026, R01-DK073973, R01-GM093825 and R01-MH083840.

Author Contributions R.M. and D.-N.W. designed the project. R.M. did all the experiments, with assistance from G.G.G. in diffraction data processing, phasing and structure refinement, and from Q.L. in phasing. R.M. and D.-N.W. wrote the manuscript.

Author Information The atomic coordinates and structure factors have been deposited in the Protein Data Bank under accession code 4F35. Reprints and permissions information is available at www.nature.com/reprints. The authors declare no competing financial interests. Readers are welcome to comment on the online version of the paper. Correspondence and requests for materials should be addressed to D.-N.W. (wang@saturn.med.nyu.edu).

METHODS

Expression and purification. A transporter protein (Q57486) from *Haemophilus influenzae*, a homologue of human NaDC1 and *Drosophila* INDY, was expressed, purified and characterized using standard protocols^{31–33}. The *Haemophilus* protein was then nominated to the cloning core of the New York Consortium of Membrane Protein Structure for the cloning of its homologues³⁴. Among the 31 clones tested, the homologous protein from *V. cholerae* (AAF95939; VcINDY) was found to give the highest expression levels. For overexpression, *E. coli* BL21-AI cells (Invitrogen) were transformed with a modified pET vector³⁴ encoding N-terminal 10X His-tagged VcINDY. After collecting the cells, membranes were solubilized in 1.2% *N*-decyl- β -maltoside (DM) and the protein was purified on a cobalt affinity column (TALON, Clontech), followed by preparative size-exclusion chromatography in buffer containing 50 mM Tris, pH 7.5, 100 mM NaCl, 50 mM lithium citrate, 5% glycerol and 0.15% DM. Seleno-L-methionine (SeMet) protein was produced and purified in the same way but in *E. coli* B834DE3 (Novagen) cells grown in minimal media containing SeMet. For the determination of the oligomeric state of purified VcINDY protein in detergent solution, protein samples were injected onto an analytical size-exclusion chromatography column (Shodex KW804, Thomson) on high-performance liquid chromatography (HPLC; Shimadzu) in buffer containing 200 mM Na₂SO₄, 50 mM Tris, pH 8.0, 3 mM NaN₃ and 0.05% *N*-dodecyl- β -maltoside³¹. Transporter proteins with similar molecular masses and well-characterized oligomeric states, the monomeric glycerol-3-phosphate transporter from *E. coli* (GlpT)³¹ and the dimeric tetracycline transporter from *Bacillus subtilis* (TetL)³⁵, were used as standards. To measure the effects of various compounds in thermostabilizing VcINDY, purified protein samples were incubated in the presence of each of these compounds (50 mM concentration) at 44 °C for 10 min, followed by size-exclusion chromatography analysis on HPLC^{31,36}.

Transport assays. Transport activity of VcINDY at 25 °C was characterized using a whole-cell assay of [¹⁴C]succinate uptake^{13,22,37}. *E. coli* BL21 p-Lys cells were transformed with the wild-type gene, mutants or empty vector. Sixty-millilitre cultures were grown to $D_{660\text{ nm}} \sim 0.7$, induced with isopropyl- β -D-thiogalactoside for 2–2.5 h and collected. Cells were washed twice with wash buffer (50 mM K-phosphate, pH 7.5) and resuspended in the same buffer to $D_{660\text{ nm}} \sim 10$. Transport was initiated by mixing the cell suspension with tenfold concentrated assay buffer at a ratio of 9:1 to yield a final concentration of 5 mM NaCl (LiCl or KCl at the same concentration), 95 mM Tris, pH 7.5 and 5 μ M [¹⁴C]succinate (stock, 54 μ Ci mmol^{−1}; Moravec Biochemicals). Aliquots of 100 μ l were taken at various time points covering the range from 0 to 5 min and the transport reaction was terminated by collecting the cells on 0.45 μ m nitrocellulose filters under vacuum, followed by washing with 4 ml of ice-cold wash buffer. The filters were incubated for 10 min in scintillation fluid before measuring radioactivity with a liquid scintillation counter^{38,39}. For the competition assay, the final buffer also included 1 mM of the test compound. For the activity measurements of mutants, their expression levels in *E. coli* cells were verified by western blot using India HisProbe-HRP (Pierce).

Crystallization. Crystals were grown at 18 °C in hanging-drop vapour diffusion by mixing equal amounts of sizing column-purified protein at 4–6 mg ml^{−1} (supplemented with 0.12% of *N*-nonyl- β -D-glucoside) and reservoir solution (29% (v/v) polyethylene glycol 1000, 50 mM lithium citrate and 50 mM MOPS, pH 6.5).

Crystallography. Crystal screening was carried out at the beamlines X25 and X29 of the National Synchrotron Light Source (NSLS) in the Brookhaven National Laboratory and at 23ID at the Advanced Photon Source at the Argonne National Laboratory. X-ray diffraction data were collected at NSLS beamline X4A with a Quantum Q4R CCD detector. There are four protein molecules in the asymmetric unit, and each contains 23 methionine residues. To collect anomalous diffraction data from SeMet crystals, the wavelength was tuned to 0.9792 Å as verified by fluorescence scan on crystals. Inverse-beam mode data collection was used and four complete diffraction data sets were collected from three crystals, with two data

sets from each end of a long crystal. The phases were obtained using a multi-crystal single-wavelength anomalous dispersion (SAD) phasing method^{23,40}. In brief, anomalous diffraction data sets were indexed and integrated using XDS⁴¹. To enhance anomalous signals, integrated intensities were scaled, analysed and merged by Scala⁴² to 3.2 Å resolution. Selenium substructure was determined by SHELXD⁴³ from the merged data. Attempts were made with various numbers of expected selenium sites, different high-resolution cutoffs and various cutoffs for the normalized structure factor E_{min} . The 92-site selenium substructure, corresponding to four molecules in the crystallographic asymmetric unit cell, was identified from the merged data that was truncated at 4.1 Å for high-resolution cutoff and 1.5 for E_{min} cutoff. The substructure was refined and completed for SAD phasing by PHASER⁴⁴ with the merged data. The SAD phases were then density modified by DM⁴⁵ to break the phase ambiguity, resulting in electron-density maps at 3.5 Å resolution of sufficient quality for model building. Model building was done in Coot⁴⁶. The first 18 residues at the N terminus and a fragment in a central loop (amino acids 240–251) were disordered in the crystals. For residues 252–259, only the backbone was visible, so a polyalanine model was constructed in that part. Model refinement to 3.2 Å resolution was accomplished using PHENIX⁴⁷ and CCP4⁴⁸ packages. For the bound citrate molecule in each of the four protein protomers in the crystallographic asymmetric unit, two have a B-factor of 90–100 Å², similar to that of the protein, whereas the other two have a B-factor of 120–137 Å². Structural figures were prepared using PyMOL⁴⁹ and Coot.

- Auer, M. *et al.* High-yield expression and functional analysis of *Escherichia coli* glycerol-3-phosphate transporter. *Biochemistry* **40**, 6628–6635 (2001).
- Li, X. D. *et al.* Monomeric state and ligand binding of recombinant GABA transporter from *Escherichia coli*. *FEBS Lett.* **494**, 165–169 (2001).
- Wang, D. N. *et al.* Practical aspects of overexpressing bacterial secondary membrane transporters for structural studies. *Biochim. Biophys. Acta* **1610**, 23–36 (2003).
- Love, J. *et al.* The New York Consortium on Membrane Protein Structure (NYCOMPS): a high-throughput platform for structural genomics of integral membrane proteins. *J. Struct. Funct. Genomics* **11**, 191–199 (2010).
- Safferling, M. *et al.* The TetL tetracycline efflux protein from *Bacillus subtilis* is a dimer in the membrane and in detergent solution. *Biochemistry* **42**, 13969–13976 (2003).
- Boulter, J. M. & Wang, D. N. Purification and characterization of human erythrocyte glucose transporter in decylmaltoside detergent solution. *Protein Expr. Purif.* **22**, 337–348 (2001).
- Hirato, T., Shinagawa, M., Ishiguro, N. & Sato, G. Polypeptide involved in the *Escherichia coli* plasmid-mediated citrate transport system. *J. Bacteriol.* **160**, 421–426 (1984).
- Law, C. J., Yang, Q., Soudant, C., Maloney, P. C. & Wang, D. N. Kinetic evidence is consistent with the rocker-switch mechanism of membrane transport by GlpT. *Biochemistry* **46**, 12190–12197 (2007).
- Law, C. J. *et al.* Salt-bridge dynamics control substrate-induced conformational change in the membrane transporter GlpT. *J. Mol. Biol.* **378**, 828–839 (2008).
- Liu, Q. *et al.* Structures from anomalous diffraction of native biological macromolecules. *Science* **336**, 1033–1037 (2012).
- Kabsch, W. Xds. *Acta Crystallogr. D* **66**, 125–132 (2010).
- Evans, P. R. An introduction to data reduction: space-group determination, scaling and intensity statistics. *Acta Crystallogr. D* **67**, 282–292 (2011).
- Sheldrick, G. M. Experimental phasing with SHELXC/D/E: combining chain tracing with density modification. *Acta Crystallogr. D* **66**, 479–485 (2010).
- Read, R. J. & McCoy, A. J. Using SAD data in Phaser. *Acta Crystallogr. D* **67**, 338–344 (2011).
- Cowtan, K. D. & Zhang, K. Y. Density modification for macromolecular phase improvement. *Prog. Biophys. Mol. Biol.* **72**, 245–270 (1999).
- Emsley, P. & Cowtan, K. Coot: model-building tools for molecular graphics. *Acta Crystallogr. D* **60**, 2126–2132 (2004).
- Adams, P. D. *et al.* PHENIX: a comprehensive Python-based system for macromolecular structure solution. *Acta Crystallogr. D* **66**, 213–221 (2010).
- Winn, M. D. *et al.* Overview of the CCP4 suite and current developments. *Acta Crystallogr. D* **67**, 235–242 (2011).
- DeLano, W. L. The PyMOL User's Manual (DeLano Scientific, 2002).

CAREERS

RESEARCH COMMUNITY European expat scientists band together abroad **p.629**

@NATUREJOBS Follow us on Twitter for the latest news and features go.nature.com/e492gf

NATUREJOBS For the latest career listings and advice www.naturejobs.com

C. J. BURTON/CORBIS



ACADEMIA

Off the tenured track

The desires to pursue personal goals, escape university pressures or get off the grant-writing treadmill convince some US professors to leave the security of a tenured post.

BY KENDALL POWELL

At the beach in Mantoloking, New Jersey, in summer 2011, the possibilities of Colin Purrington's sabbatical year stretched out before him. Purrington, then an evolutionary biologist at Swarthmore College in Pennsylvania, intended to stay on campus and was almost giddy thinking of all the undergraduate research projects he had planned, with no teaching or service duties to interrupt them. And then it hit him like a 600-page textbook. When the year was over, he did not want to return to those duties — duties that had led to miserable all-nighters and family strain.

The next day, he asked his wife, the family's

main breadwinner, what she thought of him resigning his post to become a stay-at-home father to their two children. Looking up from a Sudoku puzzle, she replied: "Whatever you'd like." Purrington's on-campus misery made the decision easy. He walked away from his tenured position, and his 14 years at Swarthmore.

For many scientists in the United States, where tenure is most common, the decision comes with much more angst. Leaving a position that they worked for decades to attain, and that is often coveted as the pinnacle of academic achievement, is a huge step. It can also leave colleagues mystified, jealous, hurt and sometimes thinking the worst — imagining research misconduct or even a scandalous affair with a student. In interviews with

professors who have left their tenured posts in the past decade, *Nature* found that the reasons for such moves ranged from the very personal — no marital prospects in a small college town — to the loftiest goals of shaping national educational or science policy.

Almost all wanted to live in a more desirable location — an indication that the age-old view that academics must 'go where the jobs are' might not lead to long-term career satisfaction. Some tenure-leavers sought to improve the balance between work and family life, or wanted a better environment for research. Most emphasized that their colleagues did not drive them away: on the contrary, talented, passionate departmental comrades were treasured. But the evidence is clear: 'giving up' ►

hard-won tenure is indeed the right move for some. Here, four researchers explain why they are happy that they relinquished those coveted posts.

CREEPING TEACHING LOADS

Purrington's thoughts of leaving Swarthmore sprouted from discussions about how to keep up with the teaching and mentoring demands of a department in which the number of students was rapidly growing. "Our department prided itself on transforming our students into loving biology for the rest of their lives," he says.

At the start of 2011, faculty members from other universities delivered a ten-year review of activities in Swarthmore's biology department. It showed how much job creep had occurred as student's demands rose — resulting in a proliferation of lab and lecture courses, requests for letters of recommendation and meetings with students, hours of summer research mentoring and extra time taken to accommodate students with special needs.

Purrington, a fastidious lecturer, also spent hours on interactive course-organizing websites such as Blackboard and Moodle. He loved teaching, but the associated preparation and paperwork was drowning him. (This year, Swarthmore actually elected to reduce its faculty teaching load from five courses per year to four.)

Purrington's wife is a physician and safety-data analyst for global pharmaceutical company Johnson & Johnson in Horsham, Pennsylvania. She has a one-hour commute, and her high-ranking position means that she is 'plugged in' almost around the clock. That makes Purrington the main on-call parent for their daughter, now 12, and son, 14. As his wife climbed the corporate ladder and his own departmental and teaching responsibilities grew, the situation became untenable. "It was doable, but it was not enjoyable," says Purrington.

When he resigned from Swarthmore last autumn, many colleagues reacted with disbelief. When they cross paths, some still ask him when he is returning 'from leave'. Purrington says that many people in academia can find a "happy, sustainable balance", but that they usually have to have a spouse with more flexibility, live-in domestic help, no children or grown children. "It was hard for me to find that balance in a department where everyone was on the edge of going insane even when most

of them had more accommodating situations than mine at home," he says.

He warns young scientists that tenured positions require personal sacrifices, especially for dual-career couples. "No one at Swarthmore had those big blocks of time in the lab to get updates on projects, look at data, make a graph," he says. "A lot of faculty members choose to come in on weekends or at night. I did that, too, when my kids were too little to care."

SCALING UP

Christof Koch, a leading scientist in the study of consciousness, spent most of the past 25 years thinking that he would have to be carried out of his Pasadena office at California Institute of Technology (Caltech) boots first on a stretcher. He adored the pure academic lifestyle, working with sharp students and brilliant scientific minds, leading a group of 25 people and publishing high-impact papers.

But in 2011, a divorce coincided with the desire for a challenge and a change of scenery. "As a mountain climber, I would say, I'm looking for a new Annapurna," he says, referring to a notorious 8,091-metre peak in Nepal.

"It was a very difficult decision to leave academia and I'm still grappling with it," says Koch. But the Allen Institute for Brain Science in Seattle, Washington, needed a chief scientific officer to head up a 250-researcher, ten-year effort to define the inner workings of the mouse visual cortex, funded with an initial US\$300 million. Koch felt that the organization offered him a new way to do neuroscience.

"That's something you can't do at a university," he says. Neuroscientists in academia, he suggests, tends to tackle questions in small units of investigator-driven labs, not big team projects. As Koch sees it, that method rewards individual discoveries but provides few paths for integrating findings into comprehensive models.

"This shift happened 50 years ago in physics. It's a huge challenge. It could fail [in neuroscience]," he notes. Novelty, after all, is what provides a publication, a PhD, grant funding and tenure. "I don't actually think the academic system is broken — it produces spectacular answers. It just needs to be complemented when dealing with unimaginable complexity," he says, referring to the brain in particular.

Koch's last day in Pasadena is on 8 April. "Caltech will take my Superman cape away from me. I'll be a mere, untenured mortal like most people on the planet," he jokes. He says that universities could benefit from greater accountability to deadlines and milestones, such as those he will have to meet for online data releases at the Allen Institute. "I'm a risk-taker," he says of leaving tenure. It was time to push up a new ascent.

TIME FOR RESEARCH

When she took a competitive teaching position at Lawrence University in Appleton, Wisconsin, straight after finishing her PhD,

mathematician Eugenie Hunsicker underestimated how much she would miss her research. Five years later, when she was up for tenure at Lawrence, Hunsicker realized that she actually wanted a position at a research-focused university. "As teaching jobs go, it was quite a good job," she says. "But I wasn't able to work on my research as much as I wanted because there were no graduate students" — a requirement for her work on difficult partial differential equations, which can model the evolution of processes or particles in physical or biological systems, but are notoriously hard to solve.

Hunsicker knew that tenure would give her better leverage on the job market. But, she says, what she had to do to get tenure at a liberal arts college versus apply for a research position were "diametrically opposed". So she focused on her tenure application at Lawrence first. As soon as it was in, and her tenure had been granted, Hunsicker began gathering her research materials for a job search.

In 2005, while on a honeymoon tour of England, Hunsicker spied an advertisement for a job at Loughborough University, UK. (When she asked British friends about the university, they replied with what every mathematician wants to hear: "It's known for sport!") She applied almost on a whim and was surprised when an interview and then an offer followed — all before her US applications had even been processed.

The teaching load was lighter than at Lawrence, similar to that in US research univer-

sity positions. But there was one key difference. "I knew in the United States, I would have to go through tenure again. In the United Kingdom, there is just a three-year probation period and the expectations are really clear." Hunsicker would be hired for a permanent position providing that she published roughly one paper per year, received good teaching evaluations from students and carried



"In the past ten years, it's become even clearer that my decision was correct."

Jackie Ying

her share of departmental duties such as serving on search committees.

Hunsicker has no regrets about snapping up the post at Loughborough. She is currently doing her own research and advising three PhD students.

"I'm quite happy here. Given an equally good job, why would I go through the tenure process a second time?" She says that the ambiguousness of the requirements for getting tenure in the United States made her



"It was a very difficult decision to leave academia and I'm still grappling with it."

Christof Koch

very uncomfortable. “I worried about any little thing that might go wrong and sway that decision.”

TIRED OF CHASING GRANTS

Jackie Ying became a professor of chemical engineering at Massachusetts Institute of Technology (MIT) in Cambridge at the age of 26. By 35, she was a tenured full professor, a rising star in the field of nanomaterials, and flush with funding. But because her research group was large and diverse, she spent most of her energy simply applying to continue her grants. She spent 75–80 hours per week at work and still struggled to find time to prepare journal manuscripts or to help students to finish dissertations. But she loved academia, and wasn't looking to move — until an unusual opportunity popped up.

In 2002, Philip Yeo, then chairman of Singapore's Agency for Science, Technology and Research (A*STAR), asked her to lead the new Institute of Bioengineering and Nanotechnology (IBN). Ying had lived in Singapore as a child. She knew it was a cosmopolitan city with a population of 5.3 million people, 38% of whom are transplants from other parts of the world.

Yeo took Ying to Singapore and showed her the immense hole that would become Biopolis, a nine-building complex of public and private labs with more than 2,000 staff members including researchers. Singapore's government is ambitious and results-oriented. “When it wants to do something, it will devote the resources to make it happen,” says Ying. At the time of Yeo's offer, she could see the writing on the wall — US funding for individual investigators was dwindling as competition grew. “In the past ten years, it has become even clearer that my decision was correct. The batting average for a grant proposal has become very low.”

As executive director of the IBN, Ying spends more time working on journal articles and conferring with her research group than she did at MIT, despite her administrative work. She directs research projects such as developing paper-based diagnostic test kits that would work like home pregnancy tests to monitor glucose, cholesterol or infections. “The way we structure our research groups is problem-centric, instead of principal-investigator-centric.”

When she left MIT in 2003, people thought Ying was crazy, she recalls. “But I had a long career in front of me.” The assured funding at the IBN has allowed her to pursue interdisciplinary projects with real-world applications — and resulted in more than 120 patents. “I actually thought it was a very important career move that would change the way I do research and live my life.” ■

Kendall Powell is a science writer based in Lafayette, Colorado.

RESEARCH COMMUNITY

Expatriate scientists get organized

European researchers form support networks abroad.

BY MICHELE CATANZARO

The Portuguese government had an unexpected critic when it proposed austerity measures including cuts to fellowships that pay for researchers to do PhD studies abroad. In June, the Portuguese Association of Researchers and Students in the United Kingdom (PARSUK) filed a complaint with the Foundation for Science and Technology, Portugal's main public research funding body. PARSUK showed that university and tuition fees for graduate students at some UK institutions cost more than the Portuguese government would provide after austerity measures; the foundation's president told PARSUK that he would consider scaling back the cuts.

Organizations of southern European scientists working abroad have proliferated in the past few years. Expatriates founded the Society of Spanish Researchers in the United Kingdom (SRUK/CERU) in June 2011 and the Society of Spanish Researchers in the Federal Republic of Germany (CERFA) in June 2012; the Association of Italian Scientists in the United Kingdom (AIS-UK) will be registered soon. The groups aim to help expats with language barriers, advise on the best places to apply for PhD and postdoc positions and organize networking events. But they also want to make a difference at home by influencing policy, enhancing the visibility of people working abroad and improving funding and opportunities.

Financial strain has been one motivator: in 2010, total Portuguese science spending declined for the first time in almost a decade. The Spanish government has cut its science budget by 39% from 2009 levels. And this year, Italy approved major cuts to research-institute budgets, with more possibly on the way (see *Nature* <http://doi.org/jrn;2012>). Scientists often leave countries hit hard by recessions: Spain, for example, has seen net emigration since 2011 after years of net immigration, says its National Institute of Statistics. Expat groups can help scientists to find opportunities abroad.

PARSUK was founded in 2008, following Luso 2007, a networking meeting of Portuguese scientists in Cambridge, UK. Since then, the 450-member group has set up annual gatherings at which researchers, politicians and company representatives from Britain and Portugal discuss ways to collaborate and cooperate. “We want to use knowledge



GETTY/M. ARCHER

gathered abroad to implement new approaches to research in Portugal,” says David Tomaz, president of PARSUK and an immunology PhD student at Imperial College London.

Last month, representatives of SRUK/CERU met a delegation from the Spanish National Quality and Accreditation Evaluation Agency in London to discuss how Spain could optimize distribution of shrinking public funds using aspects of Britain's research-evaluation systems (see *Nature* 457, 624–625; 2009). The group has spoken to the media and politicians, says Francisco Hernández, a neuroscience PhD student at the University of Cambridge and one of 94 SRUK/CERU members. This year, one of Hernández's blog posts spawned a petition for Spanish tax forms to include an option to give 0.7% of a taxpayer's contribution to research; it has collected almost 300,000 signatures.

Associations also aim to provide practical help. CERFA offers “logistic and administrative advice to people moving to Germany: from finding a house to understanding a health insurance contract in German”, says Raúl Delgado-Morales, president of the group and a biology postdoc at the Max Planck Institute for Psychiatry in Munich. CERFA, which has 50 members, plans to draw up a list of Spanish researchers in Germany for collaboration opportunities.

The AIS-UK wants to compile a database of collaborations among Italian and British scientists to raise awareness of the “vast pool of highly skilled Italians trained in prestigious UK universities”, says Emanuele Cotroneo, a biology postdoc at Imperial who backs creation of the group. “Some Italian scientists in the United Kingdom may be willing to return to Italy if they are offered positions appropriate to their experience.” But Cotroneo does not advocate UK brain drain, he says: “We think that strengthening links between countries will facilitate both emigrating and going back.” ■

GOLIATH FALLS

Identity crisis.

BY TAIK HOBSON

I'm tucked so far up Shifu's axila that — right before his arm completes its arc — my olfactory sensors experience overload.

SLAM

"Who are you?"

Contact with the floor happens in optimal hand-forearm-shoulder blade-flank sequence, while Shifu's question — the same one for the past two months — arrives somewhere in there like a distant echo. Rolling to my side, I get to my feet, right servo aimed at the forehead of the man in the white robe across from me. Saturation can't be too far off now, I think, right before I rush him and, like a closed circuit, the sequence repeats itself. Evasion. Engagement (re: olfactory alert) and Execution.

SLAM

Physical analysis of Shifu's Execution concludes an improbable amount of force; it just isn't possible for his body to manoeuvre that amount of energy sans joint augmentation. And yet every time, I end up on the ground. From what I have seen, skill level tends towards a certain personality type; the one that Shifu happens to be demonstrating is No Ego.

"Who are you?"

For me, he is my last hope — SLAM — no one else will train with me — SLAM — I do not know why he puts himself in harm's way — SLAM — the only explanation he has given me — SLAM — is this: that I am running out of time.

"Who are you?"

Shifu is, of course, referring to the time I have left to attain my upgrade; unless I achieve some higher level of understanding — and do so soon — I will have to enrol in a new, entirely different programme.

But I came here to learn Kung Fu.

There was a time when upgrades happened as a matter of course, withheld — if ever — by nothing more than a simple password; now the Diversity Dictum would see each unit further their pursuit of individuality and self-expression through subjective, real-time experiences. I am the first student to enrol in the Qi programme; a non-verbal combat narrative, and new to the Diversity Curriculum, its future

inclusion hinges upon my success. A teacher, I have learnt, must have his students.

"Their spines will regrow," I have been assured, although the two absent members from the training hall are muted reminders of how far things can go.

Tumbling Goliath is the first technique by which each student may demonstrate Kung

fu, Shifu doesn't bother to hide his disappointment.

Who am I?

I recall my meeting with the Founder, long before I was enrolled. I do not have the soundbite, but I remember what he said. "That you are a machine is not a problem."

Shifu starts to speak, but the Founder's words are all I hear. "That you think to act like a man — that is a problem."

I AM NOTHING.

I have not heard my voice for so long that I can barely recognize the sound of it. Analysis Status flashes: SATURATION, when Shifu starts coming at me.

I know that this is the end; perhaps I should have chosen a less abstract programme... the Ramsay Culinary Kitchen, for instance. Now, even as I move into position, one by one I feel my tension points break with resignation. I. Am. Nothing.

Evasion. Engagement —

Shifu rolls to a stand but doesn't say a word; from what I can see, nothing looks broken. No time to analyse; here he comes again. When next I Execute

I am neither restrained nor resigned; instead, I let his body travel the length of its intended attack, before guiding him into his fall. Unlike every other archived entry, in these last two attempts it is as though I am doing nothing at all.

And then I know who I am. I know how Shifu does what he does without joint augmentation. And I know where the force comes from.

SLAM

I am neither machine nor man; 'I' am an extension of matter. And my movements, just like Shifu's, are momentarily in sync with the physical properties of the Universe.

Gravity, for example.

All the attention in the training hall is directed at the two of us. Shifu, I can see, is smiling beneath a headful of sweat. Of course, I had to know, so I asked him.

NOW WHAT?

"Now?" Readjusting his robe, Shifu nods to one of his students, who in turn starts for a corner of the hall, where two tall panels of solid iron sit shut behind a vaulted lock.

"Release the Goliath." ■

Taik Hobson lives in Japan, where he remains well acquainted with the floor of his dojo.



JACEY

Fu competency; with the passing of the Founder it remains a strictly implemented requirement, despite the steep drop in enrolment. It is composed of three separate movements and all students start by practising with a partner.

"Who are you?"

As part of the Qi programme, I have unlimited access into my own memories. Free to review and reenact my lessons, importantly, I am allowed to remove all that is unnecessary from my practice; in itself perhaps the hardest lesson of all.

SLAM

The first thing I erased was my name.

Like everything else, Kung Fu exists within the bounds of information; each time I fall, motion sensors collate the data to form the parameter whereby I may tease apart Shifu's technique. Yet with each parametric saturation — when I am allowed a glimpse into what it is I must learn — I feel that I am drifting farther and farther away from my goal. Meanwhile, the findings are unchanged: just not possible.

Now it is Shifu's turn to attack me; it is my turn to receive and I am afraid to hurt this man with No Ego. Even as I Engage I know that my Execution will be unsatisfactory — so I do it as gently as I can. Crawling to his

➔ NATURE.COM

Follow Futures:

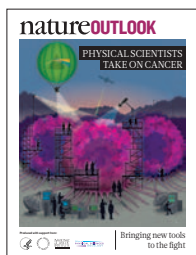
🐦 @NatureFutures

📘 go.nature.com/mtoodm

natureOUTLOOK

PHYSICAL SCIENTISTS TAKE ON CANCER

22 November 2012 / Vol 491 / Issue No. 7425



Cover art: Nik Spencer

Editorial

Herb Brody,
Lauren Gravitz,
Michelle Grayson,
Tony Scully,
Nick Haines

Art & Design

Wes Fernandes,
Alisdair Macdonald,
Nicola Hawes
Andrea Duffy

Production

Donald McDonald,
Yvonne Strong, Kelly
Hopkins, Leonora
Dawson-Bowling

Sponsorship

Reya Silao,
Yvette Smith

Marketing

Elena Woodstock,
Hannah Phipps

Project Managers

Claudia Deasy,
Christian Manco

Art Director

Kelly Buckheit Krause

Magazine Editor

Tim Appenzeller

Editor-in-Chief

Philip Campbell

Despite a huge worldwide research effort, cancer's mortality rate has barely changed over the past few decades. But as we report in this Outlook, collaborations between biologists and physical scientists are bringing fresh perspectives that are starting to bear fruit.

Cancer research was a joint enterprise between physicists and life scientists until about 40 years ago, when the focus switched to the molecular, genetic and cellular aspects of the disease (page S50). Robert Gatenby argues that so much focus on the underlying genetics of cancer may be obscuring the bigger picture (S55). New research backs him up, and shows that cancer is not strictly a disease of genetic mutations — its development and spread are influenced by the physical forces exerted on cells (S56).

Computer modelling is providing a better understanding of the interplay between physical, genetic and cellular aspects of cancer (S62). Mathematical modelling leads to better predictions of how a tumour will evolve, and which drug regimens will be most effective (S66). And nanotechnology is yielding drug carriers that can transport chemotherapies to their targets more accurately (S58), and diagnostic tools to identify cancer at an earlier stage (S64). One start-up company that uses this diagnostic approach is Applied Proteomics, co-founded by a cancer biologist and a computer scientist (S52).

Until we unravel cancer's basic principles, the battle can only progress in inches, rather than in miles. According to oncologist David Agus and Nobel prizewinning physicist Murray Gell-Mann, such leaps forward require grand theories, an encouraging publishing environment and researchers willing to test big ideas (S61).

We acknowledge the financial support of the Office of Physical Sciences–Oncology in the National Cancer Institute's Center for Strategic Scientific Initiatives in producing this Outlook. As always, *Nature* has full responsibility for all editorial content.

Lauren Gravitz
Guest Editor

CONTENTS

S50 ONCOLOGY

Getting physical

Cancer research goes back to the future

S52 MEGADATA

The odd couple

Opposites attract to solve the protein problem

S55 PERSPECTIVE

Finding cancer's first principles

Robert Gatenby says genetic data just get in the way

S56 MECHANICS

The forces of cancer

Getting to grips with flexible cells

S58 NANOTECHNOLOGY

Carrying drugs

A little help with targeting therapies

S61 PERSPECTIVE

Meeting of minds

David Agus and Murray Gell-Mann find that two heads are better than one

S62 MODELLING

Computing cancer

A simulating experience

S64 DIAGNOSTICS

Playing detective

The clues to spotting cancer earlier

S66 MATHEMATICAL MODELLING

Forecasting cancer

One step ahead of evolution

COLLECTION

S68 Nanopore-based detection of circulating microRNAs in lung cancer patients

Yong Wang, Dali Zheng, Qiulin Tan, Michael X. Wang and Li-Qun Gu

S75 The nanomechanical signature of breast cancer

Marija Plodinec et al.

S84 Mechanical waves during tissue expansion

Xavier Serra-Picamal et al.

S91 The Cancer Cell Line Encyclopedia enables predictive modelling of anticancer drug sensitivity

Jordi Barretina et al.

Nature Outlooks are sponsored supplements that aim to stimulate interest and debate around a subject of interest to the sponsor, while satisfying the editorial values of *Nature* and our readers' expectations. The boundaries of sponsor involvement are clearly delineated in the *Nature Outlook* Editorial guidelines available at http://www.nature.com/advertising/resources/pdf/outlook_guidelines.pdf

CITING THE OUTLOOK

Cite as a supplement to *Nature*, for example, *Nature* Vol XXX, No. XXXX Suppl. Sxx–Sxx (2012). To cite previously published articles from the collection, please use the original citation, which can be found at the start of each article.

VISIT THE OUTLOOK ONLINE

The *Nature Outlook Physical Scientists Take On Cancer* supplement can be found at http://www.nature.com/nature/outlook/physical_scientists_cancer

All featured articles will be freely available for 6 months.

SUBSCRIPTIONS AND CUSTOMER SERVICES

For UK/Europe (excluding Japan): Nature Publishing Group, Subscriptions, Brunel Road, Basingstoke, Hants, RG21 6XS, UK. Tel: +44 (0) 1256 329242. Subscriptions and customer services for Americas – including Canada, Latin America and the Caribbean: Nature Publishing Group, 75 Varick St, 9th floor, New York, NY 10013-1917, USA. Tel: +1 866 363 7860 (US/Canada) or +1 212 726 9223 (outside US/Canada). Japan/China/Korea: Nature Publishing Group – Asia-Pacific, Chiyoda Building 5-6th Floor, 2-37 Ichigaya Tamachi, Shinjuku-ku, Tokyo, 162-0843, Japan. Tel: +81 3 3267 8751.

CUSTOMER SERVICES

Feedback@nature.com
Copyright © 2012 Nature Publishing Group

Getting physical

Physics, maths and evolutionary biology are among the scientific disciplines providing cancer research with fresh perspective and therapeutic approaches.

BY JENNIE DUSHECK

Biology has always had its roots firmly planted in the physical world. From the earliest scientific experiments to the most recent biomedical inventions, natural philosophers and modern biologists have used all the available tools of science to study living organisms. Optics, classical mechanics and mathematics have all informed the study of life.

With the rise of biochemistry, however, the application of biology became narrower and more specific. The power and spectacular success of molecular biology — from elucidating gene function to exposing complex molecular cascades — invigorated this approach. Yet as biologists developed the tools to probe deeper into gene expression pathways, they began to neglect the big picture, a world of whole cells, tissues and organisms.

As biology begins to confront the limits of the molecular approach — which has yielded vast amounts of data but not always clear understanding — some scientists have returned to a more biomechanical view of life, and their research is starting to bear fruit. Nowhere has this change been more evident than in the field of cancer research. Cell biologist Cynthia Reinhart-King, whose lab at Cornell University studies the disruption of tissue architecture in cancer, says: “The kind of work I do in cell mechanics is often considered a new field, but if you actually look at it historically, there was a big population of scientists doing it in the 1930s, 1940s and 1950s.” That older research laid a lot of important ground work, she says. “But now we have tools that allow us to probe much deeper.”

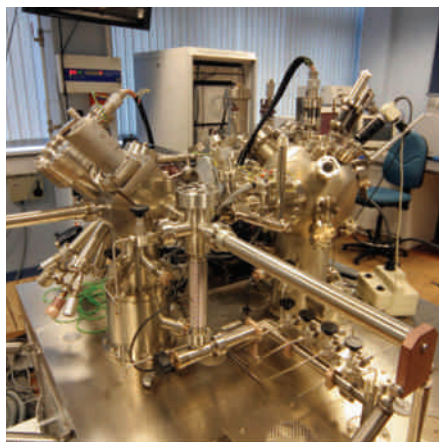
The move towards a more physical approach to cancer research stems in part from a deep well of disappointment with the war on cancer. In the 1950s and 1960s, lung cancer rates among men skyrocketed, the result of a 40-fold increase in smoking between 1910 and 1965. Spurred by these sobering statistics, President Nixon signed the US National Cancer Act in 1971, which more than doubled the annual funding for the National Cancer Institute (NCI) in just two years and charged the institute with finding a cure for cancer.

But the miracle drug never materialized. Since the 1950s, age-adjusted cancer mortality rates have declined by only 11%. Prevention, screening and successes with a handful

of cancers have saved millions of lives, but the prognosis for someone with metastatic cancer is as grim today as it was 50 years ago. The sense of failure is palpable. In 2008, *Newsweek* ran a story titled “We Fought Cancer... And Cancer Won.” When cancer geneticist Harold Varmus became director of the NCI in 2010, he told an audience: “We have not succeeded in controlling cancer as a human disease.”

TURNING TO PHYSICS

By the mid-2000s, Anna Barker, then deputy director of the NCI, noticed that many physicists, engineers and mathematicians were beginning to think about cancer, and she decided to harness their skills. “We had reached an inflection point where we knew enough about the biology to bring in other fields,” Barker says. In



The scanning tunnelling microscope gives researchers a nanoscale view of cancer.

2009, the NCI issued grants to 12 interdisciplinary centres around the United States, where investigators from both the physical sciences and oncology collaborate to address questions in one of five areas: metastasis, microenvironment, information processing, energy use, and the evolution of cancer cells.

The United States is not alone in fostering such collaborations. Cross-disciplinary oncology research in Europe receives funding from the European Union, at a national level, and at the institutional level, reports Reinhart-King, who co-authored a study on cancer research in Europe¹. In some ways, European multidisciplinary research in oncology has a longer history and deeper roots, with clinicians, basic researchers and engineers at many institutions working

side by side in ways that would be unusual in the United States. But such endeavours were not explicitly funded until recently. Scientists from other fields bring an array of different kinds of knowledge and tools to cancer research. Some are specialists in microfluidics, nanoparticles, computer science or evolutionary biology, and many have started to reframe questions about cancer. “Most [molecular] biologists don’t think in three dimensions,” Barker says.

Biomedical engineer and cancer researcher Mauro Ferrari, president of the Methodist Hospital Research Institute in Houston, Texas, gives an example. Consider that two metastases from the same primary tumour are growing in the same organ yet respond differently to the same drug, he says. A biologist wonders how identical tumours could have different levels of drug resistance, or assumes that the two metastases are not identical. But the tumours are genetically identical — what differs is their three-dimensional position in the organ, he says.

“What’s missed is the physics part of the story,” Ferrari explains. The nanoparticles that deliver the drug can penetrate the organ and reach one tumour but not the other; the difference could be due to fluid dynamics, shear forces on the blood-vessel walls, the velocity of the drug particles, and the permeability of local tissues, among other things. “If you design particles with the right physics, it changes entirely where they go,” Ferrari says (see ‘Carrying drugs’, page S58)². “I can make particles of a certain type and they will concentrate in the lung, or I can make other particles that will go to the spleen.”

“As a cancer community, we are barking up the wrong tree,” he adds. We don’t need more drugs, just better ways of deploying the ones we have.

Mathematics and complexity theory are also becoming indispensable tools. Information flows from cell to cell, from tissue to tissue, and from macroenvironment to microenvironment and back, forming intricate feedback loops that are best understood using mathematical approaches. Computational biologist Franziska Michor of the Dana-Farber Cancer Institute Physical Sciences–Oncology Center in Boston, Massachusetts, designs mathematical models to predict, and perhaps to help prevent, the evolution of cancer cells towards drug resistance or metastasis (see ‘Forecasting cancer’, page S66). Each cell, she explains, has a set of probabilities: of dividing, of dying, or

REX FEATURES

A HELPING HAND FROM PHYSICS

Biology and the physical sciences have a long history of relying on each other for major advancements. In the late 1970s, however, molecular biology began to lose touch with its physical and mathematical roots.



1600s

New microscopes made by Galileo, Antonie van Leeuwenhoek and others magnify up to x500, revealing bacteria, spermatozoa, and the banded pattern of muscle fibres.

1865

Gregor Mendel uses combinatory mathematics to explain inheritance in pea plants, laying the foundation for genetics.



1920s

Mathematicians Alfred Lotka and Vito Volterra develop simple equations for predator-prey interactions, and R. A. Fisher lays the foundations for modern statistics, population genetics and the evolutionary synthesis.

1937

Dorothy Hodgkin exploits the new field of X-ray crystallography to solve the structure of cholesterol, as well as that of penicillin (1945), vitamin B12 (1955) and insulin (1969).



1940s

Donald Griffin and Robert Galambos discover echolocation in bats.

1953

Rosalind Franklin's X-ray crystallography measurements of DNA help James Watson and Francis Crick build a model of DNA.

1972

First recombinant DNA molecule.

1977

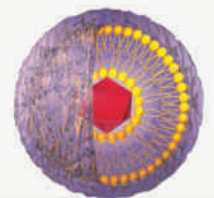
First genome sequenced.

1990

RNA interference.

1990

First gene therapy by W. French Anderson.



1995

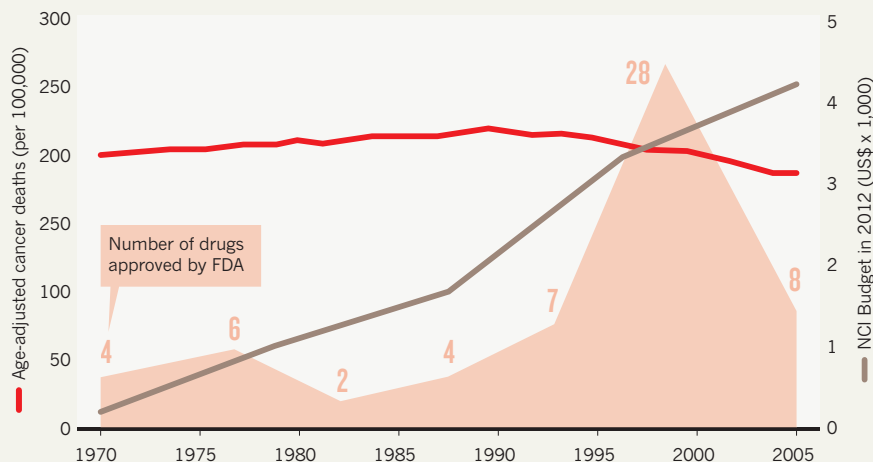
First nanoparticle drug carrier approved: Doxil.

2002

Mathematical models of the evolution of cancer cells.

DIMINISHING RETURNS OF CANCER RESEARCH

Number of cancer deaths versus spending on cancer research versus drug approval



of developing resistance. From these, it is possible to calculate the probability that a cell line will evolve resistance in different situations, and to suggest drug dosing strategies accordingly³. “One way to make progress in cancer,” Michor says, echoing Ferrari, “is just to use existing drugs in a smarter way.” Powerful insights are coming from the realization that cancer cells (as well as normal cells) respond strongly to their physical microenvironment. “Tumour cells respond to mechanical forces,” says Reinhart-King, “and those mechanical forces have been implicated in promoting cancer progression” (see ‘The forces of cancer,’ page S56)⁴.

DON'T STRESS

Physical stresses can provoke cells to turn on a set of stereotypical responses that lead to metastasis. These changes — including proliferation, increased motility and mutation — are the same strategies that bacteria use to escape danger, explains Thea Tlsty, a research oncologist at the University of California, San Francisco, and half of the duo that runs Princeton University's Physical Sciences–Oncology Center in New Jersey. “What we've been trying to do so far is kill the cancer cells,” says Tlsty. “But when you try to kill them, you stress them. And that gives the cells access to the primitive, fundamental pathways and the generation of diversity — a heterogeneity that is the hallmark of cancer.”⁵

Increasingly, researchers are wondering whether a soothing microenvironment for cancer cells might allow patients and their cancer cells to live in tenuous peace. There is considerable evidence that cancer already does this in a quarter or more of healthy adults⁵. “We are riddled with pre-malignancies and even little malignancies that don't yet manifest,” says Tlsty. “They don't express symptoms and they are being held under control. So many people die *with* these things, not *of* them.”

Cancer researchers now recognize that taming wild cancer cells — populations of cells that evolve, cooperate and roam freely through the body — demands a wider-angle view than molecular biology has been able to offer. Cross-disciplinary collaborations can approach cancer at greater spatial and temporal scales, using mathematical methods more typical of engineering, physics, ecology and evolutionary biology. The sense of failure so evident five years ago is giving way to the excitement of a productive intellectual partnership. ■

Jennie Dusheck is a science writer based in Santa Cruz, California.

1. Janmey, P. *et al.* *Assessment of Physical Sciences and Engineering Advances in Life Sciences and Oncology (APHELION) in Europe*, WTEC (2012).
2. Adrian, G. *et al.* *Biomaterials* **33**, 5504–5513 (2012).
3. Michor, F. *et al.* *Nature Rev. Cancer* **11**, 657–670 (2011).
4. Lambert, G. *et al.* *Nature Rev. Cancer* **11**, 375–382 (2011).
5. Zhang, Q. & Austin, R. H. *Annu. Rev. Condensed Matter Phys.* **3**, 363–382 (2012).



Danny Hillis (left) and Davis Agus are hoping to use protein signatures to diagnose and improve the treatment of cancer.

MEGADATA

The odd couple

An unlikely duo is trying to make sense of the avalanche of data that confronts cancer scientists, pointing the way towards a new era of research.

BY ERIK VANCE

In March 2004, oncologist David Agus was leaving his hospital in West Hollywood, California, at the end of a long day. On a whim, he cast his eye over a few magazines in the gift shop as he walked past. When he got to *Fortune* magazine, he stopped dead in his tracks. The cover picture was of an ominous, translucent cancer cell overlaid by the words: “Why We’re Losing the War on Cancer”. The story took the entire cancer research community to task and shook Agus to the core. It claimed that despite 35 years of work and more than US\$200 billion spent on US research alone, the mortality rate for cancer patients

across the world had barely budged. These were damning words to a man who had spent his entire career trying to cure patients of the disease and finding ways to stop it.

“It was very powerful,” says Agus, now an oncology researcher and physician at the University of Southern California in Los Angeles. “At first I was crestfallen. Then it was almost a call to arms.”

The *Fortune* article laid out a series of penetrating critiques of cancer research and called for a wholesale restructuring of President Richard Nixon’s ‘war on cancer’, which had created the National Cancer Institute (NCI) and has guided the US approach to cancer research ever since. The notion that cancer research was

somehow misguided would stay with Agus, gnawing at him.

He eventually found an outlet for his frustration through proteomics — the study of the body’s vast ecosystem of proteins known as the proteome. And he found a partner from outside the medical world who was adept at wading through the unthinkable vast reams of data coming from proteomic investigations. Together, the pair set about creating a computer model that could contrast a healthy proteome with those of identified cancer patients to find biomarkers for the disease. Their goal: to diagnose a cancer patient before his tumour grows. After eight years, Agus feels he has finally answered the charges levelled at researchers in the *Fortune* article — but it will be a few more years at least before he’ll know whether those answers can change the fate of his patients.

To Agus, the most critical, and personal, of the *Fortune*’s accusations was that the cancer community had become reductionist, too focused on the minutiae of just a few genes and pathways. It was a revelation of sorts. He had published many papers along these lines, but was finding cancer just too complex, with too many changes to the body’s systems occurring outside the genetic code. Finding ways to block these pathways had led to several innovative treatments, but blocking one route often forces the tumour to grow a different way.

The article strengthened doubts Agus was already beginning to have. “These complex emergent systems are impossible to understand,” he says. “Our level of understanding is just so cursory that we have to start to look for what they call, in physics, coarse-grained elements.”

For a biologist, a complex emergent system is seemingly disorganized; its constituent parts tell you little about how it functions as a whole. Coarse-grained, in this context, means shifting the focus away from those individual parts to look at multiple scales: for instance, at the level of the cell, the tumour, and the entire system. Viewing data this way is like stepping back from a pointillist painting to take in the whole scene, rather than focusing on individual dots of paint. Similarly, stepping back from a cell makes it obvious that it’s not the genes that do the heavy lifting, but the proteins they encode, Agus says. Cancer may be less about genetic mistakes than about malfunctioning proteins. But the proteome is far more varied and complex than the genome, so analysing it is a daunting proposition.

THE PROTEIN PROBLEM

“Twenty years ago, ‘proteins’ was a dirty word,” says John Blume, a molecular biologist and chief scientific officer at Applied Proteomics in San Diego, California, the company that Agus co-founded. “It was a very black art. You poured gels, you did this sort of incantation over them, and they turned blue or they turned

black or whatever — it was like trying to get things to materialize in the witches' cauldron, whereas DNA was very digital."

It is hard to overstate how much more complicated the proteome is than the genome. The genome is coded by four nucleic acids that are always the same, making analysis of the genome a problem well suited to computer analysis. Proteins, on the other hand, are constantly changing. The same proteins with the same chemical formula will have different functions depending on their shape.

But over the past few decades, advances in mass spectroscopy have allowed researchers to identify chemical components more accurately. The ability to process massive amounts of data has also improved. This combination has convinced many scientists that the time has come to pull the proteome out of the witch's cauldron and into the daylight.

Agus wanted to create a whole-body picture of the proteome at any given time using just a sample of urine or blood. From that picture, a doctor could theoretically identify a group of proteins indicating a nascent tumour. But the system is so complex that finding such a tiny anomaly would be like looking at a global climate model to determine whether a rain shower is coming to your town.

So Agus needed help. But what came next sounds more like the beginning of a bad joke than a fruitful collaboration. "I was in my lab and [former US vice-president] Al Gore came in," he recalls. "I was showing him what we are doing — proteomics and all this. And he said: 'Agus, this really would benefit from having an engineer's way of thinking attached to it.'" According to Gore, there was too much pure science and not enough problem-solving going on, Agus says. Gore thought he knew where to turn for help. He suggested that Agus call Danny Hillis, a pioneer of parallel-processing computing and former vice-president of Walt Disney Imagineering.

But Hillis was not keen to talk. "Being in the business I am, I get calls from a lot of different people," he says. "Calling [Agus] back wasn't a high priority because I knew how difficult the problem was." Then one day Hillis came into the office to find messages from Gore, venture capitalist and presidential adviser John Doerr, and entrepreneur and investor Bill Berkman, all of whom said, basically: "Call this guy back."

Hillis possesses an ideal combination of skills to help Agus: he is both a wizard with complex information systems and an exceptional businessman and entrepreneur. In the early 1980s, while working on artificial intelligence, he created one of the first parallel supercomputers, which grew into a \$65 million company called Thinking Machines. At Disney, he created business strategies, theme-park rides and giant robot dinosaurs. His current company, Applied Minds, based in Glendale, California, works with large organizations

BIG DATA, BIG BUSINESS

Hillis and Agus are just two members of a growing field of protein hunters.

The shift towards using high volumes of protein data for medicine is not unique to Applied Proteomics. Several companies and academic labs are looking carefully at diagnostics along similar lines.

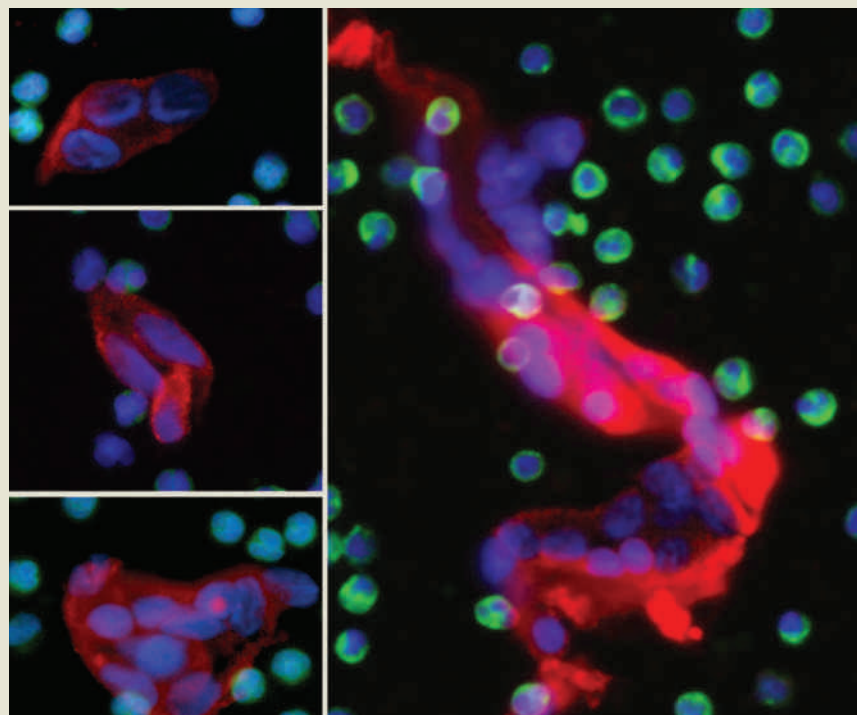
Nodality in South San Francisco, California, was founded on the premise that medicine is failing to accurately categorize patients according to which therapies might work best. The company uses a patented technique, created at Stanford University, that evaluates how cells communicate with each other. Nodality's business is based on building diagnostics, but most of its team has a background in therapeutics, so it focuses on how to match patients with specific treatments. Its first product is a test to match acute myeloid leukaemia patients with appropriate therapies.

Integrated Diagnostics in Seattle, Washington, is developing blood-based tests for the early identification of cancer, diabetes and Alzheimer's disease. The company's innovation is synthetic antibodies dubbed 'protein-catalysed capture agents', which bind to specific molecules that

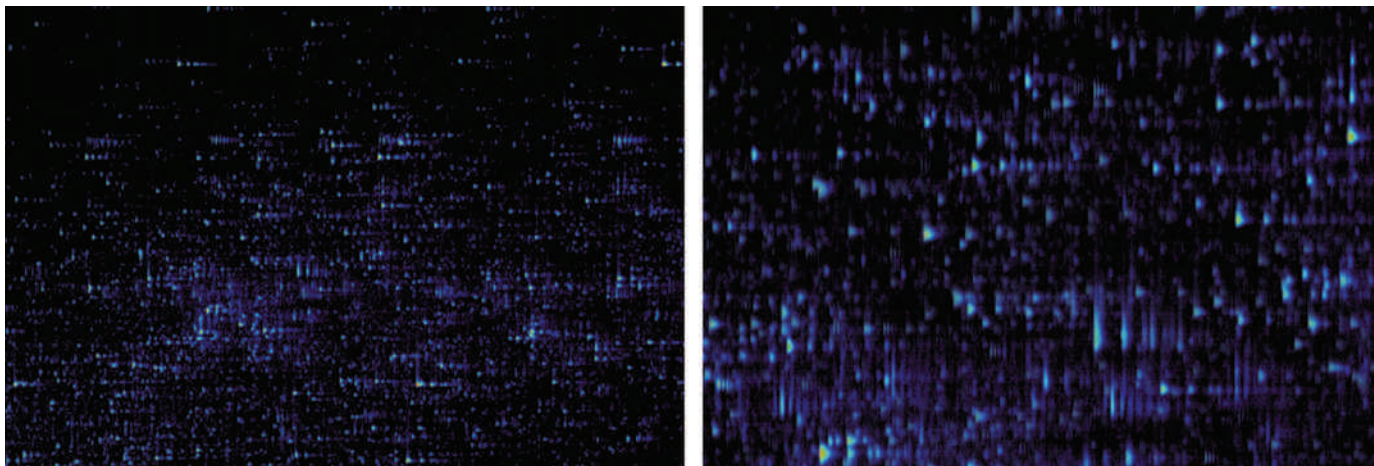
are markers of various diseases. These synthetic antibodies weigh much less than an equivalent antibody, and are more stable and less expensive than other antibodies currently used in diagnostics.

D. E. Shaw Research in New York is a computational biochemistry company set up by David Shaw, a computer scientist who made his fortune by founding a lucrative hedge fund. He swapped Wall Street for the laboratory, and in 2008 built one of the world's most powerful computers to analyse the dizzying array of ways that proteins fold. His research group also created open-source software for analysing simulations of molecular dynamics.

Epic Sciences in San Diego, California, is a cancer diagnostics company that is investigating protein and genomic biomarkers for the early identification of prostate, lung, breast, pancreatic and ovarian cancers. It is participating in 12 clinical trials in the United States, Europe and Asia as part of 40 projects looking at 15 protein or gene tumour markers, says chief executive David Nelson. **E.V.**



Blood samples from cancer patients contain normal blood cells (green and blue) and clusters of circulating tumour cells (red and blue). Epic Sciences is working to identify these circulating cancer cells and characterize them using protein or genomic markers.



Visualizations of proteins help analyze hundreds of thousands of features simultaneously, revealing both the big picture and smallest details to find disease-specific patterns.

effectively as an independent R&D department. Hillis calls it a “secret laboratory”, where engineers design everything from a voice scrambler, to shield conversations from the people sitting next to you, to vehicles for use on other planets.

Harnessing the proteome would be a monumental challenge, however, and Hillis knew that. Not only are there two million proteins with almost limitless configurations, but their concentrations in the blood vary wildly, even from one hour to the next. One protein might be 10,000 times less common than another and yet hold the key to diagnosing and understanding the manifestations of cancer. “I had looked at this before and decided it was just technically too hard,” Hillis says. But talking to Agus convinced him to try. “I got to understand how he was thinking about cancer and came to realize just how important this information was,” he says.

BUGS IN THE CODE

For two years, Agus and Hillis worked under the auspices of Applied Minds on the unwieldy proteome problem. Hillis used an engineering approach: DNA is like code, and cancer is a bug in the code. To fix the bug, you must not only understand the code, but also understand how it interacts with the computer. In biological terms, the researchers believed that the way proteins communicate between cells is more important than how they are coded for by DNA. It’s hardly a novel idea; scientists have been searching for more than a decade for cancer proteins travelling through the blood that might act as biomarkers. But according to Hillis, protein hunting — even in healthy individuals — was almost impossible. Two labs could test the same blood sample and could get very different results.

So Agus and Hillis set about building a robot assembly line that made procedures previously done on individual lab benches precisely replicable. Hillis compares it to semiconductors, which only became economically practical

when they could be made in bulk with precision.

At the end of those two years, the pair founded Applied Proteomics to create a protein diagnostic that reveals not just where a cancer is, but how it interacts with the body. Statistically speaking, the task is akin to analysing climate or earthquake data, as it involves sifting through massive amounts of noise to find a signal. Perhaps a closer comparison would be making sense of a functional magnetic resonance imaging (fMRI) brain scan. Unlike fMRI, however, which measures blood oxygen levels in the brain, proteins are not limited to the skull but found throughout the body. Given the sheer number of proteins, the complexity of each one, and their widely varying concentrations, this analysis is a massive task.

If the model works, Agus and Hillis may be able to move beyond diagnostics. If cancer proteins can be separated out from the noise of the human proteome, doctors could tailor therapies to an individual’s chemistry and target therapies for each individual cancer. With a full picture of the proteome, drugs that were previously considered failures — those that cured only a small percentage of patients — could be used in a suite of treatments tailored to individual chemistry. But this remains a distant prospect; for now, researchers must still contend with massive data loads.

“We are going to get overwhelmed by this enormous amount of genomic information,” says Robert Austin, a Princeton University physicist who studies the way tumours behave and evolve in the context of their environment. “It’s sort of like high-energy physics before the quark model came about,” he says. “We lack a ‘theory of cancer’ right now.”

MESSY DATA

Other scientists have previously tried to find patterns in the human proteome but with little success. The NCI has launched several efforts to catalogue the proteome, and the Obama administration is calling for a ‘proteome project’

analogous to the Human Genome Project, but progress has been disappointingly slow.

Applied Proteomics is the latest in a series of outsiders trying to shake up the musty halls of medicine (see ‘Big data, big business’). The Human Genome Project also integrated physicists who were comfortable with vast amounts of data. John Quackenbush, for example, was drafted into the genome project from the high-energy physics lab Fermilab, where he worked with terabytes of data in the 1980s. But he found that his controlled physics experiments could not be more different from the messy, chaotic world of the human body.

“Bringing somebody in with a new perspective and a new way to think about a problem

can be very useful,” Quackenbush says. “On the other hand, I can tell you from my experience that sometimes coming in like that you can be a little naive in thinking that having a lot of data will suddenly solve all of your problems. Big data is not a panacea.”

Neither Agus nor Hillis think this coarse-grained approach to diagnosing and treating cancer will be easy or guarantee new therapies. Yet when they talk about their work, they slip into broad, sweeping statements about the future of medicine.

“We are obligated to do things differently because the current method hasn’t worked,” Agus says. “It’s not like we are making advances every year and things are hunky dory.” And he believes that progress depends on interdisciplinary collaboration. “There is this notion that this is the century of biology — well, that’s poppycock,” he says. “This is the century of the convergence of the sciences.” ■

“It’s sort of like high-energy physics before the quark model came about. We lack a ‘theory of cancer’ right now.”

Erik Vance is a freelance science journalist based in Mexico City.

PERSPECTIVE



Finding cancer's first principles

Genomic analysis of cancer has yielded vast quantities of data. But **Robert Gatenby** would rather try to find the basic tenets of the disease.

Dazzling technological advances in molecular biology have transformed the biology of cancer and generated thousands of articles in the burgeoning fields of cancer genomics, proteomics, metabolomics and others. Yet researchers have revealed significant heterogeneity even between cancer cells in the same tumour, leading some to question the clinical value of this vast enterprise. Evolution can cause the genetic profiles in one region to be substantially different to those in distant or even adjacent sites — the conventional solution to this problem is greater investment in molecular technology so that entire cancer populations can be analysed cell by cell.

Now consider a different timeline. Suppose these technological developments had not occurred and we lacked the ability to obtain molecular data on any cancer population. Clearly, we would know less about cancer genetics, but would we also know less about cancer biology? I believe that the answer is “not necessarily”, and that we might actually know more.

Many would vigorously disagree. Most cancer biologists and oncologists take for granted that the first principles of cancer biology are genetic. Indeed, many a cancer-related publication opens with the sentence: “Cancer is a disease of the genes.” Medical students memorize the mutations found in each malignancy with the implicit assumption that this represents a full understanding. Perhaps the time has come to question these assumptions.

We hold the optimistic belief that ever more detailed molecular analysis will lead to marvellous new cancer therapies. Yet there is clear clinical evidence that existing targeted therapies generally produce mere transient responses that are ultimately defeated by the relentless evolution of cellular adaptations. So we should stop to ask: will better treatments emerge if we apply ever more sophisticated molecular technologies to smaller and smaller populations?

PRINCIPLES, NOT OBSERVATIONS

This edition of *Nature Outlook* features efforts to connect cancer biology to the physical sciences. One important lesson physicists can teach us is the explicit separation of experimental observations and system principles. Whether analysing planetary motion, atomic spectra or subatomic particles, physicists do not define a system by empirical data. Rather, they use data to support or refute a postulated theoretical framework that defines the system's governing principles. In building a framework for cancer biology, I propose that — to paraphrase evolutionary biologist Theodosius Dobzhansky — cancer, like all biology, only makes sense in the light of evolution.

In this spirit, I wonder whether genetic data are sufficient, or even necessary, to understand the evolutionary and ecological dynamics of cancer and its therapy. Darwin knew nothing of molecular genetics — his conceptual model of evolution required only an unspecified “mechanism of inheritance”. For nearly 100 years, evolutionary

biologists and ecologists observed living systems at various scales and developed the fundamental principles governing complex biological communities with no working knowledge of the underlying genetics. This was possible because the dynamics of both individual organisms and their communities are governed by phenotypic, not genotypic, interactions with environmental selection forces. In other words, understanding the principles governing living communities does not necessarily require — and may even be obscured by — genetics.

Consider cave fish. Across the world, underwater caves are populated by different species of fish, all of which have adapted to eternal darkness by developing exaggerated tactile organs and losing their eyes and skin pigment. These cave-dwelling creatures have evolved from more than 80 different species — a striking example of convergent evolution.

Genetic analysis of the world's cave-fish populations would produce a huge and highly heterogeneous data set. The data would reflect not only differences between species, but also variable genetic pathways in the same species. Such data might yield interesting insights, but the animal's fundamental biology is readily and instantly obvious simply by looking at the fish.

DATA ARE NOT ENOUGH

Like the proverbial man who looks for his car keys under the streetlight because that's where he can see best, we are drawn to intellectual places that promise high levels of information. But this does not necessarily guarantee success. Dobzhansky

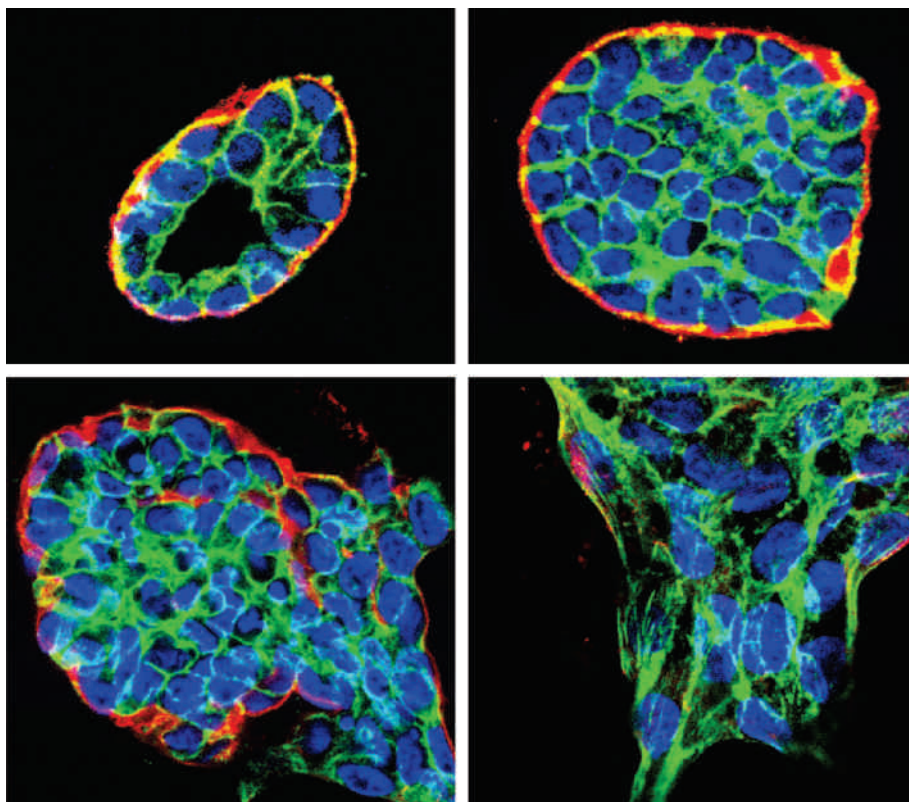
once wrote: “Scientists often have a naïve faith that if only they could discover enough facts about a problem, these facts would somehow arrange themselves in a compelling and true solution.”

The huge and complex data sets we have obtained under the strong light of molecular technology, although unquestionably useful, have caused us to neglect avenues of investigation that might ultimately allow us to arrange the data into a “true solution”. In the absence of a true understanding of cancer's evolution and ecology, we have failed to recognize the limits of these data. Without first principles, our continued confidence and unlimited investment in these technologies create an illusion of progress but may be doing more harm than good.

Ultimately, real progress in understanding cancer biology will require a formal intellectual framework. Like gravity or quantum field theory in the physical sciences, we must define the underlying principles governing the nonlinear dynamics that give rise to the vast and complex data sets being generated by the creative minds of molecular biologists. These principles will not be found until we begin to search in the right place. ■

Robert Gatenby is chairman of the departments of Radiology and Integrated Mathematical Oncology at the H. Lee Moffitt Cancer Center in Tampa, Florida.
e-mail: robert.gatenby@moffitt.org

UNDERSTANDING THE
PRINCIPLES GOVERNING
LIVING COMMUNITIES DOES
NOT NECESSARILY REQUIRE —
AND MAY EVEN BE OBSCURED
BY — GENETICS



The environment affects how cells develop, with greater stiffness leading to more cancer-like behaviour.

MECHANICS

The forces of cancer

The way cells physically interact with each other and their environment could help researchers understand the invasion and metastasis of solid tumours.

BY ERIKA JONIETZ

Hippocrates first used the term ‘carcinoma’ to describe cancerous tumours more than 2,000 years ago. But until the end of the nineteenth century, doctors knew little about solid tumours other than how much stiffer they were than the surrounding tissue. Even now, one of the most common ways people detect cancer is by discovering a lump. Yet despite the obvious contrast in hardness between a tumour and the surrounding tissue, the differences between their physical properties have largely been overlooked.

In the past 30 years, however, researchers have shown that the forces generated by, and acting on, tissues influence the way tumours grow, develop and metastasize. These forces may even be as influential as the genetic and molecular

changes at the focus of modern cancer research. “From a clinical perspective, it is not at all unimaginable that there is a connection between the mechanics of tumours and their underlying biology,” says physicist Jan T. Liphardt of the University of California, Berkeley, who heads the Bay Area Physical Sciences–Oncology Center.

In living organisms, cells are continuously exposed to physical forces, such as compression, tension, hydrostatic pressure and shear stress. They respond by modifying their behaviour and generating their own forces. “We’re finding these forces are key to the way cells divide, interact, signal, move and attach,” says Muhammad Zaman, a biomedical engineer at Boston University in Massachusetts. “There is a deeper appreciation now that cells are very touchy-feely — they’re not just these things that receive and process signals.” Such realizations have led to a

new subfield in cancer research: physical oncology, a cross-disciplinary area aimed at exploring the physical laws that affect the development and behaviour of cancer in the hope of discovering therapies and diagnostics.

Physical forces are especially important in invasion and metastasis, the processes that make most cancer lethal. Researchers are investigating how forces from both within and outside developing cancer cells interact in intricate feedback loops. This work uses both well-established and novel tools, from atomic force microscopy and three-dimensional cell culture to fluorescent beads that track how cells change their environment.

SOFT CELLS

Research in cancer physics can be divided into two basic camps. One group believes that the mechanical characteristics of malignant cells are broadly similar across all solid tumours — a theory that, if proven correct, could lead to universal approaches to diagnostics and therapeutic targets. The other group believes that although many cancers share some physical characteristics, most features will be affected by mechanical differences among the tissues of origin. If this second view is true, researchers might need to devise tests and treatments for a bewildering array of mechanical circumstances.

Josef A. Käs, a soft-matter physicist at the University of Leipzig in Germany, is in the first group: he believes that the properties he’s finding in breast and cervical cancer cells are common across tumours. He hopes to identify physical attributes of cells that would allow doctors to recognize which tumours are more likely to metastasize, regardless of where they originate. He contends that finding shared mechanical features among different cancers could provide a simpler view of the disease than the molecular picture, which is becoming increasingly diverse. Unlike biologists, he says, “physicists take a reductionist view”.

The Käs lab has developed a device — he calls it an ‘optical stretcher’ — that determines how much a cell can be deformed in order to assess its elasticity and contractility; a cell’s ability to contract is essential for movement and proliferation. Unlike tools such as optical tweezers and atomic force microscopes, the optical stretcher, which uses two laser beams pointed towards each other, can quickly measure the properties of thousands of cells. Käs has found that the elasticity and contractility of human breast epithelial cells change as they progress from normal to cancerous to metastatic, with the cells becoming softer as disease advances¹.

Käs says the device can be used to assess the likelihood of a tumour metastasizing without having to do biopsies from distant sites. He also believes it could be possible to reverse both elasticity and contractility with a drug that ‘freezes’ cancer cells, increasing their stiffness to stop them metastasizing. In order to travel to other locations in the body, tumour cells must squeeze through small gaps in the extracellular matrix

around them and between the cells in blood-vessel walls; this is much easier for softer, more pliable cells. He says he is now working with a major pharmaceutical company to identify possible anti-metastatic drugs.

Similarly, Zaman thinks it should be possible to determine which physical parameters make cancer cells most likely to develop chemoresistance³ by using a technique called microrheology, in which nanoparticles are injected into cells to quantify their viscosity and elasticity. This technique is suited to physical oncology, he says, because it can be used in three-dimensional (3D) cultures, which more closely approximate a tumour's environment in the body than the traditional 2D dish culture³.

Cells grown in dish cultures are nearly always less resistant to cytotoxic agents than those grown in 3D matrices; the main difference, Zaman says, is the forces they experience. So he cultures cancer cells in different 3D environments (stiffer or softer, or with different drug concentrations) and measures the cells' physical properties to see which ones correlate with drug resistance. There are large numbers of variables, and researchers can measure only a few at a time, but Zaman thinks the results will ultimately help doctors decide which tumours are most likely to develop chemoresistance.

MECHANICAL DIFFERENCES

It is not yet clear whether Käs and Zaman are correct in their belief that solid tumours represent a single physical system. Most physical oncology researchers hold the opposite view, believing that the forces generated by, and acting on, cancers vary among tumour types. Valerie Weaver, a bioengineer at the University of California, San Francisco, is in the latter group. Different tissues have different elastic properties, she says, which are created by interactions between tissue-specific cellular forces and the configuration of the proteins around them. "Disease is uniformly a corruption of the mechanics. But in each cancer, it's going to be different," says Weaver, who was one of the first to study 3D cultures of breast cancer cells.

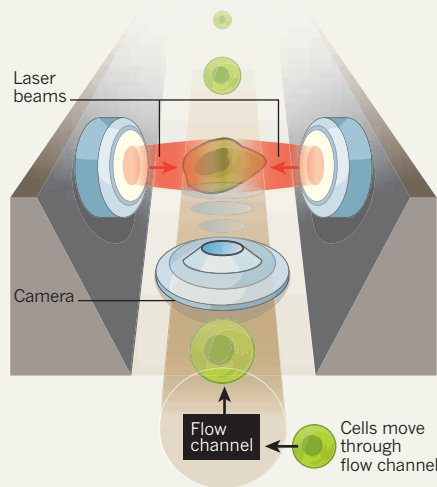
Her lab is finding differences among the mechanics of many kinds of tumour, including brain, pancreas, breast and skin cancers. Brain tumours, for example, are soft, whereas pancreatic tumours are rigid. And because cells' surface receptors can be sensitive to physical or biochemical cues, or both, from their surroundings, Weaver believes it makes sense for variations in tissue type to affect how cancer cells behave. The cues are conveyed either physically or chemically through a cell's cytoskeleton to its nucleus, where they can influence which genes are expressed — an effect that can lead to conditions that promote disease. Some genes code for enzymes that can remodel the extracellular matrix, for example, digesting collagen to open a path for invading cancer cells.

Ben Fabry also compares the mechanics of cells from different cancers in an attempt

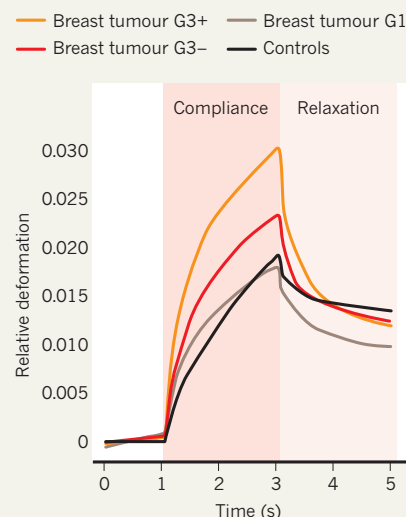
DIAGNOSING AT A DISTANCE

This optical stretcher uses two laser beams to measure cells' elasticity and contractility. Because advanced disease is associated with softer cells, the results could be used to assess whether a tumour is likely to metastasize.

Cells travel along a flow channel and are suspended in two opposing laser beams. As the laser beams are intensified, the camera takes a series of images of the cell.



Elasticity of normal breast cells and cells from tumours of increasing aggressiveness (stages G1–G3+). Cells from more aggressive tumours deform more easily.



to understand how they influence the course of disease. Fabry, a biophysicist at Friedrich-Alexander-Universität Erlangen-Nürnberg in Germany, has used fluorescent beads tightly embedded in collagen matrices to measure how various carcinoma cells affect their surrounding matrix, and to calculate their contractility⁴. Invasive breast and lung carcinoma cells turned out to be more contractile than non-invasive cells — but higher contractility does not always mean higher invasiveness. In fact, the most contractile cells Fabry has measured were from a non-invasive vulva carcinoma. He doesn't think the results are that surprising. Contrary to what Käs is finding, Fabry says: "Different cancers employ different invasion strategies, some of which benefit from a softer and more fluid-like cell phenotype, others from a stiffer phenotype; some use more contractile forces, others may use pushing forces; some cancer cells migrate collectively, others as individual cells."

The molecular mechanisms that cells use to sense and cause physical changes in their environment and in themselves — the same mechanisms that prompt them to turn cancerous — are only beginning to emerge. "One of the problems in the field of cancer mechanics is understanding and quantifying the interplay of mechanics and chemistry," says Liphardt. "When someone says, 'Oh, it's mechanics,' it's extremely likely that it's chemistry too, and vice versa."

Weaver recalls that DNA pioneer James Watson confronted her during a presentation she gave last year entitled "The Force Journey of a Cell". "He said: 'I don't see how this is going to

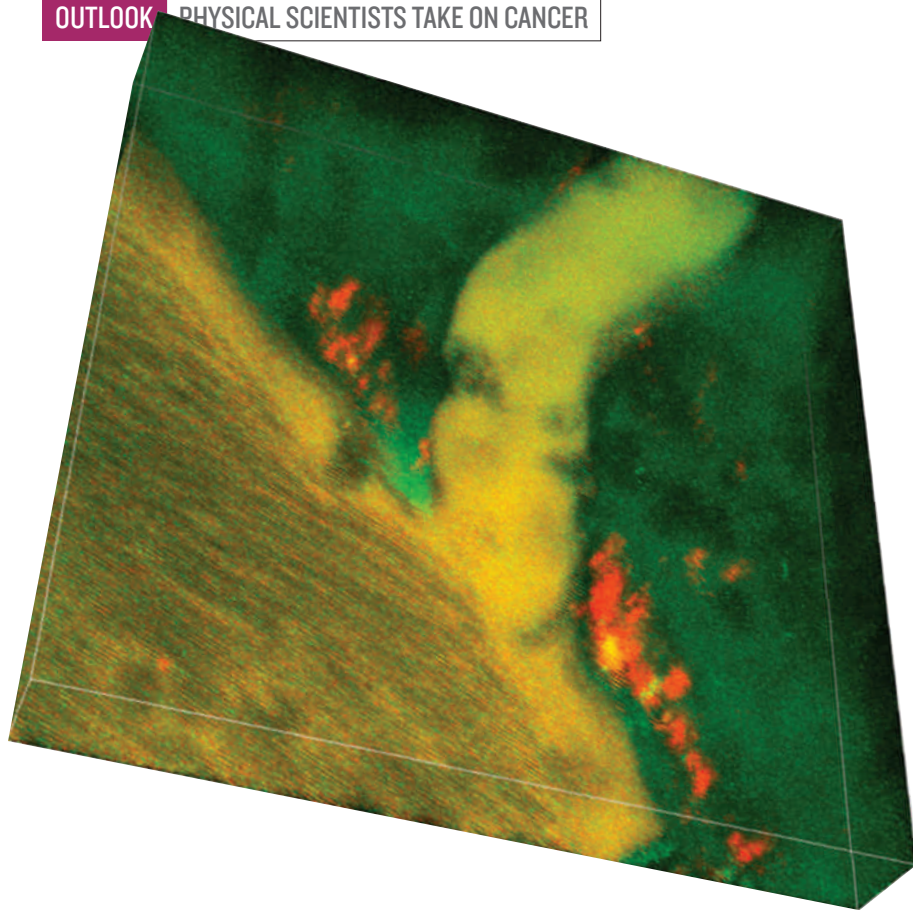
change anything. I don't see how this is going to translate into a cure.' I told him: 'Mechanics is one of the most primitive signalling systems. It is so fundamental to life and multicellular systems that it can't *not* be involved in cancer.'"

But she concedes that Watson has a point. Today's rudimentary explorations of cancer mechanics are a long way from discoveries that will lead to new therapies. Researchers studying the physical forces involved in cancer, she says, must define and understand the molecular principles underlying every aspect of the interplay between cell context and mechanics, from the nanoscale to the tissue level. Until they grasp those fundamental principles and use them to inform cancer biology — finding therapeutic targets, for example, or determining prognosis — this cross-disciplinary domain of cancer and physics will, she says, remain a "side curiosity".

Cancer mechanics is still a fledgling field. Basic questions remain to be addressed, such as how tissue mechanics relate to risk, outcome, intervention and personalized therapies. Only then can researchers face the challenge of translating these insights into clinical applications. As Weaver says: "Our hard work is just beginning." ■

Erika Jonietz is a science writer based in Austin, Texas.

1. Guck, J. et al. *Biophys J.* **88**, 3689–3698 (2005).
2. Fallica, B., Makin, G. & Zaman, M. H. *Integr. Biol.* **3**, 529–539 (2011).
3. Baker, E. L., Bonnecaze, R. T. & Zaman, M. H. *Biophys. J.* **97**, 1013–1021 (2009).
4. Koch, T. M. et al. *PLoS One* **7**(3), e33476 (2012).



A reconstructed 3D image showing the accumulation of 30-nm nanoparticles (green) in a pancreatic tumour.

NANOTECHNOLOGY

Carrying drugs

Traditional chemotherapies can be toxic but nano-sized carriers can keep them out of healthy tissue and take old drugs to new places.

BY KATHERINE BOURZAC

When Joseph DeSimone makes nanomedicines, he compares himself to a baker. He mixes drugs with different chemical 'batters', puts them in tiny moulds, cures them and then turns them out. He can mould almost any shape: discs, cubes, long sticks, roughened doughnuts, or particles shaped like pollen, viruses or red blood cells. But unlike a baker's cakes, brags DeSimone, a chemical engineer at the University of North Carolina in Chapel Hill, every particle in a batch will be identical, regardless of the recipe.

The materials scientists and chemists who work in nanotechnology are creative designers, but they're also control freaks. The ability to make particles to exact specifications, and to control their form at the nanoscale with great precision, enables researchers to control

their function. DeSimone's various shapes can squeeze through blood vessels or worm their way to the core of a tumour. And shape is just one of many properties he and others can engineer at the nanoscale. Nanoparticles with carefully controlled chemistry, size, surface charge and other properties can carry drugs to new places and give them new functions. Nano-engineered drug carriers can slip selectively into cancerous tissue, or protect the drugs they carry from being destroyed before they reach their destination.

Nanomedicine has the potential to address one of the biggest problems in cancer therapy: how to get enough of the right drug to the right place, without causing side effects or inducing resistance. As researchers learn more about the tumour microenvironment, and about how to engineer and manufacture nanoparticles that carry drugs, they are gaining more control over

the course of cancer therapy — an advance that is expected to lead to more effective treatments with fewer side effects. It is also resulting in therapies that were previously thought impossible, such as drugs that change their properties depending on where they are in the body, or that target proteins once deemed undruggable. Some labs are even testing ideas inspired by robotics and computing, such as nanoparticles that communicate with each other to increase accumulation in a tumour.

SIZE MATTERS

One of the greatest uses of nanomedicine in cancer treatments so far has been keeping toxic drugs out of healthy tissues, says Rakesh Jain, a cancer biologist at Massachusetts General Hospital in Boston who is also affiliated with several drug companies. Many traditional chemotherapies are too toxic to be given in large doses or combined with other toxic drugs. They may have precise chemical targets but they are poor at targeting specific tissues — they make their way blindly through healthy tissues and cancerous ones alike, causing harmful side effects.

Doxorubicin is used to treat a range of cancers, but it can also cause life-threatening heart damage. One of the earliest successes of nanomedicine was Doxil, a doxorubicin-carrying nanomedicine, approved in 1995, that keeps the drug out of the heart.

By the mid-1980s, researchers knew that 100-nanometre particles are too big to exit healthy blood vessels but can easily escape the leaky, hastily built vasculature that feeds tumours. Doxil was engineered to take advantage of this. To keep doxorubicin out of the heart, researchers loaded it into a lipid bubble about 100 nanometres in diameter. Lipids don't allow for much engineering control, but they readily self-assemble into bubbles. When shaken together in a water-based solution, the lipid molecules coalesce around doxorubicin particles to create drug-delivering nanoparticles. Then, to help the nanoparticles evade the immune system, researchers coat them with polyethylene glycol. Once these Doxil particles accumulate in the tumour, the drug leaks out of its carrier and attacks nearby cells.

Patients receiving Doxil have one-third the congestive heart failure incidence of those given conventional doxorubicin, resulting in "a quantum jump in quality of life", Jain says. But keeping drugs out of the wrong places is much easier than getting them into the right ones. Drugs the size of Doxil are passively excluded from healthy tissue but cannot actively make their way deep into a tumour, instead clustering at its perimeter. As a result, nanomedicines offer little or no survival benefits compared with conventional formulations, Jain says. "Now we have to improve delivery in tumours."

The nanomedicines currently being developed are more sophisticated than Doxil, but many maintain the basic design of a spherical

carrier with a coating. To improve delivery, companies such as BIND Biosciences of Cambridge, Massachusetts, are also tuning other properties such as charge, chemistry and shape. Chief executive Scott Minick describes BIND's approach as "medicinal nanoengineering". Minick was previously chief executive of Sequus Pharmaceuticals, the company that developed Doxil. But unlike Doxil, which uses simple lipids as its drug carrier, BIND's nanomedicines use polymers, which are easier to engineer. This approach means the company can build drug bubbles and direct where they go, control how quickly they release a drug, and target cancer cells according to their surface markers.

The leading candidate¹, BIND-014, is a 100-nanometre polymer sphere loaded with docetaxel, a drug that kills dividing cells. Like Doxil, BIND-014 relies on its size to leave the tumour vasculature. Unlike Doxil, however, the polymer centre has been engineered to control drug release, among other things. The outer layer is made up of two additional components: polyethylene glycol to help it evade the immune system, and binding molecules that seek out markers found only on the surface of tumour cells (see 'Nano drug carrier').

The early results of BIND-014's phase I clinical trials look promising, Minick says. "This patient population is late-stage, terminally ill, and we don't expect to see signs of efficacy," he says. Even so, there are hints that the drug is working: although the trial is still recruiting, the company has reported that, following a course of BIND-014, tumours shrank in two of 17 patients.

To design its therapies, BIND Biosciences tweaks the size, charge and other properties of each part of its drug carriers, giving it control over circulation time and drug release rate, for example. This approach allows it to make effective nanomedicines without knowing all the biological details of why a particle works as well as it does. Researchers elsewhere, however, are more deliberately taking advantage of advances in understanding the biophysics of the tumour microenvironment.

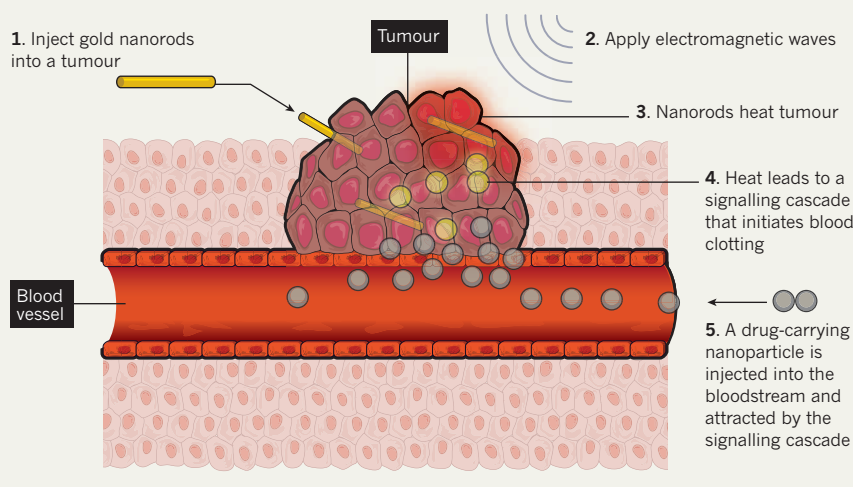
SMALL AND SQUISHY

Designing nanomedicines to seep out of the bloodstream into tumour blood vessels is only the first step in cancer drug delivery². Although a size of 100 nanometres works well for some things, it's still quite large for a drug. "Once a big nanoparticle leaks out, it's pretty much stuck," says Jeffrey Hubbell, a chemical engineer at the Ecole Polytechnique Fédérale de Lausanne in Switzerland.

Once a large particle leaves the leaky blood vessels, it has difficulty moving deep into a tumour. Making the particle smaller would improve its mobility, and is also an advantage when fighting certain tumours — particularly pancreatic and some breast cancers — that are threaded with a tough tangle of collagen,

COMMUNICATING CHEMOTHERAPIES

Reconnaissance nanoparticles lodge in a tumour and signal drug carriers to swarm to the site and accumulate at higher concentrations than are otherwise possible.



which presents a physical barrier to drugs.

But reliably making polymer nanoparticles much smaller than 100 nanometres is tricky. Kazunori Kataoka, a materials scientist at the University of Tokyo, Japan, developed the first polymer drug carrier in the mid-1980s. His company, NanoCarrier, based in Kashiwa, has now developed a 30-nanometre polymer to transport the chemotherapy drug cisplatin; it is currently undergoing phase II clinical trials in patients with pancreatic cancer.

Cisplatin usually has severe kidney toxicity, requiring patients to drink painfully large amounts of water during treatment. Kataoka says that's not the case in the NanoCarrier trials because the carrier's size allows it to move into and accumulate in the pancreatic tumour, instead of accumulating in the kidney. "We've already successfully extended survival," he says, which is heartening given how difficult pancreatic cancer is to treat. In a small phase I trial, the drug more than doubled survival time from five months to more than twelve.

Back in North Carolina, DeSimone's work moulding strangely shaped particles has a similar motivation: controlling a drug's size and shape to help it enter tumours. "We want to figure out how cancer cells get in places they're not supposed to be, and mimic that," he says, so that he and others can make drugs to follow them there.

DeSimone drew inspiration for his particle-moulding method from semiconductor manufacturing plants, which make tiny transistors by the trillions. He can precisely vary just a single property, such as stiffness, and then test how the particles move through the body. Using this manufacturing method, which has been licensed by Liquidia Technologies of Research Triangle Park, North Carolina, he can find out, for example whether a squishier

drug is better at squeezing into the centre of a tumour.

SILENCE WILL FALL

One of the most promising applications for nanoengineered drug carriers is gene silencing, in which small bits of RNA are deployed to shut down crucial cancer genes through a process known as RNA interference. Researchers know how to make RNA sequences that theoretically can turn off any given gene. But without a good delivery vehicle to test the effects of these silenced genes, finding promising therapeutic targets in animals — let alone making an RNA therapy that will work in people — is slow going, says William Hahn, an oncologist at Harvard Medical School in Boston, Massachusetts. Nanocarriers may be just the technology to push this technique forward.

Designing a nanocarrier suited to transport gene-silencing RNA is tricky, however. It must make it all the way inside a cancer cell, which requires an escort smart enough to evade destruction. Typically, if it's not cleared out by the liver, an RNA-carrying particle will bind to the cancer cell membrane, which then folds inward and pinches itself off into an acidic, destructive bubble called an endosome inside the cell.

Researchers are working on several tricks to get round this. Chemical engineer Mark Davis at the California Institute of Technology in Pasadena has developed a polymer carrier that absorbs positive charges as they are pumped into the endosome. This creates an osmotic pressure that eventually bursts the cancer cell's bubble, freeing the silencing RNA before it is destroyed.

Traditional therapies work by binding to proteins and disabling them. Unfortunately, most cancer genes produce proteins that are

NANOMEDICINE IN CLINICAL TRIALS

Several nanoscale drug carriers are currently in clinical trials.

Company	Drug	Formulation	Status	Description
Calando Pharmaceuticals	CALAA-01	A polymer nanocarrier containing gene-silencing RNA	Phase I	A polymer nanocarrier holds RNA that silences a gene in solid tumours needed for DNA synthesis and replication
BIND Biosciences	BIND-014	A polymer nanocarrier targeted to cancer cells carries docetaxel	Phase I	Targets solid or metastatic prostate cancer cells by binding to prostate-specific membrane antigen
Nippon Kayaku	NK105	A polymer nanocarrier containing paclitaxel	Phase III	Looking for progression-free survival in patients with metastatic or recurrent breast cancer
NanoCarrier	Nanoplatin (NC-6004)	A polymer nanocarrier containing cisplatin	Phase I/II	Evaluating Nanoplatin in combination with gemcitabine in patients with advanced or metastatic pancreatic cancer, with the aim of reducing kidney toxicity compared with cisplatin alone
Cerulean Pharmaceuticals	CRLX101	A pH-sensitive polymer nanocarrier releases camptothecin in the acidic environment of cancer cells	Phase I	The trial combines CRLX 101 with bevacizumab in patients with advanced renal cell carcinoma

considered undruggable by traditional means. Some of these proteins hide inside the cancer cell, out of the reach of antibody drugs that can only get to the surface. Other proteins have a physical shape that provides no foothold for a drug of any kind. Nanoengineering, Davis says, could break through these defences. With the right carrier, there is no need to go after the undruggable proteins — gene-silencing RNA can instead go directly to the genes that make them.

It can also target several cancer genes at once. “The goal has got to be to hit multiple targets simultaneously” so the tumour cannot develop resistance, says Davis. If a tumour mutates in the course of treatment, oncologists will be able to order therapies that target those new mutations.

THE LOGICAL NEXT STEP

Nanotechnology researchers such as Davis, and companies like BIND, are focused on getting more effective therapies into the clinic as quickly as possible. But most nanomedical research has been done *in vitro* and in animals; little is known about how these drugs work in people, Davis says, although a series of clinical trials is under way (see ‘Nanomedicine in clinical trials’).

Other researchers are using the tools of physical science, from robotics to computer science, to realize more fanciful ideas about future drugs. One prototype, made by George Church’s group at Harvard University in Cambridge, Massachusetts, is a drug-stuffed ‘lock box’ that opens only after performing a simple logic operation akin to those done by computer circuits. The box is made of DNA, a material Church and his colleagues chose for its design possibilities. Using a technique called DNA origami, the DNA self-assembles into a barrel shape, with locks and hinges that cause it to spring open when particular surface markers on cancer cells — the ‘keys’ — unlock them.

Church calls his DNA drug carrier a nanobot because it performs a computational logic function: when two input signals are present (two molecular markers on the targeted cancer

cell), the box generates an output (opening to release its drug payload). In one recent experiment³, the team designed a cylinder of DNA that contains a cancer drug, like gems in a jewellery box. The nanobot had two locks designed to be opened by two proteins on the surface of aggressive leukaemia cells. The researchers showed that the leukaemia cells could unlock the nanobot, but other cells in the bloodstream could not.

The logic-function idea was motivated by a clinical need. Most targeted therapies seek out just one cell surface marker. Logic-gated systems like Church’s, however, might allow for

communicate with each other to ‘swarm’ to tumours.

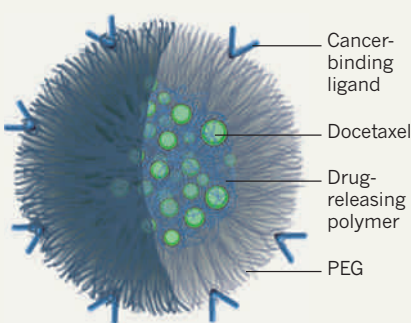
“Ninety percent of cancer deaths are caused by metastases,” says Bhatia. Finding those secondary tumours is difficult, especially when they’re new. “We want to inject a therapy that will figure out where the metastasis is” and then communicate that information to other drugs, she says, so more of the drug reaches its target. Early demonstrations⁴ showed that drug-carrying nanoparticles accumulate in a tumour in much larger numbers than they would without such communication — in one experiment, there was a 40-fold increase (see ‘Communicating chemotherapies’).

Bhatia is looking to expand this idea by incorporating design tricks from robotics. Like ants, whose individual actions are simple but who *en masse* can build a complex anthill, groups of individual robots can be programmed to swarm and perform tasks collectively. Instituting simple rules such as “maximize your distance from all neighbours” has allowed roboticists to make groups of robots that fly like bees in a swarm. If Bhatia can apply this to drugs, she might achieve even greater drug accumulation.

The work is unorthodox, but that doesn’t bother Bhatia. “We want to evolve nanomedicine away from formulations where everything is exactly the same,” she says. Indeed, the whole field is still evolving. As researchers improve their ability to control, manufacture and innovate at the nanoscale, they are opening up new paths for cancer therapy. Some may prove fruitless, but others could yield new ways to make cancer therapy less painful and more effective. ■

NANO DRUG CARRIER

BIND-014 carries its payload in a tangle of drug-releasing polymer. The PEG coating helps it circulate and binding ligands help it find the tumour.



specifically targeted drugs that go after cancer cells, such as leukaemia, but avoid healthy cells that might have a surface marker in common with the cancer cells. But the research is still in the early stages, as it is difficult to produce enough DNA boxes to test the method in animal models.

Sangeeta Bhatia, a biomedical engineer at the Massachusetts Institute of Technology, is also taking inspiration from information technology and other fields. She is emulating natural systems and robotics to make smart cocktails of cancer therapeutics that

Katherine Bourzac is a freelance journalist based in San Francisco, California.

1. Hrkach, J. *et al. Sci. Transl. Med.* **4**, 128ra39 (2012).
2. Jain, R. K. & Stylianopoulos, T. *Nature Rev. Clin. Oncol.* **7**, 653–664 (2010).
3. Douglas, S. M., Bachelet, I. & Church, G. M. *Science* **335**, 831–834 (2012).
4. von Maltzahn, G. *et al. Nature Mat.* **10**, 545–552 (2011).

PERSPECTIVE



David Agus (left) and Murray Gell-Mann

Meeting of minds

David Agus and Murray Gell-Mann show that the élites of physics and medicine can spur each other to fresh insights.

When cancer researcher and physician David Agus met particle physicist Murray Gell-Mann in 2009, they soon discovered that they occupied different worlds. Agus says their interaction showed him that “borrowing from the world of physics could help my field in unimaginable ways” and that their interaction has “shifted not only how I work and approach medicine, but also how I ask questions, how I solve problems, and how I do science”. *What follows is a conversation between the biologist and the physicist about an issue that may be blocking progress in cancer research.*

Gell-Mann: As a physicist, I wonder why it is that biology and medicine seem to have so few new theories.

Agus: Unlike physics, biology and medicine are reductionist: we first look for an experiment to answer a question, then we conduct the experiment, analyse the results, and try to find a way to explain it. We'll ask: what happens when I activate this particular receptor on that cell? But the experimental results do not always reflect what goes on in a complex human system. Cells are part of a large, intricate network, much of which we're still trying to decipher. The practice of looking at each scale — the cell, the organ, the disease and the organism, for example — and understanding how each fits into a multi-scale model is not done often enough in medicine.

Gell-Mann: Yes, and we should be encouraging speculative conjectures. In physics, we postulated the existence of quarks as fundamental constituents of particles such as the proton and neutron. Quarks have some unusual properties that make them hard to accept in theory — for example, they are permanently bound inside the neutron, proton, and so on, and cannot escape. But without them, the system of elementary particles doesn't make sense. The quark idea turned out to be correct. Is it possible to publish such broad theories in medical journals today?

Agus: Unfortunately, the literature is filled with individual conclusions — and not that many theories that aim to tie these conclusions together. Why do you think theorizing happens more in physics than in biology or in medicine?

Gell-Mann: Physics is a lot simpler. I used to wonder how close we were to a real theory of the elementary particles and their strong, weak and electromagnetic interactions. Some of us were studying symmetry properties of those particles and interactions, giving rise to simple predictions that could be verified. But the magic of ‘gauge field theory’ led us from symmetries to an actual dynamical theory, the standard model, which describes the situation in detail. It is very rare for that sort of thing to happen in biology. Deciphering the genetic code is one of the few examples.

Agus: The genetic code accounted for the existence of DNA base pairs, which led to the discovery of the molecular structure that represents the genetic code. But even if I know your DNA, I cannot use

it to determine what is going in your body at a particular moment. Similarly, I can scan your brain but it won't tell me how smart you are.

Gell-Mann: We don't even know enough about the rest of the DNA — the non-coding DNA that seems to play an important role in regulating gene expression.

Agus: Right. Along the same lines, the first molecular characterization of the human microbiome has recently been described in detail. Our body's microbial communities fulfil an important dimension in regulating what is going on at any one time in the human organism.

Gell-Mann: I have heard you refer to the microbiome when we discuss why people in the Far East don't have the same incidence of prostate cancer as those in the West. But if those same people move somewhere else, say to the United States, the rate slowly goes up towards a value near what you would find normal in their new home.

Agus: Yet a real experiment to show this would require thousands of people and decades of time. So instead, what if we make a model and the question becomes: can you look at all the available data, and do they fit the proposed model?

Gell-Mann: Can the microbiome provide the simplest explanation for the variation? Can that idea be tested?

Agus: It certainly could be an explanation. But back to the bigger picture: why is this conversation not happening in every biologist's laboratory? Why is this not the common way we are studying diseases, including cancer?

Gell-Mann: It should be. We need to develop a new generation of scientists that take observations like these and bring them together by formulating a theory. We also need policies that encourage the publication of such theories. In addition, I think we would do well to pay more attention to outliers. They're generally

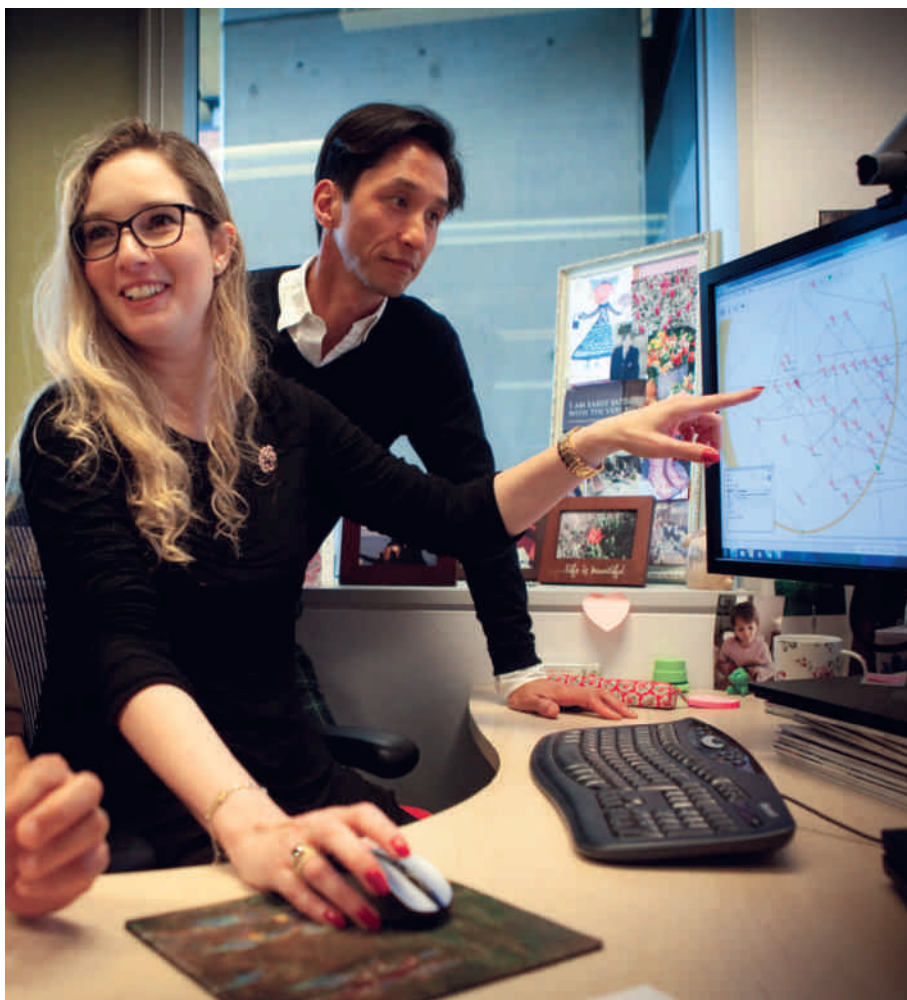
neglected because it is easy to look at common cases and figure that someday, someone will explain away those pesky outliers. Looking at outliers is tiring but important.

Agus: But imagine what focusing on them could do. Suppose I treat 100 patients with cancer and only one-third of them respond well to treatment, yet in one fortunate individual the disease vanishes altogether. There's an important clue in that outlier — the single anomaly that escapes death. Studying such outliers can provide an invaluable foundation for broad new understandings. To learn new ways of understanding the human system, we must use simplified descriptions of our observations and develop theories that help us improve health care. ■

David B. Agus is an oncologist and cancer biologist at the University of Southern California's Center for Applied Molecular Medicine in Beverly Hills. email: agus@usc.edu

Murray Gell-Mann is a physicist at the Santa Fe Institute in New Mexico, and a professor of medicine and physics at the University of Southern California. He received the Nobel Prize in Physics in 1969 for his work on particle physics.

“THE LITERATURE IS
FILLED WITH INDIVIDUAL
CONCLUSIONS — AND NOT
MANY THEORIES TO TIE THEM
TOGETHER”



Jasmin Fisher's computer models help biologists understand the molecular pathways in cancer cells.

MODELLING

Computing cancer

Software models of complex tissues and disease are yielding a better understanding of cancer and suggesting potential treatments.

BY NEIL SAVAGE

When the drug Avastin was approved as a treatment for breast cancer in 2004, physicians and researchers saw it as a powerful weapon in their armoury. Growing tumours need increased amounts of oxygen, so they send out chemical signals that coax the growth and development of new blood vessels, a process known as angiogenesis. Avastin (bevacizumab) interferes with this process by cutting off the tumour's oxygen supply, causing it to shrink. But doctors found that Avastin often left more invasive tumours in its wake. A subsequent study found that,

although Avastin did suffocate tumour cells, the lack of oxygen encouraged the growth of cancer stem cells, resulting in more aggressive tumours. The US Food and Drug Administration revoked its approval in 2011.

Cancer is not a simple disease. Tumours are made up of various types of cell in different stages of their life cycle, and these cells send out and respond to a wide range of chemical signals. They are laced with blood vessels and interact with the surrounding tissue, with the organs they invade, and with any drugs used to combat them. Gene sequencing and proteomics have yielded reams of data that scientists are only just beginning to parse. To understand this

complexity, and to explain why a drug such as Avastin doesn't work as expected, researchers are turning to computer models that help them visualize how cancer grows, generate ideas about how to combat that growth, and simulate the potential results of possible interventions.

JASMIN FISHER

BEATING THE SYSTEM

"The amount of understanding, knowledge and information we have at hand is huge, but it's too complicated to make sense of, in terms of what's going on in the system," says Jasmin Fisher, a neuroimmunologist in the Programming Principles and Tools group at Microsoft Research in Cambridge, United Kingdom.

With all this information, it's possible to miss the cancer forest for the cellular trees, says biophysicist James Glazier, director of the Bio-complexity Institute at Indiana University in Bloomington. Researchers have tended to focus on genes and proteins, but to understand and fight the disease, it must be viewed as a system, rather than merely as a set of cellular activities. According to Glazier, the recent focus on genetics and pathways in individual cells has caused many researchers to neglect the systemic view. "No amount of information about what happens inside a single cell can ever tell you what a tissue is going to do," he says. "Much of the information and complexity of tissues and life is embedded in the way cells talk to each other and the extracellular environment."

It was this need to investigate cancer as a holistic system that prompted mathematician Philip Maini, head of the Center for Mathematical Biology at the University of Oxford, UK, to model the behaviour of antiangiogenic drugs. Because these drugs are most effective when used in combination with radiation or another chemotherapy, the theory that they work strictly by cutting off blood flow and starving the tumour just didn't make sense. Maini's model shows that it is the blood-vessel density inside the tumour that holds the key to the drug's effectiveness¹.

Such modelling can be used to determine whether a drug is likely to work, or even to suggest targets for future drugs. "You can test the ideas in a simulation without even killing a rat," Glazier says.

Creating these complex simulations requires computational modelling, says Adriano Henney of the University of Heidelberg, director of the German Virtual Liver Network, a collaboration to develop computational models of the entire organ. "This approach is going to be important if we are to understand how medicines operate in complex diseases."

OPEN-SOURCE MODELLING

In one step towards such simulations, Fisher is developing computational models at Microsoft that describe molecular pathways within cells, how those pathways operate, and the way cross-talk between them affects the process of determining a cell's fate. "We look on a

biological process as if it were a computer program, so we ask ‘what is the algorithm inside the cell that is affecting behaviour?’,” she says.

Fisher calls this modelling approach “executable biology”, as it takes a biological understanding of cellular processes and turns them into a set of formal instructions that a computer could execute². For instance, a stem cell follows a different series of steps depending on whether it differentiates into a blood cell or a heart muscle cell. Several of those changes occur simultaneously and can be altered by feedback the cell receives as it matures. Because living processes are complex and nonlinear, Fisher’s program makes it easier for researchers to perform manipulations, such as changing the sequence of events or decreasing the strength of a signal, to see whether the steps they have modelled lead to an outcome that matches up with experimental results.

The challenge in developing models for different levels of organization, Maini says, lies in finding the right mathematical approach for each scale. It might be best to describe intracellular activity, such as forming a protein, by using differential equations, for example, whereas cell-to-cell signalling might require a different approach, such as rule-based programming, to define how cells interact.

To deal with these different scales, Glazier has developed an open-source modelling methodology called CompuCell3D that treats cells, components within cells, or cell clusters as discrete objects. The user can input biochemical information into a model of a cell — such as how it responds to chemical stimuli, or how strongly it sticks to other cells — and watch how the system responds³.

Glazier started developing the model in 2000, basing it on a previous model he built that simulates the growth of grains in crystal-line structures. This turned out to be similar to the way bubbles grow in liquid foam, which in turn could be extended to describe the interaction of cells in developing embryos.

IN SILICO INSIGHTS

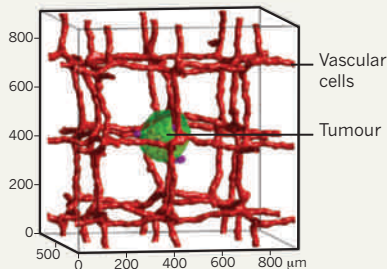
The models developed by Glazier, Fisher and others are designed to allow cancer biologists with little or no programming knowledge to create their own simulations to run *in silico* experiments. “We wanted to build a platform that would allow you to create simulations that other people could run, adapt, modify and so on, so the models would be shareable and reproducible,” Glazier says. This involves replacing detailed computer coding that describes biological processes with simplified representations of those processes that biologists can easily understand. In Fisher’s program, a biologist can select particular cells, proteins and genes, and then drag-and-drop them on a computer screen to create the conditions for the simulation.

By using CompuCell3D as a tool to build a model of a tumour, Utah State University researchers Nicholas Flann and Gregory

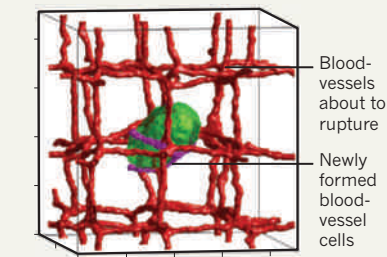
MODELLING TUMOUR GROWTH

This computer model of tumour vascularization, a process known as angiogenesis, allows for a close examination of how cellular growth is affected by blood-vessel development.

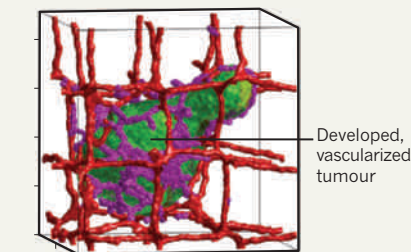
Day 15



Day 30



Day 75



Podgorski have been exploring angiogenesis, hoping to find ways to inhibit it and prevent tumour growth⁴. A microtumour emits a protein called vascular endothelial growth factor (VEGF), which signals blood vessels in nearby tissue to grow towards it. In the body, that process can take from 24 to 72 hours; on the computer, it takes about five minutes.

Flann, a computer scientist, and Podgorski, a biologist, gave the model 40 biochemical parameters, such as a cell’s ability to detect a particular growth factor, or how strongly the tip of a growing blood vessel would stick to a stromal cell in the surrounding tissue. The software then chose three parameters, changed one at random, and looked to see whether the change improved or reduced blood-vessel growth in the model. In all, there were about 100,000 possible

parameter combinations that might deprive the tumour of nutrients. To give the results statistical strength, each combination was tested 128 times, running in parallel on two large computer networks belonging to the US National Science Foundation and the US Air Force. Parallel processing allowed the researchers to perform in a few months simulations that would have taken a single processor about five years.

The first clue that the algorithm was effective was that it suggested known interventions, blocking pathways that existing drugs already act on. But it also produced other, previously unknown results. For instance, according to the model, manipulating the adhesion between the endothelial tip cells on the leading edge of blood vessels and the surrounding tissue causes the resulting vessels to become trapped, unable to provide adequate blood flow to the tumour. This, says Flann, suggests a possible avenue of attack for drug developers. In a system comprising hundreds of cells interacting, moving, secreting and reacting to chemicals, simply knowing the genetic mutation behind the tumour or the pathways within the cell would never have led to that kind of insight, says Flann. “The system is a complex spatial and dynamic system that just can’t be predicted.”

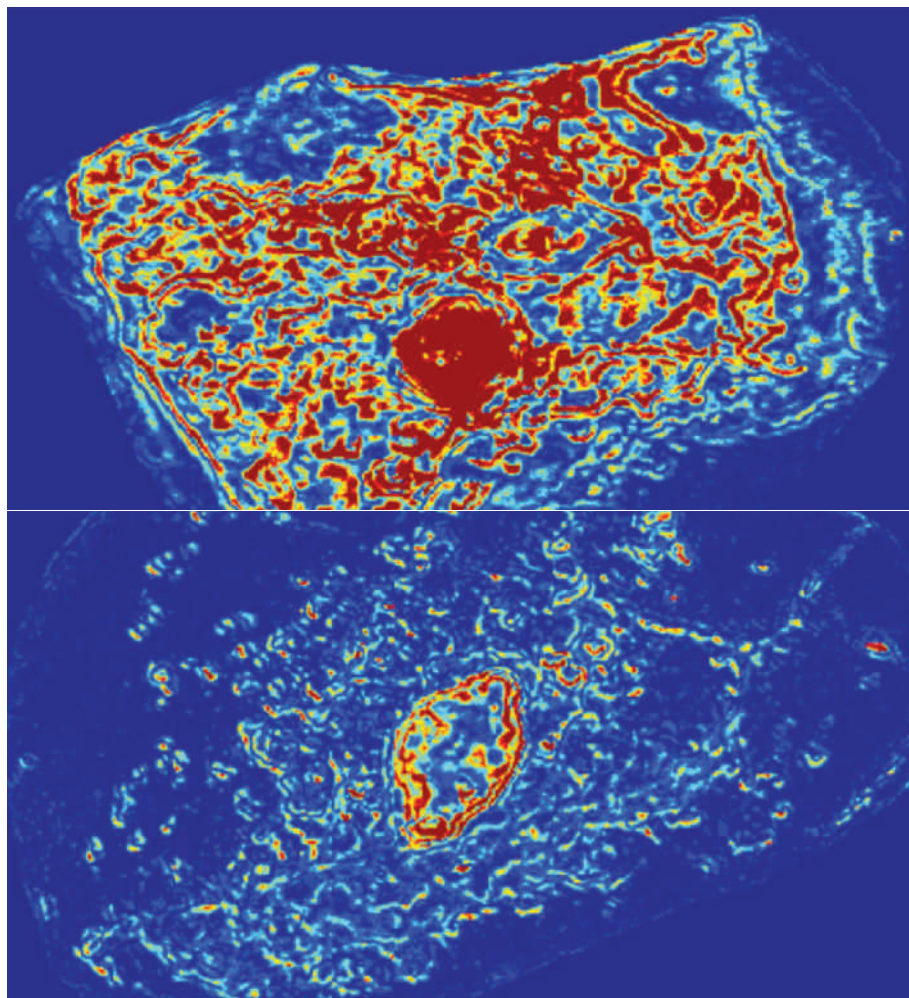
Computational models can run experiments *in silico* that would be too expensive and time-consuming to carry out in the lab. They can generate and test new hypotheses, and provide a way of tracing the steps that led to a particular outcome. But the models must also be validated, as they are no use unless they accurately represent disease in the real world. Maini worries that computational models that combine data from disparate sources — mixing mouse models and rat models with human cells, for example — might lead researchers astray. For instance, the anti-angiogenic drugs he examined starve the tumour more directly in mice than in humans, so an accurate model of human tumours is required. And the computer modellers say that scientists will need to tie the results of the computer simulations to data they can replicate in their labs.

Even so, the models are already giving scientists new ways to explore cancer’s complexity

“It’s a toolbox that is a way of handling the mass of complex data we’ve accumulated in a way that our brains can’t,” says Henney. “It’s an approach that applies engineering principles, physics, chemistry and mechanical engineering to biology. I can’t see how we can handle the complexity of the post-genome world in any other way than using mathematics and physics principles.” ■

Neil Savage is a freelance science and technology writer based in Lowell, Massachusetts.

1. Stamper, I. J. et al. *Bull. Math. Biol.* **69**, 2737–2772 (2007).
2. Fisher, J. & Henzinger, T. A. *Nature Biotechnol.* **25**, 1239–1249 (2007).
3. Swat, M. H. et al. *Meth. Cell Biol.* **110**, 325–266 (2012).
4. Mahoney, A. W. et al. *IEEE Symp. Computat. Intel. Bioinform. Computat. Biol.* 233–240 (2008).



Nanoscale density variations in cancer cells (red colour, top) compared with normal cells (bottom).

DIAGNOSTICS

Playing detective

Physical scientists are developing tools to spot cancer earlier.

BY CASSANDRA WILLYARD

Physicist Peter Kuhn views himself and his colleagues primarily as inventors and problem solvers. But the problem that he and many other physical scientists are trying to solve has plagued biologists and oncologists for decades: how to detect cancer early and stop it from spreading.

Physical scientists have long played an integral role in cancer diagnostics. Magnetic resonance imaging, computed tomography, and positron-emission tomography scans — crucial imaging technologies for identifying cancer and tracking its growth — were developed by physicists, mathematicians and engineers. Physical scientists continue to improve and combine these technologies, but they are also moving into the role of pathologist, developing tools to

help physicians spot cancer in blood and tissue samples. These new technologies, ranging from nanosensors to souped-up microscopes, promise to help find cancer earlier than previously thought possible.

Solid tumours shed cells that enter the bloodstream and travel to other parts of the body, where they can take hold, forming metastases. “This fluid phase of solid tumours is something that’s really poorly understood,” says Kuhn, who is based at the Scripps Research Institute in La Jolla, California. One reason is that circulating tumour cells are so few in number: there may be only a handful of cancer cells among the billions of cells in a tube of blood. “It’s a rare-event detection problem,” Kuhn says.

To identify cancer cells, Kuhn and his colleagues have developed a technique called fluid biopsy, which can be done using a two-millilitre

vial of blood. The researchers eliminate all the red blood cells from the sample and lay what remains on a slide in one “massive monolayer” of 10 million cells, Kuhn says. Then they apply fluorescent stains: a chemical to highlight the cells’ nuclei, an antibody that adheres to immune cells, and another antibody that tags epithelial cells. A digital microscope takes approximately 10,000 images of the slide. “Then we start slicing and dicing,” Kuhn says, using the different stains and a computer algorithm to isolate the epithelial cells that lie at the root of many important cancers — including breast, lung, colon, prostate, pancreas and liver cancer.

Once these cancerous suspects have been identified, “you can do everything you do with a regular biopsy”, Kuhn says, such as look for abnormal morphologies. Kuhn’s research indicates that the fluid biopsy can detect even more circulating tumour cells than the CellSearch assay, a test approved by the US Food and Drug Administration (FDA) that uses antibodies and magnets to isolate tumour cells.

Kuhn and his colleagues are currently investigating whether the number of circulating tumour cells can predict disease progression or treatment response, but in theory the fluid biopsy could also be useful for cancer diagnosis. The team recently showed that their technique could detect circulating tumour cells in blood samples from patients with non-small-cell lung cancer, even in the early stages of disease¹.

Realizing its potential to diagnose cancer will require some significant advances, says Kelly Bethel, a pathologist at Scripps and Kuhn’s collaborator. She is seeking grants to use the technique to search for circulating tumour cells in individuals with a high risk of cancer, such as patients with unidentified masses in their lung or pancreas. Such an approach could help physicians distinguish benign growths from malignant masses that need immediate attention.

The current version of the technology is unable to identify where a circulating tumour cell came from, but future versions might be able to provide that information — the researchers are already searching for a liver-specific marker. “All that potential exists,” Bethel says, “it’s just not well developed.”

THE PROTEIN HUNTER

Sanjiv Gambhir, chair of the radiology department at Stanford University in California, has also been frustrated by physicians’ inability to detect cancer at an early stage. A breast-cancer lump the size of a marble can contain as many as 3 billion cells, he says, and has probably already shed cells that have travelled to other parts of the body. Rather than waiting for a lump to grow to such a potentially lethal size, he is working on a way to detect tumours when they are smaller than the head of a pin.

Gambhir and his colleagues have developed

a postage-stamp-sized chip that uses magnetic nanoparticles to detect cancer proteins in the blood “at much lower levels than otherwise possible”, Gambhir says². When researchers place a drop of blood or other bodily fluid onto the chip, antibodies on its sensor strip lock on to any cancer proteins and secure them to the chip. Then they add more cancer-binding antibodies. “It’s called a sandwich assay,” Gambhir says. “You’ve trapped the thing you’re looking for between two antibodies.” The next step is to wash away any unbound material and add tiny magnetic nanoparticles that bind to the antibodies. When cancer proteins are present, the magnetic particles change the magnetic field and trip the sensor. The researchers then insert the chip into a separate device that identifies which antibodies have been bound and reveals whether any proteins known to be associated with specific cancers are present.

The chip can detect exceedingly small quantities of protein, a thousand times less than those needed for a standard ELISA assay, the method most commonly used to detect cancer proteins in the blood. The latest version of Gambhir’s chip can detect 256 different cancer proteins, improving the test’s sensitivity and specificity. But the device is only as good as scientists’ understanding of cancer biology, so the chip’s development team must work closely with biologists to decide which combinations of proteins are important. “This technology can’t work miracles,” Gambhir says. “If you don’t know what [proteins] to look for, it can’t help you.”

UNDER THE MICROSCOPE

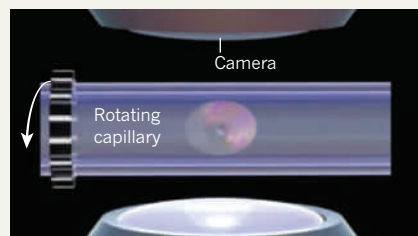
While researchers such as Gambhir are developing new devices to improve cancer diagnosis, other groups are following the same path as Kuhn, trying to boost the diagnostic potential of a centuries-old device — the microscope. VisionGate, a company based in Phoenix, Arizona, has developed an optical technology called Cell-CT, which creates three-dimensional digital images of cells. Cells are lined up single-file in a small, gel-filled tube; as the tube rotates, the microscope captures images of them from multiple angles. A computer algorithm then turns these pictures into a three-dimensional image that researchers can use to identify structural abnormalities that are associated with cancer.

“You sometimes find that the nuclei look like a beach ball that somebody sat on,” says theoretical physicist Paul Davies of Arizona State University’s Center for the Convergence of Physical Science and Cancer Biology in Tempe. Davies and his colleagues, who are testing the technology, recently reported that normal, benign and malignant breast cells from different cell lines displayed distinct morphological characteristics that probably would not have appeared in a conventional two-dimensional image³.

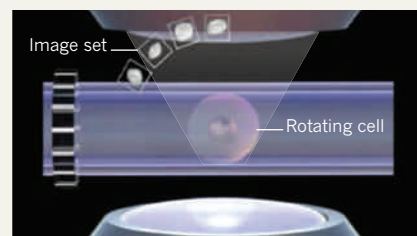
Cell-CT is the only imaging technology able to create a true three-dimensional reconstruction of a cell, says VisionGate’s chief executive,

SINGLE-CELL DIAGNOSTICS

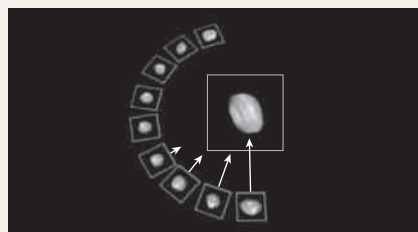
The Cell-CT cancer screening system images and analyses individual cells for morphological characteristics that are distinct to particular cancers.



1. Cells embedded in gel are transported one by one through a glass micro-capillary tube.



2. As the tube spins, each cell is scanned from multiple angles to create a set of images.



3. A computer algorithm combines these into a three-dimensional image of a cell.



4. The system then analyses the final three-dimensional cell image for structural abnormalities specific to cancer.

Alan Nelson. The rendering is so precise that the system can make hundreds of measurements within the cell to search for ‘biosignatures’ associated with cancer. “You don’t actually need a pathologist. It’s all automated,” says electrical engineer Deirdre Meldrum, director of Arizona State University’s Center for Biosignatures Discovery Automation. VisionGate is developing the technology as a screening tool for lung cancer, and has found evidence that the system can detect cancerous cells in the sputum of individuals at high risk of developing the disease.

Vadim Backman, a biomedical engineer at Northwestern University in Evanston, Illinois, has developed a microscope designed to detect even subtler signs of disease. “A limitation of [traditional] microscopy is that you can only see structures larger than half a micrometre,” Backman says. But his research suggests that the earliest signs of cancer appear as nanoscale abnormalities.

To evaluate these tiny aberrations, Backman and his colleagues have developed an instrument that combines traditional microscopy with spectroscopy. The partial-wave spectroscopic (PWS) microscope illuminates the cell and analyses the reflected wavelengths. Their research suggests that the epigenetic and genetic changes that precede cancer cause nanoscale variations in the density of the cell, even though the cell appears superficially normal. The greater the variation, or ‘disorder strength’, the closer the cell is to becoming cancerous.

As well as appearing in the location where

a tumour will occur, the abnormalities also affect nearby cells. This suggests, Backman says, that PWS could potentially be a valuable screening tool. A physician might be able to detect signs of lung cancer in cheek cells, which are easy to obtain, for example. Backman and his colleagues recently used PWS to examine rectal cells from more than 100 individuals who were undergoing colonoscopies, and found a strong correlation between cellular disorder at the nanoscale and the risk of colorectal cancer⁴.

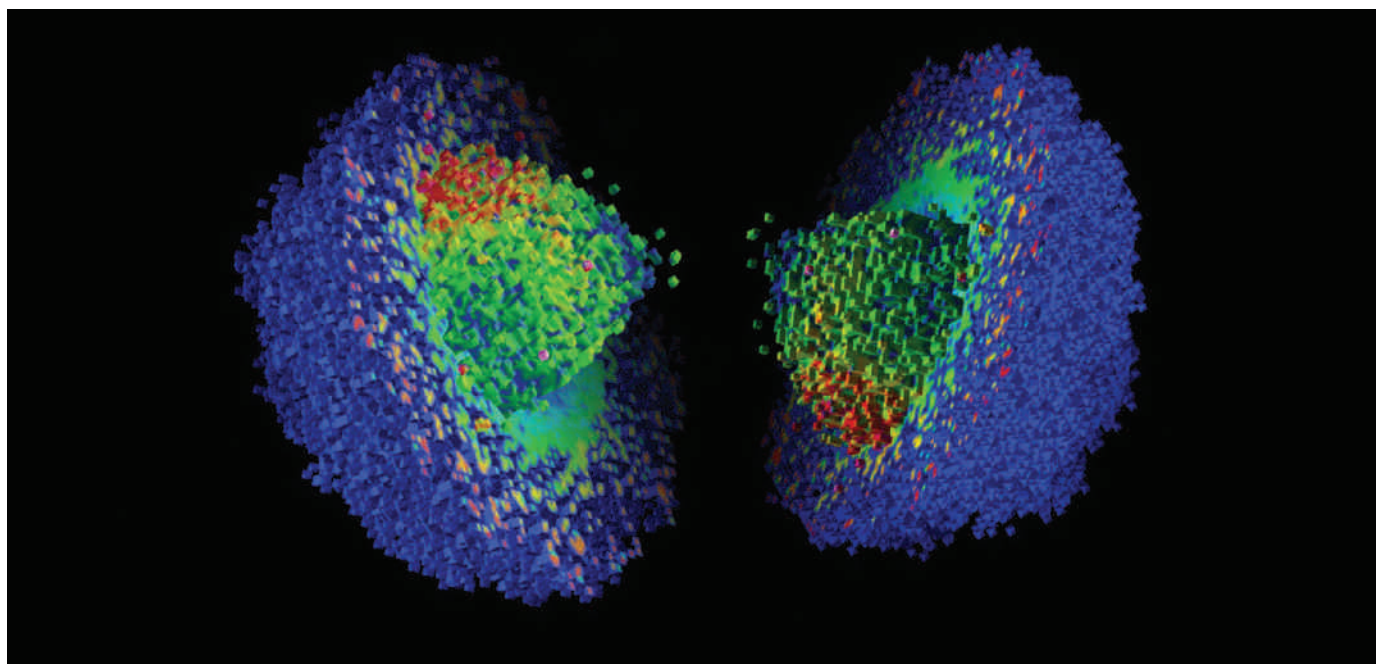
THE SOONER, THE BETTER

Physical scientists hope these tools will help oncologists detect cancer early, before it gains a foothold in the body. The five-year survival rate for lung cancer caught early is about 50% — but catching it early is incredibly difficult, because symptoms typically appear only during advanced stages of disease. Once the cancer has spread, the survival rate drops to just 1%.

Ideally, screening tools and diagnostics would not only be able to detect early signs of cancer, but also differentiate between harmless changes and abnormalities that precede the disease. However, that’s a formidable challenge that will keep Kuhn and his inventor colleagues busy for decades to come. ■

Cassandra Willyard is a freelance science writer based in Brooklyn, New York.

1. Wendel, M. *et al.* *Phys. Biol.* **9**, 016005 (2012).
2. Gaster, R. S. *et al.* *Nature Med.* **15**, 1327–1332 (2009).
3. Nandakumar, V. *et al.* *PLoS One* **7**, e29230 (2012).
4. Damania, D. *et al.* *Cancer Res.* **72**, 2720–2727 (2012).



The inside of a tumour can be visualized on a computer by using mathematical models.

MATHEMATICAL MODELLING

Forecasting cancer

Complex mathematical models are helping researchers understand cancer's evolution and providing clues on how to thwart drug resistance.

BY KATHARINE GAMMON

Einstein once called pure mathematics “the poetry of logical ideas”. It is a poetry that has allowed astronomers to understand the movement of planets, and it has shaped our understanding of the physical world around us. Now it is set to reshape our view of cancer. From speeding up clinical trials to predicting cellular mutation and evolution, mathematical models are helping to transform fundamental ideas underlying the disease.

Mathematicians are making inroads in oncology with approaches that used to be the realm of biologists: building intricate models of cancer ecology and evolution. It's a logical transition. The forces of environmental selection and adaptation that act on organisms also govern the way cancer cells develop, and a better understanding of how the disease evolves and adapts to environmental changes can help researchers find a way to stop it. “Evolutionary theory is the theory for cancer,” says Carlo Maley, a computational and evolutionary biologist at the University of California, San Francisco. “If we can engage with this evolutionary process, we can slow it down or shunt it in a direction that's more manageable.”

Cancer's heterogeneity is the main reason

it is so difficult to treat — if it retains a diverse enough population, a few impervious tumour cells can survive chemotherapy or radiation and re-establish their hold on the body. So mathematicians are creating models to predict in which direction a mutating cancer cell will change, in the hope of stopping evolution in its tracks.

ELIMINATING GUESSWORK

Through modelling, researchers can now predict the behaviour of some of the toughest cancers. Historically, oncologists have evaluated the prognosis of glioma, an aggressive form of brain cancer, on the basis of imaging and histological data. But that grading system didn't match up with reality, leading researchers at the University of Washington in Seattle and the Moffitt Cancer Center in Tampa, Florida, to develop a mathematical model based on cell proliferation, invasion rates and changes in appearance. The model marries data from imaging studies with other models that incorporate blood-vessel growth patterns and tumour microenvironment, and was able to reproduce the growth patterns of each patient's specific tumour, and also reliably predict how it would progress — validating the method and improving on the existing grading.

Such models are starting to have an impact in the clinic. Alexander Anderson, a mathematical

and computer modeller at the Moffitt centre and one of the team who worked on the glioma study, is using the model to investigate how cancer moves and spreads¹. His lab has built computer models that focus on the changes to individual cancer cells. The models integrate information from different *in vitro* experiments with factors from *in vivo* environments to gain a better understanding of how cancer progresses one cell at a time. Anderson recently used clinical data from 650 prostate-cancer patients. Each patient's tumour was sliced multiple times and stained for 250 markers. He then integrated that biopsy information into a model, creating a digital version of the biopsy. When he and his colleagues move the model forward in time and space, they can create a predictive measure of whether a tumour will be aggressive.

This detailed ability to predict invasiveness is particularly important in diseases such as prostate cancer, in which some tumours are removed unnecessarily and treated aggressively. To assess the model's predictive accuracy, Anderson's team, working with a biologist, is testing it in mice. If the model works, it would be the first to predict a tumour's aggression before the start of treatment, providing oncologists with a guide for treatment options.

Beyond evolutionary dynamics, mathematical

models are helping to reshape the way some researchers approach cancer treatments. The improved understanding of cancer evolution provided by the models provide has led some researchers to a counter-intuitive conclusion: for most cancers, targeted therapy just doesn't work. When you use drugs that target specific mutations, Anderson says, "our models tell us that you're destined to see drug resistance because there's another route to the same phenotype". Cells that survive the first wave of therapy can evolve to have the same malignant characteristics but without the same vulnerability to the drug. What's more, the evolutionary dynamics of tumours suggest that trying to eliminate cancers speeds up the development of drug resistance, reducing a patient's chances of survival. Models show that there might be a better way.

CHANGING THE GAME

Some researchers are looking for ways to hack cancer's programming and turn it against itself. Robert Gatenby, an oncologist at the Moffitt Cancer Center, has been seeking fundamental laws he can exploit. One way to attack tumours is to make them similar to each other; the more homogenous they are, the lower the odds that they will become resistant to treatment, and the greater the chances that therapy will be effective. In essence, he is looking for tricks to prevent the evolution of drug resistance.

Mathematical models allow Gatenby and others to determine the right combinations of drugs, and the optimal sequence in which to give them, to best combat resistance. In one mouse study of triple-negative breast cancer — a hard-to-treat subtype characterized by a lack of receptors for oestrogen and other hormones — researchers used models to determine when they should use different drugs, and in what sequence. The results suggested that dosing the animals with extra oestrogen would encourage the disease to adapt to a high-oestrogen environment. By guiding evolution's natural resistance mechanism, the cancers that emerged were oestrogen dependent — and were thus treatable with oestrogen-dependent cancer drugs, such as tamoxifen.

Treating cancer would be so much easier if oncologists could predict how it would react to treatment. At the moment, cancer treatment is an endless battle against an evolving foe, Gatenby says. "Cancer comes up, and we whack it and do another treatment." But he sees a better way. "We need to plan strategically how we treat patients, so that as we give one therapy, we're producing an adaptive response to be anticipated with our second therapy. Instead of whac-a-mole, we need to be playing chess."

Gatenby's team uses a game-theory model to show that cancers are good at adapting to their current situation but cannot anticipate the future. This insight gives oncologists a fundamental advantage: they can manipulate the tumour environment in ways that leave

the cancer more vulnerable. The model lets researchers discard options that would increase resistance, narrowing the range of options for treatments, doses and dosing frequency.

The evolutionary game-theory model — in which each treatment was a move in the game, made in anticipation of cancer's response — suggested the development of that vulnerability and helped clarify results from a recent clinical trial².



Prompting lung cancer to evolve one way might make traditional treatments more effective.

Patients with recurring, aggressive lung cancer who were treated with both traditional chemotherapy and a vaccine targeting the tumour-suppressing p53 protein fared better than patients who didn't receive the vaccine. The combination of treatments increased survival time by about 4 months and doubled the number of people surviving more than a year. "The tumour successfully adapted to an initial therapy, but that adaptation rendered it more susceptible to another therapy," Gatenby said. This is known as an evolutionary double bind. "We don't pretend that this could last forever, but if we could get an extra five to ten years out of evolutionary tricks, it would be a huge improvement."

DEVisING DOSING STRATEGIES

Mathematical modelling is also helping to speed up the clinical trials that test those drugs. Testing all the possible permutations of drugs and doses to determine the best course of therapy might take millions of clinical trials — and there are nowhere near enough patients or resources for that. So instead researchers are using mathematical models that make it possible to derive the same information from only a handful of experiments. Such models can describe the rate of mutation, calculate the likelihood of resistance, and even predict the chance that a certain tumour will respond to treatment.

Franziska Michor, a biostatistician at Harvard School of Public Health in Boston, Massachusetts, has built a model to predict the optimal dosing scheme for lung-cancer therapy. By accounting for the growth and death rates of different types of cell, their mutation rates, and how quickly the body metabolizes a drug, Michor's mathematical framework calculates the probability of the tumour developing

resistance for different dosing strategies. "Eventually we have to validate with mouse and human trials, but the pre-validation studies can be on a computer," Michor says. The computer model can test just about every possible combination in a few seconds — much faster than doing clinical trials. "That's the advantage of maths," she says. "If you run an infinite number of clinical trials, you will grow a really long beard. But on the computer, it works quickly."

In 2013, the Memorial Sloan-Kettering Cancer Center in New York will run the first trial based on Michor's model. Researchers will test the dosing patterns the model deemed best to prevent or delay resistance in non-small-cell lung cancer. With this disease, resistance typically appears a year after treatment ends, but Michor's model predicts that the best dosing strategy will delay resistance by another year³.

And there's more. Mathematical models can also help researchers understand, and even prevent, tumour development. Larry Norton, an oncologist at the Memorial Sloan-Kettering centre, has devised a model of tumour growth based on nineteenth-century mathematics. The S-curve model showed that while tiny tumours barely grow at all, medium-sized tumours grow at a rapid pace, and large ones grow slowly. Norton and his colleagues hypothesized that the rate at which a tumour shrinks would also be proportional to its size, with large tumours shrinking slowly and small ones rapidly.

The conventional view of chemotherapy dosing held that, because tumour growth was exponential, each treatment killed the same amount of tumour. Norton, however, used his theory to argue that giving the same total amount of chemotherapy over a shorter period of time should improve the cure rate. Because his model showed that young tumours have the fastest growth rate, he said, the less time they had to regrow between treatments, the better the cure rate would be. Norton's idea was vindicated in 2002, when a large breast-cancer trial showed that giving chemotherapy every two weeks instead of every three lowered the risk of disease recurrence by 26% over three years, even though the cumulative dose was the same.

Norton makes the point that none of this would be possible without integrating biological growth models into treatment research. "The biological sciences have become anti-maths, and it's just not working. Researchers see lots and lots of facts, but they're not connecting them together," he says. "It's like looking up at a starry sky and wondering how it worked. Only when Kepler and Newton came along did things fall into place." ■

Katharine Gammon is a freelance science writer based in Santa Monica, California.

1. Swanson, K. R. *et al. Cancer Res.* **71**, 7366–7375 (2011).
2. Basanta, D., Gatenby, R. A. & Anderson, A. R. *Mol. Pharm.* **9**, 914–921 (2012).
3. Chmielecki, J. *et al. Sci. Trans. Med.* **3**, 90ra59 (2011).

Nanopore-based detection of circulating microRNAs in lung cancer patients

Yong Wang^{1†}, Dali Zheng^{2†}, Qiulin Tan¹, Michael X. Wang^{2*} and Li-Qun Gu^{1*}

MicroRNAs are short RNA molecules that regulate gene expression, and have been investigated as potential biomarkers because their expression levels are correlated with various diseases. However, detecting microRNAs in the bloodstream remains difficult because current methods are not sufficiently selective or sensitive. Here, we show that a nanopore sensor based on the α -haemolysin protein can selectively detect microRNAs at the single molecular level in plasma samples from lung cancer patients without the need for labels or amplification of the microRNA. The sensor, which uses a programmable oligonucleotide probe to generate a target-specific signature signal, can quantify subpicomolar levels of cancer-associated microRNAs and can distinguish single-nucleotide differences between microRNA family members. This approach is potentially useful for quantitative microRNA detection, the discovery of disease markers and non-invasive early diagnosis of cancer.

MicroRNAs are a class of short (~18–22 nucleotides) non-coding RNAs that are important in development and cell differentiation, the regulation of the cell cycle, apoptosis and signalling pathways^{1,2}. Since its initial discovery in *Caenorhabditis elegans* in 1993 (ref. 3), over 17,000 microRNAs have been identified across different species, including humans⁴. In the cytoplasm, mature microRNAs are associated with an RNA-induced silencing protein complex to bind with the 3'-untranslated region of target messenger RNAs^{1,5,6}. By either repressing translation or cleaving the target messenger RNA^{1,5,6}, these microRNAs regulate around 30% of human gene expression⁵ at the post-transcriptional level. Aberrant expression of microRNAs has been found in all types of tumours^{7,8}, and different types of cancers have distinct microRNA profiles⁹. Interestingly, microRNAs can be released from the primary tumour into the bloodstream in a stable form¹⁰. Circulating microRNAs are enveloped inside exosomal vesicles and are transferable to and functional in recipient cells^{11–13}. Therefore, the detection of tumour-specific circulating microRNAs is useful for the early diagnosis, staging and monitoring of cancer^{7,8,10–13}.

Quantitative reverse transcription real-time polymerase chain reaction (qRT-PCR) assays and microarrays have been developed for the detection of microRNA. However, these methods suffer from error-prone amplification, cross-hybridization, and a lack of valid internal controls^{14,15} because the shortness of the microRNA sequences makes it difficult to design probes and primers. Other techniques based on colorimetry, bioluminescence, enzyme turnover and electrochemistry have been proposed, and nanoparticles, molecular beacons, deep sequencing^{16,17} and single-molecule fluorescence¹⁸ have also been applied to microRNA detection (for reviews, see refs 16, 17). However, many of these methods still require the labelling and chemical modification of the target or expensive instruments.

The nanopore is a molecular-scale pore structure that is able to detect, with high sensitivity, the position and conformation of a single molecule that is present within the pore lumen¹⁹. From the characteristic change in nanopore conductance, one can electrically

elucidate single-molecule kinetic pathways and quantify the target. Various nanopore sensors are being developed with broad biotechnological applications^{19–24} (for reviews, see refs 19–23), including the next generation of DNA sequencing technology^{25,26}. The development of nanopore-based microRNA detectors is a novel effort in this rapidly evolving field, and Wanunu *et al.* first reported the use of a 3 nm synthetic pore to quantify the translocation of enriched microRNAs that were hybridized to a probe²⁷. In this report, we construct a protein-nanopore-based sensor that enables sensitive, selective and direct quantification of cancer-associated microRNAs in the blood and discrimination of single-nucleotide differences in microRNA family members.

Generation of microRNA signatures in the nanopore

We used the α -haemolysin protein pore, a toxin from *Staphylococcus aureus* bacterium²⁸, as the sensor element. The translocation of single-stranded oligonucleotides through this 2 nm pore has been studied extensively^{29–32}. However, it is difficult to distinguish the translocation of different microRNAs because the sequences of all microRNAs are short and similar in length. One way of overcoming this challenge is to use a signature that can detect target microRNA in the mixture. We identified such a microRNA signature signal in the nanopore using an oligonucleotide probe.

The probe structure is shown in Fig. 1a. The capture domain of the probe was used to bind the target microRNA by Watson–Crick base pairing in the solution. Each end (3' and 5') of the capture domain was extended with a poly(dC)₃₀ signal tag. Our first target was miR-155, a lung-cancer-associated microRNA^{12,13,33}. Figure 1b illustrates a sequence of nanopore current events in the presence of miR-155 and its probe, P₁₅₅, on the *cis* side of the pore. The boxed events represent a characteristic type of multi-level block that was generated by the miR-155-P₁₅₅ hybrid. This block type was not observed in the presence of miR-155 or P₁₅₅ alone in the *cis* solution. In a multi-level block (Fig. 1c, left panel), the Level 1 state lasted for 250 ± 58 ms, which is almost equal to the entire event duration, and significantly reduced the nanopore current, with a relative residual conductance (g/g_0) of 0.15. The Level 1 state was followed

¹Department of Biological Engineering and Dalton Cardiovascular Research Center, University of Missouri, Columbia, MO 65211, ²Ellis Fischel Cancer Center and Department of Pathology and Anatomical Sciences, University of Missouri, Columbia, MO 65211, USA; [†]These authors contributed equally to this work.

*e-mail: gul@missouri.edu; wangmx@health.missouri.edu

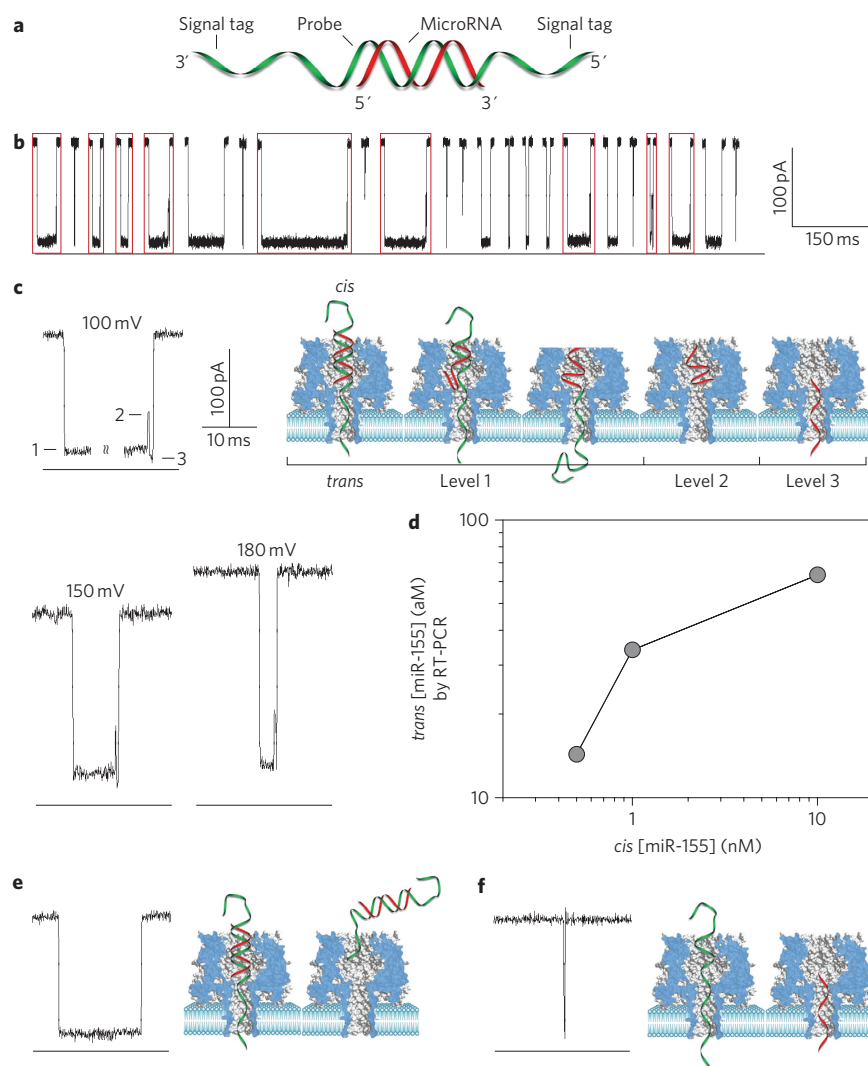


Figure 1 | Capturing single microRNA molecules in the nanopore. **a**, Molecular diagram of a microRNA (red) bound to a probe (green) bearing signal tags on each end. **b**, Sequence of nanopore current blocks in the presence of 100 nM miR-155 and 100 nM P_{155} in the *cis* solution. Traces were recorded at +100 mV in solutions containing 1 M KCl buffered with 10 mM Tris (pH 8.0). Red boxes represent the multi-level current pattern. **c**, A typical multi-level long block (from **b**) at +100 mV generated by the miR-155- P_{155} hybrid. Right panel: diagram showing the molecular mechanism of hybrid dissociation and translocation. Level 1: trapping of the microRNA-probe hybrid in the pore, unzipping of the microRNA from the probe and translocation of the probe through the pore. Level 2: unzipped microRNA residing in the pore cavity. Level 3: translocation of the unzipped microRNA through the pore. Lower panel: multi-level blocks at +150 and +180 mV. Increasing the voltage reduced the duration of Levels 1 and 3, which supports the above mechanistic model. **d**, miR-155 levels detected by qRT-PCR in *trans* solutions. Before detection, the pore current was monitored in 0.5 M/3 M (*cis/trans*) KCl at +180 mV in the presence of 1 μ M P_{155} and 0.5, 1 or 10 nM of miR-155 in the *cis* solution. A much higher probe concentration than microRNA was used to enhance their hybridization in the *cis* solution (see Supplementary Information S1). **e**, A single-level block (from **b**) generated by a trapped miR-155- P_{155} hybrid that exited the pore from the *cis* entrance without unzipping and translocation. **f**, A spike-like short block generated by the translocation of unhybridized miR-155 or P_{155} from the *cis* solution.

by a discrete current increase to the Level 2 state, which persisted for $410 \pm 20 \mu$ s, with a g/g_0 of 0.42. Finally, the current dropped to the Level 3 state and remained there for $270 \pm 30 \mu$ s before returning to the full open base level. Similar to Level 1, Level 3 almost fully reduced the pore current, with a g/g_0 of 0.08. The right panel in Fig. 1c depicts the molecular configurations that correspond to the multi-level block. The amplitude and duration of Level 1 were consistent with a configuration in which the miR-155- P_{155} complex was trapped in the nanopore at the 2.6 nm *cis* opening, with either the 3' or 5' signal tag of P_{155} occupying the 1.6–2.0 nm β -barrel. Driven by the transmembrane voltage, the signal tag in the β -barrel induced the dissociation of miR-155- P_{155} . The dissociation time (the duration of Level 1) was comparable to previously reported timescales for DNA unzipping in the pore^{34,35}. After unzipping, P_{155} left the pore through the narrower (*trans*) opening, and the Level 1

state was terminated. The Level 2 state featured large residue conductance, which should correspond to a configuration in which miR-155 unzipped from miR-155- P_{155} and temporarily resided in the nanocavity. This result is consistent with a previous finding which showed that an oligonucleotide trapped in the nanocavity can generate partial blocks³⁶. The miR-155 in the nanocavity finally passed through the β -barrel to yield the short-lived Level 3 state. The duration of Level 3 (270 μ s) was consistent with the translocation duration of miR-155 alone (220 μ s) and the timescale for DNA or RNA translocations in previous studies^{29–32}. The molecular mechanism described above was further proved by the voltage-dependent durations of Levels 1 and 3. Level 1 was shortened by a factor of 23 to 11 ms and Level 3 by a factor of 2 to 150 μ s as the voltage increased from +100 to +180 mV (Fig. 1c, lower panel). This indicated that the voltage both enhanced the unzipping of miR-155- P_{155} and

accelerated the translocation of miR-155 (ref. 30). After the electrical recording, we quantified miR-155 in the *trans* solution using qRT-PCR (Fig. 1d and Supplementary Information S1). For 0.5, 1 and 10 nM of *cis* miR-155 (1 μ M of P₁₅₅), the corresponding *trans* miR-155 concentration values were 14, 34 and 63 aM. The *trans* miR-155 identification verifies that the microRNA that unzipped from the microRNA-probe hybrid indeed translocated to the *trans* side of the pore.

The miR-155-P₁₅₅ hybrid also produced single-level long blocks that had the same conductance ($g/g_0 = 0.15$) as Level 1 of the multi-level block (Fig. 1e). The single-level block was formed by the trapped miR-155-P₁₅₅ complex that returned to the *cis* solution without unzipping and translocation. The frequency ratio of multi-level to single-level events monotonically increased with voltage, from 0.42 at +100 mV to 1.4 at +180 mV (Supplementary Table S2). This voltage-dependent frequency variation was consistent with the expectation that higher voltage increases the unzipping probability of miR-155-P₁₅₅ and decreases its probability of escaping. In addition to the characteristic long events, we observed spike-like short blocks in the same recordings (Fig. 1f). Both their duration (220 ± 21 μ s) and conductance ($g/g_0 = 0.16$) were similar to the translocation of unhybridized miR-155 or P₁₅₅ present in the *cis* solution (Supplementary Fig. S1).

The above analysis indicates two important functions performed by the signal tag of the probe: guidance of the microRNA-probe complex entrapment in the pore and inducement of the dissociation of the microRNA-probe complex. The configuration change during the unzipping process gave rise to signature current patterns, which enabled the recognition of single target microRNA molecules. Because of the specificity of the probe, the frequency of the signature signal (f_{sig}) was independent of the presence of multiple nucleic acid components (Supplementary Fig. S3) and could therefore be used to quantify target microRNA in the mixture. Overall, the signature signal ensured the high selectivity required for microRNA detection in plasma RNA extract.

Quantification of microRNAs using optimized probes

The frequency of signature events can be used to quantify microRNA by the equation $f_{\text{sig}} = k_{\text{on}} [\text{miR}]_0$, where $[\text{miR}]_0$ is microRNA concentration and k_{on} is the occurrence rate constant of signature events (Supplementary Information S2). k_{on} is a key parameter that quantifies sensitivity and can be greatly improved by optimization of the probe structure. The left panel of Fig. 2a shows the traces for detecting miR-155 using probes with a poly(dC)₃₀ tag at the 5' end (P_{5'-C30}), 3' end (P_{3'-C30}) or both ends (P₁₅₅). The right panel compares the k_{on} values for different probes. The probe without the signal tag (P_{nt}) gave the lowest k_{on} at $2.8 \pm 0.6 \times 10^4 \text{ M}^{-1} \text{ s}^{-1}$. k_{on} tripled to $6.8 \pm 1.3 \times 10^4 \text{ M}^{-1} \text{ s}^{-1}$ when the probe was attached to a poly(dC)₃₀ tag at the 5' end (P_{5'-C30}). However, k_{on} increased by a factor of 50 to $1.4 \pm 0.3 \times 10^6 \text{ M}^{-1} \text{ s}^{-1}$ when the poly(dC)₃₀ tag was attached to the 3' end (P_{3'-C30}). This orientation discrimination of single-stranded oligonucleotides in the nanopore is consistent with previous studies^{37,38}. As expected, the P₁₅₅ probe that contained both 3' and 5' poly(dC)₃₀ achieved the highest k_{on} at $2.0 \pm 0.2 \times 10^6 \text{ M}^{-1} \text{ s}^{-1}$. In addition to tag directionality, k_{on} also depends on tag length. For example, the poly(dC)₃₀ tag showed higher efficiency in the generation of signature events than a shorter tag, such as poly(dC)₈, and was more efficient than the poly(dA)₃₀ and poly(dT)₃₀ tags (unpublished data).

Using P₁₅₅ as the probe, we verified that the frequency of the signature event was proportional to the miR-155 concentration range from 10 to 100 nM (Fig. 2b, left panel). This correlation was measured at +100 mV in 1 M KCl. The frequencies in any two miR-155 concentrations, such as 10 and 25 nM, were significantly separated ($P < 0.005$). Wanunu *et al.* reported that a gradient of salt concentration across a synthetic nanopore greatly increases

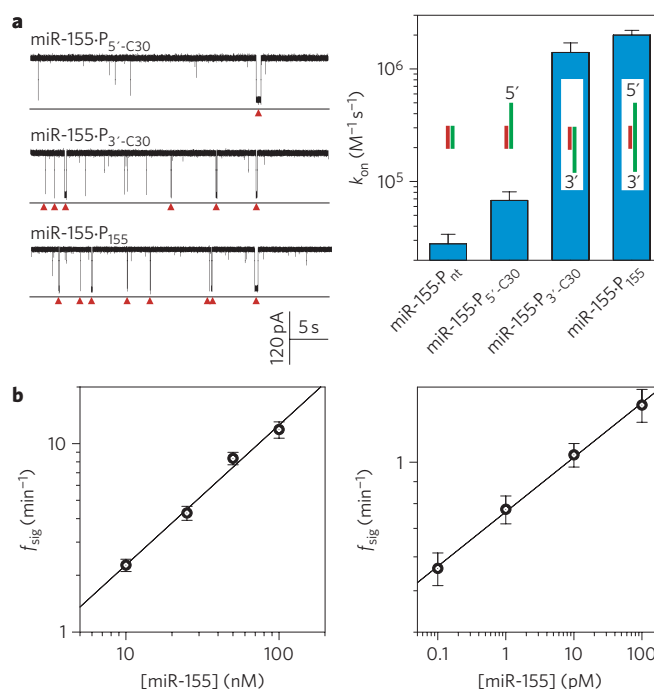


Figure 2 | Optimizing the probe sequence for enhanced detection

sensitivity. a, Left panel: current traces showing the frequencies of signature events for miR-155 hybridized to the probes P_{5'-C30} (top), P_{3'-C30} (middle) and P₁₅₅ (bottom), monitored at +100 mV in 1 M KCl. Right panel: occurrence rate constant of signature events for miR-155 detection with different probes (see Supplementary Table S3 for details). **b,** Left panel: [miR-155]— f_{sig} correlation for target concentration ranges between 10 and 100 nM in 1 M KCl. Right panel: [miR-155]— f_{sig} correlation measured in 0.2 M/3 M (*cis/trans*) KCl with much lower target concentrations (between 0.1 and 100 pM). Data in both panels were measured at +100 mV. The results between any two miR-155 concentrations were statistically significant ($P < 0.01$).

the capture rate of dsDNA³⁹. Similarly, the use of asymmetrical KCl solutions (0.2 M/3 M, *cis/trans*) allowed measurement of the frequency of microRNA events at far lower concentrations, from 0.1 to 100 pM (Fig. 2b, right panel). In addition to the use of asymmetric solutions, the application of high voltage (Supplementary Fig. S2) and the use of an engineered nanopore⁴⁰ also proved effective in increasing the event frequency for high sensitivity.

Discrimination of microRNAs with similar sequences

Among the over 1,400 human microRNAs that have been identified, many members of the same microRNA family have similar sequences or single-nucleotide polymorphisms (SNPs)⁴. The SNPs are associated with significant biological properties of cancers, such as susceptibility, prognosis and response to therapeutic agents⁴¹. However, sequence-similar microRNAs or SNPs are difficult to distinguish using current PCR or hybridization-based methods^{14–16}. Because dsDNAs that contain a single-nucleotide mismatch are identifiable in the nanopore based on their unzipping times^{35,42–44}, we decided to study whether the nanopore could distinguish single-nucleotide differences in microRNA family members.

We selected the *let-7* tumour-suppressing microRNA family^{7–9} as the target. *Let-7* is downregulated in lung cancer and is therefore useful as a biomarker and potential therapeutic agent⁴⁵. *Let-7a* and *let-7b* have two nucleotide differences (see the sequences in Supplementary Table S1), and their probes are P_a and P_b, respectively. The hybrids *let-7a*-P_a and *let-7b*-P_b were fully matched, but

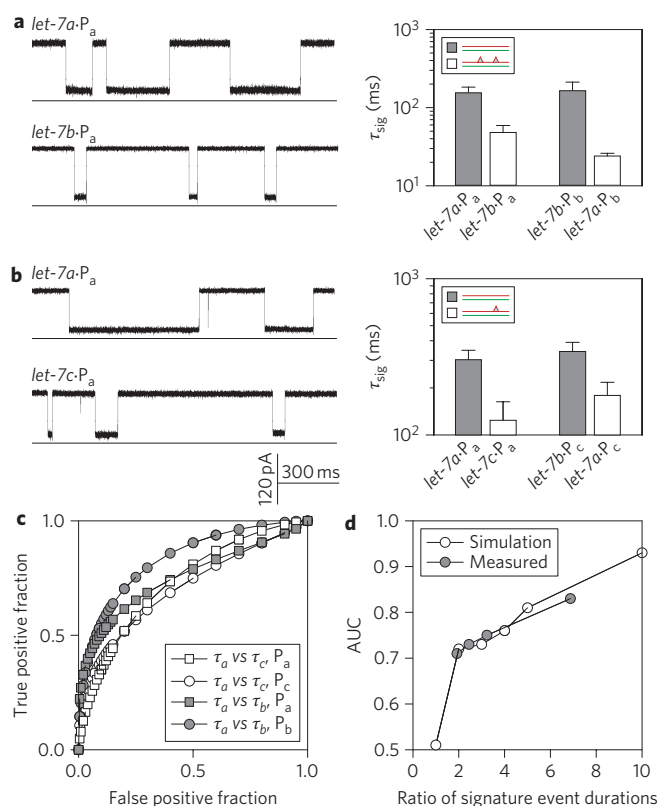


Figure 3 | Differentiation of *let-7* microRNAs that contain one or two different nucleotides. The sequences of *let-7a*, *let-7b* and *let-7c* are provided in Supplementary Table S1. **a**, Detection of *let-7a* and *let-7b* using the probe *P_a* or *P_b* at +120 mV. Left: current traces. Right: duration of signature events. **b**, Detection of *let-7a* and *let-7c* using the probe *P_a* or *P_c* at +100 mV. Left: current traces. Right: duration of signature events. See Supplementary Fig. S4 for a representative histogram and Supplementary Table S4 for raw data. **c**, ROC curves for the discrimination of events for fully matched microRNA-probe hybrids (defined as positive events) and microRNA-probe hybrids containing mismatched base pairs (defined as negative events). Open squares: *let-7a-P_a*/*let-7c-P_a*; open circles: *let-7c-P_a*/*let-7a-P_a*; filled squares: *let-7b-P_a*/*let-7a-P_a*; filled circles: *let-7b-P_a*/*let-7c-P_a*. **d**, Correlations between AUCs and the ratio of event duration for fully matched hybrids to those with mismatched base pairs. Filled circles: AUCs measured from the ROC curves in **c** (Supplementary Table S5); open circles: AUCs calculated from ROC analyses based on simulated data sets (Supplementary Fig. S5 and Table S6). The computer-generated event duration followed an exponential distribution. The ratios of event duration for ROC analysis were 1, 2, 3, 4, 5 and 10.

let-7b-P_a and *let-7a-P_b* contained two mismatches. The left panel of Fig. 3a shows the traces for *let-7a-P_a* and *let-7b-P_a*. The right panel shows that the unzipping time, τ_{sig} , at +120 mV for *let-7b-P_a* (48 ± 11 ms) is 3.2-fold shorter than that for *let-7a-P_a* (155 ± 28 ms) ($P < 0.005$), and 6.9-fold shorter when *let-7a-P_b* (24 ± 2 ms) is compared with *let-7b-P_b* (165 ± 47 ms) ($P < 0.005$). Similarly, *let-7a* and *let-7c* have only one nucleotide difference. The left panel of Fig. 3b shows the traces for *let-7a-P_a* and *let-7c-P_a*. The right panel shows that when using *P_a* and *P_c* to target *let-7a* and *let-7c* at +100 mV, respectively, τ_{sig} decreased by a factor of 2.4 from 303 ± 45 ms for *let-7a-P_a* to 124 ± 39 ms for *let-7c-P_a* ($P < 0.005$) and by a factor of 2.0 from 342 ± 49 ms for *let-7c-P_c* to 179 ± 38 ms for *let-7a-P_c* ($P < 0.005$).

We constructed receiver operating characteristic (ROC) curves to compare the durations of events for fully matched microRNA-probe hybrids and for microRNA-probe hybrids that

contain mismatches (Fig. 3c). On the basis of ROC curves, we measured the area under the ROC curve (AUC, Fig. 3d), which is an indicator of the ability to discriminate nucleotide differences between microRNAs. The AUCs varied between 0.72 and 0.83, and increased with the ratio of event duration between fully matched hybrids and mismatches. The ratio-dependent AUC was further verified using a simulation method (Fig. 3d, Supplementary Fig. S5 and Supplementary Table S6). ROC analysis strongly suggests that the nanopore is able to discriminate SNPs in microRNAs based on the duration of the signature event. The ability to discriminate SNPs in the microRNAs was tested in a mixture of 100 nM *let-7a* and *let-7c* and probed with *P_a*. On the basis of the AUCs, the optimal cut-point duration was calculated to be ~ 190 ms, which was the threshold duration that provided the best discriminatory ability (Supplementary Table S6). Block events that were longer than the optimal cut-point occurred for *let-7a-P_a*, and events that were shorter than the optimal cut-point occurred for *let-7c-P_a*. The number of events was transformed into concentrations of *let-7a* and *let-7c*, which were 85 and 120 nM, respectively. Both concentrations varied by 15–20% from the real concentration of 100 nM.

Detection of microRNA levels in lung cancer patients

Lung cancer is the leading cause of cancer mortality in men and women worldwide and is responsible for about 1.2 million deaths each year⁴⁶. Because no effective screening procedure is available, more than 70% of patients are diagnosed at advanced stages, with a five-year survival rate of less than 15% (ref. 46). At present, over one hundred microRNAs have been identified to be dysregulated in lung cancer^{7–13,17,33,41}. High levels of miR-155 and low levels of *let-7a-2* correlate with significantly poor prognoses and shorter survival times in lung cancer patients^{47,48}.

We detected plasma miR-155 in lung cancer patients using the nanopore sensor. Peripheral blood samples were obtained from six lung cancer patients and six healthy volunteers after local Institutional Review Board approval. Total plasma RNAs, which contained microRNAs, were extracted from 350 μ l of each plasma sample using a mirVana PARIS Kit (Ambion), with a final elution volume of 100 μ l. The elution volumes were then divided into two 50 μ l aliquots for the nanopore and qRT-PCR assays, respectively. One aliquot was mixed in the recording solution with or without the *P₁₅₅* probe. The nanopore current retained a low level of noise even in the presence of plasma extracts. In the absence of *P₁₅₅*, only short blocks were observed as a translocation of single-stranded oligonucleotides such as free microRNAs in the healthy individuals control group (Fig. 4a) and the lung cancer group (Fig. 4b). In the presence of the probe, distinct short and long blocks were identified in both the healthy individuals control group (Fig. 4c) and the lung cancer group (Fig. 4d). Characteristic long blocks shared the same current profile and properties as synthetic miR-155 RNA (Fig. 1). The frequency of long blocks in the lung cancer group was significantly higher than that in the healthy individuals group. More frequent short events were also observed in the presence of *P₁₅₅* (Fig. 4c,d) than without *P₁₅₅* (Fig. 4a, b). Most of these short events were contributed by the *P₁₅₅* probe, because its translocation rate was 8.4 times higher than that of microRNA (Supplementary Fig. S6). Overall, the characteristic long blocks were attributed to miR-155-*P₁₅₅* hybrids and served as signatures for the identification of single molecules of miR-155.

To normalize the assay, the frequencies of miR-155 signature events (f_{155}) for all the samples of the lung cancer and control groups were measured in the presence of a spiked-in synthetic *C. elegans* microRNA miR-39. Figure 4e shows that all the f_{155} values in the lung cancer group were higher than those in the control group ($P < 0.001$). However, Fig. 4f shows that the

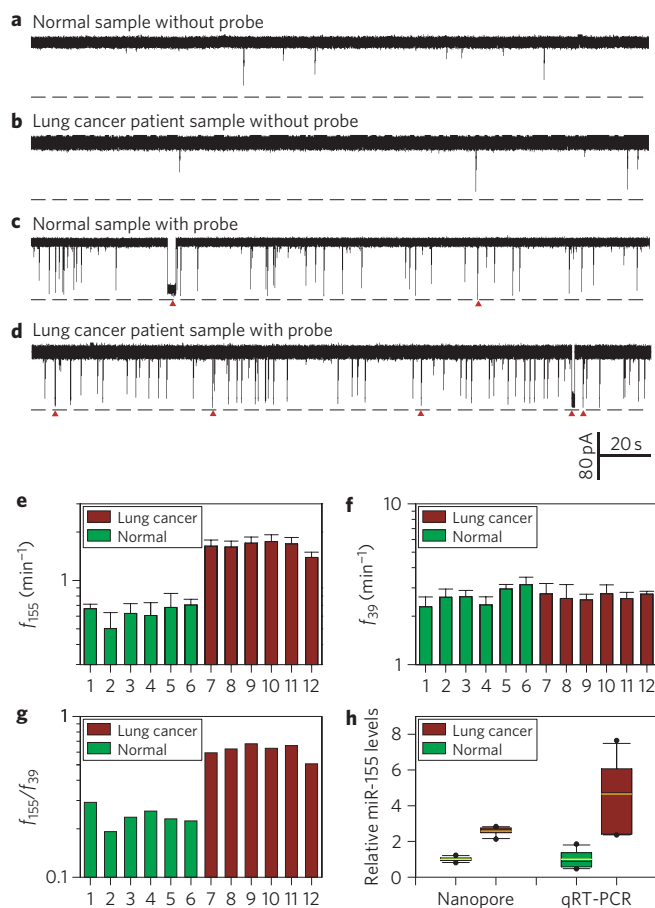


Figure 4 | Detection of miR-155 in the plasma of lung cancer patients.

a–d. Current traces for total plasma RNAs from healthy volunteers (normal sample) and lung cancer patients without (**a,b**) and with (**c,d**) the P₁₅₅ probe. Traces were recorded in 1 M KCl at +100 mV. Red arrows are signature events. Signature events were seen only in the presence of the 100 nM probe for both healthy volunteers (**c**) and lung cancer patients (**d**). **e.** Frequencies of miR-155 signature events (f_{155}) from six healthy individuals (1–6) and six patients with lung cancer (7–12) in the presence of spiked-in synthetic miR-39. **f.** Frequencies of miR-39 signature events detected using P₃₉ (sequence in Supplementary Table S1) from all the samples that were used in **e**. Each sample was measured n times ($n \geq 4$) using independent nanopores. Data are mean \pm s.d. Conditions of patients: 7, metastatic squamous lung carcinoma; 8, recurrent small-cell cancer; 9, early-stage small-cell carcinoma, status post-chemotherapy and radiation; 10, early-stage small-cell cancer, status post-chemotherapy; 11, late-stage non-small-cell carcinoma, status post-resection and post-chemotherapy; 12, late-stage adenocarcinoma, status post-chemotherapy. **g.** f_{155}/f_{39} calculated from panels **e** and **f**. **h.** Box and whisker plots of the relative miR-155 levels in healthy and lung cancer groups measured with the nanopore sensor and qRT-PCR. Boxes mark the intervals between the 25th and 75th percentiles. Black lines inside the boxes denote medians. Whiskers denote the intervals between the 5th and 95th percentiles. Filled circles indicate data points outside the 5th and 95th percentiles (see Supplementary Table S7 for raw data).

frequencies of spiked-in miR-39 events (f_{39}) were independent of the samples ($P > 0.05$). To evaluate the variability during total RNA extraction, the spiked-in miR-39 was used as an internal control and the ratio f_{155}/f_{39} was used to normalize the assays. Figure 4g shows that the mean f_{155}/f_{39} ratio in the lung cancer group (0.62 ± 0.06) was significantly higher than that in the control group (0.24 ± 0.05) ($P < 0.001$). The relative levels of

miR-155 that were measured with the nanopore were also compared using the qRT-PCR method (Fig. 4h). Collectively, the mean level of miR-155 was increased by a factor of 2.6 in the lung cancer group compared with the control group as measured by the nanopore sensor ($P < 0.001$), but a 4.3-fold increase was obtained using the qRT-PCR method ($P < 0.02$). In addition, greater variability was observed in the qRT-PCR assay. Therefore, although both the nanopore and qRT-PCR assays indicated a significant increase of miR-155 in lung cancer patient samples, the nanopore method demonstrated higher accuracy with no requirement for labelling or amplification (Fig. 4h).

Conclusion

We have designed a nanopore-based microRNA sensor that uses a programmable oligonucleotide probe to generate a signature electrical signal for the direct and label-free detection of target microRNA in a fluctuating background, such as plasma RNA extracts from clinical samples. The key component of the nanopore sensor is the probe, the sequence of which is programmable and can be optimized to achieve high sensitivity and selectivity. We expect that the probe composition will not be limited to the four nucleotides. The incorporation of unnatural compounds such as locked nucleic acids and peptide nucleotide acids into the probe sequences may enhance selectivity because of the strengthened hybridization between probe and target. The probe can also be engineered with a specific barcode through chemical modification^{31,49}, so that multiple microRNAs can be simultaneously detected using distinct probes. Our sensor can detect microRNAs, various nucleic acid fragments, genetic alterations and pathogenic DNAs/RNAs. In the future, our nanopore sensor can be devised on new membrane platforms such as a droplet–interface bilayer⁵⁰ to construct stable nanopore arrays for high-throughput microRNA detection. Overall, the nanopore method can be a useful tool for quantitative studies of microRNAs and the discovery of disease markers, which are important for non-invasive screening and the early diagnosis of diseases such as cancer.

Materials and methods

Oligonucleotides, including microRNAs and DNA probes, were synthesized and electrophoresis-purified by Integrated DNA Technologies. Before testing, the mixture of each microRNA and the probe was heated to 90 °C for 5 min, gradually cooled to room temperature and stored at 4 °C. RNase-free water was used to prepare RNA samples.

Nanopore electrical recording. The nanopore detection method has been well documented^{29,42}. The lipid bilayer membrane of 1,2-diphytanoyl-*sn*-glycerophosphatidylcholine (Avanti Polar Lipids) was formed spanning a 100–150 nm hole in the centre of a Teflon film that partitioned two chambers (*cis* and *trans*). The recording solutions on each side of the bilayer contained KCl at a desired concentration and were buffered with 10 mM Tris (pH 8.0). The α -haemolysin protein was inserted into the bilayer to form a pore from the *cis* side. MicroRNAs, DNA probes and plasma RNA extracts were also added to the *cis* solution. The voltage was given from the *trans* solution and the *cis* solution was grounded, so that a positive voltage could drive the translocation of a negatively charged DNA through the pore from *cis* to *trans*. Nanopore currents were recorded with an Axopatch 200A amplifier (Molecular Devices), filtered with a built-in four-pole low-pass Bessel filter at 5 kHz and acquired with Clampex 9.0 software (Molecular Devices) through a Digidata 1332 analog-to-digital converter (Molecular Devices) at a sampling rate of 20 kHz. Data were analysed using Clampfit 9.0 (Molecular Devices), Excel (Microsoft) and SigmaPlot (SPSS) software. Because the signature events for the microRNA:probe ($\sim 10^{-1}$ – 10^{-3} ms) were well separated from the oligonucleotide translocation events ($\sim 10^{-1}$ – 10^{-2} μ s) in duration, we set 1 ms as the boundary to collect each type of event. Data were presented as mean \pm s.d. of three independent experiments, and the differences were considered statistically significant at $P < 0.05$ using the Student's *t*-test. Nanopore measurements were conducted at 22 ± 2 °C.

Total RNA extraction from plasma. Peripheral blood samples were obtained from the University of Missouri Ellis Fischel Cancer Center with Institutional Review Board approval. Whole blood with EDTA preservative was centrifuged at 1,600g for 10 min at room temperature and the plasma was transferred to new tubes. Total RNAs containing microRNAs were extracted from 350 μ l of plasma using the

mirVana PARIS Kit (Ambion) according to the manufacturer's protocol. The final elution volume was 100 μ l.

MicroRNA quantification by qRT-PCR. A SYBR Green-based qRT-PCR assay was used for microRNA quantification. About 10 μ l of total RNA sample containing microRNAs was polyadenylated by poly(A) polymerase (Ambion) and reverse transcribed to cDNA using SuperScript III Reverse Transcriptase (Invitrogen) according to the manufacturer's instructions with a poly(T) adapter primer (5'-GCGAGCACAGAATTAATACGACTCACTATAGGTTTTTTTTTTTTTTVN-3'). Real-time PCR was performed using iQ SYBR Green Supermix (Bio-Rad) with the miR-155 specific forward primer (5'-TTAATGCTAATCGTGATAGGGGT-3') and the sequence complementary to the poly(T) adapter as the reverse primer (5'-GCGAGCACAGAATTAATACGAC-3') in an iQ5 Real-time PCR system (Bio-Rad). PCR was carried out at an initial denaturation at 95 °C for 3 min, followed by 40 cycles of 95 °C for 15 s and 60 °C for 1 min. The relative level of miR-155 was calculated using the $2^{-\Delta\Delta C_t}$ method, where the level of normal plasma was normalized as 1.

Normalization of the nanopore and qRT-PCR data using spiked-in *C. elegans* microRNA miR-39 as control. We introduced spiked-in synthetic microRNA as control to validate the nanopore sensor's capability of detecting microRNA in human samples. The spiked-in RNA oligonucleotide in the detection matches the sequence of *C. elegans* miR-39, a microRNA that is absent in the human genome. About 3.5 μ l of 1 nM synthetic miR-39 solution was introduced to each 350 μ l plasma sample after the addition of 2 \times denaturing solution (mirVana PARIS Kit) to plasma; thus the miR-39 concentration in plasma was 10 pM. The denaturing solution prevents RNAs from degradation by inhibiting endogenous plasma RNases. For each sample, both miR-155 and spiked-in miR-39 were measured using the nanopore sensor and SYBR Green-based qRT-PCR. Nanopore data and the normalization result are shown in Supplementary Table S7. In nanopore detection, the probes for miR-155 and miR-39 were P₁₅₅ and P₃₉. We first measured the signature event frequencies, f_{155} and f_{39} , of hybrids miR-155-P₁₅₅ and miR-39-P₃₉, respectively. The variability of f_{39} reflects the difference in miR-39 concentrations among samples after RNA extraction. Therefore, the ratio of the two frequencies, f_{155}/f_{39} , should eliminate this variability. Finally, the mean f_{155}/f_{39} ratio of six normal samples (A_{normal}) was used as the standard to calculate each sample's relative miR-155 level by normalizing f_{155}/f_{39} to A_{normal} , that is, $f_{155}/f_{39}/A_{\text{normal}}$.

Received 26 April 2011; accepted 29 July 2011;
published online 4 September 2011

References

1. Carthew, R. W. & Sontheimer, E. J. Origins and mechanisms of miRNAs and siRNAs. *Cell* **136**, 642–655 (2009).
2. Inui, M., Martello, G. & Piccolo, S. MicroRNA control of signal transduction. *Nature Rev. Mol. Cell Biol.* **11**, 252–263 (2010).
3. Lee, R. C., Feinbaum, R. L. & Ambros, V. The *C. elegans* heterochronic gene *lin-4* encodes small RNAs with antisense complementarity to *lin-14*. *Cell* **75**, 843–854 (1993).
4. Kozomara, A. & Griffiths-Jones, S. miRBase: integrating microRNA annotation and deep-sequencing data. *Nucleic Acids Res.* **39**, D152–D157 (2011).
5. Bartel, D. P. MicroRNAs: genomics, biogenesis, mechanism, and function. *Cell* **116**, 281–297 (2004).
6. Diederichs, S. & Haber, D. A. Dual role for argonautes in MicroRNA processing and posttranscriptional regulation of MicroRNA expression. *Cell* **131**, 1097–1108 (2007).
7. Garzon, R., Calin, G. A. & Croce, C. M. MicroRNAs in cancer. *Ann. Rev. Med.* **60**, 167–179 (2009).
8. Ortholan, C. *et al.* MicroRNAs and lung cancer: new oncogenes and tumor suppressors, new prognostic factors and potential therapeutic targets. *Curr. Med. Chem.* **16**, 1047–1061 (2009).
9. Calin, G. A. & Croce, C. M. MicroRNA signatures in human cancers. *Nature Rev. Cancer* **6**, 857–866 (2006).
10. Mitchell, P. S. *et al.* Circulating microRNAs as stable blood-based markers for cancer detection. *Proc. Natl Acad. Sci. USA* **105**, 10513–10518 (2008).
11. Kosaka, N. *et al.* Secretory mechanisms and intercellular transfer of microRNAs in living cells. *J. Biol. Chem.* **285**, 17442–17452 (2010).
12. Rabinowitz, G., Gergel-Taylor, C., Day, J. M., Taylor, D. D. & Kloecker, G. H. Exosomal microRNA: a diagnostic marker for lung cancer. *Clin. Lung Cancer* **10**, 42–46 (2009).
13. Rosell, R., Wei, J. & Taron, M. Circulating MicroRNA signatures of tumor-derived exosomes for early diagnosis of non-small-cell lung cancer. *Clin. Lung Cancer* **10**, 8–9 (2009).
14. Chen, C. *et al.* Real-time quantification of microRNAs by stem-loop RT-PCR. *Nucleic Acids Res.* **33**, e179 (2005).
15. Li, W. & Ruan, K. MicroRNA detection by microarray. *Anal. Bioanal. Chem.* **394**, 1117–1124 (2009).
16. Hunt, E. A., Goulding, A. M. & Deo, S. K. Direct detection and quantification of microRNAs. *Anal. Biochem.* **387**, 1–12 (2009).
17. Yendamuri, S. & Kratzke, R. MicroRNA biomarkers in lung cancer: MiRacle or quagMiRe? *Transl. Res.* **157**, 209–215 (2011).
18. Neely, L. A. *et al.* A single-molecule method for the quantitation of microRNA gene expression. *Nature Methods* **3**, 41–46 (2006).
19. Bayley, H. & Jayasinghe, L. Functional engineered channels and pores — (Review). *Mol. Membrane Biol.* **21**, 209–220 (2004).
20. Gu, L. Q. & Shim, J. W. Single molecule sensing by nanopores and nanopore devices. *Analyst* **135**, 441–451 (2010).
21. Howorka, S. & Siwy, Z. Nanopore analytics: sensing of single molecules. *Chem. Soc. Rev.* **38**, 2360–2384 (2009).
22. Ma, L. & Cockcroft, S. L. Biological nanopores for single-molecule biophysics. *ChemBiochem* **11**, 25–34 (2010).
23. Movileanu, L. Interrogating single proteins through nanopores: challenges and opportunities. *Trends Biotechnol.* **27**, 333–341 (2009).
24. Olasagasti, F. *et al.* Replication of individual DNA molecules under electronic control using a protein nanopore. *Nature Nanotech.* **5**, 798–806 (2010).
25. Bayley, H. Sequencing single molecules of DNA. *Current Opin. Chem. Biol.* **10**, 628–637 (2006).
26. Branton, D. *et al.* The potential and challenges of nanopore sequencing. *Nature Biotechnol.* **26**, 1146–1153 (2008).
27. Wanunu, M. *et al.* Rapid electronic detection of probe-specific microRNAs using thin nanopore sensors. *Natur Nanotech.* **5**, 807–814 (2010).
28. Song, L. Z. *et al.* Structure of staphylococcal alpha-hemolysin, a heptameric transmembrane pore. *Science* **274**, 1859–1866 (1996).
29. Kasianowicz, J. J., Brandin, E., Branton, D. & Deamer, D. W. Characterization of individual polynucleotide molecules using a membrane channel. *Proc. Natl Acad. Sci. USA* **93**, 13770–13773 (1996).
30. Meller, A., Nivon, L. & Branton, D. Voltage-driven DNA translocations through a nanopore. *Phys. Rev. Lett.* **86**, 3435–3438 (2001).
31. Mitchell, N. & Howorka, S. Chemical tags facilitate the sensing of individual DNA strands with nanopores. *Angew. Chem. Int. Ed.* **47**, 5565–5568 (2008).
32. Meller, A., Nivon, L., Brandin, E., Golovchenko, J. & Branton, D. Rapid nanopore discrimination between single polynucleotide molecules. *Proc. Natl Acad. Sci. USA* **97**, 1079–1084 (2000).
33. Donnem, T. *et al.* Prognostic impact of miR-155 in non-small cell lung cancer evaluated by in situ hybridization. *J. Transl. Med.* **9**, 6 (2011).
34. Mathé, J., Visram, H., Viasnoff, V., Rabin, Y. & Meller, A. Nanopore unzipping of individual DNA hairpin molecules. *Biophys. J.* **87**, 3205–3212 (2004).
35. Sauer-Budge, A. F., Nyamwanda, J. A., Lubensky, D. K. & Branton, D. Unzipping kinetics of double-stranded DNA in a nanopore. *Phys. Rev. Lett.* **90**, 238101 (2003).
36. Butler, T. Z., Gundlach, J. H. & Troll, M. Ionic current blockades from DNA and RNA molecules in the alpha-hemolysin nanopore. *Biophys. J.* **93**, 3229–3240 (2007).
37. Mathé, J., Aksimentiev, A., Nelson, D. R., Schulten, K. & Meller, A. Orientation discrimination of single-stranded DNA inside the alpha-hemolysin membrane channel. *Proc. Natl Acad. Sci. USA* **102**, 12377–12382 (2005).
38. Purnell, R. F., Mehta, K. K. & Schmidt, J. J. Nucleotide identification and orientation discrimination of DNA homopolymers immobilized in a protein nanopore. *Nano. Lett.* **8**, 3029–3034 (2008).
39. Wanunu, M., Morrison, W., Rabin, Y., Grosberg, A. Y. & Meller, A. Electrostatic focusing of unlabelled DNA into nanoscale pores using a salt gradient. *Nature Nanotech.* **5**, 160–165 (2010).
40. Maglia, G., Restrepo, M. R., Mikhailova, E. & Bayley, H. Enhanced translocation of single DNA molecules through α -hemolysin nanopores by manipulation of internal charge. *Proc. Natl Acad. Sci. USA* **105**, 19720–19725 (2008).
41. Cho, W. C. Role of miRNAs in lung cancer. *Expert Rev. Mol. Diagn.* **9**, 773–776 (2009).
42. Howorka, S., Cheley, S. & Bayley, H. Sequence-specific detection of individual DNA strands using engineered nanopores. *Nature Biotechnol.* **19**, 636–639 (2001).
43. Nakane, J., Wiggin, M. & Marziali, A. A nanosensor for transmembrane capture and identification of single nucleic acid molecules. *Biophys. J.* **87**, 615–621 (2004).
44. Vercouter, W. *et al.* Rapid discrimination among individual DNA hairpin molecules at single-nucleotide resolution using an ion channel. *Nature Biotechnol.* **19**, 248–252 (2001).
45. Landi, M. T. *et al.* MicroRNA expression differentiates histology and predicts survival of lung cancer. *Clin. Cancer Res.* **16**, 430–441 (2010).
46. Silvestri, G. A., Alberg, A. J. & Ravenel, J. The changing epidemiology of lung cancer with a focus on screening. *Br. Med. J.* **339**, 63053 (2009).
47. Patnaik, S. K., Kannisto, E., Knudsen, S. & Yendamuri, S. Evaluation of microRNA expression profiles that may predict recurrence of localized stage I non-small cell lung cancer after surgical resection. *Cancer Res.* **70**, 36–45 (2010).
48. Yanaihara, N. *et al.* Unique microRNA molecular profiles in lung cancer diagnosis and prognosis. *Cancer Cell* **9**, 189–198 (2006).
49. Singer, A. *et al.* Nanopore based sequence specific detection of duplex DNA for genomic profiling. *Nano Lett.* **10**, 738–742 (2010).
50. Bayley, H. *et al.* Droplet interface bilayers. *Mol. Biosyst.* **4**, 1191–1208 (2008).

Acknowledgements

The authors thank K. Gillis, T.-C. Hwang, S.-J. Chen, F. Hsieh and M. Milanick for invaluable discussions on experimental design and data analysis. This investigation was partially supported by grants from the National Science Foundation 0546165 (L.-Q.G.), the National Institutes of Health GM079613 (L.-Q.G.) and the University of Missouri Intellectual Property Fast Track Initiative (A8881, M.X.W.), and was conducted in a facility that was constructed with support from the Research Facilities Improvement Program grant no. C06-RR-016489-01 from the National Centre for Research Resources, National Institutes of Health.

Author contributions

Y.W. designed and performed the nanopore experiments, collected and analysed the nanopore data, and co-wrote the manuscript. D.Z. designed and performed the qRT-PCR

experiments, analysed the qRT-PCR data and co-wrote the manuscript. Q.T. performed molecular biology experiments, including protein synthesis. M.X.W. conceived the qRT-PCR experiments, provided the patients' samples and co-wrote the manuscript. L.-Q.G. conceived the principal idea, designed the nanopore experiments and wrote the manuscript. All the authors discussed the results and commented on the manuscript.

Additional information

The authors declare no competing financial interests. Supplementary information accompanies this paper at www.nature.com/naturenanotechnology. Reprints and permission information is available online at <http://www.nature.com/reprints>. Correspondence and requests for materials should be addressed to M.X.W. and L.-Q.G.

The nanomechanical signature of breast cancer

Marija Plodinec^{1,2}, Marko Loparic^{1,2†}, Christophe A. Monnier^{1†}, Ellen C. Obermann^{3†},
Rosanna Zanetti-Dallenbach^{4†}, Philipp Oertle¹, Janne T. Hyotyla¹, Ueli Aebi², Mohamed Bentires-Alj⁵,
Roderick Y. H. Lim^{1*} and Cora-Ann Schoenenberger²

Cancer initiation and progression follow complex molecular and structural changes in the extracellular matrix and cellular architecture of living tissue. However, it remains poorly understood how the transformation from health to malignancy alters the mechanical properties of cells within the tumour microenvironment. Here, we show using an indentation-type atomic force microscope (IT-AFM) that unadulterated human breast biopsies display distinct stiffness profiles. Correlative stiffness maps obtained on normal and benign tissues show uniform stiffness profiles that are characterized by a single distinct peak. In contrast, malignant tissues have a broad distribution resulting from tissue heterogeneity, with a prominent low-stiffness peak representative of cancer cells. Similar findings are seen in specific stages of breast cancer in MMTV-PyMT transgenic mice. Further evidence obtained from the lungs of mice with late-stage tumours shows that migration and metastatic spreading is correlated to the low stiffness of hypoxia-associated cancer cells. Overall, nanomechanical profiling by IT-AFM provides quantitative indicators in the clinical diagnostics of breast cancer with translational significance.

Physical and chemical forces mediate the order by which cells proliferate, differentiate and migrate¹ within the three-dimensional microenvironment of living tissue². Perturbations to this intricate balance^{3–5} are known to promote tumorigenesis and progression to metastasis⁶. At the molecular level, tumour initiation and progression are accompanied by complex structural changes in the extracellular matrix (ECM) and cellular architecture, which are anticipated to develop differentiable mechanical responses⁷. However, it has been difficult to reach a consensus as to how such biomechanical heterogeneities occur and what their role might be. This is due to challenges in being able to discriminate between the mechanoresponses of cells and the surrounding ECM within native tumour tissue with adequate spatial/structural resolution and force sensitivity. Not least for its implications in diagnostics and treatment, being able to understand the mechanobiology of tumorigenesis is paramount in revealing its deterministic role in cancer development and metastasis⁵.

Long-standing ambiguities exist because efforts to understand cancer biomechanics are largely polarized between tumour-level and single-cell experimentation. In accordance with conventional wisdom (breast palpation), studies on whole mouse mammary glands show that breast tumours are considerably more rigid than the surrounding tissue due to a relative stiffening of the peripheral tumour stroma^{7,8}. This notion is consistent with the increase in matrix deposition and crosslinking observed in three-dimensional cell cultures and mouse mammary glands during cancer progression^{9,10}. Paradoxically, biophysical techniques^{11–16} reveal that single (cultured) cancer cells are more compliant (or ‘softer’) than their healthy counterparts. This increase in elasticity and/or deformability is accompanied by alterations in the cytoarchitecture that have known associations with malignant transformation¹⁷. Because of their softness, cancer cells have been detected by indentation-type atomic force microscopy (IT-AFM) in tissue sections from tumours that were surgically removed from patients with

advanced cancer¹⁸. Furthermore, Cross *et al.* found that metastatic cells isolated from the pleural fluid of human patients are softer than normal cells¹², suggesting that metastasis might be promoted by cell compliance. No doubt, criticism is common on both sides of the length-scale divide. On the one hand, the mechanoresponse of whole tumours is arguably dominated by stiff structural elements in the peripheral stroma (for example, collagen^{19,20}), leaving potentially more compliant regions in the underlying cancerous core insensitive to detection. On the other hand, the relevance of single cell measurements has been questioned given the lack of a proper three-dimensional tissue environment²¹.

The diversity of biomechanical profiles underscores the importance of obtaining a holistic understanding of malignancy and how it manifests in breast tumours. This includes correlating biomechanical and microenvironmental properties at different stages of cancer progression. In this Article, we report on a comprehensive effort to correlate the nanomechanical properties of native human breast biopsies to specific histopathological markers in healthy tissue and in benign and malignant tumours. As a standard animal model, our human biopsy results are validated with systematic experiments on MMTV-PyMT (mouse mammary tumour virus-polyoma middle T antigen) transgenic mice²², which we follow from early cancer to metastasis. In bridging across length scales, our nanomechanical measurements reconcile tumour-level and single-cell measurements in both humans and transgenic mice and reveal unique mechano-markers that can be used to identify different cancer stages. Moreover, these findings suggest close correlations between cell softening, tumour hypoxia and lung metastasis.

Nanomechanical signatures of human breast biopsies

To elucidate and correlate the respective nanomechanical profiles to pathohistological findings in normal, benign and malignant biopsies, we carried out IT-AFM analyses of *ex vivo* breast tissues under physiological buffer conditions. The experimental approach

¹Biozentrum and the Swiss Nanoscience Institute, University of Basel, 4056 Basel, Switzerland, ²Maurice E. Mueller Institute for Structural Biology, Biozentrum, University of Basel, 4056 Basel, Switzerland, ³Institute of Pathology, University Hospital Basel, 4031 Basel, Switzerland, ⁴Department of Gynecology and Gynecological Oncology, University Hospital Basel, University of Basel, 4031 Basel, Switzerland, ⁵Mechanisms of Cancer, Friedrich Miescher Institute for Biomedical Research, 4058 Basel, Switzerland; [†]These authors contributed equally to this work. *e-mail: roderick.lim@unibas.ch

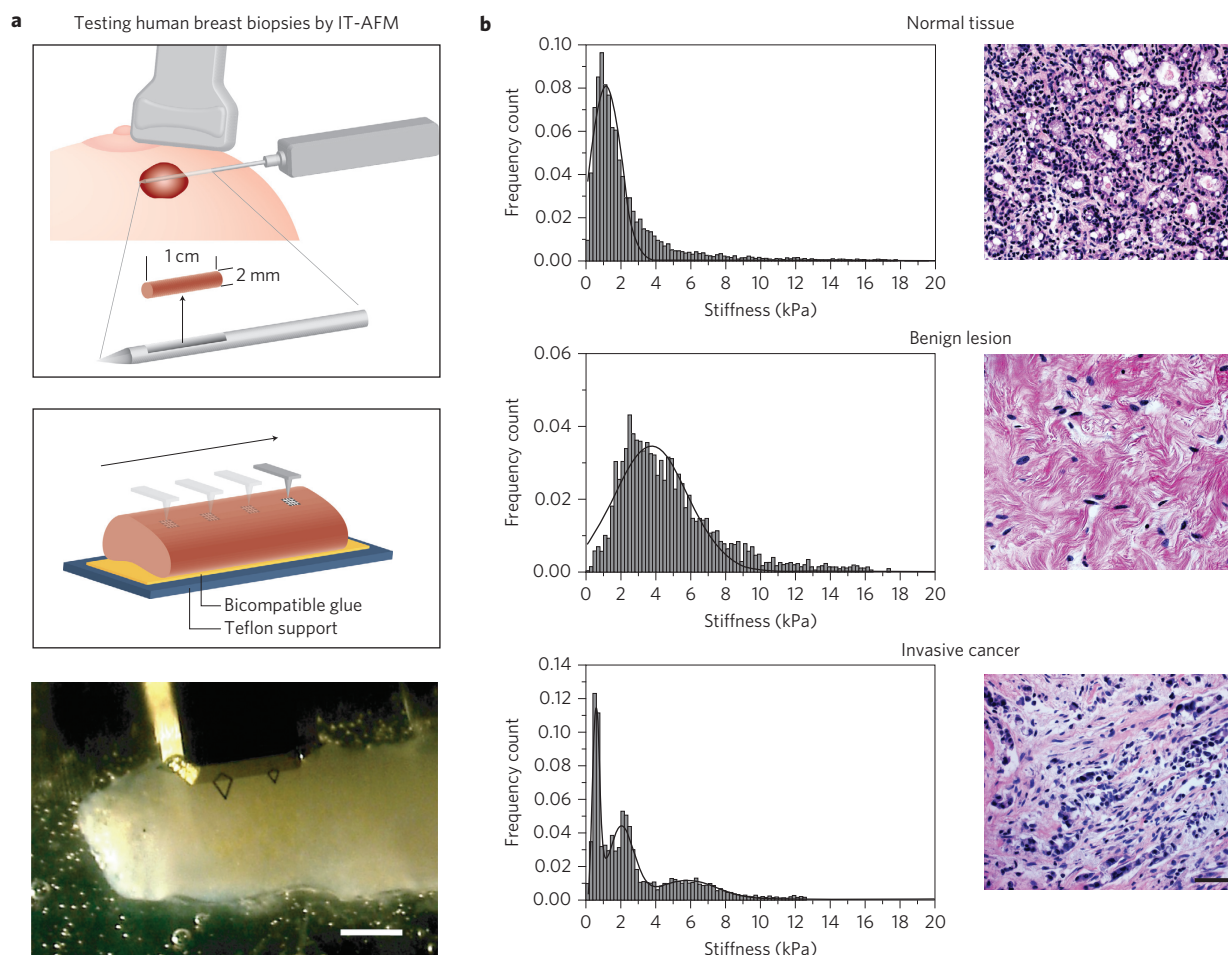


Figure 1 | Nanomechanical signatures of human breast tissue. **a**, Top: schematic of an ultrasound-guided biopsy from a patient with a suspicious lesion. Middle: multiple stiffness maps ($20 \times 20 \mu\text{m}$ each) are recorded in a defined geometrical pattern across the entire specimen. Bottom: top view of an oriented, immobilized biopsy in Ringer's solution with the cantilever positioned for IT-AFM. Scale bar, $500 \mu\text{m}$. **b**, Top left: stiffness distribution for normal mammary gland tissue is unimodal. Top right: post-AFM H&E-stained section reveals the terminal ductal lobular unit of a normal mammary gland fenced by interstitial connective tissue. Middle left: biopsy-wide histogram for a benign lesion reveals a unimodal but broader stiffness distribution with an increase in stiffness compared with the healthy biopsy. Middle right: H&E-stained section reveals extensive fibrotic stroma interspersed with fibroblasts typical for fibroadenoma. Bottom left: heterogeneous stiffness distribution with a characteristic soft peak for malignant tumour tissue is consistent with histopathology (bottom right), revealing an invasive breast carcinoma with infiltrating nests of cancer cells that have evoked a dense fibrous tissue response. Scale bar applies to all images, $50 \mu\text{m}$.

for obtaining multiple stiffness maps across entire biopsies is described in Fig. 1a. The tissue architecture and surface integrity of the biopsies were confirmed by scanning electron microscopy (SEM; Supplementary Fig. S1). Plotting a histogram of biopsy-wide stiffness values from a healthy specimen reveals a unimodal stiffness distribution of $1.13 \pm 0.78 \text{ kPa}$ (Fig. 1b, top left). Healthy ducts define the histological appearance in haematoxylin & eosin (H&E)-stained sections of the mapped specimen (Fig. 1b, top right). The benign fibroadenoma with its characteristic highly fibrotic content shows an increased stiffness of $3.68 \pm 1.92 \text{ kPa}$ (Fig. 1b, middle left). Softer features ($<2 \text{ kPa}$) presumably represent individual fibroblasts embedded in the fibrotic stroma. Post-AFM histological examination of the mapped specimen confirmed fibroblasts to be the dominant cell type within the benign lesion²³ (Fig. 1b, middle right).

In comparison, a representative cancer biopsy typically exhibits a bimodal stiffness distribution with two prominent peaks at $0.57 \pm 0.16 \text{ kPa}$ ('peak 1') and $1.99 \pm 0.73 \text{ kPa}$ ('peak 2') (Fig. 1b, bottom left). At values stiffer than 2 kPa , a broadening in the distribution indicates a marked mechanical heterogeneity across the sample, with 'peak 3' located at $5.75 \pm 1.62 \text{ kPa}$. Post-AFM H&E staining confirmed the dominance of tumour cells that

infiltrate the stroma in a cord-like pattern (Fig. 1b, bottom right). We also assigned individual stiffness peaks to specific tissue morphologies by performing more detailed measurements within defined regions of the biopsy (Fig. 2a), in particular in the core (Fig. 2b) and at the periphery (Fig. 2c). The correlation of local AFM data with matching histologies corroborated that the soft peak is typical for cancer cells (Fig. 2b) that are surrounded by stiffer peripheral stroma (Fig. 2c).

Individual biopsy-wide stiffness distributions for 30 human biopsies (8 healthy, 8 benign and 14 malignant) are displayed in Supplementary Fig. S2 and peak stiffness values are summarized in Supplementary Table S1. In general, the nanomechanical signature of healthy breast tissue is characterized by a unimodal distribution with peak stiffness from 1.13 to 1.83 kPa . The stiffness distribution across benign lesions remains uniform; however, stiffness values range from 1.91 to 3.68 kPa and thus indicate a stiffer phenotype. All 14 biopsies with cancer exhibited a characteristic stiffness profile with a dominant peak at 0.31 – 0.75 kPa , that is, at least factor of two softer than healthy mammary gland epithelium ($P < 0.0001$). The nanomechanical signature of cancer included a second peak between 1.54 and 1.99 kPa . Another feature found in

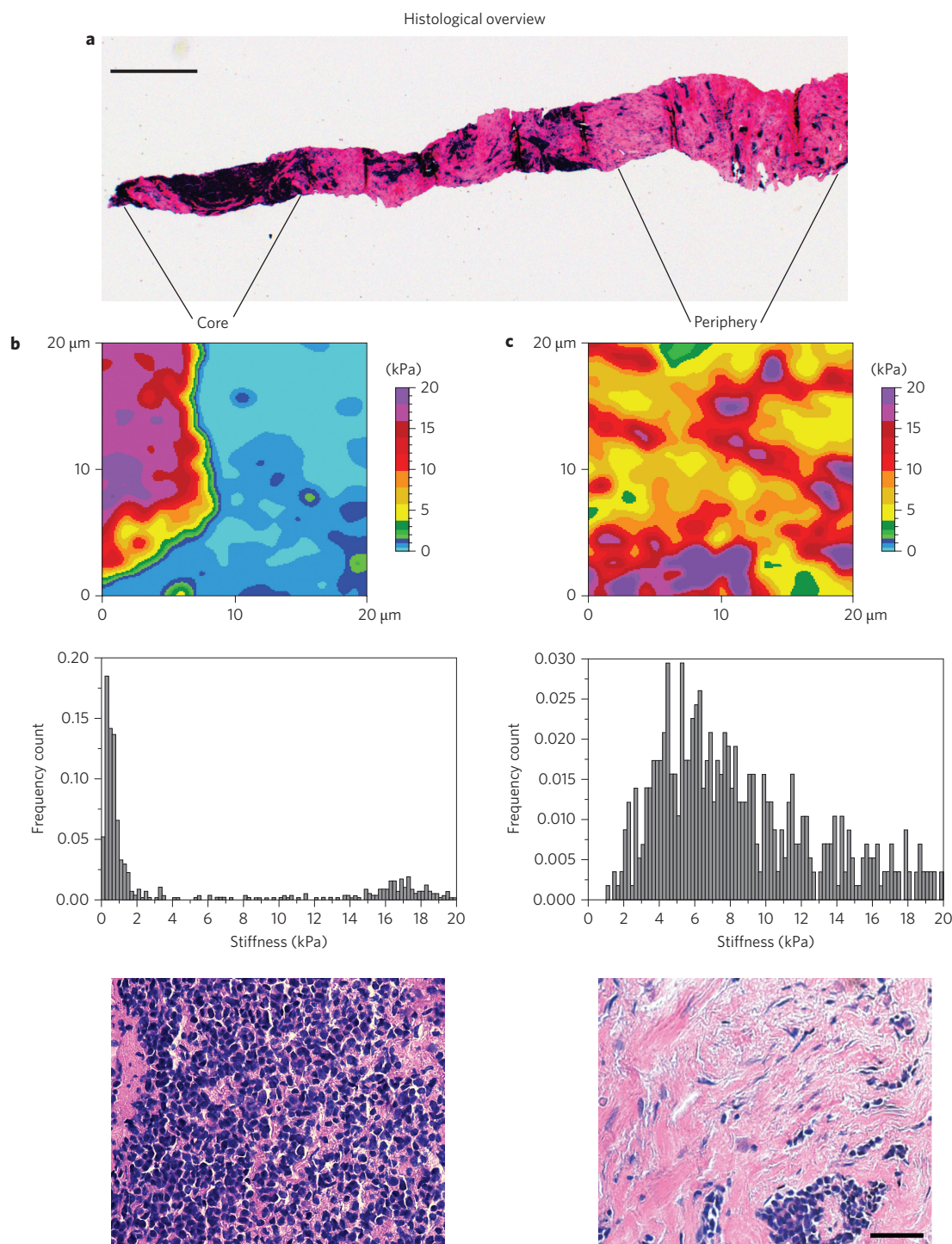


Figure 2 | Stiffness varies from core to periphery in human cancer biopsies. **a**, Post-AFM histological overview of the entire cancer biopsy with reference to the areas mapped in detail. Scale bar, 500 μm . **b**, Top: representative AFM stiffness map (24 \times 24 pixels) of the core region visualizes pronounced softness within a narrow peak of specific stiffness values (middle). Bottom: the local histology shows that the core region is densely populated with cancer cells. **c**, Top: typical stiffness map (24 \times 24 pixels) of the tumour periphery demonstrates stiff features. Middle: the corresponding stiffness distribution is broader and shifted towards stiffer values. Bottom: post-AFM histopathology reveals that the tumour periphery predominantly comprises fibrotic tissue. Scale bar, 50 μm (also applies to image in **b**).

several malignant biopsies is that the remaining stiffness values are broadly distributed up to ~ 20 kPa. This spread is indicative of the overall loss of mammary gland architecture accompanied by tumour vascularization and infiltration, and changes in the invasion-afflicted peripheral ECM^{19,24}. Interestingly, cancer biopsies often demonstrate a distinct minimum (~ 1.1 – 1.5 kPa, Supplementary Fig. S3) between the primary and secondary peaks. Because it is inversely correlated

to the average stiffness value for healthy breast tissue (Supplementary Fig. S3), we interpret the minimum to arise from the malignant transformation of healthy epithelium.

Nanomechanical staging of tumour progression

Because of the genetic and epidemiologic diversity in human patients we turned to MMTV-PyMT transgenic mice, a reliable model for

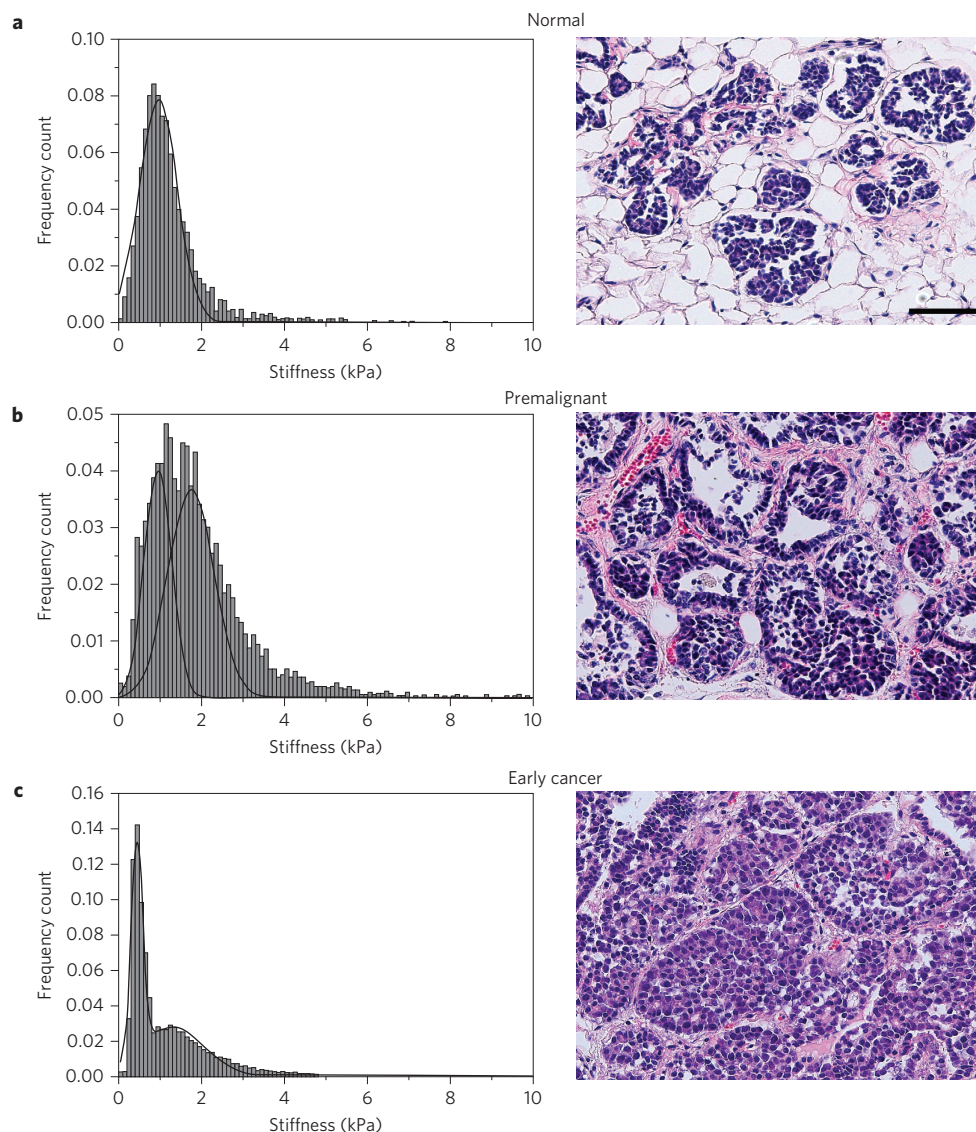


Figure 3 | Correlating the nanomechanical response with tumour progression in MMTV-PyMT mice. **a**, Left: stiffness values of normal ductal epithelium follow a uniform Gaussian distribution. Right: post-AFM H&E-stained section shows a non-lactating mammary gland with a duct surrounded by adipose tissue. **b**, Left: in the premalignant lesion, the contribution of stiffer features increases, as seen by a broader stiffness distribution with an indication of bimodality. Right: H&E-stained sections of the same tissue show extensive proliferation of epithelial cells and an increase of the surrounding stromal components. **c**, Left: in early cancer, the significant softening produces a characteristic peak that dominates the prominent bimodality of the stiffness distribution. Right: in the H&E section, cancer cells are delineated by stromal tissue. Scale bar in **a** applies to images in **b** and **c**, 50 μm .

human breast cancer, to more systematically elucidate the nanomechanical markers of tumour progression and metastasis²². For the corresponding staging of MMTV-PyMT specimens used for stiffness mapping, we monitored the loss of integrin $\beta 1$ expression, which accompanies tumour progression²² (Supplementary Fig. S4).

The biopsy-wide histogram across a normal mouse mammary gland revealed a unimodal stiffness distribution with a peak of 1.02 ± 0.42 kPa (Fig. 3a, left) that is characteristic of healthy mammary tissue, with its well-organized arrangement of densely packed epithelial cells (Fig. 3a, right). The uniform stiffness profile is comparable to that of normal human breast. It should be noted, however, that in contrast to human breast tissues, healthy murine mammary glands exhibit extensive amounts of adipose tissue (70–80%) (Supplementary Fig. S5a).

The biopsy-wide histogram of premalignant tissues shows the onset of a bimodal stiffness distribution with peaks at 0.95 ± 0.18 and 1.75 ± 0.27 kPa, as identified by peak-analysing software. The presence of soft and moderately stiffer features correlates with an

increase of stromal components surrounding the proliferative cell masses revealed in H&E stained sections (Fig. 3b, right).

In early cancer samples, this trend is more pronounced, resulting from distinct soft and stiff areas (Fig. 3c, left), as demonstrated by the peaks at 0.45 ± 0.12 and 1.29 ± 0.76 kPa, respectively. These correspond to distinct zones of densely packed cancer cells and early stromal invasion, as revealed in H&E stained sections (Fig. 3c, right). A summary of the peak stiffness values that were calculated for murine mammary tissues is presented in Supplementary Table S2.

As mentioned above, adipose tissue is prevalent in murine mammary glands and, because of its softness, could be mistaken for cancer cell clusters. Control experiments on adipose tissues demonstrated that the two cell types could be discriminated by their stiffness (Supplementary Fig. S5). Mammary adipocytes exhibit a stiffness of 0.31 ± 0.13 kPa (Supplementary Fig. S5a, middle), whereas cancer cells have a stiffness peak at 0.75 ± 0.25 kPa (Supplementary Fig. S5b, middle).

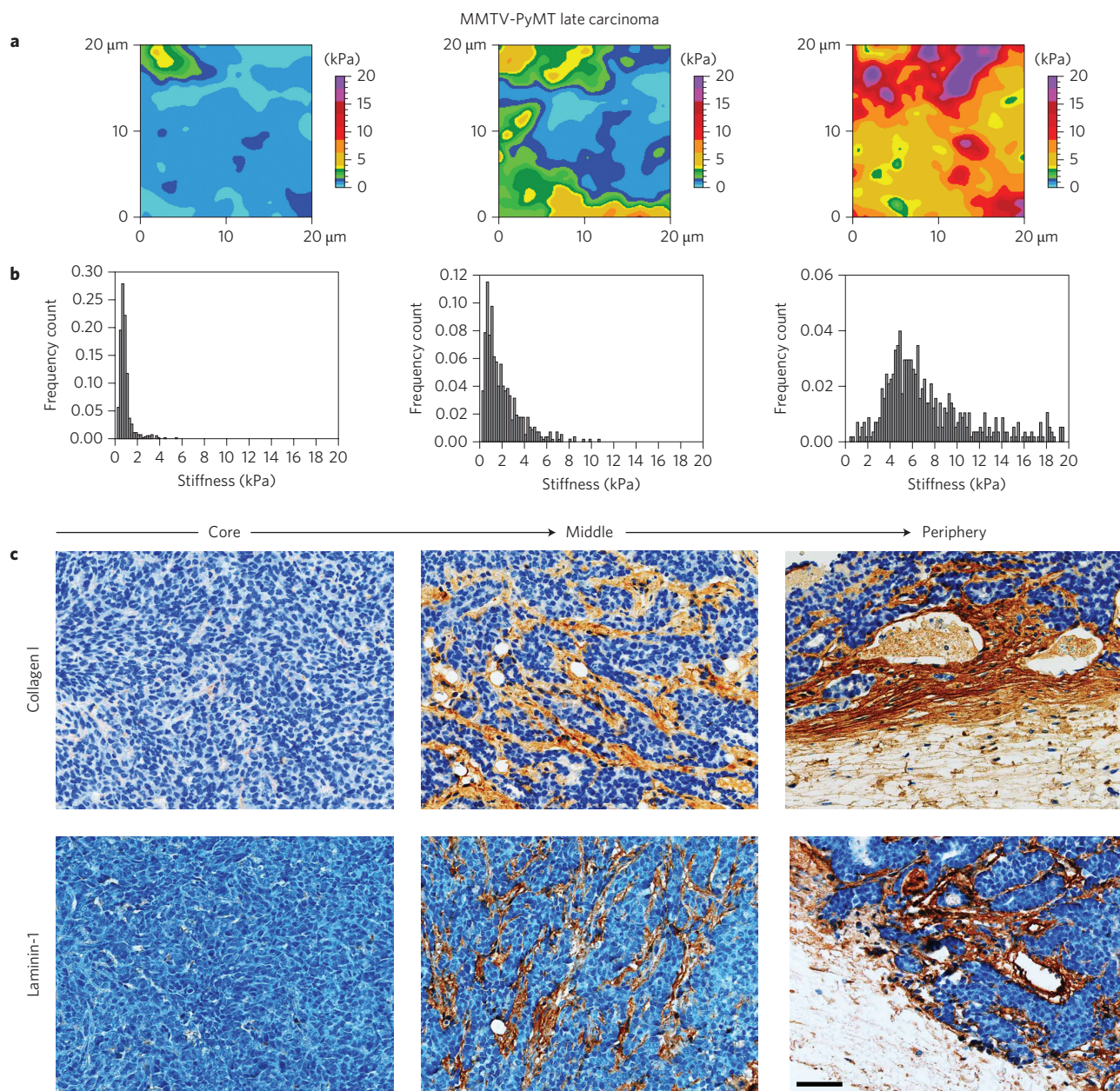


Figure 4 | Correlating local nanomechanical properties and ECM structure in late cancer. **a**, Consecutive stiffness maps (24 × 24 pixels) across the sample demonstrate a significant increase in stiffness and mechanical heterogeneity from core to periphery (left to right). **b**, Corresponding stiffness distributions change from the core to the periphery. **c**, IHC analysis (brown staining) reveals associated structural and morphological changes in collagen I (top) and laminin-1 (bottom) from core to periphery. Scale bar applies to all images, 50 μm.

Among the most substantial structural changes in mammary gland architecture that occur with the transition from normal mammary gland to early cancer are the degradation of the basement membrane that surrounds normal and premalignant glands (Supplementary Fig. S6, top) and the altered expression and organization of collagen I (Supplementary Fig. S6, bottom). In later stages of tumour progression, stromal contributions increasingly modify cancer behaviour²⁵. For example, collagen I, which is the main component of the ECM, is associated with cancer stiffening^{19,21}. Therefore, we examined the relation between local nanomechanical profiles and ECM structure in late MMTV-PyMT cancer, which corresponds to invasive ductal carcinomas in humans. Sequential stiffness maps across the specimen demonstrate gradual stiffening from the core to the periphery (Fig. 4a), with peak values shifting from 0.74 ± 0.26 kPa in the core to 5.51 ± 1.70 kPa at the periphery (Fig. 4b). At the same time, mechanical heterogeneity increases and

is most extensive at the periphery. These changes appear to be associated with distinct changes in the soft core but is subsequent immunohistochemistry (IHC) analysis (Fig. 4c).

In particular, collagen I is not detected in the soft core but is increasingly present towards the periphery (Fig. 4c, top). Also, laminin-1 expression is virtually absent from the core (Fig. 4c, bottom left), as expected in advanced cancer where the basement membrane has disintegrated²⁶. However, the increased vascularization of the mid and peripheral areas resulted in laminin-1 staining of vessel basement membranes (Fig. 4c, bottom middle and right). We conclude that the absence of laminin-1 and collagen I in the core regions contributes to the soft phenotype of cancer cells. On the other hand, the increased staining of laminin-1 and collagen I towards the periphery marks the increase of stromal invasion related to stiffening in the respective regions. Clearly, IHC analyses show that there is considerable tissue heterogeneity at

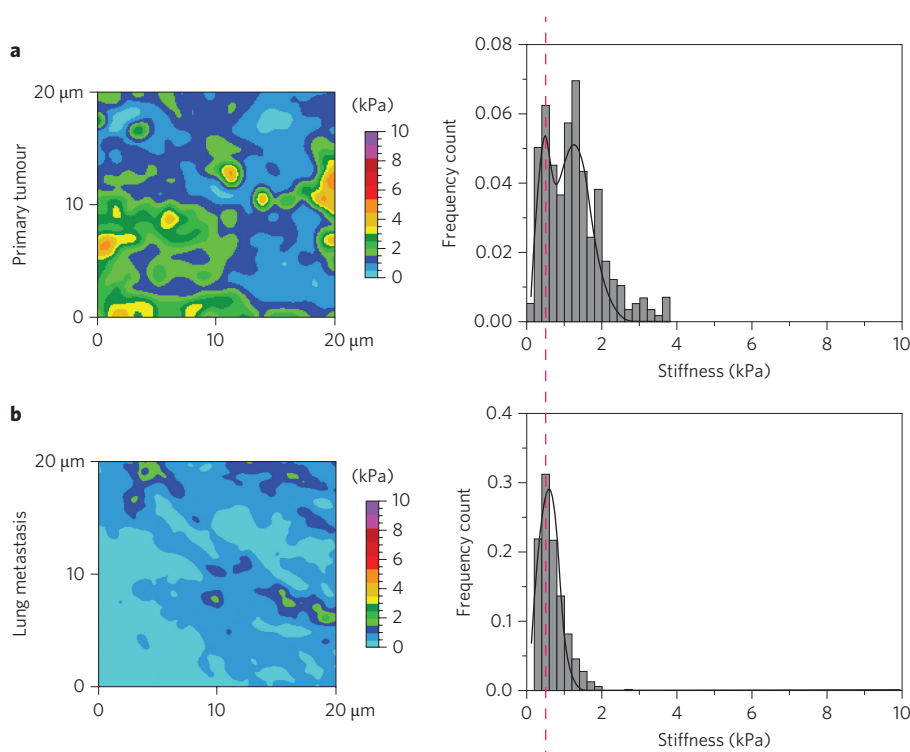


Figure 5 | Stiffness profiles of primary tumour and lung metastasis reveal a common phenotype. **a**, Left: representative AFM stiffness map (24×24 pixels) demonstrates nanomechanical heterogeneity among cancer cells in primary lesions. Right: the corresponding stiffness distribution from the map reveals two peaks representing distinct phenotypes of cancer cells, a softer one at 0.45 ± 0.15 kPa and another at 1.26 ± 0.43 kPa. **b**, Left: representative AFM stiffness map (24×24 pixels) of a metastatic lesion and the corresponding stiffness distribution (right) reveal a peak value that is almost identical to the softer peak detected at the primary tumour site (indicated by the red dashed line).

late tumour stages that is reflected in the broad range of stiffness values (Fig. 4b).

The indications that the stiffness signatures are based on distinct changes in the cytoarchitecture and ECM in MMTV-PyMT transgenic mice prompted us to follow up on this correlation in human breast cancer biopsies (Supplementary Fig. S7). Overall, the staining patterns in human biopsies diagnosed with invasive cancer were similar to those observed in the late cancer stage of MMTV-PyMT mammary tissues (Fig. 4, Supplementary Fig. S7). At the cellular level, a distinct expression of desmin and vimentin, both markers of epithelial–mesenchymal transition (EMT), was found in cancer cells, but also in the adjacent stroma of the invasive lobular (Supplementary Fig. S7c) and ductal (Supplementary Fig. S7d) carcinomas. We therefore rationalize that the soft phenotype detected in human cancer biopsies (Supplementary Fig. S2, Table S1) is an indication of tumour progression.

A soft hypoxic cell phenotype is conducive to metastasis

We next asked whether the very soft cancer phenotypes could be associated with the ability to metastasize to distant sites, in particular to the lungs where metastases frequently occur in MMTV-PyMT mice at late stages of tumour progression^{27,28}. Stiffness measurements from lungs of mice bearing late-stage tumours reveal an extremely soft peak (Supplementary Fig. S8a) that is absent in healthy lungs (Supplementary Fig. S8b; statistical differences between specimens are presented in Supplementary Table S3). Most importantly, with a stiffness peak of 0.45 ± 0.15 kPa, the softest nanomechanical phenotype present at the primary tumour site (Fig. 5a) closely corresponds to the stiffness of a metastatic lesion obtained from the lungs of the same mouse (0.56 ± 0.26 kPa, Fig. 5b).

Because a hypoxic core is a key feature of aggressive cancers²⁹, we examined whether the nanomechanical changes associated with cancer progression are related to reduced tumour oxygenation by

injecting MMTV-PyMT mice at distinct stages of tumour progression with pimonidazole (a probe that selectively binds to hypoxic cells), 90 min before tumour excision. As expected, normal glands and pre-malignant lesions were negative for hypoxia (Fig. 6, top left and middle). In contrast, early cancer exhibited central hypoxia (Fig. 6, right) that correlated well with a significant decrease of cell stiffness (Fig. 3c, left; Supplementary Table S2). In late cancer, dissemination of hypoxic cancer cells to areas of stromal invasion and to the tumour periphery (Fig. 6, bottom left) adds to the mechanical heterogeneity observed in these regions (Fig. 4b). Moreover, their presence suggests that a decreased stiffness is able to promote the metastatic spread of soft cells to the lungs (Fig. 5).

The role of mechanical properties in cancer development and progression has prompted high-powered research initiatives worldwide. Several studies in recent years have led to the notion that tumours are generally stiffer than healthy tissue³⁰ and that continuous tissue stiffening is a promoter of cancer^{10,31}. Contrary to this dogma, there are numerous studies reporting that single isolated cancer cells are significantly softer than normal cells³². However, two-dimensional systems do not recapitulate the architecture or surrounding forces to which a cell is exposed in its native tissue environment^{7,33}. Here, our work resolves the stiffness paradox by exploiting the nanomechanical sensitivity of IT-AFM³⁴ and its unprecedented spatial resolution to comprehensively investigate the mechanical properties of native breast biopsies from human patients (Supplementary Table S1). The most striking finding is that normal glandular tissue, benign lesions and malignant tumours exhibit qualitatively unique biomechanical signatures that are reproducible across different patients. Malignancies are recognized by two features: (i) mechanical heterogeneity in line with histological appearance and (ii) a characteristic stiffness peak of $0.5\text{--}0.8$ kPa measured in areas with densely packed tumour cells and little intervening stroma. Normal glandular epithelium and benign solid lesions on the other hand each exhibit a

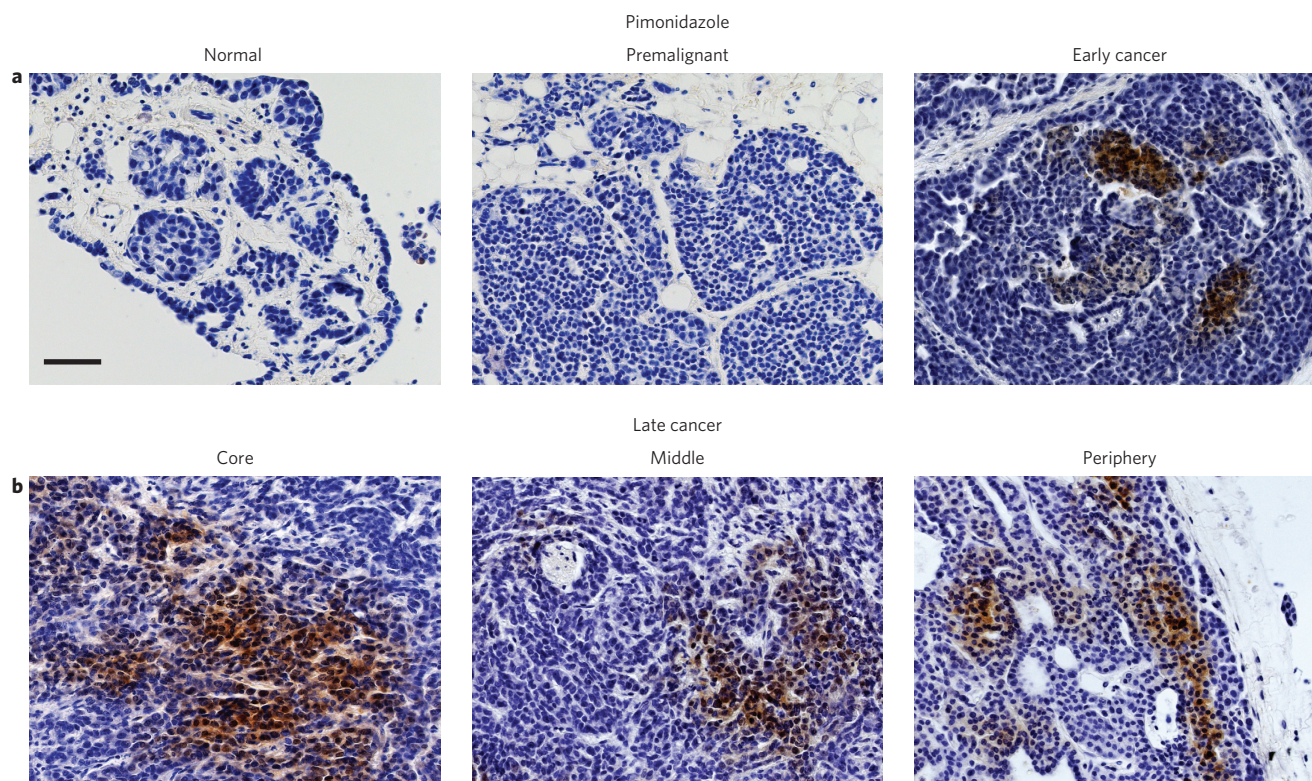


Figure 6 | Dissemination of hypoxic cancer cells increases with tumour progression. Paraffin-embedded sections of mammary gland tissues of pimonidazole (hypoxyprobe)-treated MMTV-PyMT mice at different stages were immunolabelled. **a**, Hypoxia is absent in normal glandular tissue (left) and in premalignant lesions (middle). In contrast, pimonidazole-positive cells (brown staining) reveal central hypoxia in early cancer (right). **b**, In advanced cancer stages, hypoxic cells abundant in the core region (left) are streaming towards tumour blood vessels (middle) and have disseminated to the tumour periphery (right). Scale bar applies to all images, 50 μm .

unimodal stiffness distribution with peaks at ~ 1 kPa and ~ 3 kPa, respectively. In fact, signature-based diagnoses in double-blind experiments correlate nearly 100% with conventional histopathology of the same biopsy post-AFM.

Detecting solid breast lesions by differential tissue elasticity is also the underlying principle in sonoelastography, which has emerged as a clinical, non-invasive diagnostic technique in recent years³⁵. However, the length scale of this approach does not allow for a reliable distinction of benign and malignant breast masses^{36,37}. This challenge is uniquely met by IT-AFM, which is able to differentiate between cancer and benign lesions by correlating stiffness measurements resolved at the nanometre scale across the entire length of a biopsy.

Conclusions

We have resolved the nanomechanical signatures of defined stages of tumour progression, including metastasis. Most notably, high-resolution stiffness mapping has revealed that cancer progression is not limited to matrix stiffening, as previously assumed¹⁰, but is associated with a significant softening of tumour epithelial cells in comparison to normal mammary epithelium. This distinctive softening probably went unnoticed in a recent AFM study³², because the 5 μm colloidal probe that was used only allowed for bulk measurements that did not provide sufficient resolution to distinguish between the individual tissue components (that is, the cells and ECM^{32,38}). Tumour progression to the late, invasive stage accentuates the soft peak and brings about a broadening of the stiffness distribution (Fig. 4) as a result of the cancer cells infiltrating the surrounding tissue, as well as stromal disorganization and tumour vascularization³¹.

Recent evidence shows that hypoxia promotes tumour invasion and ultimately metastases, and thus is associated with tumour

aggressiveness^{38,39}. Also, it has long been hypothesized in the field that metastatic cells need a certain degree of flexibility and deformability to escape their original niche^{40–42}. By analysing metastatic lesions in lungs from MMTV-PyMT mice we now provide the first evidence that supports this hypothesis. These data indicate a direct link between cancer cell softening in the primary tumour and aggressive behaviour leading to metastases. In conclusion, soft peaks detected in the primary tumour may serve not only as mechanobiological markers for the onset of cancer but have prognostic qualities as well.

Methods

Human biopsies. Human biopsies were obtained from the outpatient breast clinic, Department of Gynecology and Gynecological Oncology, University Hospital Basel. The study was approved by the institutional review board (ref. no. EK:157/08) and conducted in accordance with ethical guidelines. Patient recruitment was carried out with informed consent. For each patient, one out of five biopsies was used for IT-AFM analysis directly after removal, without previous knowledge of clinical data. The other four biopsies were evaluated by standard pathological procedures. Cylindrical specimens with a diameter of ~ 0.2 cm and length of 0.2–1 cm were biopsied from suspicious lesions under ultrasound guidance (Fig. 1a). Biopsies were immediately transferred to ice-cold isotonic Ringer solution (6.00 g NaCl, 0.40 g KCl, 50 g anhydrous glucose, 0.27 g CaCl_2 , 3.20 g lactic acid per 1,000 ml of distilled water) supplemented with glucose and a protease inhibitor cocktail (Complete, Boehringer Mannheim; 1 tablet per 10 ml) and kept at 4 °C to minimize tissue degradation. IT-AFM analysis was performed no later than three days after biopsy.

Mammary and lung tissue samples from MMTV-PyMT mice. All procedures involving mice were conducted in accordance with the Swiss laws regulating the use and care of animals in research and have been reviewed and approved by the Federal veterinary office. Female mice heterozygous for the PyMT transgene were obtained by breeding male PyMT mice on a FVB background with FVB females lacking the PyMT transgene. Mice were killed at different time points of tumour development²², and mammary tissues and lungs from at least six different mice were immediately excised and placed in ice-cold Ringer solution. IT-AFM was performed 1–72 h after tissue removal, after which stiffness profiles were essentially unaltered

(Supplementary Fig. S9) and tissue integrity intact as judged by RNA stability (Supplementary Fig. S9 and Supplementary Information on RNA isolation). For hypoxia assessment, mice were injected intraperitoneally with pimonidazole hydrochloride at 100 mg ml⁻¹ in 0.9% sterile saline solution (120 mg kg⁻¹, hypoxyprobe-1, HPI). After 90 min, mice were killed and tissue specimens taken for IT-AFM. Hypoxia was demonstrated by immunohistochemical analysis of pimonidazole incorporation according to a standard protocol⁴².

IT-AFM and data analysis. All preparative steps were performed in a sterile buffer environment supplemented with protease inhibitors. Each specimen was immobilized on a plastic dish with a thin layer of two-component fast drying epoxy glue (Devcon). Mechanical manipulations during sample preparation were kept minimal at all times. To level out the surface to be scanned, small wedges were placed under uneven specimens. IT-AFM was carried out with a noise-isolated FlexAFM ARTIDIS (Nanosurf AG) and a Nanowizard I atomic force microscope (JPK Instruments). To compensate for large surface corrugations on such native biological samples, we developed and implemented customized homebuilt hardware and software algorithms for automated levelling, which enabled uninterrupted AFM operation during data acquisition (see Supplementary Information on Automated levelling). A top-down microscope (S8AP0 with Imagesource DFK 31F03, Leica) was used to visually position the AFM cantilever with respect to the specimen. Four-sided pyramidal tips (205-μm-long DNP-S10 triangular silicon nitride cantilevers, resonance frequency (air) $f = 18$ kHz, nominal cantilever spring constant $k = 0.06$ N m⁻¹, tip radius = 20 nm, half-open angle of the pyramidal face of $\theta \approx 35^\circ$, Bruker) were used. The exact spring constant k of the cantilever was determined before each experiment using the thermal tune method⁴³ and the deflection sensitivity was determined in fluid using glass substrates as an infinitely stiff reference material. IT-AFM at room temperature involved recording up to 22 different 20 × 20 μm² force-volume maps over 24 × 24 point grids (576 force-displacement curves per map and a pixel size of 833 nm) and for high spatial resolution 72 × 72 point grids (5,184 force-displacement curves per map and a pixel size of 277 nm) were recorded. Force-volume maps spaced at 500 μm apart were acquired in a systematic manner across the entire sample surface (Fig. 1a). Individual force curves consisted of 512 data points, with a Z piezo-displacement between 5 and 8 μm, which were collected at 0.8–1 load/unload cycles per second. The maximum applied loading force was set to 1.8 nN, which gave indentation depths that varied approximately between 150 and 3,000 nm depending on the intrinsic mechanical differences within each biopsy (examples are shown in Supplementary Fig. S10). Force curves were analysed using the Oliver and Pharr method⁴⁴ as described previously^{45–47}. See Supplementary Methods on Oliver and Pharr analysis for further details. The stiffness values ($P_a = N\text{ m}^{-2}$) calculated from force curves were spatially plotted to yield colour-coded stiffness maps in Igor Pro 6.22 (Wavemetrics). A two-dimensional spline interpolation was performed on the stiffness maps to smooth the visual presentation of the data.

Statistics. A total of 30 human breast biopsies from female patients (Supplementary Table S1) and 27 mammary glands and 6 lungs obtained from 13 MMTV-PyMT mice were analysed. All individual stiffness values for a specimen were summarized in OriginPro 8.5 (Microcal) to obtain the distribution of stiffness values (henceforth defined as biopsy-wide histogram). The bin width was set to 200 Pa for all mammary gland specimens and 500 Pa for the murine lungs. Counts were normalized according to the total amount of measured stiffness values per specimen. For data fitting, peaks were located with the peak analysis application of OriginPro. Subsequently, a multi-peak fit was applied to the stiffness distribution. All data are given as mean ± standard deviation. The statistical significance of differences in mean values was assessed with the paired Student's *t*-test in OriginPro 8.5. Statistical significance was set at $P \leq 0.05$.

Immunohistochemical analysis. After IT-AFM, all samples were retrieved, formalin-fixed and paraffin-embedded according to standard histological procedures. Sections with a thickness of ~5 μm were cut and transferred onto coated glass slides. The first and last slides of sequential sections were routinely stained with H&E. Subsequent histopathological examination included assessing the type of lesion (invasive ductal carcinoma, fibroadenoma and so on) and a number of standard histopathological markers (extent of tumour infiltration, fibrosis, necrosis and lymphocytic infiltration). For IHC analysis of the remaining slides of human mammary tissues, the following antibodies were used: anti-collagen I (1:80; Biologo CO2111), anti-laminin (1:25; Thermo RB-082-A, Thermo Scientific), anti-vimentin (prediluted, Ventana 790-2917, Roche Diagnostics), anti-desmin (prediluted, Ventana 760-2513, Roche Diagnostics). IHC analysis of murine tissue sections for laminin was performed in the same manner as for human sections. In addition, murine sections were stained with anti-β1 integrin (1:50, Abcam, ab52971) and anti-mouse collagen I (1:800, Abcam, ab34710). In some cases, sections were treated for antigen retrieval by heat or with 10 mM Tris buffer, 1 mM EDTA, pH 9.0 and citrate buffer, pH 6.0. For collagen staining of human biopsies, sections were pre-treated with pepsin for 30 min at room temperature. Avidin/biotin was used for blocking non-specific binding of the primary antibody. For immunolabelling, sections were incubated with 100 μl antibodies correspondingly diluted in 10 mM PBS, pH 7.6 and 0.1% sodium azide. Staining was visualized with horseradish peroxidase (HRP)-conjugated secondary antibodies (DakoCytomation). Sections

were examined with an upright light microscope (Carl Zeiss) at the magnifications indicated.

Received 29 June 2012; accepted 29 August 2012;
published online 21 October 2012

References

- Ingber, D. E. *et al.* Cellular tensegrity—exploring how mechanical changes in the cytoskeleton regulate cell-growth, migration, and tissue pattern during morphogenesis. *Int. Rev. Cytol.* **150**, 173–224 (1994).
- Park, C. C., Bissell, M. J. & Barcellos-Hoff, M. H. The influence of the microenvironment on the malignant phenotype. *Mol. Med. Today* **6**, 324–329 (2000).
- Needham, D. Possible role of cell cycle-dependent morphology, geometry, and mechanical-properties in tumor-cell metastasis. *Cell Biophys.* **18**, 99–121 (1991).
- Paszek, M. J. & Weaver, V. M. The tension mounts: mechanics meets morphogenesis and malignancy. *J. Mammary Gland Biol.* **9**, 325–342 (2004).
- Kumar, S. & Weaver, V. Mechanics, malignancy, and metastasis: the force journey of a tumor cell. *Cancer Metast. Rev.* **28**, 113–127 (2009).
- Kass, L., Erler, J. T., Dembo, M. & Weaver, V. M. Mammary epithelial cell: influence of extracellular matrix composition and organization during development and tumorigenesis. *Int. J. Biochem. Cell B* **39**, 1987–1994 (2007).
- Butcher, D. T., Alliston, T. & Weaver, V. M. A tense situation: forcing tumour progression. *Nature Rev. Cancer* **9**, 108–122 (2009).
- Sinkus, R. *et al.* High-resolution tensor MR elastography for breast tumour detection. *Phys. Med. Biol.* **45**, 1649–1664 (2000).
- Paszek, M. J. *et al.* Tensional homeostasis and the malignant phenotype. *Cancer Cell* **8**, 241–254 (2005).
- Levental, K. R. *et al.* Matrix crosslinking forces tumor progression by enhancing integrin signaling. *Cell* **139**, 891–906 (2009).
- Rosenbluth, M. J., Lam, W. A. & Fletcher, D. A. Force microscopy of nonadherent cells: a comparison of leukemia cell deformability. *Biophys. J.* **90**, 2994–3003 (2006).
- Cross, S. E., Jin, Y. S., Rao, J. & Gimzewski, J. K. Nanomechanical analysis of cells from cancer patients. *Nature Nanotech.* **2**, 780–783 (2007).
- Lekka, M. *et al.* Elasticity of normal and cancerous human bladder cells studied by scanning force microscopy. *Eur. Biophys. J. Biophys.* **28**, 312–316 (1999).
- Ward, K. A., Li, W. L., Zimmer, S. & Davis, T. Viscoelastic properties of transformed-cells—role in tumor-cell progression and metastasis formation. *Biorheology* **28**, 301–313 (1991).
- Lam, W. A., Rosenbluth, M. J. & Fletcher, D. A. Chemotherapy exposure increases leukemia cell stiffness. *Blood* **109**, 3505–3508 (2007).
- Guck, J. *et al.* Optical deformability as an inherent cell marker for testing malignant transformation and metastatic competence. *Biophys. J.* **88**, 3689–3698 (2005).
- Suresh, S. Biomechanics and biophysics of cancer cells. *Acta Mater.* **55**, 3989–4014 (2007).
- Lekka, M. *et al.* Cancer cell detection in tissue sections using AFM. *Arch. Biochem. Biophys.* **518**, 151–156 (2012).
- Weaver, V. M. *et al.* Matrix crosslinking forces tumor progression by enhancing integrin signaling. *Cell* **139**, 891–906 (2009).
- Erler, J. T. & Weaver, V. M. Three-dimensional context regulation of metastasis. *Clin. Exp. Metastasis* **26**, 35–49 (2009).
- Weaver, V. M., DuFort, C. C. & Paszek, M. J. Balancing forces: architectural control of mechanotransduction. *Nature Rev. Mol. Cell. Biol.* **12**, 308–319 (2011).
- Lin, E. Y. *et al.* Progression to malignancy in the polyoma middle T oncogene mouse breast cancer model provides a reliable model for human diseases. *Am. J. Pathol.* **163**, 2113–2126 (2003).
- Lundin, M., Lundin, J., Helin, H. & Isola, J. A digital atlas of breast histopathology: an application of web based virtual microscopy. *J. Clin. Pathol.* **57**, 1288–1291 (2004).
- Weaver, V. M. *et al.* Tensional homeostasis and the malignant phenotype. *Cancer Cell* **8**, 241–254 (2005).
- Egeblad, M. & Werb, Z. New functions for the matrix metalloproteinases in cancer progression. *Nature Rev. Cancer* **2**, 161–174 (2002).
- Albrechtsen, R., Nielsen, M., Wewer, U., Engvall, E. & Ruoslahti, E. Basement membrane changes in breast cancer detected by immunohistochemical staining for laminin. *Cancer Res.* **41**, 5076–5081 (1981).
- Guy, C. T., Cardiff, R. D. & Muller, W. J. Induction of mammary tumors by expression of polyomavirus middle T oncogene: a transgenic mouse model for metastatic disease. *Mol. Cell Biol.* **12**, 954–961 (1992).
- Fantozzi, A. & Christofori, G. Mouse models of breast cancer metastasis. *Breast Cancer Res.* **8**, 212 (2006).
- Guppy, M. The hypoxic core: a possible answer to the cancer paradox. *Biochem. Biophys. Res. Commun.* **299**, 676–680 (2002).
- Sedwick, C. Valerie Weaver: overcoming cancer's stiff resistance. *J. Cell. Biol.* **193**, 802–803 (2011).
- Lopez, J. I., Kang, I., You, W. K., McDonald, D. M. & Weaver, V. M. *In situ* force mapping of mammary gland transformation. *Integr. Biol. (Camb.)* **3**, 910–921 (2011).

32. Suresh, S. Biomechanics and biophysics of cancer cells. *Acta Biomater.* **3**, 413–438 (2007).
33. Alcaraz, J. *et al.* Collective epithelial cell invasion overcomes mechanical barriers of collagenous extracellular matrix by a narrow tube-like geometry and MMP14-dependent local softening. *Integr. Biol. (Camb.)* **3**, 1153–1166 (2011).
34. Stolz, M. *et al.* Early detection of aging cartilage and osteoarthritis in mice and patient samples using atomic force microscopy. *Nature Nanotech.* **4**, 186–192 (2009).
35. Thomas, A. *et al.* Real-time elastography—an advanced method of ultrasound: first results in 108 patients with breast lesions. *Ultrasound Obst. Gyn.* **28**, 335–340 (2006).
36. Burnside, E. S. *et al.* Differentiating benign from malignant solid breast masses with US strain imaging. *Radiology* **245**, 401–410 (2007).
37. Xu, H. Y. *et al.* Axial-shear strain imaging for differentiating benign and malignant breast masses. *Ultrasound Med. Biol.* **36**, 1813–1824 (2010).
38. Wong, C. C. L. *et al.* Hypoxia-inducible factor 1 is a master regulator of breast cancer metastatic niche formation. *Proc. Natl Acad. Sci. USA* **108**, 16369–16374 (2011).
39. Erler, J. T. *et al.* Lysyl oxidase is essential for hypoxia-induced metastasis. *Nature* **440**, 1222–1226 (2006).
40. Fritsch, A. *et al.* Are biomechanical changes necessary for tumour progression? *Nature Phys.* **6**, 730–732 (2010).
41. Wirtz, D., Konstantopoulos, K. & Searson, P. C. The physics of cancer: the role of physical interactions and mechanical forces in metastasis. *Nature Rev. Cancer* **11**, 512–522 (2011).
42. Erler, J. T., Jeffrey, S. S. & Giaccia, A. J. Hypoxia promotes invasion and metastasis of breast cancer cells by increasing lysyl oxidase expression. *Breast Cancer Res.* **7**, S57 (2005).
43. Sader, J. E., Larson, I., Mulvaney, P. & White, L. R. Method for the calibration of atomic-force microscope cantilevers. *Rev. Sci. Instrum.* **66**, 3789–3798 (1995).
44. Oliver, W. C. & Pharr, G. M. An improved technique for determining hardness and elastic-modulus using load and displacement sensing indentation experiments. *J. Mater. Res.* **7**, 1564–1583 (1992).
45. Plodinec, M., Loparic, M. & Aebi, U. Atomic force microscopy for biological imaging and mechanical testing across length scales. *Cold Spring Harb. Protoc.* **2010**, pdb top86 (2010).
46. Loparic, M. *et al.* Micro- and nanomechanical analysis of articular cartilage by indentation-type atomic force microscopy: validation with a gel-microfiber composite. *Biophys. J.* **98**, 2731–2740 (2010).
47. Plodinec, M. *et al.* The nanomechanical properties of rat fibroblasts are modulated by interfering with the vimentin intermediate filament system. *J. Struct. Biol.* **174**, 476–484 (2011).

Acknowledgements

The authors thank U. Mueller for excising tissues from MMTV-PyMT mice, T. Nguyen and P. Hirschmann for technical assistance with histology and IHC, and R. Suetterlin for advice on IHC. B. Bircher is acknowledged for his contribution to AFM data analysis, T. Pfändler for logistic support concerning clinical samples and A. Roulier for help with the drawing in Fig. 1. The authors also thank U. Sauder for SEM sample preparation, D. Mathys for SEM imaging and P. Demougin for RNA extraction. This work is funded by the National Centre of Competence in Research ‘Nanoscale Science’, Swiss National Science Foundation (to C.-A.S.), and the Commission for Technology and Innovation (CTI) supporting university–industry partnerships (Project 11977.2 PFNM-NM within the project ARTIDIS ‘Automated and Reliable Tissue Diagnostics’ awarded to R.Y.H.L. in partnership with Nanosurf AG). R.Z.D. is supported by Krebsliga Beider Basel (grant no. 22-2010). The laboratory of M.B.-A. is supported by the Novartis Research Foundation, the European Research Council (ERC starting grant no. 243211-PTPsBDC), the Swiss Cancer League and the Krebsliga Beider Basel.

Author contributions

M.P., R.Y.H.L. and C.-A.S. conceived the study and designed experiments. M.P., M.L. and R.Y.H.L. developed all customized hardware and software solutions for AFM. M.P. and E.C.O. performed pathohistological and IHC analysis of human and murine tissues. R.Z.D. recruited patients and provided human biopsies. M.P., C.A.M. and P.O. performed AFM experiments. M.P., M.L., C.A.M., J.T.H., P.O. and R.Y.H.L. analysed AFM data. M.B.-A. provided MMTV-PyMT mice and was involved in the analysis of murine tissues. M.P., U.A., R.Y.H.L. and C.-A.S. wrote the paper. All authors discussed the results and commented on the manuscript.

Additional information

Supplementary information is available in the online version of the paper. Reprints and permission information is available online at <http://www.nature.com/reprints>. Correspondence and requests for materials should be addressed to R.Y.H.L.

Competing financial interests

The University of Basel has filed patents on the technology and intellectual property related to this work based on the inventions of M.P., M.L. and R.Y.H.L.

Mechanical waves during tissue expansion

Xavier Serra-Picamal^{1,2†}, Vito Conte^{1†}, Romaric Vincent¹, Ester Anon^{1,3}, Dhananjay T. Tambe⁴, Elsa Bazellieres¹, James P. Butler^{4,5}, Jeffrey J. Fredberg⁴ and Xavier Trepat^{1,2,6★}

The processes by which an organism develops its shape and heals wounds involve expansion of a monolayer sheet of cells. The mechanism underpinning this epithelial expansion remains obscure, despite the fact that its failure is known to contribute to several diseases, including carcinomas, which account for about 90% of all human cancers. Here, using the micropatterned epithelial monolayer as a model system, we report the discovery of a mechanical wave that propagates slowly to span the monolayer, traverses intercellular junctions in a cooperative manner and builds up differentials of mechanical stress. Essential features of this wave generation and propagation are captured by a minimal model based on sequential fronts of cytoskeletal reinforcement and fluidization. These findings establish a mechanism of long-range cell guidance, symmetry breaking and pattern formation during monolayer expansion.

Epithelial monolayer expansion is increasingly regarded as a mechanical phenomenon in which physical forces not only drive cell motions but also trigger and feedback to signalling pathways^{1–3}. Each cell in the sheet is now known to generate forces on its underlying substrate¹, to transmit forces through intercellular junctions so as to create long-ranged gradients of tension⁴, and to migrate preferentially along the direction of maximum principal stress⁵. Despite such recent discoveries, the ultraslow dynamics of epithelial expansion remain poorly understood.

To study such dynamics, we developed an experimental approach that combines soft lithography^{6,7}, traction force microscopy⁴ and monolayer stress microscopy⁵. A polydimethylsiloxane (PDMS) membrane was fabricated with a rectangular opening and deposited on a polyacrylamide gel that had been coated with collagen I. We then seeded Madin–Darby Canine Kidney (MDCK) epithelial cells and allowed them to adhere and proliferate (Fig. 1a). On reaching confluence and a relatively high cell density, the monolayer sheet exhibited features typical of a stable epithelium including apico-basal polarity and accumulation of cortical actin at cell–cell junctions (Fig. 1b,c). Moreover, the tight junction protein ZO-1 (zona occludens 1) and the adherens junction protein E-cadherin co-localized at the lateral membranes of the cells (Fig. 1c).

Sudden removal of the PDMS membrane triggered collective cellular migration towards newly available free space (Figs 1a–c, 2a–c and Supplementary Movie S1). Over the course of 600 min, the total area of the monolayer sheet more than doubled, with less than half of the total area being attributable to proliferation (Fig. 1d inset) and the rest being attributable to cell spreading and flattening (Fig. 1b and Supplementary Text S2). In this process, the actin cytoskeleton exhibited a pronounced reorganization; it formed protrusions and transverse stress fibres in cells both at the leading edge and well behind it (Fig. 1c and Supplementary Movie S2). These changes in actin organization were paralleled by pronounced changes in the size and shape of focal adhesions (Fig. 1c). Cells did not undergo a full transition to a mesenchymal state, however;

although E-cadherin was partially internalized, tight junctions remained intact and the monolayer expanded as a cohesive unit (Fig. 1c). Moreover, whereas a number of genes traditionally associated with the epithelial to mesenchymal transition such as those encoding paxillin, vinculin and β -actin exhibited changes in expression, others such as those encoding E-cadherin, vimentin and ZO-1 did not (Supplementary Fig. S1).

The internal dynamics of the monolayer were remarkable, both in terms of the distribution of cellular velocities and underlying tractions exerted by each cell on its substrate. Shortly after removal of the PDMS stencil, migration outwards was limited to cells at the leading edge (Fig. 2d), whereas cells back from the leading edge remained virtually immobile. With increasing time, however, cell movement penetrated progressively deeper into the monolayer and gave rise to a pattern of velocities characterized by an outer boundary layer of outward velocities at the edges and an inner region of negligible velocities at the centre (Fig. 2e). A similar evolution of cellular velocities was recently reported after monolayer wounding, thus supporting the notion that progressive cell mobilization away from the leading edge is a general response of cell collectives to the release of physical boundaries⁸. Traction forces exerted by cells on the underlying substrate exhibited similar spatial organization, with boundary layers of large tractions at both edges and virtually no traction at the centre. Fluctuations of both velocities and tractions increased with time and progressively expanded towards the monolayer midline (Fig. 2f,i).

If each cell in the monolayer has the capability to exert tractions on its substrate across focal or fibrillar adhesions, it also has the capability to exert stresses on its immediate neighbours across cell–cell junctions^{5,9,10}. Using monolayer stress microscopy⁵ (Methods and Supplementary Texts S1 and S2), we measured corresponding inter- and intra-cellular stresses, which we refer to together simply as monolayer stresses. Shortly after the stencil was lifted, the average normal stress ($\bar{\sigma}$) was largely tensile (positive) but was restricted to thin boundary layers at the leading edges, whereas the centre of the monolayer remained relaxed (Fig. 2j).

¹Institute for Bioengineering of Catalonia, Barcelona 08028, Spain, ²Facultat de Medicina, Universitat de Barcelona, and Ciber Enfermedades Respiratorias, Barcelona 08036, Spain, ³Laboratoire Matière et Systèmes Complexes (MSC), Université Paris Diderot, and Unité Mixte de Recherche 7057 CNRS, F-75205 Paris Cedex 13, Paris, France, ⁴School of Public Health, Harvard University, Boston, Massachusetts 02115, USA, ⁵Brigham and Women's Hospital, Harvard Medical School, Boston, Massachusetts 02115, USA, ⁶Institució Catalana de Recerca i Estudis Avançats (ICREA), Barcelona 08010, Spain. [†]These authors contributed equally to this work. ★e-mail: xtrep@ibecbarcelona.eu.

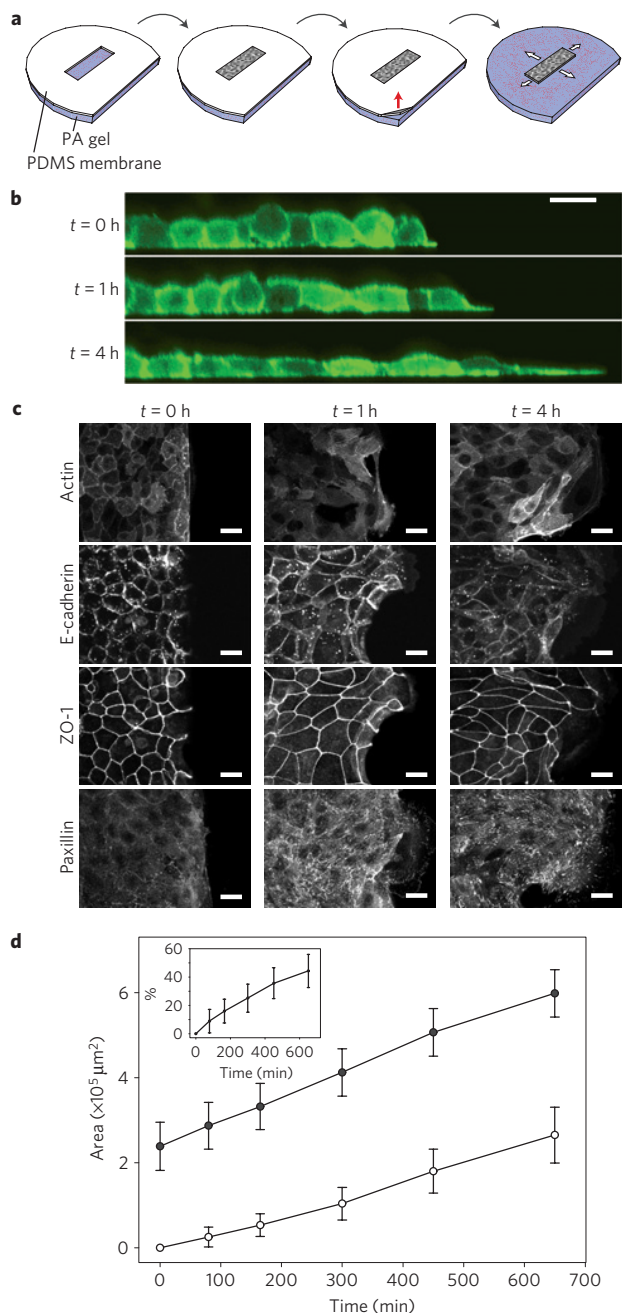


Figure 1 | Experimental model. **a**, A PDMS membrane is deposited on a collagen-coated polyacrylamide (PA) gel. Cells are seeded and allowed to attach only over the gap defined by the PDMS membrane. When confluent cells reach a relatively high confluence, the PDMS membrane is peeled off and cells start invading the surrounding space. **b**, Transversal view of LifeAct MDCK cells at the specified time points after the PDMS membrane was removed; scale bar, 20 μm . **c**, Basal actin (LifeAct-GFP), E-cadherin, ZO-1 and paxillin immunofluorescence micrographs before, 1 h after and 4 h after removing the membranes. Scale bars, 15 μm . **d**, Cell sheet area (filled circles) and cell sheet area due to proliferation (white circles) at different time points. The area due to proliferation was calculated by counting the number of cells in the monolayer at distinct time points and then multiplying the number of new cells by the average cell area. Data are mean \pm s.d. ($n = 5$). Inset: relative contribution of cell proliferation to cell sheet area.

With time, these boundary layers became markedly heterogeneous but systematically grew to encompass increasing numbers of

cells; cell–cell tension transmission exhibited a growing scale of length (Fig. 2k), and the maximum intercellular shear stress ($\bar{\mu}$) followed a similar pattern (Fig. 2m,n). Taken together, these findings demonstrate that force transmission from cell-to-cell, and cellular migration across the epithelial sheet, are initiated at the leading edge and progressively penetrate towards the centre (Supplementary Movie S3).

Moreover, these stress fields were anisotropic. At each position in the monolayer plane, the maximum (σ_{max}) and minimum (σ_{min}) principal stresses⁵ were represented as an ellipse aligned with corresponding principal orientations (Fig. 2p). Throughout epithelial expansion, stress ellipses tended to be spindle-shaped and thus revealed pronounced stress anisotropy. The maximum principal stress orientation tended to be perpendicular to the leading edge and thus roughly parallel to local cell motion (Fig. 2q). As described previously, this mode of local cell guidance defines plithotaxis^{2,5}.

Superposed on systematic monolayer spreading were large-scale spatio-temporal fluctuations of tractions, monolayer stresses and cellular velocities (Fig. 2f,i,l,o). To better characterize the systematic evolution of mechanical patterns, we averaged these variables over the observable monolayer length (corresponding to the y coordinate), thereby reducing the dimensionality of the system to only one spatial dimension and one temporal dimension. All data could then be represented as kymographs in the x – t plane (Methods). Kymographs of cellular velocity (v_x) revealed motility patterns that were not restricted to the initial phase of inward mobilization (Fig. 3a). To the contrary, after reaching the monolayer midline at ~ 150 min, the two fronts of cell motility coalesced and then continued towards the leading edges. When cells are cohesive and mass is conserved, cellular velocities must be linked to the rate of cell deformation (strain rate, $\dot{\epsilon}_{xx}$; ref. 11) through the expression $\dot{\epsilon}_{xx} = \partial v_x / \partial x$. Remarkably, kymographs of $\dot{\epsilon}_{xx}$ revealed clear evidence of wave-like crests of strain rate that were launched at each leading edge, propagated away from and back to the leading edge at roughly twice the speed of the advancing front edge, and spanned the entire monolayer (Fig. 3b). To distinguish these mechanical waves from other known types of mechanical wave, and because they inscribe an X-shape on the kymograph, we call them X-waves.

To study the physical origin of the X-wave, we next focused on traction generation and stress transmission in the monolayer. Whereas traction kymographs demonstrated extrema at the leading edge, monolayer stresses were highest at the monolayer midline, indicating that local force generation was globally integrated and transmitted through cell–cell junctions to give rise to a stress build-up (Fig. 3c,d). Importantly, monolayer stress at the midline oscillated in time (Fig. 3g,h and Supplementary Movie S4); these oscillations were in phase with fluctuations of cell area (Fig. 3f,h) and demonstrated phase quadrature with strain rate (Fig. 3e). Contrary to long-held assumptions (reviewed in ref. 12), these observations establish that on the ultraslow timescales of cellular migration the dominant cellular stresses in the monolayer are elastic, not viscous.

In the absence of appreciable inertia, there can exist no exchange between kinetic and potential energy storage as is usually associated with propagation of passive mechanical waves, thus suggesting that the mechanism underlying the observed propagation might be active. To investigate this possibility, we inhibited myosin using blebbistatin. Blebbistatin prevented the formation of stress fibres (Supplementary Fig. S2) and had little effect on the velocity of the leading edge, thus confirming previous reports in wound scratch assays⁸. Blebbistatin caused traction forces and intercellular stresses to be abrogated, however (Supplementary Fig. S2 and Movie S5). A well-defined front of strain rate could be clearly identified nonetheless, but this front was stationary, did not propagate

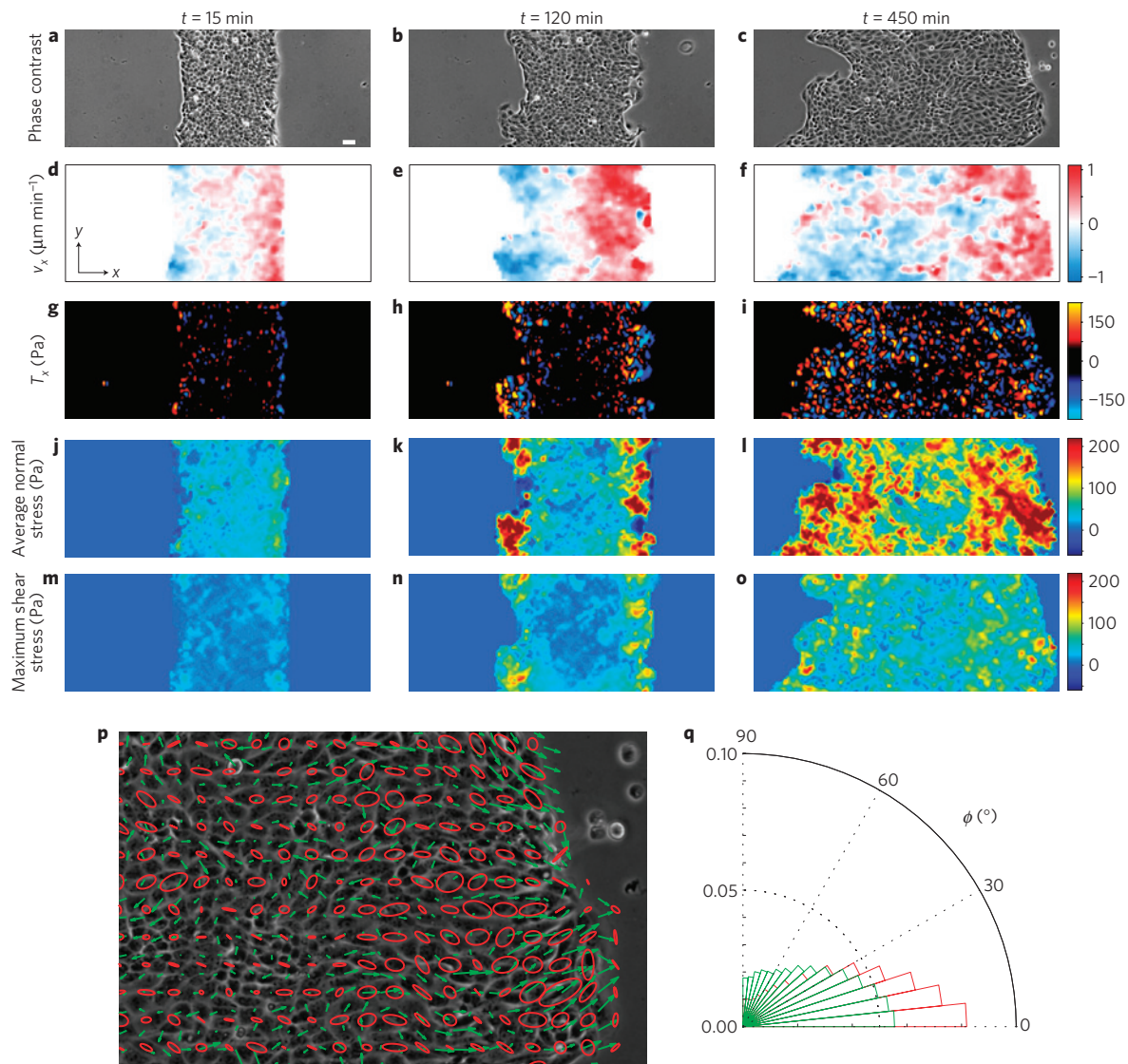


Figure 2 | Maps of cell velocity, cell substrate tractions and monolayer stresses. **a–o**, Phase-contrast images (**a–c**), velocity v_x (**d–f**), tractions T_x (**g–i**), average normal stress $\bar{\sigma}$ (**j–l**) and maximum shear stress $\bar{\mu}$ (**m–o**) at 15 min (**a,d,g,j,m**), 120 min (**b,e,h,k,n**) and 450 min (**c,f,i,l,o**) after removing the PDMS membrane. **p**, Principal stress ellipses (red) and velocity vectors (green) of a magnified region from **c**. **q**, Probability distribution of the major axis of the principal stress ellipse (red) and the velocities (green), where 0° represents alignment with the x axis and 90° represents alignment to the y axis. Scale bar, $50 \mu\text{m}$.

and dispersed or attenuated after about 450 min. Together, these findings indicate that the propagating mechanical wave involves a contractile component.

To study the role of intercellular adhesion in monolayer stress transmission and wave propagation, we disrupted cell–cell junctions by chelation of extracellular calcium⁵ after 280 min of monolayer expansion (Supplementary Fig. S3 and Movie S6). Within 20 min of calcium chelation, the monolayer lost its structural integrity and isolated cells were seen to escape from the leading edge. Monolayer stress exhibited a sharp drop and wave crests vanished (Supplementary Fig. S3). Restoration of calcium levels 45 min later rescued monolayer stresses and wave propagation but, remarkably, wave propagation restarted at the very edge of the monolayer. These data highlight a central role for cell–cell junctions in the generation and propagation of X-waves. They show, further, that these waves are not restricted to the case of sudden release of a physical constraint.

Across experiments, monolayer expansion exhibited various levels of symmetry breaking (Supplementary Fig. S4). As in

the symmetric case (Fig. 3), experiments in which symmetry was spontaneously broken showed propagation of velocity fronts back from each leading edge but, on collision, one of the two fronts penetrated past the midline into the opposite side of the monolayer before propagating back towards the leading edge (Supplementary Fig. S4a,b). As such, the characteristic time for the velocity front to complete one cycle of inward and outward propagation was longer than in the symmetric case. Symmetry breaking in multicellular systems is a widespread process that remains poorly understood^{13–15}. Our findings suggest that symmetry breaking during monolayer expansion originates at the very edge of the monolayer boundaries at the very onset of migration (Supplementary Fig. S4 and Movie S7), with the highest stresses restricted to the first few rows of the fastest leading edge.

Waves in chemical systems, as in the Belousov–Zhabotinsky reaction, rely on temporal competition between reaction times and diffusion times, and a generalization of this idea to non-equilibrium mechano-chemical systems was recently proposed¹⁶.

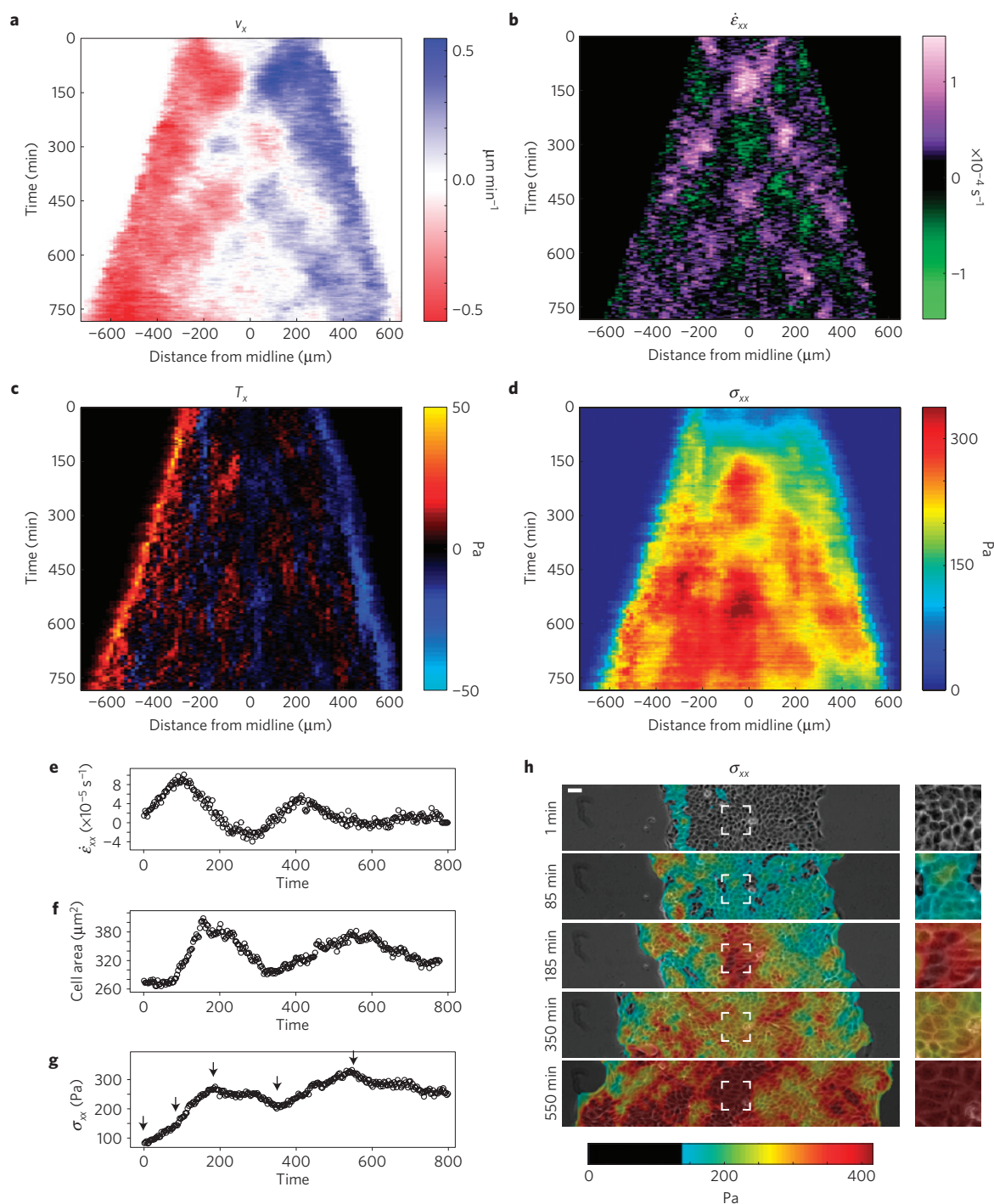


Figure 3 | Dynamic behaviour of a cell sheet expanding nearly symmetrically. **a–d**, Kymographs of velocity v_x (**a**), strain rate $\dot{\epsilon}_{xx}$ (**b**), tractions T_x (**c**) and monolayer stress component σ_{xx} (**d**). Boundary artefacts attributable to particle image velocimetry have been suppressed from **b** (Supplementary Fig. S5). **e–g**, Average value of $\dot{\epsilon}_{xx}$ (**e**), cell area (**f**) and σ_{xx} (**g**) at the monolayer midline (average over a strip of width 125 μm centred at the midline). **h**, Overlay of monolayer stress component σ_{xx} on phase-contrast images. The right square panels are a magnification of the highlighted region in the left panels. Scale bar, 50 μm .

Alternatively, wave propagation can also originate from threshold phenomena that are rapid, coupled with refractory phenomena that are slow, as in propagation of the action potential¹⁷. Although it remains unclear how comparable mechanisms might account for the mechanical waves reported here, a minimal one-dimensional mechanical model captures the observed phenomenology without invoking chemical factors or their associated reaction, diffusion and advection. The model treats the monolayer as a collection of springs

(cells) of elastic constant k connected in series (Fig. 4a). Each cell is allowed to generate a self-propelling force F_i . This propelling force can be transmitted through elastic forces to neighbouring cells and by frictional forces to the underlying gel substrate. The position x_i of a generic node (cell–cell junction) is affected by the force F_i , by the elastic responses f_i^e and f_{i+1}^e of the two cells joined at that node, and by the viscous friction f_i^v between those two cells and the gel substrate (Fig. 4b), represented as a dashpot of constant viscosity η

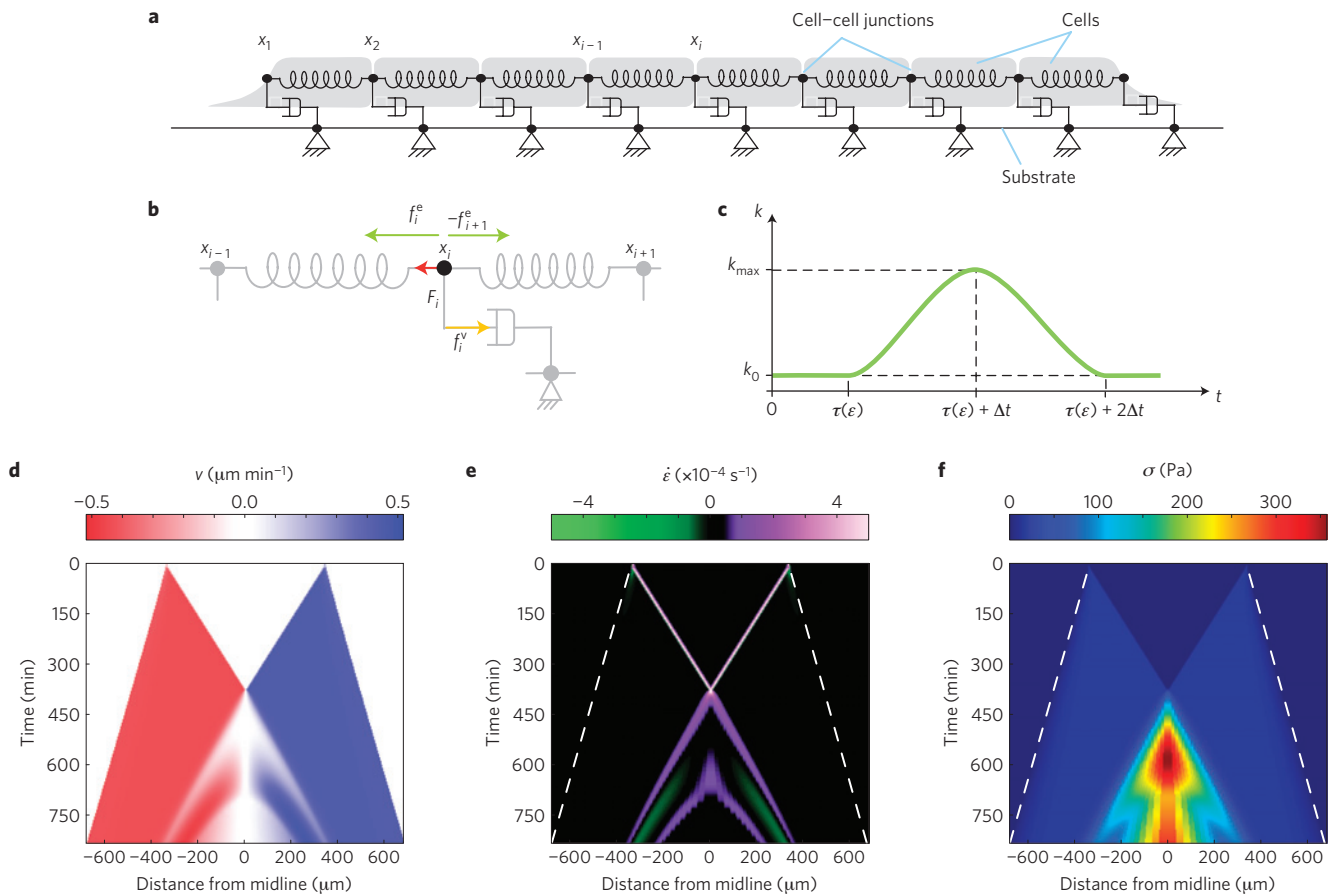


Figure 4 | Essential features of wave generation and propagation are captured by a minimal model based on sequential fronts of cytoskeletal reinforcement and fluidization. **a**, Schematic of the one-dimensional *in silico* model for a line of elastic epithelial cells sliding viscously on a rigid substrate in response to self-propelling forces. **b**, Schematic of the nodal force balance. Forces are represented through arrows and all act at the generic node x_i (for the sake of the clarity, they have been drawn as acting at points in the proximity of node x_i). Self-propelling force F_i is in red; viscous force f_i^v is in yellow; elastic forces f_i^e and f_{i+1}^e are in green. **c**, Dependence of the spring constant k on strain and time. When a spring reaches a strain threshold ϵ_{th} , it undergoes one phase of reinforcement (stiffening) followed by one phase of fluidization (softening). **d**, *In silico* velocity kymograph. **e**, *In silico* strain rate kymograph. **f**, *In silico* stress kymograph.

(Fig. 4a). Thus, force balance at each node x_i reads

$$F_i + k\epsilon_i - k\epsilon_{i+1} - \eta\dot{x}_i = 0$$

where ϵ_i denotes the strain undergone by the spring connecting nodes x_{i-1} and x_i , and \dot{x}_i denotes the velocity of node x_i .

In the context of this model we first considered the two most widely invoked mechanisms for monolayer expansion, namely, that force generation is restricted to the first few leading cell rows, or that each cell in the monolayer is mechanically self-propelled. Simulation of each of these scenarios results in monolayer expansion but fails to account for the generation and propagation of X-waves (Supplementary Text S3). In contrast, such waves are captured with only two assumptions. The first is that a cell acquires a motile phenotype only when an adjacent cell either creates space¹⁸ or pulls on the shared intercellular junction¹⁹, either of which would promote local cell unjamming^{5,20,21} and lead naturally to the propagation of a strain-rate front followed by a stress build-up (Supplementary Text S3). If, second, the cell is assumed to possess a threshold of strain beyond which the cytoskeleton first reinforces²² but then fluidizes²³, then strain rate fronts and stress differentials become reiterated in time. As they elicit effects on cellular mechanical properties that are nonlinear in character but opposite in sign, and, importantly, as they act over disparate scales of time^{23,24}, reinforcement and fluidization taken together are shown to be sufficient to sustain a propagating mechanical

wave with many of the same features as the X-waves demonstrated experimentally (Fig. 4d–f and Supplementary Movie S8). A role for reaction–diffusion–advection mechanisms or for gene oscillators cannot be ruled out, but to explain these mechanical waves, such mechanisms need not be invoked.

In view of this relationship, pattern formation during development is widely attributed to cellular sensing of local chemical differentials that become reiterated over the span of a great many cells. Although there is little doubt that such reiterated chemical differentials are necessary to explain patterning, it remains unclear whether they are sufficient. For example, large multicellular systems are typically heterogeneous, dynamic and noisy. In such systems, can the reaction, diffusion and advection of chemical factors act with sufficient precision to transmit requisite information over distances spanning a great many cells? This question and others have led to the hypothesis that pattern formation requires another feedback mechanism, and that such a mechanism is provided by physical forces^{2,16,25–28}. It is now well established that local physical forces can be transduced into local intracellular signals to activate local regulatory protein networks^{29–32}, but patterns of stress and strain reiterated in time and over space across a multicellular tissue have never before been observed. Our finding of a slow mechanical wave constitutes the first direct evidence of such reiterated mechanical patterns and thus provides a natural candidate to trigger mechanotransduction

pathways during wound healing, morphogenesis and collective cellular invasion in cancer.

Methods

Cell culture. MDCK strain II cells were cultured in minimum essential media with Earle's Salts and L-glutamine (Gibco) supplemented with 10% fetal bovine serum (FBS; Gibco), 100 U ml⁻¹ penicillin and 100 µg ml⁻¹ streptomycin.

Microfabrication of the PDMS membranes. PDMS membranes were fabricated according to procedures described previously^{7,33}. Briefly, SU8-50 masters containing rectangles of 300 × 2,500 µm were raised using conventional photolithography. Uncured PDMS was spin-coated on the masters to a thickness lower than the height of the SU8 feature (35 µm) and cured for 2 h at 60 °C. A thicker border of PDMS was applied at the edges of the membranes for handling purposes. PDMS was then peeled off from the master and kept in ethanol at 4 °C until use.

Preparation of polyacrylamide gels. Polyacrylamide gel preparation was adapted from protocols described in refs 34,35. Glass-bottom dishes were activated by using a 1:1:14 solution of acetic acid/bis-silane/ethanol. The dishes were washed twice with ethanol and air-dried for 10 min. For 3 kPa gels, a stock solution containing a concentration of 5.5% acrylamide, 0.09% bisacrylamide, 0.5% ammonium persulphate, 0.05% tetramethylethylenediamine, 0.4% of 200-nm-diameter red fluorescent carboxylate-modified beads (Fluospheres, Invitrogen) and 2 mg ml⁻¹ NH-acrylate was prepared. A drop of 10 µl was added to the centre of the glass-bottom dishes, and the solution was covered with 12-mm-diameter glass coverslips. After polymerization, gels were washed with PBS and incubated with 100 µl of a collagen I solution (0.1 mg ml⁻¹, Millipore) overnight at 4 °C. Gels were washed afterwards with PBS and incubated with cell culture media with 10% FBS for 6 h.

Cell patterning on soft substrates. One hour before seeding the cells, the PDMS membranes were air dried and incubated in a solution of 2% Pluronic F-127 (Sigma-Aldrich) in PBS to avoid damage of the gel coating due to the PDMS membrane. The membranes were then washed twice with PBS and air dried for 20 min, and they were deposited on the surface of the polyacrylamide gel. A small volume (8 µl) containing 15,000 cells was placed on the exposed region of the polyacrylamide gel defined by the PDMS membrane. Once the cells were attached to the polyacrylamide gel (20 min), the unattached cells were washed away and 200 µl of medium was added. Twelve hours after seeding the cells, 2 ml of medium was added and the PDMS membranes were carefully removed with tweezers before the beginning of the experiment.

Time-lapse microscopy. Multidimensional acquisition routines were performed on an automated inverted microscope (Nikon Eclipse Ti) equipped with thermal, CO₂ and humidity control, using MetaMorph (Universal Imaging) software. Time-lapse recording started approximately 30 min after removing the PDMS membrane. The interval between image acquisition was 1 min and a typical experiment lasted for 20 h. To capture the full width of the expanding cell sheet, two images were acquired at ×10 for every time point, approximately overlapping laterally by 10%. The two images were accurately stitched with subpixel resolution using custom-made MatLab software.

Fluorescence microscopy. Immunofluorescence microscopy experiments were carried out by fixing the cells with 3% paraformaldehyde (Sigma-Aldrich) in PBS, permeabilizing with 0.5% Triton X-100 (Sigma-Aldrich) in PBS, and blocking with 10% FBS (Sigma-Aldrich) in PBS.

Primary antibodies mouse anti-E-cadherin (BD Transduction Laboratories), rabbit anti-ZO-1 (Zymed, Invitrogen) and mouse anti-paxillin (BD Transduction Laboratories) diluted at 1:1,000, 1:500 and 1:100, respectively, in 10% FBS in PBS were incubated for 1 h at room temperature, and were detected using secondary antibodies goat anti-mouse and donkey anti-rabbit (Invitrogen). A spectral confocal microscope (Nikon Eclipse C1si) was used for high-resolution image acquisition.

Cell area measurements. The contour of each cell was determined using a segmentation algorithm (Greylevel Watershed for ImageJ, D. Sage, Biomedical Image Group, EPFL). Phase-contrast images were pre-processed by contrast enhancement followed by a Gaussian blur. To limit the over-sampling inherent to water-shedding algorithms, we set up the appropriate limits for the cell area and eccentricity.

Velocity measurements. Velocity fields were computed using custom-made particle image velocimetry software on the phase-contrast images. The interrogation window was either 64 × 64 pixels or 96 × 96 pixels, and the time interval between consecutive analysed images was 1 min. Monolayer boundaries were computed using a home-made algorithm based on the standard deviation of each interrogation window in the phase-contrast images.

Traction microscopy. Traction forces were computed using Fourier transform traction microscopy with a finite gel thickness⁴. Gel displacements between any experimental time point and a reference image obtained after monolayer trypsinization were computed using home-made particle imaging velocimetry software. To reduce systematic biases in subpixel resolution and peak-locking effects, we implemented an iterative process ($n = 4$ iterations) based on a continuous window shift technique.

Monolayer stress microscopy. Monolayer stresses were computed using monolayer stress microscopy⁵. Monolayer stress microscopy uses traction forces and straightforward force balance demanded by Newton's laws to map the two-dimensional stress tensor σ in the monolayer:

$$\sigma = \begin{pmatrix} \sigma_{xx} & \sigma_{xy} \\ \sigma_{yx} & \sigma_{yy} \end{pmatrix}$$

By rotating these stress components at each point in the cell sheet, we computed the magnitude of the two principal stress components σ_{\max} and σ_{\min} and their corresponding, mutually perpendicular, principal orientations. For each point in the monolayer, we then computed the average normal stress within and between cells defined as $\bar{\sigma} = (\sigma_{\max} + \sigma_{\min})/2$ and the maximum intercellular shear stress defined as $\bar{\mu} = (\sigma_{\max} - \sigma_{\min})/2$.

Kymographs. For each pixel in the monolayer, we computed the distance to the closest leading edge. Next we computed the median values of velocities, tractions, monolayer stresses and strain rates of all pixels located at a given distance from the leading edge. These median values were then represented on a unidimensional segment whose width was the mean width of the monolayer. This operation was repeated for each experimental time point.

Quantification of gene expression. MDCK monolayers were collected at 0, 3, and 7 h of monolayer expansion. The total RNA was extracted using the PARIS kit (Applied Biosystems) according to the manufacturer's instructions. RNA was quantified by the absorbance at 260 nm, and reverse transcribed into complementary DNA using the high-capacity RNA-to-cDNA master mix (Applied Biosystems). Quantitative PCR was performed with the 7500 fast real-time PCR system and software (Applied Biosystems). TaqMan gene expression assays Cff02668852_g1, Cff02651495_m1, Cff02628470_m1, Cff02624268_m1, Cff02667774_m1, Cff02645536_m1, and Cff03023880_g1 were used to detect vimentin, paxillin, ZO-1, E-cadherin, β -catenin, vinculin and β -actin, respectively. Quantitative real-time PCR values were normalized to an internal control s18 (TaqMan probe Cff02624915_g1), averaged and expressed relative to gene expression before cell migration (0 h).

Received 31 January 2012; accepted 30 May 2012; published online 8 July 2012

References

- Du Roure, O. *et al.* Force mapping in epithelial cell migration. *Proc. Natl Acad. Sci. USA* **102**, 2390–2395 (2005).
- Trepat, X. & Fredberg, J. J. Plithotaxis and emergent dynamics in collective cellular migration. *Trends Cell Biol.* **21**, 638–646 (2011).
- Leckband, D. E., le Duc, Q., Wang, N. & de Rooij, J. Mechanotransduction at cadherin-mediated adhesions. *Curr. Opin. Cell Biol.* **23**, 523–530 (2011).
- Trepat, X. *et al.* Physical forces during collective cell migration. *Nature Phys.* **5**, 426–430 (2009).
- Tambe, D. T. *et al.* Collective cell guidance by cooperative intercellular forces. *Nature Mater.* **10**, 469–475 (2011).
- Nikolic, D. L., Boettiger, A. N., Bar-Sagi, D., Carbeck, J. D. & Shvartsman, S. Y. Role of boundary conditions in an experimental model of epithelial wound healing. *Am. J. Physiol. Cell Physiol.* **291**, C68–C75 (2006).
- Poujade, M. *et al.* Collective migration of an epithelial monolayer in response to a model wound. *Proc. Natl Acad. Sci. USA* **104**, 15988–15993 (2007).
- Matsubayashi, Y., Razzell, W. & Martin, P. 'White wave' analysis of epithelial scratch wound healing reveals how cells mobilise back from the leading edge in a myosin-II-dependent fashion. *J. Cell Sci.* **124**, 1017–1021 (2011).
- Maruthamuthu, V., Sabass, B., Schwarz, U. S. & Gardel, M. L. Cell-ECM traction force modulates endogenous tension at cell-cell contacts. *Proc. Natl Acad. Sci. USA* **108**, 4708–4713 (2011).
- Liu, Z. *et al.* Mechanical tugging force regulates the size of cell-cell junctions. *Proc. Natl Acad. Sci. USA* **107**, 9944–9949 (2010).
- Blanchard, G. B. *et al.* Tissue tectonics: Morphogenetic strain rates, cell shape change and intercalation. *Nature Methods* **6**, 458–464 (2009).
- Chen, X. & Brodland, G. W. Multi-scale finite element modeling allows the mechanics of amphibian neurulation to be elucidated. *Phys. Biol.* **5**, 015003 (2008).
- Gros, J., Feistel, K., Viebahn, C., Blum, M. & Tabin, C. J. Cell movements at Hensen's node establish left/right asymmetric gene expression in the chick. *Science* **324**, 941–944 (2009).

14. Wan, L. Q. *et al.* Micropatterned mammalian cells exhibit phenotype-specific left-right asymmetry. *Proc. Natl Acad. Sci. USA* **108**, 12295–12300 (2010).
15. Brangwynne, C., Huang, S., Parker, K. K., Ingber, D. E. & Ostuni, E. Symmetry breaking in cultured mammalian cells. *In Vitro Cell Dev. Biol. Anim.* **36**, 563–565 (2000).
16. Bois, J. S., Julicher, F. & Grill, S. W. Pattern formation in active fluids. *Phys. Rev. Lett.* **106**, 028103 (2011).
17. Hodgkin, A. L. & Huxley, A. F. A quantitative description of membrane current and its application to conduction and excitation in nerve. *J. Physiol.* **117**, 500–544 (1952).
18. Carmona-Fontaine, C. *et al.* Contact inhibition of locomotion in vivo controls neural crest directional migration. *Nature* **456**, 957–961 (2008).
19. Weber, G. F., Bjerke, M. A. & Desimone, D. W. A mechanoresponsive Cadherin-Keratin complex directs polarized protrusive behavior and collective cell migration. *Dev. Cell* **22**, 104–115 (2012).
20. Angelini, T. E. *et al.* From the cover: Glass-like dynamics of collective cell migration. *Proc. Natl Acad. Sci. USA* **108**, 4714–4719 (2011).
21. Garrahan, J. P. Dynamic heterogeneity comes to life. *Proc. Natl Acad. Sci. USA* **108**, 4701–4702 (2011).
22. Riveline, D. *et al.* Focal contacts as mechanosensors: Externally applied local mechanical force induces growth of focal contacts by an mDia1-dependent and ROCK-independent mechanism. *J. Cell Biol.* **153**, 1175–1186 (2001).
23. Treppe, X. *et al.* Universal physical responses to stretch in the living cell. *Nature* **447**, 592–595 (2007).
24. Bursac, P. *et al.* Cytoskeletal remodelling and slow dynamics in the living cell. *Nature Mater.* **4**, 557–561 (2005).
25. Eyckmans, J., Boudou, T., Yu, X. & Chen, C. S. A Hitchhiker's guide to mechanobiology. *Dev. Cell* **21**, 35–47 (2011).
26. Mammoto, T. & Ingber, D. E. Mechanical control of tissue and organ development. *Development* **137**, 1407–1420 (2010).
27. Shraiman, B. I. Mechanical feedback as a possible regulator of tissue growth. *Proc. Natl Acad. Sci. USA* **102**, 3318–3323 (2005).
28. Montell, D. J. Morphogenetic cell movements: Diversity from modular mechanical properties. *Science* **322**, 1502–1505 (2008).
29. del Rio, A. *et al.* Stretching single talin rod molecules activates vinculin binding. *Science* **323**, 638–641 (2009).
30. Hoffman, B. D., Grashoff, C. & Schwartz, M. A. Dynamic molecular processes mediate cellular mechanotransduction. *Nature* **475**, 316–323 (2011).
31. Johnson, C. P., Tang, H.-Y., Carag, C., Speicher, D. W. & Discher, D. E. Forced unfolding of proteins within cells. *Science* **317**, 663–666 (2007).
32. Zhang, H. *et al.* A tension-induced mechanotransduction pathway promotes epithelial morphogenesis. *Nature* **471**, 99–103 (2011).
33. Ostuni, E., Kane, R., Chen, C. S., Ingber, D. E. & Whitesides, G. M. Patterning mammalian cells using elastomeric membranes. *Langmuir* **16**, 7811–7819 (2000).
34. Kadow, C. E., Georges, P. C., Janmey, P. A. & Benigno, K. A. in *Methods in Cell Biology* Vol. 83 (eds Wang Yu-Li, E. & Discher, Dennis) 29–46 (Academic, 2007).
35. Yeung, T. *et al.* Effects of substrate stiffness on cell morphology, cytoskeletal structure, and adhesion. *Cell Motil. Cytoskeleton* **60**, 24–34 (2005).

Acknowledgements

We thank M. Bintanel for technical assistance, S. Garcia and A. Carreras for help with polyacrylamide gels and micropatterning, the Nanotechnology Platform from Barcelona Science Park, J. J. Munoz for help with the numerical implementation of the model, and P. Roca-Cusachs, D. G. Miguez, D. Navajas, R. Farre and J. Alcaraz for discussions. This research was supported by the Spanish Ministry for Science and Innovation (BFU2009-07595 and FPU fellowship XS), the European Research Council (Grant Agreement 242993) and the National Institutes of Health (R01HL102373, R01HL107561).

Author contributions

X.S.-P. and X.T. designed experiments; X.S.-P. performed all experiments. E.B. and X.S.-P. performed gene expression experiments; X.S.-P., R.V., V.C. and X.T. analysed data; D.T.T. contributed software; V.C. built the computer model and performed simulations; X.S.-P., V.C., J.J.F. and X.T. wrote the manuscript; all authors discussed and interpreted results and commented on the manuscript; X.T. supervised the project.

Additional information

The authors declare no competing financial interests. Supplementary information accompanies this paper on www.nature.com/naturephysics. Reprints and permissions information is available online at www.nature.com/reprints. Correspondence and requests for materials should be addressed to X.T.

The Cancer Cell Line Encyclopedia enables predictive modelling of anticancer drug sensitivity

Jordi Barretina^{1,2,3,†*}, Giordano Caponigro^{4*}, Nicolas Stransky^{1*}, Kavitha Venkatesan^{4*}, Adam A. Margolin^{1†*}, Sungjoon Kim⁵, Christopher J. Wilson⁴, Joseph Lehar⁴, Gregory V. Kryukov¹, Dmitriy Sonkin⁴, Anupama Reddy⁴, Manway Liu⁴, Lauren Murray¹, Michael F. Berger^{1†}, John E. Monahan⁴, Paula Morais¹, Jodi Meltzer⁴, Adam Korejwa¹, Judit Jané-Valbuena^{1,2}, Felipa A. Mapa⁴, Joseph Thibault⁵, Eva Bric-Furlong⁴, Pichai Raman⁴, Aaron Shipway⁵, Ingo H. Engels⁵, Jill Cheng⁶, Guoying K. Yu⁶, Jianjun Yu⁶, Peter Aspesi Jr⁴, Melanie de Silva⁴, Kalpana Jagtap⁴, Michael D. Jones⁴, Li Wang⁴, Charles Hatton³, Emanuele Palescandolo³, Supriya Gupta¹, Scott Mahan¹, Carrie Sougnez¹, Robert C. Onofrio¹, Ted Liefeld¹, Laura MacConaill³, Wendy Winckler¹, Michael Reich¹, Nanxin Li⁵, Jill P. Mesirov¹, Stacey B. Gabriel¹, Gad Getz¹, Kristin Ardlie¹, Vivien Chan⁶, Vic E. Myer⁴, Barbara L. Weber⁴, Jeff Porter⁴, Markus Warmuth⁴, Peter Finan⁴, Jennifer L. Harris⁵, Matthew Meyerson^{1,2,3}, Todd R. Golub^{1,3,7,8}, Michael P. Morrissey^{4*}, William R. Sellers^{4*}, Robert Schlegel^{4*} & Levi A. Garraway^{1,2,3*}

The systematic translation of cancer genomic data into knowledge of tumour biology and therapeutic possibilities remains challenging. Such efforts should be greatly aided by robust preclinical model systems that reflect the genomic diversity of human cancers and for which detailed genetic and pharmacological annotation is available¹. Here we describe the Cancer Cell Line Encyclopedia (CCLE): a compilation of gene expression, chromosomal copy number and massively parallel sequencing data from 947 human cancer cell lines. When coupled with pharmacological profiles for 24 anticancer drugs across 479 of the cell lines, this collection allowed identification of genetic, lineage, and gene-expression-based predictors of drug sensitivity. In addition to known predictors, we found that plasma cell lineage correlated with sensitivity to IGF1 receptor inhibitors; AHR expression was associated with MEK inhibitor efficacy in *NRAS*-mutant lines; and *SLFN11* expression predicted sensitivity to topoisomerase inhibitors. Together, our results indicate that large, annotated cell-line collections may help to enable preclinical stratification schemata for anticancer agents. The generation of genetic predictions of drug response in the preclinical setting and their incorporation into cancer clinical trial design could speed the emergence of ‘personalized’ therapeutic regimens².

Human cancer cell lines represent a mainstay of tumour biology and drug discovery through facile experimental manipulation, global and detailed mechanistic studies, and various high-throughput applications. Numerous studies have used cell-line panels annotated with both genetic and pharmacological data, either within a tumour lineage^{3–5} or across multiple cancer types^{6–12}. Although affirming the promise of systematic cell line studies, many previous efforts were limited in their depth of genetic characterization and pharmacological interrogation.

To address these challenges, we generated a large-scale genomic data set for 947 human cancer cell lines, together with pharmacological profiling of 24 compounds across ~500 of these lines. The resulting collection, which we termed the Cancer Cell Line Encyclopedia (CCLE), encompasses 36 tumour types (Fig. 1a and Supplementary Table 1; see also <http://www.broadinstitute.org/ccle>). All cell lines were characterized by several genomic technology platforms. The mutational status of >1,600 genes was determined by targeted massively parallel sequencing, followed by removal of variants likely to be germline events (Supplementary Methods). Moreover, 392 recurrent mutations affecting 33

known cancer genes were assessed by mass spectrometric genotyping¹³ (Supplementary Table 2 and Supplementary Fig. 1). DNA copy number was measured using high-density single nucleotide polymorphism arrays (Affymetrix SNP 6.0; Supplementary Methods). Finally, messenger RNA expression levels were obtained for each of the lines using Affymetrix U133 plus 2.0 arrays. These data were also used to confirm cell line identities (Supplementary Methods and Supplementary Figs 2–4).

We next measured the genomic similarities by lineage between CCLE lines and primary tumours from Tumorscape¹⁴, expO, MILE and COSMIC data sets (Fig. 1b–d and Supplementary Methods). For most lineages, a strong positive correlation was observed in both chromosomal copy number and gene expression patterns (median correlation coefficients of 0.77, range = 0.52–0.94, $P < 10^{-15}$, for copy number, and 0.60, range = 0.29–0.77, $P < 10^{-15}$, for expression, respectively; Fig. 1b, c and Supplementary Tables 3 and 4), as has been described previously^{3–5,15}. A positive correlation was also observed for point mutation frequencies (median correlation coefficient = 0.71, range = –0.06–0.97, $P < 10^{-2}$ for all but 3 lineages; Supplementary Fig. 5), even when *TP53* was removed from the data set (median correlation coefficient = 0.64, range = –0.31–0.97, $P < 10^{-2}$ for all but 3 lineages; Fig. 1d and Supplementary Table 5). Thus, with relatively few exceptions (Supplementary Information), the CCLE may provide representative genetic proxies for primary tumours in many cancer types.

Given the pressing clinical need for robust molecular correlates of anticancer drug response, we incorporated a systematic framework to ascertain molecular correlates of pharmacological sensitivity *in vitro*. First, 8-point dose–response curves for 24 compounds (targeted and cytotoxic agents) across 479 cell lines were generated (Supplementary Tables 1 and 6, and Supplementary Methods). These curves were represented by a logistical sigmoidal function with a maximal effect level (A_{\max}), the concentration at half-maximal activity of the compound (EC_{50}), a Hill coefficient representing the sigmoidal transition, and the concentration at which the drug response reached an absolute inhibition of 50% (IC_{50}).

Broadly active compounds, exemplified by the HDAC inhibitor LBH589 (panobinostat), showed a roughly even distribution of A_{\max} and EC_{50} values across most cell lines (Fig. 2a). In contrast, the RAF inhibitor PLX4720 had a more selective profile: A_{\max} or EC_{50} values for most cell lines could be categorized as ‘sensitive’ or ‘insensitive’ to

¹The Broad Institute of Harvard and MIT, Cambridge, Massachusetts 02142, USA. ²Department of Medical Oncology, Dana-Farber Cancer Institute, Harvard Medical School, Boston, Massachusetts 02115, USA. ³Center for Cancer Genome Discovery, Dana-Farber Cancer Institute, Harvard Medical School, Boston, Massachusetts 02115, USA. ⁴Novartis Institutes for Biomedical Research, Cambridge, Massachusetts 02139, USA. ⁵Genomics Institute of the Novartis Research Foundation, San Diego, California 92121, USA. ⁶Novartis Institutes for Biomedical Research, Emeryville, California 94608, USA. ⁷Department of Pediatric Oncology, Dana-Farber Cancer Institute, Boston, Massachusetts 02115, USA. ⁸Howard Hughes Medical Institute, Chevy Chase, Maryland 20815, USA. [†]Present addresses: Novartis Institutes for Biomedical Research, Cambridge, Massachusetts 02139, USA (J.B.); Sage Bionetworks, 1100 Fairview Ave. N., Seattle, Washington 98109, USA (A.A.M.); Department of Pathology, Memorial Sloan-Kettering Cancer Center, New York, New York 10065, USA (M.F.B.).

*These authors contributed equally to this work.

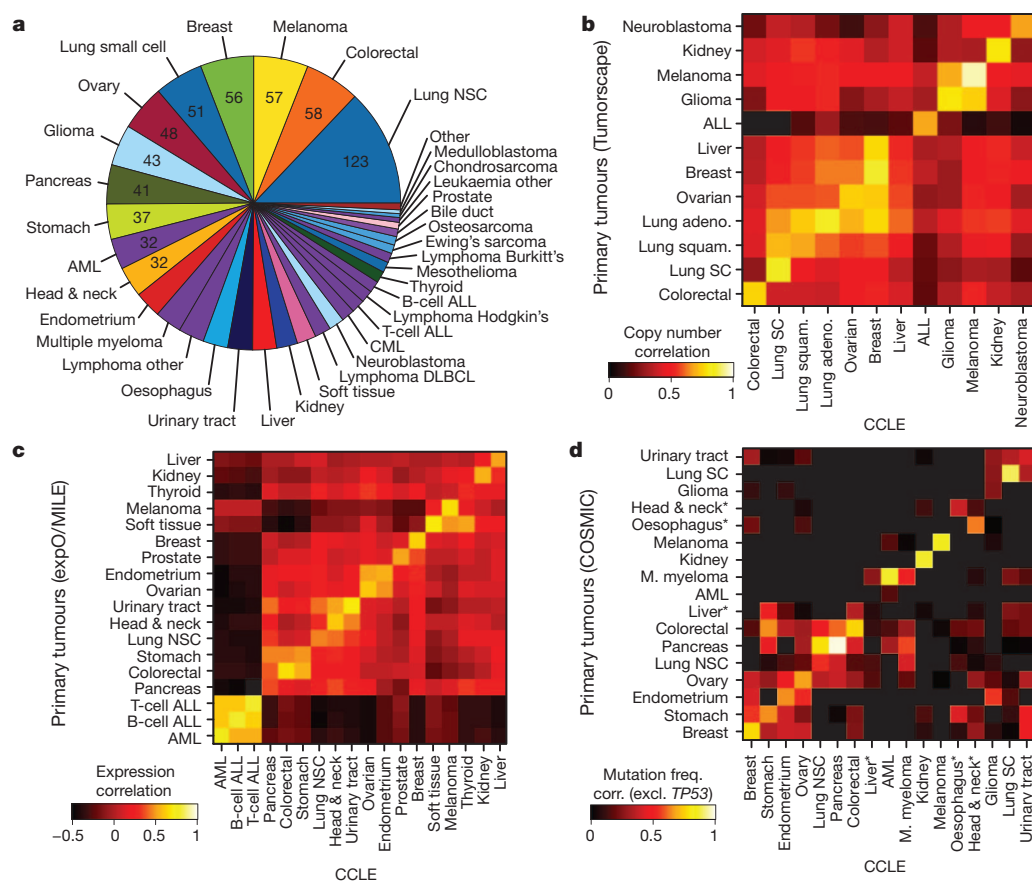


Figure 1 | The Cancer Cell Line Encyclopedia. **a**, Distribution of cancer types in the CCLE by lineage. **b**, Comparison of DNA copy-number profiles (GISTIC G-scores) between cell lines and primary tumours. The diagonal of the heat map shows the Pearson correlation between corresponding tumour types. Because cell lines and tumours are separate data sets, the correlation matrix is asymmetric: the top left showing how well the tumour features correlate with the average of the cell lines in a lineage, and the bottom right showing the converse. **c**, Comparison of mRNA expression profiles between cell lines and primary tumours. For each tumour type, the log fold change of the 5,000 most variable genes is calculated between that tumour type and all others. Pearson correlations between tumour type fold changes from primary tumours and cell lines are shown as a heat map. **d**, Comparison of point mutation frequencies between cell lines and primary tumours in COSMIC (v56), restricted to genes that are well represented in both sample sets but excluding *TP53*, which is highly prevalent in most tumour types. Pairwise Pearson correlations are shown as a heat map. Asterisk indicates that the correlations of oesophageal, liver, and head and neck cancer mutation frequencies are restored when including *TP53*.

PLX4720, with sensitive lines enriched for the *BRAF*^{V600E} mutation (Fig. 2a). To capture simultaneously the efficacy and potency of a drug, we designated an 'activity area' (Fig. 2b and Supplementary Fig. 6). The 24 compounds profiled showed wide variations in activity area, and those with similar mechanisms of action clustered together (Supplementary Fig. 7).

Genomic correlates of drug sensitivity may be extracted by predictive models using machine learning techniques^{6,10}. We therefore assembled all CCLE genomic data types into a matrix wherein each feature was converted to a z-score across all lines (Supplementary Methods). Next, we adapted a categorical modelling approach that used a naive Bayes classification and discrete sensitivity calls, or an elastic net regression analysis¹⁶ for continuous sensitivity measurements. Both approaches were applied to all compounds and genomic data with or without gene expression features (Supplementary Methods). Prediction performance was determined using tenfold cross-validation, and the elastic net features were bootstrapped to retain only those that were consistent across runs (Supplementary Methods).

Out of >50,000 input features, the regression-based analysis identified multiple known features as top predictors of sensitivity to several agents (Supplementary Table 7 and Supplementary Figs 8 and 9), with robust cross-validated performance (Supplementary Fig. 10 and 11). For example, activating mutations in *BRAF* and *NRAS* were among the top four predictors of sensitivity in models generated for the MEK inhibitor PD-0325901 (ref. 10) (Fig. 2c). Additional predictive features for MEK inhibition included expression of *PTEN*, *PTPN5* and *SPRY2* (which encodes a regulator of MAPK output). *KRAS* mutations were also identified, albeit with a lower predictive value (Fig. 2c, Supplementary Tables 8 and 9 and Supplementary Fig. 8).

Other top predictors included *EGFR* mutations and *ERBB2* amplification/overexpression for erlotinib⁸ and lapatinib¹⁷, respectively;

BRAF^{V600E} for RAF inhibitors (PLX4720 (ref. 18) and RAF265); *HGF* expression and *MET* amplification for the MET/ALK inhibitor PF-2341066 (ref. 19); and *MDM2* overexpression for Nutlin-3 (ref. 20) sensitivity. Variants affecting the *EXT2* gene, which encodes a glycosyltransferase involved in heparin sulphate biosynthesis, were significantly correlated with erlotinib effects (Supplementary Fig. 12). This observation is intriguing in light of a report linking heparin sulphate with erlotinib sensitivity²¹. In addition, *NQO1* expression was identified as the top predictive feature for sensitivity to the Hsp90 inhibitor 17-AAG, a quinone moiety metabolized by NAD(P)H:quinone oxidoreductase (NQO1). NQO1 produces a high-potency intermediate (17-AAGH2)²², and has previously been identified as a potential biomarker for Hsp90 inhibitors²³.

Because some genetic/molecular alterations occur commonly in specific tumour types, lineage may become a confounding factor in predictive analyses. Indeed, a classifier built using the entire cell-line data set performed suboptimally when applied exclusively to melanoma-derived cell lines (Fig. 2d), whereas a model built with only melanoma cell lines performed better (Fig. 2d). Predictive features in the melanoma-only model showed a strong overexpression of genes regulated by the transcription factors MITF and SOX10 (Supplementary Table 10), which may also help predict RAF inhibitor drug sensitivity in melanoma cell lines.

Nonetheless, lineage emerged as the predominant predictive feature for several compounds. For example, elastic net studies of the HDAC inhibitor panobinostat identified haematological lineages as predictors of sensitivity (Fig. 2e and Supplementary Fig. 9). Interestingly, most clinical responses to panobinostat and related compounds (for example, vorinostat and romidepsin) have been observed in haematological cancers. Similarly, most multiple myeloma cell lines (12 of 14 lines tested) exhibited enhanced sensitivity to the IGF1 receptor inhibitor

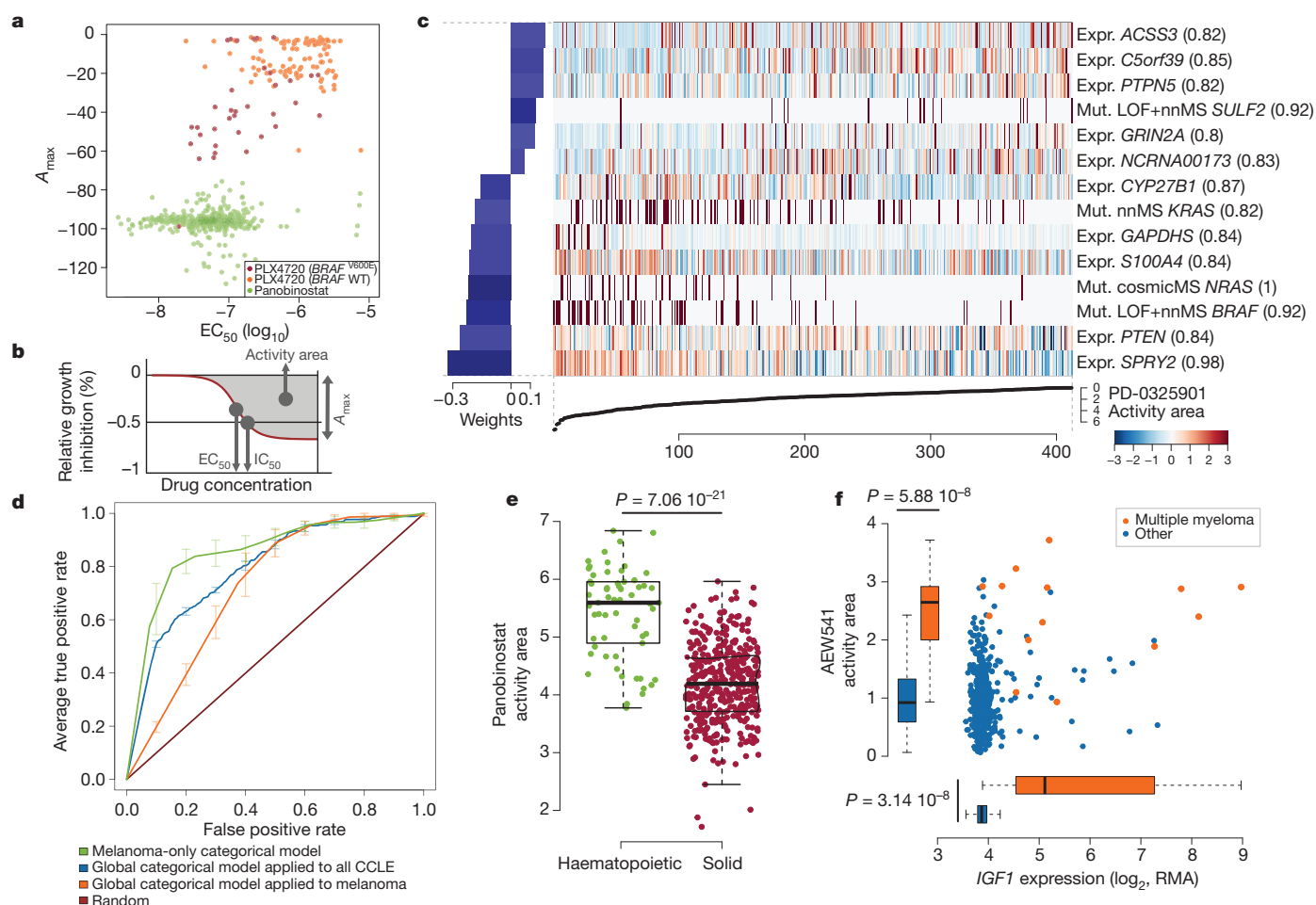


Figure 2 | Predictive modelling of pharmacological sensitivity using CCLE genomic data. **a, b,** Drug responses for panobinostat (green) and PLX4720 (orange/purple) represented by the high-concentration effect level (A_{\max}) and transitional concentration (EC_{50}) for a sigmoidal fit to the response curve (**b**). **c,** Elastic net regression modelling of genomic features that predict sensitivity to PD-0325901. The bottom curve indicates drug response, measured as the area over the dose–response curve (activity area), for each cell line. The central heat map shows the CCLE features in the model (continuous z-score for expression and copy number, dark red for discrete mutation calls), across all cell lines (x axis). Bar plot (left): weight of the top predictive features for sensitivity (bottom) or insensitivity (top). Parentheses indicate features present in >80% of models after bootstrapping. LOF, loss of function mutation; nnMS, non-neutral missense mutation (Supplementary Methods).

AEW541 (Fig. 2f and Supplementary Figs 8 and 9) and showed high *IGF1* expression (Fig. 2f). Interestingly, elevated *IGF1* expression also correlated with AEW541 sensitivity (Supplementary Fig. 9). The CCLE results indicate that multiple myeloma may be a promising indication for clinical trials of *IGF1* receptor inhibitors²⁴ and that these drugs may have enhanced efficacy in cancers with high *IGF1* or *IGF1R* expression.

Whereas *BRAF* and *NRAS* mutations are known single-gene predictors of sensitivity to MEK inhibitors, several ‘sensitive’ cell lines lacked mutations in these genes, whereas other lines harbouring these mutations were nonetheless ‘insensitive’ (Fig. 2c). The elastic net regression model derived from the subset of cell lines with validated *NRAS* mutations identified elevated expression of the *AHR* gene (which encodes the aryl hydrocarbon receptor) as strongly correlated with sensitivity to the MEK inhibitor PD-0325901 (Fig. 3a). This finding was interesting in light of previous studies indicating that a related MEK inhibitor (PD-98059) may also function as a direct *AHR* antagonist²⁵. We therefore hypothesized that the enhanced sensitivity of some *NRAS*-mutant cell lines to MEK inhibitors might relate to a coexistent dependence on *AHR* function.

d, Specificity and sensitivity (receiver operating characteristic curves) of cross-validated categorical models predicting the response to a MEK inhibitor, PD-0325901 (activity area). Mean true positive rate and standard deviation ($n = 5$) are shown when models are built using all lines (global categorical model, in blue and orange), or within only melanoma lines (green). **e,** Activity area values for panobinostat between cell lines derived from haematopoietic ($n = 61$) and solid tumours ($n = 387$). The middle bar, median; box, inter-quartile range; bars extend to $1.5\times$ the inter-quartile range. **f,** Distribution of activity area values for AEW541 relative to *IGF1* mRNA expression. Orange dots, multiple myeloma cell lines ($n = 14$); blue dots, cell lines from other tumour types ($n = 434$). Box-and-whisker plots show the activity area or mRNA expression distributions relative to each cell line type (line, median; box, inter-quartile range), with bars extending to $1.5\times$ the inter-quartile range.

To test this hypothesis, we first confirmed the correlation between *AHR* expression and sensitivity to MEK inhibitors in a subset of *NRAS*-mutant cell lines (Fig. 3b and Supplementary Fig. 13). Next, we performed short hairpin RNA (shRNA) knockdown of *AHR* in cell lines with high or low *AHR* expression (Fig. 3c). Silencing of *AHR* suppressed the growth of three *NRAS*-mutant cell lines with elevated *AHR* expression (Fig. 3d–f), but had no effect on the growth of two lines with low *AHR* expression (Fig. 3g, h). The growth inhibitory effect was confirmed with two additional shRNAs, where evidence for dose dependence was also apparent (Fig. 3i, j). We also tested the hypothesis that allosteric MEK inhibitors may suppress *AHR* function by measuring the effect of PD-0325901 and PD-98059 on endogenous *CYP1A1* mRNA, a transcriptional target of *AHR* in some contexts. Both compounds reduced *CYP1A1* levels in *NRAS*-mutant melanoma cells (IPC-298 and SK-MEL-2; Fig. 3k) but not in neuroblastoma cells (CHP-212; Fig. 3k), indicating that other factors may govern *CYP1A1* expression in the latter lineage. Together, these results suggest that *AHR* dependency may co-occur with MAP kinase activation in some *NRAS*-mutant cancer cells, and that elevated *AHR* may serve as a

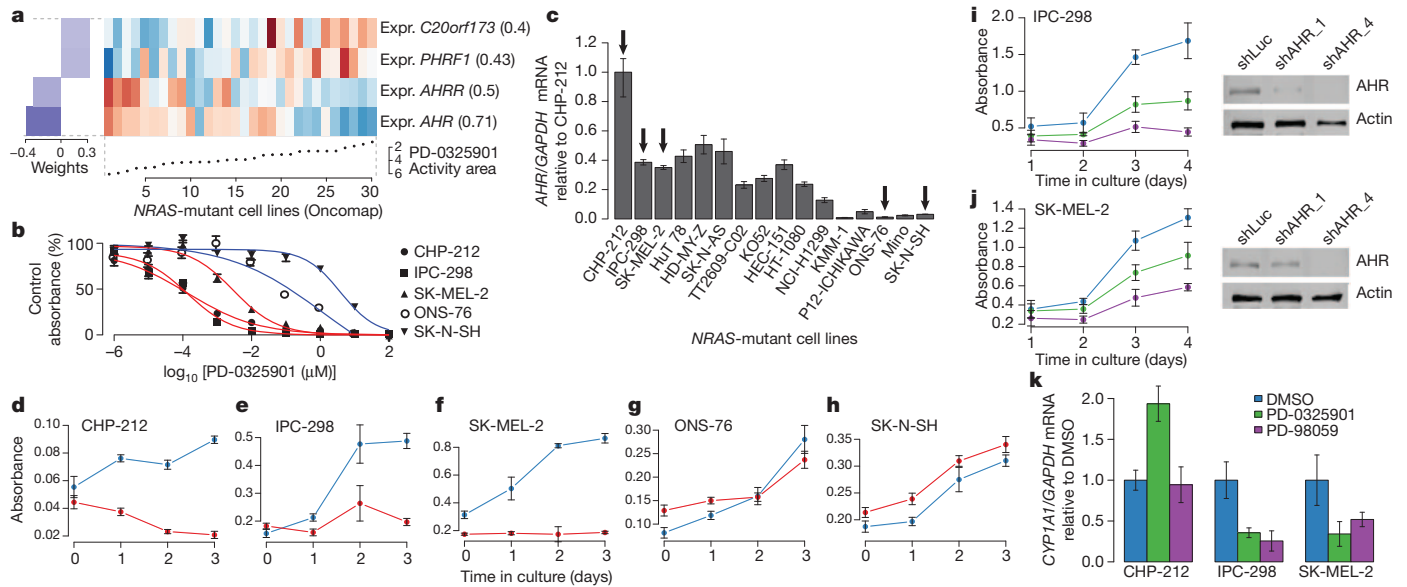


Figure 3 | AHR expression may denote a tumour dependency targeted by MEK inhibitors in NRAS-mutant cell lines. **a**, Predictive features for PD-0325901 sensitivity (using the 'varying baseline' activity area) in validated NRAS-mutant cell lines. **b**, Growth inhibition curves for NRAS-mutant cell lines expressing high (red) or low (blue) levels of AHR mRNA in the presence of the MEK inhibitor PD-0325901. **c**, Relative AHR mRNA expression across a panel of NRAS-mutant cell lines (arrows indicate cell lines where AHR dependency was analysed). **d–h**, Proliferation of NRAS-mutant cell lines displaying high (**d–f**) and low (**g, h**) AHR mRNA expression, after introduction of shRNAs against mechanistic biomarker for enhanced MEK inhibitor sensitivity in this setting.

We also looked for markers predictive of response to several conventional chemotherapeutic agents (Supplementary Fig. 7 and Supplementary Table 6) and identified *SLFN11* expression as the top correlate of sensitivity to irinotecan (Fig. 4a), a camptothecin analogue that inhibits the topoisomerase I (TOP1) enzyme. *SLFN11* expression

also emerged as the top predictor of topotecan sensitivity (another TOP1 inhibitor; Supplementary Figs 8 and 14). Overall, 12 of 16 lineages showed significant *SLFN11* associations for topotecan or irinotecan sensitivity (Pearson's $r \geq 0.2$, Supplementary Fig. 14b). This finding was independently validated using data from the NCI-60 collection (Supplementary Fig. 15). *SLFN11* knockdown did not affect steady-state growth sensitivity profiles (Supplementary Fig. 14d–f).

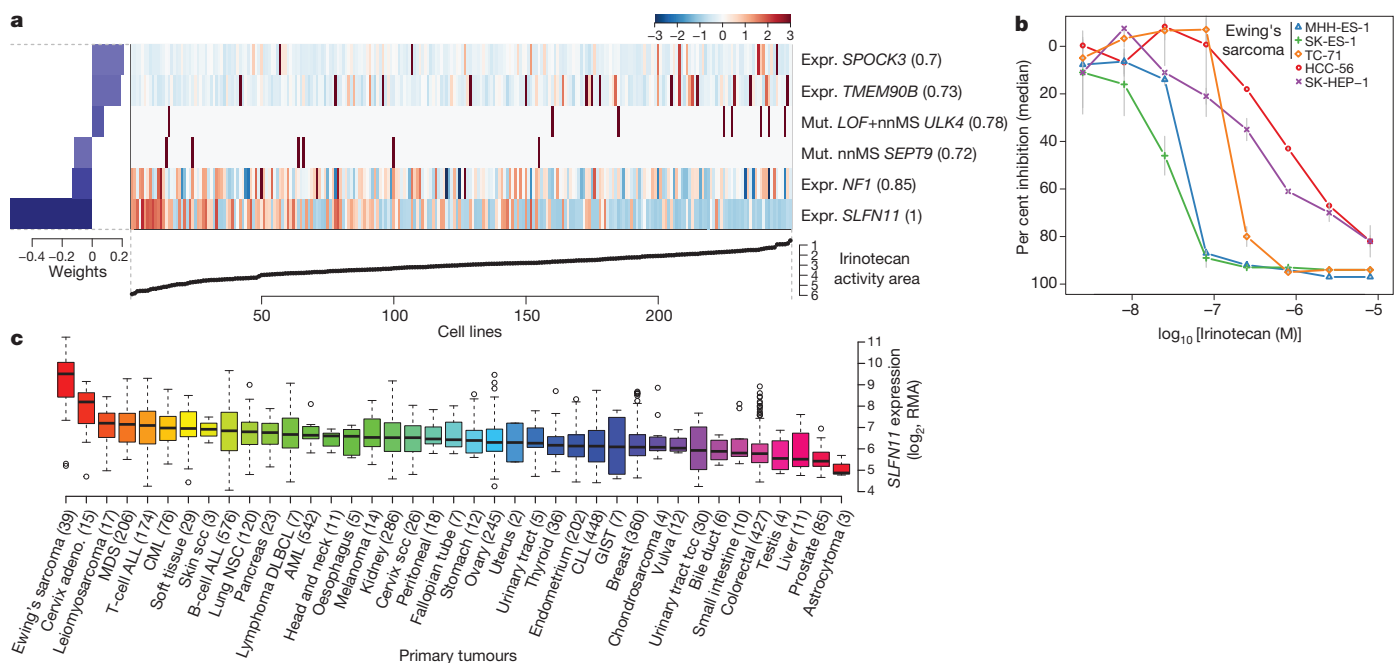


Figure 4 | Predicting sensitivity to topoisomerase I inhibitors. **a**, Elastic net regression analysis of genomic correlates of irinotecan sensitivity is shown for 250 cell lines. **b**, Dose-response curves for three Ewing's sarcoma cell lines (MSS-ES-1, SK-ES-1 and TC-71) and two control cell lines with low *SLFN11* expression (HCC-56 and SK-HEP-1). Grey vertical bars, standard deviation of the mean growth inhibition ($n = 2$). **c**, *SLFN11* expression across 4,103 primary tumours. Box-and-whisker plots show the distribution of mRNA expression for each subtype, ordered by the median *SLFN11* expression level (line), the inter-quartile range (box) and up to 1.5x the inter-quartile range (bars). Sample numbers (n) are indicated in parentheses.

the mean growth inhibition ($n = 2$). **c**, *SLFN11* expression across 4,103 primary tumours. Box-and-whisker plots show the distribution of mRNA expression for each subtype, ordered by the median *SLFN11* expression level (line), the inter-quartile range (box) and up to 1.5x the inter-quartile range (bars). Sample numbers (n) are indicated in parentheses.

All three Ewing's sarcoma cell lines screened showed both high *SLFN11* expression and sensitivity to irinotecan (Fig. 4b and Supplementary Fig. 14). Ewing's sarcomas also exhibited the highest *SLFN11* expression among 4,103 primary tumour samples spanning 39 lineages (Fig. 4c), suggesting that TOP1 inhibitors might offer an effective treatment option for this cancer type. Towards this end, several ongoing trials in Ewing's sarcoma are examining irinotecan-based combinations, or the addition of topotecan to standard regimens²⁶. For some lineages with high *SLFN11* expression (for example, cervical adenocarcinoma), topoisomerase inhibitors already comprise a standard chemotherapy regimen. In other tumours where topoisomerase inhibitors are commonly used (for example, colorectal and ovarian cancers), a range of *SLFN11* expression was observed, raising the possibility that high *SLFN11* expression might enrich for tumours more likely to respond. If confirmed in correlative clinical studies, *SLFN11* expression may offer a means to stratify patients for topoisomerase inhibitor treatment.

By assembling the CCLE, we have expanded the process of detailed annotation of preclinical human cancer models (<http://www.broadinstitute.org/ccle>). Genomic predictors of drug sensitivity revealed both known and novel candidate biomarkers of response. Even within genetically defined sub-populations—or when agents were broadly active without clear genetic targets—elastic net modelling studies identified key predictors or mechanistic effectors of drug response. Additional efforts that increase the scale and provide complementary types of information (for example, whole-genome/transcriptome sequencing, epigenetic studies, metabolic profiling or proteomic/phosphoproteomic analysis) should enable additional insights. In the future, comprehensive and tractable cell-line systems provided through this and other efforts²⁷ may facilitate numerous advances in cancer biology and drug discovery.

METHODS SUMMARY

A total of 947 independent cancer cell lines were profiled at the genomic level (data available at <http://www.broadinstitute.org/ccle> and Gene Expression Omnibus (GEO) using accession number GSE36139) and compound sensitivity data were obtained for 479 lines (Supplementary Table 11). Mutation information was obtained both by using massively parallel sequencing of >1,600 genes (Supplementary Table 12) and by mass spectrometric genotyping (OncoMap), which interrogated 492 mutations in 33 known oncogenes and tumour suppressors. Genotyping/copy number analysis was performed using Affymetrix Genome-Wide Human SNP Array 6.0 and expression analysis using the GeneChip Human Genome U133 Plus 2.0 Array. Eight-point dose–response curves were generated for 24 anticancer drugs using an automated compound-screening platform. Compound sensitivity data were used for two types of predictive models that used the naive Bayes classifier or the elastic net regression algorithm. The effects of *AHR* expression silencing on cell viability were assessed by stable expression of shRNA lentiviral vectors targeting either this gene or luciferase as control. The effect of compound treatment on *AHR* target gene expression was assessed by quantitative RT–PCR. A full description of the Methods is included in Supplementary Information.

Received 25 July 2011; accepted 1 March 2012.

1. Caponigro, G. & Sellers, W. R. Advances in the preclinical testing of cancer therapeutic hypotheses. *Nature Rev. Drug Discov.* **10**, 179–187 (2011).
2. MacConaill, L. E. & Garraway, L. A. Clinical implications of the cancer genome. *J. Clin. Oncol.* **28**, 5219–5228 (2010).
3. Lin, W. M. *et al.* Modeling genomic diversity and tumor dependency in malignant melanoma. *Cancer Res.* **68**, 664–673 (2008).
4. Neve, R. M. *et al.* A collection of breast cancer cell lines for the study of functionally distinct cancer subtypes. *Cancer Cell* **10**, 515–527 (2006).
5. Sos, M. L. *et al.* Predicting drug susceptibility of non-small cell lung cancers based on genetic lesions. *J. Clin. Invest.* **119**, 1727–1740 (2009).
6. Dry, J. R. *et al.* Transcriptional pathway signatures predict MEK addiction and response to selumetinib (AZD6244). *Cancer Res.* **70**, 2264–2273 (2010).
7. Garraway, L. A. *et al.* Integrative genomic analyses identify MITF as a lineage survival oncogene amplified in malignant melanoma. *Nature* **436**, 117–122 (2005).
8. Greshock, J. *et al.* Molecular target class is predictive of *in vitro* response profile. *Cancer Res.* **70**, 3677–3686 (2010).
9. McDermott, U. *et al.* Identification of genotype-correlated sensitivity to selective kinase inhibitors by using high-throughput tumor cell line profiling. *Proc. Natl Acad. Sci. USA* **104**, 19936–19941 (2007).

10. Solit, D. B. *et al.* BRAF mutation predicts sensitivity to MEK inhibition. *Nature* **439**, 358–362 (2006).
11. Staunton, J. E. *et al.* Chemosensitivity prediction by transcriptional profiling. *Proc. Natl Acad. Sci. USA* **98**, 10787–10792 (2001).
12. Weinstein, J. N. *et al.* An information-intensive approach to the molecular pharmacology of cancer. *Science* **275**, 343–349 (1997).
13. Thomas, R. K. *et al.* High-throughput oncogene mutation profiling in human cancer. *Nature Genet.* **39**, 347–351 (2007).
14. Beroukhi, R. *et al.* The landscape of somatic copy-number alteration across human cancers. *Nature* **463**, 899–905 (2010).
15. Ross, D. T. *et al.* Systematic variation in gene expression patterns in human cancer cell lines. *Nature Genet.* **24**, 227–235 (2000).
16. Zou, H. & Hastie, T. Regularization and variable selection via the elastic net. *J. R. Stat. Soc. B* **67**, 301–320 (2005).
17. Konecny, G. E. *et al.* Activity of the dual kinase inhibitor lapatinib (GW572016) against HER-2-overexpressing and trastuzumab-treated breast cancer cells. *Cancer Res.* **66**, 1630–1639 (2006).
18. Tsai, J. *et al.* Discovery of a selective inhibitor of oncogenic B-Raf kinase with potent antitumor activity. *Proc. Natl Acad. Sci. USA* **105**, 3041–3046 (2008).
19. Zou, H. Y. *et al.* An orally available small-molecule inhibitor of c-Met, PF-2341066, exhibits cytoreductive antitumor efficacy through antiproliferative and antiangiogenic mechanisms. *Cancer Res.* **67**, 4408–4417 (2007).
20. Müller, C. R. *et al.* Potential for treatment of liposarcomas with the MDM2 antagonist Nutlin-3A. *Int. J. Cancer* **121**, 199–205 (2007).
21. Nishio, M. *et al.* Serum heparan sulfate concentration is correlated with the failure of epidermal growth factor receptor tyrosine kinase inhibitor treatment in patients with lung adenocarcinoma. *J. Thorac. Oncol.* **6**, 1889–1894 (2011).
22. Guo, W. *et al.* Formation of 17-allylamino-demethoxygeldanamycin (17-AAG) hydroquinone by NAD(P)H:quinone oxidoreductase 1: role of 17-AAG hydroquinone in heat shock protein 90 inhibition. *Cancer Res.* **65**, 10006–10015 (2005).
23. Kelland, L. R., Sharp, S. Y., Rogers, P. M., Myers, T. G. & Workman, P. DT-Diaphorase expression and tumor cell sensitivity to 17-allylamino, 17-demethoxygeldanamycin, an inhibitor of heat shock protein 90. *J. Natl Cancer Inst.* **91**, 1940–1949 (1999).
24. Moreau, P. *et al.* Phase I study of the anti insulin-like growth factor 1 receptor (IGF-1R) monoclonal antibody, AVE1642, as single agent and in combination with bortezomib in patients with relapsed multiple myeloma. *Leukemia* **25**, 872–874 (2011).
25. Reiners, J. J. Jr, Lee, J. Y., Clift, R. E., Dudley, D. T. & Myrand, S. P. PD98059 is an equipotent antagonist of the aryl hydrocarbon receptor and inhibitor of mitogen-activated protein kinase kinase. *Mol. Pharmacol.* **53**, 438–445 (1998).
26. Wagner, L. M. *et al.* Temozolomide and intravenous irinotecan for treatment of advanced Ewing sarcoma. *Pediatr. Blood Cancer* **48**, 132–139 (2007).
27. Garnett, M. J. *et al.* Systematic identification of genomic markers of drug sensitivity in cancer cells. *Nature* <http://dx.doi.org/10.1038/nature11005> (this issue).

Supplementary Information is linked to the online version of the paper at www.nature.com/nature.

Acknowledgements We thank the staff of the Biological Samples Platform, the Genetic Analysis Platform and the Sequencing Platform at the Broad Institute. We thank S. Banerji, J. Che, C. M. Johannessen, A. Su and N. Wagle for advice and discussion. We are grateful for the technical assistance and support of G. Bonamy, R. Bruschi III, E. Gelfand, K. Gravelin, T. Huynh, S. Kehoe, K. Matthews, J. Nedzel, L. Niu, R. Pinchback, D. Roby, J. Slind, T. R. Smith, L. Tan, V. Trinh, C. Vickers, G. Yang, Y. Yao and X. Zhang. The Cancer Cell Line Encyclopedia project was enabled by a grant from the Novartis Institutes for Biomedical Research. Additional funding support was provided by the National Cancer Institute (M.M., L.A.G.), the Starr Cancer Consortium (M.F.B., L.A.G.), and the NIH Director's New Innovator Award (L.A.G.).

Author Contributions For the work described herein, J.B. and G.C. were the lead research scientists; N.S., K.V. and A.M.M. were the lead computational biologists; M.P.M., W.R.S., R.S. and L.A.G. were the senior authors. J.B., G.C., S.K., P.M., J.M., J.T., A.S., N.L. and K.A. performed cell-line procurement and processing; P.M. and K.A. performed or directed nucleic acid extraction and quality control; S.G., W.W. and S.B.G. performed or directed genomic data generation; C.J.W., F.A.M., E.B.-F., I.H.E., P.A., M.D.S., K.J. and V.E.M. performed pharmacological data generation; N.S., K.V., G.V.K., A.R., M.F.B., J.C., G.K.Y., M.D.J., T.L., M.R. and G.G. contributed to software development; N.S., K.V., A.A.M., J.L., G.V.K., D.S., A.R., M.L., M.F.B., A.K., P.R., J.C., G.K.Y., J.Y., M.D.J., L.W., C.H., E.P., J.P.M., V.C. and M.P.M. performed computational biology and bioinformatics analysis; J.B., G.C., N.S., L.M., J.E.M., J.J.-V., M.P.M., W.R.S., R.S. and L.A.G. performed biological analysis and interpretation; N.S., K.V., A.A.M., J.L., A.R., M.L., L.M., A.K., J.J.-V., J.C., G.K.Y. and J.Y. prepared figures and tables for the main text and Supplementary Information; J.B., G.C., N.S., K.V., A.A.M., J.L., G.V.K., J.J.-V., M.P.M. and L.A.G. wrote and edited the main text and Supplementary Information; J.B., G.C., N.S., K.V., S.K., C.J.W., J.L., S.M., C.S., R.C.O., T.L., L.M.C., W.W., M.R., N.L., S.B.G., K.A. and V.C. performed project management; J.P.M., V.E.M., B.L.W., J.P., M.W., P.F., J.L.H., M.M. and T.R.G. contributed project oversight and advisory roles; and M.P.M., W.R.S., R.S. and L.A.G. provided overall project leadership.

Author Information Data have been deposited in the Gene Expression Omnibus (GEO) using accession number GSE36139 and are also available at <http://www.broadinstitute.org/ccle>. Reprints and permissions information is available at www.nature.com/reprints. The authors declare competing financial interests: details accompany the full-text HTML version of the paper at www.nature.com/nature. Readers are welcome to comment on the online version of this article at www.nature.com/nature. Correspondence and requests for materials should be addressed to L.A.G. (Levi_Garraway@dfci.harvard.edu) or R.S. (robert.schlegel@novartis.com).